

AD 713 561

AD 713 561



Army Science Conference Proceedings

16 - 19 June 1970

Volume II

Principal Authors M thru Z

D D C
RECEIVED
NOV 6 1970
RECEIVED
E

Reproduced by
**NATIONAL TECHNICAL
INFORMATION SERVICE**
Springfield, Va. 22151

Distribution of this
document is unlimited

This document has been approved
for public release and under the
distribution is unlimited

**OFFICE, CHIEF OF RESEARCH AND DEVELOPMENT
DEPARTMENT OF THE ARMY**

All experiments involving live animals that are reported in the Proceedings were performed in accordance with the principles of laboratory animal care as promulgated by the National Society of Medical Research.

ACCESSION NO.	
WHITE SECTION	<input checked="" type="checkbox"/>
BUFF SECTION	<input type="checkbox"/>
UNANNOUNCED	<input type="checkbox"/>
JUSTIFICATION	
BY	
DISTRIBUTION/AVAILABILITY CODES	
DIST.	AVAIL. IND. W/ SPECIAL



DEPARTMENT OF THE ARMY
OFFICE OF THE ADJUTANT GENERAL
WASHINGTON, D.C. 20310

IN REPLY REFER TO
AGDA (M) (8 Sep 70) CRDDM

24 September 1970

SUBJECT: 1970 Army Science Conference, Volume III

SEE DISTRIBUTION

1. Inclosed for your information and use is Volume III of the 1970 Army Science Conference Proceedings. This volume contains the unclassified papers by principal authors M thru Z which were presented at the conference, 16-19 June 1970, U. S. Military Academy, West Point, New York.
2. Volumes I, II and IV of the Proceedings are being distributed separately.
3. Chiefs of Army Staff agencies and major commanders on the distribution list will insure that copies of the documents are placed in Technical Libraries where they will be available for reference.

BY ORDER OF THE SECRETARY OF THE ARMY:

1 Incl
Vol III, 1970 Army
Science Conference Proceedings

Kenneth G. Wickham
KENNETH G. WICKHAM
Major General, USA
The Adjutant General

(See page 2 for distribution)

DISTRIBUTION:

Chief Scientist, Department of the Army
Office of the Adjutant General, ATTN: Army Library
The Surgeon General, ATTN: Medical Library
Chief of Engineers, ATTN: Scientific Advisor

Commanding Generals:

US Army Materiel Command, ATTN: Chief Scientist
US Army Missile Command
US Army Electronics Command
US Army Mobility Equipment Command
US Army Munitions Command
US Army Test & Evaluation Command
US Army Weapons Command
US Army Tank-Automotive Command
US Army Combat Developments Command

Commanding Officers:

Aberdeen Proving Ground
Picatinny Arsenal
Rock Island Arsenal
Dugway Proving Ground
Edgewood Arsenal
Frankford Arsenal
Watervliet Arsenal
Natick Laboratories
Harry Diamond Laboratories
Walter Reed Army Institute of Research
US Army Biological Center
US Army Research Office-Durham
US Army R&D Group (Far East)
US Army R&D Group (Europe)
US Army Satellite Communications Agency
US Army Foreign Science & Technology Center
US Army Ballistic Research Laboratories
US Army Human Engineering Laboratories
US Army Cold Regions Research and Engineering Center
US Army Materials & Mechanics Research Center
US Army Nuclear Effects Laboratory
US Army Electronics R&D Laboratory
US Army Engineer R&D Laboratory
US Army Medical Research and Nutritional Laboratory
US Army Surgical Research Unit, Brooke Army Medical Center
US Army Research Institute of Environmental Medicine
US Army Land Warfare Laboratory
US Army Atmospheric Sciences Laboratory
US Army Engineer Nuclear Cratering Group
US Army Coastal Engineering Research Center
US Army Mobility Equipment R&D Center
US Army Electronics Components Laboratory
US Army Desert Test Center
US Army White Sands Missile Range

DISTRIBUTION (Continued)

Commanding Officers:

US Army Aeronautical Research Laboratory
US Army Materiel Systems Analysis Agency
US Army Aviation Materiel Laboratory

Chief

US Army Element Research Office, Latin America
Superintendent

US Military Academy

Directors:

US Army Waterways Experiment Station
US Army Engineer Topographic Laboratories
Combat Operations Research Group
US Army Manpower Resources R&D Center
US Army Advanced Ballistic Missile Defense Agency
US Army Infantry Board
Institute for Exploratory Research
Letterman Army Institute of Research
US Army Institute of Dental Research

Copies furnished:

Director of Defense Research and Engineering
Defense Documentation Center
Director, Armed Forces Institute of Pathology

Commandants:

Industrial College of the Armed Forces
National War College
Armed Forces Staff College

Chief of Naval Research

Director, US Naval Research Laboratories

Commanders:

Air Force Institute of Technology
Office of Aerospace Research (RRG)
Aeronautical Systems Division, ATTN: ASNPD Library

Atomic Energy Commission
National Aeronautics and Space Agency
National Institutes of Health
National Science Foundation
National Academy of Sciences
Research Analysis Corporation
Director, Center for Research and Social Systems

PROCEEDINGS
OF THE
1970 ARMY SCIENCE CONFERENCE
UNITED STATES MILITARY ACADEMY, WEST POINT, N. Y.
16 - 19 JUNE 1970

VOLUME III
Principal Authors M through Z

a

INTRODUCTION

1. This seventh in a series of Army Science Conferences was held at the United States Military Academy, 16-19 June 1970. "The Needs of the Modern Soldier in His Current and Future Environment", was the theme of this year's conference. In carrying out this theme, the conference presented a cross section of the many significant scientific and engineering programs carried out by the Department of the Army.

2. These Proceedings of the 1970 Army Science Conference are a compilation of all papers presented at the conference and the supplemental papers that were submitted. The Proceedings consist of four volumes, three unclassified and one classified.

3. Our purposes for soliciting these papers were:

a. To stimulate the involvement of scientific and engineering talent within the Department of the Army.

b. To demonstrate Army competence in research and development.

c. To provide a forum wherein Army personnel can demonstrate the full scope and depth of their current projects.

d. To promote the interchange of ideas among members of the Army scientific and engineering community.

4. It is hoped that the information contained in the volumes will be of benefit to those who attended the conference and to others interested in Army research and development.



A. W. BETTS
Lieutenant General, GS
Chief of Research and Development

TABLE OF CONTENTS
 PROCEEDINGS OF THE 1970 ARMY SCIENCE CONFERENCE

<u>Author</u>	<u>Title</u>	<u>Vol</u>	<u>Page</u>
Aamot, H. W. C.	See Quinn, W. F.	3	161
Agee, F. J. Jr. Spangler, G. E.	Testing for an Organic Superconductor	1	1
Ahlvin, R. G. Hammit, G. M., II	Rapid Assessment of Aircraft Landing Sites	1	15
Akers, W. A. Sulzberger, M. B.	The Friction Blister	1	29
Amato, J. J. Rich, N. M. Lawson, N. S. Gruber, R. P. Billy, L. J.	Temporary Cavity Effects in Blood Vessel Injury by High Velocity Missiles	1	43
Atha, L. C.	An Investigation of the Dynamic Pressure Response of Fluoric Transmission Lines	1	59
Auerbach, A.	See Rothwarf, F.	3	243
Baer, P. G.	Prediction of High Velocity Solid Propellant Gun Performance by Gas Dynamic Computer Program	1	73
Baker, J. W., II	Social Status Variables in the Military and Their Effect on Expressing Aggression	1	89
Baldini, A. A.	Determination of Latitude and Longitude of Unknown Stations from Photographs of a Satellite Against Stellar Background Independent of Any Distance	1	99
Baranowski, J. J. Higgins, V. J.	Analysis and Application of Gallium Arsenide Avalanche Transit Time Devices	1	113

<u>Author</u>	<u>Title</u>	<u>Vol</u>	<u>Page</u>
Bartoshuk, L. M.	Alteration of Taste Qualities Through Natural Products	1	129
Bean, G. T.	See Daly, P. J.	4	45
Beatrice, E. S. Powell, J. O. Landers, M. B. Bresnick, G. H.	Retinal Damage by Q-Switched Ruby Laser	1	143
Billy, L. J.	See Amato, J. J.	1	43
Blair, J. R. Sperrazza, J.	Wound Data and Munitions Effectiveness as Based Upon Battlefield Surveys in Vietnam	4	1
Bluhm, J. I. Gordon, B. E., Jr. Morrissey, R. J.	Exploitation of Contoured Double Cantilever Beam Specimens in Crack Growth and Arrest Studies	1	159
Bowie, D. R.	See Brown, H. A., Jr.	4	15
Brand, C. S.	See Morris, G. E.	3	17
Bresnick, G. H.	See Beatrice, E. S.	1	143
Broomfield, C. A.	See Morrisett, J. D.	3	31
Brown, H. A., Jr. Callahan, J. J. Wulkow, E. A. Penski, E. C. Bowie, D. R.	A Physical Model for the Penetration of Clothing by Chemical Agents	4	15
Brown, J. W.	Response of Selected Materials to High-Speed Fragment Impact	1	173
Bukalski, S. H.	See Klebers, J.	4	173
Burns, F. C.	See Priest, H. F.	3	147
Callahan, J. J.	See Brown, H. A., Jr.	4	15

<u>Author</u>	<u>Title</u>	<u>Vol</u>	<u>Page</u>
Campagnuolo, C. J. Gehman, S. F.	A Flueric Oscillator for Military Timer Applications	1	187
Cash, C. H.	See Hatcher, J. L.	2	17
Chase, R. P.	Computer Operated Automatic Fuze Testing Systems	1	201
Chen, Pi-Fuay	See O'Connor, D. C.	3	103
Choi, C. S.	See Trevino, S. F.	3	345
Christensen, C. R.	See Daniel, A. C.	1	233
Civjan, S.	Properties of n-Butyl-a-Cyanoacrylate Restorative Materials	1	209
Cook, C. F. Jr.	See Kohn, J. A.	2	277
Cooper, E. B.	See Lutcher, C. L.	2	355
Corrado, A. P.	An Experimental Investigation of a Flueric Explosive Initiator	4	29
Corrie, J. D.	See Rinnovatore, J. V.	4	245
Corrie, J. D.	See Steward, W. B.	4	323
Costantino, J. Pontelandolfo, C. Reago, D.	Optimization Analysis of a Compact Lightweight Laser Rangefinder	1	223
Crozier, D.	See Dangerfield, H. G.	4	59
Daly, P. J. Sims, W. S. Bean, G. T.	Night Vision Viewers Using Thermal Techniques	4	45
Dangerfield, H. G. Crozier, D.	Biological Effects of Staphylococcal Enterotoxin B	4	59
Daniel, A. C. Guenther, B. D. Christensen, C. R.	Echo Amplification in Magnetic Materials with Application to Pulse Compression Radar	1	233

<u>Author</u>	<u>Title</u>	<u>Vol</u>	<u>Page</u>
Davidson, T. E. Throop, J. F. Reiner, A. N.	The Role of Fracture Toughness and Residual Stresses in the Fatigue and Fracture Behavior of Large Thick-Walled Pressure Vessels	1	249
De Santis, G. C.	The Internal and External Flow Field Associated with Parachutes During Inflation	1	265
Di Persio, R.	See Simon, J.	4	307
Drake, J. L. Sakurai, A.	Far Field Characteristics of Ground Shock Induced by Explosions	1	281
Dunkel, T. B.	See Lutchter, C. L.	2	355
Dunn, R. L.	An Electro-Magnetic Technique for Wire Location	4	73
Eckart, D. W.	See Kohn, J. A.	2	277
Eigelsbach, H. T. Hornick, R. B. Schricker, R. L. Hankins, W. Griffith, W. R.	Pathogenesis, Prophylaxis, and Therapy of an Incapacitating Disease ¹	4	55
Essenwanger, O.	The Characteristic Coefficients Technique for Probability Models of Wind Profiles in Missile Design and Environment Analysis	1	291
Ferrick, J. H. Heise, C. J.	Experimental Superconducting Alternators with Iron-Core and Iron-Free Armatures	1	307
Figge, I. E. Sr.	"Tetra-Core": A Three-Dimensional Space Structure	4	97
Finck, P. A.	A Research Concept for the Interpretation of Human Missile Wounds by the Pathologist	1	319

<u>Author</u>	<u>Title</u>	<u>Vol</u>	<u>Page</u>
Fishbein, W. Frost, E. Vander Meer, W.	Investigation of Radar Anomalies	4	111
Foiani, D. L.	See Gaule', G. K.	4	127
Ford, D.	See Rothwarf, F.	3	243
Frantz, J. W.	See Nerdahl, M. C.	3	59
Frost, E.	See Fishbein, W.	4	111
Gambino, L. A.	Advanced Computational Algorithms for Large Scale, Three Dimen- sional, Artillery Survey Applica- tions	1	323
Gardner, L. B.	See Iversen, R. J.	2	151
Garono, L. E.	Denver Earthquakes	1	339
Gaule', G. K. Foiani, D. L.	A New Approach to Detection of Enemy Arms Caches	4	127
Gehman, S. E.	See Campagnuolo, C. J.	1	187
Gerben, M. J.	See Jones, L. G.	2	195
Gibson, W. H.	The Application of a Solid State Helium-Neon Gas Laser to Missile Guidance	1	353
Gilbert, R. M.	See Rosado, J. A.	4	261
Gillis, E. A. Kezer, O. F. Taschek, W. G.	Open Cycle Hydrocarbon-Air Fuel Cell Power Plant	1	363
Gold, L. M. Shinaly, F.	Mathematical Model for Pro- jectile Body	1	379
Goldman, R. F.	Tactical Implications of the Physiological Stress Imposed by Chemical Protective Clothing Systems	1	393

<u>Author</u>	<u>Title</u>	<u>Vol</u>	<u>Page</u>
Gordon, B. E., Jr.	See Bluhm, J. I.	1	159
Grant, J. W.	See Jackson, G. A.	2	165
Gray, W. Merkel, G.	Simulation of High Altitude Ionized Air with an Artificial Dielectric	1	409
Greenberg, M.	See Quinn, W. F.	3	161
Greveris, H. A.	M16 Rifle/Ammunition Malfunction Modeling	1	425
Griffith, W. R.	See Eigelsbach, H. T.	4	85
Gruber, R. P.	See Amato, J. J.	1	43
Guenther, B. D.	See Daniel, A. C.	1	233
Haber, G.	See Stiber, S.	4	339
Hackley, B. E., Jr.	See Morrisett, J. D.	3	31
Hammit, G. M., II	See Ahlvin, R. G.	1	15
Hankins, W.	See Eigelsbach, H. T.	4	85
Harris, D. L.	A Deterministic View of Spectrum and Cross-Spectrum Analysis	2	1
Harrison, A.	See Richardson, A. E.	3	207
Hartley, L. H.	See Jones, L. G.	2	195
Hatcher, J. L. Cash, C. H.	Radar Polarization Diversity Effects on Target Reradiated Phase Front	2	17
Hawie, M. C.	See Russ, D. S.	4	277
Hawkins, A. L.	See Jameson, R. L.	2	181
Hay, D. R.	See Kowalick, J. F.	2	291
Hays, G.	See Henry, J. N.	2	49

<u>Author</u>	<u>Title</u>	<u>Vol</u>	<u>Page</u>
Heise, C. J.	See Ferrick, J. H.	1	307
Heiser, F. A.	Anisotropy of Fatigue Crack Propagation in Hot Rolled Banded Steel Plate	2	33
Henry, J. N. Matsumoto, T. Hays, G.	Obstacles in Oxygen Transport During Aeromedical Evacuation	2	49
Herman, R. H. Rosensweig, N. S. Stifel, F. B. Herman, Y. F.	The Effect of Diet on Jejunal Enzymes	2	59
Herman, Y. F.	See Herman, R. H.	2	59
Revenor, R. A.	A Mathematical Analysis of the Propagation and Reflection of Plane Electromagnetic Waves in a Non-Homogeneous Isotropic Medium	2	71
Higgins, V. J.	See Baranowski, J. J.	1	113
Hildebrandt, P. K.	See Nims, R. M.	3	75
Hill, J. L. E. Streett, W. B.	Phase Behavior in Fluid Mixtures at High Pressures I: Experimental	2	85
Hogan, R. P.	See Jones, L. G.	2	195
Hornick, R. B.	See Eigelsbach, H. T.	4	85
Howe, P. M.	Detonation Structure in Condensed Phase Explosives	2	99
Hu, K. H. Loconti, J. D.	T-T Indicating Systems	2	109
Huber, W. A.	Automated Raw Environmental Data Processing	2	125

<u>Author</u>	<u>Title</u>	<u>Vol</u>	<u>Page</u>
Hung, H. M.	Mechanical Dispersion of a Machine Gun System with Stochastic Excitations	2	139
Hurt, L. J.	Controllable Rocket Motor for AHM Interceptor Missile	4	143
Huxsoll, D. L.	See Nims, R. M.	3	75
Iacono, V. D.	See Spano, L. A.	3	287
Ingram, R. R., Jr. McHugh, R. F. Jr. Lewis, J. H.	Human Incapacitation Produced by Burns	4	157
Ionno, J. A.	See Lutchter, C. L.	2	355
Iqbal, Z	See Trevino, S. F.	3	345
Iverson, R. J. McGarvey, J. W. Gardner, L. B.	Holographic Inspection of Laminate Bonds	2	151
Jackson, G. A. Grant, J. W.	Linear Suspension System Parameter Identification	2	165
Jacobs, H.	See Morris, G. E.	3	17
Jameson, R. L. Hawkins, A. L.	Detonation Pressure Measurements in TNT and Octol	2	181
Jonas, G. H.	See Regan, J. M.	4	217
Jones, L. G. Hartley, L. Mason, J. W. Hogan, R. P. Gerben, M. J. Krueze, L.	The Effects of Muscular Leg Exercise on Neuroendocrine Blood Levels	2	195
Kapsalis, J. G. Walker, J. E., Jr. Wolf, M.	New Foods for Military Use. A Physico-Chemical Approach to Research and Development	2	207

<u>Author</u>	<u>Title</u>	<u>Vol</u>	<u>Page</u>
Kezer, O. F.	See Gillis, E. A.	1	363
Kinas, E. N.	See Riffin, P. V.	4	229
Kirshenbaum, A. D. Taylor, F. R.	Gaseous Illuminant Pyrotechnic Systems	2	221
Klebers, J. Bukalski, S. H.	A Theoretical and Experimental Evaluation of a Biconical Antenna Nuclear Electromagnetic Pulse Simulator	4	173
Klein, N.	The Effect of Structure on Radiation Chemical Reactivity	2	237
Klein, R. D. Thomas, C. B.	The Development of Combat Related Measures for Small Arms Evaluation	2	249
Knight, J. A.	The Development of a Kalman Filtering Algorithm for Hybrid Navigation in Army Aircraft	2	263
Kohn, J. A. Cook, C. F., Jr. Eckart, D. W.	Direct Solution of Complex Crystal Structures by Electron Microscopy	2	277
Kowalick, J. F. Hay, D. R.	The Nature and Formation of the Bond in the Explosive Bonding of Metals	2	291
Kramer, D. N. Sech, J. M.	A New Sensitive Method for the Detection and Quantitative Analysis of Ammonia and Aliphatic Amines	2	303
Kronenberg, S. Lux, R. Nilson, K.	Reduction of Biological Effectiveness of X-Rays at Very High Dose Rates	2	315
Krueze, L.	See Jones, L. G.	2	195
Landers, M. B.	See Beatrice, E. S.	1	143

<u>Author</u>	<u>Title</u>	<u>Vol</u>	<u>Page</u>
Lawson, N. S.	See Amato, J. J.	1	43
Lawton, W. D.	See Tyeryar, F. J., Jr.	3	361
Lewis, J. H.	See Ingram, R. R., Jr.	4	157
Lewis, R. W. Roylance, M. E. Thomas, G. R.	Rubber Toughened Acrylic Polymers for Armor Applica- tions	2	327
Lindesmith, L. A.	See Lutchter, C. L.	2	355
Loconti, J. D.	See Hu, K. H.	2	109
Low, R. D. H.	A More Rigorous Expression for the Rate of Droplet Growth	2	341
Lutchter, C. L. Lindesmith, L. A. Pettyjohn, F. S. Steudel, W. T. Dunkel, T. B. Ionno, J. A. Cooper, E. B.	Observations on Early Detec- tion and Therapy of the De- fibrination Syndrome in Meningococemia	2	355
Lux, R.	See Kronenberg, S.	2	315
Mason, J. W.	See Jones, L. G.	2	195
Matsumoto, T.	See Henry, J. N.	2	49
McDysan, L. Mitchell, E. M.	ABM Discrimination Technology	4	189
McGarvey, J. W.	See Iversen, R. J.	2	151
McHugh, R. F., Jr.	See Ingram, R. R., Jr.	4	157
Merendino, A. B. Vitali, R.	Target Reaction to Continuous and Particulate Shaped Charge Jets	4	205
Merkel, G.	See Gray, W.	1	409

<u>Author</u>	<u>Title</u>	<u>Vol</u>	<u>Page</u>
Meyers, R. E.	Kinematics of Diffusion, Fluids and Plasma by Continuous Movement and Finite Velocities	3	1
Mical, R. D.	See Trevino, S. F.	3	345
Mitchell, E. M.	See McDysan, L.	4	189
Mooney, T. R.	See Morris, G. E.	3	17
Morris, G. E. Jacobs, H. Brand, C. S. Mooney, T. R.	Threshold Effects of Chemical Mixtures in the HCN Laser	3	17
Morrisett, J. D. Broomfield, C. A. Hackley, B. E., Jr.	Conformational Studies on the Active Site of Acetylcholinesterase by Electron Paramagnetic Resonance	3	31
Morrissey, R. J.	See Bluhm, J. I.	1	159
Morrow, S. I.	The Preparation and Properties of New Oxidizers for Propellants, $\text{NH}_4\text{ClO}_4\text{-KClO}_4$ and $\text{NH}_4\text{ClO}_4\text{-NH}_4\text{NO}_3$ Mixed Crystals	3	47
Nerdahl, M. C. Frantz, J. W.	Development of a Mathematical Model for Designing Functional Controls of a Soft-Recoil Mechanism	3	59
Nilson, K.	See Kronenberg, S.	2	315
Nims, R. M. Huxsoll, D. L. Hildebrandt, P. K. Walker, J. S.	Investigation of a New Disease of Military Dogs	3	75
Oatman, L. C.	Electrophysiological Measures of Cross-Sensory Interaction in the Central Nervous System ¹	3	87
O'Connor, D. C. Chen, Pi-Fuay	Applications of Sensing Arrays to Photogrammetry and Metrology	3	103

<u>Author</u>	<u>Title</u>	<u>Vol</u>	<u>Page</u>
Ohmstede, W. D.	A Similarity Model for Atmospheric Turbulence Structure in the Planetary Boundary Layer	3	117
Pardue, A. L., Jr.	CO ₂ Laser Pulsing Produced by Cavity-Length Modulation	3	131
Penski, E. C.	See Brown, H. A., Jr.	4	15
Pettyjohn, F. S.	See Litcher, C. L.	2	355
Pontelandolfo, C.	See Costantino, J.	1	223
Powell, J. O.	See Beatrice, E. S.	1	143
Prask, H. J.	See Trevino, S. F.	3	345
Priest, G. L.	See Priest, H. F.	3	147
Priest, H. F. Burns, F. C. Priest, G. L.	Use of Activation Analysis for Determining Weight of Pellet in M34 Primers	3	147
Quinn, W. F. Aamot, H. W. C. Greenberg, M.	Field Test of a Steam Condenser Heat Sink Concept	3	161
Ramsley, A. O.	Modern Counter-Surveillance in Combat Clothing	3	177
Rao, K. R.	See Trevino, S. F.	3	345
Reago, D.	See Costantino, J.	1	223
Redpath, B. B.	A Concept of Row Crater Enhancement	3	191
Regan, J. M. Jonas, G. H.	The Generation and Penetration Characteristics of High Density Shaped Charge Jets	4	217
Reiner, A. N.	See Davidson, T. E.	1	249
Rich, N. M.	See Amato, J. J.	1	43

<u>Author</u>	<u>Title</u>	<u>Vol</u>	<u>Page</u>
Richardson, A. E. Harrison, A.	The Determination of Aluminum and Chlorine in Composite Propellants by Non-Destructive Activation Analysis Using a Mixture of 14.5 MeV and Slow Neutrons	3	207
Riffin, P. V. Kinas, E. N.	Development of New High Fragmentation Shell Steel	4	229
Rinnovatore, J. V. Corrie, J. D.	Effect of Environment on Crack Propagation in High Strength Steel	4	245
Roberts, T. G.	On the Propagation of High Intensity Relativistic Electron Beams	3	221
Romba, J. J.	Tactics in the Development of Mine Detector Dogs	3	235
Rosado, J. A. Gilbert, R. M. Vault, W. L. Tompkins, J. E.	Internal Electromagnetic Pulses in Irradiated Enclosures	4	261
Rosati, V. J.	See Strozyk, J. W.	3	303
Rosensweig, N. S.	See Heyman, R. H.	2	59
Rothwarf, F. Auerbach, A. Ford, D.	The Use of Martensite Materials in the Design of Thermally Activated Springs	3	243
Roylance, M. E.	See Lewis, R. W.	2	327
Rudland, R. S.	See Vause, C. R.	3	371
Russ, D. S. Hawie, M. C.	Reentry Measurements Program	4	277
Sakurai, A.	See Drake, J. L.	1	281
Schoening, J. P.	The Insignificant Twig Which Cries "Alarm" When the Enemy Moves Down the Jungle Trails	4	293

<u>Author</u>	<u>Title</u>	<u>Vol</u>	<u>Page</u>
Schricker, R. L.	See Eigelsbach, H. T.	4	85
Sech, J. M.	See Kramer, D. N.	2	303
Seely, W. B.	The Effect of Undifferentiated Mass Punishment on the Cohesiveness of the Group and the Attractiveness of the Rebel	3	259
Shinaly, F.	See Gold, L. M.	1	379
Simon, J. Di Persio, R.	Predictions of Shaped Charge Warhead Lethality Effectiveness	4	307
Sims, W. S.	See Daly, P. J.	4	45
Snead, J. L.	See Sollott, G. P.	3	275
Sollott, G. P. Snead, J. L. Strecker, R. A.	Chemiluminescent Organic Phosphides	3	275
Spangler, G. E.	See Agee, F. J.	1	1
Spano, L. A. Iacono, V. D.	Microclimate-Controlled (Thermalibrium) Clothing Systems for Military Applications	3	287
Sperrazza, J.	See Blair, J. R.	4	1
Studel, W. T.	See Lutcher, C. L.	2	355
Steward, W. B. Corrie, J. D.	New Techniques for Entry into Explosive Warheads	4	323
Stiber, S. Haber, G.	Feasibility Study, RF Detonation of Command-Detonated and Pressure-Electric Mines	4	339
Stifel, F. B.	See Herman, R. H.	2	59
Strange, J. N. Whalin, R. W.	Creation of Massive Offshore Surf Zones by Underwater Explosions	4	353

<u>Author</u>	<u>Title</u>	<u>Vol</u>	<u>Page</u>
Strecker, R. A.	See Sollott, G. P.	3	275
Streett, W. B.	See Hill, J. L. E.	2	85
Strozyk, J. W. Rosati, V. J.	Neodymium YAG Laser for Optical Radar Applications	3	303
Sulzberger, M. B.	See Akers, W. A.	1	29
Taschek, W. G.	See Gillis, E. A.	1	363
Tate, H. N.	A Lightweight Electronic Scanning Radar	3	317
Taylor, F. R.	See Kirshenbaum, A. D.	2	221
Thomas, C. B.	See Klein, R. D.	2	249
Thomas, G. R.	See Lewis, R. W.	2	327
Throop, J. F.	See Davidson, T. E.	1	249
Tinder, L. E.	Comparative Analysis of Mandibular and Mid-Face Fractures in Missile and Blunt Trauma: 4,015 Cases	3	329
Tompkins, J. E.	See Rosado, J. A.	4	261
Trevino, S. F. Choi, C. S. Iqbal, Z. Mical, R. D. Prask, H. J. Rao, K. R.	Structure and Lattice Dynamics of Metal Azides and Their Relation- ship to Stability	3	345
Tyeryar, F. J., Jr. Lawton, W. D.	Genetic Transformation in the Genus <u>Pasteurella</u>	3	361
Vander Meer, W.	See Fishbein, W.	4	111
Vault, W. L.	See Rosado, J. A.	4	261

<u>Author</u>	<u>Title</u>	<u>Vol</u>	<u>Page</u>
Vause, C. R. Rudland, R. S.	Mass Flow, Velocity and In- Flight Thrust Measurements by Ion Deflection	3	371
Vitali, R.	See Merendino, A. B.	4	205
Walker, J. E., Jr.	See Kapsalis, J. G.	2	207
Walker, J. S.	See Nims, R. M.	3	75
Whalin, R. W.	See Strange, J. N.	4	353
Wolf, M.	See Kapsalis, J. G.	2	207
Wulkow, E. A.	See Brown, H. A., Jr.	4	15

KINEMATICS OF DIFFUSION, FLUIDS AND PLASMA
BY CONTINUOUS MOVEMENT AND FINITE VELOCITIES

RONALD E. MEYERS
DESERET TEST CENTER
FORT DOUGLAS, UTAH

1. INTRODUCTION

Einstein [1], Chandrasekhar [2], and others using Markov processes have derived parabolic differential equations governing physical processes such as Brownian motion, diffusion, and stellar dynamics. Unfortunately, a mathematically admissible limiting process used in these derivations leads to infinite particle velocities. While Einstein and Chandrasekhar realized the drastic nature of the approximations employed in the parabolic formulation, there has been widespread indiscriminate use and generalization of their equations without regard to the fundamental limitations imposed by those approximations.

It is believed that the following is the framework of a general theory which provides a systematic, comprehensive, and useful approach to studying phenomena based on particulate motion. The present "hyperbolic" theory is a modification and generalization of a hyperbolic diffusion model [3] and attempts to represent more accurately the physical process of diffusion. The approach will be to describe first the kinematics of a single particle moving continuously under general conditions. This is done by representing the motion of one realization of a single particle by a complete power series expansion in time. Then, the Dirac delta function [4,5] is used to give expression to the localization of a single particle's physical mass and to bridge the gap between probability theory and determinism. Under the condition that all the terms of the power series expansion are known, which is the same as knowing the initial position, the initial velocity, and all initial higher derivatives, the position of the particle at any later time is known exactly or "deterministically." At any time its positions in the infinite state space (i.e., configuration space, velocity space, acceleration space, and the spaces of all the other time derivatives) are known in the limit of certainty and expressed by Dirac delta functions. These generalized functions in the infinite-state space are the limiting cases of conditional probability distributions in which the variances go to zero.

A differential equation is found for these conditional probability distributions in the infinite-state space. By the application of the laws of probability, the general differential equation is found for the joint probability of a particle being at one place at one time and another place at another time. This theory is generalized to include the motion of any number of particles in the infinite-state space.

The utility of the equations in the infinite-state space is not limited by a lack of knowledge of the infinite set of initial conditions necessary to solve the differential equation in the infinite state space. Instead, it is found that integration over velocity space, acceleration space, and all the other spaces except configuration space yields the continuity equation, the momentum equation, the energy equation, and all other Eulerian equations for a one particle or multiparticle system. For all these systems the formal relationships between the Eulerian and the Lagrangian properties become evident.

In a straightforward manner, integration with respect to configuration space over the Eulerian properties of the diffusing ensembles provide the Lagrangian properties. As an example, G. I. Taylor's [6] Lagrangian diffusion equation is derived from the Eulerian equations.

2. DERIVATION OF HYPERBOLIC DIFFERENTIAL EQUATIONS GOVERNING KINEMATICS

Consider first the properties of a single particle, k , which moves continuously. If its triplet position coordinates at time t , $k R_i(t)$, $i=0$, and its i -th time derivatives, $k R_i(t)$, $i=1,2,3, \dots$, can be represented by a power series, Eq. (1), and if the remainder tends toward zero for all τ, t , then

$$k R_i(\tau) = k R_i(t) + (\tau-t) k R_{i+1}(t) + \frac{(\tau-t)^2}{2!} k R_{i+2}(t) + \dots \quad (1)$$

where

$$k R_i(\tau) = k R_{i1}(\tau)\hat{i} + k R_{i2}(\tau)\hat{j} + k R_{i3}(\tau)\hat{k}.$$

It is clear that the state of the particle at time $\tau > t$ may then be completely specified by a function of the $k R_{ij}(t)$, where j indicates the j -th component. The exchange of time symbols, τ and t , will also allow an expansion in the backward time direction and demonstrates the time reversibility of the system [7].

To represent a physical fluid one must consider the statistics of the ensemble of the many particles comprising the fluid. If many particles were to undergo continuous movements, then the movement of the collection of these particles could be described by a power series with a distribution of values for each of the terms of the power series corresponding to the various values of $k R_i(t)$. In such a collection the various properties of the movement of the collection of particles may be represented in a manner similar to the calculations of the following expected values.

As a rule of summation

$$\langle \underset{k}{R}(\tau) \rangle = \langle \underset{k}{R}(t) + (\tau-t) \underset{k}{R}_{k+1}(t) + \frac{(\tau-t)^2}{2!} \underset{k}{R}_{k+2}(t) + \dots \rangle \quad (2)$$

As a rule of exponentiation

$$\langle (\underset{k}{R}(\tau))^n \rangle = \langle (\underset{k}{R}(t) + (\tau-t) \underset{k}{R}_{k+1}(t) + \frac{(\tau-t)^2}{2!} \underset{k}{R}_{k+2}(t) + \dots)^n \rangle \quad (3)$$

and

$$\langle (\underset{k}{R}(\tau))^m (\underset{k}{R}(\tau))^n \rangle = \langle (\underset{k}{R}(t) + (\tau-t) \underset{k}{R}_{k+1}(t) + \dots)^m \cdot (\underset{k}{R}(t) + (\tau-t) \underset{k}{R}_{k+1}(t) + \dots)^n \rangle \quad (4)$$

where

$$\langle \underset{k}{R}_i(t) \rangle = \frac{1}{N} \sum_{k=1}^N \underset{k}{R}_i(t), \text{ etc.} \quad (5)$$

As the number of particles N becomes very large, it may be that the distribution of values of $\underset{k}{R}_i(t)$ becomes continuous; nevertheless, since $\underset{k}{R}_i(t)$ represents motion of physical particles, it seems reasonable to assume that values of $\underset{k}{R}_i(t)$ are bounded for all finite t and τ . However, this is not necessarily true if t or $\tau \rightarrow \infty$. It is clear that such expected values as the above represent the significant and measurable properties of the ensemble of particles. Differential equations from which these properties and all other statistical properties may be derived will be developed in what follows.

Let a vector space S have dimensions $3N^\infty$. Let a vector \underline{a} in space S have components $\underset{k}{a}_{ij}$ where the particle label k goes from 1 to N , the derivative number i goes from 0 to ∞ by integer steps, and the cartesian direction component j goes from 1 to 3. One can consider $\underset{k}{R}(\tau)$ with components $\underset{k}{R}_{ij}(\tau)$ to be a vector in this space. Let \underline{s} and \underline{r} also be vectors on the same space S . Vector $\underset{k}{R}(\tau)$ can be referred to as a state vector; in the context of probability theory it is a vector random variable. For two vectors \underline{a} and \underline{b} in space S , the statement $\underline{a} \leq \underline{b}$ will be interpreted as $\underset{k}{a}_{ij} \leq \underset{k}{b}_{ij}$. (Ordinarily a vector space cannot be ordered and the inequality of vectors in this paper has the above specified interpretation.) The state vector, $\underset{k}{R}(\tau)$, is a constrained vector in space S such that

$$\underset{k\ell}{R}_i(\tau) \leq \underset{k}{R}_i(\tau) \leq \underset{ku}{R}_i(\tau), \text{ where } \ell \text{ and } u \text{ indicate the lower and upper bounds respectively. Under certain conditions } \underset{k\ell}{R}_i(\tau) \text{ and}$$

$\underset{ku}{R}_i(\tau)$ may go to $-\infty$ and $+\infty$ respectively. This allows treatment of the parabolic equations as hyperbolic equations in their asymptotic forms [8].

If the position and all the derivatives of the k -th particle are given at time t , say $\underset{k}{r} = \underset{k}{R}(t)$, then at any time $\tau > t$ by substituting $\underset{k}{r} = \underset{k}{R}(t)$ into Eq. (1), one knows deterministically that the particle will have position and derivatives at time τ given by

$$k_{i+1}^R(\tau) = k_{i+1}^R + (\tau-t)k_{i+2}^R + \frac{(\tau-t)^2}{2!}k_{i+3}^R + \dots \quad (6)$$

Therefore, the conditional probability density, $f(\tau, k_{i+1}^S | t, k_{i+1}^R)$, representing the position of the particle in the infinite state space is

$$f(\tau, k_{i+1}^S | t, k_{i+1}^R) = \delta[k_{i+1}^S - k_{i+1}^R(\tau)] \quad (7)$$

where

$$f(\tau, k_{i+1}^S | t, k_{i+1}^R) d_{k_{i+1}^S} = P[k_{i+1}^S < k_{i+1}^R(\tau) < k_{i+1}^S + d_{k_{i+1}^S} | k_{i+1}^R(t) = k_{i+1}^R] d_{k_{i+1}^S} \quad (8)$$

and

$$\delta[k_{i+1}^S - k_{i+1}^R(\tau)] = \prod_{i,j} \delta[k_{i+1}^S - k_{i+1}^R(\tau)] \quad (9)$$

where $\prod_{i,j}$ indicates the product over all i, j where $i=0,1,2,3,\dots$, and $j=1,2,3$. $P[k_{i+1}^S < k_{i+1}^R(\tau) < k_{i+1}^S + d_{k_{i+1}^S} | k_{i+1}^R(t) = k_{i+1}^R] d_{k_{i+1}^S}$ is the probability that $k_{i+1}^R(\tau)$ takes on a value between k_{i+1}^S and $k_{i+1}^S + d_{k_{i+1}^S}$ at time τ under the condition that $k_{i+1}^R(t) = k_{i+1}^R$ at time t .

Each $\delta[k_{i+1}^S - k_{i+1}^R(\tau)]$ in Eq. (9) has the following properties

$$\delta[k_{i+1}^S - k_{i+1}^R(\tau)] = 0 \quad k_{i+1}^S \neq k_{i+1}^R(\tau) \quad (10a)$$

$$\delta[k_{i+1}^S - k_{i+1}^R(\tau)] = 0 \quad k_{i+1}^S \neq k_{i+1}^R(\tau) \quad (10b)$$

$$\int_{-\infty}^{+\infty} \delta[k_{i+1}^S - k_{i+1}^R(\tau)] d_{k_{i+1}^S} = 1 \quad (11a)$$

$$\int_{-\infty}^{+\infty} \delta[k_{i+1}^S - k_{i+1}^R(\tau)] d_{k_{i+1}^S} = 1 \quad (11b)$$

The Dirac-delta function, $\delta[k_{i+1}^S - k_{i+1}^R(\tau)]$, is not a function in the ordinary sense but is a generalized function in the Lighthill [5] sense, the difference being that this is a generalization to a delta function of an infinite number of variables. The integral of Eq. (11b) is an infinitely iterated integral and the $d_{k_{i+1}^S}$ is an infinite product of the $d_{k_{i+1}^S}$. Another example of an infinitely iterated integral is the Wiener integral [9,10].

A differential equation for $f(\tau, k_{i+1}^S | t, k_{i+1}^R)$ will now be developed: Taking the partial derivative of Eq. (7) with respect to τ gives

$$\frac{\partial f(\tau, k_{i+1}^S | t, k_{i+1}^R)}{\partial \tau} = \frac{\partial}{\partial \tau} \{ \delta[k_{i+1}^S - k_{i+1}^R(\tau)] \} = \sum_{i,j} \delta' [k_{i+1}^S - k_{i+1}^R(\tau)] \cdot \frac{\partial (k_{i+1}^S - k_{i+1}^R(\tau))}{\partial \tau} \cdot \prod_{\ell, m} (\ell, m \neq i, j) \delta[k_{i+1}^S - k_{i+1}^R(\tau)] \quad (12)$$

$$\frac{\partial (k_{i+1}^S - k_{i+1}^R(\tau))}{\partial \tau} = -k_{i+2}^R(\tau) \quad (13)$$

MEYERS

Since $\delta [k_{i+1,j}^S - k_{i+1,j}^R(\tau)] = 0$, unless $k_{i+1,j}^S = k_{i+1,j}^R(\tau)$, we can replace $k_{i+1,j}^R(\tau)$ by $k_{i+1,j}^S$. Eq. (12) now becomes

$$\frac{\partial f(\tau, k_{i+1,j}^S | t, k_{i+1,j}^R)}{\partial \tau} = - \sum_{i,j} (k_{i+1,j}^S)^{\delta [k_{i+1,j}^S - k_{i+1,j}^R(\tau)]} \cdot \prod_{\ell, m} (\ell, m \neq i, j) \delta [k_{\ell m}^S - k_{\ell m}^R(\tau)] \quad (14)$$

Now taking the partial derivative of Eq. (7) with respect to k_{ij}^S gives:

$$\frac{\partial f(\tau, k_{i+1,j}^S | t, k_{i+1,j}^R)}{\partial k_{ij}^S} = \frac{\partial}{\partial k_{ij}^S} \{ \delta [k_{i+1,j}^S - k_{i+1,j}^R(\tau)] \} = \sum_{i,j} \delta' [k_{i+1,j}^S - k_{i+1,j}^R(\tau)] \frac{\partial}{\partial k_{ij}^S} \prod_{\ell, m} (\ell, m \neq i, j) \delta [k_{\ell m}^S - k_{\ell m}^R(\tau)] \quad (15)$$

Comparing Eqs. (14) and (15), it is seen that

$$\frac{\partial f(\tau, k_{i+1,j}^S | t, k_{i+1,j}^R)}{\partial \tau} + \sum_{i,j} k_{i+1,j}^S \frac{\partial f(\tau, k_{i+1,j}^S | t, k_{i+1,j}^R)}{\partial k_{ij}^S} = 0. \quad (16)$$

This is the hyperbolic differential equation in the state space S. Under the rather unrestrictive conditions represented by Eq. (1), it can completely describe the kinematics of a single particle in continuous motion given the initial conditions at $t, k_{i+1,j}^R$. Eq. (16) governs the "transition" probability density in the infinite dimensional space. It describes the infinite dimensional space rate of change of the density of the particle with respect to its time rate of change. One may consider it hyperbolic along the real line in the infinite dimensional space since it possesses the real characteristics

$$\frac{ds_{ij}}{d\tau} = s_{i+1,j}$$

which may be obtained by differentiating Eq. (6) or by taking moments on Eq. (16). The moments method is pursued in the following sections.

Eq. (16) represents the differential equation for the conditional probability density, $f(\tau, k_{i+1,j}^S | t, k_{i+1,j}^R)$. The joint probability density, $f(\tau, k_{i+1,j}^S; t, k_{i+1,j}^R)$, can be obtained from the product of the marginal probability density, $f(t, k_{i+1,j}^R)$, and the conditional density, $f(\tau, k_{i+1,j}^S | t, k_{i+1,j}^R)$, with the aid of a law of probability theory [11,12].

$$f(\tau, k_{i+1,j}^S; t, k_{i+1,j}^R) = f(\tau, k_{i+1,j}^S | t, k_{i+1,j}^R) f(t, k_{i+1,j}^R), \quad (17)$$

where

$$f(t, k_{i+1,j}^R) d_{k_{i+1,j}^R} = P [k_{i+1,j}^R < k_{i+1,j}^R(t) < k_{i+1,j}^R + d_{k_{i+1,j}^R}] d_{k_{i+1,j}^R}$$

and

$$f(\tau, k_{i+1,j}^S; t, k_{i+1,j}^R) d_{k_{i+1,j}^S} d_{k_{i+1,j}^R} = P [k_{i+1,j}^S < k_{i+1,j}^S(\tau) < k_{i+1,j}^S + d_{k_{i+1,j}^S}; k_{i+1,j}^R < k_{i+1,j}^R(t) < k_{i+1,j}^R + d_{k_{i+1,j}^R}] d_{k_{i+1,j}^S} d_{k_{i+1,j}^R}$$

$P[\underline{k}^r < \underline{k}^R(t) < \underline{k}^r + d_{\underline{k}^r}] d_{\underline{k}^r}$ is the probability that $\underline{k}^R(t)$ takes on a value between \underline{k}^r and $\underline{k}^r + d_{\underline{k}^r}$ at time t , and $P[\underline{k}^s < \underline{k}^R(\tau) < \underline{k}^s + d_{\underline{k}^s}; \underline{k}^r < \underline{k}^R(t) < \underline{k}^r + d_{\underline{k}^r}] d_{\underline{k}^s} d_{\underline{k}^r}$ is the joint probability that $\underline{k}^R(\tau)$ takes on a value between \underline{k}^s and $\underline{k}^s + d_{\underline{k}^s}$ at time τ , and $\underline{k}^R(t)$ takes on a value between \underline{k}^r and $\underline{k}^r + d_{\underline{k}^r}$ at time t .

Multiplying Eq. (16) by $f(t, \underline{k}^r)$ gives the differential equation for the joint probability density, Eq. (18a), and integration over \underline{k}^r provides the absolute probability density at \underline{k}^s , Eq. (18b).

$$\frac{\partial f(\tau, \underline{k}^s; t, \underline{k}^r)}{\partial \tau} + \sum_{i,j} k_{i+1,j}^s \frac{\partial f(\tau, \underline{k}^s; t, \underline{k}^r)}{\partial k_{ij}^s} = 0 \quad (18a)$$

$$\frac{\partial f(\tau, \underline{k}^s)}{\partial \tau} + \sum_{i,j} k_{i+1,j}^s \frac{\partial f(\tau, \underline{k}^s)}{\partial k_{ij}^s} = 0 \quad (18b)$$

Also by deduction, the exchange of τ and t and k_{ij}^s and k_{ij}^r yield

$$\frac{\partial f(\tau, \underline{k}^s; t, \underline{k}^r)}{\partial t} + \sum_{i,j} k_{i+1,j}^r \frac{\partial f(\tau, \underline{k}^s; t, \underline{k}^r)}{\partial k_{ij}^r} = 0 \quad (18c)$$

These are standard forms which may be compared with various plasma and gas dynamics equations [13].

For finite velocities

$$\frac{ds_{oi}}{d\tau} = s_{1i}$$

is finite and, therefore, the response time is nonzero. For parabolic cases the response time is zero. For more pertinent discussion on partial differential equation properties see Courant [14]. One notes that Eq. (16), along the characteristics, may be rewritten as

$$\frac{df(\tau, \underline{k}^s | t, \underline{k}^r)}{d\tau} = 0,$$

a total and exact differential equation. The significance of this result, to be demonstrated later, is that given the absolute probability density at time t , which may be considered as the distribution of conditions or states at time t , upon integration along the characteristics one may determine the distribution at any later time.

The above derivation utilized the delta function concept. The above equations, and subsequent ones, could have been derived from a $3N^\infty$ Markov process and are completely consistent with it. The conditions for a Markov process are given by Ornstein and Uhlenbeck [15], and Bharuchba-Reid [16]. By utilizing the Markov property, the connection between various events at various times and in various spaces may be constructed.

3. MANY PARTICLE SYSTEMS

Two particle diffusion. Consider two marked particles designated $k=1, k=2$. There corresponds a conditional probability density $f(\tau, \underline{k}^s | t, \underline{k}^r)$, $k=1,2$, irrespective of the interactions between the two particles. The conditional probability density for two

particles, $f(\tau, {}_1\mathcal{S}, {}_2\mathcal{S} | t, {}_1\mathcal{R}, {}_2\mathcal{R})$, therefore, must be related to the conditional probability density for each particle by

$$f(\tau, {}_1\mathcal{S}, {}_2\mathcal{S} | t, {}_1\mathcal{R}, {}_2\mathcal{R}) = f(\tau, {}_1\mathcal{S} | t, {}_1\mathcal{R})f(\tau, {}_2\mathcal{S} | t, {}_2\mathcal{R}). \quad (19)$$

The differential equations governing $f(\tau, {}_k\mathcal{S} | t, {}_k\mathcal{R})$, $k=1,2$, are

$$\frac{\partial f(\tau, {}_k\mathcal{S} | t, {}_k\mathcal{R})}{\partial \tau} + \sum_{i,j} k^{S_{i+1,j}} \frac{\partial f(\tau, {}_k\mathcal{S} | t, {}_k\mathcal{R})}{\partial k^{S_{i,j}}} = 0, \quad k=1,2. \quad (20)$$

Multiplying Eq. (20) with $k=1$ by $f(\tau, {}_k\mathcal{S} | t, {}_k\mathcal{R})$ with $k=2$ and multiplying Eq. (20) with $k=2$ by $f(\tau, {}_k\mathcal{S} | t, {}_k\mathcal{R})$ with $k=1$ yields the following set of equations:

$$\begin{aligned} & f(\tau, {}_2\mathcal{S} | t, {}_2\mathcal{R}) \frac{\partial f(\tau, {}_1\mathcal{S} | t, {}_1\mathcal{R})}{\partial \tau} + \\ & + \sum_{i,j} 1^{S_{i+1,j}} \frac{\partial f(\tau, {}_1\mathcal{S} | t, {}_1\mathcal{R})}{\partial 1^{S_{i,j}}} \cdot f(\tau, {}_2\mathcal{S} | t, {}_2\mathcal{R}) = 0 \end{aligned} \quad (21a)$$

$$\begin{aligned} & f(\tau, {}_1\mathcal{S} | t, {}_1\mathcal{R}) \frac{\partial f(\tau, {}_2\mathcal{S} | t, {}_2\mathcal{R})}{\partial \tau} + \\ & + \sum_{i,j} 2^{S_{i+1,j}} \frac{\partial f(\tau, {}_2\mathcal{S} | t, {}_2\mathcal{R})}{\partial 2^{S_{i,j}}} \cdot f(\tau, {}_1\mathcal{S} | t, {}_1\mathcal{R}) = 0 \end{aligned} \quad (21b)$$

Utilizing Eq. (19) and adding Eqs. (21a,b) yields the differential equation governing $f(\tau, {}_1\mathcal{S}, {}_2\mathcal{S} | t, {}_1\mathcal{R}, {}_2\mathcal{R})$.

$$\begin{aligned} & \frac{\partial f(\tau, {}_1\mathcal{S}, {}_2\mathcal{S} | t, {}_1\mathcal{R}, {}_2\mathcal{R})}{\partial \tau} + \\ & + \sum_{i,j,k} k^{S_{i+1,j}} \frac{\partial f(\tau, {}_1\mathcal{S}, {}_2\mathcal{S} | t, {}_1\mathcal{R}, {}_2\mathcal{R})}{\partial k^{S_{i,j}}} = 0 \end{aligned} \quad (22)$$

If Eq. (22) is multiplied by the absolute probability density $f(t, {}_1\mathcal{R}, {}_2\mathcal{R})$, the differential equation governing the joint probability density $f_{1,2} = f(\tau, {}_1\mathcal{S}, {}_2\mathcal{S}; t, {}_1\mathcal{R}, {}_2\mathcal{R})$ is

$$\frac{\partial f_{1,2}}{\partial \tau} + \sum_{i,j,k} k^{S_{i+1,j}} \frac{\partial f_{1,2}}{\partial k^{S_{i,j}}} = 0, \quad k=1,2 \quad (23)$$

By deduction

$$\frac{\partial f_{1,2}}{\partial t} + \sum_{i,j,k} k^{R_{i+1,j}} \frac{\partial f_{1,2}}{\partial k^{R_{i,j}}} = 0 \quad (23a)$$

Integrating Eq. (23) in a manner similar to that used in the integrations performed on the one particle system over the various spaces gives the partial differential equations governing the two particle system in the remaining unintegrated spaces. Continuity, momentum, and energy equations, for example, as well as the relations between correlations and moments, may be obtained in this manner.

N-particle systems. Extending the above derivation to N particles, and letting

$f_{1,2,\dots,N} = f(\tau, 1^S, 2^S, \dots, N^S; t, 1^R, 2^R, \dots, N^R)$ yields

$$\frac{\partial f_{1,2,\dots,N}}{\partial \tau} + \sum_{i,j,k} k^{S_{i+1,j}} \frac{\partial f_{1,2,\dots,N}}{\partial k^{S_{i,j}}} = 0 \quad k=1,2,\dots,N. \quad (24)$$

This is a very general equation. It is the differential equation governing the motion of N marked particles. From it one may derive all kinematic relationships governing the continuous motion of the N particles in any spaces desired. The general solution to this equation under initial condition is presented by Meyers and Fletcher [17]. By averaging the contributions of the various particles diffusing past points separated in space and time, it is possible to construct the space-time statistical properties of a fluid or plasma. In other words, the fluid or plasma ensemble may be constructed by a superposition of the diffusing subensembles. The remainder of the present paper will consider the properties of subensembles of diffusing particles. The relationship of the statistics of the diffusing subensembles to the statistics of an incompressible fluid will be presented in a separate contribution [18].

4. THE EULERIAN EQUATIONS

The Eulerian kinematic equations for the diffusing ensemble of particles may now be derived from Eq. (18b). Integrating Eq. (18b) over all variables except k^S yields the continuity equation in the configuration space, k^S_0 .

$$\int_{-\infty}^{+\infty} \frac{\partial}{\partial \tau} f(\tau, k^S) \frac{d_k^S}{d_k^S_0} + \int_{-\infty}^{+\infty} \sum_{i,j} k^{S_{i+1,j}} \frac{\partial f(\tau, k^S)}{\partial k^{S_{i,j}}} \frac{d_k^S}{d_k^S_0} = 0$$

$$\frac{\partial f(\tau, k^S_0)}{\partial \tau} + \nabla_{k^S_0} \cdot (E[k^R_{k^S_1}(\tau) | k^R_{k^S_0}(\tau)] f(\tau, k^S_0)) = 0 \quad (25)$$

where

$$E[k^R_{k^S_1}(\tau) | k^R_{k^S_0}(\tau)] f(\tau, k^S_0) = \int_{-\infty}^{+\infty} k^S_{k^S_1} f(\tau, k^S) \frac{d_k^S}{d_k^S_0}.$$

The notation for the conditional expected values is in a standard form (e.g., Brunk [11]). $E[k^R_{k^S_1}(\tau) | k^R_{k^S_0}(\tau)]$ is the expected value of the velocity of the k -th particle at time τ under the condition that its position in configuration space is given also at time τ . Multiplying Eq. (18b) by $k^S_{k^S_1}$ and integrating over all variables except k^S_0 yields a momentum equation in configuration space, k^S_0 .

$$\begin{aligned} & \frac{\partial}{\partial \tau} (E[k^R_{k^S_1}(\tau) | k^R_{k^S_0}(\tau)] f(\tau, k^S_0)) + \\ & + \nabla_{k^S_0} \cdot (E[k^R_{k^S_1}(\tau) | k^R_{k^S_0}(\tau)] f(\tau, k^S_0)) - \\ & - E[k^R_{k^S_2}(\tau) | k^R_{k^S_0}(\tau)] f(\tau, k^S_0) = 0 \end{aligned} \quad (26)$$

where

$$E[\underset{k^s}{R}(\tau), \underset{k^s}{R}(\tau) | \underset{k^s}{R}(\tau)] \cdot f(\tau, \underset{k^s}{s}_0) = \int_{-\infty}^{+\infty} \underset{k^s}{k^s}_1 \underset{k^s}{k^s}_1 f(\tau, \underset{k^s}{s}) \frac{d \underset{k^s}{s}}{d \underset{k^s}{s}_0}$$

and

$$E[\underset{k^s}{R}(\tau) | \underset{k^s}{R}(\tau)] \cdot f(\tau, \underset{k^s}{s}_0) = \int_{-\infty}^{+\infty} \underset{k^s}{k^s}_2 f(\tau, \underset{k^s}{s}) \frac{d \underset{k^s}{s}}{d \underset{k^s}{s}_0}$$

An energy equation may be derived from (18b) by multiplying by the dyadic, $\underset{k^s}{k^s}_1 \underset{k^s}{k^s}_1$, and integrating in a manner similar to that used in Eqs. (25) and (26). Equations with higher Eulerian moments may be similarly obtained. These equations establish the formal connection between the equations of statistical mechanics and the Eulerian "balance" equations of classical continuum mechanics.

5. THE LAGRANGIAN MOMENTS

Integration of the above Eulerian momentum equation over $\underset{k^s}{k^s}_0$ provides the following relationship between the Lagrangian position and the Lagrangian velocity:

$$\begin{aligned} 0 &= \int_{-\infty}^{+\infty} \left\{ \frac{\partial}{\partial \tau} (E[\underset{k^s}{R}(\tau) | \underset{k^s}{R}(\tau)] f(\tau, \underset{k^s}{s}_0)) + \right. \\ &+ \underset{k^s}{v} \cdot (E[\underset{k^s}{R}(\tau), \underset{k^s}{R}(\tau) | \underset{k^s}{R}(\tau)] f(\tau, \underset{k^s}{s}_0)) - \\ &- E[\underset{k^s}{R}(\tau) | \underset{k^s}{R}(\tau)] f(\tau, \underset{k^s}{s}_0) \left. \right\} d \underset{k^s}{s}_0 \\ &= \frac{d}{d \tau} E[\underset{k^s}{R}(\tau)] + E[\underset{k^s}{R}(\tau), \underset{k^s}{R}(\tau) | \underset{k^s}{R}(\tau)] \cdot f(\tau, \underset{k^s}{s}_0) \Big|_{-\infty}^{+\infty} - E[\underset{k^s}{R}(\tau)] \end{aligned} \quad (27)$$

$$\frac{d}{d \tau} E[\underset{k^s}{R}(\tau)] = E[\underset{k^s}{R}(\tau)] \quad (28)$$

It should be emphasized that all Lagrangian terms may be obtained from integration over Eulerian terms in the above manner.

Multiplying Eq. (18b) by the various products of $\underset{k^s}{k^s}_i$ and integrating provides more Eulerian moment equations in a more direct fashion from which one may obtain the following supplementary Lagrangian relationships:

$$\frac{d}{d \tau} E[\underset{k^s}{R}_i(\tau)] = E[\underset{k^s}{R}_{i+1}(\tau)] \quad (29)$$

$$\begin{aligned} \frac{d}{d \tau} E[\underset{k^s}{R}_i(\tau), \underset{k^s}{R}_j(\tau)] &= E[\underset{k^s}{R}_{i+1}(\tau), \underset{k^s}{R}_j(\tau)] + \\ &+ E[\underset{k^s}{R}_i(\tau), \underset{k^s}{R}_{j+1}(\tau)], \text{ etc.} \end{aligned} \quad (30)$$

where

$$E[\underset{k^s}{R}_i(\tau)] = \int_{-\infty}^{+\infty} \underset{k^s}{k^s}_i f(\tau, \underset{k^s}{s}) d \underset{k^s}{s}, \quad (31)$$

$$E[\underset{k^s}{R}_i(\tau), \underset{k^s}{R}_j(\tau)] = \int_{-\infty}^{+\infty} \underset{k^s}{k^s}_i \underset{k^s}{k^s}_j f(\tau, \underset{k^s}{s}) d \underset{k^s}{s}, \text{ etc.} \quad (32)$$

It becomes obvious that Lagrangian differentiation for one particle obeys the ordinary calculus of differentiation in the argument of the expectation sign. It also follows that integration with respect to time is permitted.

6. THE DERIVATION OF THE EQUATION OF LAGRANGIAN DIFFUSION

For stationary, homogeneous turbulence in a coordinate system in which there is no mean translation and under the condition that in every trial case the single particle movement starts at the origin, one has from Eq. (30) for $i = j = 0$

$$\frac{d}{d\tau} E[{}_{k^{\sim}0}R(\tau), {}_{k^{\sim}0}R(\tau)] = E[{}_{k^{\sim}1}R(\tau), {}_{k^{\sim}0}R(\tau)] + E[{}_{k^{\sim}0}R(\tau), {}_{k^{\sim}1}R(\tau)] \quad (33)$$

$$= \int_0^\tau \{E[{}_{k^{\sim}1}R(\tau), {}_{k^{\sim}1}R(\xi)] + E[{}_{k^{\sim}1}R(\xi), {}_{k^{\sim}1}R(\tau)]\} d\xi + E[{}_{k^{\sim}1}R(\tau), {}_{k^{\sim}0}R(0)] + E[{}_{k^{\sim}0}R(0), {}_{k^{\sim}1}R(\tau)] \quad (34)$$

$$= \int_0^\tau \{E[{}_{k^{\sim}1}R(\tau), {}_{k^{\sim}1}R(\xi)] + E[{}_{k^{\sim}1}R(\xi), {}_{k^{\sim}1}R(\tau)]\} d\xi \quad (35)$$

Consider for the moment the dyadic, $E[{}_{k^{\sim}1}R(\tau), {}_{k^{\sim}1}R(\xi)] + E[{}_{k^{\sim}1}R(\xi), {}_{k^{\sim}1}R(\tau)]$.

By the condition of stationarity, $E[{}_{k^{\sim}1}R(\tau), {}_{k^{\sim}j}R(\tau)] = E[{}_{k^{\sim}1}R(\xi), {}_{k^{\sim}j}R(\xi)] = E[{}_{k^{\sim}1}R(0), {}_{k^{\sim}j}R(0)]$ for $i = j \neq 0$, and therefore describes a tensor independent of time. By the use of Eq. (1) one has

$$E[{}_{k^{\sim}1}R(\tau), {}_{k^{\sim}j}R(\xi)] = E[{}_{k^{\sim}1}R(\tau), {}_{k^{\sim}j}R(\tau) + (\xi - \tau) {}_{k^{\sim}j+1}R(\tau) + \frac{(\xi - \tau)^2}{2!} {}_{k^{\sim}j+2}R(\tau) + \dots] = E[{}_{k^{\sim}1}R(\tau), {}_{k^{\sim}j}R(\tau)] + (\xi - \tau) E[{}_{k^{\sim}1}R(\tau), {}_{k^{\sim}j+1}R(\tau)] + \frac{(\xi - \tau)^2}{2!} E[{}_{k^{\sim}1}R(\tau), {}_{k^{\sim}j+2}R(\tau)] + \dots \quad (36)$$

Because $E[{}_{k^{\sim}i}R(\tau), {}_{k^{\sim}j}R(\tau)]$, ($i = j \neq 0$), is constant,

$$\frac{d}{d\tau} E[{}_{k^{\sim}i}R(\tau), {}_{k^{\sim}j}R(\tau)] = E[{}_{k^{\sim}i+1}R(\tau), {}_{k^{\sim}j}R(\tau)] + E[{}_{k^{\sim}i}R(\tau), {}_{k^{\sim}j+1}R(\tau)] = 0, \text{ for } (i = j \neq 0). \quad (37)$$

Differentiating (37) yields

$$2E[{}_{k^{\sim}i+1}R(\tau), {}_{k^{\sim}j+1}R(\tau)] = -\{E[{}_{k^{\sim}i+2}R(\tau), {}_{k^{\sim}j}R(\tau)] + E[{}_{k^{\sim}i}R(\tau), {}_{k^{\sim}j+2}R(\tau)]\}, (i = j \neq 0). \quad (38)$$

By successive differentiation of (38) and substitution of (37) the following relations are obtained:

$$E \left[\frac{d^{2n} {}_{k^{\sim}i}R(\tau), {}_{k^{\sim}j}R(\tau)}{d\tau^{2n}} \right] + E \left[\frac{{}_{k^{\sim}i}R(\tau) d^{2n} {}_{k^{\sim}j}R(\tau)}{d\tau^{2n}} \right] =$$

$$= E\{(-1)^{n_2} \left[\frac{d^n R_i(\tau)}{d\tau^n} \right] \left[\frac{d^n R_j(\tau)}{d\tau^n} \right] \}, \quad (i = j \neq 0), \quad (39)$$

and

$$E \left[\frac{d^{2n+1} R_i(\tau)}{d\tau^{2n+1}} \frac{d^{2n+1} R_j(\tau)}{d\tau^{2n+1}} \right] + E \left[\frac{d^{2n+1} R_i(\tau)}{d\tau^{2n+1}} \frac{d^{2n+1} R_j(\tau)}{d\tau^{2n+1}} \right] = 0 \quad (40)$$

(i = j ≠ 0)

Substituting (39) and (40) into (36) yields the equation for the correlation dyadic of the derivatives,

$$\begin{aligned} \frac{1}{2} \{ E[\frac{d R_i(\tau)}{d\tau} \frac{d R_j(\xi)}{d\xi}] + E[\frac{d R_i(\xi)}{d\xi} \frac{d R_j(\tau)}{d\tau}] \} &= E[\frac{d R_i(\tau)}{d\tau} \frac{d R_j(\tau)}{d\tau}] + \\ &+ (\xi - \tau) \cdot (0) - \frac{(\xi - \tau)^2}{2!} E[\frac{d^2 R_i(\tau)}{d\tau^2} \frac{d^2 R_j(\tau)}{d\tau^2}] + \frac{(\xi - \tau)^3}{3!} \cdot (0) + \\ &+ \frac{(\xi - \tau)^4}{4!} E[\frac{d^4 R_i(\tau)}{d\tau^4} \frac{d^4 R_j(\tau)}{d\tau^4}] + \dots, \quad (i = j \neq 0). \end{aligned} \quad (41)$$

We define the derivative correlation coefficients with the aid of a normalization with respect to the velocity standard deviations.

$$k_{i\ell}^V(\tau) = k_{i\ell}^R(\tau) / (E[k_{i\ell}^R(\tau) R_{im}(\tau)])^{\frac{1}{2}}, \quad (42)$$

(i ≠ 0; n = ℓ = m = 1, 2, 3) .

$\frac{1}{2} \{ E[k_{i\ell}^V(\tau) k_{i\ell}^V(\xi)] + E[k_{i\ell}^V(\xi) k_{i\ell}^V(\tau)] \}$ then defines the velocity correlation coefficient dyadic. It is noted that the correlation coefficients depend only on the even function $(\xi - \tau)^2$, hence Eq. (35) becomes

$$\begin{aligned} \frac{d}{d\tau} E[k_{o\ell}^R(\tau) k_{om}^R(\tau)] &= E[k_{1\ell}^R(0) k_{1m}^R(0)] \int_0^\tau \{ E[k_{1\ell}^V(0) k_{1m}^V(\xi)] + \\ &+ E[k_{1\ell}^V(\xi) k_{1m}^V(0)] \} d\xi. \end{aligned} \quad (43)$$

Integrating again with respect to τ yields Batchelor's [19,20] generalization of G. I. Taylor's [6] equation of Lagrangian diffusion.

$$\begin{aligned} E[k_{o\ell}^R(\tau) k_{om}^R(\tau)] \Big|_0^T &= E[k_{1\ell}^R(0) k_{1m}^R(0)] \cdot \int_0^T \int_0^\tau \{ E[k_{1\ell}^V(0) k_{1m}^V(\xi)] + \\ &+ E[k_{1\ell}^V(\xi) k_{1m}^V(0)] \} d\xi d\tau. \end{aligned} \quad (44)$$

7. RELATIONSHIP BETWEEN EULERIAN AND LAGRANGIAN CORRELATION FUNCTIONS FOR ONE DIFFUSING PARTICLE

To find the relationship between the Eulerian and Lagrangian correlation functions for the diffusion of the particle designated k from the origin, consider the joint probability density $f(\tau, k_{\vec{s}}; t, k_{\vec{r}})$. Its differential Eqs. (18a) and (18c) yield the

MEYERS

continuity and momentum equations. Integration of (18c) over all state space variables except $k_{\omega 0}^S$ and $k_{\omega 0}^R$ yields

$$\frac{\partial f(\tau, k_{\omega 0}^S; t, k_{\omega 0}^R)}{\partial \tau} + \nabla_{k_{\omega 0}^R} \cdot \{E[k_{\omega 1}^R(t) | k_{\omega 0}^R(\tau), k_{\omega 0}^R(t)] \cdot f(\tau, k_{\omega 0}^S; t, k_{\omega 0}^R)\} = 0 \quad (45)$$

Multiplying Eq. (18a) by $k_{\omega 1}^R$ and integrating yields a momentum equation as a function of the correlation function

$$\frac{\partial \{E[k_{\omega 1}^R(t) | k_{\omega 0}^R(\tau), k_{\omega 0}^R(t)] \cdot f(\tau, k_{\omega 0}^S; t, k_{\omega 0}^R)\}}{\partial \tau} + \nabla_{k_{\omega 0}^S} \cdot \{E[k_{\omega 1}^R(\tau), k_{\omega 1}^R(t) | k_{\omega 0}^R(\tau), k_{\omega 0}^R(t)] f(\tau, k_{\omega 0}^S; t, k_{\omega 0}^R)\} = 0. \quad (46)$$

Differentiating (45) with respect to τ and taking the divergence of (46) with respect to $k_{\omega 0}^R$ allows elimination of the flux

$E[k_{\omega 1}^R(t) | k_{\omega 0}^R(\tau), k_{\omega 0}^R(t)] \cdot f(\tau, k_{\omega 0}^S; t, k_{\omega 0}^R)$ with the result

$$\frac{\partial^2 \{f(\tau, k_{\omega 0}^S; t, k_{\omega 0}^R)\}}{\partial \tau \partial t} = \nabla_{k_{\omega 0}^R} \cdot [\nabla_{k_{\omega 0}^S} \cdot \{E[k_{\omega 1}^R(\tau), k_{\omega 1}^R(t) | k_{\omega 0}^R(\tau), k_{\omega 0}^R(t)] \cdot f(\tau, k_{\omega 0}^S; t, k_{\omega 0}^R)\}] . \quad (47)$$

With the change of variables $T = \tau - t$, $t' = t$, $k_{\omega 0}^S = k_{\omega 0}^S - k_{\omega 0}^R$, $k_{\omega 0}^R = k_{\omega 0}^R$, Eq. (47) transforms to Eq. (48):

$$\left(\frac{\partial^2}{\partial T^2} - \frac{\partial}{\partial T \partial t'} \right) f(T+t', k_{\omega 0}^S + k_{\omega 0}^R; t', k_{\omega 0}^R) = (\nabla_{k_{\omega 0}^S} - \nabla_{k_{\omega 0}^R}) \cdot [\nabla_{k_{\omega 0}^S} \cdot \{E[k_{\omega 1}^R(T+t'), k_{\omega 1}^R(t') | k_{\omega 0}^R(T+t'), k_{\omega 0}^R(t')]\} \cdot f(T+t', k_{\omega 0}^S + k_{\omega 0}^R; t', k_{\omega 0}^R)] . \quad (48)$$

When the probability density and the correlation function depend only upon the differences $T = \tau - t$, and $k_{\omega 0}^S = k_{\omega 0}^S - k_{\omega 0}^R$, and for the condition that in every case the particle movement starts at the origin at time $t' = 0$, $f(t', k_{\omega 0}^R) = \delta(k_{\omega 0}^R)$. Integration of Eq. (48) over $k_{\omega 0}^R$ provides

$$\frac{\partial^2 f(T, k_{\omega 0}^S)}{\partial T^2} = \nabla_{k_{\omega 0}^S} \cdot [\nabla_{k_{\omega 0}^S} \cdot \{E[k_{\omega 1}^R(T), k_{\omega 1}^R(0) | k_{\omega 0}^R(T)] \cdot f(T, k_{\omega 0}^S)\}] . \quad (49)$$

The dyadic $E[k_{\omega 1}^R(T), k_{\omega 1}^R(0) | k_{\omega 0}^R(T)]$ is recognized as the Eulerian velocity correlation function dyadic. Multiplication of (49) by the dyadic $k_{\omega 0}^S k_{\omega 0}^S$ and integration over $k_{\omega 0}^S$ yields an alternate method of obtaining the previously derived equation relating the second moment of position to the velocity correlation function:

$$\frac{d^2 E[k_{\omega 0}^R(T), k_{\omega 0}^R(T)]}{dT^2} = 2E[k_{\omega 1}^R(T), k_{\omega 1}^R(0)] \quad (50)$$

MEYERS

where

$$E\left[\frac{R_{k^{\sim}1}}{k^{\sim}1}(\tau), \frac{R_{k^{\sim}1}}{k^{\sim}1}(0)\right] = \int_{-\infty}^{+\infty} E\left[\frac{R_{k^{\sim}1}}{k^{\sim}1}(T), \frac{R_{k^{\sim}1}}{k^{\sim}1}(0) \mid \frac{R_{k^{\sim}0}}{k^{\sim}0}(T)\right] \cdot f(T, \frac{S_o}{k^{\sim}0}) d\frac{S_o}{k^{\sim}0} \quad (51)$$

Eq. (51) is the relationship between the Eulerian and Lagrangian correlation functions for one particle diffusion in homogeneous steady turbulence.

In cartesian notation Eq. (49) may be written in terms of the velocity correlation tensor Q_{ij} ,

$$\frac{\partial^2 f}{\partial T^2} = \sum_{i,j} \frac{\partial^2 f}{\partial k_{oi}^2 \partial k_{oj}^2} Q_{ij} \quad i,j = 1,2,3 \quad (52)$$

Under isotropic conditions the velocity correlation tensor may be written in terms of two scalar functions $\bar{f} = \bar{f}(S_o, T)$ and $\bar{g} = \bar{g}(S_o, T)$, the longitudinal and lateral velocity correlation functions, respectively, for the diffusing particle [21,22]:

$$Q_{ij} = (\bar{f} - \bar{g}) \frac{k_{oi}^2 k_{oj}^2}{k_o^2} + \bar{g} \delta_{ij} \quad (53)$$

where

$$k_o^2 = k_{o1}^2 + k_{o2}^2 + k_{o3}^2.$$

Under conditions for spherically symmetric diffusion Eq. (52) reduces to an important new form [8].

$$\frac{\partial^2 f}{\partial T^2} = \frac{1}{k_o^2} \frac{\partial^2 [k_o^2 (\bar{f} - \bar{g}) f]}{\partial k_o^2} + \frac{1}{k_o^2} \frac{\partial}{\partial k_o} \left[k_o^2 \frac{\partial f \bar{g}}{\partial k_o} \right] \quad (54)$$

Multiplying Eq. (54) by $4\pi k_o^{n+2}$ and integrating over the range of k_o from 0 to ∞ provides the prescription for finding the ordinary differential equation governing the n-th radial moments when they exist. For $n = 2$ one has

$$\frac{\partial^2}{\partial T^2} E\left[\frac{S_o^2}{k_o^2}\right] = 2E[\bar{f} + 2\bar{g}] \quad (55)$$

Eqs. (49), (52), and (54) represent the Eulerian partial differential equations for one particle diffusion in terms of the Eulerian space-time correlation functions for the diffusing particle. It is possible to construct the Eulerian differential equations for many particle diffusion in an analogous manner [23].

8. CONCLUSION

The kinematic equations governing the motion of any number of marked particles in an infinite-state space have been formulated. Integrations over these hyperbolic partial differential equations provide partial differential equations governing the joint, marginal, and conditional probability densities of the particles in fewer dimensions. Moments generated on the probability densities provide the Eulerian and Lagrangian properties of the particle ensembles. Thus, the connections between classical continuum theories, using

MEYERS

partial differential equations, and more recent statistical approaches, using probability densities, correlations and generation of moments, have been established through a more general theory.

The imposition of formal constraints such as stationarity and homogeneity allowed a correspondence derivation of G. I. Taylor's diffusion equation from the new theory. It is believed that the further application of the new formalism of the differential equations in the state space will provide a powerful tool in both properly posing and solving such complicated problems as relative and meandering diffusion [24], the kinematics of turbulence flows, meteorological dynamics, and plasma interactions. Use of the new hierarchy of equations may be particularly pertinent in atmospheric diffusion applications where there exist scales as large or larger than any particular experiment, and a particular experiment may span several scales as a function of time. It is in these cases that parabolic approximations are most suspicious. In making a closure to the equations of motion, care must be taken not to violate seriously the new kinematic formulation. Perhaps the most useful aspect of the new theory is its simplicity and comprehensiveness. This allows physical insight into the process of connecting statistical and continuum formulations to experimental application.

ACKNOWLEDGMENT

The author would like to thank Dr. S. K. Kao, Professor of Atmospheric Sciences, University of Utah, for helpful guidance on, and review of, the paper; Dr. Harvey J. Fletcher, Professor of Mathematics, Brigham Young University, and Dr. John N. Cannon, Professor of Mechanical Engineering, Brigham Young University, for constructive critique on the mathematical and physical adequacy of the development; and Mr. William D. Ohmstede, Research Meteorologist, Department of the Army, Fort Huachuca, Arizona, for encouragement and many helpful discussions.

REFERENCES

- [1] Einstein, A., 1956: Investigations on the Theory of the Brownian Movement, New York, Dover Ed.
- [2] Chandrasekhar, S., 1943: Stochastic Problems in Physics and Astronomy, Reviews of Modern Physics, Vol. 15, No. 2, 89 pp.
- [3] Meyers, R. E., 1967: Derivation of an Atmospheric Hyperbolic Turbulent Diffusion Equation, U. S. Army ECOM Technical Report No. 6026.
- [4] Jones, D. S., 1966: Generalized Functions, N. Y., McGraw-Hill Book Co., Inc.
- [5] Lighthill, M. J., 1964: Fourier Analysis and Generalized Functions, Cambridge, Cambridge University Press, 79 pp.
- [6] Taylor, G. I., 1921: Proceeding London Math. Soc., 20, 196.
- [7] Wu, Ta-You, 1966: Kinetic Equations of Gases and Plasmas, Reading, Massachusetts, Addison-Wesley, p 17ff.

MEYERS

- [8] Meyers, R. E., 1970: Application of Hyperbolic Diffusion Theory: Gaussian Diffusion, To be published.
- [9] Wiener, N., 1966: Nonlinear Problems in Random Theory, Cambridge, Massachusetts, M. I. T. Press, 131 pp.
- [10] Fosdick, L. D., 1968: The Monte Carlo Method in Quantum Statistics, S I A M Review, Vol. 10, No. 3, p. 315.
- [11] Arley, N. K., and Buck, N. C., 1950: Probability and Statistics, N. Y., Chapman and Hall, Limited, p 23ff.
- [12] Brunk, H. D., 1965: An Introduction to Mathematical Statistics, Waltham, Massachusetts, Blaisdell Publishing Company, 429 pp.
- [13] Vlasov, A. A., 1959: Many-Particle Theory, Moscow-Leningrad, 1950, trans. AEC-tr-3406, Washington, D.C.
- [14] Courant, R., and Hilbert, D., 1962: Methods of Mathematical Physics, Vol. II, New York, John Wiley and Son, 830 pp.
- [15] Ornstein, L. S., and Uhlenbeck, G. E., 1930: On the Theory of the Brownian Motion, Physical Review, Vol. 36, No. 3.
- [16] Bharuchba-Reid, A. T., 1960: Elements of the Theory of Markov Processes and their Applications, New York, McGraw.
- [17] Meyers, R. E., and Fletcher, H. J., 1970: General Solution to Kinematic Equations, To be published.
- [18] Meyers, R. E., 1970: Kinematics of an Incompressible Fluid, To be published.
- [19] Batchelor, G. K., 1949: Australian J. Sci. Research, 2, 437.
- [20] Batchelor, G. K., 1951: Inst. Fluid Dynamics and Appl. Math., Lecture Ser. No. 4, University of Maryland, College Park.
- [21] Hinze, J. O., 1959: Turbulence, New York, McGraw-Hill Book Co., Inc., p 142ff.
- [22] Batchelor, G. K., 1959: The Theory of Homogeneous Turbulence, Cambridge, Cambridge University Press, 197 pp.
- [23] Meyers, R. E., and Fletcher, H. J., 1970: Many Particle Diffusion, To be published.
- [24] Gifford, F., 1957: Relative Atmospheric Diffusion of Smoke Puffs, Journal of Meteorology, Vol. 14, No. 5, 410.

THRESHOLD EFFECTS OF CHEMICAL
MIXTURES IN THE HCN LASER

GEORGE E. MORRIS, HAROLD JACOBS, CHARLES S. BRAND
THOMAS R. MOONEY, MAJ, USMA
U.S. ARMY ELECTRONICS COMMAND, ELECTRONIC COMPONENTS
LABORATORY, FORT MONMOUTH, NEW JERSEY

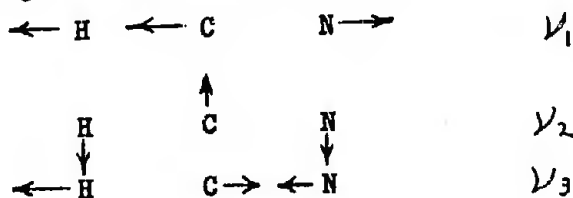
INTRODUCTION

The purpose of this report is to describe the basic mechanisms of the HCN laser which has two strong radiation lines of 337 μm and 311 μm . Experiments have been conducted in which flow rates have been varied and the power output noted as a function of tube pressure and current. This gives us insight into the chemical kinetics of CH_3CN (acetonitrile) as a fuel for the HCN laser.

The function and behavior of many impurity gases have also been studied, with CO_2 and O_2 giving enhancement in current threshold and power output. These additives have been studied over a wide range of mixture ratios, discharge currents, and total tube pressure. It is thought that the mechanism of enhancement of the HCN laser by CO_2 is a resonant transfer process.

MOLECULAR SPECTROSCOPY OF THE HCN MOLECULE

The molecular spectroscopy of the HCN laser has been developed by D. R. Lide and A. G. Maki¹. The laser action takes place between vibrational-rotational levels of the electronic ground state of HCN molecules. As a linear triatomic molecule, hydrogen cyanide has three normal modes of vibration. A symmetric mode along the axis of the molecule, a two-fold degenerate bending mode transverse to the axis, and an asymmetric mode along the axis. The frequencies associated with a particular type mode are designated as ν_1, ν_2, ν_3 , and are illustrated as



Each of these normal modes can be considered to be an harmonic oscillator approximately independent of the others. The vibrational levels of the HCN molecule is characterized by a triplet of integers representing the number of quanta of each of the three normal modes, for example (n_1, n_2, n_3) where n_1 represents the number of quanta in the symmetrical axial mode etc. The superscript notation, l , is an indicator of the degeneracy of the bending mode.

The vibrational levels responsible for submillimeter laser radiation are the (11^1_0) and the (04^0_0) . These are approximately 2800 cm^{-1} above ground state and are shown in Fig. 1. The vibrational levels are split due to molecular rotation into rotational levels labeled by appropriate J numbers. The transition $J = 10 (11^1_0)$ $J = 9 (04^0_0)$ results in the emission of $337 \mu\text{m}$ radiation.

The fact that $J = 10 (11^1_0)$ and $J = 10 (04^0_0)$ are nearly coincident enhances population inversion since a path is provided between the two vibrational levels. This exchange of vibrational energy is known as "Fermi Resonance" or "Fermi's Golden Rule",² and is believed to enhance population inversion.

The mechanisms for $337 \mu\text{m}$ radiation is as follows: A population inversion between $J = 10 (11^1_0)$ and $J = 9 (04^0_0)$ occurs resulting in radiation at $337 \mu\text{m}$ wavelength. Molecules which make this transition thermalize quickly, (in the order of 10^{-7} to 10^{-6} sec) due to collisions and transfer into the (11^1_0) vibrational band at $J = 10$. Therefore the depleted population inversion is rapidly replenished and this process can continue such that CW laser action is possible.

Lide and Maki¹ have further estimated that the gain at $337 \mu\text{m}$ should be 2.5 times the gain at $311 \mu\text{m}$ for the gas temperature at $300 - 400^\circ\text{K}$. As the rotational temperature changes due to molecular collisions, one would expect the relative gain of the two different wavelengths to vary. This will be verified from the experiments to be reported.

CHEMICAL MIXTURES - EXPERIMENTAL DESCRIPTION

The details of the laser used for all the chemical mixing experiments is shown in Fig. 2. A multiport input was provided for different gases and each one was monitored and controlled by calibrated flow meters. A constant flow was attained by using a 170 CFM pump. Radiation was coupled out through a 3 mm hole in one mirror and detected by a Golay cell. A far infrared monochrometer was used to insure that only the $337 \mu\text{m}$ line was observed. (There was the possibility the $10.6 \mu\text{m}$ radiation would be generated when CO_2 was added.) CH_3CN was used as the fuel for generating the HCN under direct current discharge.

A host of gases were mixed with the CH_3CN fuel at controlled mixture ratios, tube pressures, and discharge currents. These include CCl_4 , He, H_2O_2 , air, N_2 , CH_3OH , H_2O , CO, NH_4OH , CO_2 , O_2 . For each combination of CH_3CN and a test gas the laser performance was evaluated. We chose total relative power and current threshold, (the minimum current necessary to achieve oscillation) as the criteria for performance and compared the mixtures against the results of CH_3CN alone. The following statements can be made about the above additives. CCl_4 , N_2 when used as test gas decreased the relative output power. H_2O , CO, He, when added, appeared to be inert and passive to the laser performance and could be added in large amounts with little or no degradation. Only the last three, (NH_4OH , CO_2 and O_2) gave noticeable improvements in relative power and/or current threshold and are now discussed in more detail. Figures 3 through 8 are used to summarize the laser behavior.

The output from a lock-in amplifier was plotted vs. total discharge current in Fig. 3. The total pressure was held constant at 0.4 Torr. The control curve using CH_3CN alone, when compared with mixtures of CH_3CN and O_2 and CH_3CN and CO_2 , indicate that the presence of additives of CO_2 or O_2 greatly enhance performance. At lower levels the O_2 and CO_2 additives curves have the same effect. In Fig. 4, the threshold current required for oscillation for the same ratios as in Fig. 1 are noted as a function of total pressure. For all useable pressure ranges the presence of CO_2 or O_2 significantly decreases the threshold current. Again we note the similarity of the CO_2 and O_2 curves at pressure up to about 0.6 Torr. One interpretation which would explain the similarity of the effects of the O_2 and CO_2 additives is that during the electric discharge process in CH_3CN , the oxygen is converted to carbon dioxide, and the actual enhancement effects which were found are due to the presence of CO_2 .

There was the possibility that CO was being formed from the CO_2 or O_2 products, which might account for the observed improvements in laser operation. This was shown not to be the case. In Fig. 5 no significant enhancement was noted in relative output due to the presence of CO. Furthermore, in Fig. 6 all of the ratios of CH_3CN to CO tried gave about the same current threshold as the control curve of CH_3CN alone. Figures 7 and 8 show the effects of other mixture ratios of CO_2 and CH_3CN and O_2 and CH_3CN . In both cases the flow rate ratios of 1:1 resulted in the lowest current threshold over normally operating ranges, i.e., 0.3 Torr to 0.5 Torr. Small increases in relative power were noted for mixtures of NH_4OH and CH_3CN .

POSSIBLE MECHANISM OF CHEMICAL ADDITIVES

The exact cause for the decrease in current threshold and the shift to lower current ranges with the addition of O_2 and CO_2 is not known at this time. The fact that the same power can be

obtained from these mixtures at significantly lower current (See Fig. 3) with essentially the same tube voltage indicates that the laser efficiency has been increased.

There is the possibility that this increase in efficiency is due to a resonant transfer of energy from excited CO_2 or O_2 into the HCN vibrational spectrum. If this actually is occurring, then pumping to the (11^1_0) level or depletion of the (04^0_0) level would be more efficient and result in greater population inversions, hence greater laser efficiency. Weber and Deutsch³, have reported a vibrational energy level of CO_2 at about 2800 cm^{-1} , the (20^0_0) state. An energy level such as this could produce the desired interaction.

FLOW RATE EXPERIMENTS

Experiments to determine the performance of an HCN laser as a function of pump speed were also conducted. The set-up is shown in Fig. 9. A flow meter was calibrated to give the mass flow rates of CH_3CN and three mechanical pumps with a total capacity of 61 CFM were connected in parallel at the output end of the laser. Pump valves were used to control pumping speed. An oil bath was used to stabilize the temperature of the liquid fuel during evaporation.

The experimental procedure was as follows: Generally a particular laser tube pressure and discharge current were fixed as constant. Pumping speed was then adjusted by means of the pump flow valves shown in Fig. 9. The calibrated flow meter* was then adjusted to maintain the desired tube pressure. At each such point relative power of the $337 \mu\text{m}$ line and the $311 \mu\text{m}$ line was recorded. These lines are tuned independently by the motion of one mirror. A series of readings formed the curves shown in Fig. 10 through Fig. 12.

In Fig. 10 the variation of relative output vs. relative flow rate is shown for assorted discharge circuits at 0.4 Torr pressure. One sees approximately a linear increase with pumping speed for all currents. This variation continues until a power saturation is reached, (the point where power no longer increased with pumping speed.) Further pumping now causes a decrease in laser output of the $337 \mu\text{m}$ line. It is important to note that the relative flow rate of the CH_3CN which gives the maximum output increases with increasing discharge current. For example, the maximum power obtainable for a discharge current of 0.3 amps occurs for a relative flow rate of 5, and the maximum for 0.8 amp occurs at a flow rate of 7.5.

*The flow meter was calibrated in cc/sec of liquid CH_3CN under operating conditions. The calibration curve is linear for relative flow rates greater than 4.5 and follows the equation, volume flow = (Relative Flow Rate - 3.5) $\times 8.8 \times 10^{-4}$ cc/sec. Mass Flow = specific gravity of CH_3CN \times volume flow rate = $0.781 \times$ volume flow rate.

Fig. 11 shows the relative laser power output vs. relative flow rate for two different discharge currents (0.5 amps, 0.7 amps) at a constant tube pressure of 0.3 Torr. The 337 μm and the 311 μm lines are plotted together for comparison. Once again the sharp power saturation effect occurs for both radiation lines. The most interesting observation, however, is the following: (1) for very low flow rates, the 337 μm line was present but the 311 μm line was not; (2) the ratio 337 μm power/311 μm power decreases for increasing pump speed and in fact for the condition of 0.5 amps discharge the two lines become almost equal. The interpretation of these observations will be discussed in detail later in this paper.

The variation of relative output as a function of mass flow rate in cc/sec for different laser tube pressures is shown in Fig. 12. The current was held constant at 0.65 amps. A trend is shown from these pressure dependence curves where the maximum relative output shifts towards higher flow rates as tube pressure decreases. Also from Figures 10, 11, and 12 it is seen that one can increase the output power of the HCN laser by increasing pumping speed. This was found to be true for all pressure and current combinations considered; however, if one pumps too hard a saturation of power and even a decrease in output for high pumping will occur. An optimum pump speed exists and strongly depends on the particular total tube pressure and discharge current chosen.

THEORY OF PUMP RATE EXPERIMENTS

The general behavior of the flow rate curves, Figs. 10-12, can be divided into three general regions: I. The region which shows an approximately linear increase with pump speed; II. The region where saturation occurs and power does not increase with further pumping, and finally, III. The region where power decreases with added pumping.

Region I. What is occurring here is believed to be a cooling effect on the gases in the laser tube. This can be clarified as follows: As the laser continues to run the HCN molecules reach an equilibrium rotational temperature which is 300-400°K. When this occurs the two vibrational levels that are responsible for 337 μm laser action, namely the (11¹0) and (04⁰0) levels, thermalize at this temperature to a Boltzmann distribution, and the population inversion between the $J = 10$ (11¹0) and $J = 9$ (04⁰0) levels are determined by this distribution. As the pumping speed is increased the molecules spend less time in the discharge and are replaced more rapidly with "cool" HCN molecules. The lowering of the average gas temperature enhances the population inversion resulting in the observed power increase. This result is consistent with work reported by O. M. Stafsudd.⁴

The observed change in the ratio 337 μm power/311 μm power at increased pump speeds (Fig. 11) also indicates a gas cooling effect.

Lide and Maki¹ reported that the theoretical and experimental ratio is 2.5 for the temperature range from 300 - 400°K. We have found that for slow flow rates, i.e., a relative flow of 4.3, at a pressure of 0.3 Torr and 0.5 amps discharge current, that the ratio is about 2.5. However, the ratio was found not to remain constant and varied greatly. Since the 311 μ m and 337 μ m are parallel transitions, this change in the ratio of power is indicative of a rotational cooling effect. As the distribution of the laser levels change with a decrease in gas temperature, the population inversion increases and likewise power.

Regions II and III. It is theorized that the time necessary for the formation of HCN from the dissociation of CH₃CN is rather long. This conclusion is drawn from A. Murai⁵ where an HCN laser operating pulsed in a sealed-off condition at 0.6 Torr pressure required approximately 15 seconds after the first pulse was initiated before maximum output power was reached. This is thought to be caused by a gradual build-up in the HCN concentration. Now, if for a flowing system the molecules are swept through the interaction region faster than the formation rate for HCN, one would expect a decrease in the HCN concentration and an eventual decrease in output power, which was observed in these experiments. From the tube pressure, system volume, and mass flow rate of CH₃CN in cc/sec one can calculate the residence time for molecules, (the time a molecule spends in the laser before it is pumped out). This is done by taking the ratio, (total molecules in the system at a fixed pressure)/(molecules per second introduced into the laser system). Calculation of residence times at maximum output power vary between 2 and 14 seconds, for tube pressures between 0.25 Torr to 0.50 Torr respectively for 0.65 amps discharge current. This agrees with Murai's results and indicates long residence times for CH₃CN molecules are necessary for maximum output power.

Added information is given by the shift in the power peak towards higher flow rates when discharge current is increased or when tube pressure is lowered. (See Fig. 10 and Fig. 12). This occurs since for high currents the number of electron impacts are high and formation of large amounts of excited HCN take place more rapidly. Similarly by lowering the tube pressure the mean free path of electrons becomes longer and the average electron energy again goes up as in the high current case, thus the pump speed can be increased since the formation rate is increased. Both conditions have been observed experimentally.

CONCLUSIONS

The mechanism of the HCN laser has been discussed. We conclude that when either CO₂ or O₂ is used as an additive gas to CH₃CN in an HCN laser, a lowering of current threshold by 50% is observed. Also for fixed currents, a higher relative output power is obtainable. There is an indication that the enhancement

mechanism is related to resonant transfer processes.

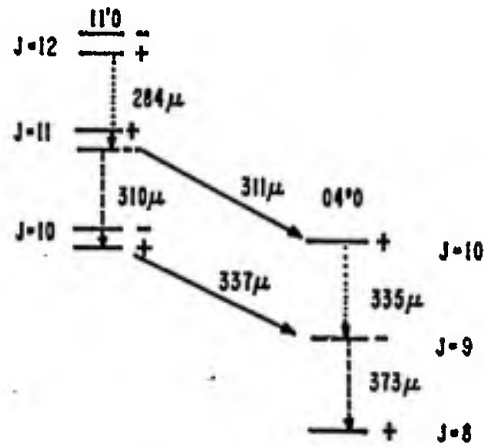
With respect to the flow rate experiments, one can obtain an increase in power from the CH_3CN (HCN) laser by increasing pump speed. However, there is a limit to this effect, where further increases in pump speed can bring about a decrease in power. The mechanism for this situation is due to the slow formation rate of HCN molecules after CH_3CN decomposition. Experiments indicate that several seconds are required to form substantial densities of HCN after the electric discharge has been started.

ACKNOWLEDGMENTS

The authors gratefully acknowledge the contributions of Mr. J. C. Danielson, Mr. J. D. Schumacher, Dr. Ronald C. Hofer, and MAJ Charles Green in this study.

REFERENCES

1. D. R. LIDE and A. G. MAKI, "On the Explanation of the So-Called CN Laser," *Applied Physics Letters*, Vol. II, No. 2, 15 July 1967, pp. 62-64
2. A. S. DAVYDOV, "Quantum Mechanics," Pergamon Press Ltd., 1965, pp. 294-295.
3. M. J. WEBER and T. F. DEUTSCH, "Pulsed and Steady State Infrared Emission Studies of CO_2 Laser Systems," *IEEE Journal of Quantum Electronics*, Vol. QE-2, No. 9, Sep 1966, pp. 369-375.
4. O. M. STAFSUDD and Y. C. YEH, "The CW Gain Characteristics of Several Gas Mixtures at 337 μm ," *IEEE Journal of Quantum Electronics*, Vol. 5, No. 7, July 1969, pp. 277-380.
5. A. MURAI, "Long Time Operation of HCN Laser by Pulsed Discharges in a Seal-Off Tube," *Physics Letters*, Vol. 28A, No. 8, 27 Jan 1969, pp. 540-541.



ENERGY DIAGRAM OF HCN SPLITTINGS
OF THE 11'0 LINES ARE DUE TO I-TYPE DOUBLING

- PUMP TRANSITIONS
- LINES PREVIOUSLY SEEN PULSED
- NEW SUBMILLIMETER TRANSITIONS

Fig. 1

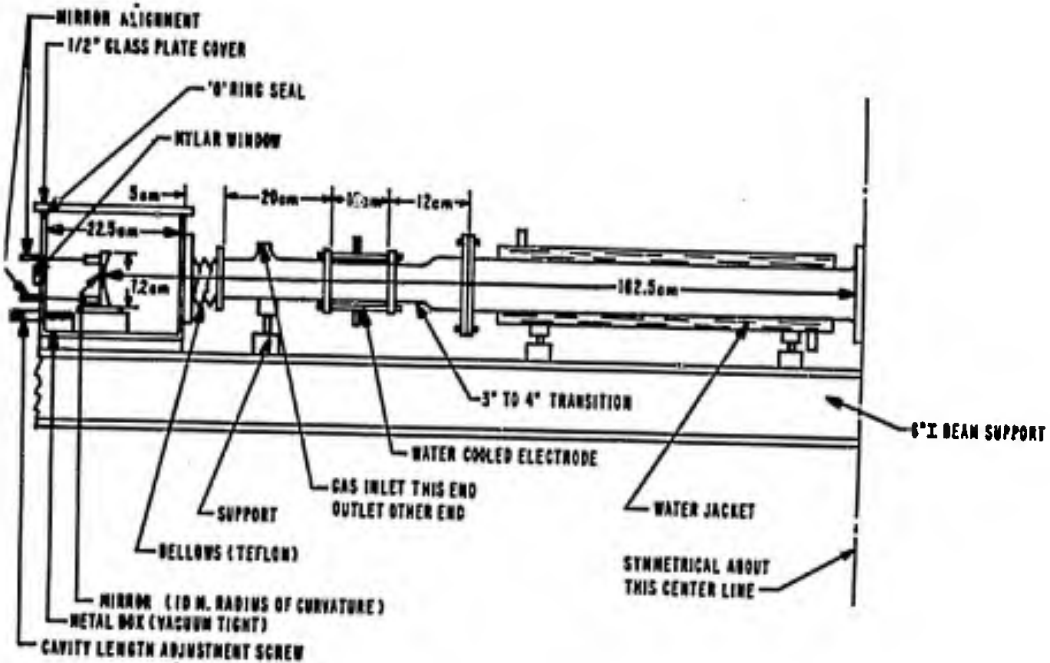


Fig. 2 - HCN Laser used in gas mixture experiments.

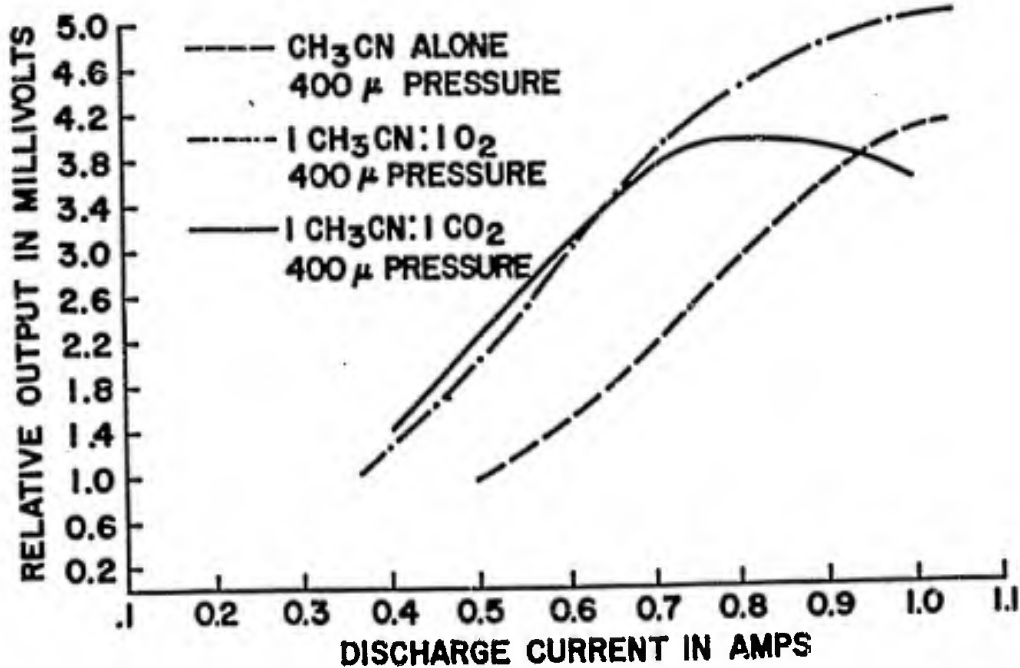


Fig. 3 - Relative output vs. discharge current for CO₂ and O₂ mixtures.

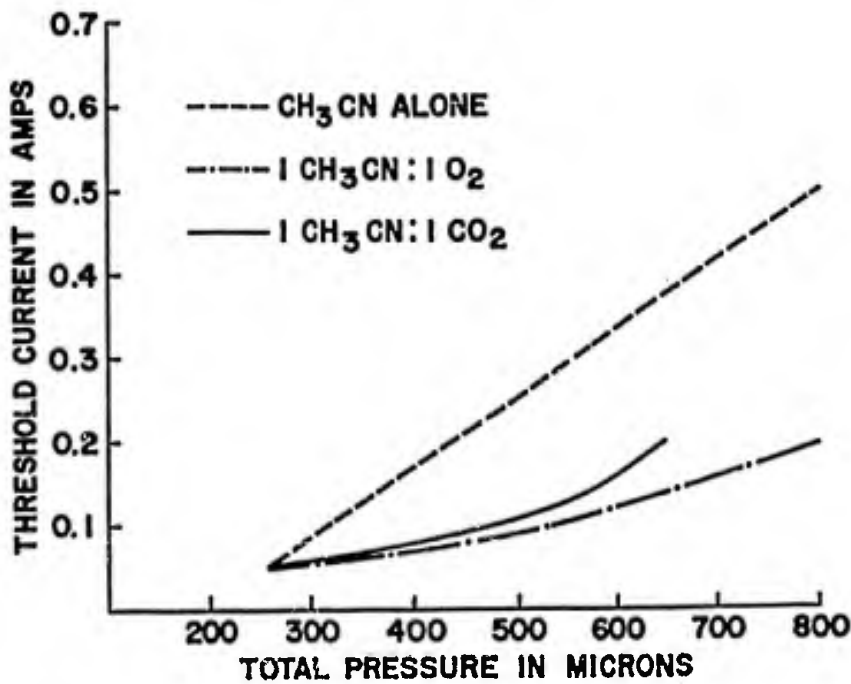


Fig. 4 - Comparison of laser threshold current for CO₂ and O₂ mixtures.

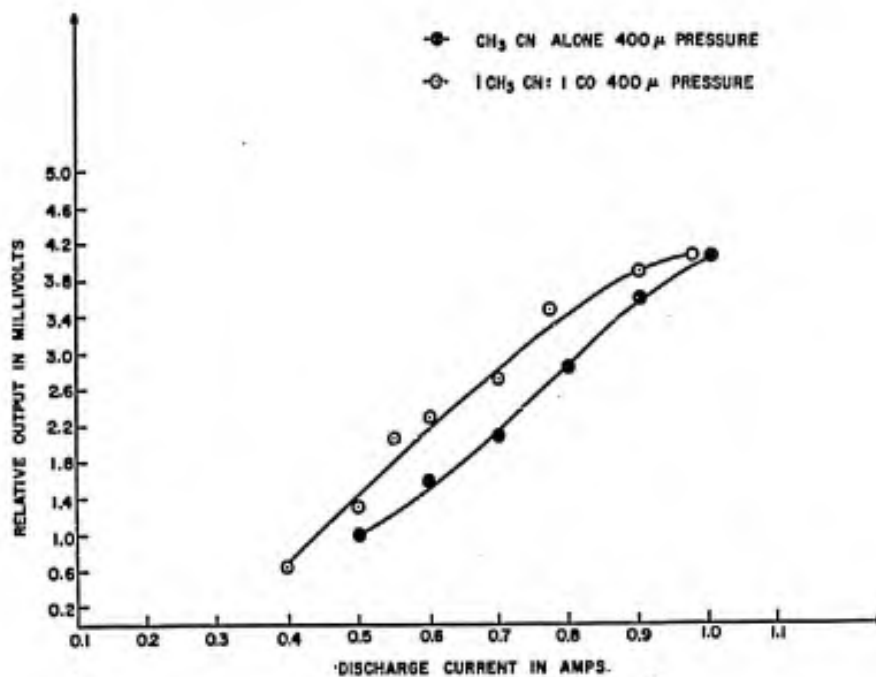


Fig. 5 - Relative output vs. discharge current for CO mixture and CH₃CN.

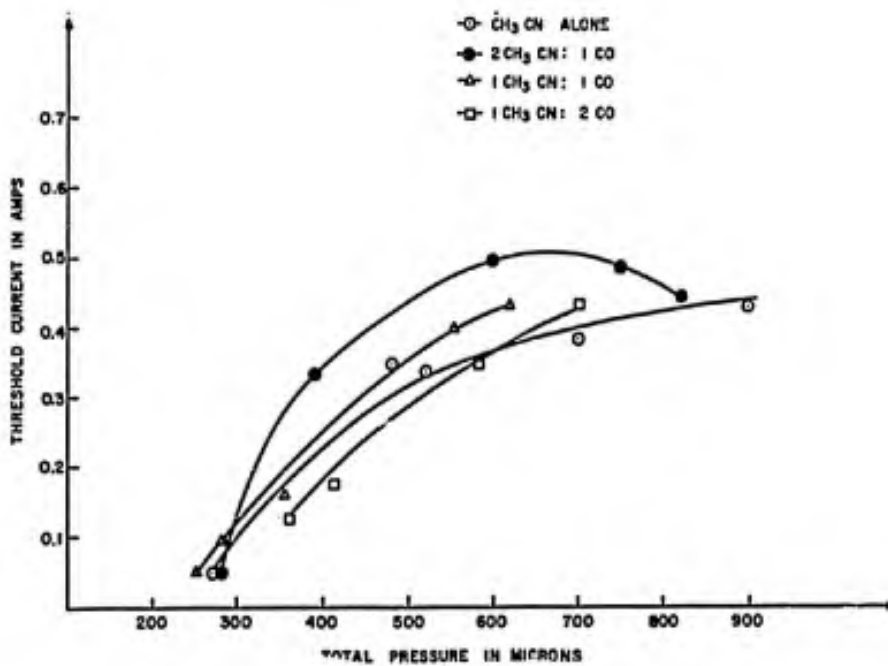


Fig. 6 - Threshold current vs. tube pressure for CO mixtures.

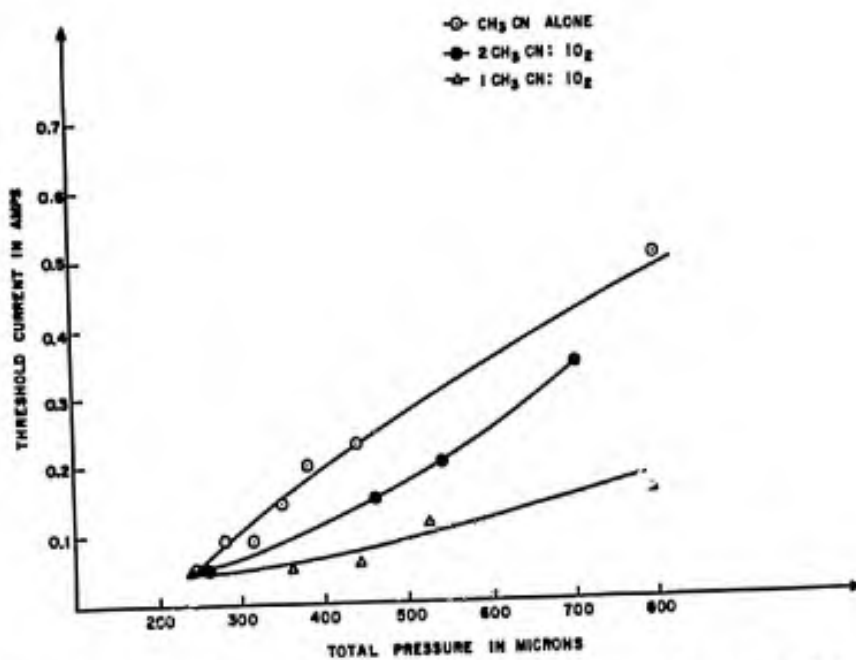


Fig. 7 - Threshold current vs. tube pressure for O₂ mixtures.

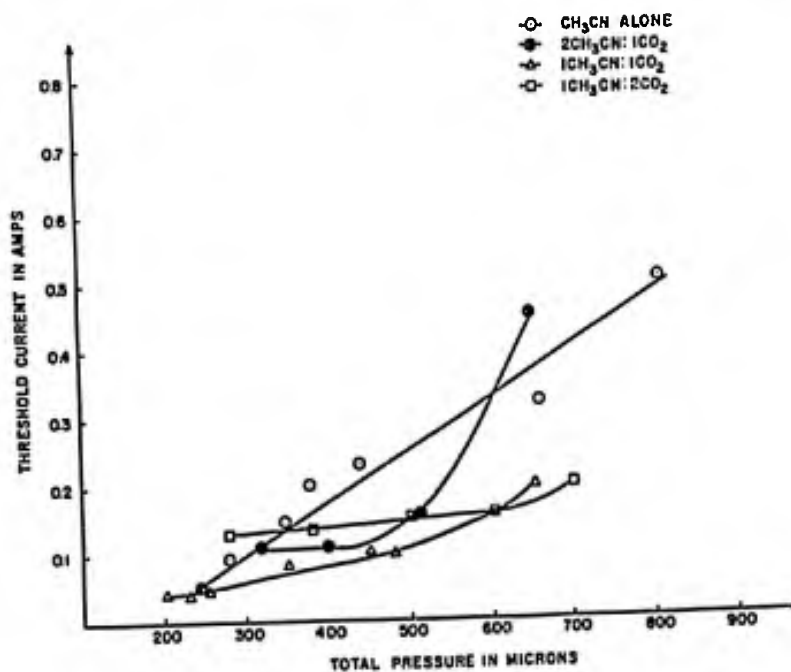


Fig. 8 - Threshold current vs. tube pressure for CO₂ mixtures.

MORRIS, JACOBS, BRAND, MOONEY

M1- FIXED MIRROR 4 METERS CURVATURE (POLISHED STEEL)
 M2- TUNABLE MIRROR 4 METERS CURVATURE WITH 3mm COUPLING HOLE (POLISHED STEEL)
 ELECTRODES - ALUMINUM

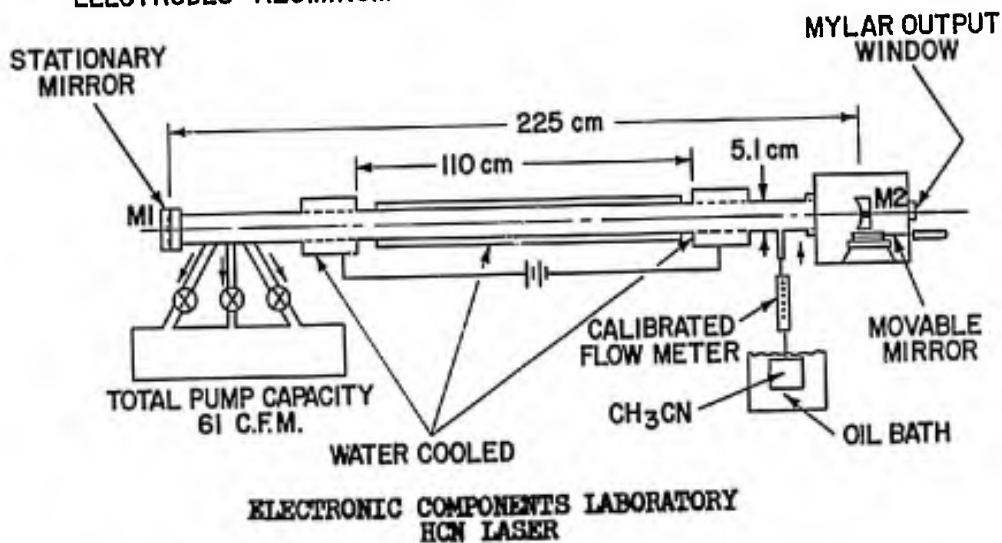


Fig. 9 - HCN laser used in flow rate experiments.

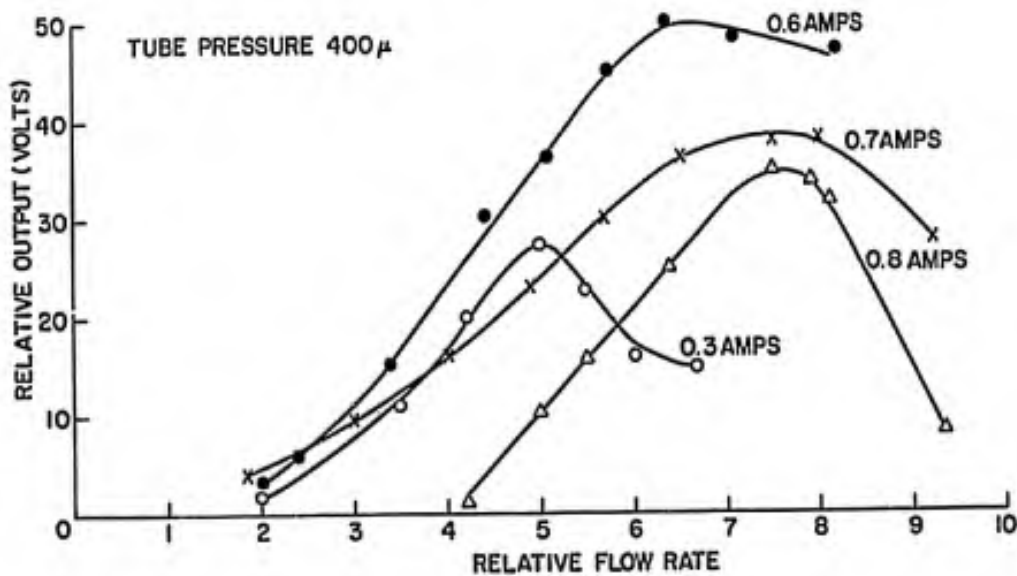


Fig. 10 - Variation in 337 μm power with flow rate.

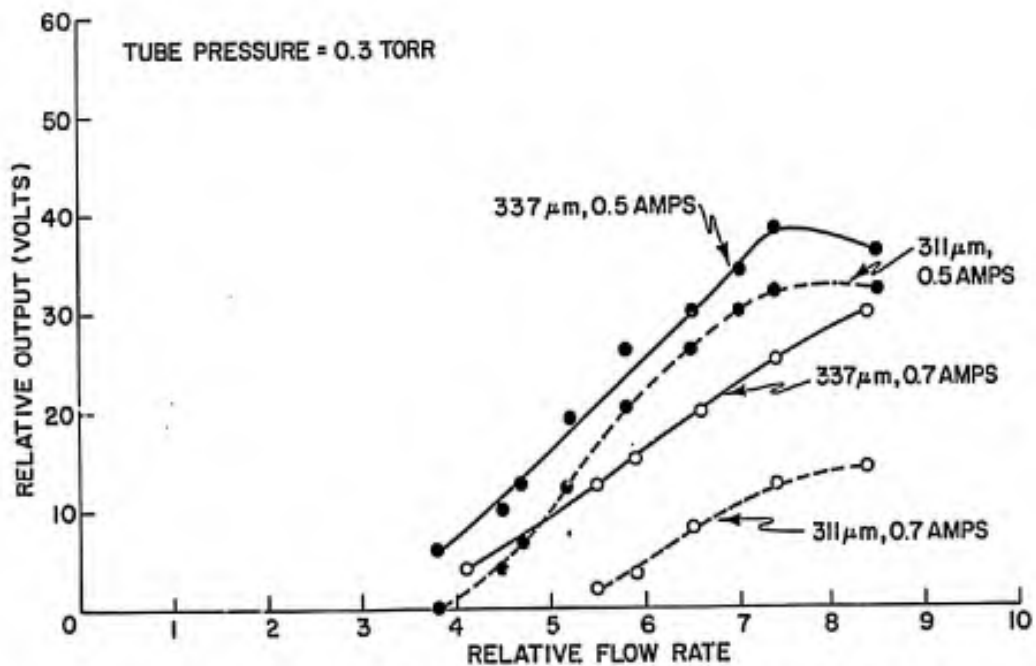


Fig. 11 - Variation in 337 μm and 311 μm power with flow rate.

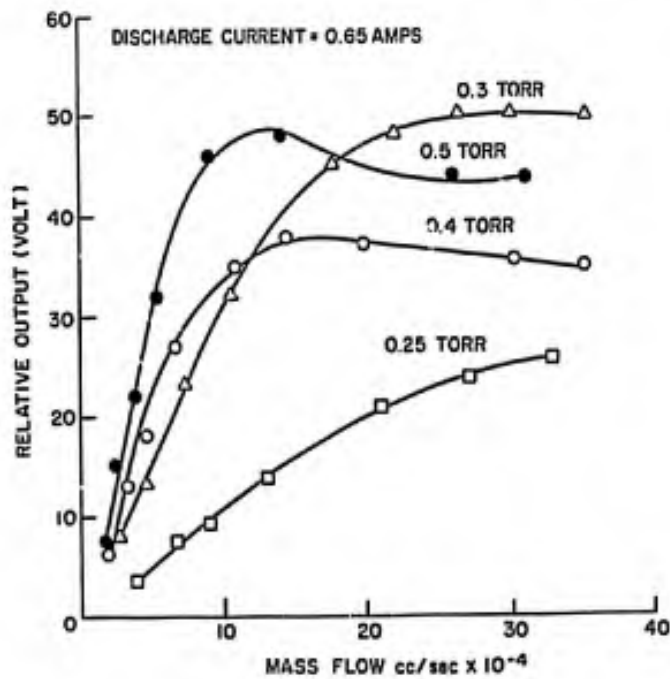


Fig. 12 - Power vs. mass flow rate for 337 μm line.

CONFORMATIONAL STUDIES ON THE ACTIVE SITE OF ACETYLCHOLINESTERASE
BY ELECTRON PARAMAGNETIC RESONANCE

JOEL D. MORRISETT, CPT, MSC, CLARENCE A. BROOMFIELD AND
BRENNIE E. HACKLEY, JR.
MEDICAL RESEARCH LABORATORY
EDGEWOOD ARSENAL, MARYLAND

The role of acetylcholinesterase (Acetylcholine acetylhydrolase, E.C. 3.1.1.7) in the transmission of nervous impulses at the synaptic junction has been widely studied and its importance to animal life has been well established. Inactivation and reactivation of the functioning state of this enzyme have been examined in detail and such processes bear great relevance to this nation's military posture, both defensive and offensive.

Of special concern to us from a defensive point of view is the problem of the so-called "refractory" anticholinesterases. Poisoning by these agents is not reversed by oxime therapy because of the phenomenon of "ageing", the spontaneous dealkoxylation or dealkylation from the phosphonyl group attached to the active site serine residue. In order to develop a more effective defense against agents of this type, it is necessary to have a complete understanding of the chemical reactions involved, the conformational changes in the enzyme which might occur in the course of these reactions, and the relationships between the acetylcholinesterase molecule and its environment in the living cell.

Our laboratories have undertaken studies directed toward the elucidation of structure-function relationships in this enzyme. In particular, we are interested in the geometry and stereochemistry of the active site, which is believed to contain (a) an anionic binding site involving glutamic or aspartic acid, (b) an activating group such as the imidazole of a histidine residue, and (c) an esteratic site involving a seryl hydroxyl group.

In order to examine the active site region of this enzyme, we selected the spin-labeling method developed by McConnell and his associates at Stanford University. Several factors influenced our choice of this technique: (1) A method with high sensitivity was needed because, when in concentrated solution,

MORRISETT, BROOMFIELD and
HACKLEY

the membrane-free enzyme tends to undergo aggregation which often results in irreversible denaturation of the native tertiary structure. (2) We recognized that this enzyme is usually localized on a membrane in the living organism and that the conformation of the active site region of the membrane-bound enzyme might be significantly different from that of the purified, membrane-free molecule. Thus, we needed a single method which could be used to study both optically transparent solutions of the enzyme and optically opaque suspensions of membranes. Electron paramagnetic resonance (EPR) suited our needs admirably. (3) Finally, we desired a method which would be highly specific and allow us to study only acetylcholinesterase, and no other contaminating species which might be present. We were able to fulfill this requirement by combining the very selective phosphonofluoridate moiety with a nitroxyl radical, thereby producing a spin-label capable of tagging the reactive seryl residue at the active site.

We have prepared two such spin-labels (I, II) of widely differing size (Figure 1). Their mode of reaction is illustrated in Figure 2.

Spin-labels behave as molecular telephones, reporting to the investigator the nature of the local environment in which they reside. In the case of acetylcholinesterase, one may study the conformation at the active site of the enzyme by comparing the line shape of the EPR spectrum of the free, unbound nitroxyl radical to that of the covalently attached spin probe. The unbound label gives a simple spectrum in which the three narrow lines are of approximately equal width and height (Figure 3). However, when the label is attached to the macromolecule, its freedom of motion becomes dependent upon the tumbling motion of the macromolecule and the motional freedom around the bond of attachment. This resulting restriction in the motion of the radical is reflected in a broadening of the three principal hyperfine lines of the spectrum. Two excellent reviews and references therein adequately describe additional theoretical considerations relevant to the method of spin-labeling (1,2).

In preliminary experiments, we spin-labeled 4 types of membranes, which are known to have acetylcholinesterase bound to their surfaces. Among these were human erythrocytes, ox erythrocytes, rat brain nerve ending particles and particles from the electric organ of the eel, *Electrophorus electricus*. In a typical experiment, the membranes were equilibrated with the desired buffer, then treated with the nitroxyl phosphonate. Excess spin label was removed by sedimenting the membranes by centrifugation, discarding the supernatant, and resuspending the pellet in fresh buffer. Normally, the wash procedure is repeated six times, all operations being carried out at 5°. Figure 4 shows the EPR

MORRISETT, BROOMFIELD and
HACKLEY

spectrum obtained from spin-labeled nerve ending particles in 0.1 M phosphate buffer, pH 7.4. The spectrum indicates that the radical possesses a high degree of mobility and is not greatly constrained by attachment to the enzyme. Since the high field line is the most sensitive to this freedom of motion, we have used its relative magnitude (as compared to the middle field line) as a semi-quantitative measure of the degree of mobility of the spin label. For this spectrum that ratio is 0.72, compared to a ratio of 0.92 for unbound reagent. When the particles are equilibrated with Earle's solution, a physiological buffer containing ions essential for respiration, this ratio is diminished to 0.51 (Figure 5). This decreased mobility for the spin probe may result from either (1) a nearby conformation change on the enzyme and/or membrane which is induced by the bridging effect of the divalent cations present in the buffer, or (2) the binding of the cations at the nearby anionic site. Of all the membrane systems we have studied by spin labeling, the nerve ending particles (synaptosomes) are the most difficult to prepare, yet they are richest in membrane-bound acetylcholinesterase. However, these membranes also contain lower levels of other enzymes, which are known to react with fluorophosphonates and thus can be labeled by the nitroxylorganophosphonate. In order to evaluate the magnitude of this problem, a critical control experiment was performed. The membranes were first washed twice with and resuspended in buffer containing 10^{-6} M 1,5-bis(4-allyldimethyl-ammoniumphenyl) pentan-3-one dibromide (III, Figure 6). At the concentration used, this compound specifically and reversibly inhibits acetylcholinesterase while leaving unaffected other esterases which might be present. While the active site of acetylcholinesterase was reversibly protected by this inhibitor, the other esterases which might have been present were irreversibly blocked with diisopropylphosphonofluoridate (DFP). The reversible inhibitor was then removed by two wash cycles and the membranes were spin-labeled in the usual manner. The signal of the resulting EPR spectrum (Figure 7) was significantly reduced in amplitude, yet the overall spectral line shape remained unchanged. This result indicated that spin-labeled esterases on the membrane other than acetylcholinesterase do not significantly alter the spectrum or make little contribution to it.

In most cases, the EPR spectrum of the spin-labeled membranes indicated that the radical was highly mobile. In fact, we were not absolutely certain that all excess unattached spin-label had been washed out until we performed a control experiment to evaluate this possibility. In this case, the suspension of nerve ending particles was initially treated with diisopropylphosphonofluoridate (DFP), then treated with the spin-labeling reagent in the routine manner, and finally washed six times with buffer. The EPR signal of membranes so treated was barely detectable at the spectrometer conditions normally employed.

MORRISETT, BROOMFIELD and
HACKLEY

One of the difficulties encountered in working at the pH region where acetylcholinesterase exhibits its highest enzymic activity, i.e., pH 7.0 - 7.5 is that the phosphorylated enzyme can undergo "ageing", resulting in release of the nitroxyl radical from the enzyme while the phosphoryl moiety remains attached at the active site serine residue. Figure 8 indicates three mechanisms whereby this process may occur. The first mechanism proceeds by acid catalysis and is highly dependent upon the stability of the carbonium ion which can be formed by cleavage of the carbon-oxygen bond. The second mechanism employs base catalysis with nucleophilic displacement of the alkoxide by hydroxide ion, and is dependent on the leaving properties of the alkoxide. The third reaction shows a base-catalyzed elimination mechanism which is governed by the acidity of the proton alpha to the carbon-oxygen bond. It has been demonstrated that for phosphorylated acetylcholinesterase, the first mechanistic route of ageing is the most important below pH 7.5.

Fleisher and Harris have described experiments in which this problem was obviated by performing inhibition studies in 0.01 M borate buffer at pH 8.8 and 5° (4). Under these conditions, little if any ageing occurs with methylpinacolylphosphonofluoridate, which is known to age quite rapidly under physiological conditions. When synaptosomes were spin-labeled under these conditions, the resulting EPR spectrum (Figure 9) had both the same line curvature and almost the same ratio (0.49) of high and center field lines as synaptosomes labeled in the physiological buffer at pH 7.4 (0.51). This result demonstrated that we were, in fact, observing only signals from radicals attached to the membrane-bound enzyme.

When the temperature of spin-labeled synaptosomes was raised from 5° to 25° for 24 hours, the resonance signal almost disappeared (Figure 10a). However, upon addition of the nonionic detergent, Lubrol W, to the preparation, the signal became more discernable (Figure 10b). As the concentration of detergent was increased, the amplitude of the signal increased concomitantly (Figure 10c). It is significant to note that the diminished signal generally possesses the same line shape as that displayed before the temperature was raised. This indicates that the diminution of the signal is not caused by conformational changes which restrict the motion of the spin probe. The signal recovered after the detergent treatment contains two spectral components, one corresponding to unbound radical resulting from ageing, and the other corresponding to the remaining membrane-bound radical. Thus, the question arises as to how the spectrum can be so drastically reduced to a signal possessing the original mobility. Other workers have also observed this time-dependent loss of spin concentration in biological systems. Drott and Lee have observed the slow disappearance of the signal from spin-labeled cytochrome c bound to

MORRISETT, BROOMFIELD and
HACKLEY

submitochondrial membrane fragments (5), and Calvin, et al. have reported the reduction of nitroxyl radicals in lobster nerve (6). It appeared to us that these observations of signal diminution or loss might be related to the presence of sulfhydryl groups on the membranes. To test this possibility several experiments were performed. In the first, spin-labeled nerve ending particles were treated with iodoacetamide under conditions normally used to block reactive sulfhydryl groups. The resulting preparation did not suffer drastic signal diminution when held at 25° for 24 hours. Furthermore, the EPR spectrum of these particles indicated that the spin probe was in a slightly more confined environment than before the alkylation of the thiol moieties (Figure 11). In a second confirmatory experiment, soluble, membrane-free acetylcholinesterase was labeled with I. Permitting a solution of this material to sit at 25° for 24 hours produced absolutely no change in the EPR spectrum. The reduction of nitroxyl radicals by the thiol function has been demonstrated unequivocally (7). Presumably, the reaction proceeds via the coupling of the thiol and nitroxyl radicals destroying the paramagnetic center of each, thereby resulting in the diminution of the resonance signal. Clearly, the experimental results just described and the operation of this mechanism require that the sulfhydryl group and the nitroxyl moiety be in close proximity on the membrane, and in an environment which excludes other agents which might result in further oxidation or irreversibility of the process. It is logical to expect that when the detergent is added to the suspension of spin-labeled membranes which has lost its EPR signal, disruption of the native membrane and/or enzyme conformation occurs, thereby making the sulfhydryl and nitroxyl groups more distant from each other. This would result in the regeneration of the original paramagnetic radicals. Several additional experiments have been designed to provide further corroboration for this hypothesis and are now in progress.

Finally, we attempted to answer the question of whether or not the conformation at the active site of acetylcholinesterase is affected by dissociation of the enzyme molecules from the membrane by comparing the ESR spectrum of the solubilized enzyme with the spectra of the membrane-bound preparations just discussed. A partially purified preparation of electric eel acetylcholinesterase was spin-labeled at pH 8.8 to minimize "ageing" of the labeled enzyme. After 5 minutes the enzymic activity had dropped to less than 1% of the original value, and the reaction mixture was immediately passed through a column of Sephadex G-25 to remove excess reagent. The EPR spectrum of the resulting spin-labeled enzyme, (Figure 12) was similar, but not identical to that obtained with the membrane-bound enzyme. It is noteworthy that this spectrum contains a broad component on the low-field side of the first principal line and between the first and second lines. This indicates that, most probably, two different spectral components are superimposed upon each other; the narrow component results from

MORRISETT, BROOMFIELD and
HACKLEY

a freely rotating spin-label and the broader component comes from a probe residing in a more confined environment. The concept of two distinctive types of active sites on this enzyme is supported by the work of Leuzinger et al. who have examined the C-terminal residues by hydrazinolysis and carboxypeptidase A digestion and find that there are two types of polypeptide chains, suggesting that the enzyme has a dimeric hybrid structure (8).

From these studies, we have gained several new pieces of information about the active site of acetylcholinesterase. First, the active site appears to be quite spacious and/or located superficially on the enzyme. Second, the conformation at the active site is detectably, but not greatly affected by removing the enzyme molecule from the membrane. Third, there appears to be on the membrane a sulfhydryl group located close enough to the active site of the membrane-bound enzyme to interact with the attached nitroxyl radical.

We have come to the conclusion that perhaps a more space-filling spin probe such as II would be more sensitive than I to conformational changes in the relatively open active site region. For this reason, we have recently prepared this new steroidal phosphonyl nitroxide and are using it in experiments currently underway.

ACKNOWLEDGEMENTS

We wish to express our thanks to Mr. Michael Lochner for his technical assistance, to Dr. Edward Poziomek for the use of his electron paramagnetic resonance spectrometer, and especially to Mrs. Margaret Filbert for supplying the membrane preparations and for her helpful suggestions.

MORRISETT, BROOMFIELD and
HACKLEY

REFERENCES

1. Hamilton, C.L. and McConnell, H.M., in A. Richard, N. Davidson (editors). Structural Chemistry and Molecular Biology, W.H. Freeman and Company, San Francisco, 1968, p. 115.
2. Griffith, O.H. and Waggoner, A.S., Accounts Chem. Res., 2, 17 (1969).
3. Cohen, J.A. and Oosterbaan, R.A., in O. Eichler and A. Farah (editors). Handbook der Experimentellen Pharmakologie, Erganzungswerk XV, Berlin, 1963, pp 104 and 324.
4. Fleisher, J.H. and Harris, L.W., Biochem. Pharmacol., 14, 641 (1965).
5. Drott, H.R. and Lee, C.P., private communication.
6. Calvin, M., Wang, H.H., Entive, G., Gill, D., Ferruti, P., Harpold, M.A. and Klein, M.P., Proc. Nat. Acad. Sci. U.S.A., 63, 1 (1969).
7. Morrisett, J.D. and Drott, H.R., J. Biol. Chem., 244, 5083 (1969).
8. Leuzinger, W., Goldberg, M. and Cauvin, E., J. Mol. Biol. 40, 217, (1969).

MORRISETT, BROOMFIELD and
HACKLEY

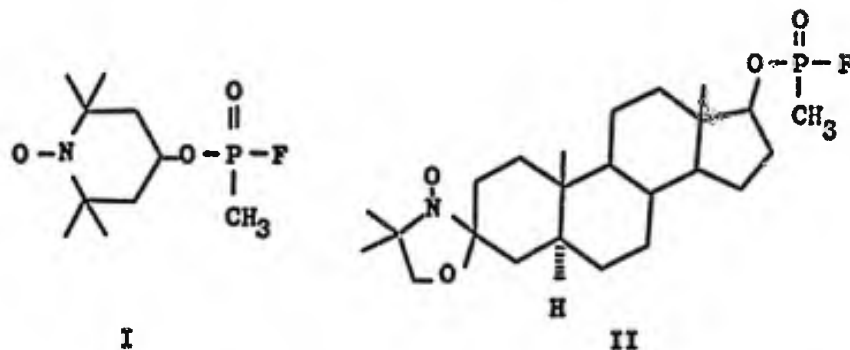


Figure 1: 1-oxyl-2,2,6,6-tetramethyl-4-piperidinylmethylphosphono-
fluoridate (I) and N-oxyl-4',4'-dimethyloxazolidine of
5 α -androstan-3-one-17 β -ol (II).

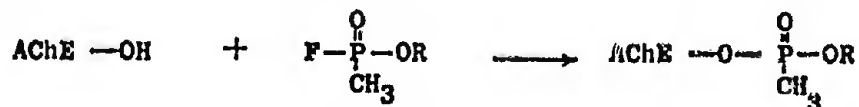


Figure 2: Mode of reaction of the nitroxylorganophosphonates (I and
II) with acetylcholinesterase.

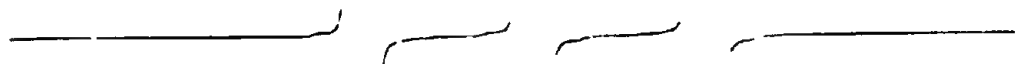


Figure 3: EPR spectrum of I in 0.1M phosphate buffer, pH 7.4.



Figure 4: EPR spectrum of nerve ending particles spin-labeled with I_1 in 0.1 M phosphate buffer, pH 7.4.

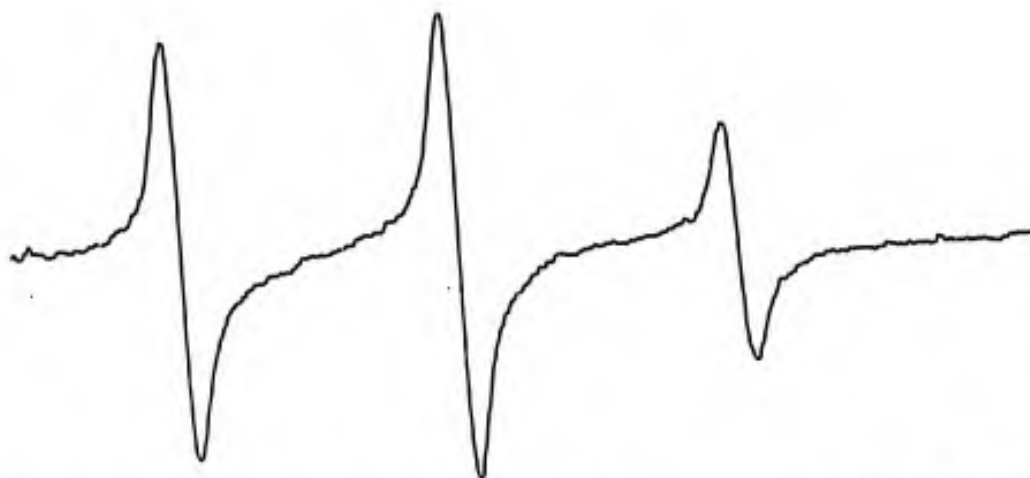
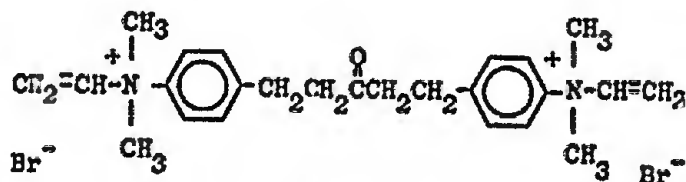


Figure 5: EPR spectrum of nerve ending particles spin-labeled with I_1 in Earle's physiological buffer (pH 7.4) containing ions essential for respiration.

MORRISETT, BROOMFIELD and
HACKLEY



III

Figure 6: 1,5-BIS (4-allyldimethylammoniumphenyl) pentan-3-one dibromide (III). This compound inhibits acetylcholinesterase at 10^{-8} M and butyrylcholinesterase at 10^{-5} M. At 10^{-6} M the inhibition ratio is AChE to BChE, 217,000 to 1 (3).

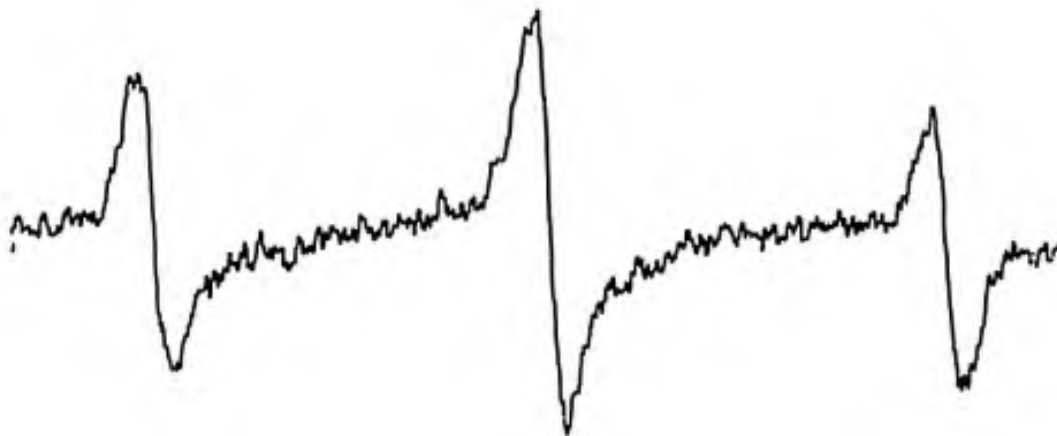


Figure 7: EPR spectrum of nerve ending particles pretreated with diisopropylphosphonofluoridate in the presence of inhibitor (III), then spin-labeled with I in Earle's buffer, pH 7.4, in the absence of III.

MORRISETT, BROOMFIELD and
HACKLEY

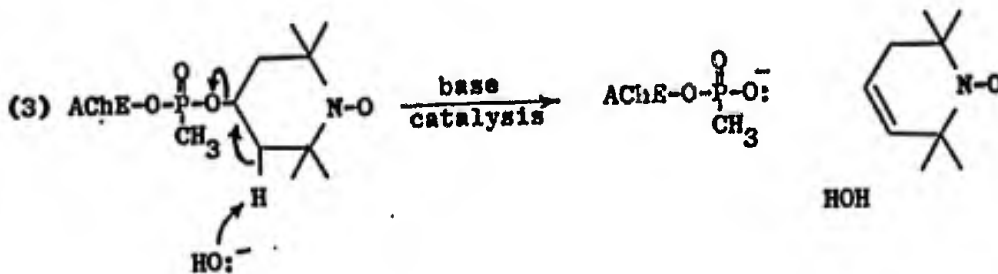
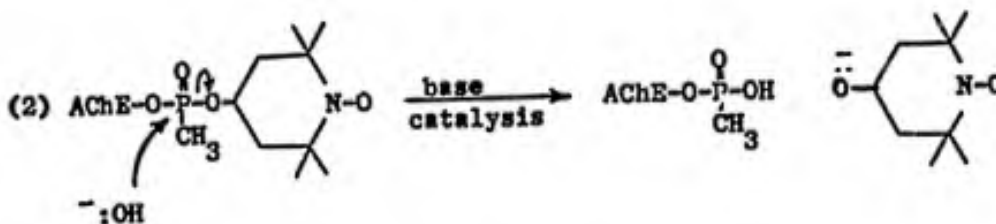
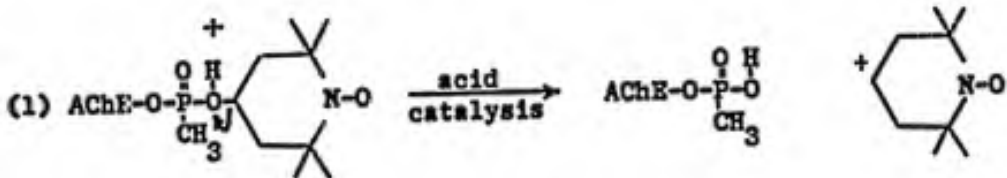


Figure 8: Mechanistic routes by which ageing may proceed.

MORRISETT, BROOMFIELD and
HACKLEY

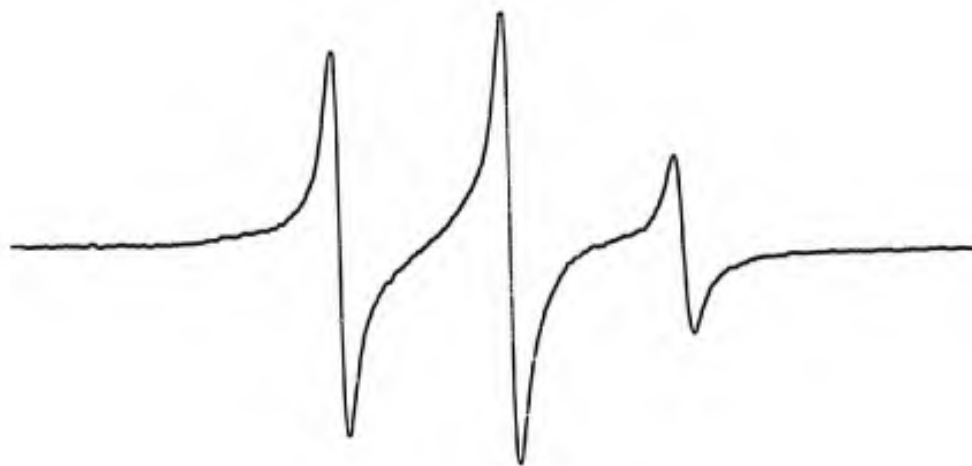


Figure 9: EPR spectrum of spin-labeled nerve ending particles in 0.01 M borate buffer, pH 8.8 (conditions of minimal ageing),

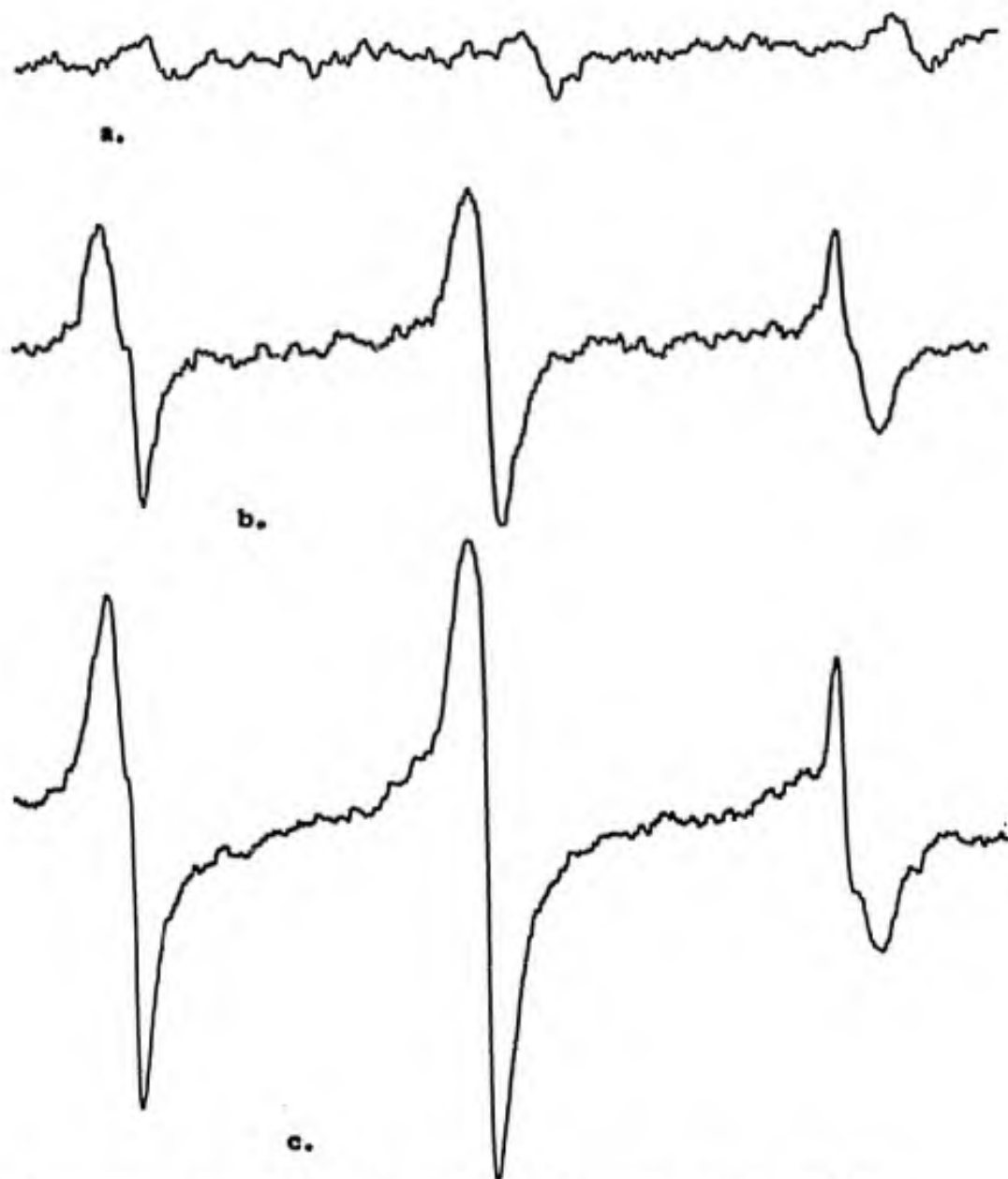


Figure 10: EPR spectrum of spin-labeled nerve ending particles (a) after temperature was raised from 5° to 25° for 24 hours, (b,c) after 24 hours at 25° then addition of increasing amounts of the non-ionic detergent, Lubrol W.

MORRISETT, BROOMFIELD and
HACKLEY

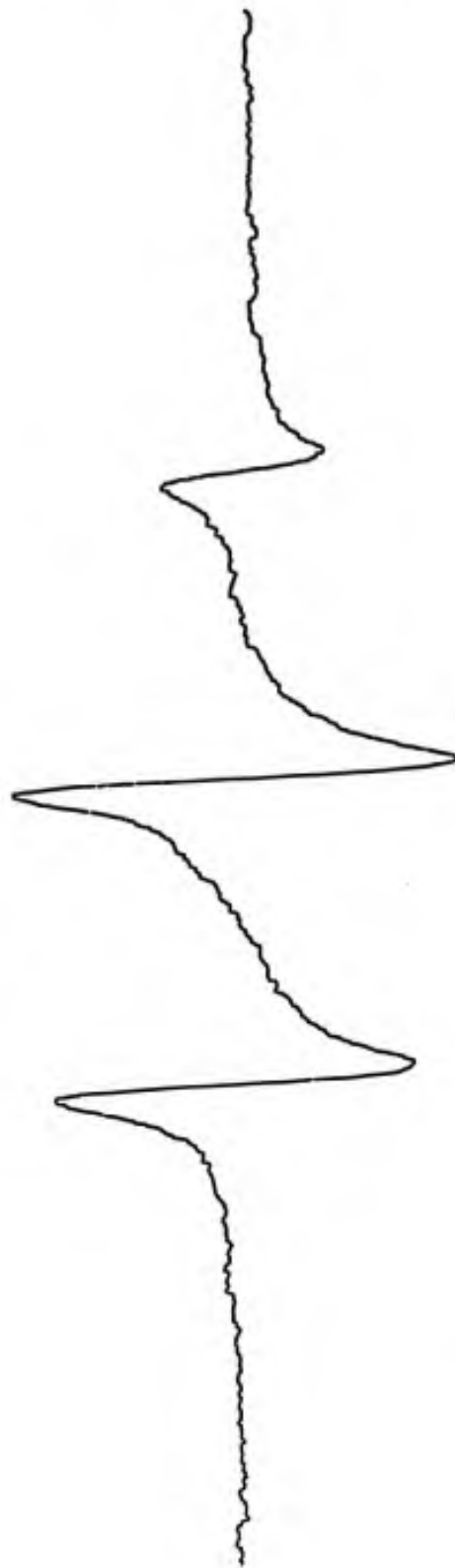


Figure 11: EPR spectrum of nerve ending particles first spin-labeled with I then alkylated with iodoacetamide in Earle's buffer, pH 7.4.

MORRISETT, BROOMFIELD and
HACKLEY

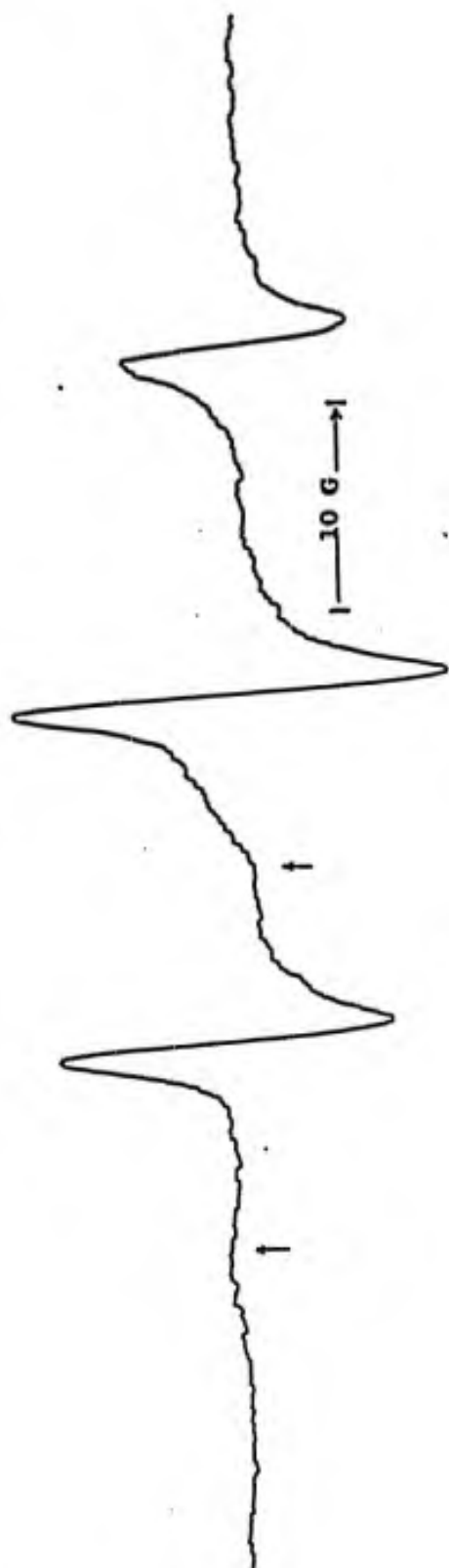


Figure 12: EPR spectrum of soluble, membrane-free acetylcholinesterase (from electric eel) spin-labeled with I in 0.1 M KCl, 0.01 M borate, pH 8.8.

THE PREPARATION AND PROPERTIES OF NEW OXIDIZERS FOR PROPELLANTS,
 $\text{NH}_4\text{ClO}_4\text{-KClO}_4$ and $\text{NH}_4\text{ClO}_4\text{-NH}_4\text{NO}_3$ MIXED CRYSTALS

SCOTT I. MORROW
PICATINNY ARSENAL
DOVER, N. J.

INTRODUCTION:

In spite of intensive efforts to synthesize new oxidizers in the post-Sputnik era, no new species has been obtained to rival in a practical way the old stand-by, ammonium perchlorate, for use in solid propellant rockets. In a new approach to this problem we proposed that new mixed crystal oxidizer "alloys" could be made from isomorphous components. This indeed proved to be the case for we were able to demonstrate that ammonium perchlorate could be stabilized and rendered less moisture sensitive by incorporating its isomorph, potassium perchlorate into its crystal lattice. Success in this work (8) prompted us to extend our investigations to include synthesis and characterization of ammonium perchlorate-ammonium nitrate oxidizer "alloys".

EXPERIMENTAL PROCEDURE:

Preparation of Ammonium Perchlorate-Potassium Perchlorate Mixed Crystals

By Isothermal Coprecipitation A new technique was used in the work reported here. Previously (8) we had made the mixed crystals by standard phase rule procedures in 10-15 gram batches in sealed glass tubes after the manner of Simanova and Shul'ts (14). Our new method, involving intermittent hand grinding with a mortar and pestle enclosed in suitable, vapor-tight containers, was capable of giving up to about a quarter of a pound of crystal product.

Analysis and Characterization of Ammonium Perchlorate-Potassium Perchlorate Mixed Crystals

Chemical Analysis and Chemical and Physical Characterization These methods were described in a previous paper (8).

MORROW

Preparation of Ammonium Perchlorate-Ammonium Nitrate Mixed Crystals

By Isothermal Coprecipitation The data of Karnaukhov (5) was used for calculations on the $\text{NH}_4\text{ClO}_4\text{-NH}_4\text{NO}_3\text{-H}_2\text{O}$ system at 25°C for carrying out our experiments. The ternary Gibbs diagram is shown in Figure 1. Two sets of conditions were used, which differed primarily in the manner and intensity of grinding used during crystal growth. Results of these experiments are shown in Tables III and IV.

Analysis and Characterization of Ammonium Perchlorate-Ammonium Nitrate Mixed Crystals

Chemical Analysis of Solid Phases The Kjeldahl procedure was used to establish the composition to within 4% from the NH_4^+ ion concentration. In most cases these are the values reported here in lieu of final, complete analytical results from Crobaugh Laboratories.

DTA Thermograms of the mixed crystals and pure salts were obtained on a Du Pont No. 900 unit equipped with a standard cell for operations at moderately high temperatures. Samples were run in 2 mm glass tubes in direct contact with Chromel-Alumel thermocouples. Sample depth was about 4 mm and heating rates were $20^\circ\text{C}/\text{min}$.

Explosive Testing This was done with standard methods in this Laboratory, which have been described by Clear (3).

Polarizing Microscopy Deliquescence was determined by means of the test described by this author (10).

DISCUSSION:

Theoretical Considerations

Ideality of the $\text{NH}_4\text{ClO}_4\text{-KClO}_4\text{-H}_2\text{O}$ System We tested the data of Simanova and Shul'ts by phase rule methods to determine the Roseboom classification and the degree of ideality of the behavior of ammonium perchlorate and potassium perchlorate in water at 25.0°C . Both Blasdale (1) and Ricci (13) have described the Roseboom classification of mixed crystals. In addition to Roseboom's original five types, Ricci added a sixth (11). We also reviewed the subject recently (7) giving particular consideration to the synthesis problem with relation to the degree of ideality of the system.

Ricci (12) has described methods for theoretical treatment of phase rule data on mixed crystal systems based on thermodynamic principles. Using Simanova and Shul'ts data, we obtained the relationship shown in Figure 2, which is characteristic of a

MORROW

Rooseboom Type I case. We also obtained values for R_1 and R_S , which are the mole ratios of the interchangeable ions in the liquid and solid phases, as was defined in the last-mentioned paper. In an ideal case the relationship between $\log R_1$ and $\log R_S$ is a linear one. As can be seen from Figure 4, Ricci's alums, A-1 through A-4 (12), show this ideality over the range indicated. The ternary perchlorate mixed crystal system, S-1 with water as the solvent shows a slight deviation from ideality at the one extreme. It is evident, however, that this system affords a favorable prototype for studying by phase rule methods the formation and properties of a continuous series of heat sensitive mixed crystals.

Isomorphous Relation Between NH_4ClO_4 and NH_4NO_3 Crystal data for these two salts (4), shows that insofar as the "normal" orthorhombic forms are concerned, the two crystals are related isomorphously. Their lattice constants are not as close to one another as in the case of ammonium perchlorate and potassium perchlorate, though. This could have a definite bearing on their ability to form mixed crystals, according to Morrow (9). In addition to the similarity between these forms both species revert to structures of higher symmetry, cubic, at elevated temperatures. These respective cubic forms probably have some mutual solubility. One can conclude that the two salts might very well tend to form mixed crystals by precipitation from water in the presence of one another. These observations have been experimentally verified by Karnaukhov (5), who asserted "that the investigated salts are isomorphous and form continuous solid solutions at any ratios".

Explosive Parameters Official data from an Army bulletin (15) and from our own tests on explosive properties is shown in Table 1. Our tests showed that ammonium perchlorate has a higher explosion temperature at the 5 sec. point than ammonium nitrate. It is also much less sensitive to moisture than the latter salt. Ammonium nitrate has an additional unfavorable property in that it undergoes five phase changes, with appreciable accompanying changes in density, over a range of less than 200°C . This causes problems in maintaining the mechanical integrity of the propellant grain. Such propellants tend to be difficult to ignite and to burn slowly also.

Ideality of the NH_4ClO_4 - NH_4NO_3 - H_2O System at 25°C When the data of Karnaukhov on this ternary system was examined by the methods described above, the solubility relationship shown in Figure 3 was found to be suggestive of a Rooseboom Type IV case. It is not possible from the data available to determine if there is an horizontal portion in the curve between the points A and B, as is found in Type IV systems. However, it is evident that there may be a discontinuity in the series of mixed crystals and that the two different types may be present. The curve, K-1, shown in Figure 4 is a further indication of the lack of ideality of the behavior

Table I

Oxidizer Explosive Properties

<u>Property or Test</u>	<u>NH₄ClO₄</u>	<u>NH₄NO₃</u>
Impact Sensitivity 2 Kg. Weight, in Picatinny Test (Note 1.)	21 (18)	40+ (15)
Explosion Temperature, °C, 5 sec. point (Note 2.)	403	232
100°C Heat Test, % loss 1st 48 hours	0.02	0.74
Structural Transition Temperatures, °C	240	-60, -18, 32, 84, 125
Melting point, °C	dec.	169.9

Note 1. This value is from our tests with material of particle size < 149 > 74 microns. Figures below in brackets are sample weights in mg.

2. This is our value with particle sizes given in Note 1.

of the salt pair in water at 25.0°C.

Practical Considerations

Cost Ammonium nitrate is extremely attractive from the standpoint that it is a very cheap chemical produced in large quantities by many different manufacturers.

Synthesis of Mixed Crystals

NH₄ClO₄-KClO₄ One of the most important factors in crystal synthesis experiments, as we were to discover, is the weight ratio of water to salt. If there is too little water in relation to the amount of salt present, it is difficult to reach true equilibrium. In our earlier work in preparing NH₄ClO₄-KClO₄ mixed crystals we used a 1:1 water-salt ratio which proved to be quite satisfactory. This same ratio was used to test our new mortar and pestle procedure for making the mixed crystals on approximately a six-fold expanded scale. Results indicated that for all practical purposes we attained equilibrium and formed an essentially homogeneous product within a weeks time.

NH₄ClO₄-NH₄NO₃ Two series of experiments were carried out. Compositions and explosive properties of some of the products are shown in Tables III and IV. In the first series of experiments samples 1, 2, and 3, Table IV, were prepared in the same way as the NH₄ClO₄-KClO₄ mixed crystals described above. Weight ratios of water to salt in these preparations were 1:2, 1:4, and 1:4 respectively.

In the second series of experiments, samples 4, 5, and 6, Table III, the weight ratio of water to salt was 1:3. A unique feature of this series was that the experiments were performed simultaneously and treated as nearly alike as possible. Also as vigorous grinding conditions as possible were used as this was judged to be a most critical variable.

Characterization of Mixed Crystals

Chemical Analysis of NH₄ClO₄-KClO₄ We found that we could accurately judge how successful we had been in attaining chemical equilibrium in our experiments by comparing the composition of the "fines" and largest particles obtained by pulverizing and screening the samples. Results of such analyses are shown in Table II. In the case of both samples there is not a large difference in compositions of large and small particle size fractions after grinding. Some variation is unavoidable inasmuch as a little of the liquid phase adheres to the products. Upon drying this deposits a coat of a different composition on the crystals. These analyses show that the mortar and pestle synthesis technique was quite effective under the conditions employed here.

Table II

Compositions of Experimental AP (NH₄ClO₄)-KP
(KClO₄) Mixed Crystals Determined by NH₄⁺
Analysis (Note 3)

<u>Sample No.</u>	<u>Particle size, microns</u>	<u>Target AP Content, % by wt.</u>	<u>Actual AP, Content, % by wt. by analysis</u>	<u>Difference, % by wt.</u>
1	<210 >177	50.0	49.32	2.31
	<44	"	51.63	
2	unground	80.0	80.02	4.30
	<210 >44	"	80.99	
	<44	"	76.69	

Note 3. Except in the case of the unground crystals, samples were pulverized and separated into different particle size fractions by screening.

Chemical Analysis of $\text{NH}_4\text{ClO}_4\text{-NH}_4\text{NO}_3$ Analytical data on out products is shown in Table III. In the cases of samples 4 and 6 it was evident that a fairly good degree of homogeneity had been attained in the crystals. Since particularly vigorous grinding had been used in preparing these crystals, it is obvious by comparison to conditions used to make homogeneous $\text{NH}_4\text{ClO}_4\text{-KClO}_4$ mixed crystals, that the $\text{NH}_4\text{ClO}_4\text{-NH}_4\text{NO}_3$ types are much more difficult to prepare. This is not surprising when one considers the lack of ideality predicted theoretically for this system. It must be born in mind, that the "fines", 44 micron particles, are a relatively small fraction by weight of all of the particle fractions and that they no doubt represent the thin surface layers of the crystals. For this reason the actual composition of the unground crystals does not differ too much from the composition of the largest particle fraction. Evidently in the case of samples 3 and 5 use of less vigorous grinding conditions led to lack of attainment of equilibrium. This same condition exists in the case of preparation of sample 2, where mild grinding was also used.

Table III

Compositions of Experimental AP (NH_4ClO_4)-
AN (NH_4NO_3) Mixed Crystals Determined by
 NH_4^+ Analysis (Note 3)

<u>Sample No.</u>	<u>Particle Size, Microns</u>	<u>AP Content, % by wt. by analysis</u>	<u>Difference, % by wt.</u>
4	unground	7.3	4.5
	<210>44	6.6	
	<44	11.1	
3	>149	31.0	54.7
	<44	85.7	
5	unground	53.9	25.5
	<210>44	49.0	
	<44	74.5	
2	>149	97.5	8.0
	<44	89.5	
6	unground	87.0	3.2
	<210>44	87.0	
	<44	83.8	

DTA of $\text{NH}_4\text{ClO}_4\text{-NH}_4\text{NO}_3$ Thermograms of Mixed crystal samples and pure components are shown in Figure 5. Curves 3, 4, and 5 in this figure were obtained with samples 4, 5, and 6 of Table III, respectively. Pure NH_4NO_3 shows the structural transition endotherms described by Bracuti (2) at about 50 and 124°C. The endotherm at about 170°C is due to melting. NH_4ClO_4 , on the other hand, has only one structural transition endotherm at about 240°C. In the case of curve 3 for mixed crystals with NH_4ClO_4 as the minor component the two NH_4NO_3 -type transition endotherms are slightly displaced with respect to temperature from that of the pure compound. The phenomenon associated with the endotherm at about 155°C has not yet been identified. The decomposition exotherms above 270°C occur at a slightly lower temperature than those for pure NH_4NO_3 . Curve 4 for mixed crystals with about a 1:1 weight ratio of components has the same three major endotherms as in the former case, but they are much weaker. The exothermic decomposition of this material resembles that of pure NH_4NO_3 somewhat.

For the mixed crystal which is composed primarily of NH_4ClO_4 , curve 5, the three endotherms discussed above have become very weak and the decomposition behavior seems to be a hybrid of that of the two components. A marked feature in all three mixed crystal thermograms is the absence of the well-characterized transition endotherm of ammonium perchlorate. This figure clearly illustrates that heat effects due to phase changes in ammonium nitrate are diminished progressively as ammonium perchlorate is introduced into its crystal lattice. Also the initial decomposition effects in the mixed crystals occur at lower temperatures than in pure ammonium perchlorate.

Explosive Properties of $\text{NH}_4\text{ClO}_4\text{-NH}_4\text{NO}_3$ Explosion temperature and impact sensitivity for a different series of samples than those used in the DTA experiments were determined. This data is summarized in Table IV.

All samples were $\langle 149 \rangle 74$ micron particle size, which is standard in our work. Except in the case of sample 2 the explosion temperatures of the mixed crystals at the 5 second point are lower than that of pure NH_4ClO_4 . The impact sensitivity of the mixed crystals except for sample 1 is less than that of pure NH_4ClO_4 .

Deliquescence of $\text{NH}_4\text{ClO}_4\text{-NH}_4\text{NO}_3$ We showed by the deliquescent test (10) that except at low levels of NH_4ClO_4 of the order of 13%, the mixed crystals are more resistant to moisture as a function of increasing NH_4ClO_4 content. When NH_4ClO_4 comprises 50 percent or more by weight of the mixed crystal, their deliquescence is much less than that of pure NH_4NO_3 .

Table IV

Explosive Properties of Experimental AP (NH_4ClO_4)-
AN (NH_4NO_3) Mixed Crystals

<u>Sample</u>	<u>AP</u> <u>Content, %</u> by wt.	<u>Explosion</u> <u>Temp., °C</u> at 5 sec. pt.	<u>Impact Sens-</u> <u>itivity, P.A., 2 KG</u> wt., in.
NH_4ClO_4	100	403	21 (18 mg)
1	84.2	374	19 (17 mg)
2	89	443	40+ (17 mg)
3	49	383	40+ (16 mg)
NH_4NO_3	0	232	40+ (15 mg)

SUMMARY:

We continued our demonstration of the new principle that isomorphous and phase rule concepts can be used as a theoretical guide for obtaining valuable new oxidizer "alloys". New synthesis techniques were explored to facilitate preparation of NH_4ClO_4 - KClO_4 and NH_4ClO_4 - NH_4NO_3 "alloys" on an expanded scale. We found that it was considerably more difficult to make the latter type of homogeneous mixed crystals. This was due to the theoretically predicted lack of ideality of the behavior of this salt pair in water. It was shown that introduction of NH_4ClO_4 into the crystal lattice of NH_4NO_3 tends to increase the latter's thermal stability and decrease its sensitivity to moisture. At the same time NH_4NO_3 appears to reduce the impact sensitivity of NH_4ClO_4 . These are desirable effects from a propellant and explosive standpoint.

CONCLUSIONS:

Guidelines established in this work can serve as a useful model for investigation of not only other new oxidizer "alloy" systems but also similarly in a more general way in inorganic mixed crystal chemistry. Not only do the NH_4ClO_4 - KClO_4 mixed crystal "alloys" have interesting properties from a propellant and explosive standpoint but so do those of NH_4ClO_4 - NH_4NO_3 . The latter "alloys" hold promise for development of a low-cost rocket oxidizer and explosive ingredient.

ACKNOWLEDGEMENTS:

We thank Messrs. N. Gelber, R. Croom, H. Vaughan, J. Campisi, and Dr. A. Beardell for their help. Army Research Office Consultants Professor J. E. Ricci and Dr. C. P. Saylor also participated in this effort.

MORROW

REFERENCES

1. Blasdale, W. C., Equilibria in Saturated Salt Solutions, Chemical Catalog Co., Inc., N. Y., 1927
2. Bracuti, A. J., Picatinny Arsenal Technical Memorandum No. 1905, September 1969
3. Clear, A. J., Standard Laboratory Procedures for Determining Sensitivity, Brisance, and Stability of Explosives, Picatinny Arsenal Technical Report No. 3278, December 1965
4. Donnay, J. D. H., Donnay, G., Cox, E. G., Kennard, O., and King, M. V., Crystal Data Determinative Tables, Second Edition, Williams and Heintz Map Corp., Washington, D. C., 1963
5. Karnaukhov, A. S., Zh. Neorgan. Khimii, 2, 915 (1957)
6. McCrone, W. C., Fusion Methods in Chemical Microscopy, Interscience Publishers Inc., N. Y., 1957
7. Morrow, S. I., "Problems in the Synthesis of Mixed Crystals", 24th Annual Northwest Regional ACS Meeting, U. of Utah, Salt Lake City, Utah, June 13, 1969
8. Morrow, S. I., Proceedings of the 1969 US Army Munitions Command Science Conference, June 18-19, 1969, Picatinny Arsenal, Dover, N. J., pgs. 725-740
9. Morrow, S. I., J. Chem. Ed., 46, 580 (1969)
10. Morrow, S. I., paper to be submitted to Inter/Micro 70, Chicago, Ill., July 1, 1970
11. Ricci, J. E., J. Amer. Chem. Soc., 57, 805 (1935)
12. ibid, 62, 2723 (1940)
13. Ricci, J. E., The Phase Rule and Heterogeneous Equilibrium, Dover Publications Inc., N. Y., 1966
14. Simanova, S. A., and Shul'ts, M. M., Zhurnal Neorganicheskoy Khimii, 12, No. 1, 223-230 (1967)
15. Smith, S. D., Engineering Design Handbook, AMCP 706-177, USAMC, March 1967

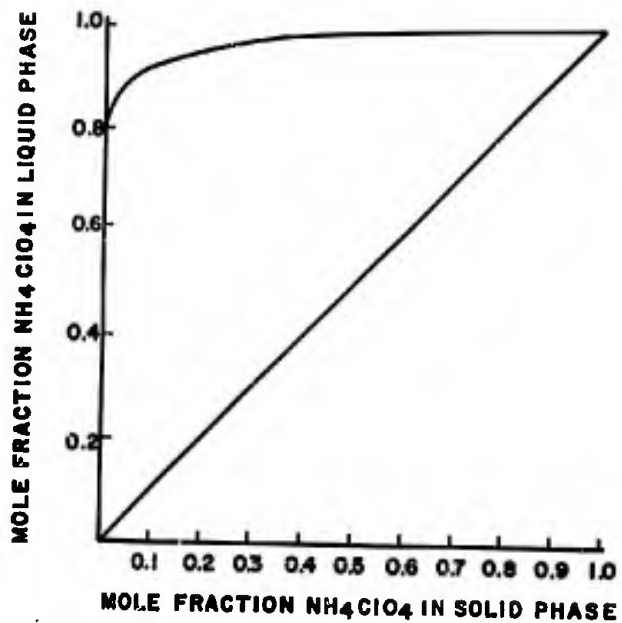
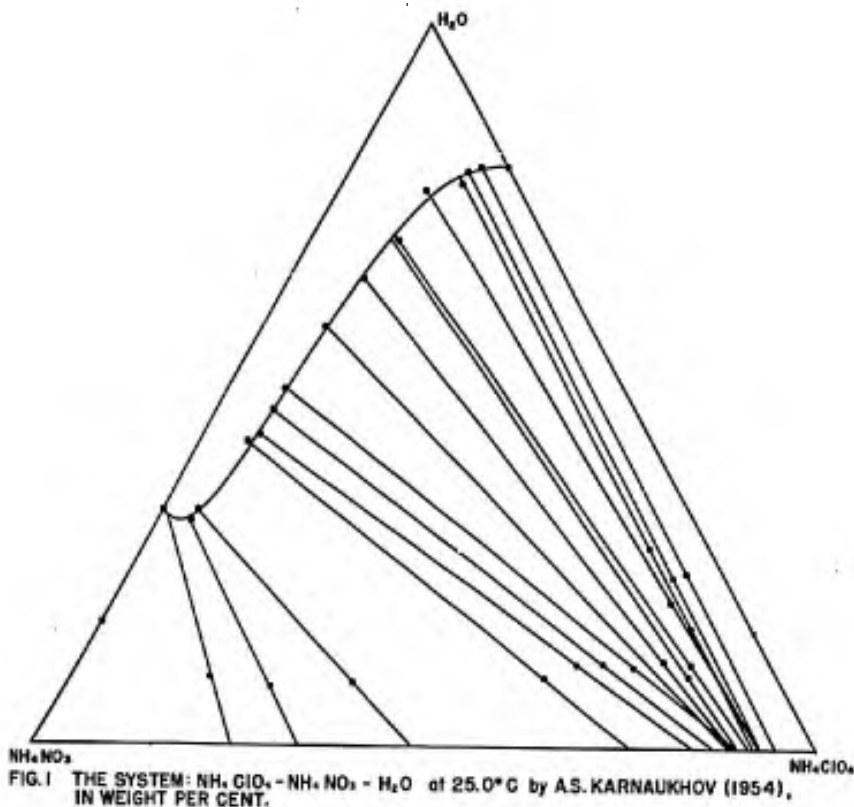


FIG. 2 THE SYSTEM: NH_4ClO_4 - KClO_4 - H_2O 25.0°C , SIMANOVA AND SHUL'TS (1967)

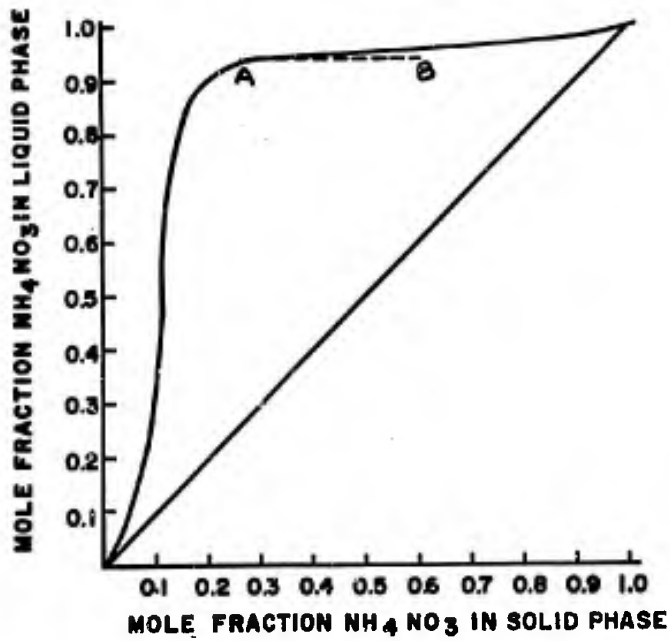


FIG.3 THE SYSTEM: $\text{NH}_4\text{ClO}_4 - \text{NH}_4\text{NO}_3 - \text{H}_2\text{O}$
 25.0°C, KARNAUKHOV (1954)

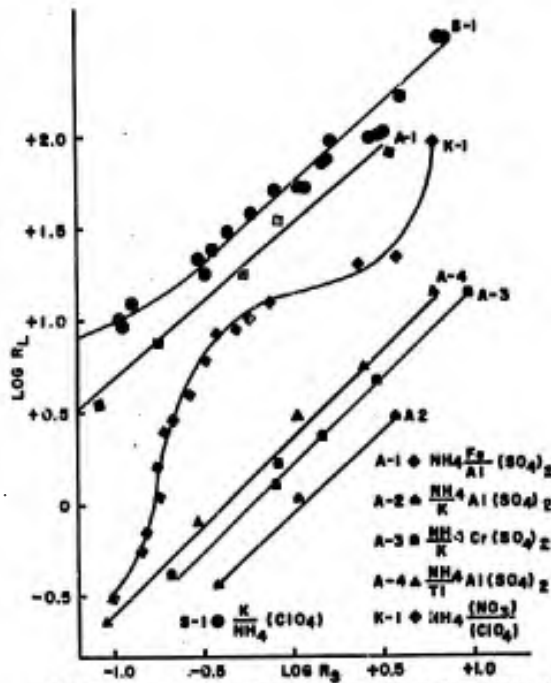


FIG.4 SALT DISTRIBUTION IN AP-KP-H₂O & APAN-H₂O
 SYSTEMS COMPARED TO THOSE IN IDEAL ALUM SYSTEMS.

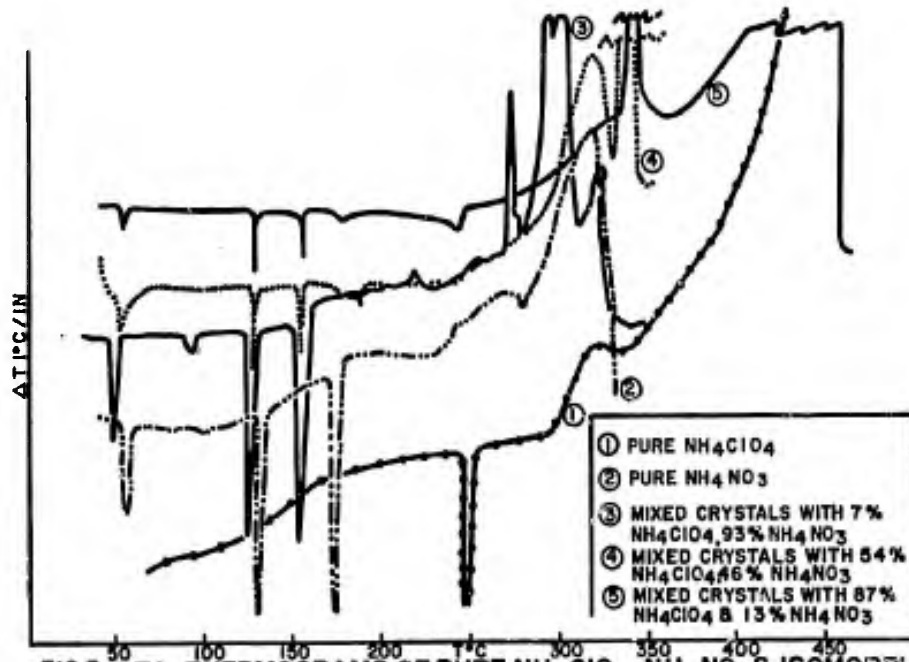


FIG.5 DTA THERMOGRAMS OF PURE NH_4ClO_4 , NH_4NO_3 & ISOMORPHOUS MIXED CRYSTALS THEREOF.

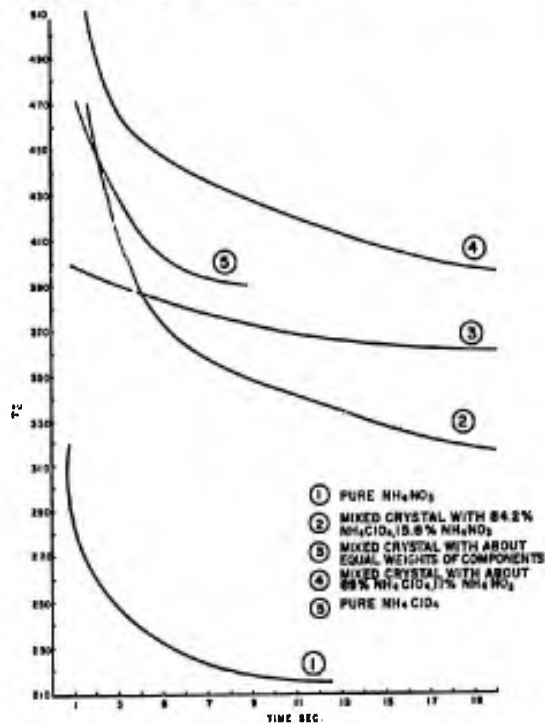


FIG.6 EXPLOSION TEMPERATURE CURVES OF AMMONIUM PERCHLORATE, AMMONIUM NITRATE, AND MIXED CRYSTALS THEREOF

DEVELOPMENT OF A MATHEMATICAL MODEL FOR DESIGNING
FUNCTIONAL CONTROLS OF A SOFT-RECOIL MECHANISMMICHAEL C. NERDAHL AND JERRY W. FRANTZ
U. S. ARMY WEAPONS COMMAND
ROCK ISLAND, ILLINOIS

Investigation of a revolutionary recoil cycle for artillery began in 1957 with the modification of a standard 105mm Howitzer and subsequent evaluation tests to demonstrate what is now called a "soft-recoil" cycle. An experimental firing fixture was designed and fabricated in 1964. Extensive firing tests, made from this fixture, allowed for examination of the accuracy, durability, and functioning to confirm the technical feasibility of using this recoil system in the field. A prototype artillery weapon, the XM204, (Figure 1) has been built for Military Potential Testing and Evaluation. It consists of: Cannon, 105mm Howitzer, XM205; Recoil Mechanism, XM46; and Carriage, XM44.

In any artillery weapon, combustion of the powder charge produces a gas pressure which propels the projectile downrange and exerts a force on the breech tending to move the weapon in a direction opposite that of projectile motion. When the cannon is rigidly attached to the supporting structure, the complete weapon is exposed to the full propellant force (exceeding two million pounds in large guns). Therefore, in large artillery, a recoil mechanism is introduced between the cannon and the carriage to protect the major portion of the structure and to limit the ground reactions. This is accomplished by providing a controlled resistance to the allowable motion of the recoiling parts and by storing some of the recoil energy for return of the cannon to its starting (or "in battery") position.

In conventional artillery, the recoil cycle begins with propellant ignition when the recoiling mass is stationary. The gas pressure then accelerates the projectile and the recoil mass in opposite directions. The recoiling mass moves against the resisting force produced by the recoil mechanism until its speed is brought to zero within some limited amount of recoil travel. The mass is then returned to battery position in a controlled manner by energy stored during recoil in a spring element.

NERDAHL* and FRANTZ

The new XM46 Recoil Mechanism is based on the soft-recoil cycle described as follows: The recoiling parts are mechanically held against a gas spring force acting in the direction of firing; upon release, acceleration in the direction of firing occurs; propellant ignition is initiated automatically when the proper velocity is attained; the firing impulse overcomes the momentum of the recoiling parts, reverses their direction of travel, and forces them against the gas spring until they pass the latch position; and the gas spring returns the recoiling parts to the latch point, thus completing the cycle.

The difference between the conventional and the soft-recoil cycle is illustrated in Figure 2. In either case, the recoiling mass (M_R) of an artillery weapon is subjected to a force system that first puts the mass in motion, then controls the motion, and finally returns the velocity to zero at the end of the cycle. The free body diagram of the recoiling parts under such a force system is shown in Figure 3.

Motion of a system may be predicted by solution of the differential equation:

$$(1) \quad M_R \ddot{x} = A(t) - D(t)$$

where

$A(t)$ = Summation of forces causing positive accelerations

$D(t)$ = Summation of forces causing negative accelerations

and both may be considered as functions of time. Since the firing cycle begins with the recoiling parts at rest, the initial conditions will be

$$x = 0 \quad \text{and} \quad \dot{x} = 0 \quad \text{at} \quad t = 0$$

If a definition of $A(t)$ and $D(t)$ can be assumed, the system could be depicted as in Figure 4.

A graphical interpretation of the solution to Equation 1 is given by the following equations, which hold at any instant ($t = t_i$)

$$(2) \quad M_R \dot{x} \Big|_{t=t_i} = \Sigma \text{ Areas under curve of } A(t) \\ - \Sigma \text{ Areas under curve of } D(t)$$

$$(3) \quad M_R x \Big|_{t=t_i} = \Sigma \text{ Moment of area under } A(t) \text{ around } t = t_i \\ - \Sigma \text{ Moment of area under } D(t) \text{ around } t = t_i$$

By defining

I = Area Under the Breech Force Curve

and assuming that the function $D(t)$ [Resistance to Recoil] can be held constant (R) by an unspecified method of control, some useful design relationships may be developed. If, for a conventional cycle, a length of recoil (ℓ = allowable maximum displacement from original position) is chosen and noting that at the end of recoil, $\dot{x} = 0$ when $x = \ell$

$$(4) \quad R_{\text{conventional}} = \frac{I^2}{2M_R \ell + 2\bar{a}I} + W_R \sin \epsilon$$

For an ideal soft-recoil cycle with the same values of ℓ , but noting that $\dot{x} = 0$ and $x = 0$ at the end of recoil.

$$(5) \quad R_{\text{soft recoil}} = \frac{1}{4} \left[\frac{I^2}{2M_R \ell + 2\bar{a}I} \right] + W_R \sin \epsilon$$

if

$$(6) \quad \dot{x}_{\text{firing}} = - \frac{I}{M_R} \left[\frac{1}{2} - \frac{1}{\frac{8M_R \ell}{\bar{a}I} + 4} \right]$$

If the breech force imposed an instantaneous impulse, the term \bar{a} would equal zero. Then, for $\epsilon = 0^\circ$, a perfect soft-recoil cycle could reduce the constant force applied to the carriage by a factor of approximately four.

The lower recoil force level gives the soft recoil system the following advantages over conventional recoil:

(a) improved firing stability; (b) simplified ground anchoring requirements, and (c) a resultant reduction in emplacement and displacement times.

The cycle time is also reduced since the recoiling mass is closer to the battery position at the beginning of counterrecoil.

Several inherent problems must be considered in developing a soft recoil mechanism. Primary areas are those involving the ammunition characteristics of:

(a) impulse variation due to zoning (for range) or to projectile type; (b) variations in ignition delay — the time lapse between hitting the primer and establishing a breech pressure; and (c) possibility of a misfire or hangfire — an excessively long ignition delay.

NERDAHL* and FRANTZ

Since a soft-recoil mechanism reduces force levels by initiating the breech force after the recoiling parts have been given a desired momentum, the triggering of the firing mechanism must be directly related to the velocity of the recoiling mass. Consequently, the firing mechanism must be set by the gun crew to match the charge selected. This dependence on human behavior adds the usual requirement for protection against the possibility of malfunction due to human error—"idiotproofing."

"Something-for-nothing" is rarely attained and a soft-recoil cycle requires such additional functional controls as:

- (a) A latch mechanism to hold the recoil mass against the gas spring until the firing cycle is initiated;
- (b) A velocity sensor to match the firing velocity to the propellant charge;
- (c) A mechanical trip to initiate firing at a limiting displacement if the firing velocity is not reached;
- (d) An automatic reduction of the drive force to prevent an increase in velocity after firing in case of ignition delay;
- (e) A front buffer to protect the system in case of a misfire;
- (f) A rear buffer to protect the system if, through human error, a maximum impulse charge is fired at the wrong velocity setting;
- (g) An automatic reset for the latch mechanism; and
- (h) A counterrecoil control to protect the latch mechanism.

Mathematical prediction of system motion requires that the operational characteristics of these functional controls be defined by logic decisions that can be made on a digital computer. This simulation requires continuous monitoring of time, velocity, displacement, and pressure, in order to answer the following questions:

- Has firing been initiated?
- Has the firing velocity been reached?
- Has the mechanical trip initiated firing?
- Has ignition delay been simulated?
- Has the drive force been removed?
- Has the breech force been applied?
- Has a misfire occurred?
- Has the front buffer functioned?
- Has the mass changed direction?
- Has the mass returned to latch?
- Has the mass exceeded the maximum overtravel position?
- Has counterrecoil begun?
- Has the cycle ended?

Development of the mathematical models used in the design of the functional controls began with the application of the moment-area method to the problem. This allowed for: establishment of limits on such parameters as lengths allowed for runup, coast, forward buffing and rear buffing; determination of approximate firing velocities for each impulse level; and the estimation of the gas spring force required to obtain the maximum firing velocity in the displacement limit chosen. This simplified model enabled the engineer to size a practical recoil mechanism design schematically shown in Figure 5. The direction of fluid flow is indicated in Figure 6.

The forces shown are those that exist when the displacements x , y and $x-y$ are increasing in magnitude and the sign convention is based on the assumption that the breech force $[B(t)]$ causes a positive acceleration. As the recoiling mass (M_R) moves in a positive direction, the oil will flow from P_1 to P_4 through the orifice areas $[a_i]$ with flow velocities $[v_i]$. Size of the orifice areas will vary with position of the spear buffer, with functioning of the velocity sensor used to trip the firing mechanism, and with the direction of fluid flow. By assuming:

- (a) Incompressible fluid flow,
- (b) Adiabatic gas laws, $[P_0, V_0 = \text{Initial gas pressure volume}]$
- (c) Constant friction forces,
- (d) Constant discharge coefficients (c_i), and,
- (e) System filled with fluid (density $=\sigma$) as long as pressures are positive;

the system can be considered to have one degree of freedom and its motion may be predicted by solution of the differential equation

$$(7) \quad \left[M_R + \left(\frac{A_4 - A_R}{A_4} \right) M_P \right] \ddot{x} =$$

$$B(t) + (W_R + W_P) \sin \epsilon - (F_p + F_g) \frac{\dot{x}}{|\dot{x}|}$$

$$+ A_3 P_3 - \begin{cases} A_2 P_2 & \text{if } x > 0 \\ \text{or} \\ A_2 P_1 & \text{if } x \leq 0 \end{cases} - A_1 P_1$$

while the force applied to the supporting structure is given by

$$(8) \quad R = A_1 P_1 + A_2 P_2 - A_3 P_3 + (F_p + F_g) \frac{\dot{x}}{|\dot{x}|}$$

Since the velocity (v_i) of oil flow through an orifice (a_i) may be

NERDAHL* and FRANTZ

related to the velocity of the recoiling parts by volume relations, the equations

$$(9) \quad v_1 = \frac{A_1 + BA_2}{a_1} \dot{x}$$

$$(10) \quad v_2 = \frac{A_1 + A_2}{a_2} \dot{x}$$

$$(11) \quad v_3 = \frac{A_R}{a_3} \dot{x}$$

may be written, where

$$(12) \quad B = \begin{cases} 1 & \text{if } x < 0 \\ 0 & \text{if } x \geq 0 \end{cases}$$

Then, the pressure drop across the orifice (a_i) may be written as

$$(13) \quad \Delta p_{a_i} = \frac{\sigma}{2g} \frac{v_i^2}{c_i} \frac{v_i}{|v_i|}$$

where the last term changes the direction of the pressure drop with the direction of fluid flow.

The gas pressure is defined by:

$$(14) \quad P_N = \frac{P_o}{\left[1 - \frac{A_N A_R}{A_4 V_o} x \right]^k}$$

and, the oil pressure in the recuperator is defined by

$$(15) \quad P_4 = \frac{1}{A_4} \left[W_p \sin \epsilon + A_N P_N + F_{fp} \frac{\dot{x}}{|\dot{x}|} - M_p \left(\frac{A_4 - A_R}{A_4} \right) \ddot{x} \right]$$

Then, all pressures may be evaluated in terms of x and \dot{x} and Equation 7 may be rewritten as:

$$(16) \quad \left[M_R + \left(\frac{A_4 - A_R}{A_4} \right)^2 M_P \right] \ddot{x} =$$

$$B(t) + \left[W_R + \left(\frac{A_4 - A_R}{A_4} \right) W_P \right] \sin \epsilon$$

$$- \frac{A_R A_N}{A_4} P_N - \left[F_P + F_g + \frac{A_R}{A_4} F_{fp} \right] \frac{\dot{x}}{|\dot{x}|}$$

$$- \frac{\sigma}{2g} \left[(A_1 + BA_2) \frac{v_1^2}{c_1^2} + (A_1 + A_2) \frac{v_2^2}{c_2^2} + A_R \frac{v_3^2}{c_3^2} \right] \frac{\dot{x}}{|\dot{x}|}$$

It should be noted that solution of the motion equation (Either Equation 7 or 16) is based on the implied assumption that the supporting structure is rigid.

The effect of possible carriage motion was also studied. The model shown schematically in Figure 7 has two degrees of freedom, translation of the recoiling parts (η_A) and rotation of the carriage (ϕ). Then, after defining system energy, use of LaGranges Equation yields the following pair of simultaneous motion equations:

$$(17) \quad \{M_A (\eta_A + Y_T \cos \epsilon + Z_T \sin \epsilon)^2$$

$$+ M_B [(Y_T + \eta_B \cos \epsilon - \zeta_B \sin \epsilon)^2 + (Z_T + \eta_B \sin \epsilon + \zeta_B \cos \epsilon)^2]$$

$$+ M_D (Y_D^2 + Z_D^2) + (I_A + I_B + I_D)\} \ddot{\phi} =$$

$$M_A (\eta_A + Y_T \cos \epsilon + Z_T \sin \epsilon) [\dot{\phi}^2 (\zeta_A - Y_T \sin \epsilon + Z_T \cos \epsilon) - 2\dot{\phi} \dot{\eta}_A]$$

$$+ B(t) (\zeta_1 - \zeta_A) - c\dot{\phi} - k (\phi + \phi_{static})$$

$$+ (\zeta_A - Y_T \sin \epsilon + Z_T \cos \epsilon) [R(t) - BF - (\mu_1 |S_1| + \mu_2 |S_2|) \frac{\dot{\eta}_A}{|\dot{\eta}_A|}]$$

$$- \{W_A (\eta_A + Y_T \cos \epsilon + Z_T \sin \epsilon) \cos (\epsilon + \phi)$$

$$+ W_B [Y_T \cos \phi - Z_T \sin \phi + \eta_B \cos (\epsilon + \phi) - \zeta_B \sin (\epsilon + \phi)]$$

$$+ W_D (Y_D \cos \phi - Z_D \sin \phi)\}$$

NERDAHL* and FRANTZ

$$(18) \quad M_A \ddot{\eta}_A - M_A (\zeta_A - Y_T \sin \epsilon + Z_T \cos \epsilon) \ddot{\phi} = \\ M_A (\eta_A + Y_T \cos \epsilon + Z_T \sin \epsilon) \dot{\phi}^2 + R(t) - B(t) \\ - BF - W_A \sin (\epsilon + \phi) - (\mu_1 |S_1| + \mu_2 |S_2|) \frac{\dot{\eta}_A}{|\dot{\eta}_A|}$$

By defining

$$(19) \quad -x = \eta_A - \eta_{A0}$$

these equations could be combined with Equation 16 of the basic model to relate recoil mechanism functioning to linear motion of the recoiling mass and rotation of the total weapon around a fixed pivot point.

Justification for development of this particular model must be based on an examination of the environment in which an artillery weapon is expected to perform. The wide variety of anticipated firing conditions may be related to carriage motion by describing the emplacement rigidity: The weapon may be firmly anchored to the ground (as it would be during some firing tests, or while at a relatively permanent emplacement, or when frozen to the ground) or it may be emplaced in soft sand which offers little resistance to weapon motion. The weapon could also be anchored by bracing it against a solid support in such a manner that linear motion is prevented while rotational motion is almost unrestrained. From experience, a rigid mounting has been shown to produce the highest loads in the recoil mechanism. Therefore, the simple model (Equation 16) was used to establish the mechanism control parameters; and the more complex model (Equations 16, 17, 18 and 19) were used to determine whether total weapon motion would compromise functioning of the controls.

In using these models to design the functional controls, the following systematic procedure was employed. Values chosen were based on the numerical solution (by high speed digital computer) of the appropriate equations.

After choosing a reasonable limit for runup (X_{runup}) and estimating the maximum required firing velocity (V_{Fmax}) by using the moment - area method, Equation 16 was solved with various initial gas pressures until the value of V_{Fmax} was attained just before X_{runup} was reached.

The second step was to design the control orifice of the rear buffer. To ensure the resetting of the mechanical latch, the minimum impulse round must be fired from the latch position. This will allow any round to be fired from the same position. Therefore,

the variable control orifice was designed to protect the system from damage if a maximum impulse round was fired by mistake from the latch position. This was accomplished by defining the force which would be applied to the supporting structure and by solving a version of Equation 7 for values of x , \dot{x} , and \ddot{x} (relating a force level to the maximum recoil stroke). Then, an algebraic solution for a_1 from Equations 8 through 15 defined the orifice area at any travel x .

The third step in the design procedure was to provide for control of the counterrecoil motion. During this portion of the cycle, $x > 0$; $\dot{x} < 0$ and $B(t)$ is equal to zero. Then, an examination of Equation 16 shows that the term $(A_R A_N/A_4) P_N$ defines the driving force (force which increases the magnitude of the acceleration) during counterrecoil. If hydraulic throttling completely balanced this driving force, making the acceleration zero, a constant velocity would be obtained. This limiting velocity is defined by the equation

$$(20) \quad \frac{A_1^3}{a_1^2} + \frac{(A_1 + A_2)^3}{a_2^2} + \frac{A_R^3}{a_3^2} = \frac{2gc^2}{\sigma \dot{x}^2} \frac{A_R A_N}{A_4} P_N$$

To control the velocity, (\dot{x}), any one of the control orifices (a_i) could be used by making it small compared to the remaining openings. In this particular weapon, a_3 was sized to limit the maximum counterrecoil velocity and a_1 was modified to provide the pressure drop (across a_1) and the resultant retarding force which would lower the terminal velocity to an acceptable value as the mass approached the latch (battery) position at the end of the cycle.

The fourth control to be considered was the choice of a firing velocity for each expected impulse. Ideally, the recoiling parts should return to latch with a velocity that is high enough to provide the overtravel necessary to reset the latch mechanism and yet low enough to limit the force produced by functioning of the rear buffer. These conflicting requirements were studied by use of the mathematical model to evaluate the effects of latch velocity variation until an acceptable value was determined. At this time, a maximum and a minimum impulse charge for each zone (assuming no ignition delay) was used as an input and the firing velocity varied until the acceptable latch velocity was obtained. Ignition delay effects were then evaluated.

The final step was to design an external front buffer to dissipate the energy of the recoiling parts in the case of a misfire. The simple model described previously was modified by the addition of a term describing a constant hydraulic throttling force for this buffer. A variable orifice was then sized to bring the speed of the recoiling mass from maximum velocity to zero in a stroke of 10 inches.

The two degree-of-freedom model was then used to evaluate the effect of carriage motion since the design procedure was based on an assumed rigid supporting structure. As anticipated, the motion of a secondary mass (rotation of the carriage) reduced the sustained values of recoil resistance. However, predicted peak loads were similar for both models. The only control that was significantly affected by carriage motion was the firing velocity. The two degree-of-freedom model required slightly lower firing velocities to attain the desired latch velocity than did the rigid model. This indicates that the final settings of the velocity sensor should be made on the carriage.

Use of these mathematical models provided practical benefits. The more important of these are summarized here.

1. The first studies made to define the initial nitrogen pressure pointed out a required design change (See Figure 5) in the value of the orifice a_2 , and showed that the relative sizes originally chosen for A_R and A_3 had to be altered to minimize the pressure drop across the piston head which placed a limit on the maximum attainable firing velocity. (runup velocity)
2. During the runup period, the orifice a_2 is really the effective combination of the opening indicated and the circular opening for the spear buffer (See Figure 5). Therefore, the spear buffer must have a cross sectional area large enough to prevent limiting runup velocity.
3. These two original difficulties actually pointed the way to obtaining simple yet adequate control of the counterrecoil velocity by limiting fluid flow through a_3 and a_1 .
4. The lowest charge rounds were found to have such a slow pressure buildup that any ignition delay will allow the recoiling mass to attain a runup velocity so great that these rounds cannot provide an adequate latch velocity. Therefore, if these zone charges are adopted as standard a mechanism for firing without releasing the latch must be provided.
5. Predictions of maximum pressures, velocities, accelerations, and displacements were available to the engineer as a basis for component design.

NERDAHL* and FRANTZ

The normal course of artillery development is, as in other fields, toward the bigger and more powerful, and the next logical application of the soft-recoil cycle will be to a larger caliber weapon. Since adaptation problems will increase with larger size and greater impulse, a reasonably accurate source of performance predictions should be available. Correlation of firing tests with mathematical predictions will increase the value of these models by allowing evaluation of both model acceptability and input data accuracy. This will allow the ordnance engineer to establish future designs of soft-recoil mechanisms in a larger caliber with greater confidence, at lower cost, and in a shorter time.

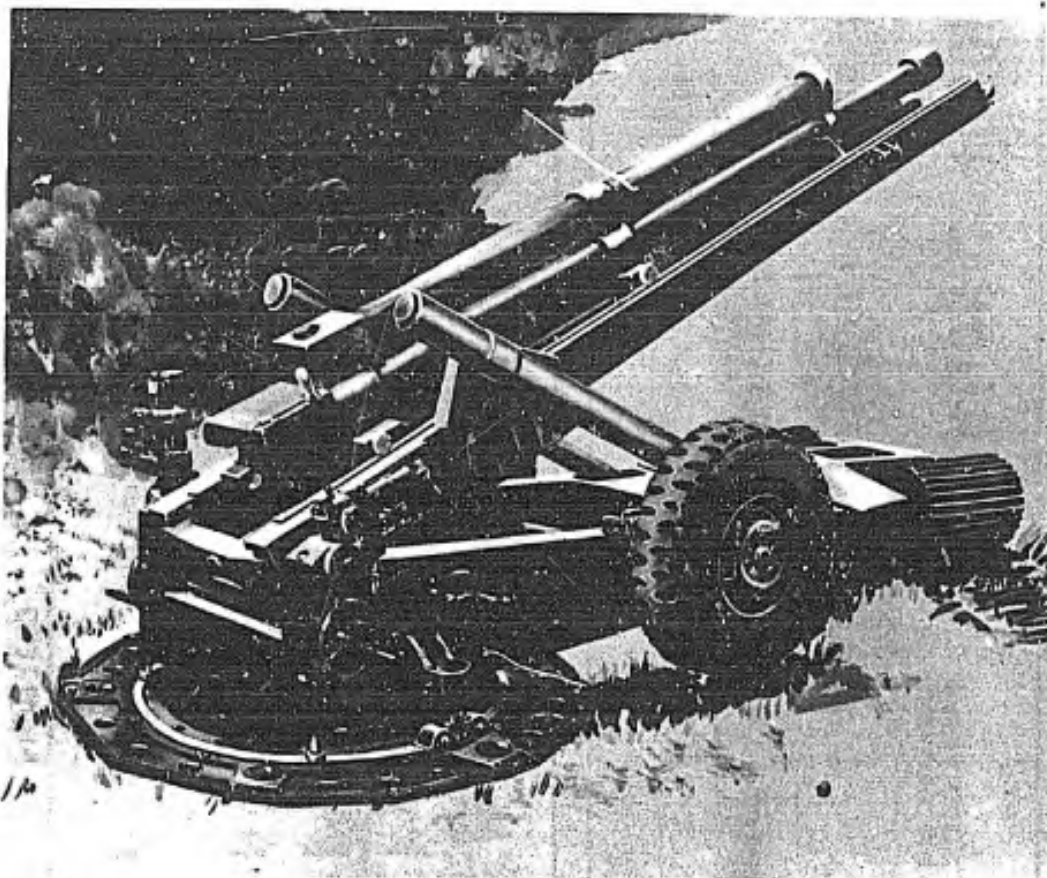


FIGURE 1
Howitzer, Light, Towed: 105mm, Soft Recoil, XM204
(Artist's Sketch)

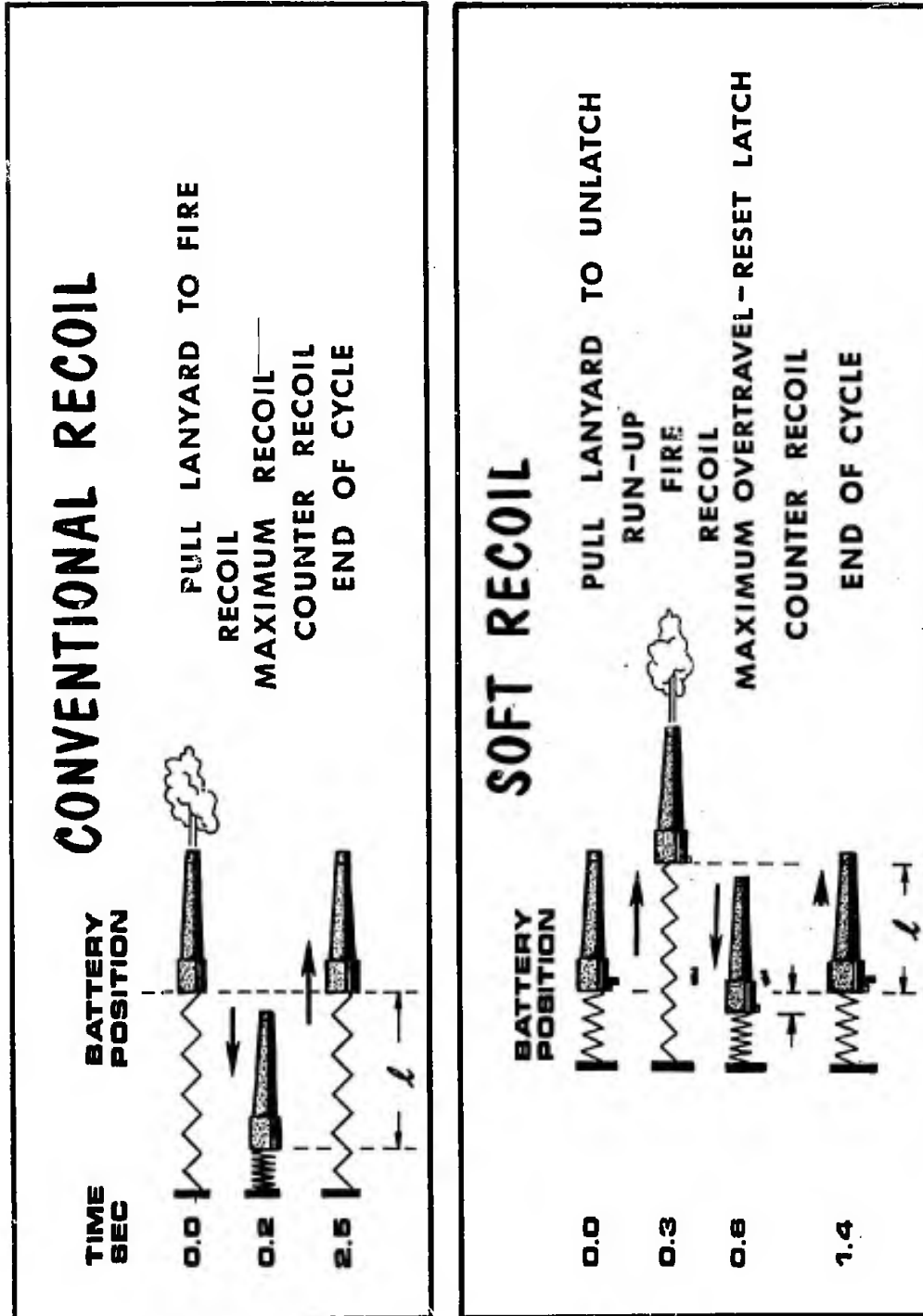


FIGURE 2 COMPARISON OF CYCLES

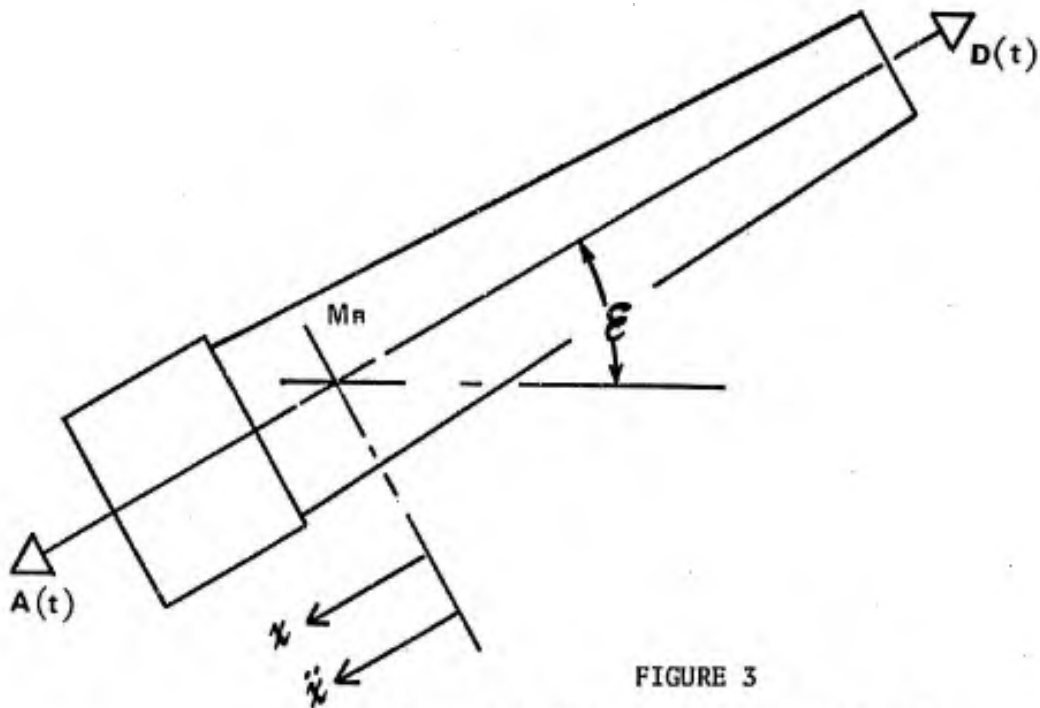


FIGURE 3
Free Body Diagram of Recoiling Mass

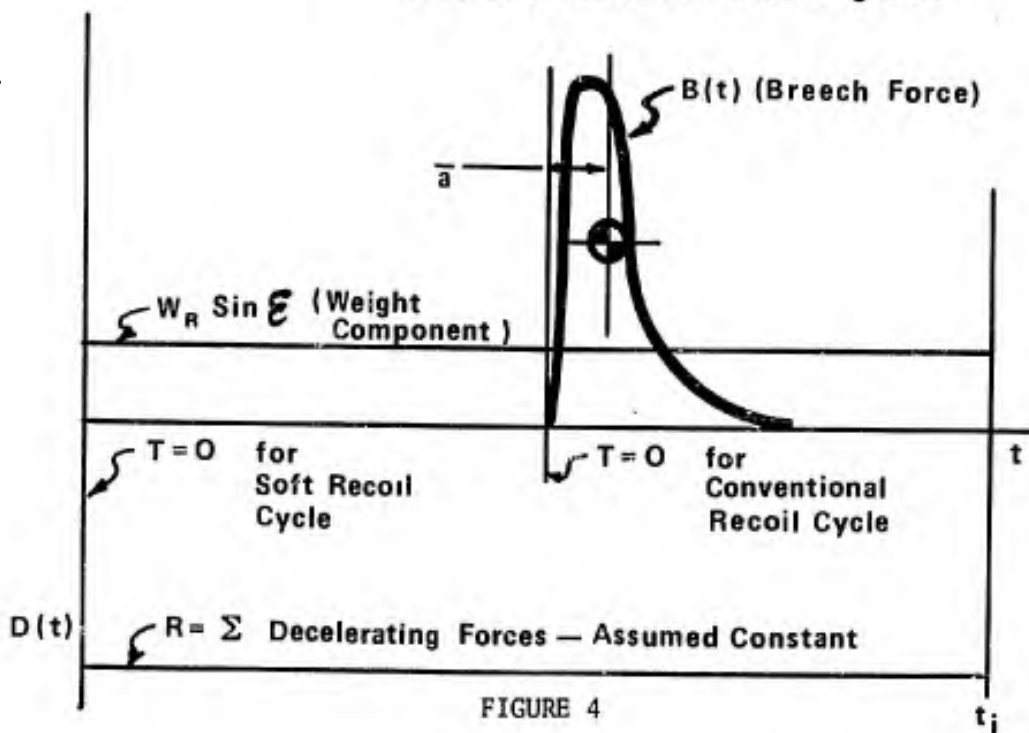


FIGURE 4
Graphical Representation of Forces on Recoiling Mass as a Function of Time

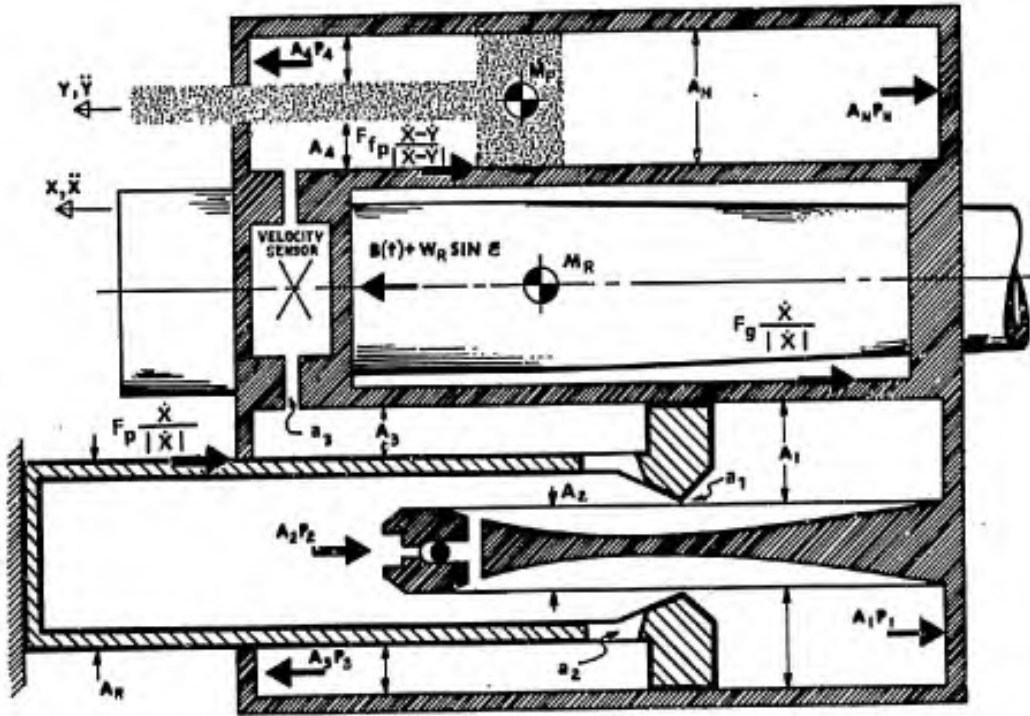


FIGURE 5

Schematic Diagram of Soft Recoil Mechanism
Showing Forces On Recoiling Parts

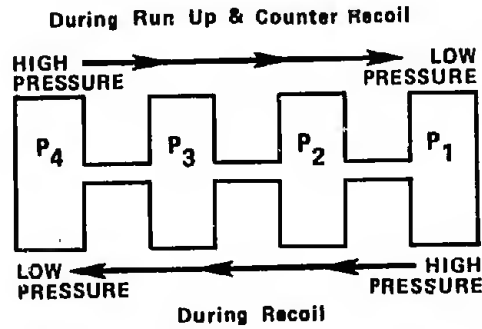
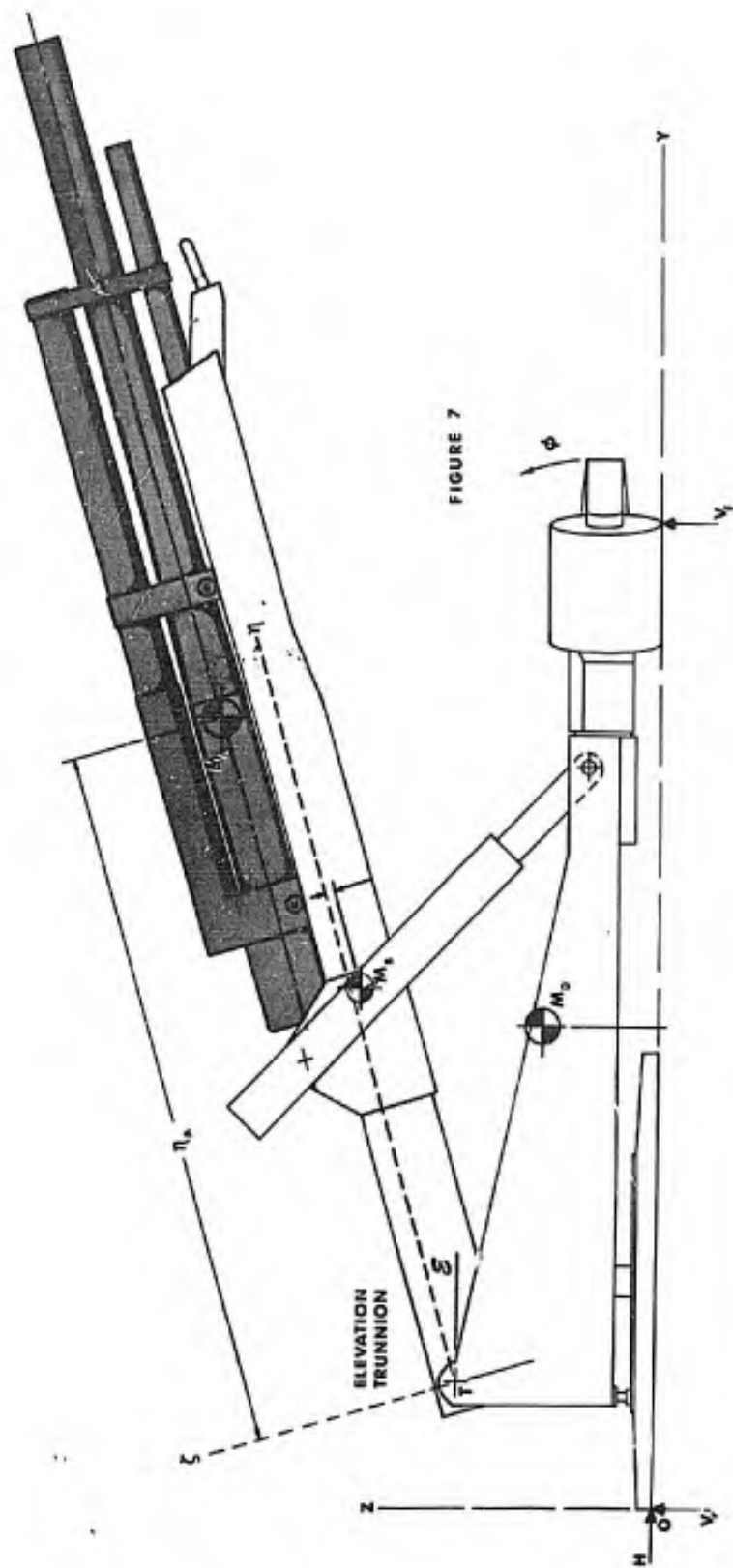


FIGURE 6

Direction of Oil Flow



INVESTIGATION OF A NEW DISEASE OF MILITARY DOGS

ROBERT M. NIMS, COLONEL, VC; DAVID L. HUXSOLL, MAJOR, VC;
PAUL K. HILDEBRANDT, MAJOR, VC AND JERRY S. WALKER, MAJOR, VC
WALTER REED ARMY INSTITUTE OF RESEARCH
WASHINGTON, D. C. 20012

In July 1968, an epizootic of a fatal hemorrhagic disease, characterized by unilateral or bilateral epistaxis, began in U. S. military dogs in Southeast Asia (Fig. 1). The disease appeared to be the same as Tropical Canine Pancytopenia (TCP) described by the British in military dogs in Singapore as early as 1963 (4,5,7), and was similar to a disease reported by the French in military dogs in Tunisia (1,2).

It became apparent that this new disease was a serious problem to combat units dependent on military dogs in Southeast Asia. Death losses have totaled 179 dogs during the first 16 months of the epizootic (Fig. 2) and further deaths are anticipated. A coordinated investigation of the disease was initiated at the Veterinary Department, 9th U. S. Army Medical Laboratory, Vietnam and the Division of Veterinary Medicine, Walter Reed Army Institute of Research, with the objective of determining the cause and nature of the disease and means of control.

When this epizootic commenced, little was known about the disease except that severe anemia and/or leucopenia accompanied the hemorrhage and that nearly all cases were fatal. Most animals appeared to be in good physical condition and there were no obvious signs of illness prior to the onset of bleeding. Death from epistaxis or other hemorrhage usually occurred within a week, although some dogs survived the initial epistaxis but had recurrent episodes days or weeks later. Initially, epistaxis was considered a manifestation of the acute stage of the disease; however, careful examination of clinical records and field investigations indicated that a febrile episode of 3 to 5 days' duration preceded epistaxis by 2 or more months. From a further investigation of cases an incubation period of 9 to 15 days was established. This was based on the time from first possible exposure to the onset of fever and is supported by laboratory findings (Fig. 3).

NIMS, HUXSOLL,
HILDEBRANDT and WALKER

During the febrile phase the dogs are lethargic, anorexic and frequently suffer marked weight loss. This is accompanied by a progressively lowered red blood cell and white blood cell count and an elevated erythrocyte sedimentation rate. As the febrile phase subsides, the dogs progress to a subclinical phase of variable duration, during which they regain lost weight and stamina. Hematologic examinations, however, reveal a leucopenia and/or anemia. Although acute or chronic epistaxis or other forms of hemorrhage later occur in some of these dogs, others do not develop epistaxis but become progressively debilitated, eventually becoming non-effective as working military animals (6).

Necropsy findings are similar in all forms of the disease. Petechial and ecchymotic hemorrhages are found on mucosal and serosal surfaces of most organs and in subcutaneous tissues (Fig. 4). Lymph nodes are swollen and hemorrhagic. Hemorrhages occur most frequently in the urinary bladder, kidney, gastrointestinal tract and lung.

The most prominent histopathologic finding is a plasma cell infiltrate surrounding vessels, particularly veins. This is evident in numerous organs, especially the meninges, kidney and lymphopoietic system (Fig. 5). There are varying degrees of hemosiderosis and erythrophagocytosis in the lymph nodes.

Heavy tick infestation has consistently been observed to coincide with incidence of TCP, providing strong circumstantial evidence that the tick may be the primary vector of the disease.

Treatment of dogs in the terminal phases of the disease has been disappointing. Dogs with epistaxis did not respond to hematinic drugs. Massive transfusions of whole blood were not effective for treating dogs with hemorrhage. A variety of antibiotics have been used in such dogs with no apparent benefit.

Disease has been produced in laboratory dogs by inoculation with blood from affected animals. These dogs have developed all signs common to the natural disease, and histologic examination of tissues has disclosed similar lesions.

Intracytoplasmic inclusions, morphologically identified as Ehrlichia canis, family Rickettsiaceae, have consistently been demonstrated in monocytes of experimentally infected dogs (Fig. 6). These are observed in peripheral blood smears and in impression smears of lung, kidney, spleen and liver tissue, stained with Wright's or Giemsa stain. Identical inclusions have been found in naturally occurring cases (3).

Blood specimens, collected from affected dogs from diverse geographic locations and inoculated into susceptible laboratory dogs, produced disease indistinguishable from natural cases of Tropical Canine Pancytopenia (Table I). This suggests that TCP has a widespread

NIMS, HUXSOLL,
HILDEBRANDT and WALKER

distribution in the tropical and semitropical regions of the world.

Other significant findings which bear mentioning are:

(1) A wide variety of other animal species have proven insusceptible to infection, and there is no evidence of transmissibility to man.

(2) Attempts to grow the Ehrlichia in embryonating eggs and a wide variety of tissue culture cell lines have been unsuccessful.

(3) There is no evidence that the disease spreads from dog to dog in the absence of a vector. Control dogs, caged for months alongside experimentally infected dogs, have not become infected.

(4) There has been no apparent change in the infectivity or the disease characteristics of 2 separate isolates of TCP which have each undergone 10 serial passages in laboratory dogs.

(5) In a preliminary study, infection was successfully prevented by the administration of tetracycline 2 days prior to and 14 days following inoculation of dogs with infective material. This was evidenced by the failure of other susceptible dogs to become infected when inoculated with their blood 30 days after treatment was discontinued.

(6) Infected dogs may develop a carrier state and remain a potential source of infection. Two laboratory dogs, inoculated more than 1 year ago, remain infected, as evidenced by the ability of their blood to infect other animals.

Studies are currently in progress to delineate the possible role of the tick in the transmission of Tropical Canine Pancytopenia; to develop other in-vivo and in-vitro systems for the isolation and replication of Ehrlichia canis; to develop a sero-diagnostic test for Ehrlichia sp.; to describe, in more detail, the pathogenesis of TCP, especially the mechanism responsible for the hemorrhagic manifestations, and the effects of breed and age; and to devise methods for the treatment, control and prevention of Tropical Canine Pancytopenia.

Acknowledgment - Recovery of E. canis from a dog contracting the disease in the Persian Gulf area was accomplished by Dr. John Seamer of the Microbiological Research Establishment, Porton, England.

NIMS, HUXSOLL,
HILDEBRANDT and WALKER

REFERENCES

1. Bobin, A., Chabassol, C., deBrux, J., Fiehrer, A., Guillot, G., Michel, C., and Pigoury, L.: Syndrome hemorrhagique thrombotique thrombocytopenique du chien en Tunisie. *Rev. Path. Gen.*, 62, (1962): 317-334.
2. Durand, M.: Note sur L'Hepato-Nephrite hemorrhagipare du Chien Berger en Tunisie. Historique, Resume Clinique. *Inst. Pasteur de Tunis, Arch.*, 38, (1961): 33-50.
3. Huxsoll, D. L., Hildebrandt, P. K., Nims, R. M., Ferguson, J. A., and Walker, J. S.: Ehrlichia canis - The Causative Agent of a Hemorrhagic Disease of Dogs? *Vet. Rec.*, 85, (1969): 587.
4. MacVean, D. W.: That New Dog Disease. *Malaysian Kennel Review*, 66, (1968).
5. Spence, J. B., Giam, C. H., Theis, J. H.: A New Canine Disease Syndrome. *Vet. Rec.*, 81, (1967): 328-329.
6. Walker, J. S., Rundquist, J. D., Taylor, R., Wilson, B. L., Andrews, M. R., Barck, J., Hogge, A. L., Huxsoll, D. L., Hildebrandt, P. K., and Nims, R. M.: Clinical and Clinicopathologic Findings in Tropical Canine Pancytopenia. *J. A. V. M. A.*, (in press).
7. Wilkins, J. H., Bowden, R. S. T., and Wilkinson, G. T.: A New Canine Disease Syndrome. *Vet. Rec.*, 81 (1967): 57-58.

NIMS, HUXSOLL,
HILDEBRANDT and WALKER



Fig. 1--Dog with a typical case of epistaxis.

NIMS, HUXSOLL,
HILDEBRANDT and WALKER

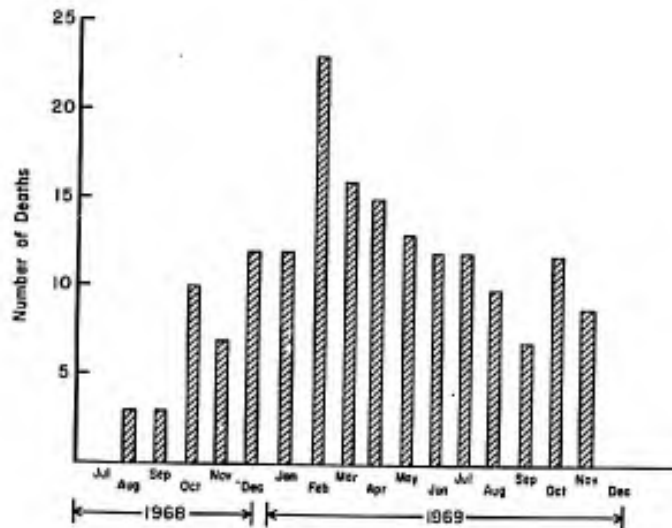


Fig. 2--Deaths from TCP in U. S. military dogs, Vietnam, August 1968 through November 1969.

NIMS, HUXSOLL,
HILDEBRANDT and WALKER

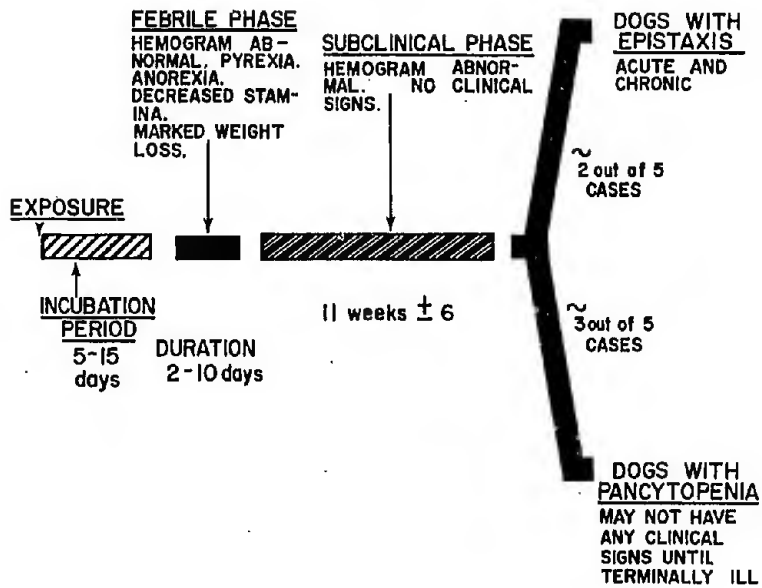


Fig. 3--Graphic representation of the clinical course of TCP.

NIMS, HUXSOLL,
HILDEBRANDT and WALKER



Fig. 4 a--Rear leg of dog with skin reflected, illustrating subcutaneous edema and hemorrhage.



Fig. 4 b--Ecchymotic hemorrhages of the mucosa of urinary bladder.

NIMS, HUXSOLL,
HILDEBRANDT and WALKER

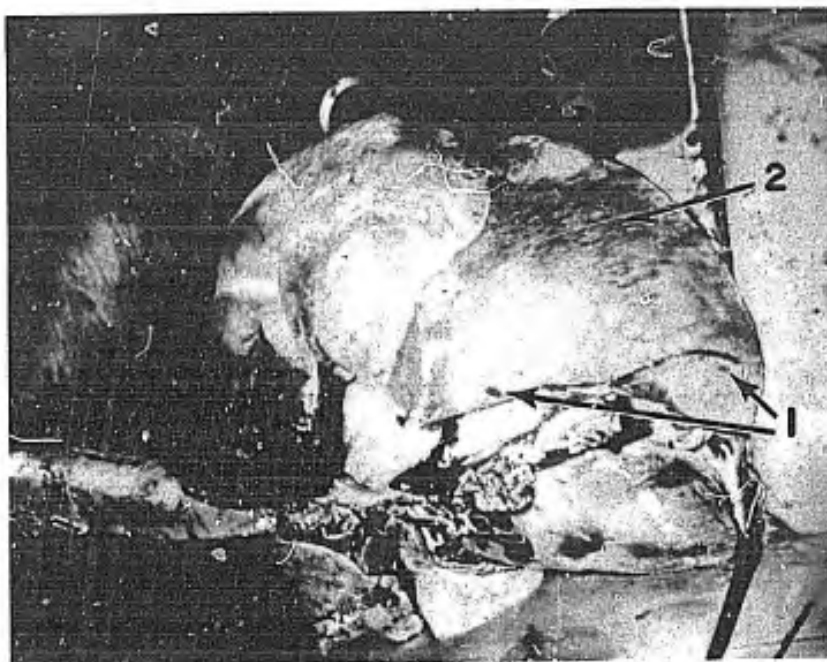


Fig. 4 c--Ecchymotic hemorrhages (1) and mottled area (2) of lung.

NIMS, HUXSOLL,
HILDEBRANDT and WALKER

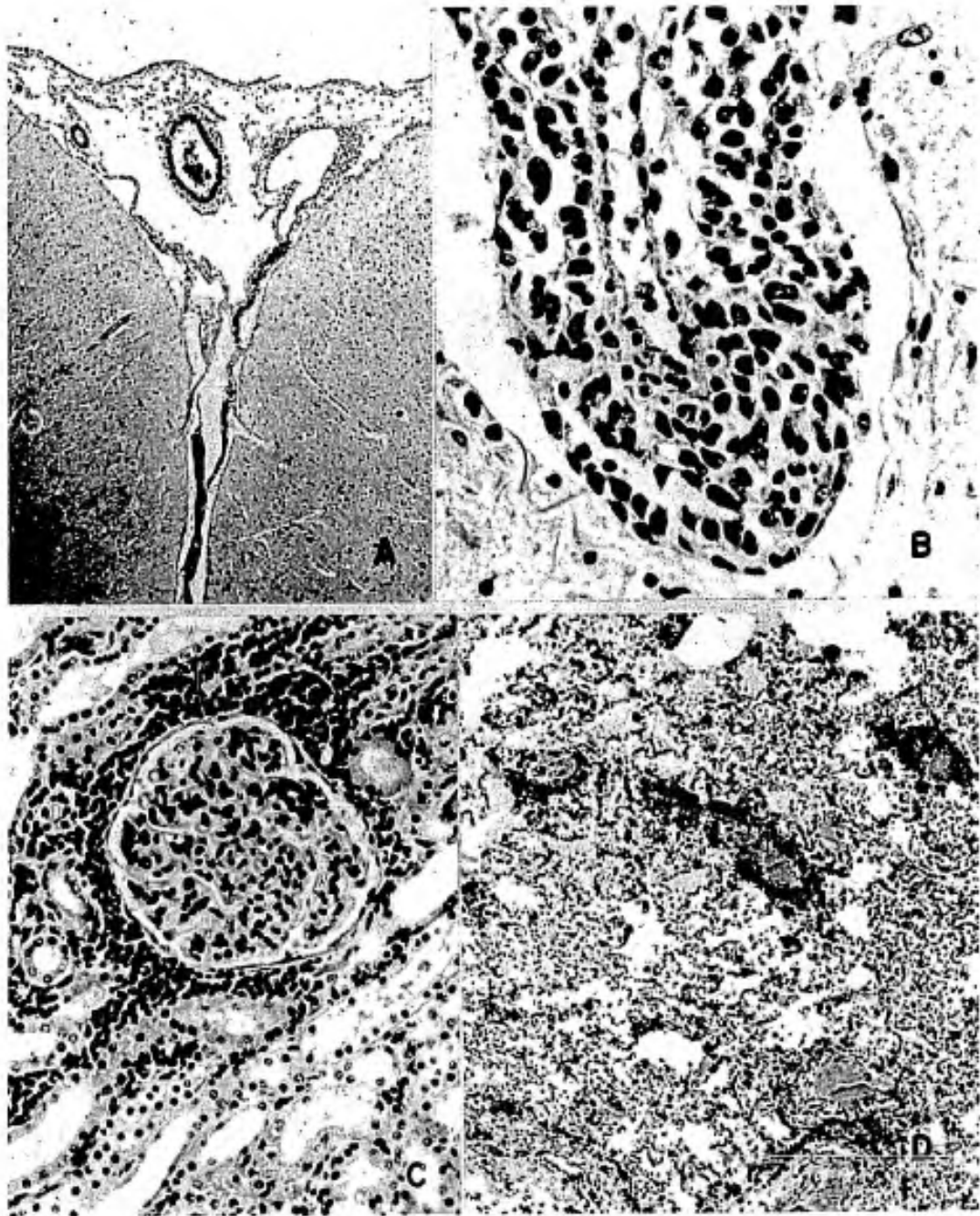


Fig. 5--Microscopic lesions of TCP. H&E stain.
a. Brain & meninges. Perivenous plasma cell infiltrate; X 45.
b. Perivenous plasma cells. Meninges; X 760.
c. Plasma cells surrounding glomerulus. Kidney; X 190.
d. Plasma cells cuffing. Pulmonary veins; X 76.

NIMS, HUXSOLL,
HILDEBRANDT and WALKER

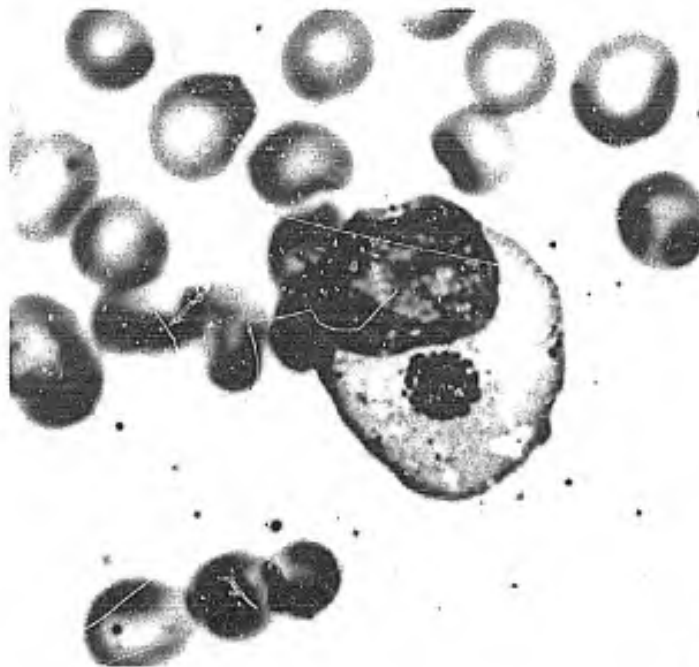


Fig. 6--Photomicrograph of inclusion of Ehrlichia canis in a monocyte.

LOCATION	TCP CONFIRMED BY PATHOLOGY	<u>Ehrlichia canis</u> CONFIRMED		NUMBER OF ISOLATES	SOURCE OF ISOLATE (BREED)
		FROM NATURAL CASES	BY TRANSMISSION IN DOGS		
OKINAWA	+	+	+	1	GERMAN SHEPHERD
REPUBLIC OF VIETNAM	+	+	+	1	GERMAN SHEPHERD
PUERTO RICO	+	-	+	4	3 GERMAN SHEPHERDS
VIRGIN ISLANDS	+	+	+	3	1 GERMAN SHEPHERD 1 OLD ENG SHEEP DOG 1 MIXED BREED
FLORIDA	-	-	+	1	GERMAN SHEPHERD
PERSIAN GULF*	-	-	+	1	GERMAN SHEPHERD

*Note: Confirmed by Microbiologic Research Establishment, Porton, England.

Table I--Geographic Distribution of Tropical Canine Pancytopenia.

ELECTROPHYSIOLOGICAL MEASURES OF CROSS-SENSORY
INTERACTION IN THE CENTRAL NERVOUS SYSTEM¹

LYNN C. OATMAN
HUMAN ENGINEERING LABORATORIES
USA ABERDEEN RESEARCH & DEVELOPMENT CENTER
ABERDEEN PROVING GROUND, MARYLAND

INTRODUCTION

The development of modern weapons and related training devices often results in the production of man-machine systems in which the human must operate controls in response to information obtained through visual and auditory channels. The human operator is placed in many military situations where sensory interactions can occur between the visual and auditory systems, since an operator must simultaneously monitor a visual display and listen to one or more incoming messages. For example, the aircraft controller must keep track of several objects on his radar screen as well as communicate with his aircraft, and the airplane pilot must monitor his flight instruments as well as listen for instructions through his ear-phones.

The known anatomical connections between the auditory and visual-sensory systems within the central nervous system would lead one to expect the occurrence of cross-sensory interactions, i.e., where the stimulation of the visual sensory system would affect the perception of a stimulus presented to the auditory sensory system. Several investigators (1, 9, 10) have presented evidence supporting the potential for sensory interaction to occur within the central nervous system.

¹In conducting the research described herein, the investigator adhered to the Guide for Laboratory Animal Facilities for Laboratory Animal Resources, National Academy of Sciences, National Research Council. This research meets the requirements of AR 70-18, Experimental Animal Care.

OATMAN

However, a large amount of psychophysical research concerned with sensory interaction between the visual and auditory systems has been contradictory--particularly the data showing whether visual stimulation can improve the threshold of hearing. Since Child and Wendt (5, 6) reported that a brief photic pulse presented to the visual system would facilitate the perception of auditory stimuli at threshold, the psychophysical evidence for facilitation at threshold, (7, 14, 18) and at suprathreshold levels (12) has continued to increase impressively. It should be noted that other investigators (8, 11, 16, 4, 13) failed to find evidence of an interaction between the visual and auditory sensory systems.

It is difficult to reconcile these diverging results, however, in the absence of other explanations "attention" is frequently invoked to explain cross-sensory facilitation and inhibition, where one may be more attentive to the primary stimulus and this may serve to enhance performance, or one's attention may be distracted by multiple-input conditions and this may degrade one's performance.

Since the human operator's capacity to receive, process, store, and act upon information is limited, some kind of selective process occurs within the central nervous system where relevant sensory stimuli are perceived while irrelevant stimuli are rejected (2, 3, 10). It is evident that a mass of sensory information impinges upon the central nervous system, most of which one is not aware of, until his attention is focused on them. For example, if one is reading, one is consciously aware of the text material, but not normally aware of the pressure of the book against one's hands, the shoes on one's feet, or the watch around one's wrist. Most of the time the central nervous system suppresses these sensory inputs, but if one calls his attention to these irrelevant stimuli, one becomes aware of them. In other words, the central nervous system operates like a biological filter--rejecting information from one sensory system when it is necessary to pay attention to information coming in another sensory system. It is necessary that an individual be able to filter irrelevant information, if he is to continue to function in an integrated manner. Therefore, it is important that one understand this filtering process, especially in military situations where human operators must acquire and act upon information received through auditory and visual channels.

The present research was conducted to provide electrophysiological evidence of cross-sensory interactions and to investigate the physiological mechanisms responsible for the filtering process that controls sensory input to the central nervous system.

METHOD

Surgical Procedure. Under sodium pentobarbital anesthesia, six female cats weighing approximately 2.5 Kg were implanted with chronic electrodes placed on the round window (RW) and bilaterally in the cochlear nucleus (CN) and auditory cortex (AC). The electrodes were stereotaxically implanted through small holes bored in the skull according to coordinates in the stereotaxic atlas of Snider and Niemer (17). The deep electrodes were concentric and were made of 0.010-inch Formvar-coated stainless-steel wire inserted into 25-gauge hypodermic stock. Both the wire and the hypodermic stock were insulated with vinyl coating (Stoner-Mudge) up to one millimeter from the tip. The tips were one millimeter apart. The cortical electrodes were flattened monopolar silver-ball electrodes placed on the dura over the auditory cortex. The round-window electrode was a 0.010-inch stainless-steel wire with a ball tip in polyethylene tubing. The indifferent electrode was a stainless-steel screw over the frontal sinus, and another stainless-steel screw at the posterior part of the skull was used as an internal ground for the animal.

After the electrodes were fixed to the skull with dental cement, the cat was removed from the stereotaxic apparatus and placed into a head holder where a stainless-steel ball electrode was implanted on the round window of each cat. After the electrode was placed on the round window and anchored to the wall of the bulla, it was led under the skin to the top of the head, where all of the electrodes were terminated in a 19-pin Ampheno connector on the vertex of the skull. The assembly was fixed to the skull with dental cement. At the time of the round-window implantation, the tendons of the stapedius and tensor tympani muscles were cut in five of the six experimental animals and were left intact in the sixth. About a month after recovery from the brain and round-window implant, another operation was performed on the opposite ear, and the stapes was removed in each cat (Fig. 1).

Histology. At the end of the experiment, the cats were sacrificed with an overdose of Lethane administered intravenously. Electrolytic lesions were produced at the recording sites of each concentric electrode. The lesion current was 1 milli-ampere for 15 seconds. The brain was removed and placed in formalin and potassium ferrocyanide for 24 hours. All placements were verified histologically using unstained, frozen sections (15). Histological verification was obtained for all six cats which confirmed the electrode placements in the cochlear nucleus of the cats' auditory pathways.

Visual and Acoustic Stimulation. The tests were made in a sound-attenuating chamber which had a visual display mounted on one end wall, a response key and a liquid food dipper mounted in the floor, and a driver speaker, with sound tube attached, mounted in the top of the box (Fig. 2).

The cats' task was to learn the visual discrimination for food reinforcement. The cats were gradually deprived of food until they were on a 22-hour deprivation schedule. Then they learned the visual discrimination task, with Purina tuna mixed with water as food reinforcement. All cats received either 100 trials or 50 food reinforcements, each day of training until they reached a criterion of 20 consecutive correct responses.

The visual stimuli consisted of a large and a small concentric ring presented successively for discrimination. The large outer ring was 1/8-inch wide and had a diameter of one inch and the small inner ring was 1/8-inch wide with a diameter of 3/4 inch. Luminance measurements were made on the stimulus figures with a Pritchard Spectrophotometer (Model 1970-PR). The luminance was 7.17 foot-Lamberts for the outer ring and 8.47 foot-Lamberts for the inner ring. Figure 3 shows a schematic diagram of the stimulus presentation. The large outer ring was presented first, which served as a warning stimulus for the cat to attend to the stimuli. Then the smaller inner ring was presented. The cat had to respond to the onset of the small inner ring to receive food reward. If the cat responded between the onset of the large outer ring and the onset of the small inner ring, it received no reinforcement and the onset of the next trial was delayed 25 seconds. In order to increase the cats' attentiveness, the temporal interval (t_1) between the onset of the large and small concentric rings was varied randomly between one and six seconds. The exposure duration of the small inner concentric ring was four seconds and the time between trials was 25 seconds.

Auditory clicks were presented continuously at a rate of one per second during the presentation of the successive visual discrimination task, but they were not synchronized with the onset of the visual display. The auditory clicks were generated by a 90-microsecond square-wave pulse obtained from Tektronix waveform (Type 162) and pulse generators (Type 163). The rectangular pulses were led through a high-pass filter (Allison Labs, Model 2-B, attenuation 30 dB per octave) set at 9,600 Hz, a decade attenuator (General Radio, GR-1450), and a Dynakit power amplifier (Mark III, 60 watt). From the power amplifier the clicks were delivered to a hypersonic driver speaker (University T-50) and led through a 1-3/8 inch diameter, eight-inch long Phenolic sound tube through the sound-attenuating chamber into a nine-inch, 1/4 inch inside diameter Tygon tube which terminated at the entrance to the external auditory meatus of the cat (Fig. 1). The clicks were presented at a peak intensity of 90 dB SPL (re 0.0002

OATMAN

microbar). The click intensity was measured with a calibrated condenser microphone (Bruel and Kjaer type 4135). The sound-pressure measurements were made in the sound attenuated cubicle, where the condenser microphone was placed perpendicular to and just in front of the end of the sound tube. The voltage output from the microphone was observed osciloscopically, and the decade attenuator was used to obtain the necessary sound levels. The highest wave was measured from base line to peak to calculate the sound intensity. The sound pressure was calibrated at 1 dyne per square centimeter and other sound pressures for different intensities were inferred from that intensity, since the output from the speaker was linear through 120 dB.

Data Collection and Procedure. Simultaneous recordings were obtained from the round window (cochlear microphonics and $N_1 - N_2$ responses), the cochlear nucleus and the auditory cortex to click stimuli. Recordings were obtained from the unrestrained animals via a Microdot shielded cable connected to an electroencephalograph (Grass Model 7) located outside the sound-attenuating cubicle. At the same time, the click-evoked potentials were recorded on a 14-channel FM tape recorder (Sangamo 4700). The tape speed was 7-1/2 i.p.s. and the band pass was from 0 to 2,500 Hz for FM, but 50 to 35,000 Hz for direct record. From the FM tape recorder the click-evoked potentials were fed into a Bio-Data variance computer (Model 204), averaged with a computer of average transients (Technical Measurement Corporation, CAT 1000) and displayed on a Tektronix storage oscilloscope (Type 564) or plotted on an X-Y plotter (Mosley Model 7000 AM).

After the electrodes were checked, the data were collected in recording sessions consisting of a control period, an experimental period, and a control period, which were designed to alter the attentive state of the animals. The data were collected under four different attentive states: 1) a pre-test control in which the cat was awake, relaxed, and nonattentive to any identifiable stimuli, 2) a pre-discrimination period during the test which was just prior to the onset of the visual discrimination when the cat was mildly attentive, anticipating the onset of the visual discrimination, 3) during the presentation of the visual discrimination stimuli when the cat was attentive since appropriate behavioral responses were obtained to the visual stimuli, and 4) a post-test control period similar to the pre-test control period. The evoked responses to 50 clicks were averaged on the computer of average transients for each of the four different attentive states, i.e., while the cat was relaxed, while the cat was anticipating the onset of the visual discrimination, while the cat was attending to the visual discrimination, and while the cat was relaxed again. The 50 click-evoked responses, averaged while the cat was attending to the visual discrimination, included only those evoked potentials presented between the onset of the large outer concentric ring and the presentation of the small inner concentric ring (Fig. 3).

RESULTS

The data consist of plots of the averages of 50 click-evoked potentials from the three electrode locations: round window (LRW), cochlear nucleus (LCN), and auditory cortex (LAC). The peak-to-peak (first largest positive to first largest negative) amplitude of these averaged evoked responses was measured by ruler to the nearest millimeter and then converted into microvolts. Evoked potentials influenced by bodily movement were discarded from the data as were those responses obtained on discrimination trials in which the cat failed to respond and received no food reinforcement. No attempt was made to analyze the different components of the evoked response.

Figure 4 shows an example of representative averaged auditory evoked potentials for cat number 28 for each of the four attentive states: pre-test control (cat non-attentive, relaxed but awake), pre-discrimination (cat alert, somewhat attentive), during-discrimination (cat very attentive), and post-test control (cat non-attentive, relaxed but awake). The figure shows that the mean peak-to-peak amplitude of click-evoked potentials recorded from the auditory pathway were of a smaller amplitude when the cats were very attentive than when they were non-attentive. This reduction in amplitude occurred at all three electrode locations. All six cats showed that with a mild degree of attention (pre-discrimination) the amplitudes of the click-evoked potentials at the cochlear nucleus and the auditory cortex were reduced when compared to the control periods. However, when the attention of the animals was focused upon the visual discrimination, the amplitudes of these evoked potentials were further reduced. The top wave forms in Figure 4 shows the cochlear microphonic (CM) and $N_1 - N_2$ responses to a single click. Likewise, when the animal was very attentive (during-discrimination), the amplitudes of the $N_1 - N_2$ responses of the auditory nerve (LRW) were reduced when compared with the control periods. It should be noted that although the $N_1 - N_2$ responses were reduced in amplitude when the cats were very attentive (during-discrimination) little or no change occurred in the amplitude of the cochlear microphonic. It was necessary to increase the number of responses to 100 in order to obtain the maximum resolution of the $N_1 - N_2$ responses from the computer of average transients. Therefore, the missing data of the pre-discrimination condition at the round window (LRW) resulted from an insufficient number of evoked responses during that condition.

The variance of the 50 averaged responses is presented below the mean for the cochlear nucleus and auditory cortex in Figure 4. The variance for the round-window response was discarded since the computer could not be properly calibrated in the variance mode. The figure shows

OATMAN

that the evoked potentials become more variable with increased attention at the auditory cortex. The highest variance occurred when the cats were most attentive, whereas the lowest variance occurred during the control periods when the cats were non-attentive. Differences in variance also occurred between the cochlear nucleus and the auditory cortex. For all of the attentive states, the variance in the cochlear nucleus was much lower than the variance in the auditory cortex.

All of the data are summarized in Figures 5, 6, 7, and 8. The figures show the mean peak-to-peak amplitude in microvolts as a function of increased attention for the five cats with middle-ear muscles cut and the cat with muscles intact. The columns in the graphs represent different attentive states; the pre-test and post-test were control periods, with the cat relaxed, awake, and non-attentive. The experimental period consisted of two parts: (a) pre-discrimination (cat mildly attentive, prior to the visual discrimination), (b) during-discrimination (cat very attentive, onset of outer and inner rings). The number (N) below each column refers to the number of averages upon which the condition means were based. The limits around each mean for the cochlear nucleus and the auditory cortex represent 95 percent confidence levels. No confidence levels are included for the round-window means since the variance could not be obtained from the computer.

At the auditory cortex (Fig. 5) the mean peak-to-peak amplitudes decreased as a function of increased attention for cats with middle-ear muscles cut as well as for the cat with its middle-ear muscles intact. In the cats with middle-ear muscles cut, comparing the pre-discrimination period with the during-discrimination period, the figure shows that the mean amplitude was reduced 30 percent, which was significant at the .02 level ($t= 2.34$, $df= 4065$). The mean amplitude reduced in the cat with the middle-ear muscles intact was not different from the cats with their muscles cut. The percentage of amplitude reduction between the pre-discrimination and the during-discrimination periods was 29 percent which was significant at the .01 level ($t= 2.64$, $df= 684$).

At the cochlear nucleus (Fig. 6) in cats with the middle-ear muscles cut, the mean amplitude of the pre-discrimination period as compared with the during-discrimination period was reduced 26 percent which was significant at the .01 level ($t= 21.01$, $df= 3232$). Although there was an overall reduction in amplitude between the cats with the middle-ear muscles cut and the cat with the middle-ear muscles intact, the amplitude reduction probably reflects a poor electrode placement in PC-29 rather than any action on the part of the middle ear muscles. The percentage of

OATMAN

amplitude reduction for the cat with the middle-ear muscles intact was 20 percent between the pre-discrimination and the during-discrimination, which was significant at the .01 level ($t = 7.87$, $df = 930$).

At the round window (Fig. 7) in cats with middle-ear muscles cut, the mean amplitude of the N_1 response in the during-discrimination period was reduced 46 percent when compared with the pre-test period. Since the variance was not available for this electrode placement, a t test was not applied to the two mean amplitudes. However, it may be assumed that a distribution of evoked responses around the means would be similar to the distribution observed in the cochlear nucleus and that the two means would be significantly different in amplitude. The amplitude of the evoked potentials from the cats with middle-ear muscles severed was much larger than for the cat with its middle-ear muscles intact. This was probably due to a poor electrode placement, since this cat had the least sensitivity of the six cats. The percentage of amplitude reduction of the N_1 response was 40 percent between the pre-test period and the during-discrimination period, and this reduction is similar to that of cats with middle-ear muscles severed.

Figure 8 shows the cochlear microphonic response recorded at the round window for cats with middle-ear muscles cut, as well as for the cat with middle-ear muscles intact. The graph shows the mean peak-to-peak amplitude of the cochlear microphonic in microvolts as a function of increased attention. No significant differences were found between the pre-test or post-test periods and the during-discrimination period for the cats with middle-ear muscles cut and intact. Again, the overall reduction in amplitude between cats with middle-ear muscles cut and the cat with middle-ear muscles intact was probably due to a poor electrode placement in PC-29.

DISCUSSION AND CONCLUSIONS

The results indicate that the attentive state of the animal significantly affects the amplitude of click-evoked responses recorded all along the auditory pathway. These data provide evidence that cross-sensory interactions occur within the central nervous system. The present evidence suggests that the nature of the cross-sensory interaction is inhibitory and that the response modifications in the auditory pathways are due to a central inhibitory mechanism which influences $N_1 - N_2$ responses in the cochlea but does not influence the cochlear microphonics.

In the present experiment, as the animal was more attentive to the relevant visual stimuli, a selective process occurred within the central

OATMAN

nervous system where the irrelevant stimuli were suppressed. According to traditional concepts the suppression of irrelevant information and the facilitation of relevant sensory information during attention would take place exclusively at the cortex. In light of the results of this experiment, this concept is no longer tenable. It appears that stimuli can be suppressed at very early stages in the afferent auditory pathways, and that sensory information is transmitted to the cerebral cortex only after having been subjected to a "filtering" at a peripheral level.

Since these results clearly demonstrate a filtering process within the central nervous system, this experiment provides support for Broadbent's (2) theory that the human operator may function as a one-channel data-processing system having limited capacity. In other words, information from only one source can gain access to the central nervous system at any given time, so that one item of information must be processed before another item can enter the processing system. This implies that the cross-sensory interactions would complicate any attempt to use more than one modality simultaneously to increase the information transmitted to a human operator.

REFERENCES

1. Ades, H. W. Central Auditory Mechanisms. In J. Field, H. W. Magoun, and V. E. Hall, (Eds.), Handbook of Physiology: Neurophysiology, American Physiological Society, Washington, D. C. 1959, Chapter 24, Pp. 585-613.
2. Broadbent, D. E. Perception and Communication. London, 1958.
3. Broadbent, D. E. The approach to information processing through behaviour. In Information Processing in the Nervous System, Vol. III. of Proceedings of the International Union of Physiological Sciences, XXII International Congress Leiden, 1962, Pp. 9-14.
4. Brown, A. E. and Hopkins, H. K. Interaction of the auditory and visual sensory modalities. J. Acoust. Soc. Am., 1967, 41, 1-6.
5. Child, I. L. and Wendt, G. R. The magnitude and temporal course of facilitation of hearing by vision. Psychol. Bull., 1936, 33, 596.
6. Child, I. L. and Wendt, G. R. The temporal course of the influence of visual stimulation upon the auditory threshold. J. Exp. Psychol., 1938, 23, 109-127.

OATMAN

7. Gregg, L. W. and Brogden, W. J. The effect of simultaneous visual stimulation on absolute auditory sensitivity. J. Exp. Psychol., 1952, 43, 179-186.
8. Gulick, W. L. and Smith, F. L. The effect of intensity of visual stimulation upon auditory acuity. Psychol. Record, 1959, 9, 29-32.
9. Hernandez-Peon, R. Reticular mechanisms of sensory control. In W. A. Rosenblith (Ed.), Sensory Communication. M.I.T. Press, Cambridge, Mass., 1961, Chapter 26, Pp. 497-520.
10. Hernandez-Peon, R. Physiological mechanisms in attention. In R. W. Russell (Ed.), Frontiers in Physiological Psychology. Academic Press, New York, 1966, Pp. 121-144.
11. Howarth, C. I. and Treisman, M. Lowering of an auditory threshold produced by a light signal occurring after the threshold stimulus. Nature, 1958, 182, 1093-1094.
12. Karlovich, R. S. Sensory interaction: Perception of loudness during visual stimulation. J. Acoust. Soc. Am., 1968, 44, 570-575.
13. Karlovich, R. S. Auditory thresholds during stroboscopic visual stimulation. J. Acoust. Soc. Am., 1969, 45, 1470-1473.
14. O'Hare, J. J. Intersensory effect of visual stimuli on the minimum audible threshold. J. Gen. Psychol., 1956, 54, 167-170.
15. Siegel, J. A rapid procedure for locating deep electrode placements. Physiol. Behavior, 1968, 3, 203-204.
16. Sheridan, J. A., Cimbalo, R. S., Sills, J. A., and Alluisi, E. A. Effects of darkness, constant illumination, and synchronized photic stimulation on auditory sensitivity to pulsed tones. Psychonom. Sci., 1966, 5, 311-312.
17. Snider, R. and Niemer, W. T. A stereotaxic atlas of the cat brain. University of Chicago Press, Chicago, 1961.
18. Watkins, W. H. Photic facilitation of tonal signal detection in a forced-choice situation. Psychonom. Sci., 1966, 6, 477-478.

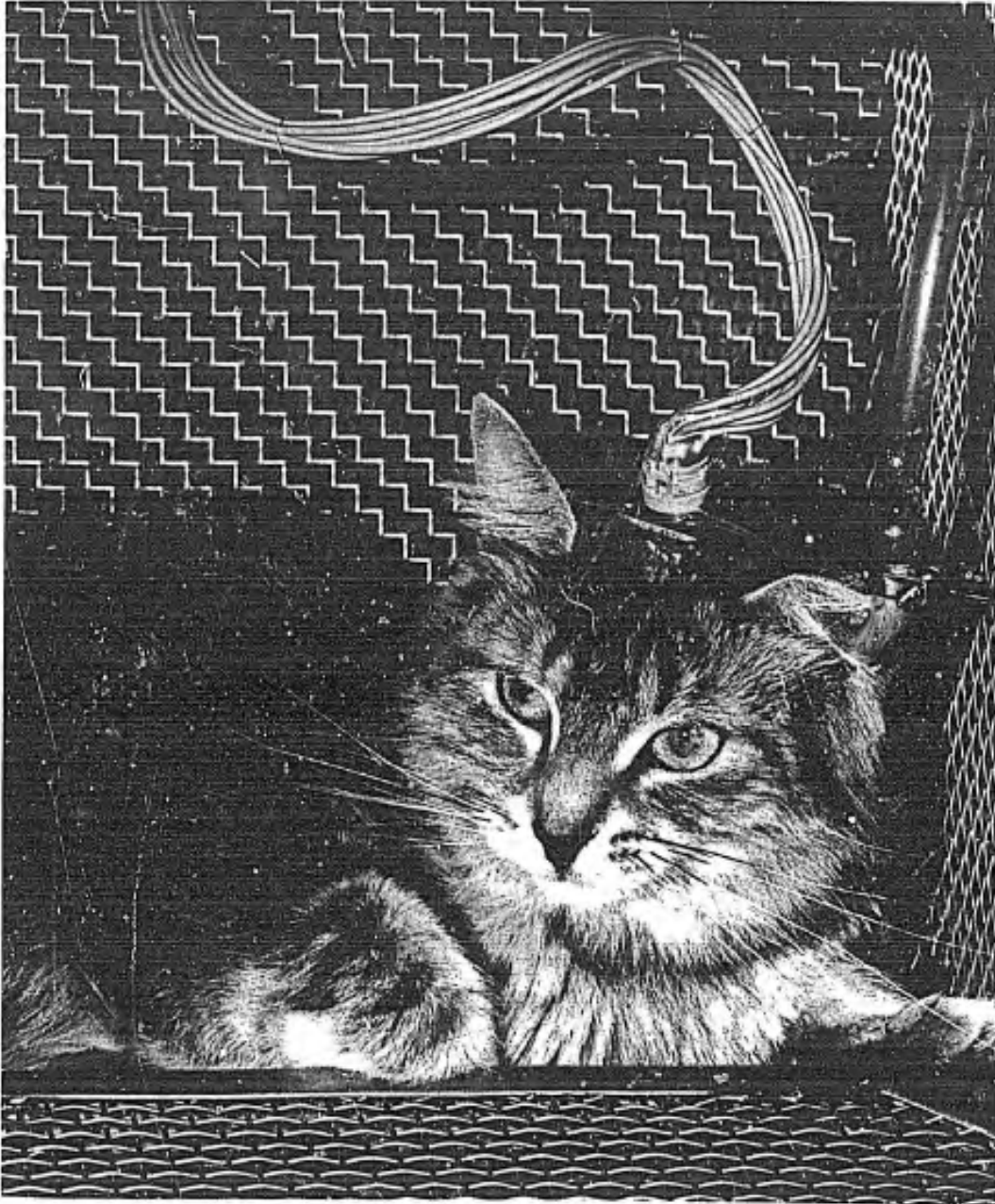


Figure 1. Photograph showing the EEG cable connection and sound-tube connection to the cat.

OATMAN

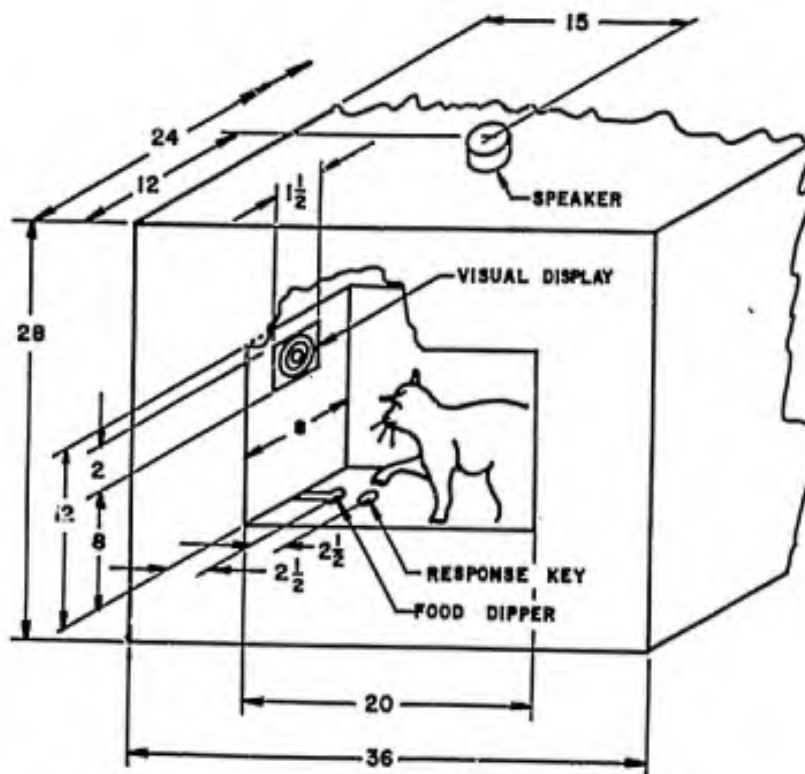


Figure 2. Diagram of sound-attenuating chamber.

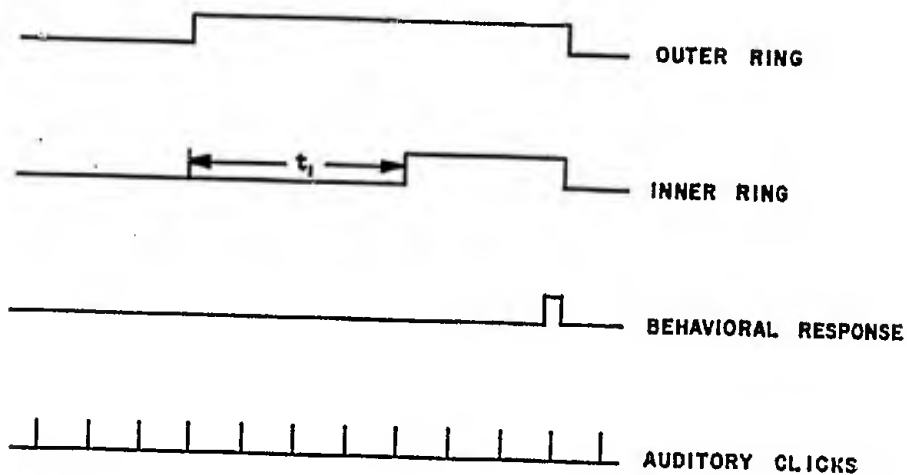


Figure 3. Schematic diagram of the stimulus presentation.

OATMAN

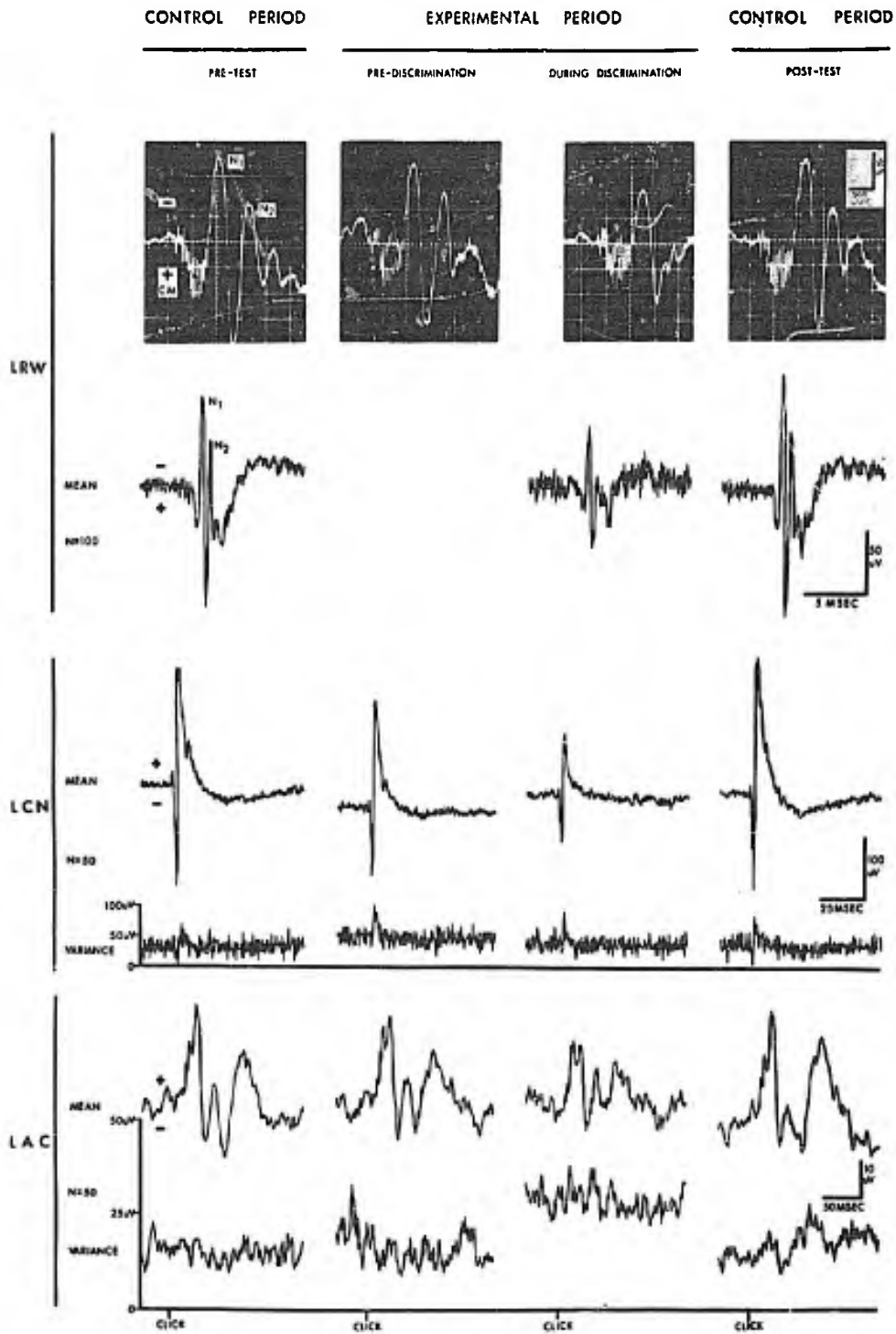


Figure 4. Mean evoked potentials recorded from left round window (LRW), left cochlear nucleus (LCN), and left auditory cortex (LAC) for different attentive states.

OATMAN

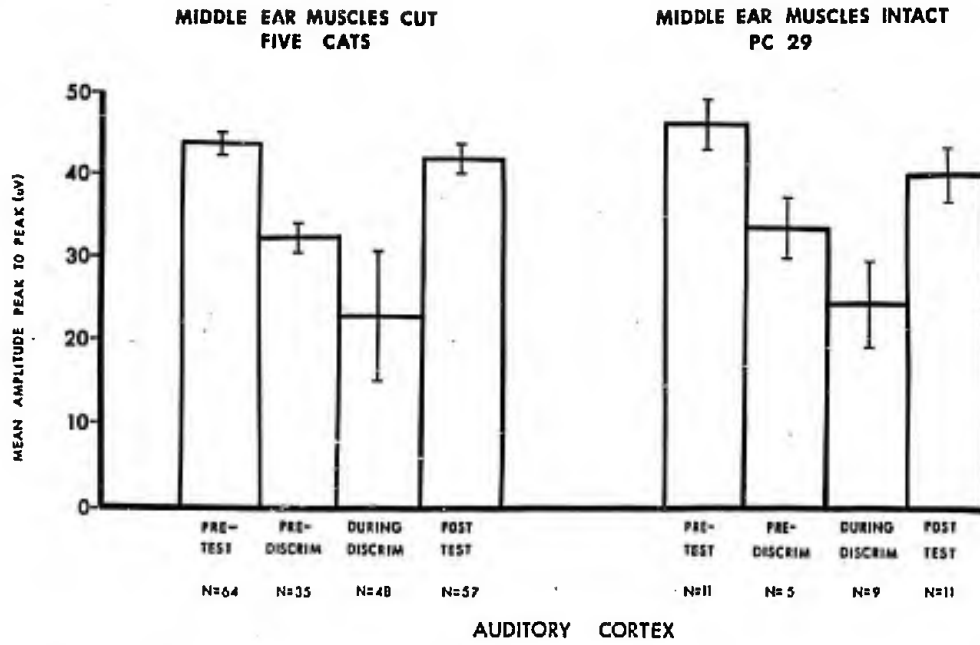


Figure 5. Mean amplitude of evoked potentials as a function of increased attention.

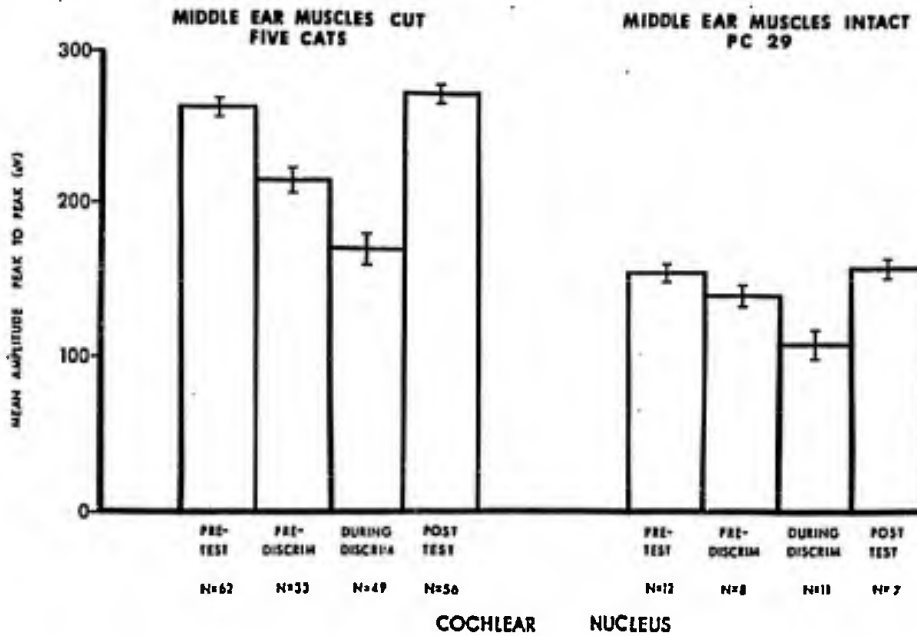


Figure 6. Mean amplitude of evoked potentials as a function of increased attention.

OATMAN

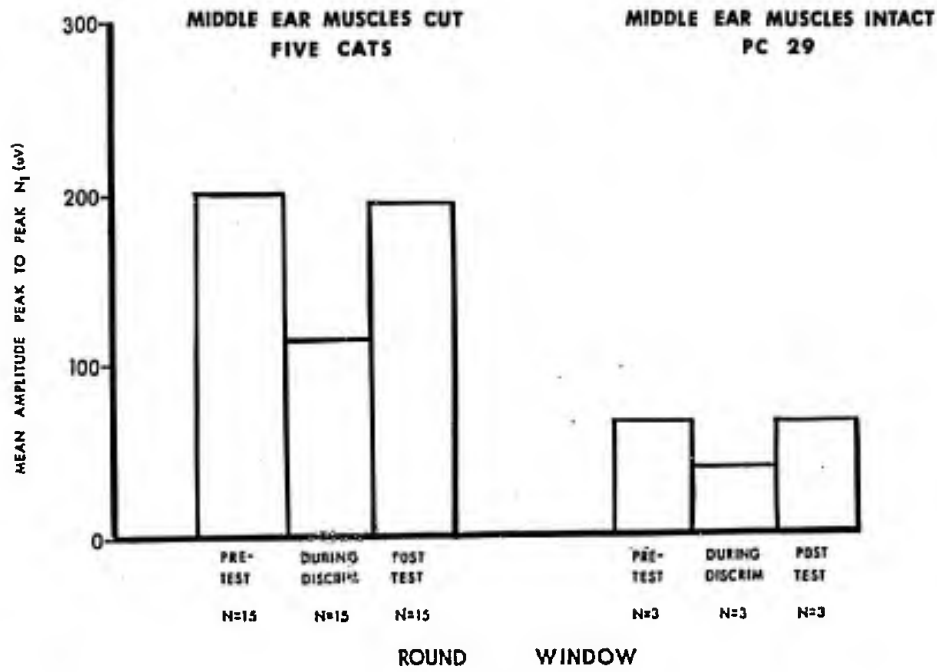


Figure 7. Mean amplitude of evoked potentials as a function of increased attention.

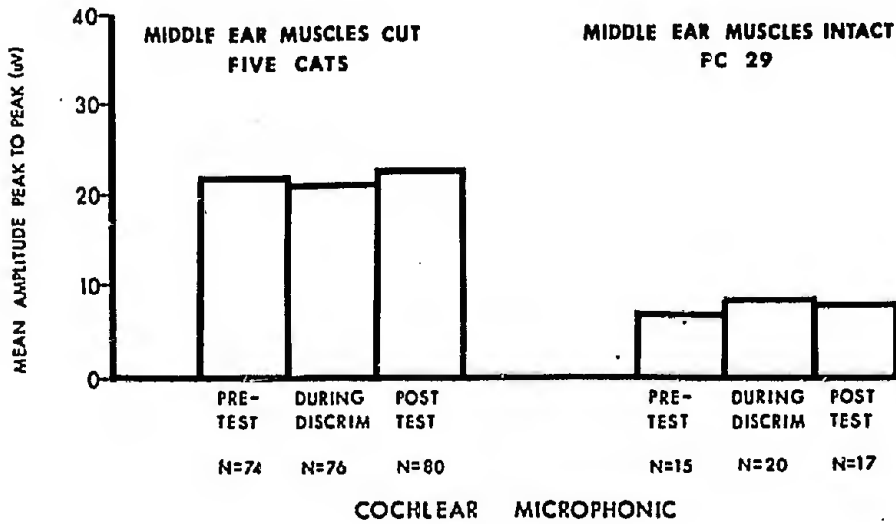


Figure 8. Mean amplitude of evoked potentials as a function of increased attention.

APPLICATION OF SENSING ARRAYS TO PHOTOGRAMMETRY
AND METROLOGYDESMOND C. O'CONNOR, PI-FUAY CHEN*
US ARMY ENGINEER TOPOGRAPHIC LABORATORIES
FORT BELVOIR, VIRGINIA

INTRODUCTION

Many inquirers have found in living systems inspiration for the solution of engineering problems in data processing, recognition and detection, and mensuration. In particular, the human eye has always posed a challenge, and as sensor array technology advances, eye analogues could offer great possibilities for the substitution of arrays for film in a wide variety of situations where cameras are used to produce metric records. It is not inconceivable that a camera with an array in the focal plane could be made to generate metric data about any image projected onto it, such as a stellar field. This would virtually generate coordinates in realtime.

A series of investigations by O'Connor [1] provided the basis for this paper. O'Connor found, as had others before him, that the performance of the human eye in a simple visual acuity task in photogrammetric measurement could not be simply explained in terms of the properties of light, the optical properties of the eye, and the dimensions of the retinal receptors. Experimental results showed that the standard deviation of optical settings may be of the order of $1/24$ of the dimensions of the finest foveal cone.

The classical, or "static," theories of vision have proved unable to resolve this paradox, and a new set of "dynamic" theories is evolving based on image perturbation caused by the involuntary physiological nystagmus, and neural and central factors up to the brain.

The physiological nystagmus oscillates the diffraction pattern of an object continuously across the retina for conversion into nerve fiber discharge. The nature and extent of the movements, their role in vision, and the mechanisms underlying their operation continue to be the subject of research. With a great measure of agreement amongst investigators, the following movements have been shown to be present during fixation:

O'CONNOR, CHEN*

a. A "tremor" of mean amplitude of the order of 10 to 15 seconds of arc, and frequency ranging from 20 to 100 c.p.s., with the maximum amplitude occurring at about 50 c.p.s. The maximum angular velocity is of the order of 20 minutes of arc per second.

b. A series of very rapid "flicks" or "saccades", whose amplitude ranges from 1 to 25 minutes of arc, occurring irregularly at intervals ranging from 0.03 to 5 seconds. The angular velocity is of the order of 600 minutes of arc per second.

c. Slow, unidirectional "drifts" of up to 5 to 6 minutes of arc in the intervals between the flicks, of angular velocity of the order of 1 minute of arc per second.

The movements are shown approximately in Figure 1 [2].

There appears little doubt that the physiological nystagmus operates to compensate for the grossness of the retinal array in minute visual tasks, and produces nerve fiber discharges. It is, however, the subtle interplay between the elements of the neural system as these discharges are processed and transmitted that provide the most startling effects. The dynamic theory of vision presents a picture of reciprocal overlap, neural recovery cycles, and multiplication of pathways at geniculate and cortex producing neural amplification, border inhibitions, accentuation of gradients, and control of thresholds.

An investigation has been designed to simulate the nystagmus and neural aspects of the visual system in terms of sensor arrays.

This paper is concerned with the perturbation of an image across a linear array in order to increase its resolution. Two techniques are described, one a mechanical perturbation as mentioned by O'Connor [3], and the other an electronic perturbation after Chen [4]. The full neural simulation will be undertaken progressively as the perturbation technique is solved. In this electronic system, "perturbation" corresponds to the involuntary eye movements. A zero sensing error is obtained by the introduction of an optimal perturbation signal [5] into the system. In another words, the size of the receptors used in the system and complexity of the system are greatly reduced by the introduction of the perturbation. A moderate size of receptor-array, which eliminated the lead problem, is thus possible.

Since the sensing array system is capable of detecting the position, velocity, area, and some simple shapes of the object-image the application of the system to metrology and photogrammetry is obvious. Possible applications of the sensing array systems to the above two fields are considered. Extensions of the idea in the future are suggested with some general comments. Finally, the relationship between the suggested techniques and the state-of-the-art

O'CONNOR, CHEN*

of electronics is discussed.

THE SENSING ARRAY SYSTEM

A sensing array system based on the concepts described in the previous section is devised. A block diagram of the system is shown in Figure 2. The system consists of a receptor-array, memory (for some applications the memory may be omitted), signal processor, an output indicator, and a control unit.

A brief description of the system's operation follows. The object-image in the sample space is projected onto the receptor-array through an optical coupling device consisting of mirrors. The receptor-array senses and converts the optical image signals into electrical signals. These electrical signals are then stored in the memory. The signal processor, which follows the memory, operates on the stored signals and produces a signal denoting either the position velocity, area, or shape of the object image, depending upon the type and the function of the signal processor being used. This signal is then displayed by the output indicator. It is also sent to the memory. A control unit is used to control all the system functions.

The array system is capable of detecting position, velocity, area, and some simple shapes of a moving object-image in a 2 or 3-dimensional form. The receptor-array is the primary section of the system being considered here. It converts the image signal into electrical signals which can be processed electronically. It is assumed to consist of many equally spaced elements (a matrix of elements) which have an output of "1" when illuminated by an amount of the input image equal to or greater than its threshold value and a "0" otherwise. If a coordinate system is defined with respect to the receptor matrix, the image position can be determined by noting which receptor elements are energized by an object-image. Velocity information is obtained by introducing time into the receptor-array measurements. Velocity measurements require the use of a memory and logic circuits. The area of an image is obtained by summing up all outputs energized by the object-image. Some simple shapes of the object-image are detected by using pattern recognition techniques. A relatively complicated signal processor is required for this case.

As stated previously, the receptor-array is one of the most important parts of the system. A theory is developed which relates the size of the receptor arrays and the complexity of the input object-image. A receptor-array having square photo surface elements is assumed for analysis. The elements of the receptor array are assumed to be packed closely so that in effect, no dead-space (or inactive area) exists. The theory is then extended to the cases where certain dead-spaces are assumed for the receptor-array. Both one- and two-dimensional receptor-arrays are considered [4]. The size of the receptor-array used depends on the complexity of the object-image and the desired resolution (or detecting accuracy) of

the system. Not only this, the size of the receptor-array also directly determines the memory size and the complexity of the electronic signal processor and, therefore, directly determines the total cost of the entire system. For the system being considered, in order to detect a rotating square to an angular position resolution of one degree, a receptor-array containing elements of 314×314 is required. To detect a moving cube within an angular position resolution of one degree, two receptor-arrays each having elements of 628×628 are needed. With this size of receptor-array, a translation velocity error of approximately 0.16 per cent can be obtained [4].

For angular position resolutions better than one degree, a larger size of receptor-array that is beyond the state-of-the-art of the sensing array technology is required. To the authors' best knowledge, some research organizations both in government and private industries have done some experiments on mosaic sensing arrays [6], [7], [8], [9]. The largest array ever tested was constructed at RCA Laboratories [6] and consisted of a 256×256 matrix of receptor elements. The primary problem with these arrays is in connecting leads to each sensor element of the array since the arrays were fabricated in a very small size, approximately 1 inch square in order to sense a good resolution from the object-image. In order to avoid this problem, most large receptor-arrays today use a time-share readout device to read the output signal either from a row or a column of the array one sensor element at a time. In this way, only a single wire is needed to be connected to a row (or column) of the array instead of a group of some hundred leads.

However, one may also avoid the complex lead problem associated with a large receptor-array if some method is devised that significantly increases the sensing resolution of a small size receptor-array. The method proposed here is based on concepts arising from involuntary eye movements. The object-image is moved around on the receptor-array by a perturbation signal, which corresponds to the involuntary eye movements, of zero average value. The output of all receptor elements is then summed and the high frequency components due to the perturbation are removed by a lowpass filter. The filtered output with respect to the input is significantly more linear than the original case without perturbation. Therefore, the degree of the sensing accuracy is improved by an order of magnitude or more [4]. Sine waves and ramp functions were used as the perturbation signals. The theory was then extended to seek an optimal perturbation signal. It was proved that for a linear array having square sensing elements, a family of triangular waveforms with their amplitudes equal to or larger than half the size of the receptor elements are the optimal perturbation signals [5]. By introducing an optimal perturbation signal into the system, a zero sensing error is obtained. A scheme for producing the perturbation signal for a two-dimensional receptor-array is shown in Figure 3. The moving mirrors

O'CONNOR, CHEN*

are controlled by a servomechanism in such a way as to produce the perturbation effect of the object-image on the receptor-array. A zero sensing error was also obtained when a sweep function is applied electronically to the signal processor. For this case the constraint of keeping the average value of the perturbation signal equal to zero is not required. Since the mechanical part to produce the perturbation signal is not needed, the system can detect the object-image moving in higher velocity. The system is also relatively simple and more reliable.

Once the perturbation is introduced into the system, the receptor size can now be conveniently determined by the largest variation of the input object position and the size of the sensing element and dead-space being used. The maximum size of the sensing element available is governed by the uniformity of the sensing area of each element that is in turn determined by the system resolution requirement.

APPLICATIONS

1) Since the system can detect the relative position of points in an object field, one can apply the system to a wide range of metrology problems, for example, obtaining the coordinates of satellites' images against stellar backgrounds or determining shimmer of a star against its background sky by appropriately utilizing a telescope as a means of coupling to normalize the input object-image of interest into a convenient size for the receptor-array to sense.

2) The array system can be used to remotely track an object of interest in a battle field, such as a moving tank because it can detect velocity of a moving object. This may lead to an optical radar concept.

3) The array system can be applied to a process control to detect gain size and other dimensional properties of objects.

4) The perturbation concepts may be used to simplify the RATNA type optical characteristic recognition machine available commercially because the perturbation method can reduce the size of the sensing array of the machine enabling the entire system to be reduced in size, complexity, and cost.

5) By using a large enough two-dimensional array and the introduction of the perturbation signal, the system is theoretically capable of sensing a black and white photography and reproduce its image faithfully on the output indicator instantly. This may lead to replacing the photographic film. In order to see the whole photograph image instantly on the output indicator, a time-share reading scheme would not be used. Fortunately, the perturbation effect can reduce the size of the receptor-array and that of the system, thus, avoiding

a system complexity problem.

Presently, a one-dimensional experimental sensing array is being built and tested. The system is designed to measure the relative position of a point light with respect to its reference axis which is the bottom edge of the receptor. Both electronic and mechanical perturbations are employed. A linear array of size 1 x 31 is used. The array has elements of size 0.0045 in. x 0.005 in. with 0.0005 in. gaps in between the elements. Only outputs from the bottom eight elements are utilized. Following each sensing element of the array, a de amplifier consisting of a FET transistor and three other conventional transistors is used to amplify the small output signal from the sensor element. An operational amplifier is utilized to act as a threshold gate where the electronic perturbation signal may be applied. The mechanical perturbation is achieved by oscillating the point light around in the receptor. An optical coupling device is placed in between the light source and the receptor to form a rectangular shape point light on the receptor. For the mechanical perturbation, the size of the point light is adjusted to be approximately 0.005 in. x 0.01 in. with its longer side in the horizontal direction. The perturbation amplitude B is set in such a way that the point light covers about three element length, that is approximately 0.015 in. in one case, and five element length, that is approximately 0.025 in. in the other case for a cycle of oscillation. For the electronic perturbation, twice size of the point light is used. A sweep waveform of amplitude 1 volt, frequency 1000 Hz is supplied to threshold gates as electronic perturbation signal. An adder is used to sum the output from all the operational amplifiers. This adder, in turn, produces an output voltage whose amplitude is proportional to the position of the point light with respect to the bottom edge of the receptor. This voltage is then indicated by a digital voltmeter.

In the mechanical perturbation case, the center line of the point light is supposed to be measured, while for the electronic perturbation, the far edge of the point light from the reference axis is detected. A simplified diagram of this system is shown in Figure 4. The measurement data which indicates the input position versus the output voltage for two cases of perturbation is shown in Figure 5 and Figure 6.

From Figure 5, it is noted that almost linear relationship for input position versus output voltage is obtained for the middle part of the curve. This suggests that the relative position measurement of accuracy better than 0.001 in. can be achieved by using the sensing array technique. For the electronic perturbation, the effect due to the dead-space of the receptor remains exists. This appears as dips and flat portions on the measurement curve shown in Figure 6. It is suggested that some means be considered in the future for smoothing this curve.

ADVANTAGES AND EXTENSIONS OF THE IDEA

As stated in the previous sections, the introduction of signal perturbation will result in the reduction of the system's receptor-array to a moderate size. Hence, there will be no need for adapting the time-share reading scheme. Input information can then be read, processed and reproduced on the output indicator in a much shorter time compared to the conventional array systems. The complicated, huge mechanical scanning device can be eliminated. Since the system operates at a higher speed, the detectable velocity of the input object can be higher. Because the perturbation effect linearizes the non-linear transfer function of the system's receptor, a more accurate detected output can be obtained for a system of equivalent complexity. The lead problem of receptor is now eliminated since the use of a large receptor-array can be avoided.

The perturbation idea can also be extended to linearize many non-linearities and nonlinear devices not only in the field of electronics but others as well [10]. The improvement of the sensing accuracy is one of its extensions. The theories and experiments developed so far are restricted only to the type of receptor-array having square sensing elements. It may be fruitful to study whether different geometries of the sensor elements and their distribution, if the statistic input data to the system is known, would further improve the system's resolution or simplify the system's complexity. Complex shape detection may be studied by using pattern recognition techniques.

RELATIONSHIP BETWEEN THE SUGGESTED TECHNIQUE AND THE STATE-OF-THE-ART OF ELECTRONICS

The receptor-array technology is closely related to the fields of thin film, chip matrices, fiber optics, memory, and optical devices such as mirror and lens, etc. The suggested technique may thus affect any of the above fields in many ways.

One thing for sure is that the procedure of making fiber optics will be simplified, if the fiber optics are to be utilized in the construction of the arrays because the suggested technique does not require extremely small sensor elements.

CONCLUSIONS

The performance and function of the human eye are reviewed. A sensing array system devised by using the concept of the involuntary human eye motion is considered. The system's receptor-array is reduced to a moderate size by the introduction of the perturbation effect, thus decreasing the system's complexity and cost, while retaining equivalent or better system resolutions. Also, the serious lead problem of the receptor-array and the complicated, huge, mechanical scanning device are eliminated.

Applications of the array systems to metrology photogrammetry are discussed. A one-dimensional experimental sensing array is built and tested. The experimental results show that the system can detect the relative position of an object-image of accuracy better than 0.001 in. Suggestions are made to the extension of the idea in the future.

REFERENCES

- [1] O'Connor, D. C., "Visual Factors Affecting the Precision of Coordinate Measurement on Photographic Plates," GIMRADA Research Note No. 21, 13 Jan. 1967.
- [2] Pritchard, R. M., "Stabilized Images on the Retina," Scientific American, 204, 6, 72-78, June 1961.
- [3] O'Connor, D. C., "Some Factors Affecting the Precision of Measurements on Photographic Plates," International Society of Photogrammetry Symposium on Spatial Aerotriangulation, Urbana, Illinois, March 1966 and photogrammetria, 22, 77-97 1967.
- [4] Chen, P. F., "Position and Velocity Detecting Systems Using Pattern Recognition Concepts," University of Virginia, Doctor of Science Dissertation, August 1968.
- [5] Chen, P. F., "Optimal Perturbation Signal Waveform for Sensing Arrays," Will appear in IEEE Trans. on Instrumentation and Measurement, May 1970 Issue.
- [6] Weimer, P. K., Sadasiv G. and Pike, W. S., "Solid-State Digital Scanning of Mosaic Sensors (phase III)," RCA Laboratories, Princeton, N. J., Technical Report AFAL-TP-68-82, Apr. 1968.
- [7] Irwin, E. L., Saboe, J. M. and Schuster, M. A., "Monolithic Infrared Mosaic Sensors," Westinghouse Defense and Space Center, Third Interim Technical Report F33615-67-1895, April 1968.
- [8] Dyck, R. H., "Photosensor Arrays - the Key to Simpler Character Reader," Electro-Optical Systems Design, Sept-Oct Issue, 1969.
- [9] Weimer, P. K., et al, "Solid-State Digital Scanning of Mosaic Sensors," RCA Laboratories, Technical Report AFAL-TR-65-188, August 1965.
- [10] Gibson, J. E., "Nonlinear Automatic Control," McGraw Hill Book Company, New York, 1963.

O'CONNOR, CHEN*

Figure 1. An approximation showing the nature and extent of the involuntary eye movements which carry an image across the retina during fixation. The three movements are a 'drift' (curved lines) away from the center of vision; a faster 'flick' (straight lines) back towards the center; and a high frequency 'tremor' superimposed on the drift. The magnitude of the movements is very small; the diameter of the patch of the fovea shown is only about 15 minutes of arc. From Pritchard [2].

Figure 2. General system block diagram.

Figure 3. Scheme for producing two-dimensional perturbation signals.

Figure 4. One-dimensional sensing array system.

Figure 5. Input position versus output voltage for mechanical perturbation.

Figure 6. Input position versus output voltage for electronic perturbation.

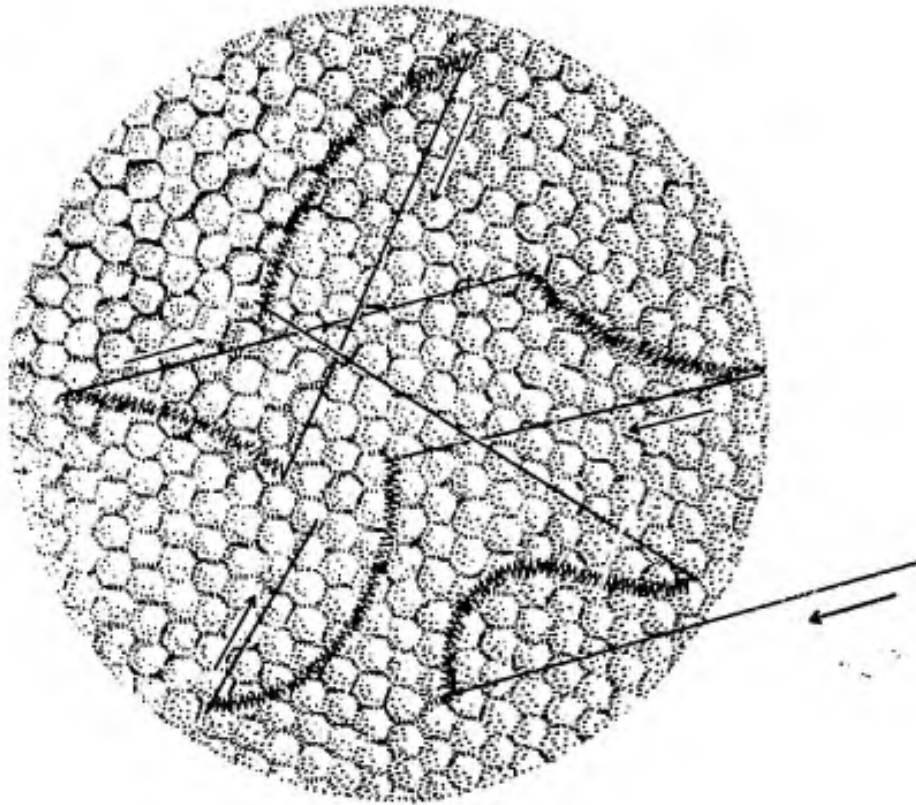


Figure 1

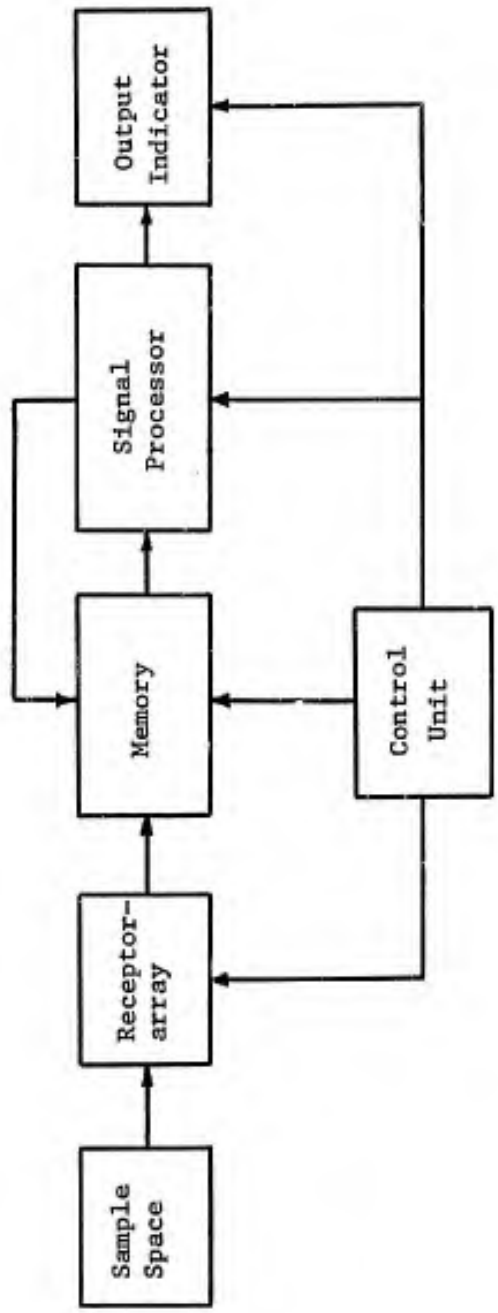


Figure 2

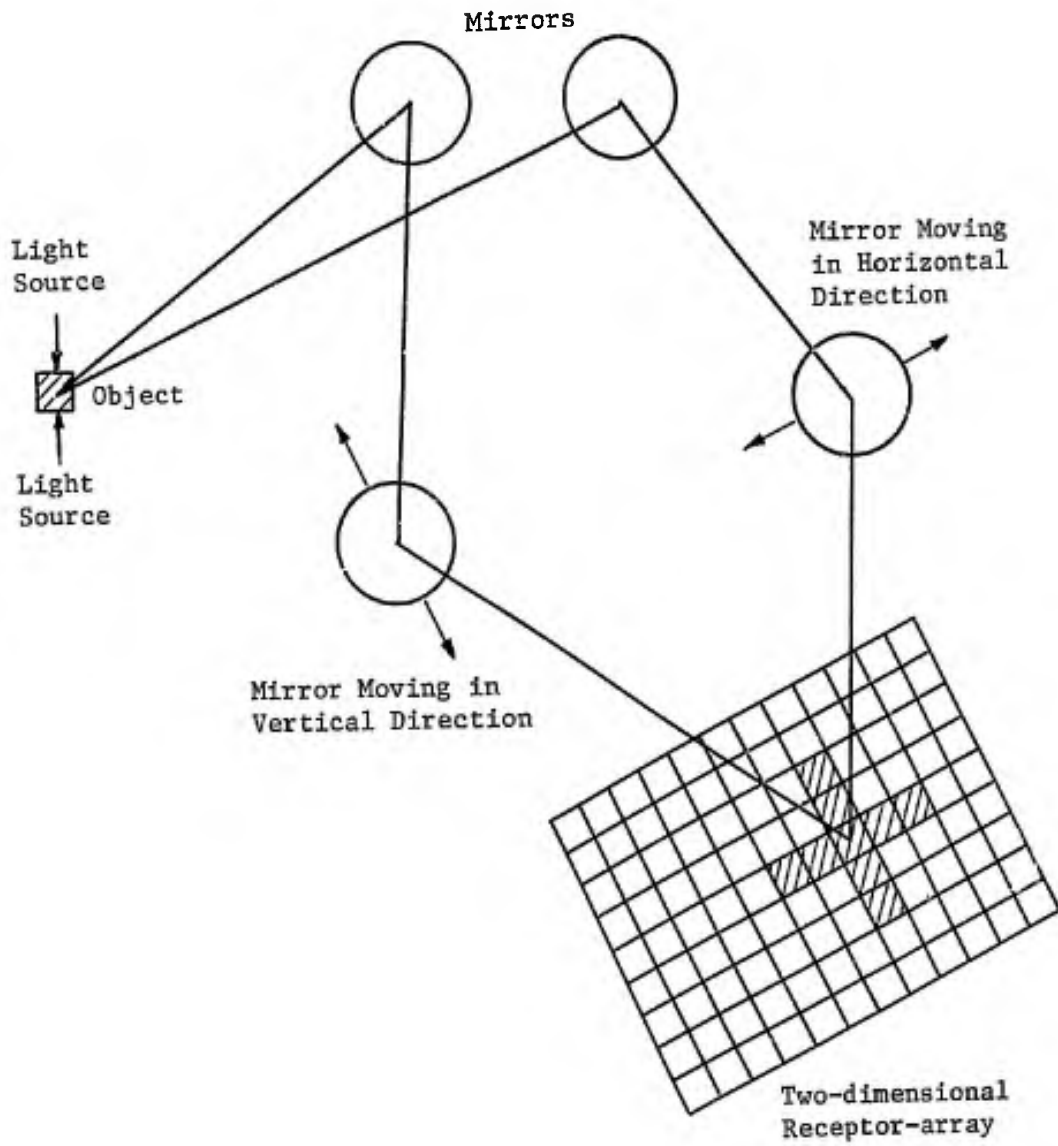


Figure 3

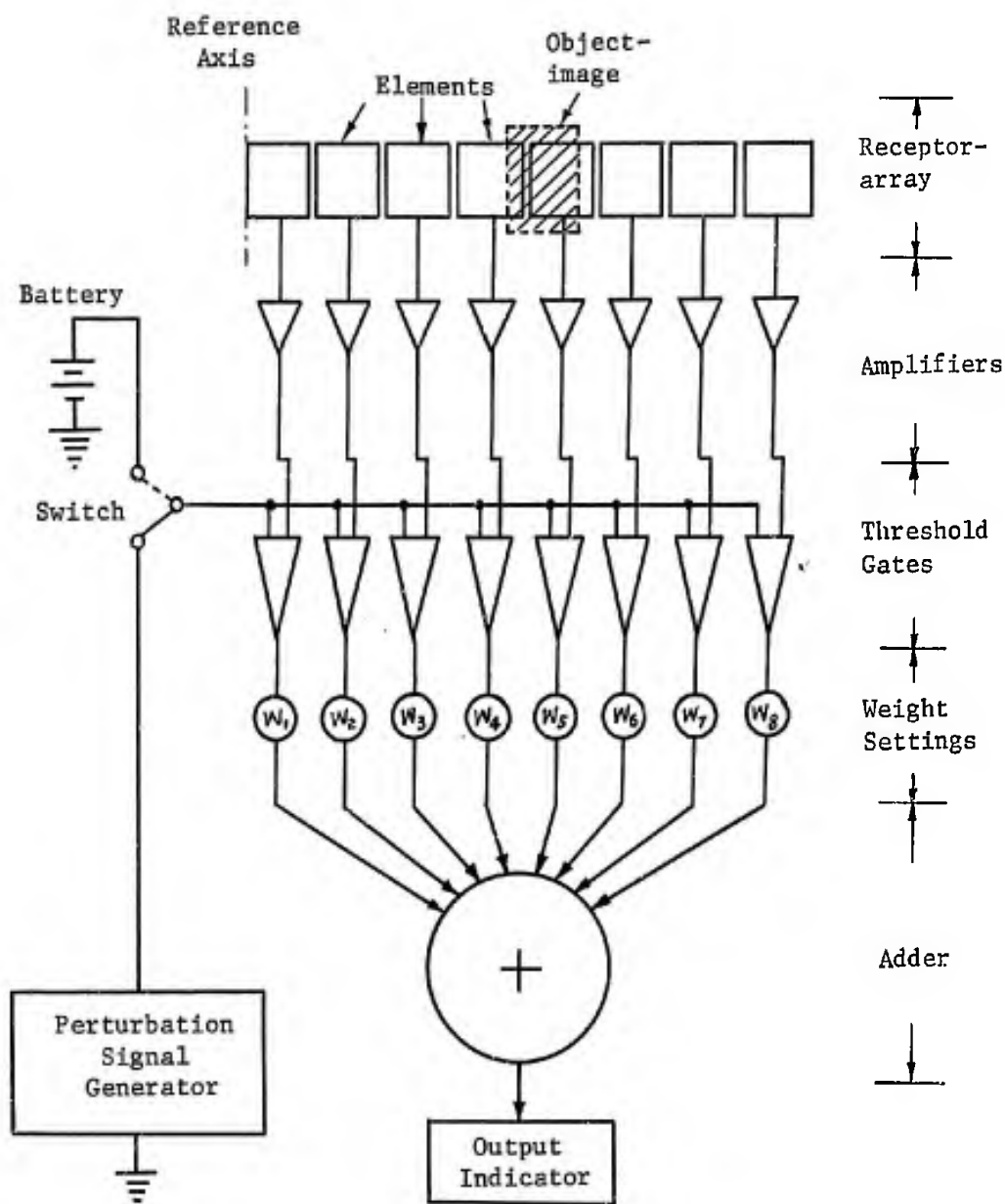


Figure 4

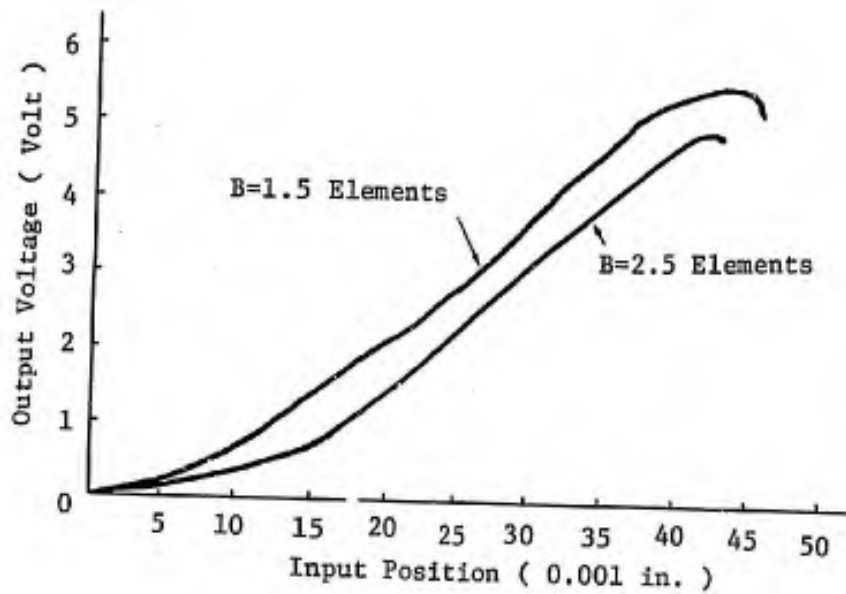


Figure 5

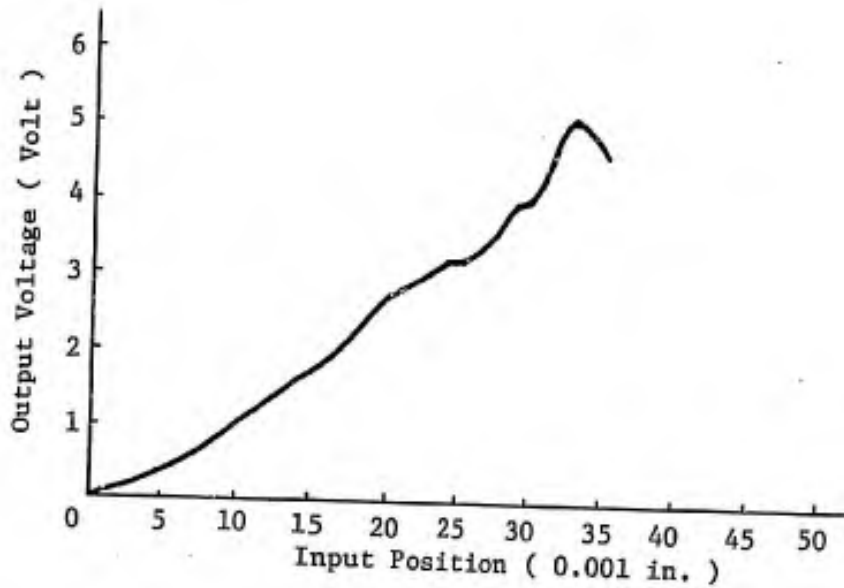


Figure 6

A SIMILARITY MODEL FOR ATMOSPHERIC TURBULENCE STRUCTURE
IN THE PLANETARY BOUNDARY LAYER

WILLIAM D. OHMSTEDE
ATMOSPHERIC SCIENCES LABORATORY, USAECOM
FORT HUACHUCA, ARIZONA

INTRODUCTION

The modern Army confronts the meteorologist with many challenging problems which require him to develop techniques to evaluate the effects of complicated atmospheric phenomena on Army operations and materiel. At the Atmospheric Sciences Laboratory, we have strived to develop generalized models of atmospheric phenomena which may be adapted to meet current and anticipated requirements.

The planetary boundary layer, the lowest 1000 meters of the atmosphere, is of special interest because most Army operations and materiel function within it. This layer of air is characteristically turbulent. This property not only affects the overall behavior of the layer, but also directly influences Army operations and materiel. Meaningful measurements of atmospheric turbulence are difficult to obtain, and techniques must be developed for assessing the turbulence structure from simple observations or, in some cases, no observations at all.

At the 1964 Army Science Conference, we reported (1) on the development of a preliminary model for the structure of the wind and turbulence in the planetary boundary layer. Since then, considerable progress has been made (2) in developing more general models, but these models have proved to be only partially successful, due principally to the difficulty in representing the turbulence effects in the models. The models proved effectively that current concepts are inadequate for predicting turbulence structure in the planetary boundary layer.

The pragmatic relationships which have been used to predict turbulence are largely phenomenological and usually applicable only to simplified situations. Consequently, these concepts lack generality, and there are no guidelines to evaluate their limitations. The objective of the study reported here was to develop, from basic principles, a rational hypothesis for the prediction of turbulence structure in

OHMSTEDE

the planetary boundary layer, including means to assess the limitations and methods to further generalize the hypothesis.

UNDERSTANDING THIS REPORT

The scope of this report is extensive; space limitation demands that the reader be familiar with the cited references. Definitions are generally consistent with the Glossary of Meteorology (3). The intent of the report is to convey the ideas involved in the development and their consequences rather than to establish a catalog of equations. Consequently, the development is illustrated by a few examples instead of the complete system of equations. The analysis tools are presented so that the interested reader may reproduce for himself the development of any or all equations.

The mathematical notation is concise. Superscript indices are used to denote the individual components of vectors and tensors. The index implies a numerical index (i, j , or $k = 1, 2$, or 3). Parentheses are used when powers of vector components occur. Subscript indices denote partial differentiation, e.g., $a_t = \partial a / \partial t$ and $a_i = \partial a / \partial x^i$. Exceptions to this rule are the standard notations c_v , c_p , K_h , K_m . The Einstein summation convention is followed; that is, a repeated index (i or j) implies summation of the term over all values assumed by that index (1,2,3).

The Reynolds principle of averaging physical variables is fundamental to the theory of turbulence (4). An arbitrary physical variable (a) at a particular space-time point has the representation

$$a = \bar{a} + \hat{a},$$

where \bar{a} is the meteorological (averaged) variable and \hat{a} is the turbulent fluctuation ($\bar{\hat{a}} = 0$). If a product occurs with another arbitrary physical variable (b), the result, after averaging, is

$$\overline{ab} = \bar{a} \cdot \bar{b} + \overline{\hat{a}\hat{b}}.$$

A table of mathematical symbols is provided at the end of this report.

BASIC PRINCIPLES

The assumption that basic physical principles which are observed and verified in the laboratory are also applicable to natural phenomena is the foundation upon which science is based; in particular, the meteorologist is concerned with the physical principles which describe the state and dynamics of the mixture of gases known as air. The basic physical principles for this report, taken from Monin and Yaglom (4), stated functionally are the thermodynamic equation of state and the dynamic equations which govern the conservation of mass, momentum, and energy, that is, the continuity equation, the equation

OHMSTEDE

of motion, and the equation of total energy.

The basic independent variables are time (t) and the position coordinates ($x^i | i=1,2,3$) of a cartesian system. We shall use a coordinate system which lies on a conformal projection which rotates with the earth and has the third axis normal to the surface of geopotential height.

The dependent physical variables are the statistical averages of the gross effects of molecular interactions for an ensemble of air molecules which is called an air parcel. The basic physical variables are the thermodynamic state variables - density (ρ), pressure (p), and temperature (T) - and the velocity components ($u^i = Dx^i/Dt | i = 1,2,3$). Additional dependent variables representing the dynamic effects of molecular interactions, e.g., the viscous stress tensor ($\sigma^{ij} | i,j = 1,2,3$), are introduced.

The operator D/Dt , termed the Lagrangian operator, occurs in all dynamic equations and implies the time rate of change of the operand for a given air parcel. Lagrangian properties are difficult to measure so it is more common to use the Eulerian operator. The Lagrangian and Eulerian operators are related through the identity,

$$Da/Dt = a_t + u^i a_i .$$

The Eulerian operator applied to the operand a is the expression on the right of the equation above. The Eulerian operator is nonlinear since it involves products of dependent variables.

The basic physical principles are applicable to the atmosphere in the sense that they cannot be violated. However, these principles are inappropriate for the atmosphere because the physical variables as defined are not "measureable" in a practical sense. When one measures physical variables at several space points within the atmosphere, it is generally observed that there are significant fluctuations of these properties in space and time. Furthermore, the time and space scales of these disturbances vary over a wide range.

The scale of "horizontal" inhomogeneities is confined only by the size of the globe. Fortunately, the scale of vertical inhomogeneities is limited by the shallowness of the atmosphere and the proximity to the air/earth boundary. Many scales of atmospheric disturbances occur. There are large-scale synoptic weather systems which are the principal interest of most meteorologists. These systems are considered to be deterministic. At the other end of the scale are the quasi-random systems which are called turbulence. Between these limiting scales is a miscellany of other types of inhomogeneities. This report is primarily concerned with the scales of the nondeterministic turbulent fluctuations. The time and space scales of these disturbances are of the order of several minutes and deka-

OHMSTEDE

meters or less. The turbulence range can be further subdivided into the energy-containing, inertial, and viscous subranges, the latter being the smallest scale disturbances.

The turbulence problem for the meteorologist is analogous to the molecular problem of the physicist. A complete description of the motion of each molecule is impractical so the physicist defines variables which represent the gross effects of many molecular interactions. Similarly, the meteorologist defines variables which represent the gross effects of interactions of many turbulent fluctuations. However, the Reynolds averaging process introduces turbulent interaction terms which are the covariances of the turbulent fluctuations, e.g., the Reynolds stress tensor ($\tau^{ij} | i, j=1, 2, 3$) and the turbulent mass flux vector ($\mu^i | i=1, 2, 3$). Later, we shall define yet higher-order terms which consist of multiple products of turbulent fluctuations.

The meteorological Lagrangian and Eulerian operators are not equivalent to the physical ones. Following Lettau (5), we define the identity

$$da/dt = a_t + \bar{u}^i a_i,$$

where the left and right sides of the identity are the meteorological Lagrangian and Eulerian operators applied to the operand a . It follows that

$$Da/Dt = da/dt + \bar{u}^i a_i.$$

The last term in this expression leads to turbulent interaction terms when the averaging process is applied.

From this point on, the report will deal only with the meteorological variables. Therefore, the overbar which has been used to denote an averaged variable will be deleted, and it is to be understood that a symbol denotes the meteorological and not the physical variable. For clarity, the overbar is retained for turbulent interaction variables which are not denoted by a special symbol.

The basic meteorological equations are analogous to the physical equations. For example, the continuity equation is expressed by

$$d\rho/dt + \rho u_i^i + \mu_i^i = 0.$$

The fundamental difficulty with the basic meteorological equations is that they contain a family of esoteric unknowns which have been called the turbulent interaction terms. Dynamic equations for these terms can be derived, but they would appear to be of little help since they contain yet higher-order products of the fluctuations which are also unknown. Closure of the set of equations is never

OHMSTEDE

obtained no matter how many times the process is repeated. Thus, we cannot derive explicit a priori expressions for the interaction terms. This dilemma (more unknowns than equations) is the reason why turbulence is called the unsolvable problem. To bring closure of the system of equations, we must introduce approximations and analysis techniques which eliminate at some finite level the yet higher-order terms.

DEVELOPMENT OF THE HYPOTHESIS

This development is based upon the system of dynamic equations for the turbulent fluctuations. These equations describe complicated interactions of thermodynamic and kinematic variables in a nonequilibrium compressible fluid. The role of the pressure fluctuations in these interactions is poorly understood; yet, this is the variable which couples the kinematics to the thermodynamics.

Pressure fluctuations are intimately related to acoustical phenomena (broadly including atmospheric tides). Since these disturbances travel at about the speed of sound, they are not considered to be turbulence. Indeed, it is generally accepted that the pressure fluctuations are not relevant to the thermodynamic turbulent interactions. The rejection of the pressure fluctuations leads to the first postulate of this hypothesis, which is expressed by the equation

$$\dot{u}_i^i = -(c_v/c_p) \dot{u}_i^i p_i/p \approx \dot{u}^3 g/c^2 .$$

The last term is an approximation which is useful in practical applications.

The complete development of the first postulate (not reproduced here) is based on the premise that the pressure fluctuations are passive in thermodynamic turbulent interactions, and consequently the advection of internal energy (per unit volume) by turbulent velocity fluctuations is directly related to the work performed by these velocity fluctuations. On the other hand, the pressure fluctuation gradients play an important, but little understood, role in the dynamics of the velocity fluctuations. It can be shown that these pressure fluctuations are related to fluctuations of kinetic energy. This matter will be dealt with later.

Dynamic equations for the turbulent interaction terms may be derived from the system of equations for the fluctuations. For example,

$$\overline{d\delta^2/dt} + 2[\overline{\delta^2 u_i^i} + (\rho/r)u_i^i r_i] + [(\overline{\delta^2 \dot{u}_i^i})_i + \overline{\delta^2 \dot{u}_i^i}] = 0 ,$$

OHMSTEDE

$$d\mu^j/dt + [\mu^j u_i^i + \mu^i u_i^j - \tau^{ij} \rho r_i / r - \bar{\delta}^2 p_j / \rho^2] + [(\bar{\rho} \bar{u}^j \bar{u}^i)_i + \bar{\delta} \bar{p}_j / \rho] = \bar{\delta} \sigma_1^j / \rho .$$

The first postulate has been used in these equations with the result that the inhomogeneity of the mean density field is expressed by the potential density (r) gradient rather than the density. Similarly, equations for temperature fluctuations would involve the potential temperature. These results represent the pragmatic manifestation of the first postulate.

All dynamic equations for turbulent interaction terms consist of four groups of terms which we call, from left to right, the Lagrangian term, the generative terms, the dispersive terms, and the dissipative or molecular interaction terms. (The first equation above has no dissipative term since we have followed the convention of neglecting molecular self-diffusion.) The generative terms are important since they couple the dynamics of the turbulent interaction terms with the inhomogeneities of the meteorological variables. The turbulent interaction terms which occur in the generative terms derive their primary contribution from disturbances whose time and space scales occur in the energy-containing subrange. The dispersive terms obtain their major contribution from disturbances lying in the inertial subrange, and, of course, the dissipative terms lie in the viscous subrange. Consequently, the turbulence process consists of a cascade of breakdowns of inhomogeneities through the various scales. For very large Reynolds number flow, which is usually the case in the planetary boundary layer, the time and space scales of these different interactions are widely separated.

The elementary development of the hypothesis presumes that the Lagrangian term is negligible so that a quasi-balance exists between the generative group of terms and the combination of the dispersive and dissipative terms. More generally, the hypothesis considers the entire hierarchy of dynamic equations for turbulent interactions. As we proceed to higher-order interaction terms, the time and space scales become correspondingly smaller. Hence, for any situation, the hypothesis presumes that there is a finite level where a quasi-balance exists. There is no real loss of generality and a major gain in simplicity if we develop the hypothesis for the most elementary situation.

The second postulate of the hypothesis is that a given turbulent interaction term is functionally related to the sum of the generative terms, each weighted with a proportionality factor. We shall now show that the proportionality factors are appropriate Lagrangian time scales. The approach is illustrated for the density variance.

The dynamic equation for the density fluctuation may be written in the following form:

$$d\delta(t+t')/dt' = -\{\delta(t+t')u_i^i + (\rho/r)\bar{u}^i(t+t')r_i\} - \{[\delta(t+t')\bar{u}^i(t+t')]_i - \mu_1^i\} ,$$

OHMSTEDE

where t is fixed and t' is a parameter which is within the limits of several minutes or less. Let $\beta(t)$ denote the fluctuation at a reference point with fixed time t and a fixed space point. The above equation is supposed to be applicable to the space-time point on the mean trajectory passing through the reference point. We assume that $(\rho r_1/r)$ and u_1^1 are essentially independent of t' along the trajectory since t' is small. If this is not a good assumption, then we would be required to deal with the yet higher-order terms to reduce the time scale.

Integration with respect to t' is tantamount to integration along the trajectory. We multiply the preceding equation by $\beta(t)$, integrate the product over the interval $-\tau < t' < 0$, and then apply the averaging process. Consequently, we have

$$\overline{\beta^2}(t) = \overline{\beta(t)\beta(t-\tau)} - \left(\int_{-\tau}^0 \overline{\beta(t)\beta(t+t')} dt' \right) u_1^1 - \left(\int_{-\tau}^0 \overline{\beta(t)\beta^1(t+t')} dt' \right) \rho r_1/r - \left(\int_{-\tau}^0 \overline{[\beta(t)\beta(t+t')\beta^1(t+t')]_1} dt' \right) .$$

The term $\overline{\beta(t)\beta^1(t+t')}$ represents a Lagrangian correlation function. For $t'=0$, it is simply equal to μ^1 . Since turbulence is a quasi-random process, the correlation converges to zero as t' becomes large. Thus, the integral of the correlation function asymptotically approaches a fixed value as τ increases. Similar results apply to the other correlation functions. We must choose τ as small as possible and yet obtain with small error the limiting values of the integrals. Similarly, τ must be large enough so that the correlation $\overline{\beta(t)\beta(t-\tau)}$ is negligible. It is very important to recognize that this hypothesis is applicable only to quasi-random processes for which the Lagrangian correlation functions converge to zero in a reasonably short time interval. Organized disturbances which maintain correlation over long time periods are considered deterministic and should be treated as such. The Lagrangian time scales shall be defined as follows:

$$T_L(a,b) \equiv \frac{G}{\int_{-\tau}^0 \overline{a(t)b(t+t')} dt'} \overline{ab}(t)$$

As a result of the development given above, we may write the approximate equation

$$\overline{\beta^2} = -T_L(\beta,\beta)\overline{\beta^2}u_1^1 - T_L(\beta,\beta^1)\rho\mu^1r_1/r - T_L[\beta,(\beta\beta^1)_1] \cdot (\overline{\beta^2\beta^1})_1 .$$

For large Reynolds number flows, the scales of the variances and covariances are widely separated from the scales of the dispersive and dissipative terms. Therefore, we can assume that the Lagrangian time scales of the dispersive and dissipative terms are negligible in comparison with the Lagrangian time scales for the variances and covariances. Thus, we obtain the desired result for the second postulate,

OHMSTEDE

$$\overline{\delta^2} = -\{T_L(\beta, \beta) \overline{\delta^2} u_i^i + T_L(\beta, \bar{u}^i) \rho u^i r_i / r\} .$$

Similarly, we may derive the result

$$\mu^j = -\frac{1}{2}\{T_L(\beta, \bar{u}^j) \mu^j u_i^i + T_L(\beta, \bar{u}^i) \mu^i u_i^j - T_L(\bar{u}^j, \bar{u}^i) \rho \tau^j r_i / r - T_L(\beta, \beta) \overline{\delta^2} p_j / \rho^2\} .$$

It should be evident to the reader how this process may be applied to any of the variables for which we have a dynamic equation.

The significance of the second postulate is that we can now obtain closure of the system of equations since we have eliminated the yet higher-order terms. For the elementary case, we can derive state equations for the turbulent interaction terms and thus eliminate the need for solving dynamic equations for these variables. The principal drawback of the second postulate is that it introduces a family of new unknowns which we have called Lagrangian time scales. The second postulate has practical significance only if we can generate explicit relationships for the Lagrangian time scales.

Lagrangian time scales have long been of interest to specialists in atmospheric diffusion. Since Lagrangian properties are very difficult to observe, there have recently been attempts to relate these to Eulerian properties. The empirical studies of Mickelsen (6) in 1955 were the first significant step in this direction. For his experimental diffusion problem, he showed that the Lagrangian time scale was proportional to an Eulerian length scale divided by a characteristic velocity scale. The length scale is the mean speed times the Eulerian time scale. The characteristic velocity scale is the square root of the variance of the velocity fluctuations in the direction of the diffusion. Although the Mickelsen postulate has recently been verified by theoretical analysis (7,8), a need exists for continued theoretical and experimental research on this matter.

Lagrangian time scales are on the forefront of research today, and we can anticipate significant progress in this area in the near future. For the present, the third postulate of this hypothesis is essentially the same as that of Mickelsen except more general.

The details of the third postulate are best presented in combination with the results of the second postulate. Let u^i represent the square root of the variance of u^i ($i=1,2,3$). Then, for example, we have

$$\frac{1}{2} \overline{\delta^2} = -\gamma \{L(\beta, \beta) \cdot (u_i^i / u^i) + L(\beta, \bar{u}^i) \cdot (\rho u^i r_i / u^i r)\}$$

and

$$\mu^j = -\gamma \{L(\beta, \bar{u}^j) \cdot (\mu^j u_i^i / u^i) + L(\beta, \bar{u}^i) \cdot (\mu^i u_i^j / u^i)\}$$

$$+ \gamma \{ L(\bar{u}^j, \bar{u}^i) \cdot (\rho \tau^{j1} r_i / u^1 r) + L(\bar{\delta}, \bar{\delta}) \cdot (\bar{\delta}^2 / \rho^2) \cdot (\delta^{ij} p_i / u^1) \} ,$$

where γ is a constant and the various L parameters are the appropriate Eulerian length scales. The reader should note that the superscript of the characteristic velocity scale corresponds with the subscript of the associated meteorological variable.

The constant γ should be equal to approximately 0.3 if our third postulate is to be in agreement with the results of Mickelsen. However, it may be preferable to leave the evaluation of the constant to future empirical research. We may find that the constant for covariant correlation functions differs from that for autocorrelation functions, but for the present we shall retain the simplified form of the third postulate which uses a single unspecified Mickelsen constant.

It should be evident to the reader how the third postulate may be applied to any state equations derived from the second postulate. The equations involving density fluctuations have been used to illustrate the development because of their simplicity. The corresponding equations for the Reynolds stress tensor are more complicated and, furthermore, a special problem arises.

It was previously noted that the pressure fluctuations occur in connection with the fluctuations of kinetic energy. In the dynamic equations for off-diagonal elements of the Reynolds stress tensor, the pressure fluctuation gradient terms function as added dispersive terms and may be treated as such. On the other hand, this does not appear to be the case for the diagonal elements. Indeed, it appears improper to attempt to deal with the variance of an individual velocity component independent of the other components. Velocity is a vector and the individual components cannot be analyzed as if they were independent scalar variables. On the other hand, the sum of the variances of the fluctuations of the velocity components may be treated as a scalar variable. Multiplied by $\frac{1}{2}$, this variable is simply the kinetic energy per unit mass of the turbulence (denoted by k).

If we apply our hypothesis to the variable k , we may anticipate that the values predicted by the hypothesis will be smaller than the observed values which usually contain contributions from intermediate-scale disturbances that we have not considered to be turbulence. For example, the land surface of the earth is rarely homogeneous - a woods here, an open farm there, and a city yonder. The inhomogeneities in boundary conditions generate disturbances in the lower atmosphere which are very difficult to deal with. These disturbances become manifest as intermediate-scale fluctuations of the horizontal velocity components which contribute significantly to the variances. To my knowledge, no one has yet developed an adequate method to cope with the gross effect of these and other intermediate-scale disturbances.

OHMSTEDE

It bears repeating that our hypothesis, in the present stage of development, is applicable only to the small-scale disturbances which we have called turbulence. The value of k predicted by the hypothesis consists of only the small-scale contributions to the variances. In the lower atmosphere, the vertical velocity fluctuations are predominantly small-scale so that the portion of the predicted k associated with the vertical component is essentially the same as the observed variance. Ohmstede (9) has suggested that the observed spectra of the horizontal velocity components may be explained by the superposition of two independent spectrum functions - one being essentially intermediate scale and the other predominantly small scale. Furthermore, he contends that the small-scale spectrum functions of the horizontal components are similar to the spectrum function of the vertical component. This postulate is at least partially confirmed by results published by Cramer and Record (10), and Panofsky and Busch (11); however, further research is required to complete the verification of the concept and establish quantitative relationships.

In consonance with the preceding concepts, the fourth postulate of this hypothesis is that the contributions of the generative terms to the small-scale kinetic energy per unit mass (k) are partitioned, not necessarily equally, but in constant proportions, to the small-scale variances of the individual components of the velocity fluctuations. In particular, we assume the following general form for the elementary case,

$$\frac{1}{2}(v^k)^2 = \gamma \{ C^{ik} L(\bar{u}^i, \bar{u}^j) \cdot (\tau^{ij} u_j^i / v^j) + D^{ik} L(\beta, \bar{u}^i) \cdot (u^i p_1 / v^i \rho^2) \}$$

where C and D are presumed to be constant tensors having the property

$$\sum_k C^{ik} = \sum_k D^{ik} = 1, \quad i = 1, 2, 3.$$

For a particular case which is of practical interest, the fourth postulate can be shown to be almost identical to an equation proposed by Panofsky and McCormick and verified by Prasad and Panofsky (11). This may also be interpreted as a partial verification of the fourth postulate.

The fourth postulate is essential from a practical standpoint because we must have a means to evaluate the various Mickelsen velocity scales. The evaluation of the various Eulerian length scales necessitates recourse to observations and empirical studies. Panofsky and coworkers (11), working on grants from the Atmospheric Sciences Laboratory, have analyzed an extensive set of turbulence data with remarkable results. They developed several universal spectra and cospectra relationships for the turbulence structure. We may derive from their results universal relationships for some of the Eulerian length scales which are of practical interest to this hypothesis.

OHMSTEDE

The analyses of Panofsky are incomplete; not all spectra of interest were analyzed. Furthermore, almost all analyses were applied to observations taken in the lowest 100 meters of the atmosphere; turbulence observations above 100 meters are practically nonexistent. Consequently, there is a need for further elaboration of the Panofsky analyses. For the present, it is proposed that the various Eulerian length scales occurring in the elementary statement of the hypothesis may be represented by a function of the form $\kappa S \lambda$. In this expression, λ is the universal length scale reported by Appleby and Ohmstede at the 1964 Army Science Conference, κ is a constant which is different for each variance and covariance, and S is a function of atmospheric stability. According to the results of Panofsky, S can be taken as unity during unstable and neutral conditions, but S decreases with increasing stability. Furthermore, the dependence of S on stability is different for each variance and covariance. Additional empirical research is needed to establish firm relationships for various S functions. This discussion of the Eulerian length scales has been necessarily brief; the interested reader should consult the reports of Panofsky to appreciate the problem involved.

Our general hypothesis states that, for any situation, closure of the hierarchy of dynamic equations for turbulent interactions can be obtained at a level of finite order by equating each turbulent interaction term at that level to the sum of products of the associated generative terms and ratios of appropriate Eulerian length and velocity scales. For the elementary case, we obtain a closed system of implicit state equations which can be used to solve for the variances and covariances needed for practical applications. Admittedly, the current knowledge of turbulence structure is insufficient to permit us to apply the more general statement of the hypothesis which involves the higher terms. The principal value of the general hypothesis is that it offers a means to estimate the limitations of the elementary hypothesis when applied to general situations.

PRAGMATIC CONSEQUENCES OF THE HYPOTHESIS

The hypothesis should be helpful in the development and improvement of the generalized models previously discussed. We shall note only two recurring problems to which the hypothesis may be applied.

The meteorological literature is replete with attempts to define variables known as the eddy conductivity (K_h) and eddy viscosity (K_m). Some of the more generally accepted relationships for these variables, gleaned from the literature, did not function satisfactorily in our planetary boundary layer model. We obtain from this hypothesis explicit equations for K_h and K_m .

Recently there has been considerable speculation regarding the ratio K_m/K_h which in former years was assumed to be equal to unity. The hypothesis predicts an explicit function for this ratio which, as far as we know, is the first instance where a relationship

OHMSTEDE

has been derived from basic principles.

Another problem of recurring interest is the prediction of the vertical profiles of wind, density, and temperature in the surface boundary layer for different conditions of atmospheric instability. The hypothesis provides explicit relationships for these profiles based on a unique stability parameter which always remains finite even in the limiting case of free convection.

The elementary relationships which have been described to illustrate the application of the hypothesis are similar to, but also significantly different from, extant relationships in current usage. The real test of the differences comes when we program the hypothesis into the general planetary boundary layer model (2) - the ultimate arbiter.

CONCLUSIONS

Turbulence is said to be the unsolvable problem. General theories of turbulence can only be approximations and their application necessitates recourse to empirical studies to complete the development. The hypothesis reported here is no exception to this rule.

Postulates two and three of the hypothesis are related to analyses performed in conjunction with turbulent diffusion; the major difference is that turbulent diffusion is usually concerned with effects, whereas this hypothesis stresses cause as well as effects. The reader may find it interesting to compare the hypothesis with the summary of turbulent diffusion theory reported by Csanady (12). The results of the hypothesis are superficially similar to the more conventional works of Businger (13), Hanna (14), Lettau (15) and others, but the approach differs markedly. In short, the hypothesis has no known parallel.

The weakest parts of the hypothesis are postulates three and four. The hypothesis shares this shallowness with the whole field of turbulent diffusion. In the coming decade, we shall strive for substantial progress in these areas so that we may better apply our knowledge to solve practical problems. There is a need for new ideas, for example, the work of R. E. Meyers reported at this Army Science Conference. It is the author's opinion that real progress will be made when we better understand the role of the pressure fluctuations in the turbulence dynamics.

I wish that this could be reported as a proven theory rather than just a hypothesis. While much work remains to complete the development and validate the hypothesis, it does establish a general concept which can guide future basic research toward practical goals.

OHMSTEDE

NOMENCLATURE

a or b	Arbitrary dependent variable
c	Speed of sound in air
c_v and c_p	Specific heats at constant volume and pressure
C^{ik} or D^{ik}	Constant tensors
g	Acceleration of gravity
$k = \frac{1}{2} \overline{u^i u^i}$	Kinetic energy per unit mass of the turbulence
l	Mixing length (see Ref. 1)
$L(\hat{a}, \hat{b})$	Eulerian length scale for covariance of a and b
p	Pressure
r	Potential density
S	Stability function for Eulerian length scale
t or t'	Time
$T_L(\hat{a}, \hat{b})$	Lagrangian time scale for covariance of a and b
u^i	Vector coordinates of velocity
x^i	Space coordinates
γ	Mickelsen constant
δ^{ij}	Kronecker delta; $\delta^{ij} = 1$ if $i = j$, $\delta^{ij} = 0$ if $i \neq j$
κ	Constant for Eulerian length scale
$u^i = \overline{\rho u^i}$	Vector components of the turbulent mass flux
ρ	Density
σ^{ij}	Elements of the viscous stress tensor
τ	Temporal limit of integration
$\tau^{ij} = -\overline{u^i u^j}$	Elements of the Reynolds stress tensor
$u^i = \sqrt{\overline{(u^i)^2}}$	Mickelsen velocity scales, $i = 1, 2, 3$

OHMSTED

REFERENCES

1. Appleby, J. F., and W. D. Ohmstede, Army Science Conference, June 1964 (AD 612 121).
2. Ohmstede, W. D., "Numerical Solution of the Transport and Energy Equations in the Planetary Boundary Layer," Tech. Report ECOM-6020, April 1966 (AD 633 694).
3. American Meteorological Society, Glossary of Meteorology, Boston, 1959.
4. Monin, A. S., and A. M. Yaglom, Statistical Hydromechanics, Part 1, JPRS 37,763; Joint Pub. Res. Svc., Washington, D. C., Sept. 1966.
5. Lettau, H. H., J. Meteorol., 11, p. 196, 1954.
6. Mickelsen, W. R., "An Experimental Comparison of the Lagrangian and Eulerian Correlation Coefficients in Homogeneous Isotropic Turbulence," NACA Tech. Report 3570, Oct. 1955.
7. Smith, F. B., USAEC Meteorological Meeting, Sept. 11-14, 1967, AECL-2787, pp. 476-483.
8. Wandel, C. F., and O. Kofoed-Hansen, J. Geophys. Research, 67, pp. 3089-3093, 1962.
9. Ohmstede, W. D., "Estimating the Distribution of an Aerosol Within a Forest," Interim Report, ASL, USAECOM, March 1968.
10. Cramer, H. E., and F. A. Record, "Properties of Turbulent Energy Spectra and Cospectra in the Atmospheric Surface Layer," R&D Tech. Report ECOM-64G1-F, March 1969 (AD 687 337).
11. Panofsky, H. A., et al., "Properties of Wind and Temperature at Round Hill, South Dartmouth, Mass.," R&D Tech. Report ECOM-0035-F, Aug. 1967 (AD 659 430); R&D Tech. Report ECOM-68G2-F, Oct. 1968 (AD 680 911).
12. Csanady, G. T., "Development of the Theoretical and Technological Prerequisites to Field Investigation of Particulate Agent Behavior," Report Nr. 1, Qtrly Progress Report, Dec. 1965, Contract DA18-035-AMC-399(A), Edgewood Arsenal, Md.
13. Businger, J. A., J. Geophys. Research, 66, p. 2425, 1961.
14. Hanna, S. R., J. Atmos. Sci., 25, pp. 1026-1033, 1968.
15. Lettau, H. H., Phys. Fluids, 10, 9(Part II), pp. S79-S83, 1967.

CO₂ LASER PULSING PRODUCED BY CAVITY-LENGTH MODULATION

ALBERT L. PARDUE, JR., 1LT, OrdC
 US ARMY MISSILE COMMAND
 REDSTONE ARSENAL, ALABAMA 35809

INTRODUCTION

In recent years Q-switching in CO₂ lasers, conventionally achieved by rotating mirrors, has aroused considerable interest. This technique not only produces high peak power outputs, but the resulting pulsing provides information on the various laser level lifetimes and molecular relaxation processes [1,2]. Two methods of varying the cavity length -- the use of a moving mirror by Bridges [3] and rotating an NaCl plate internal to the cavity by Carswell and Wood [4] -- produced an effect that Bridges termed "reactive Q-switching." This effect exhibits two advantages over the conventional Q-switching: 1) the average power of the resulting pulses is approximately equal to the CW power, and 2) the pulse repetition rate can be greatly extended.

Reactive Q-switching results from sweeping the longitudinal resonator modes through the gain profiles of the CO₂ lasing media. In the conventional (single-pass) laser experimental setup such as that used by Bridges and Carswell, the effective optical cavity length is less than 200 cm, so that the axial mode interval or spacing is greater than the Doppler half-linewidth for CO₂. Thus only one mode can oscillate in a given transition at a given time, and it is possible to have a situation where no mode is oscillating at a given instant.

In the experiment reported here, the reactive Q-switching effect was obtained in a CO₂-N₂-He multimode multipass laser oscillator using various numbers of passes (ranging from 4 to 32), for which the axial mode interval is less than the Doppler half-linewidth for CO₂. As in Bridges' study, a moving mirror was used to vary the optical cavity length. The mirror was moved at various velocities, in both the constant velocity and sinusoidal velocity modes. Contrary to what the previous experiments might suggest, the characteristic pulsing

PARDUE

occurred even though the mode structure consisted of a number of modes above threshold. There were at least two and in most cases more than two modes oscillating under a given Doppler linewidth.

EXPERIMENTAL

Instrumentation. The multipass CO₂ laser oscillator and amplifier is described in detail in the literature [5-8]. The particular instrument used in this study consisted of a White-type mirror system with a 15-cm tube [5], shown in the functional diagram of Fig. 1. Off-axis aluminum disks were used as electrodes, with a separation between electrode centers of 2.7 meters. The White mirror section of the cavity used gold-coated, copper substrate mirrors with a 3-meter separation. The mode structure in the laser oscillator was controlled by 1) a mask placed 7 cm in front of the split mirrors in the White mirror system, and 2) a beam-restricting circular aperture placed outside the Brewster angle NaCl window. During the study it was found that the additional limiting provided by the circular aperture is necessary to achieve pulses that decay to zero. A gold-coated, stainless steel substrate, flat mirror external to the White mirror system was used to facilitate alignment of the laser beam onto a moving mirror. This movable end mirror, weighing approximately 6 grams and consisting of a flat gold-coated front surface on a cervite substrate, was moved along the axis of the laser cavity by a Mössbauer transducer. The entire lasing structure was mounted on a vibration isolation table to minimize the mechanical vibration, and a 10- μ F capacitor was used to filter out unwanted electronic noise from the dc power supply.

Procedure. The block diagram of Fig. 2 includes the additional, data-collecting instrumentation, and Fig. 3 is a photograph of the experimental laboratory setup. Tests were made for various values of N (number of passes) while moving the mirror at selected velocities (from 0.5 to 40.0 cm/sec) for each pass setting. The majority of the experiments used the constant velocity mode, with the mirror being moved in a sawtooth fashion along the axis of the cavity. The pulsing produced by this mode was studied for N = 4, 8, 16, 20, and 32 passes. Pulsing was briefly examined for N = 20 passes with the mirror in the sinusoidal velocity mode. To achieve the sinusoidal cavity-length modulation, the dc voltage supply (Fig. 2) was replaced by a low frequency generator amplified by a McIntosh amplifier, and the control unit was appropriately adjusted.

In the multipass laser, the axial mode spacing can be easily adjusted in increments by changing the number of optical passes in the cavity, and this characteristic was used to study pulsing for several mode spacings. Beat notes between modes were observed for all values of N, using a Ge:Hg detector and Panoramic spectrum analyzer.

The laser output in the time domain was viewed by a Tektronix 555 CRO. The CRO sweep was triggered by a velocity signal from the transducer, which signal was delayed to insure that the laser pulses

PARDUE

were observed during the linear portion of the sawtooth displacement of the mirror. A waveshape feedback control unit was used with the transducer to insure that the displacement of the transducer was linear.

Gas pressures were initially set at 0.1 torr CO₂, 0.5 torr N₂, and 2.7 torr He, which provided lasing, and were then adjusted the slight amount necessary to achieve maximum power at each pass number setting. Pressures were measured by a Wallace and Tiernan gauge connected to the end plate that supported the full White mirror. The output mirror shown in Fig. 2, i.e., an NaCl disk oriented perpendicular to the laser emission axis, was used for the higher values of N. To obtain sufficient gain for lasing at N = 4 and 8, this disk was removed and replaced by an NaCl Brewster angle window and a germanium flat mirror.

RESULTS AND DISCUSSION

Unless specifically mentioned as sinusoidal, the discussion in this section concerns results obtained with the mirror in the constant velocity mode.

Mode Spectrum. The difference between the mode structure of a conventional laser [3,4] and that of the multipass laser oscillator is illustrated in Fig. 4. In the conventional type the effective optical cavity length (L) is less than 200 cm, so that the axial mode interval is greater than the Doppler half-linewidth for CO₂ (Fig. 4-A), or $c/2L > 50$ MHz. It is clear from the diagram that if L is varied sufficiently a mode corresponding to a given integer "n" can enter and leave a gain transition, thereby producing a laser pulse. The dominant effect of the moving mirror is to sweep a "comb" of modes through the gain profiles. Since the change in L is small, there is no appreciable change in mode spacing as viewed in the localized frequency region of the line. Because of the strong competition between the transition lines due to the thermalization of vibrational-rotational levels by molecular collisions, only one line will oscillate at a given instant.

The mode structure of the multipass laser oscillator resulted in a number of modes being above threshold (Fig. 4-B), i.e., $c/2L_{\text{eff}} < 50$ MHz, at all values of N. The effective cavity length L_{eff} is given by the relation $L_{\text{eff}} \approx NL$,* where L is the axial separation between the White mirrors and N is the number of passes. Because of the skewness of the paths within the White cell and the distance added by the outside placement of the movable mirror, the actual L_{eff} is slightly larger than NL. The approximate axial mode interval is given by $c/2NL$. As the number of passes between mirrors is increased, the axial mode spacing is reduced and the number of modes above threshold is consequently increased.

*For a single-pass conventional laser, $L_{\text{eff}} = L$ since $N = 1$.

PARDUE

Beat notes were observed on the spectrum analyzer at all values of N . The 4-pass laser had an axial mode separation of 12.3 MHz and, in the nonmodulated condition, had a minimum of two modes oscillating in the multipass laser cavity. At $N = 8$, beat notes between modes were observed at 6.1, 12.2, and 18.3 MHz, giving an axial mode interval of 6.1 MHz and indicating that four longitudinal modes were oscillating. At $N = 16$, the beat notes occurred at 3.05, 6.1, 9.15, and 12.2 MHz, indicating a 3.05-MHz mode spacing with five modes oscillating. Higher pass settings gave similar results with a corresponding increase in number of modes above threshold.

Pulse Repetition Rate. The pulsing associated with the reactive Q-switching phenomenon was obtained in the multipass laser oscillator even though several modes were oscillating above threshold. This pulsing was similar in pulse width and repetition rate to that observed in conventional straight lasers [3,4] which have only one mode oscillating at a given instant. At all values of N in the constant velocity mode, the pulses occurred at a pulse time separation equivalent to the time required for the end mirror to move $\lambda/2$. Consequently, the pulse repetition rate was directly proportional to the mirror velocity. Pulse repetition rates ranged between 1 and 60 kHz, with pulse halfwidths as small as 5 μ sec. The following cases are cited as examples: for the 4-pass laser, the pulse repetition rate at a 40-cm/sec mirror velocity was 42 kHz with a pulse width of 6 μ sec; at the same velocity the 16-pass laser produced a pulse rate of 60 kHz with a pulse width of 6 μ sec; at a mirror velocity of 26.0 cm/sec the 20-pass configuration had a pulse repetition rate of 36.7 kHz with a pulse width of 5 μ sec.

Pulse Amplitude Consistency. Unlike the prior work, the periodic pulses in the multipass CO₂ laser exhibited constant amplitude at all constant mirror velocities, which ranged from 0.5 to 40.0 cm/sec. Bridges reports that at low mirror velocities, such as 1.6 and 5.9 cm/sec, conditions are such that the lasing oscillation jumps between transition P lines, giving pulsing with varying amplitudes. As can be seen in Fig. 5, the pulsing in the 4-pass configuration was regular in waveform shape and amplitude at these and even lower velocities. At all velocities the output pulse had a sharp leading edge. "Post lasing" was observed at low mirror velocities, as was generally true for all values of N , with the duration depending on the mirror velocity and consequently the arrival of the next pulse; however, as the mirror velocity increased, this post lasing region gradually vanished and the pulses became symmetrical (Fig. 6).

There was no competition or switching between lines, such as that reported by Bridges, and no evidence of "break up" frequency described by Carswell.*

*A point at which the system misses pulses and the amplitude becomes irregular from pulse to pulse.

PARDUE

Pulse Power. The laser output was chopped to allow a comparison of the peak pulse power output of the modulated laser with the CW level of the free-running or nonmodulated laser. In some cases the reactive Q-switched pulses had an apparent peak pulse amplitude 10 times as high as the CW output level. The average power was approximately equal to the CW power. It was observed that the pulsed output at low mirror velocities decayed between the pulses to a "quasi-zero" level (apparent zero line of pulses); as the mirror velocity was increased, this level dropped and finally became true zero.

Figure 7 shows the chopped laser output of the 4-pass configuration at zero mirror velocity (A) and at a 1.0 cm/sec velocity (B). A pulsing phenomenon occurred with mirror motion but the quasi-zero level never dropped to zero. This quasi-zero level was gradually lowered with increasing velocities and became zero at an 8.0-cm/sec mirror velocity, as shown in Fig. 8. The Q-switched pulses (Fig. 8) had an apparent peak pulse amplitude of 10 times the CW nonmodulated output level. The pulses had a pulse width (6 μ sec) and repetition rate (12.4 kHz) similar to those obtained by Bridges and Carswell, and showed the post-lasing output noted by the latter. The time duration between the pulses at the point where the quasi-zero level becomes zero is interpreted here as a measure of the recovery time of the system. The time interval between pulses was found to be 82 μ sec. At mirror velocities above 8.0 cm/sec, the pulse amplitude decreased but the quasi-zero level remained at zero. In addition, the pulse width broadened slightly. For the 20-pass configuration, the axial mode spacing was 2.47 MHz and at minimum five modes were above threshold. However, a very definite Q-switching effect was obtained, as is shown in Fig. 9 for a 26.0-cm/sec mirror velocity. With a pulse repetition rate of 36.7 kHz and pulse width of 5 μ sec, the peak pulse power was approximately six times the CW laser output. At this velocity the post-lasing output had vanished but the pulsing did not decay completely to zero between pulse peaks.

One measure of the degree to which the output decays to zero between pulses is the ratio $\Delta P/P_{\max}$, where $\Delta P = P_{\max} - P_{\min}$, or ΔP is the difference between pulse peak amplitude and the quasi-zero level. Plotting $\Delta P/P_{\max}$ versus velocity gives the same correlation as shown by the preceding traces: as the mirror velocity is increased, the quasi-zero level approaches zero. The trend shown in Fig. 10 for $N = 8$ was typical of all optical cavity lengths.

As was noted earlier, it was found that limiting the beam size inside the laser cavity was necessary to achieve pulses that decayed to zero, with the ease of obtaining such pulses directly dependent on the degree of such restriction. At all path length settings, the circular aperture was stopped down to approximately 5 mm, which gave essentially a TEM_{00q} mode output and a beam size of approximately 5 mm.

PARDUE

Sinusoidal Mode. A limited number of runs were made with the transducer driven in the sinusoidal mode and using the 20-pass configuration. The resulting distribution of pulses, shown in Fig. 11, was very similar to that for the constant velocity mode, i.e., the pulses were regular in waveform, and the time separation was equivalent to the time required for the end mirror to move $\lambda/2$.

CONCLUSIONS

It is apparent that the reactive Q-switching pulsing in the CO₂ laser is not restricted to the conventional straight laser [3,4] where only one mode oscillates at a given instant. In the conventional laser the restriction to one such mode appeared to be the major factor. However, the lengthening of the laser cavity in the multipass CO₂ laser provided similar pulse widths and repetition rates. Even at low mirror velocities (~ 0.5 cm/sec), pulsing was found to be repetitive in waveform shape and amplitude, whereas under similar conditions in the conventional straight laser, irregular pulsing was observed.

This study is still in the preliminary stage, and the significance of the results and potential application have not been explored. One interesting characteristic observed in the spectrum analysis, in addition to those reported, will be included in the study. Although the beat note pattern of the laser output was very erratic in the free-running state, the waveform in the perturbed laser oscillator was to a great extent frequency stabilized.

ACKNOWLEDGMENTS

The author gratefully acknowledges valuable suggestions and assistance from Dr. Odis P. McDuff, University of Alabama, and from Dr. George J. Dezenberg and Dr. William B. McKnight, of the US Army Missile Command.

REFERENCES

1. Kovacs, M. A., Flynn, G. W., and Javan, A., "Q-Switching of Molecular Laser Transitions," Applied Physics Letters, Vol. 8, Feb 1966, p. 62.
2. Flynn, G. W., Kovacs, M. A., Rhodes, C. K., and Javan, A., "Vibrational and Rotational Studies Using Q-Switching of Molecular Gas Lasers," Applied Physics Letters, Vol. 8, Feb 1966, pp. 63-65.
3. Bridges, T. J., "Competition, Hysteresis and Reactive Q-Switching in CO₂ Lasers at 10.6 Microns," Applied Physics Letters, Vol. 9, Aug 1966, pp. 174-176.
4. Carswell, A. I., and Wood, J. I., "High-Speed Reactive Q-Switching in CO₂ Lasers," IEEE Journal of Quantum Electronics, Vol. QE-4, May 1968, pp. 294-296.

PARDUE

5. Dezenberg, G. J., Roy, E. L., and Merritt, J. A., "Properties of a 15-cm Inside Diameter Multipath CO₂ Laser Amplifier and Oscillator," Applied Optics, Vol. 9, Feb 1970, pp. 516-517.
6. Dezenberg, G. J., and Merritt, J. A., "The Use of a Multipath Cell as a CO₂-N Gas Laser Amplifier and Oscillator," Applied Optics, Vol. 6, Sept 1967, pp. 1541-1543.
7. Bickart, C. J., and Fulton, John N., "Investigation of a Multi-traverse 10.6 Micrometer Oscillator Amplifier," Research and Development Technical Report ECOM 3176, US Army Electronics Command, Fort Monmouth, New Jersey, Sept 1969.
8. Kogelnik, H., and Bridges, T. J., "A Nonresonant Multipass CO₂ - Laser Amplifier," IEEE Journal of Quantum Electronics, Feb 1967, pp. 95-96.

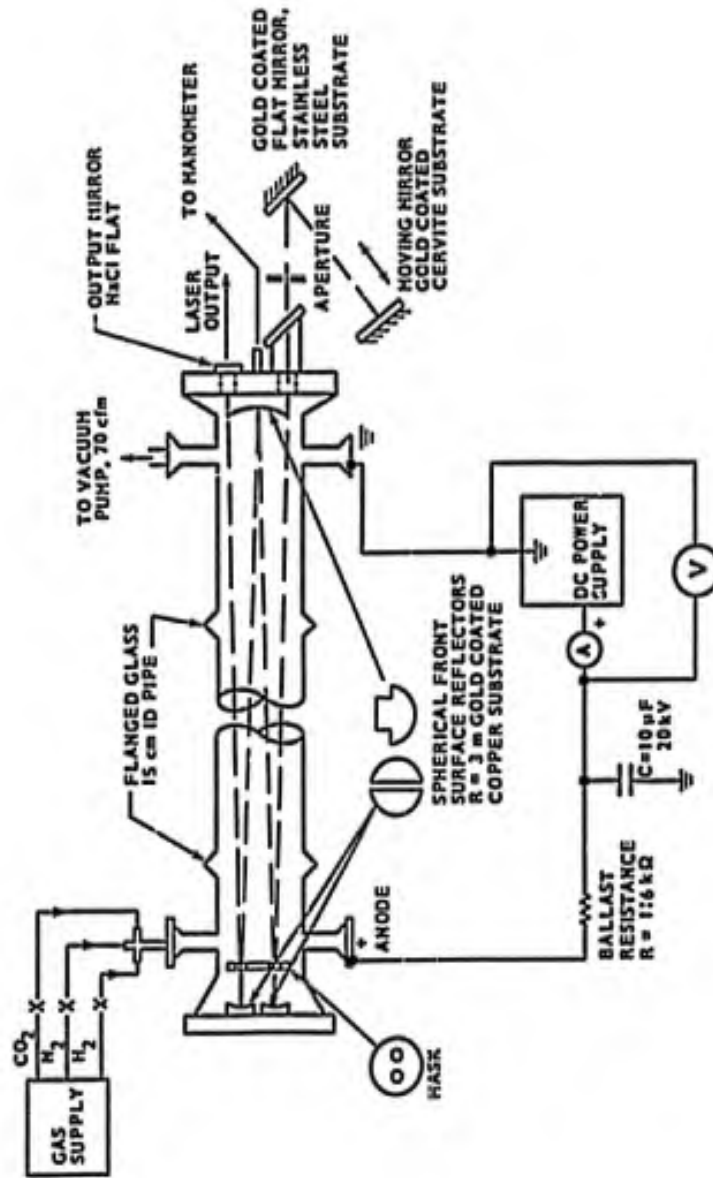


Fig. 1. Functional Diagram of Multipass Laser Oscillator with Ray Path Shown for 4 Passes

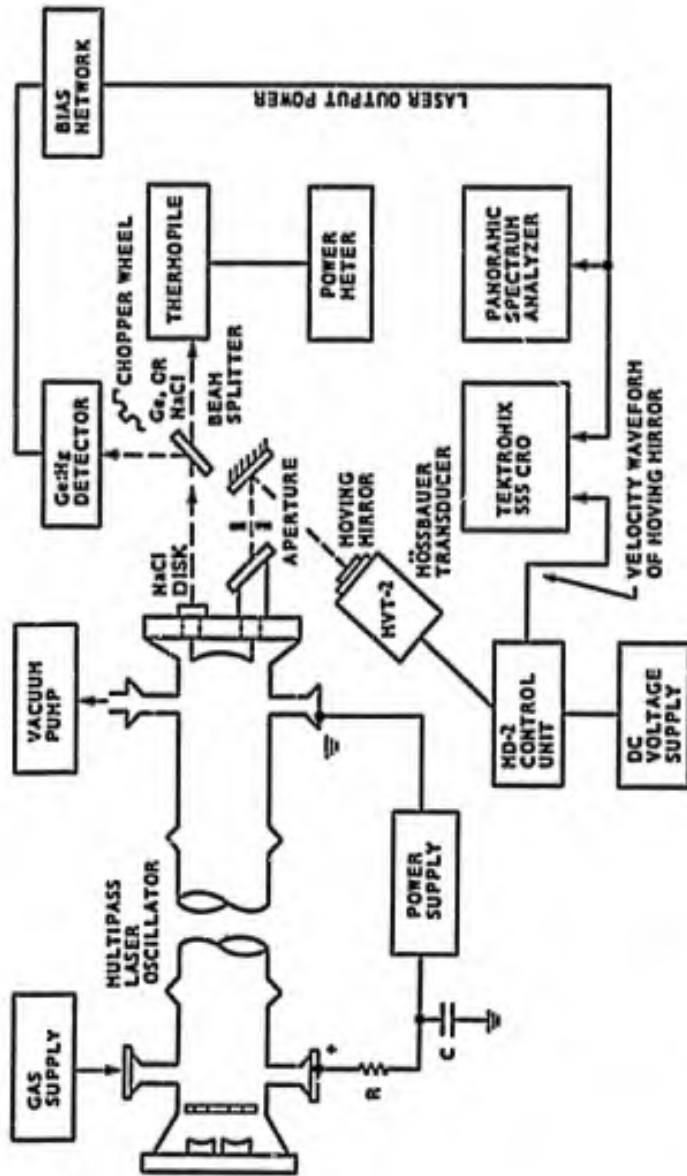


Fig. 2. Block Diagram of Experimental Apparatus - Multipass CO₂ Laser

PARDUE

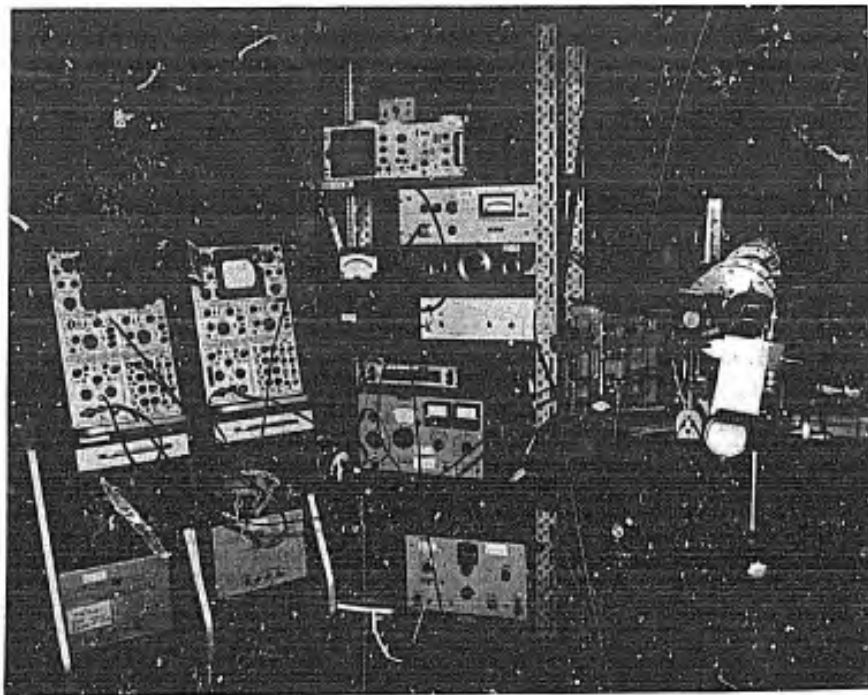
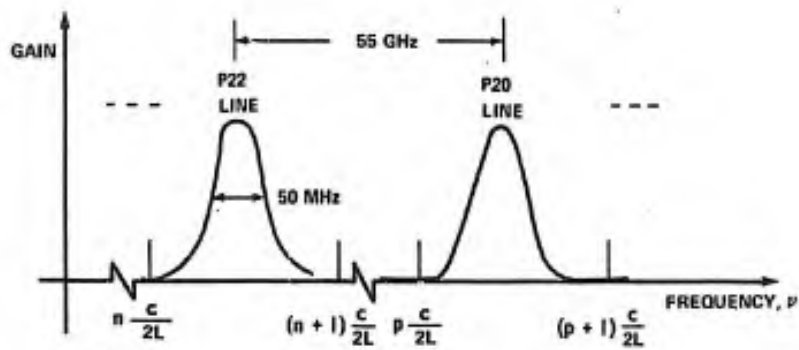
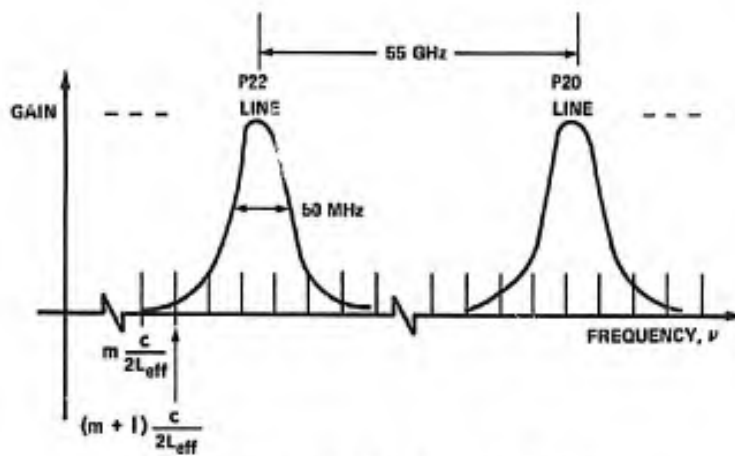


Fig. 3. Experimental Apparatus for Length-Modulated Multipass CO₂ Laser

PARDUE



A. Type Used by Bridges [3] and Carswell [4]



B. Typical Multipass Laser Oscillator

Fig. 4. Resonator Mode Spectrum for CO_2 Laser.

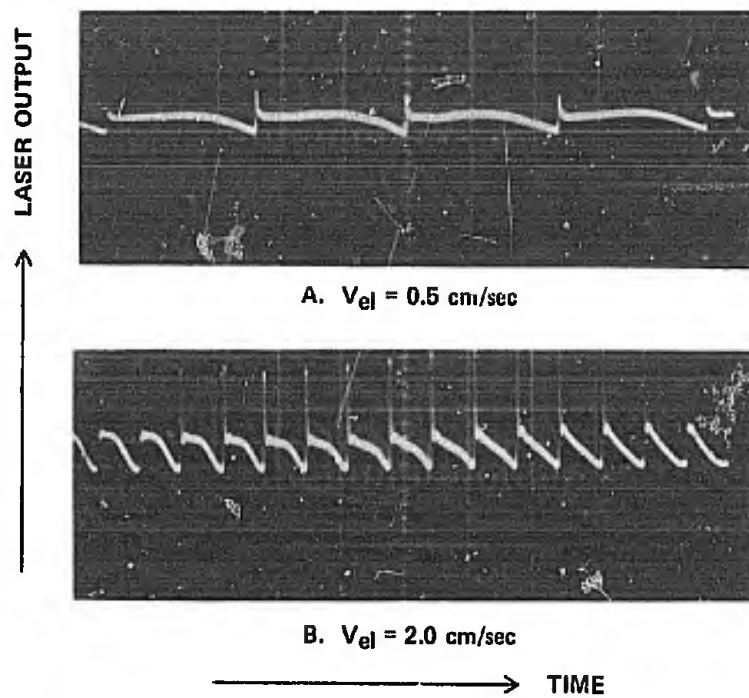


Fig. 5. Time Variation of Laser Output for Different Mirror Velocities (V_{e1}):
 $N = 4$; Discharge Current = 100 mA;
Time Base = 0.5 msec/cm

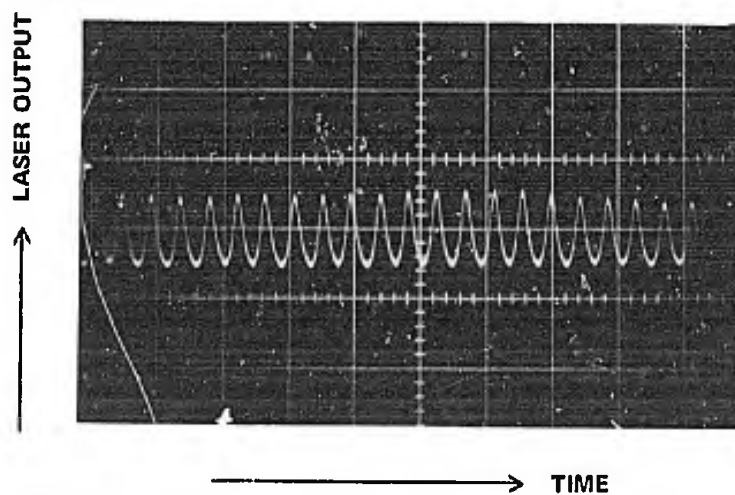


Fig. 6. Time Variation of Laser Output: $N = 16$;
Discharge Current = 50 mA; $V_{e1} = 31.25$ cm/sec;
Time Base = 50 μ sec/cm

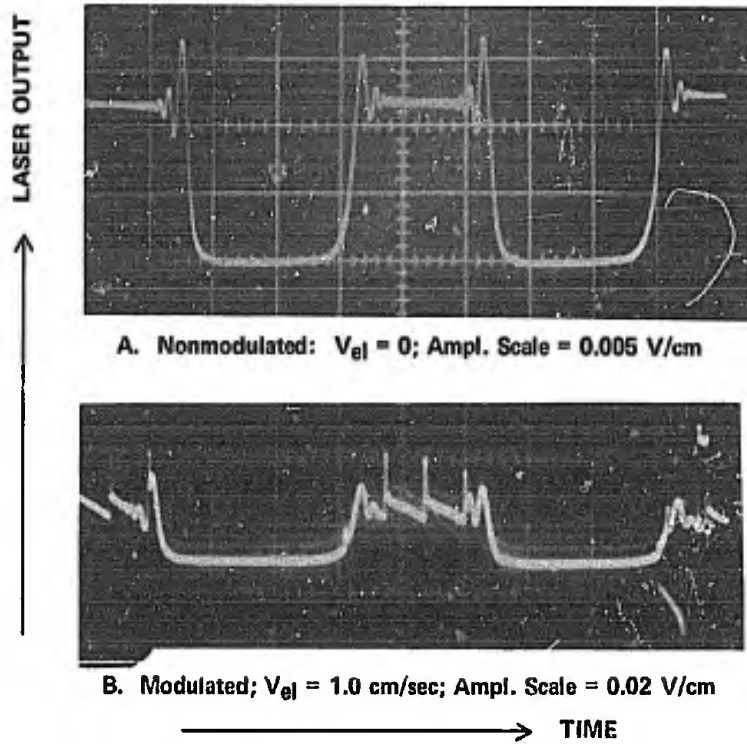


Fig. 7. Time Variation of Chopped Laser Output:
 $N = 4$; Discharge Current = 100 mA;
Time Base = 0.5 msec/cm

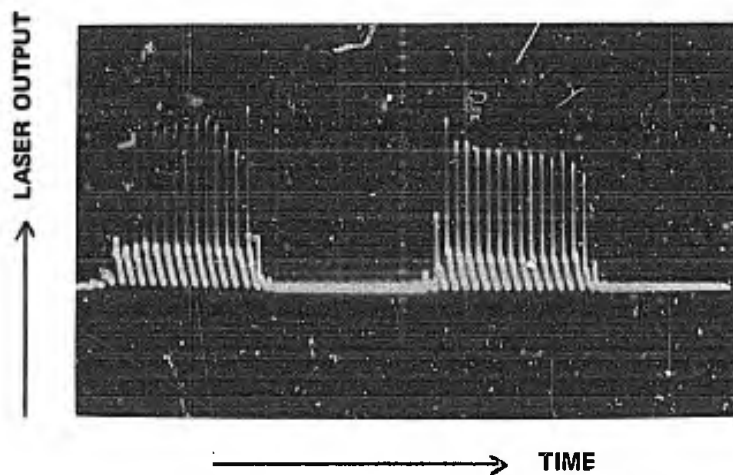


Fig. 8. Time Variation of Chopped Laser Output:
 $N = 4$; Discharge Current = 100 mA;
 $V_{e1} = 8.0$ cm/sec; Time Base = 0.5 msec/cm;
Amplitude Scale = 0.05 V/cm

PARDUE

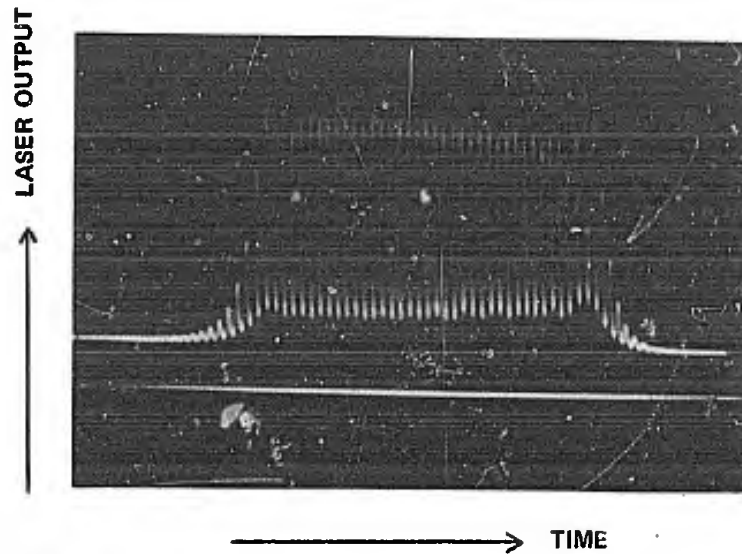


Fig. 9. Upper Trace, Time Variation of Chopped Laser Output: $N = 20$; Discharge Current = 50 mA; Time Base = 0.2 msec/cm. Lower Trace, Velocity Waveform of Transducer: $V_{e1} = 26.0$ cm/sec

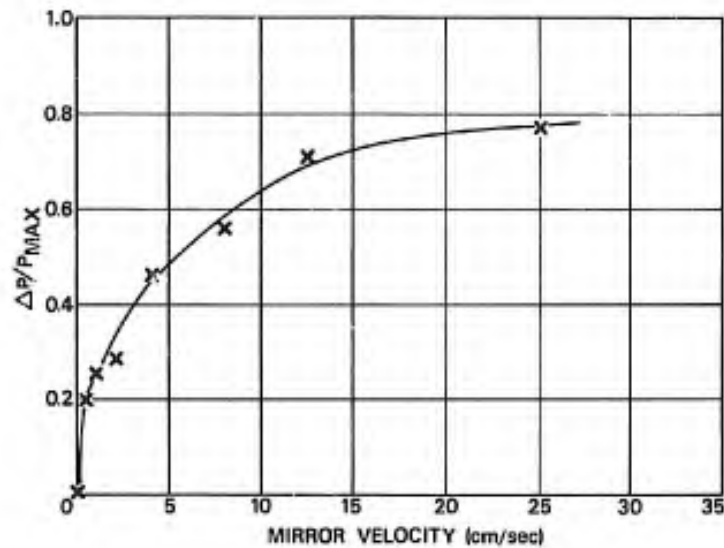


Fig. 10. $\Delta P/P_{max}$ versus Constant Mirror Velocity. $N = 8$, $P_{CW} = 2.75$ W, Discharge Current = 100 mA.

PARDUE

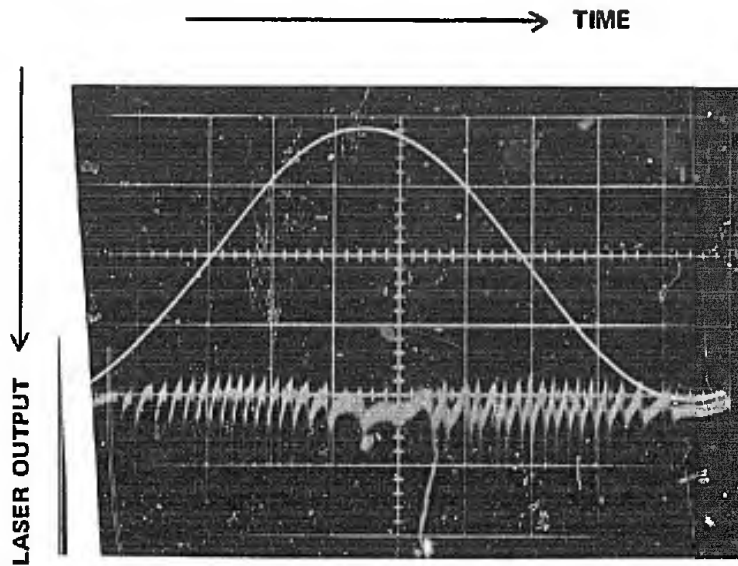


Fig. 11. Upper Trace, Velocity Waveform
of Transducer: $f = 100$ Hz. Lower
Trace, Time Variation of Laser Output:
 $N = 20$; Time Base = 1 msec/cm.

USE OF ACTIVATION ANALYSIS FOR DETERMINING WEIGHT
OF PELLET IN M34 PRIMERS

HOMER F. PRIEST, FORREST C. BURNS*, GRACE L. PRIEST
ARMY MATERIALS AND MECHANICS RESEARCH CENTER
WATERTOWN, MASSACHUSETTS

The use of rapid fire weapons such as the minigun has focused attention on the problem of hangfires. A hangfire in the minigun is defined as a cartridge which gives an action time greater than four milliseconds. Since the electrically operated minigun fires up to 6000 rounds per minute, a hangfire is considered to be the most serious malfunction, because the cartridge may explode either in the weapon causing a stoppage and possible gun damage or outside the weapon where flying particles may injure personnel, with possible loss of life and equipment.

From a study at Frankford Arsenal, it was concluded that low pellet weight in the M34 primer (more than 20% below specification) which is used in the minigun 7.62 mm. round, tends to produce cartridge hangfires due to insufficient output of hot gases and particles to adequately ignite the propellant charge.

Methods considered for 100% nondestructive quality assurance of the M34 primer pellet weight at a production rate in excess of 10 million per day were:

(1) Weigh pellet before insertion in the cup. In the current manufacturing process, the pellet is formed in the cup from wet explosive dough, and, therefore, final dry weight of the pellet would have to be determined in the finished primer. Weighing of the completed primer is not only too slow a process, but the allowable variations in the weight of the components other than the pellet are such that variations in the pellet weight could be easily masked.

(2) Incorporate a radioactive isotope in the pellet mix so that radiation sensing could be used to determine the pellet weight. It was at this point the authors of this paper became involved in the problem. Consideration of the addition of a radioactive isotope to the pellet mix in a concentration sufficient to ensure adequate

precision in radiation counting showed that because of the large number of primers manufactured, the supply of isotope would be complex and costly, and the large quantities of primers containing radioactive isotope in any one location would constitute a severe radiation hazard requiring special handling and shielding.

(3) Incorporate an additive in the pellet mix or select an element in the pellet mix which could be irradiated by a neutron source to make it sufficiently radioactive to give adequate counting precision but would rapidly decay back to normal, thereby eliminating the handling and shielding problem.

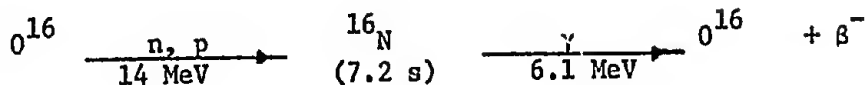
The criteria established to aid in selecting a candidate isotope were:

- a. The isotope must have a reasonable neutron capture cross section so that the neutron source does not have to be impractically large.
- b. The isotope must be present in the pellet in a high enough concentration to ensure a high count rate when activated.
- c. The isotope must have a unique radiation pattern so that discriminators can isolate its gamma rays easily from those of other isotopes present.
- d. The isotope must have a short half-life so that it can be easily activated to a high level but will decay rapidly to safe levels of radiation.

In Table I the various elements present in the primer as major components are shown with the radioactive species to be expected from irradiation with accelerator-produced neutrons (14 MeV).

It will be noted that copper, a major component of the primer (58.9%) in terms of weight, produces 0.511 MeV gamma rays from positron annihilation. The nature of this radiation is such that it will completely mask virtually all the other isotopes produced with the exception of nitrogen-16 from oxygen which, with its 6.1 MeV gamma ray, is a very unique source of radiation. Thus the most practical element to use for activation analysis of the pellet is oxygen, which meets all four criteria, and already constitutes 26.53% of the pellet weight.

Fortunately, as part of a basic AMMRC research program of impurities in ultrapure materials, a very advanced irradiation, transfer, and counting system (1) for 14 MeV activation analysis of oxygen in solids had been developed. This system utilizes 14 MeV neutrons to irradiate the oxygen which is converted to radioactive nitrogen according to the following nuclear reaction:



The radioactivity of the nitrogen is measured, and since this is directly proportional to the oxygen content, the weight of the pellet is determined. The radioactivity decays back to normal within a few minutes so there is no hazard in subsequent handling of the primers.

An analysis consists of three parts: irradiation, pneumatic transfer, and counting. The unknown and standard cylindrical samples in special irradiation capsules, which are mounted on the irradiation head as shown in Figure 1, undergo complex motions to ensure uniform irradiation and are transported pneumatically to the uncapping and counting subsystem (shown in Figure 2) where the samples are removed from the irradiation capsules and the radioactivity is counted. The printed data from the counting system provides all necessary information to calculate the weight of oxygen in the primer and thus the pellet weight. Corrections are made for geometry effects, decay, and oxygen in the other primer components and the primer sample holder.

Figure 3 is an exploded view and cross section of the M34 primer showing the component parts of cup, pellet, paper disc, and anvil, and a cross section of an assembled primer.

In order to accommodate the M34 primer, special holders were made which had a cavity for the primer at the geometrical center as shown in Figure 4.

Primer pellet weights have been determined by analyzing the primer for oxygen utilizing lucite as an oxygen containing standard sample for comparison, and in most cases the same primers have also been analyzed utilizing the copper/oxygen ratio whereby the copper in the cup-anvil combination in the primer was used as an internal standard by comparing the 0.511 MeV positron annihilation radiation from ${}^{62}\text{Cu}$ (produced by the reaction $\text{Cu}^{63} (n, 2n) {}^{62}\text{Cu}$) to the 6.1 MeV gamma from ${}^{16}\text{N}$ (produced by the reaction ${}^{16}\text{O} (n, p) {}^{16}\text{N}$) from the oxygen in the primer. In the copper internal standard method, which is directly applicable to a production inspection system, two single channel analyzers have their windows at 0.511 MeV and 6.1 MeV respectively and the two radiations are counted simultaneously. When using the copper in the cup and anvil as an internal standard, the actual determination of the pellet weight is not required. The ratio of copper to oxygen, after necessary corrections, is a measure of the pellet weight, and rejection or acceptance can be based on the ratio.

The results of the initial feasibility study (2) showing

PRIEST, BURNS*, and PRIEST

the determination of the pellet weights on a group of specially selected primers are given in Table II. Included for comparison are some copper/oxygen ratios on the same primers.

Based on these results, it was decided to proceed with further studies to obtain data required to design a production inspection system. A sampling of production primers was analyzed, and some typical results are shown in Table III.

The variations in pellet weight are well within the specified tolerances for the M34 primer. The copper/oxygen ratio results are not quite as accurate, although a very low pellet weight always gives a high ratio. The absolute value of the ratios are different because they depend on the settings of the single channel analyzers which were purposely changed during this series of analyses.

Based on the results obtained on production primers, a contract was awarded to Cambridge Engineering, Inc. (3) to develop the concepts and design specifications for a production inspection system for 100% nondestructive quality assurance inspection of the M34 primer at the required high production rate of more than 10 million/day at a reasonable cost per item. The authors supplied all technical details and maintained constant surveillance of the contract. Figures 5 and 6 show schematically how such a system would operate. Parallel channels of 5 rows of primers, with anvils up, are continuously fed under the neutron generator target face to give an irradiation time of five seconds. The irradiated primers are transported by a stepping carrier through the 8 ft. thick concrete shield to an unloader where they pass into 10 parallel counting channels, each individual primer passing at a controlled speed between two scintillation crystals for counting the ^{16}N and ^{62}Cu for 0.5 sec. The data is supplied to a small digital computer which decides on acceptance or rejection of the primer. Each system would have the capability of inspecting 13 primers/second or 374,400 primers per 8 hours. To meet a higher inspection rate, multiple systems would be required.

Conclusions

A 100% inspection of M34 primers for low pellet weight has been demonstrated to be feasible and specifications for an actual manufacturing quality assurance system have been developed based on activation analysis for oxygen in the pellet.

PRIEST, BURNS*, and PRIEST

LITERATURE CITATIONS

1. "Irradiation, Transfer, and Counting System for Neutron Activation Analysis of Short-Lived Components in Inhomogeneous Samples", Homer F. Priest, Forrest C. Burns, and Grace L. Priest, Anal. Chem. April, 1970.
2. "Feasibility Study on Use of Activation Analysis For Determining Weight of Pellet in M34 Primers", Homer F. Priest, Grace L. Priest, and Forrest C. Burns, AMMRC TN 68-06, September 1968.
3. "M-34 Primer Quality Assurance System", Cambridge Engineering, Inc., Waltham, Mass., 1-6823C, February 1969.

TABLE I
ISOTOPIES WHICH WOULD BE PRODUCED IN THE M34 PRIMER BY 14 MeV NEUTRONS

Component	Element	Weight % Present	Radioactive Species Produced	Energy γ Rays MeV	Half-Life
Pellet	Aluminum	7.00	Sodium 24 Magnesium 27	2.75, 1.38 0.834	15 hour 9.5 min.
	Barium	16.80	No Significant		
	Hydrogen	0.52	None		
	Nitrogen	10.62	Nitrogen 14	0.511	10 min.
	Oxygen	26.53	Nitrogen 16	6.1	7.2 sec.
	Lead	16.35	No Significant		
	Antimony	9.05	Antimony 120 Antimony 122	1.18 0.061, 0.075	16.4 min. 3.5 min.
	Sulfur	5.95	No Significant		
	Carbon	7.16	No Significant		
	Cup & Anvil	Copper		Copper 62 Copper 64	0.511 0.511
Zinc			Zinc 63 Zinc 65	0.67, 0.96 1.12	38 min. 245 day

TABLE II

DETERMINATION OF PELLET WEIGHT AND THE COPPER/OXYGEN RATIOS
FOR N34 PRIMERS*
14 MeV Neutron Activation Analysis (Weight in Grains)

Specified Pellet Weight	Corr. O Weight**	Pellet Weight Based on Corr. O Weight**	Ratio $\frac{\text{Cu}}{\text{O}}$
0.26	0.084	0.261	—
0.26	0.077	0.236	—
0.26	0.079	0.241	—
0.26	0.076	0.231	—
0.26	0.084	0.260	7.449
0.26	0.069	0.204	7.326
0.26	0.085	0.264	6.288
0.39	0.109	0.357	—
0.39	0.134	0.449	—
0.39	0.120	0.397	—
0.39	0.111	0.361	—
0.39	0.119	0.394	6.101
0.39	0.115	0.378	6.312
0.39	0.112	0.366	6.052
0.54	0.147	0.500	—
0.54	0.190	0.660	—
0.54	0.148	0.500	—
0.54	0.147	0.500	—
0.54	0.170	0.585	4.033
0.54	0.157	0.535	4.313
0.54	0.159	0.545	4.410

* Original Special Primers Supplied.

** Correction made for oxygen in primer cup, anvil, and paper.

TABLE III
 DETERMINATION OF PELLET WEIGHT AND OF THE COPPER/OXYGEN RATIO
 FOR PRODUCTION M34 PRIMERS
 14 MeV Neutron Activation Analysis (Weight in Grains)

Primer Desig- nation	Corr. O Weight*	Pellet Weight			Ratio
		Based on Corr. O Weight*	% Dev. From Spec. (0.600)**	% Dev. From Mean	$\frac{\text{Cu}}{\text{O}}$
a. Production M34 Primers, Manufacturer #1					
1	0.168	0.576	- 4.00	+ 1.59	4.699
2	0.169	0.581	- 3.17	+ 2.47	4.653
3	0.172	0.594	- 1.00	+ 4.76	4.304
4	0.173	0.596	- 0.67	+ 5.11	4.134
5	0.155	0.530	-11.67	- 6.53	4.412
6	0.160	0.547	- 8.83	- 3.53	4.310
7	0.170	0.584	- 2.67	+ 3.00	4.091
8	0.165	0.565	- 5.83	- 0.35	4.171
9	0.171	0.588	- 2.00	+ 3.70	4.037
10	0.151	0.513	-14.50	- 9.52	4.446
11	0.164	0.563	- 6.17	- 0.71	4.219
12	0.165	0.567	- 5.50	- 0.00	4.161
b. Production M34 Primers, Manufacturer #2					
1	0.159	0.543	- 9.50	- 3.72	8.858
2	0.169	0.580	- 3.33	+ 2.84	8.172
3	0.151	0.513	-14.50	- 9.04	9.094
4	0.161	0.551	- 8.17	- 2.30	8.461
5	0.167	0.575	- 4.17	+ 1.95	8.144
6	0.178	0.617	+ 2.83	+ 9.40	8.302
7	0.166	0.569	- 5.17	+ 0.89	8.315
8	0.164	0.562	- 6.33	- 0.35	8.412
9	0.155	0.530	-11.66	- 6.03	9.028
10	0.157	0.535	-10.83	- 5.14	8.573
11	0.176	0.607	+ 1.17	+ 7.62	7.912
12	0.171	0.587	- 2.17	+ 4.08	8.149
c. Production M34 Primers, Manufacturer #3					
1	0.173	0.598	- 0.33	+ 0.34	7.015
2	0.196	0.683	+13.83	+14.59	6.812
3	0.167	0.575	- 4.17	- 3.52	7.062
4	0.168	0.579	- 3.50	- 2.85	6.896
5	0.164	0.562	- 6.33	- 5.70	7.405
6	0.177	0.610	+ 1.67	+ 2.35	6.981
7	0.176	0.608	+ 1.33	+ 2.01	6.806
8	0.157	0.537	-10.50	- 9.90	7.017

* Correction made for oxygen in primer cup, anvil, and paper.

** M34 individual pellet weight specification = 0.600 -0.120.

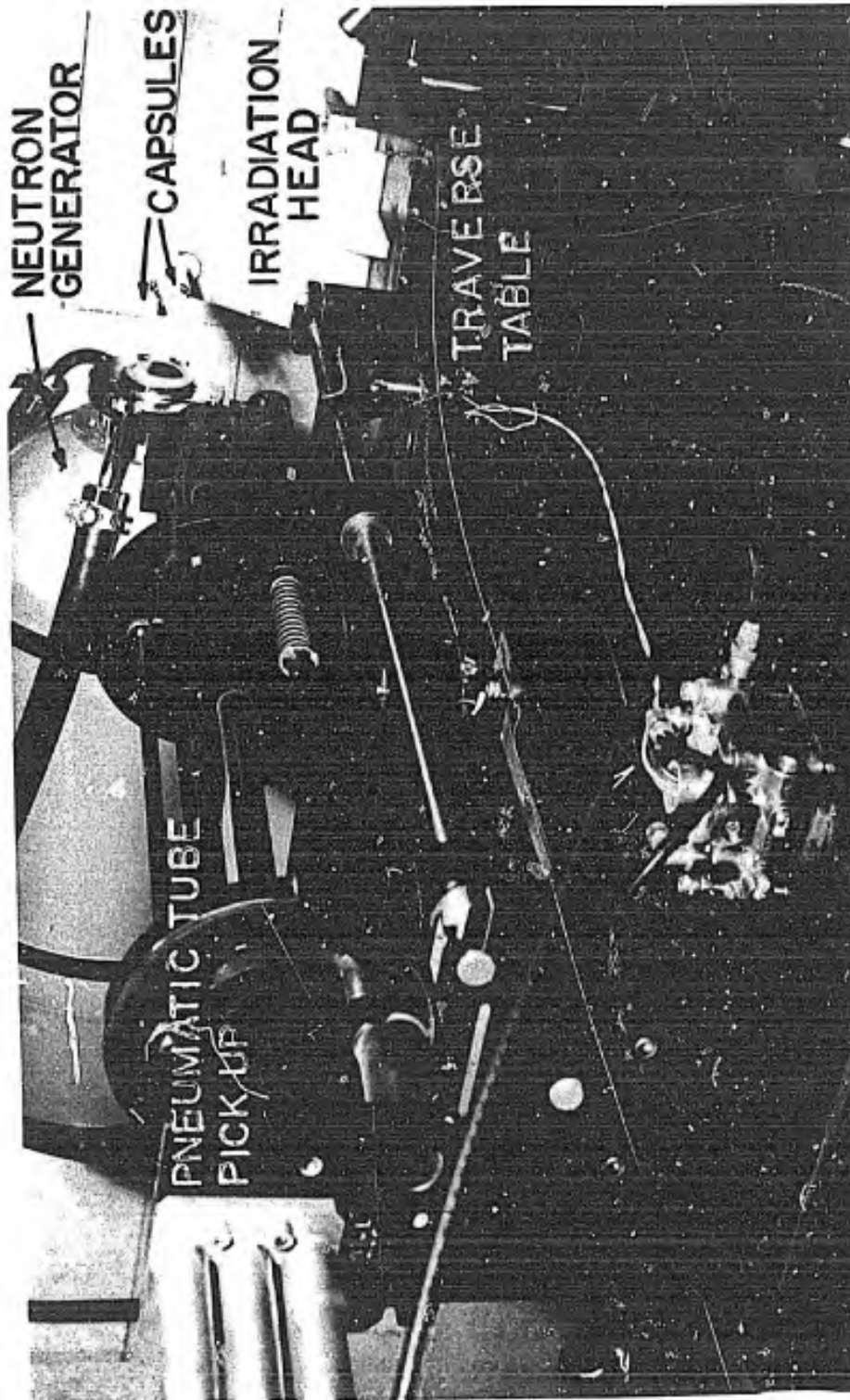


FIGURE 1 IRRADIATION AND TRANSFER SYSTEM



Figure 2. UNCAPPING AND COUNTING SYSTEM

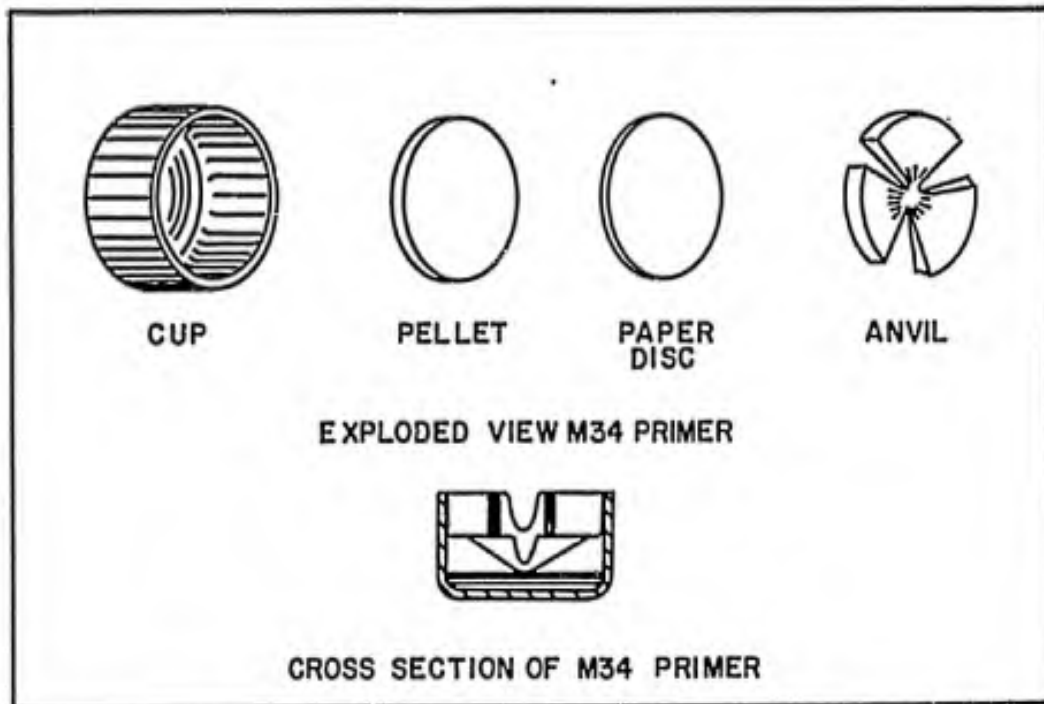


Figure 3. EXPLODED VIEW AND CROSS SECTION OF M34 PRIMER

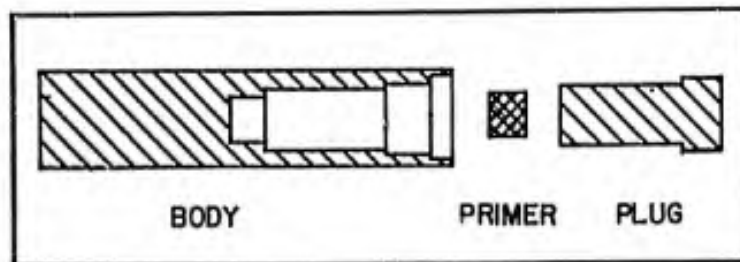


Figure 4. SPECIAL HOLDER FOR M34 PRIMER

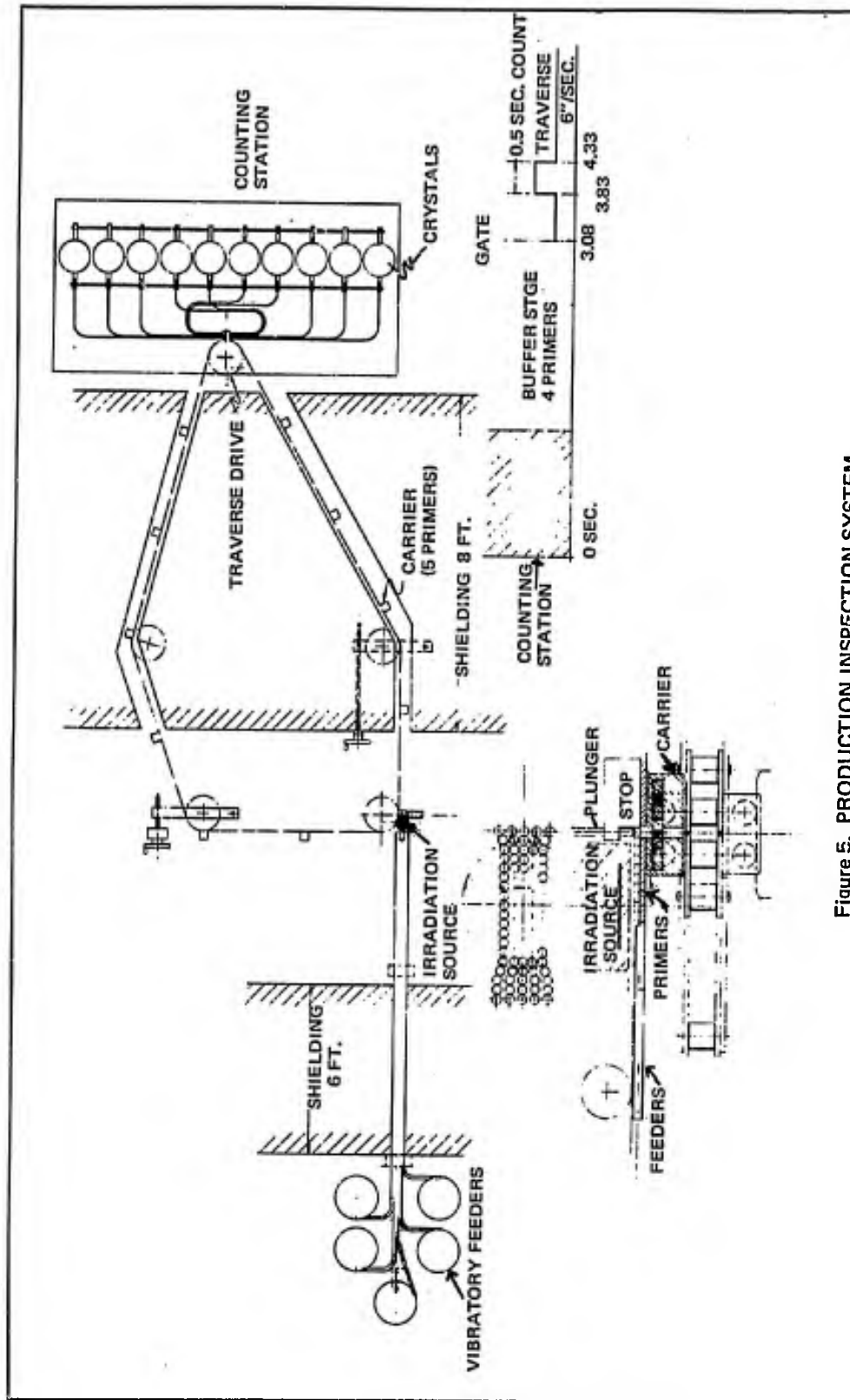


Figure 5. PRODUCTION INSPECTION SYSTEM

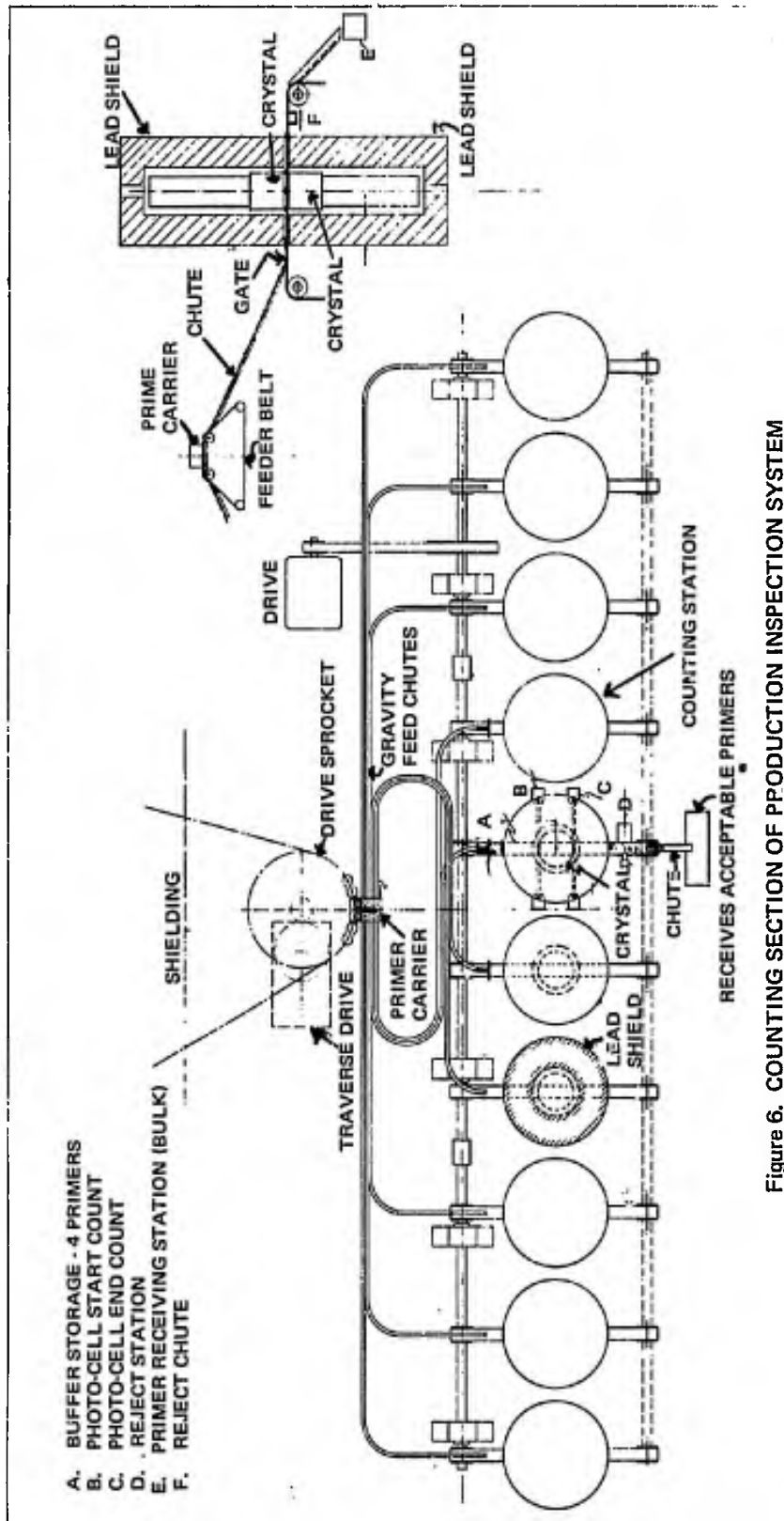


Figure 6. COUNTING SECTION OF PRODUCTION INSPECTION SYSTEM

FIELD TEST OF A STEAM CONDENSER
HEAT SINK CONCEPT

WILLIAM F. QUINN, HALDOR W. C. AAMOT, MARCUS GREENBERG
U. S. ARMY COLD REGIONS RESEARCH AND ENGINEERING LABORATORY
HANOVER, NEW HAMPSHIRE

The protection against nuclear attack afforded by deeply burying strategic installations is generally well recognized. Such installations must often be self-sustaining and function during and after attack conditions on essentially a closed cycle system. This places upon the system the requirement that all of the waste heat associated with power generation by a buried power plant be contained and stored underground for some specified period of time. A functional and economical heat rejection system is an important design consideration for such installations.

The rejection of waste heat developed in the operation of hardened underground power plants presents the designer with several alternatives in his choice of a heat sink. Such alternatives include water (either at the in-situ ground temperature or at some lower temperature provided by mechanical refrigeration), an ice-water mixture utilizing the latent heat of fusion, a chemical solution at a depressed temperature below the freezing point of water, the surrounding ground, or some combination of these alternatives.

Prior analytical and laboratory studies have considered water, chilled water, chilled brine, and ice-water systems. (1,2,3,4)* In all these studies the use of the surrounding medium as the primary heat sink has never been considered in detail. At the request of the Nuclear Power Division, Office, Chief of Engineers, the U. S. Army Cold Regions Research and Engineering Laboratory conducted a study to determine the feasibility of such a concept. This concept as developed by OCE's Missiles and Protective Structures Branch and the Nuclear Power Division involved the disposal of turbine exhaust steam generated by a nuclear powered turbine by discharging into rock tunnels. The condensate would be collected

*See bibliography

QUINN, AAMOT,
GREENBERG

and reused in the power cycle after appropriate chemical treatment. The primary advantages of this concept are that it obviates the need to store and maintain large quantities of heat sink substances (water, ice, etc.) underground and also permits use of tunnels for other than just heat sink purposes. If existing tunnels can be used, the concept becomes economically attractive.

Although the study looked feasible theoretically^(5,6), a field test was required to establish its practicability. The field test was conducted to study saturation levels, heat transfer coefficients and to validate the analytical approach for predicting the amount and rate of heat storage by the rock. Although a field test of an ice-water heat sink concept was reported in the literature⁽⁷⁾, no information was available involving the use of rock as a steam condenser.

SITE DESCRIPTION

The site selected for this study was located in a magnetite mine owned and operated by Republic Steel Corporation in Mineville, New York (approximately 5 miles west of Port Henry). The test was conducted 2250 ft below the ground surface in a tunnel roughly 10 ft high by 13 ft wide. The tunnel had been constructed by the drill, blast and muck method which caused some fracturing of the face rock.

The drift for the entire length of the test area is in a granitic gneiss made up mainly of quartz and feldspar and sparsely disseminated magnetite; its compressive strength is between 30,000 to 43,000 psi⁽⁸⁾. The general dip in the location is approximately 25 degrees downward to the left (northeast) and the strike is approximately parallel to the drift. The ores and adjacent rock in this drift are possibly Grenville Metasediments⁽⁹⁾. Four stations within a 300-ft length of tunnel were selected for temperature observations and thermocouple assemblies were installed to depths of 40 ft in the roof, floor and two side walls at each of the four stations. The position of each station within the test area is given on Figure 1. The granitic gneiss contacts a biotite gneiss at varying distances from the tunnel face (at least 15 ft at Stations 1 and 2). The location of rock bolts is also shown in the figure. Rock bolting (29 bolts total) was limited to those sections of roof which were obviously loose. The tunnel floor was sloped at a grade of 0.75% toward the northwest; this provided the desired gravity flow of condensate to a collection point at Bulkhead B.

Average apparent specific gravities for the rock were: 2.85 (178 pcf) - granitic gneiss, 3.17 (198 pcf) - biotite gneiss, and 4.79 (298 pcf) - magnetite ore.

QUINN, AAMOT,
GREENBERG

Several core samples were used for thermal conductivity tests by Professor Francis Birch of Harvard University. Thermal conductivities were measured with divided-bar systems similar to that described by Birch⁽¹⁰⁾. Results of these tests are summarized below:

Summary - Average Thermal Conductivities

Rock Type	Environment	Core Orientation	
		Vertical	Horizontal
Granitic Gneiss	Air Dry 104°F	1.97 Btu/ft hr°F	2.24 Btu/ft hr°F
	Soaked 104°F	2.02	2.32
	Soaked 77°F	2.11	2.36
Biotite Gneiss	Air Dry 104°F	1.12 Btu/ft hr°F	
	Soaked 104°F	1.15	
	Soaked 77°F	1.14	

PRETEST ANALYSIS

As no specific mission requirements were imposed, the assumed heat rejection rates and button-up times were selected as being reasonably representative of a realistic situation.

Thermodynamic Process

The measured ambient rock and air temperatures in the test area were initially constant at 60°F and the air was 100% saturated. The partial pressure of the vapor (saturated vapor pressure) for this temperature condition is 0.25 psia and the average total atmospheric pressure was 15.25 psia (corresponding to an elevation of 1075 ft below sea level). The partial pressure of the vapor is governed by its dew point, in this case the rock surface temperature (condenser temperature). With the introduction of steam into the tunnel, the rock surface temperature gradually rises resulting in a corresponding increase in the dew point and associated vapor pressure.

The total pressure (air pressure plus vapor pressure) was maintained constant at atmospheric throughout the test by the continuous venting of air through a water trap. Thus, the partial pressure of air (difference between total pressure and vapor pressure) continuously decreased. The vapor pressure can rise to a maximum of 15.25 psia corresponding to a dew point (rock surface temperature) of 213.8°F. Changes in atmospheric pressure during the test resulted in a dew point variation from 213.6 to 214.0°F.

The experiment is completed when the rock surface temperature reaches about 213.6°F at which time all of the air has been displaced and the tunnel is filled with pure steam. Now the rock can no longer accept heat at the same constant rate and the steam flow rate must be reduced or the excess steam will either overflow

QUINN, AAMOT,
GREENBERG

through the vent or it will pressurize the tunnel.

It was qualitatively concluded that the transfer coefficient between the tunnel atmosphere and the rock will increase during the course of the test as air is continuously vented from the test area. It was also estimated that initially for an air-rich mixture, the transfer coefficient would probably be on the order of $1.2 \text{ Btu/ft}^2\text{hr}^\circ\text{F}^{(11)}$.

Prediction of Air and Rock Surface Temperatures

Heat transfer to the rock was approximated using an analytical model which considers the test tunnel to be represented by a hollow cylinder in an infinite medium initially at a constant temperature with heat flow at a constant rate by conduction in the radial direction. The problem has been treated by Carslaw and Jaeger⁽¹²⁾. The solution can be expressed as a dimensionless relationship between temperature rise at the surface (ΔT) and time (t):

$$\frac{\Delta T k}{a \dot{q}} = f \left(\frac{\alpha t}{a^2} \right)$$

An exact analytical solution of the basic equation is not possible. DA Technical Manual TM-855-4⁽¹¹⁾ provides a numerically computed graph of these dimensionless functions. A numerical solution of the equation was also developed by Stanley and Fellers⁽¹³⁾. The underlying assumptions are: a homogeneous rock material with constant thermal conductivity (k) and diffusivity (α), a circular tunnel cross-section of radius (a) and a constant heat flux (\dot{q}). The actual situation involves a heterogeneous rock material with variable thermal properties, a rectangular tunnel cross-section with rounded corners, and a slightly variable heat flux.

For the Mineville experiment, a flux vs warmup time curve was prepared. As the tunnel was rectangular rather than circular, an equivalent radius was used on the basis of equal perimeters: $a = 2(10+13)/2\pi = 7.33 \text{ ft.}$ The following rock properties, estimated from handbook values⁽¹⁴⁾, were used (the experiment was designed prior to the measurement of thermal properties): $k = 1.7 \text{ Btu/ft hr}^\circ\text{F}$, $C_p = 0.19 \text{ Btu/lb }^\circ\text{F}$, and $\rho = 177 \text{ lbs/ft}^3$. The theoretical time-temperature relationship is given on Figure 2. A temperature of 212°F was originally taken to represent the maximum dew point temperature. A period of 20 days was considered to be a reasonable length of time to permit a comprehensive evaluation of both the thermal and physical processes. Entering the graph at 20 days a heat flux of $60 \text{ Btu/ft}^2\text{hr}$ is found to be required. The tunnel surface area is in the order of $\sqrt{2} (13+10) \times 300 = 13,800 \text{ ft}^2$ which represents a demand load of $\sqrt{60 \times 13,800} = 828 \times 10^3 \text{ Btu/hr.}$ Assuming that the heat from the saturated steam is solely its heat of condensation at 212°F (970 Btu/lb), the steam production required is:

QUINN, AAMOT,
GREENBERG

$(828 \times 10^3 \text{ Btu/h}) / (0.97 \times 10^3 \text{ Btu/lb}) = 854 \text{ lb/hr}$. A 5% allowance for end losses and steam quality results in a total requirement of 896 lb/hr. Heat dissipation by the condensate was not considered. Assuming boiler feedwater at 60°F, the boiler was sized as follows:

Heat of vaporization at 212°F	970 Btu/lb
Water enthalpy at 212°F	181
	<u>1151</u>
Water enthalpy at 60°F	28
Energy required	<u>1122 Btu/lb</u>

Boiler size: $(1122)(896)/3412 = 295 \text{ KW}$

The predicted change in surface temperature with time is given on Figure 3. The curve depicting the vapor-air mixture temperature with time is only an approximation. Between the beginning and completion of the test, the temperature difference between the rock surface and tunnel atmosphere was expected to decrease exponentially. Radial temperature gradients were also predicted for various times.

TEST PLAN

The 300 ft section of tunnel was sealed off by welded steel bulkheads which were insulated with foamed-in-place urethane. Pipes, tracks and ballast were left in place within the test area; however, they were removed at the bulkhead locations. Ditches were excavated on both sides of the track to provide channels for the condensed water to return to the boiler area. The ballast beneath the track varied in thickness from 18 to 24 inches.

Although the concept involved the recovery and reuse of the condensate, it was decided to waste the condensate in this experiment after recording its flow rate and temperature. Steam was developed by a 296-kW electric boiler continuously operated at approximately 460 volts. A constant heat output by the boiler was selected as being a reasonable approximation to the waste heat generated in the development of the essentially constant power level utilized in operating an underground facility. Distribution of steam within the test area incorporated a two-pipe system. One pipe (pipe X) conveyed the steam in a header running the full length of the test area with nineteen (19) vertical riser pipes, spaced at 15 ft intervals, discharging steam in essentially equal quantities throughout the tunnel. This system provided an even distribution of steam. The other pipe (pipe Y) discharged steam at a single point, 22 ft from Bulkhead B; this system permitted steam diffusion throughout the entire test area.

The original plan was to inject steam through pipe X until the air temperature was within a few degrees of the saturated steam temperature. At that time the steam would be injected through pipe Y in order to compare diffusion under the two distribution systems.

QUINN, AAMOT,
GREENBERG

When a saturated steam condition had been reached in the test area, it was planned to reduce the constant heat input to approximately three-quarters of its initial rate. This would simulate a reduction in demand on an underground power generating facility and would thereby prolong the effective usefulness of the heat sink.

The following quantities were monitored during the experiment:

Input -- water flow, steam flow, bulkhead pressure, boiler pressure, pipeline pressure, and steam quality
Output -- condensate weight and temperature, rock temperatures and bulkhead temperatures

POST-TEST TUNNEL CONDITION

Prior to discussing the experimental results, it is useful to have an appreciation of the rock distress caused by the introduction of live steam. Such information is of considerable assistance in appraising the results.

Upon termination of the test and after overnight cooling, the access door in bulkhead B was opened to reveal a pile of rock rubble about 5 ft deep. Prior to the clean-up operation a muck pile averaging 5 ft in depth covered the floor from bulkhead B for a distance of 70 ft into the test area. From 70 ft to 115 ft (vicinity of Sta. 2) a heavy fall of ground occurred which enlarged the drift from 13 to 17 ft in width and from 10 to 35 ft in height. The rubble pile in this region was about 30 ft high. The remainder of the tunnel was covered with a pile of rubble about 2.5 ft deep. The mucking operation required the removal of 323 car loads or roughly 2585 tons of rock. This represents an average of about 3 ft of rock fall from the two walls and roof.

Figure 4 shows the tunnel condition in the vicinity of Station 1. The severed thermocouple wires can be seen hanging from the ceiling. Note the smooth texture of the roof and walls and the tendency for the corners to round out. In some cases the rock bolts held sections of roof intact, in others the bolts remained in place and the rock spalled away. As noted above considerable distress developed in the vicinity of Station 2 (Figure 5). The catastrophic collapse is attributed to an open seam less than 1/32 inch wide which diagonally intersected the tunnel as shown on Figure 1. Although several other seams were present in the test area, they were oriented normal to the tunnel axis and did not develop the distress pattern found at Station 2.

The pile of debris had a slabby nature and resembled a very tight dry stone wall. Slabs developed during spall ranged from fines up to about 8 inches in thickness. It was interesting to note the similarities between this rubble pile and those associated

QUINN, AAMOT,
GREENBERG

with failure attributed to erosion of gouge-filled seams in unlined hydraulic tunnels⁽⁵⁾.

TEST RESULTS

The test was begun at 1030 hours on 18 June 1968 and was conducted for 37.2 days (892 hours) ending at 1415 hours on 25 July.

As previously mentioned, it was planned to use pipe X to distribute steam uniformly throughout the major portion of the experiment. This plan was aborted after 10 1/2 hours of testing because a large slab fell and broke the pressurized pipe X header. Steam was then diverted to pipe Y for the remainder of the test, dumping the entire steam load between Stations 3 and 4. A comparison of the air temperature measured 1 inch from the rock surface on the west side of the tunnel as shown on Figure 6 indicates that the distribution of steam longitudinally throughout the test area was relatively uniform. The air temperature at Station 1 is consistently about 3 to 4°F less than at Stations 2 and 3 indicating a slight longitudinal variation (3 to 4°F/100 ft). A definite temperature stratification existed with the floor being particularly cooler (Fig. 7). Improvement in the heat transfer coefficient with time between the air and rock surface is indicated on Figure 8 which shows a continual decrease in the average temperature difference with time between the air and rock surface at Stations 1, 2, and 3. An overall average temperature difference is given in the figure.

The air temperature variation with time at Station 3 is shown on Figure 9 together with bulkhead B, 25 ft from Station 3 and the temperature of the condensate leaving the tunnel. The air temperature increased from 60°F on 18 June to 200°F on 7 July (19 days). Starting on 8 July a distinct air cooling was recorded at Station 3 and the same tendency was observed at the bulkhead. An explanation for this sudden drop in the heating curve was not obvious at that time. The primary explanation for the cooling trend became evident after the test when the bulkhead door was opened and the rubble pile was observed.

The event log maintained during the test cited numerous rock falls on the 7th and 8th of July and again on 17, 19, 20 and 21 July. This continual fall of roof rock exposed additional cooler surface for condensation and a larger mass for heating and thereby slowed the rate of heating of the tunnel atmosphere. Although it was evident that rock fall was taking place during the experiment, the magnitude of the fall was not fully appreciated until the test was completed.

The quantity of heat introduced to the test area was quite uniform. The average daily boiler pressure was used to determine the enthalpy of steam in the boiler and the temperature of the returning condensate was used for computing the residual heat in the water

QUINN, AAMOT,
GREENBERG

leaving the test area. The resulting average heat input, assuming a 13,800 ft² surface area, varies between 59 and 60 Btu/ft² hr. A comprehensive assessment of test results was complicated by the successive loss of temperature sensors occurring continuously throughout the test.

ANALYSIS

Surface Transfer Coefficients

As shown on Figure 8, temperature differences between the air-vapor and rock surface decreased with time thereby indicating an increase in the combined surface transfer coefficient. For a temperature difference of 4°F and heat input rates of 59 to 60 Btu/ft² hr, a combined surface transfer coefficient on the order of 15 is indicated. During the early days of the test, temperature differences of 6 to 8°F were observed representing coefficients of 7 to 10 Btu/ft² hr°F.

Measured vs. Predicted Surface Temperatures

Establishing a correlation between measured and predicted temperature was complicated by the problem of rock fall which retarded the rate of temperature rise. Had roof spall not occurred, the air temperature would have increased more rapidly than observed.

An indication of the significance of rock fall, both in terms of magnitude and time, may be obtained from Figure 9. Two discontinuities are evident in the relationship between condensate temperature and time. Between 23 and 25 June the condensate temperature remained relatively constant while the tunnel air temperature continued to increase. From about 9 to 17 July the condensate temperature remained nearly constant, after which it tended to decrease (except for 16 July). A possible explanation for this behavior is that the condensate in flowing past the rock rubble on the tunnel floor was giving up some of its heat to the numerous rock slabs (and their associated high surface areas) lying on the tunnel floor. The decrease in air temperature on the west wall at Station 3 and the leveling out of the bulkhead B temperature probably indicate a substantial rock fall within the test area subsequent to about 9 July. The slope of the condensate temperature vs time curve up to about 23 June indicates that substantial rock fall probably did not develop prior to that time.

The temperature gradient in the floor differed from those observed in the wall and/or roof. The heat stored in the rock surrounding Station 1 was estimated using radial distance-temperature curves for 0600 hrs on 24 June. This amounted to an average heat flux of 77 Btu/ft² hr to the roof, 69 Btu/ft² hr in each wall and 44 Btu/ft² hr in the floor. Although these values are only approximations of the heat budget, they do indicate that heat storage in the floor was

QUINN, AAMOT,
GREENBERG

considerably less than either in the walls or roof during the early stages of the experiment and prior to the rockfalls. This lower heat transfer to the floor was due to a combination of factors: (a) the temperature stratification existing in the tunnel, which represented an air-rich mixture of air and vapor near floor level and consequently a poorer transfer condition, (b) the insulating effect of the water layer flowing along the floor and (c) the gradual build-up of fallen rock.

Figure 10 compares the average measured rock surface temperature vs time with the theoretical curve assuming a flux of 59 Btu/ft² hr. The measured temperatures are greater than predicted during the early portion of the test although they do intersect after about 22 days. As previously mentioned, the exposure of cool rock surface due to spalling resulted in prolonging the warm up period over what it would have been had no spalling developed. It would therefore appear that the mathematical model tends to overpredict warm up times which is undesirable for this design application. Analytical predictions of the time required for the rock surface to reach the limiting temperature must be modified to account for the relatively slow heat transfer to the floor. Such adjustment can be most easily applied by reducing the amount of surface area exposed for heat transfer or in effect theoretically increasing the heat flux. A theoretical curve (Figure 10) so adjusted, is compared with average surface temperatures measured in the walls and roof at Stations 1, 2, and 3. The departure from the theoretical curve on the 8th day undoubtedly represents the influence of rock fall. A more detailed analysis of the experimental results is presented in the project final report⁽¹⁶⁾.

CONCLUSIONS

A comparison between the theoretical and measured results is particularly difficult because of the rock fall which occurred throughout the test, but the following conclusions can be drawn from the results of this experiment:

1. An unlined tunnel, constructed by drilling and blasting, was the primary cause of slabbing in the roof. The following expedients would reduce, or may possibly eliminate this effect: lining the tunnel, using rock bolts or roof screening, or machine boring the tunnel. The test did show that steam with an unstable cross-section such as the rectangular drilled and blasted tunnel used in this experiment could result in serious consequences.

2. As indicated in figure 6, the longitudinal distribution of steam within the 300 ft test area was remarkably uniform. Although most thermocouples at the far end of the tunnel were eventually lost, the uniform mixing during the early stages of the test was readily demonstrated by measurement.

QUINN, AAMOT,
GREENBERG

3. The heat transfer coefficient between rock and air mixed with steam is at least ten times as much as that between rock and air alone. The continued improvement in heat transfer was primarily due to the venting of air throughout the test.

4. Heat transfer to the floor was less than that to either the walls or ceiling. This results in two unfavorable conditions: (a) a departure from radial flow causing a decrease in warm-up time, and (b) the greater extraction of heat from returning condensate.

5. Analytical predictions of the time required for the rock surface to reach the condensing temperature must be modified to account for the relatively low heat transfer coefficient at the floor. Such an adjustment can be most easily made by theoretically reducing the amount of surface area exposed for heat transfer, i.e., increasing the heat flux. For this particular test, a theoretical flux adjustment of 13 to 15% would have been appropriate. Although such an adjustment is considered to be conservative, full-term validation was not possible in this field experiment.

6. In the event that rock debris can be tolerated in either all or a portion of the tunnel space, the advantageous use of spalled rock for additional heat sink capacity was made obvious by this experiment.

ACKNOWLEDGMENTS

Many people participated in the experiment. We are especially grateful to Republic Steel Corporation and the staff at the Adirondack Ore Mines under Mr. William A. Blomstran, District Manager. Their support of this project was always timely, responsive, and cooperative.

Richard Guyer, USACRREL Electronics Technician, installed and checked out the temperature-monitoring systems. Four Scientific and Engineering Enlisted Men from our Laboratory provided valuable contributions to the project in general and to solving the many problems which are always encountered in putting such a field test together, making it work, and monitoring outputs. The contributions of SP David Karr and SP Joseph Wilhelm are particularly appreciated; they were involved in designing the experiment and assembling the components in the field. They were then most ably assisted by SP Brian Murray and SP Ted Maffei in monitoring the test during execution. This monitoring involved 24-hour coverage, 7 days a week for 38 days.

The authors appreciate the constructive comments and criticisms of Messrs. R. Berg, F. Croxy, E. F. Lobacz and F. Sanger of the USACRREL staff.

QUINN, AAMOT,
GREENBERG

BIBLIOGRAPHY

1. U. S. Army Cold Regions Research and Engineering Laboratory (USACRREL) "Studies of Underground Heat Sink Concept (U)," March 1966, Draft Report.
2. Parson, Brinckenhoff, Hall and MacDonald, "Feasibility Study-Icing of Underground Reservoirs (U)," February 1958.
3. Tien, Chi, "Analysis of a Sub-Ice Heat Sink for Cooling Power Plants," USA Snow, Ice, and Permafrost Research Establishment (SIPRE), Research Report No. 60, July 1960.
4. Dill, R. S. and Peavy, B. A., "Some Observations on the Use of Underground Reservoirs as Heat Sinks," National Bureau of Standards Report 4795, July 1956.
5. Hubbard, Frank R., III, "Tunnel Condenser Concept (U)," Nuclear Power Field Office, Ft. Belvoir, VA, August 1967.
6. (Classified reference)
7. Peavy, B. A. and Dill, R. S., "Heat Absorbing Capacity of an Underground Reservoir Used as a Heat Sink," National Bureau of Standards Progress Report 4740, July 1956.
8. Farrell, P. F., "Raise Boring, Republic Steel Corporation, Old Bed-Harmony Mine, Mineville, New York," Mining Congress Journal, January 1967.
9. Personal communication with Mr. William Blomstran, District Manager, Republic Steel Adirondack Ore Mines, September 1968.
10. Birch, F., "Flow of Heat in the Front Range, Colorado," Bulletin Geological Society of America, 61, p. 567-630, June 1950.
11. Department of the Army Technical Manual, TM 5-855-4, "Heating and Air Conditioning of Underground Installation," August 1965.
12. Carslaw, H. S. and Jaeger, J. C., "Conduction of Heat in Solids," Oxford Clarendon Press, 1959, page 338.
13. Stanley, L. E. and Fellers, G. E., "Temperatures in an Infinite Medium Surrounding a Cylindrical Constant Heat Flux," USACRREL Technical Note, October 1968, Draft.
14. Clarke, S. P., Jr., "Handbook of Physical Constants," The Geological Society of America, Inc., 1966.
15. Cooke, J. B., Libby, S. B., and Madill, J. T., "Kemano Tunnel Operation and Maintenance," The Engineering Journal, Engineering Institute of Canada, August 1962.
16. Quinn, W. F., Aamot, H.W.C., and Greenberg, M., "Field Test of a Steam-Rock Condenser Heat Sink Concept," USACRREL, July 1969. (Draft)

QUINN, AAMOT,
GREENBERG

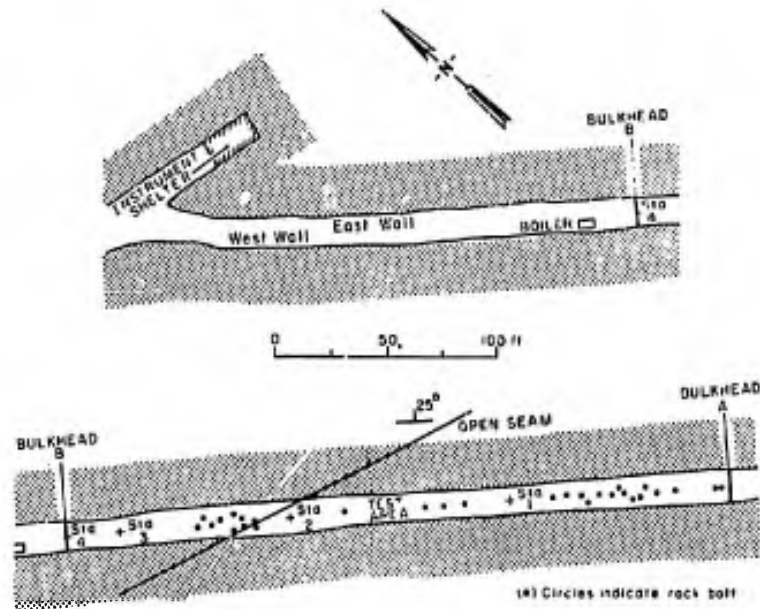


Figure 1. Plan view of tunnel, heat sink test, Mineville, N. Y.

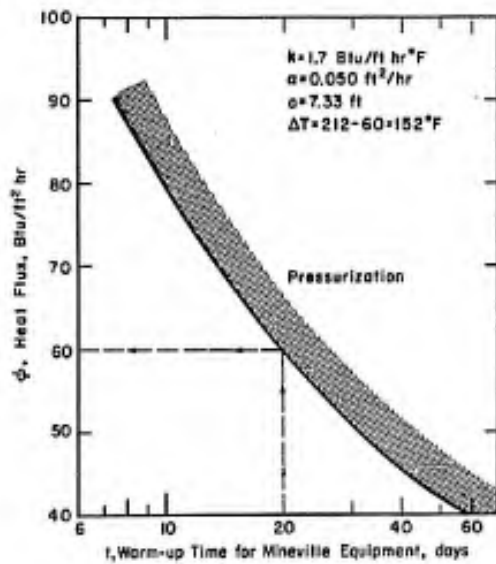


Figure 2. Theoretical relationship between heat flux and warm-up time for Mineville experiment.

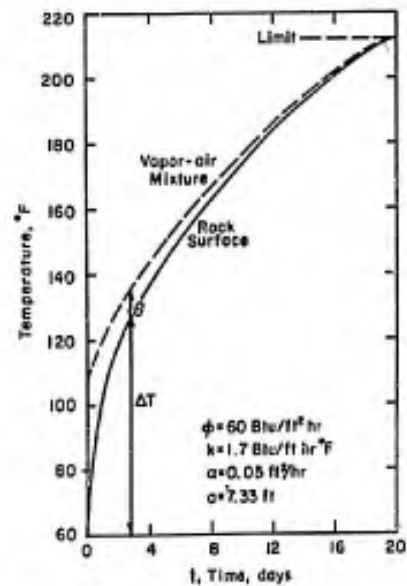


Figure 3. Theoretical vapor-air and rock surface temperatures vs time.

QUINN, AAMOT,
GREENBERG,



Figure 4. Post-test view in vicinity
of Station 1.

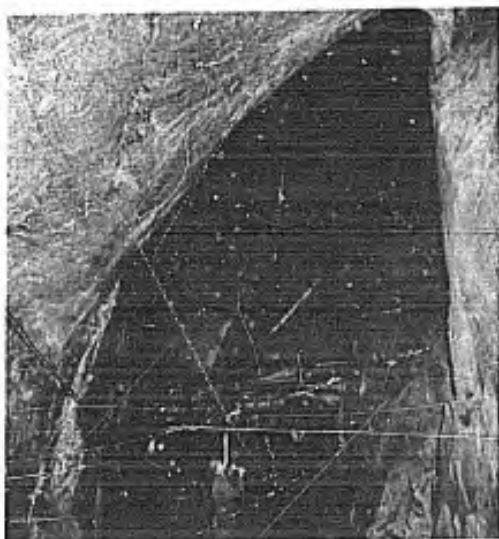


Figure 5. Cathedral-like roof devel-
oped at Station 2.

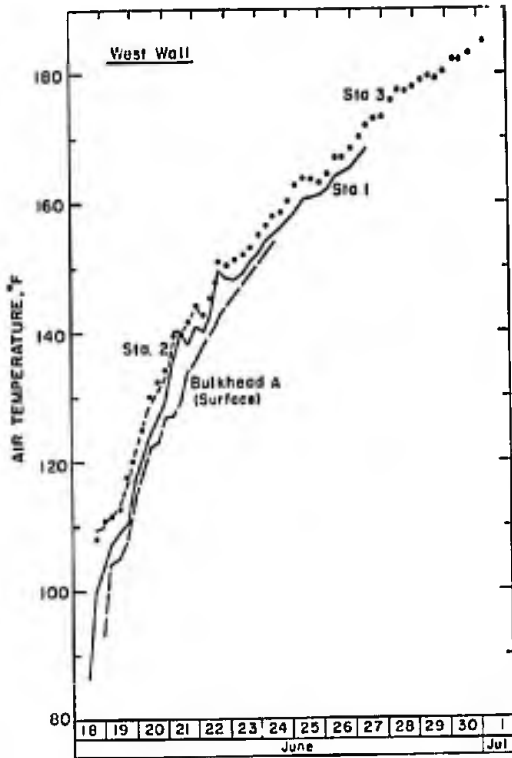


Figure 6. Air temperature vs time for various stations (west wall).

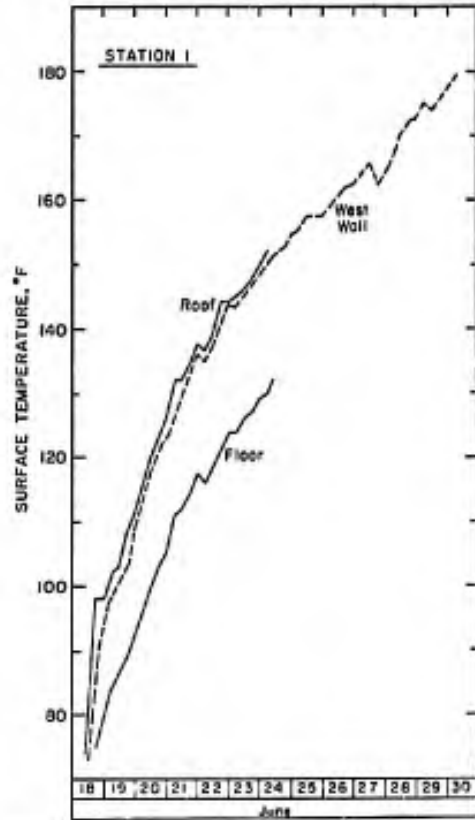


Figure 7. Surface temperature vs time, Station 1.

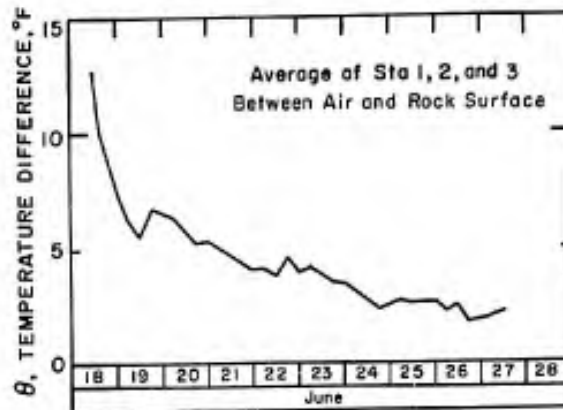


Figure 8. Overall average temperature difference (θ) between air and rock surface.

QUINN, AAMOT,
GRUENBERG

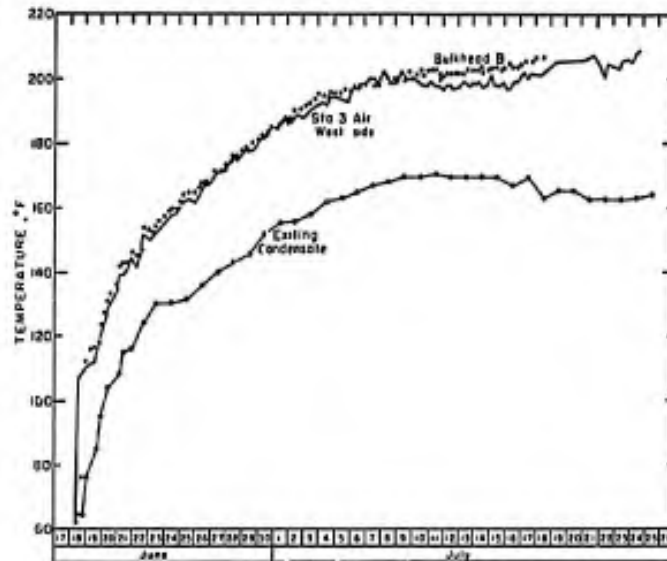


Figure 9. Measured temperature vs time..
(Condensate, Bulkhead B, Station 3 Air).

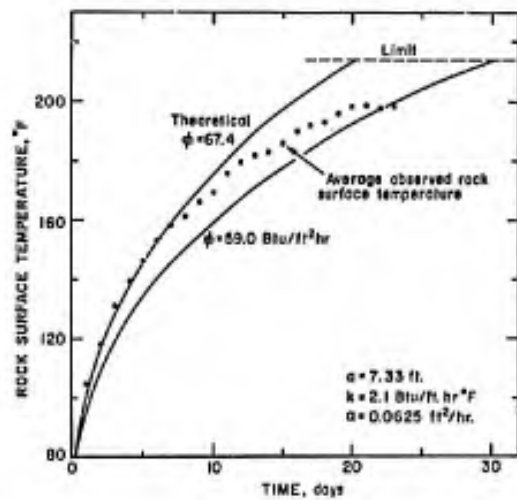


Figure 10. Adjusted theoretical sur-
face temperature - time relationship.

MODERN COUNTER-SURVEILLANCE IN COMBAT CLOTHING

A. O. RAMSLEY
U. S. ARMY NATICK LABORATORIES
NATICK, MASSACHUSETTS

INTRODUCTION

Before World War II, personal camouflage was needed only in daylight, because night-time surveillance was limited to use of the naked eye. Since that time surveillance devices have been developed that enable an enemy to observe military personnel effectively, both by day and night. Both aerial photography and the sniper scope extend vision into the infrared, allowing an observer to take advantage of differences in the reflection properties of terrain and clothing. An image intensifier increases his visual sensitivity at night by many orders of magnitude. Because the present military environment emphasizes the use of small, mobile units, the Combat Development Objectives Guide states that an individual soldier must have maximum freedom from enemy observation, if he is to complete his mission successfully. This paper describes the development of a colorant system for combat clothing that satisfies the reflectance requirements for camouflage protection against detection by all of these modern surveillance devices, as well as by visual observation.

The Problem

These surveillance devices function on the basis of the radiation that is reflected from troops and other objects in the terrain. Figure 1 shows the regions of the spectrum in which each device operates to its best advantage, and illustrates that these devices depend primarily on infrared radiation. The sniper scope makes use of a band of light near 1000 nanometers (nm), while both the image intensifier and infrared photography are most responsive to that portion of the infrared that lies just beyond the visible spectrum (700 to 900 nm).

The reason for counter-surveillance measures is to minimize the probability of detection of individual soldiers to effectively low levels. This requires a low contrast between a uniform

RAMSLEY

and the background against which it is viewed, by whatever detection device may be used. The contrast of an object in a uniformly illuminated field depends largely on the reflectances of the object and the background. To develop an effective camouflage colorant system, one must know the reflection properties of both the uniform and typical terrains. Figure 2 shows the reflectances of typical leaves, both fresh and dry, in the region of the spectrum we are considering. Figure 3 is a comparable set of curves for some soil specimens.

Earlier research has led to colorant systems now in use for camouflage against visual observation and detection by the sniper-scope. It has also been possible to devise relatively simple colorant systems to provide camouflage against visual surveillance and that by either infrared photography or the image intensifier. In the past, however, it had not been possible to develop colorant systems that afford suitable camouflage protection against all four methods of surveillance; visual observation, infrared photography, the image intensifier, and the sniperscope.

The Objective

Our long-range goal is a significant reduction in the probability of detection of our troops by an enemy using visual observation and any of the modern surveillance devices. The objective of this research study is the development of a system for coloring combat clothing and equipment to provide camouflage against surveillance by the four systems cited above.

The Criterion

Figures 2 and 3 show that the reflectances of common components of the terrain are higher in the near infrared than in the visible spectrum. They also show that the reflectance curves for terrains vary from one location to another. To cope with variations in terrain coloration, it has been possible to select compromise colors for visual camouflage. In an analogous manner, it should be possible to define criteria for counter-measures against detection by other devices, that is, levels of reflectance that clothing should have in each spectral region to assure generally low contrast in a variety of terrains.

Based on known physical data and field observations, a criterion has been derived that represents the spectral reflectance of ideal camouflage in terrains that contain substantial vegetation, when viewed by the four surveillance systems used to their best advantage. A uniform that has a reflectance curve between 400 and 1200 nm similar to that shown in Figure 4 can be expected to afford camouflage protection against observation by the four devices we are considering. The lower values of reflectance at the longer wave-

RAMSLEY

lengths pertain to the use of the sniperscope, where illuminating and viewing conditions significantly differ from those of the others.

TECHNICAL APPROACH

The Idealized Curve

The idealized curve of Figure 4 has a higher reflectance at wavelengths between 700 and 900 nm than it does at wavelengths beyond 900 nm. This is the feature of the theoretical curve that is most difficult to duplicate in reality. Dyes known to absorb strongly at 1000 nm have been used to control the reflectance to levels deemed necessary to afford camouflage against sniperscope observation. Such dyes, however, absorb even more strongly between 700 and 900 nm than they do at 1000 nm. Thus, one should not expect to duplicate, by simply reflection processes alone, a reflectance curve that has lower reflectances near 1000 nm than it does at shorter wavelengths.

The idealized curve, itself, provides a clue to the starting point for research. Its shape resembles the apparent reflectance curves obtained for fluorescent surfaces, in that one part of the curve rises to values that are higher than those at the longer wavelengths that usually define a maximum reflectance base line. This led to the proposal that the idealized curve could be duplicated by dyes that had fluorescent emission in the near infrared, if such colorants could be found.

Infrared Fluorescence

When a dye absorbs electromagnetic radiation, the molecule is elevated to an energetic (excited) state that is short-lived. For the molecule to return to its original ground state, the absorbed energy must be dissipated quickly by one or more available paths. For most dyes on fabric, these paths usually involve photo-chemical processes or direct conversion to heat. Fluorescence, however, is observed when the absorbed energy is directly re-emitted as electromagnetic radiation without being diverted into alternative paths.

Early literature references to luminescence in the infrared begin with that of Pauli in 1911,⁽¹⁾ who claimed to be the first to have observed luminescence in the infrared. Dhere and co-workers^(2,3) reported in 1936 that the fluorescence of the living leaf of the geranium extends as far into the infrared as 830 nm. In a survey of about 200,000 mineral specimens, Barnes⁽⁴⁾ reported that nearly 1500, representing about 75 mineral types, exhibited some degree of infrared fluorescence. Prior to the present work, the only example in the literature of an organic textile dye that exhibits infrared fluorescence on fabric was reported by Stearns in 1943.⁽⁵⁾

RAMSLEY

Experimental Approach

It is clear from the foregoing that the first phase of the experimentation was a search for dyes that exhibit fluorescence in the near infrared. Figure 5 shows the absorption and fluorescence spectra of a thiazine dye, Methylene Blue, in methanol. A characteristic of the fluorescence process is that the wavelengths of emitted light are longer than those of the light that was absorbed. For many dyes, the difference in wavelength between the absorption and fluorescence peaks is 50 to 100 nm. In this research we have sought dyes that fluoresce in the near infrared. For a dye to fluoresce near 750 nm, for example, it should absorb light in the red end of the visible spectrum. Such dyes are green or blue, a fact that provided another clue in our search for colorants by which the idealized curve could be reproduced on a textile fabric.

The second phase of our research was to develop a means of incorporating a selected infrared fluorescent dye into a colorant formulation to provide the other characteristics shown in the idealized curve. This combination of colorants was then applied to a fabric in such a manner as to preserve the fluorescence.

The third phase of the study was a preliminary field evaluation of the prototype fabric, using the sniperscope, the image intensifier, and infrared photography.

EXPERIMENTAL RESULTS

Survey of Dyes

To detect fluorescence in the near infrared, in our survey of dyes we used a specially designed photometer.⁽⁶⁾ The specimen is illuminated with a tungsten lamp limited by selected filters⁽⁷⁾ to the visible spectrum. Light emerging from the specimen by reflection and fluorescence is intercepted in front of the photo-detector by a filter that transmits only light in the near infrared. Since the reflected light is limited to the visible spectrum, the only energy that reaches the detector is that produced by fluorescence in the infrared. The spectral response curve for the infrared fluorophotometer rises to a peak at about 830 nm and has a band width of about 130 nm. This is similar to the spectral response curve shown for infrared photography in Figure 1.

In the search for useful colorants, 250 dyes were applied to a variety of fabrics and examined with the infrared fluorophotometer. Of these, 75 displayed some degree of infrared fluorescence, a fact not previously reported in the literature.^(8,9) Table I is a list of those dyes that were found to fluoresce most strongly, while Table II lists those that were moderately fluorescent. The numerical values in the last column show the relative intensity of

RAMSLEY

TABLE I

DYES THAT FLUORESCENCE MOST STRONGLY IN THE INFRARED

<u>C. I. Name</u>	<u>Chemical Type</u>	<u>Fabric Type</u>	<u>Fluorescence Intensity</u>
Basic Blue 4	oxazine	polyacrylic	160
Basic Blue 3	oxazine	polyacrylic	155
Direct Blue 108	oxazine	polyamide	96
Direct Blue 106	oxazine	polyamide	82
Direct Blue 109	oxazine	polyamide	72
Direct Blue 107	oxazine	polyamide	68
Direct Violet 54	oxazine	polyamide	63
Basic Blue 9	thiazine	polyacrylic	62

TABLE II

DYES THAT FLUORESCENCE MODERATELY IN THE INFRARED

<u>C. I. Name</u>	<u>Chemical Type</u>	<u>Fabric Type</u>	<u>Fluorescence Intensity</u>
Basic Violet 4	triarylmethane	polyacrylic	48
Basic Green 3	triarylmethane	polyacrylic	45
Basic Blue 26	triarylmethane	polyacrylic	45
Basic Blue 36	triarylmethane	polyacrylic	42
Direct Blue 1	disazo	cotton	42
Acid Green 16	triarylmethane	polyamide	41
Acid Green 3	triarylmethane	polyamide	40
Direct Blue 25	disazo	cotton	37
Basic Violet 3	triarylmethane	polyacrylic	37
Basic Green 1	triarylmethane	polyacrylic	37
Direct Blue 14	disazo	cotton	36
Direct Blue 109	oxazine	cotton	35
Basic Violet 5	azine	polyacrylic	33
Direct Blue 22	disazo	cotton	32
Basic Blue 7	triarylmethane	polyacrylic	32
Basic Blue 9	thiazine	cotton	32

RAMSLEY

fluorescence as measured by the fluorophotometer.

From the dyes listed in Table I, Basic Blue 4 was selected for further consideration and applied to a variety of fabric types. It was found that the fluorescence for this dye was most intense when applied to acrylic fibers, less so on polyamide, and absent on cotton. Because the dye molecules can interact with certain fibers in a manner that quenches fluorescence, it is important to choose a fabric substrate that will allow the return of the excited state molecule to the ground state by fluorescence.

Application to Fabric

Figure 6 shows the spectral curve for combined fluorescence and reflectance for Basic Blue 4 applied to an acrylic fabric when illuminated with a xenon arc used as a simulated daylight source. This figure also shows the curve for a dyed specimen in which Basic Blue 4 was included in a formulation to produce an olive green shade.

Although the curve for the olive green shade does not match the idealized curve in the infrared, the important feature to note is that the reflectance is higher in the intermediate region than it is at the longer wavelengths. As pointed out earlier, this is the most difficult feature of the idealized curve to reproduce. The task that remained was to find a means of lowering the entire infrared portion of the curve to proper levels, while still preserving the effect of fluorescence in the region between 700 and 900 nm.

When dyes that were known to absorb at longer wavelengths were added directly to the formulation, fluorescence was quenched. Light emitted by fluorescence was simply re-absorbed by neighboring molecules of the absorbing colorant before it could emerge from the surface of the fabric.

A technique of blending two fibers was also attempted. One lot of acrylic fibers was dyed with the fluorescent formulation. The other lot (cotton) was dyed with a vat dye that absorbed strongly throughout the near infrared to about 1200 nm. When these lots were thoroughly blended to form a uniformly colored surface, the expected fluorescence was almost entirely lost, presumably for the reason described above. The conclusion from both of these attempts was that fluorescent portions of the fabric must be separated from absorbing areas sufficiently to allow the fluorescent emission to emerge from the fabric surface before it is re-absorbed by other colorants.

The problem of quenching was eventually overcome by devising a 2-component grid pattern.⁽¹⁰⁾ A fabric was made by weaving two black rayon yarns alternately with four undyed acrylic yarns in

RAMSLEY

both the warp and filling directions. This produced a checkered fabric in which the undyed areas were about 1/8 inch square, as shown in Figure 7. The rayon contained carbon black, a colorant that strongly absorbs all wavelengths of light we are considering. As woven, the fabric consists of two distinct areas, one having high reflectance, the other low. The fabric was then dyed with the fluorescent dye formulation illustrated in Figure 6 to produce an over-all olive green shade.

Figure 8 shows the reflectance curve for an area of the fabric, both before and after dyeing. The effect of the black yarns was to lower the level of reflectance of the fabric before dyeing to about 30 per cent. If non-fluorescent dyes had been used, the resulting reflectance curve would have been lower than the upper curve at all wavelengths. By fluorescence, however, it was possible to lift the reflectance curve above that of the undyed fabric within a narrow range of wavelengths. By separating the fluorescent areas from the non-fluorescent areas sufficiently, each area is able to act independently of the other without quenching the fluorescence.

Evaluation

When the dyed fabric is viewed at distances beyond 15 feet, the checkered pattern blends into a uniform shade that is indistinguishable from olive green. To estimate the effectiveness of the general technique, observations were made with the devices we have been discussing. The experimental fabric was displayed as a panel about six feet long and four feet high, with a similar panel of a standard fabric. Both panels were erected at the northern edge of an open field with a background of brush, tall weeds, and trees.

Photographs of the panels were made at noon on a sunny day in September, using Polaroid infrared film and a Wratten 87 filter that excluded all visible light. The spectral response of the film under these conditions is that shown for infrared photography in Figure 1. The close-up view in Figure 9 shows the local setting for the panels. Figure 10 is a view of the panels in the same setting photographed at a range of about 30 meters.

Both photographs demonstrate that the standard fabric appears conspicuously dark against a background one often encounters in a field situation. The experimental fabric shows that the use of infrared fluorescence with the 2-component grid pattern technique permits a control of reflectance to levels that decrease the contrast of a fabric when viewed by infrared photography against typical field backgrounds.

Night-time observations were also made with an image intensifier. These showed that, for this surveillance device too, the contrast was much lower for the experimental fabric than for the comparison fabric, which appeared conspicuously dark. Spectrophoto-

RAMSLEY

metric measurements show that the reflectance of the experimental fabric near 1000 nm is close to 25 per cent, a value that affords camouflage protection against observation with the sniperscope.

CONCLUSIONS

To reduce the effectiveness of modern surveillance systems, it is necessary that the reflectance of fabrics for combat clothing follow an idealized spectral reflectance curve that covers the visible spectrum and the infrared to about 1200 nm. This curve rises from low values in the visible spectrum to a maximum in the region between 700 and 900 nm and falls to somewhat lower values beyond 900 nm. The shape of this curve is such that it can be duplicated only by using colorants that are fluorescent in the near infrared. As part of this research, a survey of dyes disclosed for the first time that about 75 dyes were fluorescent in the infrared.

An infrared fluorescent dye alone was not able to confer the reflectance properties needed for camouflage against the variety of surveillance devices we are considering. In fact, fluorescence was quenched, when other dyes were added to bring experimental reflectance curves into conformity with the idealized curve. It was, therefore, necessary to separate physically the fluorescent dyes from colorants needed to lower the general level of reflectance in the infrared.

To avoid quenching of fluorescence and at the same time lower the infrared reflectance, a special technique was devised for using these dyes. A checkered fabric was designed in which part of the fabric consisted of strongly absorbing yarns and part consisted of yarns that were later dyed with infrared fluorescent dyes. In this manner, the two components of the over-all coloring system were able to perform their necessary functions independently and without interference, with the result that a reflectance curve was obtained that had the camouflage characteristics described by the idealized curve.

Field observations with infrared photography and an image intensifier confirmed the camouflage value of the newly developed colorant formulation, because the experimental fabric was far less conspicuous in a typical terrain than currently used fabrics. Thus, a single coloring system for clothing can afford camouflage protection against visual observation and detection by infrared photography, the sniperscope, and the image intensifier, when that coloring system is based on dyes that are fluorescent in the near infrared.

RAMSLEY

REFERENCES

1. Pauli, W. E., *Ann. Phys.*, 34, 739 (1911).
2. Dhere, C., and Raffy, A., *Compt. Rend.*, 200, 1146 (1935).
3. Dhere, C., and Biermacher, O., *Compt. Rend.*, 203, 412 (1936).
4. Barnes, D. F., *Infrared Luminescence of Minerals*, Geol. Survey Bul. 1052-C, U. S. Printing Office, Washington, 1958.
5. Stearns, E. I., *J. Opt. Soc. Amer.*, 33, 27 (1943).
6. Ramsley, A. O., U. S. Patent 3,422,266, January 14, 1967.
7. Ramsley, A. O., *J. Opt. Soc. Amer.*, 57, 111 (1967).
8. Ramsley, A. O., *Color Engineering*, 5, 20 (1967).
9. Ramsley, A. O., *Amer. Dyestuff Repr.*, 57, 611 (1968).
10. Ramsley, A. O., and Walwood, J. T., Patent pending.

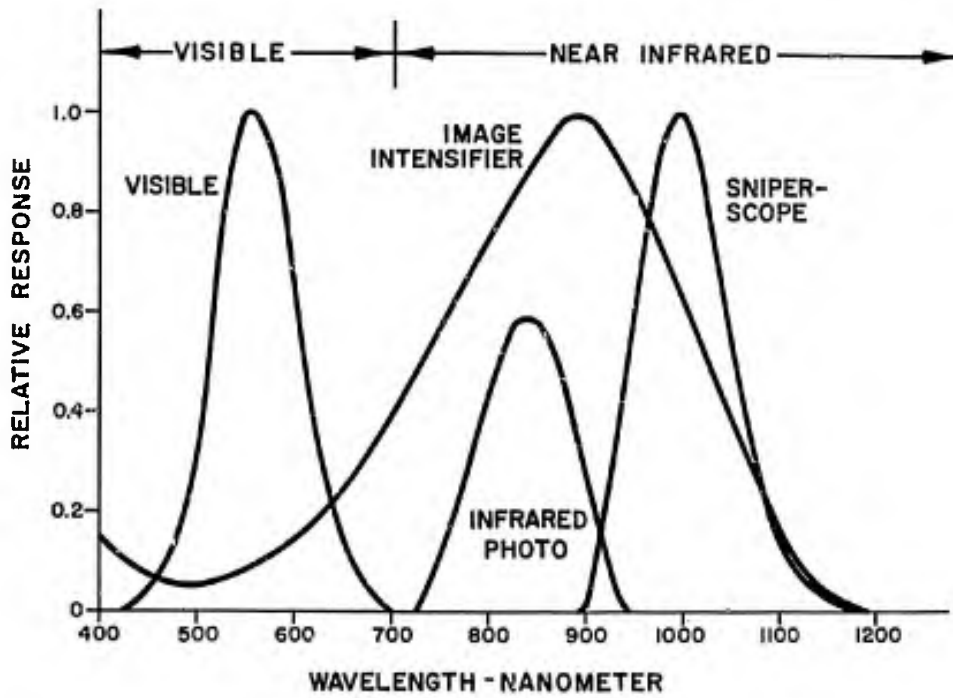


Fig.1: Response as a function of wavelength for human vision, an image intensifier, infrared photography, and the sniper scope.

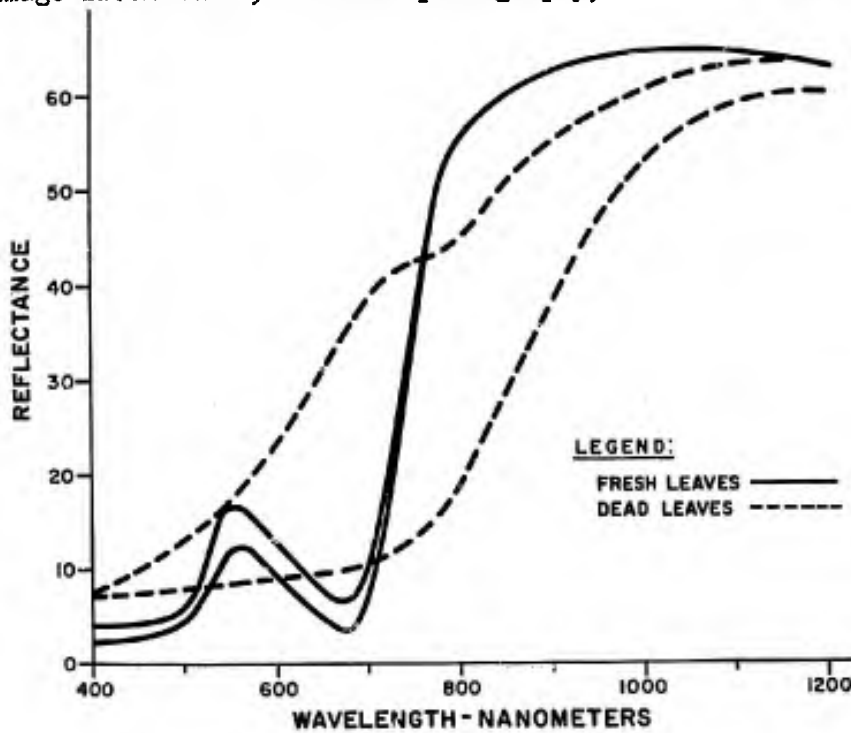


Fig. 2: Range of spectral reflectance for typical fresh leaves (—————) and dry leaves (- - - - -).

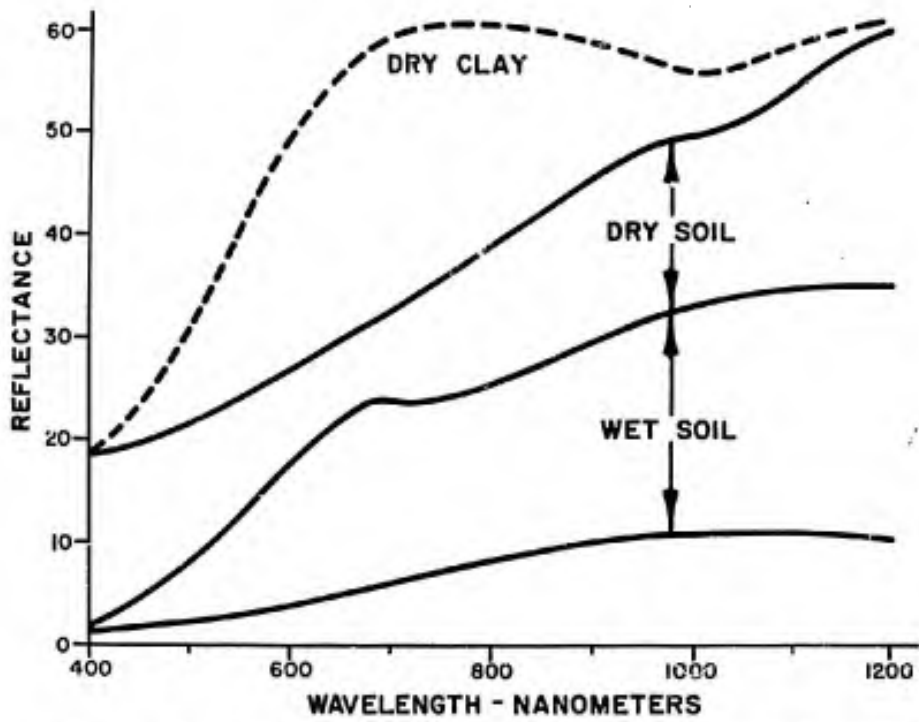


Fig. 3: Spectral reflectance curves for typical wet and dry soils.

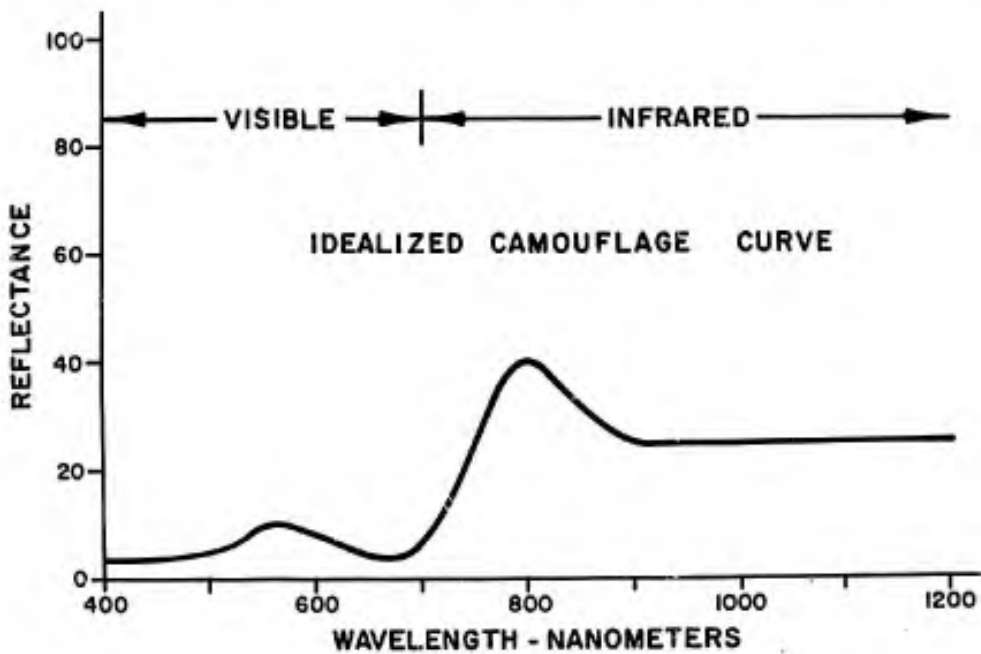


Fig. 4: Idealized spectral reflectance curve for camouflage in typical vegetated terrains.

RAMSLEY

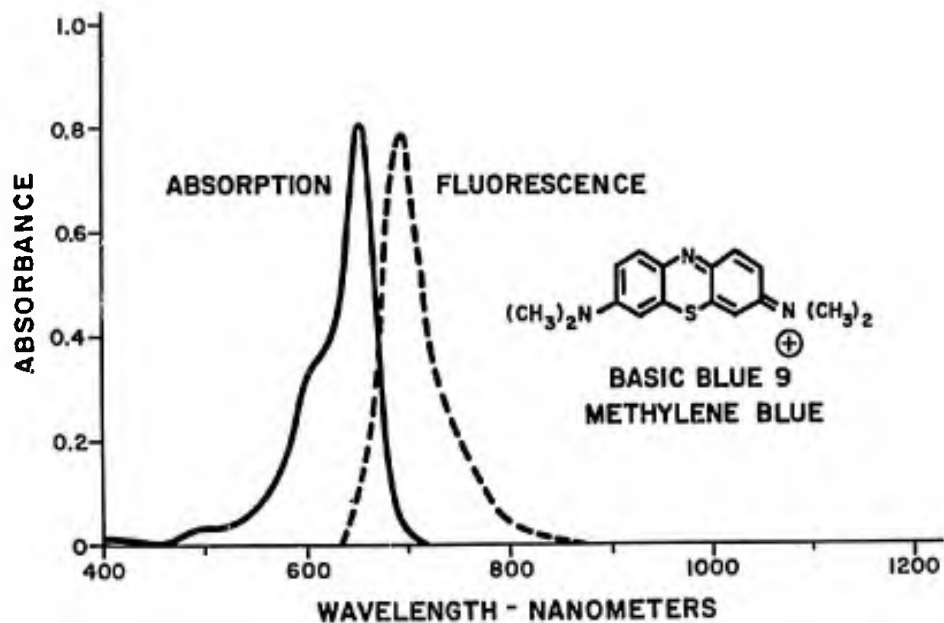


Fig. 5: Absorption and fluorescence spectra of Basic Blue 9 (Methylene Blue) in methanol.

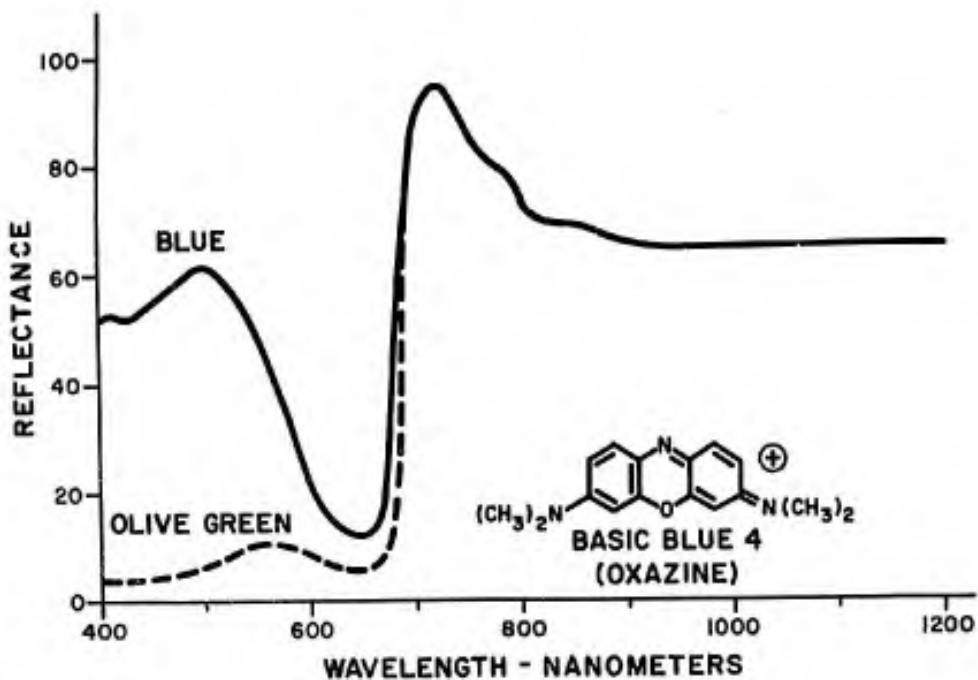


Fig. 6: Combined reflectance and fluorescence curve for an acrylic fabric dyed using Basic Blue 4 alone and in a dye formulation to produce an olive green shade.

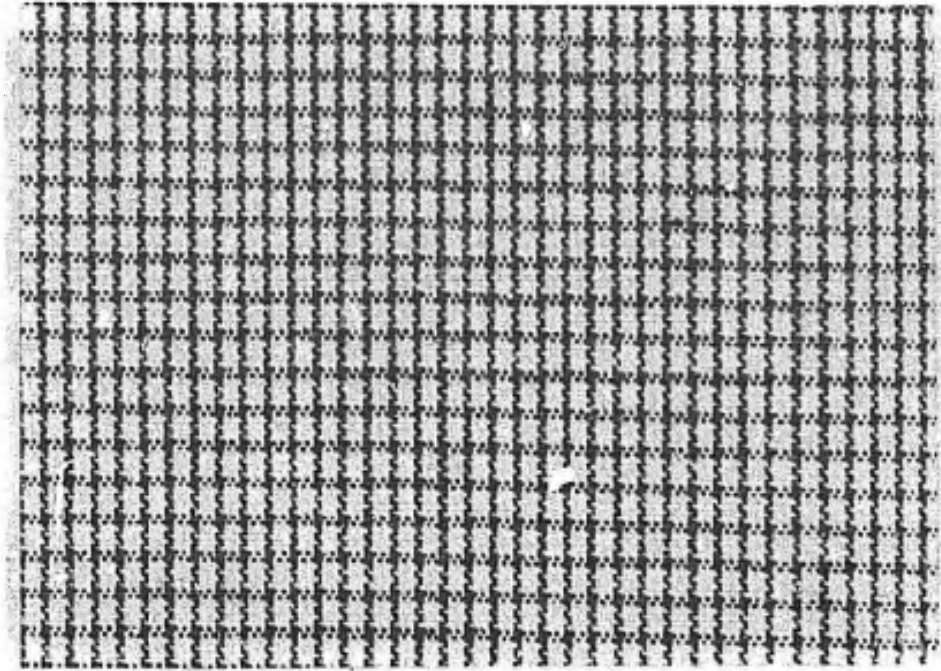


Fig. 7: Fabric made by alternating black rayon yarns and undyed acrylic yarns in both warp and filling directions.

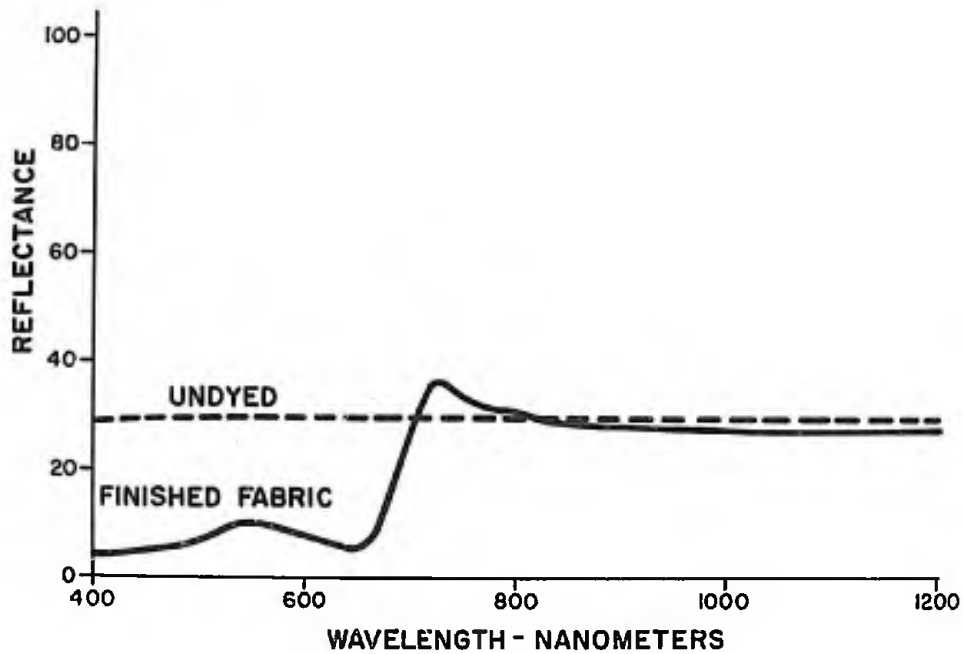


Fig. 8: Reflectance curves of the 2-component grid fabric before and after dyeing with infrared dyes to an olive green shade.

RAMSLEY

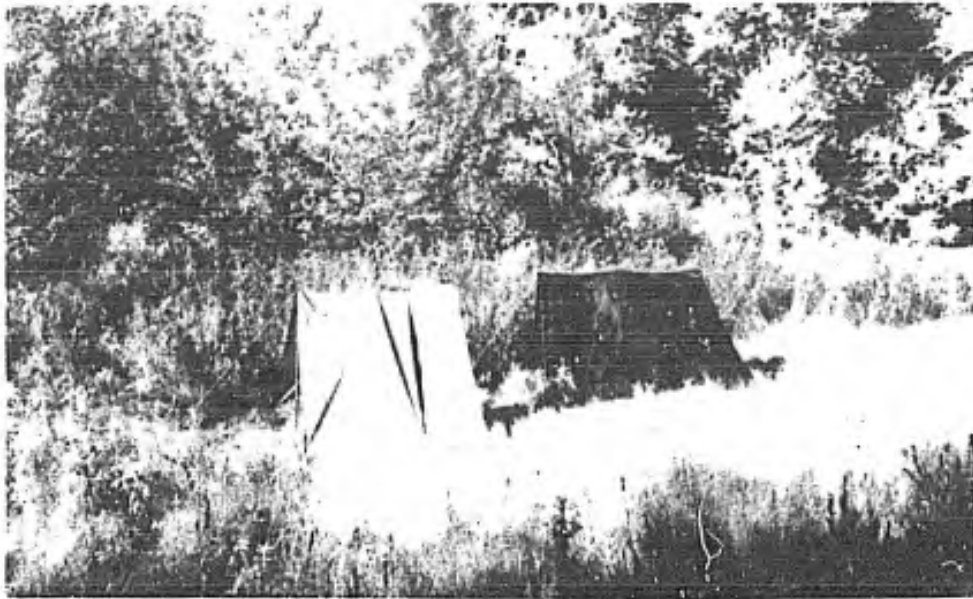


Fig. 9: Close-up infrared photograph of panels made with the experimental fabric on the left and a standard fabric on the right.



Fig. 10: Infrared photographs of panels at 30 meters with the experimental fabric on the left and a standard fabric on the right.

A CONCEPT OF ROW CRATER ENHANCEMENT

BRUCE B. REDPATH
U. S. ARMY ENGINEER NUCLEAR CRATERING GROUP
LIVERMORE, CALIFORNIA

INTRODUCTION. Linear craters formed by the simultaneous detonation of a row of buried explosives will probably have a wider application than single charges in the explosive excavation of engineering structures such as canals, channels and harbors. Most cratering experience to date has been with single charges, and an analytical procedure for the design of a row of charges to excavate a crater with a specified configuration has been lacking. There are no digital computer codes having direct application to a row of charges as there are for single charges⁽¹⁾. This paper derives a simple relationship which can be used to design row charges with some assurance of achieving the desired result and with considerable flexibility in the choice of explosive yield of the individual charges.

BACKGROUND. A characteristic of row craters is that their width (W_a) and depth (D_{ar}) are generally larger than the diameter ($2R_a$) and depth (D_a) of a single crater excavated by a charge equal in yield to one of the charges in the row. This characteristic is called enhancement, and the size of a row crater can be expressed in terms of enhanced single crater dimensions. Because enhancement increases as the charge spacing is decreased, the size of a row crater can be altered by changing the layout of the charges rather than their yield. This concept found particular application in the design of detonation programs for the Interoceanic Canal Studies (IOCS) where, in response to potentially severe ground shock hazards, the total yield of a number of critical detonations was reduced by employing relatively closely spaced charges⁽²⁾.

It became apparent in developing the nuclear excavation technology for the IOCS that the results of existing row crater experiments were too inconsistent for direct quantitative application to the design of detonation programs. Fig. 1, which illustrates the scatter in existing data, shows the dimensions of several of these row craters as a function of charge spacing and relative to single

REDPATH

crater dimensions. It was primarily in response to the need of the IOCS program that an attempt was made to arrive at a quantitative rule relating enhancement and spacing.

The successful development of a relationship between enhancement and spacing would mean that a row charge design could be based on single crater dimensions, and these dimensions can be acquired either from calibration shots or from the computational techniques currently in use at institutions such as the Lawrence Radiation Laboratory in Livermore, California.

This paper presents results of a row crater experiment designed to test a concept of the dependence of enhancement on charge spacing.

CONCEPT. The following assumptions were made in deriving a plausible connection between row crater size and charge spacing:

- (1) A decrease in the spacing of the explosives in a row is equivalent to increasing the apparent yield of each explosive.
- (2) The cross sectional geometry of a row crater is a hyperbola, is not dependent on charge spacing over the range of interest (spacing = $0.5 R_a$ to $1.2 R_a$), and is the same as optimum (largest) single crater in the same medium.
- (3) The volume of apparent crater excavated by each charge in a row is independent of charge spacing and is greater, by some factor 'k', than the volume of the largest crater excavated by a single charge of the same yield.

The second assumption implies that the width and depth of a row crater will be enhanced equally at any given spacing, and that the depth of burst (DOB) of the charges should be the optimum single charge depth increased by the amount of enhancement. The assumption of a hyperbolic cross section is, in fact, an experimental observation.

The third assumption can be stated:

$$A_r e^2 S = k V_s$$

where A_r = cross section area of optimum single crater or unenhanced row crater

e = enhancement

S = charge spacing

k = volume excavated by a charge in a row relative to a single charge of the same yield

REDPATH

V_s = volume of optimum single charge crater

so that:
$$e = \left[\frac{k V_s}{A_s S} \right]^{1/2}$$

i.e. the enhancement of row crater dimensions is inversely proportional to the square root of the charge spacing.

Fig. 2 is a schematic cross section of a crater illustrating the elements of hyperbolic geometry. The area A_r and the volume V_s are easily evaluated for any crater.

The equation above can also be written:

$$e = \left[\frac{k V_s}{A_r R_a (S/R_a)} \right]^{1/2}$$

and it is interesting to note that the quantity:

$$\frac{V_s}{A_r R_a}$$

varies only over the range of 1.05 to 1.15 for an extremely wide range of crater geometries, and has a value of approximately 1.1 for almost all existing craters. As a consequence, the enhancement equation can be simplified to:

$$e = \left[\frac{1.1 k}{(S/R_a)} \right]^{1/2}$$

It is evident that the volume factor k is now the most important unknown.

The volume factor k , which can be thought of as the efficiency of a row charge relative to a single charge, has been determined in a number of experiments and some of these values are listed in Table I.

It is believed that the large variations in the value of k have been caused by the lack of a consistent design procedure and less than optimum placement of charges in some experiments. The next section discusses further work on the experimental determination of k .

TABLE I
Volume Efficiency of Row Charges

Experiment	Medium	$k = \frac{\text{Volume per row charge}}{\text{Single crater volume}}$
Pre-GONDOLA II (3)	Shale	0.82 (entire crater)
Pre-GONDOLA III Phase II (4) (S=0.6 R _a)	Shale	0.78
Pre-GONDOLA III Phase II (S=1.0 R _a)	Shale	1.05
Pre-BUGGY II (C) (5)	Alluvium	1.12
Pre-BUGGY II (D)	Alluvium	1.18
DUGOUT (6)	Basalt	1.70*

} linear section of crater

EXPERIMENT. The enhancement concept described above was the basis for a series of row cratering experiments using 1-ton charges of nitromethane. The objectives were to verify the inverse square root relation between enhancement and charge spacing and to determine the relative efficiency of row charges. The experiment was conducted as part of Phase III of Project Pre-GONDOLA III in October 1969 by the U. S. Army Engineer Nuclear Cratering Group in a shale medium adjacent to the Fort Peck Reservoir in Montana.

The single crater dimensions shown in Fig. 3 had been obtained previously by detonating 1-ton charges in an adjacent area (7). The following parameters are applicable to the optimum 1-ton single crater:

$$R_a = 27 \text{ ft}$$

$$D_a = 13 \text{ ft}$$

$$\theta = 33^\circ$$

The value of k was judged to be approximately 1.1 on the basis of information available from previous experiments (Table I). The value of $[V_s / (A_r R_a)]$ is 1.1 so that the equation for enhancement was assumed to be:

$$e = \left[\frac{1.21}{S/R_a} \right]^{1/2}$$

* The value of k = 1.70 for DUGOUT is suspect because more than 40 additional tons of the explosive (nitromethane) were poured into the charge cavities to replace leakage which occurred during filling operations.

REDPATH

A total of six row charges with five combinations of DOB and spacing and one duplication were detonated. Table II summarizes the shot layouts. An additional objective of this series was to test several schemes for smoothly connecting one row crater to another, however, this aspect of the experiment will not be discussed here. Also, in some rows the placement of the end charges differed from the remainder of the row.

A topographic map of the row craters is shown in Fig. 4. It should be noted that the center rows (A1 and B1) were detonated and surveyed before the other rows. When the rows at the ends of the center craters were fired they deposited some material in the center craters.

The crater dimensions were averaged over the linear section* of each crater and are shown in Fig. 5 together with the 1-ton single crater dimensions. Despite the scatter, it is evident that the row crater dimensions plot along lines which pass through zero and the peaks of the single charge curves. This indicates that the cross sections of the rows are very similar to that of the optimum single charge crater, i.e., the cross section geometry is being scaled up as if the yield had been increased.

The dimensions are shown in Fig. 6 in the format of enhancement vs. charge spacing. A curve which varies as the inverse square root of the charge spacing has been drawn through the data points in Fig. 6. The widths show less scatter about this curve than the depths, and the two rows with a spacing of $0.85 R_a$ demonstrate the scatter inherent in the data. The predicted enhancement is also shown in Fig. 6 and it is evident that the craters were larger than anticipated. There are two primary factors which may account for this. First, there is no single charge 1-ton crater immediately adjacent to the rows; previous experience in this region has demonstrated that the surface layer and its effect on crater dimensions are variable. Consequently, the size of the single crater to which the enhancements are referenced may be incorrect. An increase of 10% in the reference crater dimensions would shift the observed values of enhancement onto the predicted curve. Second, it is very probable that the factor k , assumed to be 1.1, is actually higher. If the size of the reference crater were correct, then the observed row crater dimensions indicate that k is approximately 1.3.

Crater volume excavated per ton of explosive is plotted against charge spacing in Fig. 7 together with a volume computed for

*The linear section of a row crater is generally the portion bounded by points midway between the two charges at each end. In some of the rows the position of the end charges was varied for other reasons. Dimensions were measured only over the portion of the rows where the charge layout was uniform.

TABLE II
Pre-GONDOLA III Phase III Row Charges

Row	Charge Spacing S/R_a Absolute	Depth of Burst Scaled Absolute	Number of Charges	Predicted Enhancement	Predicted Dimensions $Wa/2$	Predicted Dimensions Dar
A1	1.0	143 λ	6	1.10	29.7 ft	14.3 ft
A2	0.85	155	7	1.20	32.4	15.6
A3	1.15	133	5	1.03	27.8	13.4
B1	0.7	170	7	1.32	35.6	17.2
B2	0.85	155	6	1.20	32.4	15.6
B3	0.55	192	9	1.49	40.4	19.4

$$\left[\lambda = ft/kt^{1/3.4} \right]$$

REDPATH

the reference crater on the basis of its geometry. The row craters averaged approximately 17,000 cu. ft. per ton of explosive compared with about 13,000 cu. ft. for the optimum one-ton single crater. The assumption that the volume excavated by each charge is not dependent on charge spacing appears to be valid.

The row charge detonations were photographed with high speed motion picture cameras and mound surface velocities were obtained from analysis of the films. The peak mound surface velocities are plotted as a function of scaled depth of burst in Fig. 8 together with maximum single charge mound surface velocities observed in previous Pre-GONDOLA experiments. Although the row charge velocities appear to be more dependent on depth of burst than the single charge mound surface velocities, they are approximately the same as the single charge velocities. It is interesting to note that row crater dimensions increased as the peak mound surface velocity decreased, and that the largest of the six row craters had depth of burst and a peak mound surface velocity [~ 80 ft/sec] which would be characteristic of a retard or mound in the case of a single charge in the same material. Previously, craters have not been produced in either shale or dry hard rock when peak mound surface velocities were observed to be less than about 100 ft/sec.

It will be noted that more charges were used in the rows with the closer charge spacings. This was done to insure that the craters would have a reasonable ratio of length to width and not be elliptical in plan.

APPLICATION. In order to illustrate application of the concept, assume that we wish to excavate a 15 ft. deep channel in rock and that 1-ton charges are desirable from a construction and economic standpoint. What is the appropriate charge spacing and DOB assuming that the optimum single crater has the following properties:

$$\begin{aligned}r_a &= 150 \text{ ft/kt}^{1/3.4} \\d_a &= 90 \text{ ft/kt}^{1/3.4} \\ \text{optimum dob} &= 140 \text{ ft/kt}^{1/3.4} \\ \theta &= 37^\circ\end{aligned}$$

and assuming, for the present, that $k = 1.2$.

The required scaled crater depth is

$$\frac{15}{.001^{1/3.4}} = 114 \text{ ft/kt}^{1/3.4}$$

so that the necessary enhancement of single crater depth is

$$e = \frac{114}{90} = 1.27$$

REDFATH

the appropriate charge spacing will be given by

$$\frac{S}{R_a} = \frac{1.1 k}{e^2}$$

$$= 0.82, \text{ say } 0.8,$$

therefore,

$$S = 0.8 R_a$$

$$= 0.8 \times 150 \times .001^{1/3.4}$$

$$= 15.7 \text{ ft, say } 16 \text{ ft.}$$

and the DOB will be

$$= 140 \times 1.27 \times .001^{1/3.4}$$

$$= 23.3 \text{ ft, say } 23 \text{ ft.}$$

It is interesting to note that if enhancement were not used, then each charge would require a yield of

$$\left[\frac{15 \text{ ft.}}{90 \text{ ft/kt}^{1/3.4}} \right]^{3.4} = 2.3 \text{ tons}$$

in order to excavate the same channel.

CONCLUSIONS. It appears that the concept relating enhancement and charge spacing is essentially correct. The experiment based on this concept indicates that enhancement does vary inversely as the square root of the charge spacing, provided that the depth of burst is increased correspondingly. The volume of material excavated by a charge in a row does not appear to vary with the spacing of the charges. The efficiency of a row charge in excavating shale appears to be about 30 percent greater than a series of single charges. The relative efficiencies of row charges and single charges in other media should be determined empirically.

The observation that mound surface velocity decreased with increasing crater size, and the association of the largest row crater with a velocity characteristic of a single charge retarder or mound, would suggest that peak mound surface velocity should be used cautiously as a row charge design tool.

A departure from a row charge design consisting of charges spaced one radius apart and buried at optimum DOB for a single charge has been, in the past, an uncertain procedure. It is believed that there is now a flexible and reliable basis for row charge design.

This concept has already found application to the feasibility studies of an interoceanic canal, however, it is anticipated

REDPATH

that it will find the widest application to excavation projects with chemical explosives where emplacement costs can be reduced by employing smaller charges.

REFERENCES

1. Terhune, R. W., Stubbs, T. F., Cherry, J. T., "Nuclear Cratering on a Digital Computer". Proceedings of the ANS Topical Meeting, Engineering with Nuclear Explosives, Las Vegas, Nevada, January 14-16, 1970.
2. Toman, John, "Summary of Nuclear Excavation Applications". Proceedings of the ANS Topical Meeting, Engineering with Nuclear Explosives, Las Vegas, Nevada, January 14-16, 1970.
3. Day, Walter, et.al., "Technical Director's Summary Report - Project Pre-GONDOLA II", PNE-1112, U. S. Army Engineer Nuclear Cratering Group, Lawrence Radiation Laboratory, Livermore, California (in press)
4. Lattery, J., et.al., "Summary Report - Project Pre-GONDOLA III Phase II", PNE-1117, U. S. Army Engineer Nuclear Cratering Group, Lawrence Radiation Laboratory, Livermore, California (in press)
5. Spruill, J. L. and Videon, F. F., "Studies of the Pre-BUGGY II Apparent Craters", PNE-315F, U. S. Army Engineer Nuclear Cratering Group, Lawrence Radiation Laboratory, Livermore, California, June 1965
6. Nordyke, M. D., "Technical Directors Summary Report - Project DUGOUT", PNE-600F, Lawrence Radiation Laboratory, Livermore, California, May 1965.
7. Cress, J. P., et.al., "Summary Report - Project Pre-GONDOLA III Phase I", PNE1114, U. S. Army Engineer Nuclear Cratering Group, Lawrence Radiation Laboratory, Livermore, California, (in press).

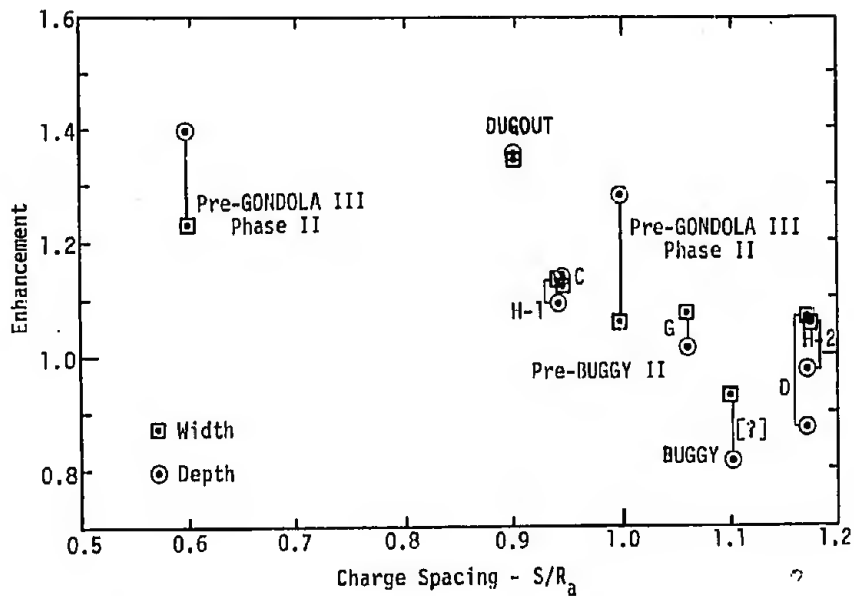


Fig.1 Enhancement of row crater dimensions as a function of charge spacing

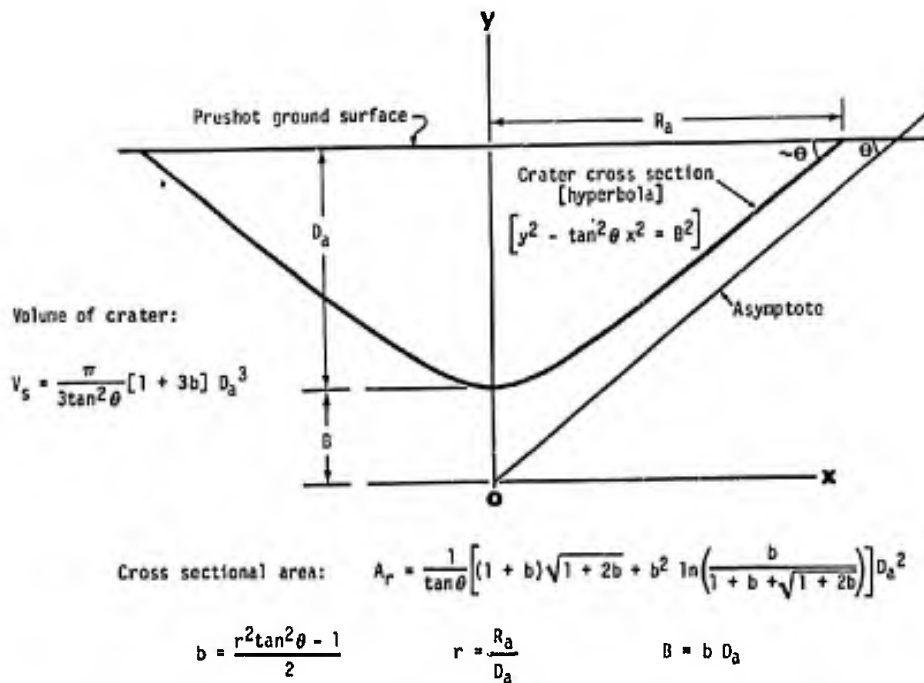


Fig.2 Schematic cross section of a crater illustrating hyperbolic geometry

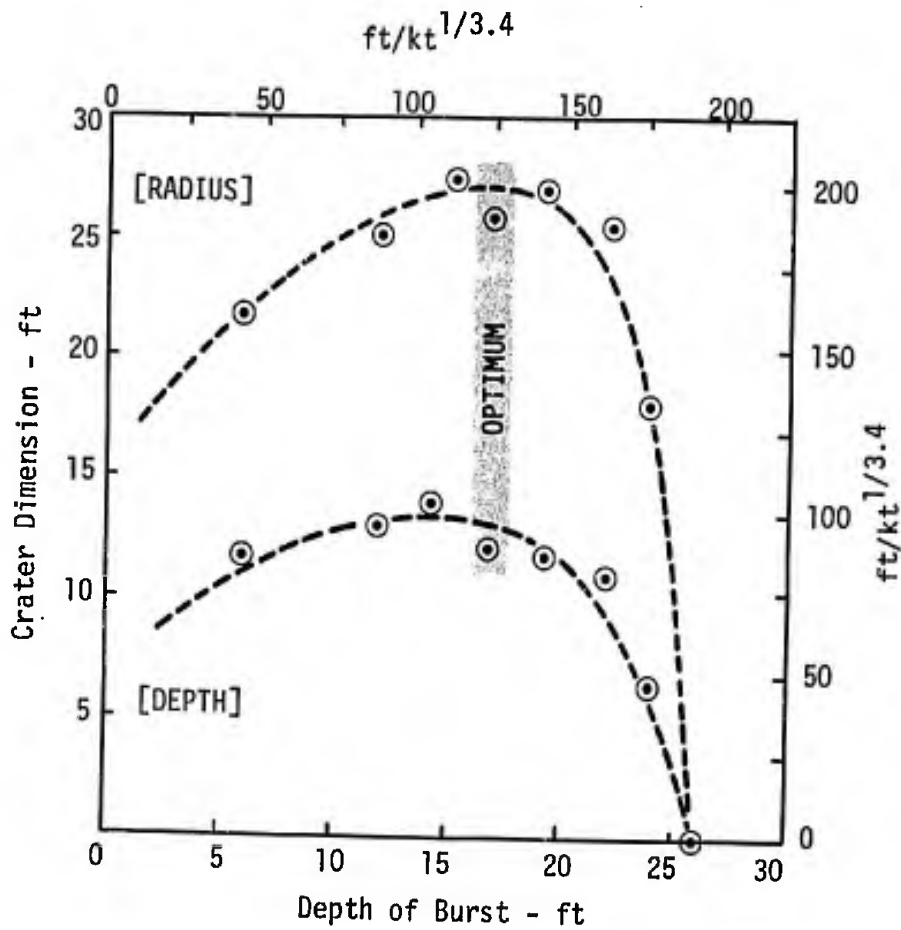


Fig.3 Crater dimensions vs depth of burst for 1-ton charges in shale.

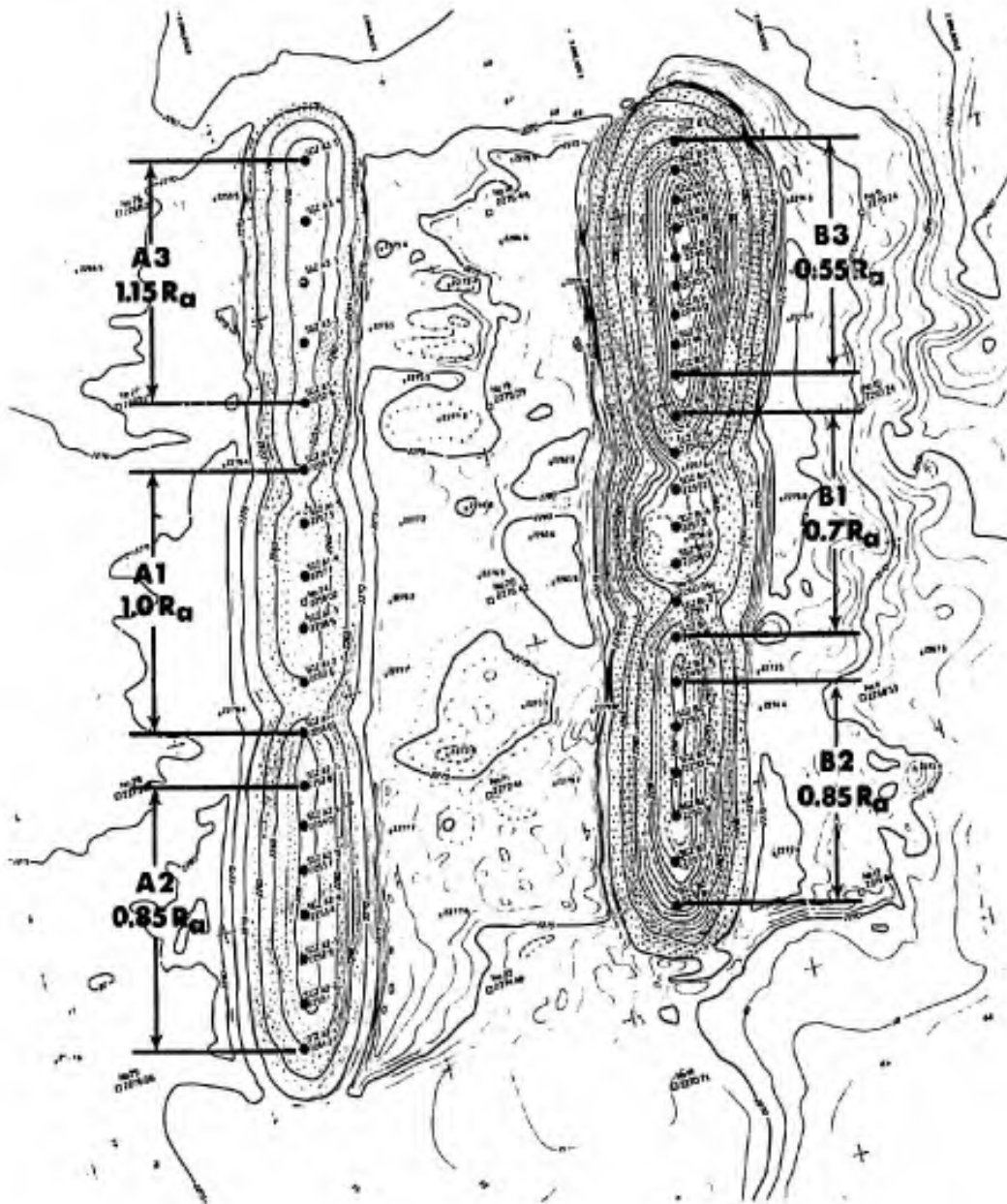


Fig.4 Topographic map of the Pre-GONDOLA III Phase III row crater experiment.

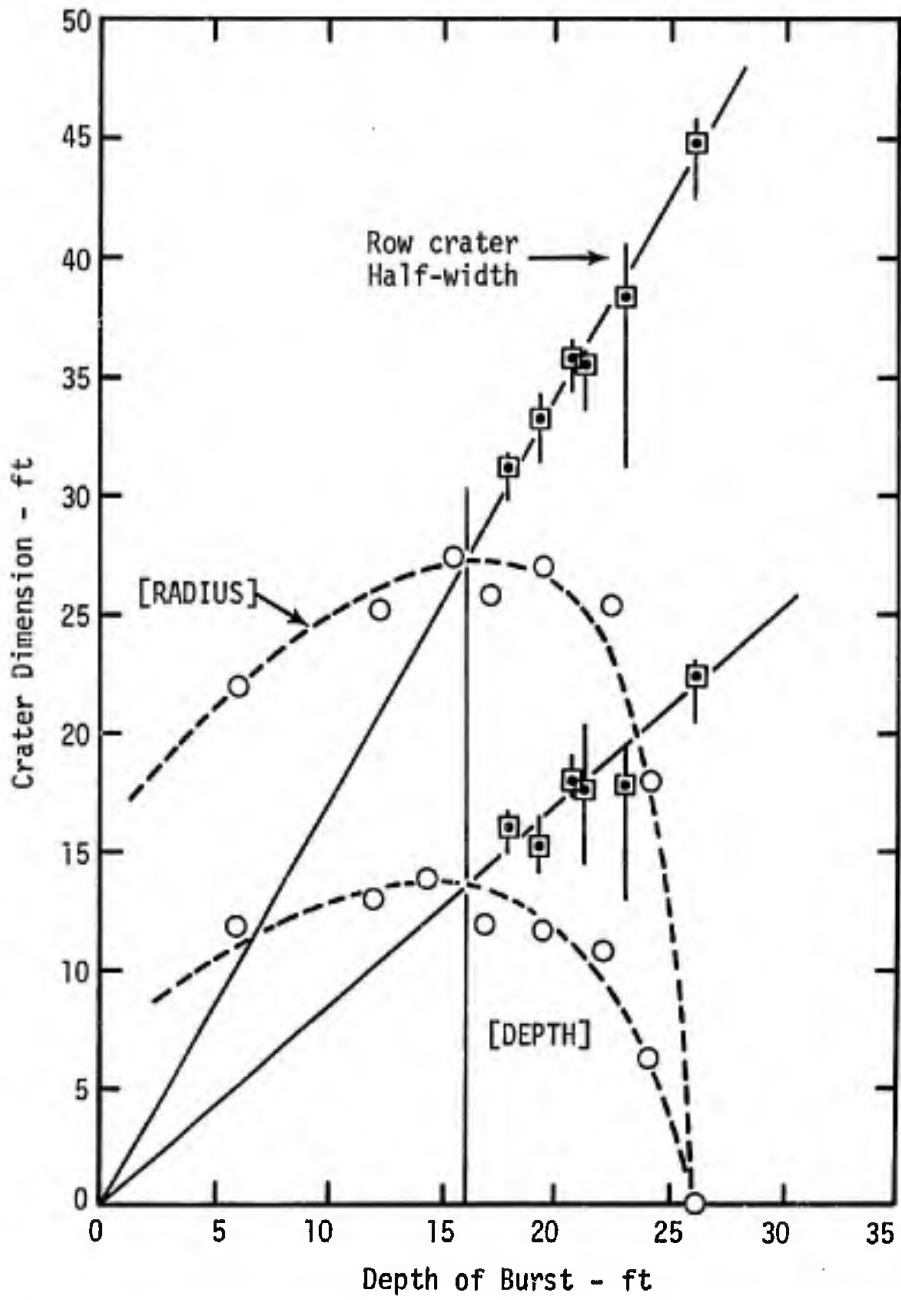


Fig.5 Dimensions of single and row craters vs depth of burst.

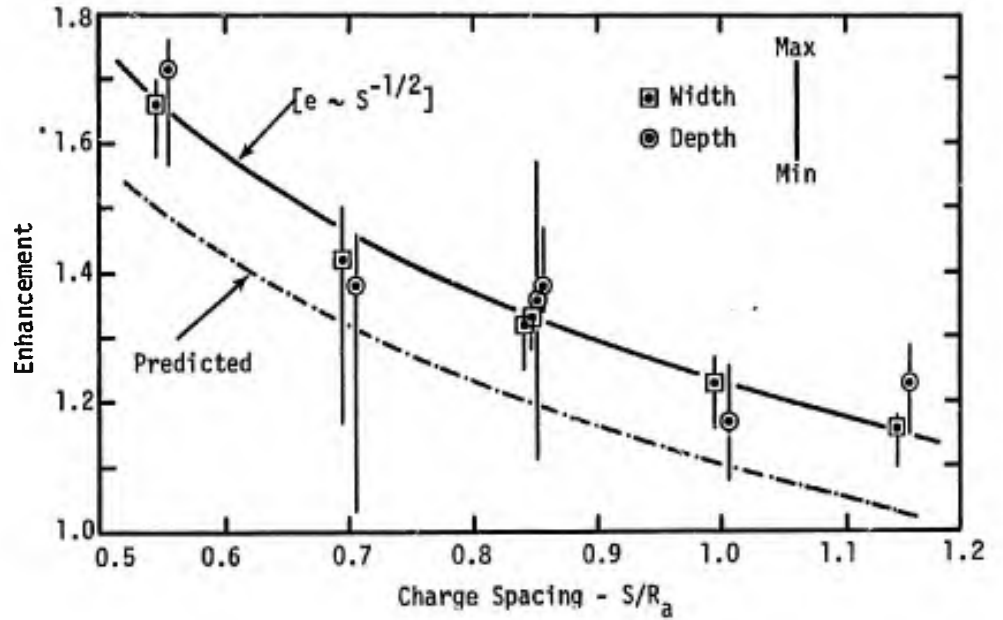


Fig.6 Enhancement of Pre-GONDOLA III Phase III row crater dimensions as a function of charge spacing.

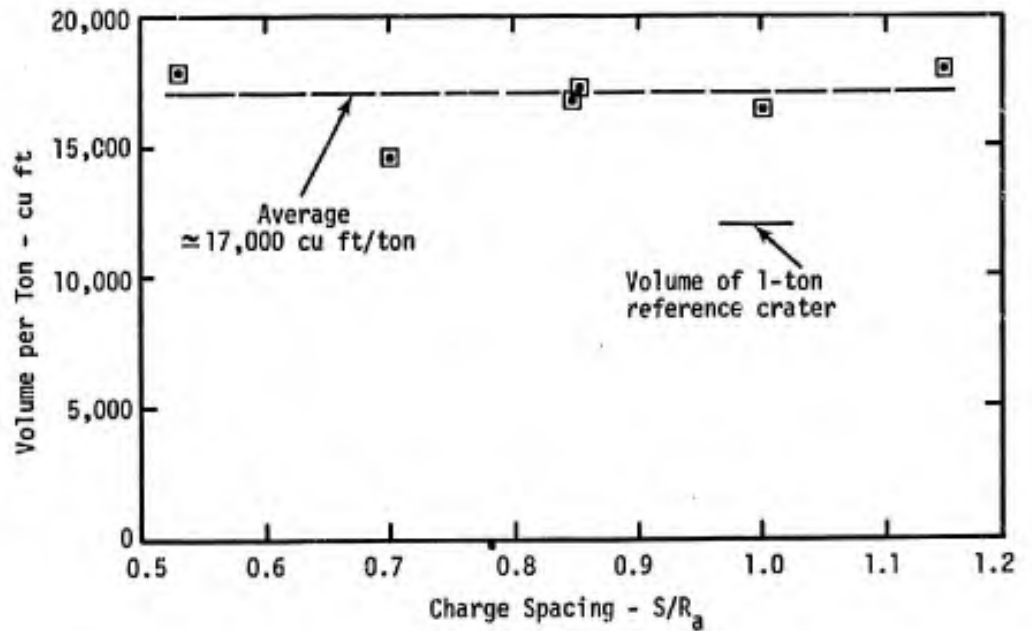


Fig.7 Volume of apparent crater per ton of explosive as a function of charge spacing.

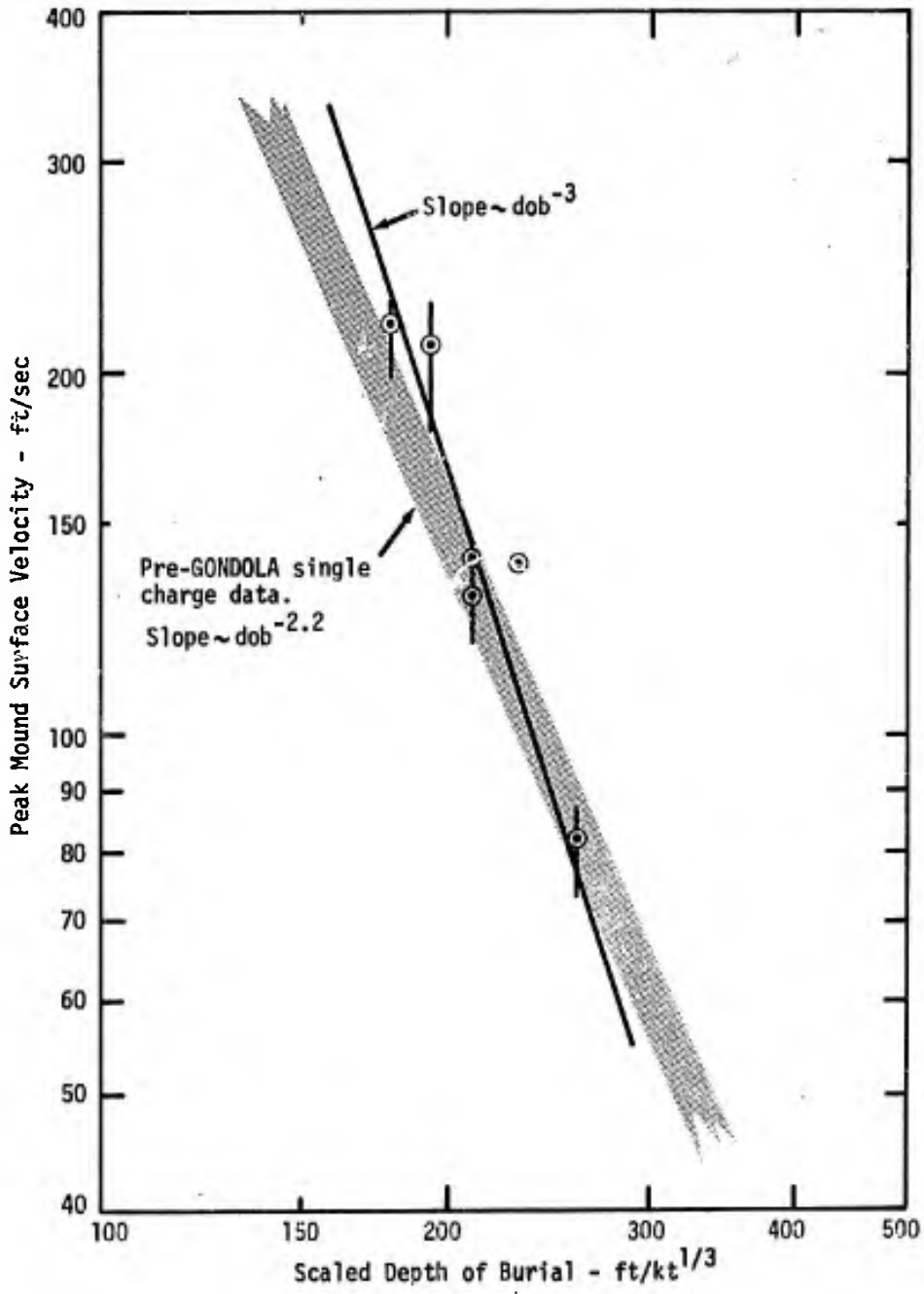


Fig.8 Variation of maximum surface velocity with depth of burst

THE DETERMINATION OF ALUMINUM AND
CHLORINE IN COMPOSITE PROPELLANTS
BY NON-DESTRUCTIVE ACTIVATION ANALYSIS
USING A MIXTURE OF 14.5 MEV AND SLOW NEUTRONS

A. E. RICHARDSON and ALEX HARRISON*
BIOLOGICAL-CHEMICAL-METALLURGICAL BRANCH
WHITE SANDS MISSILE RANGE, NEW MEXICO

X-ray fluorescence methods have been developed for the nondestructive analysis of composite propellants by Alley and Higgins (1, 2). It was believed, however, that by means of neutron activation a method of analysis might be developed which would not be as sensitive to matrix effects and particle size. The primary purpose of the neutron activation analysis would be for quality control of composite propellants with a composition of approximately 70% ammonium perchlorate, 15% aluminum, and 15% binder plus minor additives. The determination of aluminum and chlorine will give a complete analysis of the composite propellant. The ammonium perchlorate percentage can be obtained directly by multiplying the chlorine percentage by the appropriate stoichiometric factor. The polymer percentage can then be obtained by subtracting the sum of aluminum and ammonium perchlorate from one hundred.

Several nuclear reactions were studied, but the $^{27}\text{Al}(n,p)^{27}\text{Mg}$ reaction with 14.5 MeV neutrons and the $^{37}\text{Cl}(n,\gamma)^{38}\text{Cl}$ reaction with slow neutrons gave the best results. It was found possible to produce a useful mixture of 14.5 MeV and slow neutrons, so that both aluminum and chlorine could be determined simultaneously from a single irradiation. It was necessary to make a Compton correction for ^{24}Na produced from $^{27}\text{Al}(n,\alpha)$ by 14.5-MeV neutrons in order to obtain reproducible results for ^{38}Cl . The method was developed and evaluated by comparing a series of batches of known composition with a given batch whose composition was also known.

As this work was being completed, Rison and co-workers reported the application of activation analysis to the determination of nitrogen in propellants and explosives (3) and to the determination of phosphorus in composite propellants (4). Portions of the material presented herein were published in Analytical Chemistry (5).

EXPERIMENTAL

Sample Preparation. All but one of the samples were prepared from cylindrical slugs from the Propulsion Laboratory, U. S. Army Missile Command, Redstone Arsenal, Alabama. These cured propellant slugs contained ammonium perchlorate, aluminum, binder, and other minor additives such as iron(III) oxide. One sample from the propellant storage facilities at White Sands Missile Range contained only ammonium perchlorate, aluminum, and binder. The samples were prepared for irradiation by pushing, without rotating, a sharpened cork-borer through the cylindrical slugs. The inside diameter of the cork-borer was chosen to be exactly the same as that of an 8-ml polyethylene container in which the sample was to be placed. The plug of propellant was pushed carefully into the polyethylene container and any protruding material was carefully shaved off. The prepared sample exactly filled the container and ranged in weight from 12.2692 to 13.0536 grams.

Irradiation. The source of neutrons was a Texas-Nuclear Model 9505 150 kV neutron generator which had a maximum output of approximately 10^{11} n/sec and gave a 14.5-MeV flux of as high as 10^9 n/cm²-sec at 3 cm from the target. Samples irradiated inside a 30-cm cubic polyethylene box with a 15-cm cubic cavity and 7.5-cm wall thickness were about 10 cm from the target and were subjected to fluxes upwards of 10^8 n/cm²-sec for 14.5-MeV neutrons and 10^7 n/cm²-sec for slow neutrons. A sulfur disk monitor was used to estimate the 14.5-MeV flux at 3 cm.

Forty-five irradiations were performed, 35 with 14.5-MeV neutrons and 10 with mixtures of 14.5-MeV and slow neutrons. A simple rotation procedure was used to make sure that standards and unknowns were subjected to the same doses of neutrons during irradiation. Three samples were taped together and forced over a spindle which was rotated at a rate of approximately 20 rpm during irradiations. The method of positioning the samples on the rotation device in front of the neutron generator is shown in Figure 1. Care was taken to see that all three rotating samples swept out the same circular region. For irradiations with only 14.5-MeV neutrons, samples were rotated at a position about 3 cm from the tritium target in line with the deuteron beam. For irradiations using the mixture of 14.5-MeV and slow neutrons, samples were rotated inside the polyethylene box.

Counting. After irradiation, the samples were manually removed from the target position and placed upright on a 3 X 3 inch NAI(Tl) crystal which was covered by a beta shield. Counts, taken for 1 or 4 min live time for ²⁷Mg and 10 min for ³⁸Cl, were accumulated on a TMC 400-channel analyzer. The counts under the photopeak were integrated manually and corrected for decay, and the 3 samples irradiated simultaneously were compared with each other.

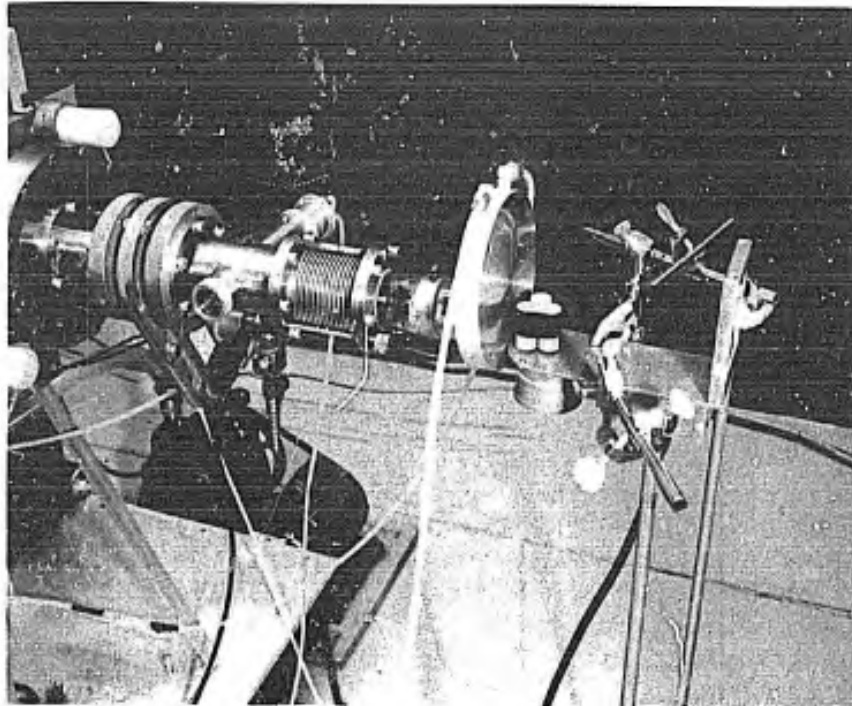


Fig. 1 Arrangement of Propellant Samples Next to the Target of the Neutron Generator

For the decay corrections, the mean time for a count was taken as the linear average of the starting and ending times. It was observed that anomalously low counting results, off by as much as several per cent, were obtained when the fractional dead time was higher than about 30% and the counting duration was longer than 20% of the half-life. This error was minimized by keeping the fractional dead time below 30%.

For the decay corrections to irradiation end, the mean time for the count was determined by using the linear average of the starting and ending times for the count. Assuming a fixed fractional dead time, it can be shown (6) that for a counting duration of 20% of the half-life the error resulting from such linear averaging of time is only 0.08% on the high side and for 40% of the half-life, only 0.32% on the high side. When comparing a standard and an unknown, an error will arise only when the standard and an unknown, respectively, are counted for different fractions of a half-life.

RICHARDSON and HARRISON*

Only when counting rates are very high and there is a fast drop off in the fractional dead time from one sample to the next will there be a significant difference in the half-life fractions. If there is a fast drop off in fractional dead time during a given count, and thus from one sample to the next, the above listed error values will not hold anyway.

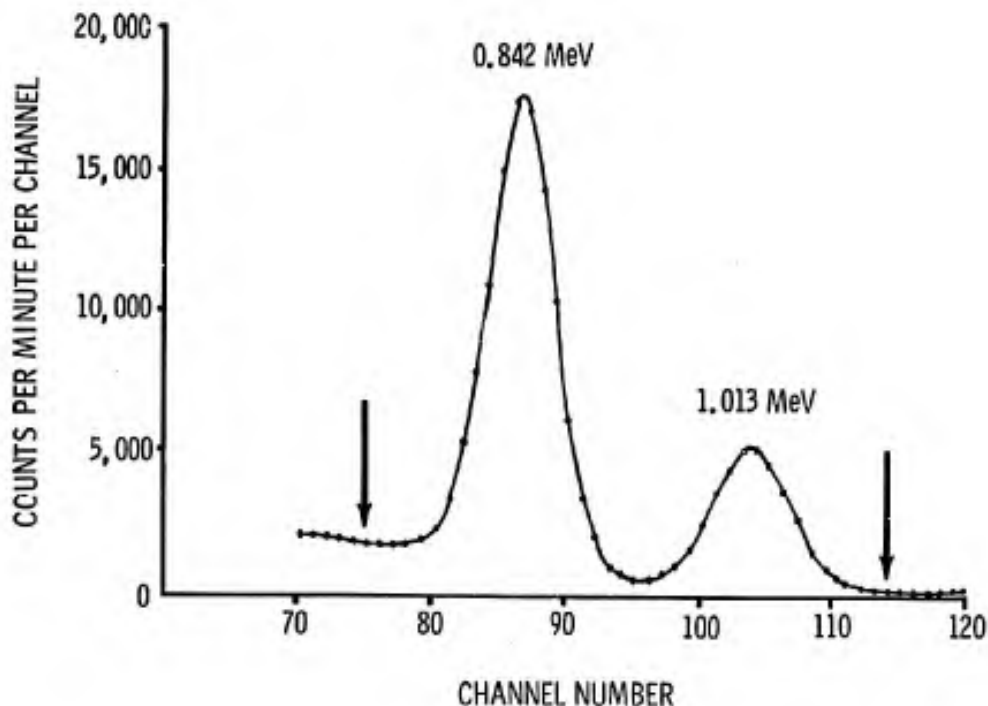


Fig. 2 Typical Gamma Scintillation Spectrum of ^{27}Mg for Composite Propellant (Increment per channel is slightly larger than 0.01 MeV.)

Determination of Aluminum by $^{27}\text{Al}(n,p)^{27}\text{Mg}$ Reaction. Magnesium-27 has a half-life of 9.5 min and emits gammas of 0.842- and 1.013-MeV energies. The integrated counts for each sample were obtained by summing the counts for channels in the range of about 75 through 114 and subtracting $(40/3)$ times the total number of counts in the next three channels. For the above range, the two magnesium peaks were at channels 86 and 104, respectively. (Figure 2 shows a typical gamma scintillation spectrum of ^{27}Mg .) Slight variations from these calibrations produced no noticeable effect on the results, and the subtraction gave an adequate correction for Compton tails from higher energy gammas. A possible

RICHARDSON and HARRISON*

interference was from the 0.847-MeV peak of 2.58 hr ^{56}Mn produced from $^{56}\text{Fe}(n,p)$. However, because of the small percentages of iron in the samples used, the effect did not become noticeable until about 30 min after irradiation end by which time all counting of ^{27}Mg was completed.

When only 14.5-MeV neutrons were used, counting was started about 2 min after irradiation end and counts were taken for 1 min live time. When the mixture of neutrons was used, counting was begun after 6 min and counts were for 4 min live time. Zero-time activities ranged downward from about 6×10^5 cpm for 5-min irradiations at the 3-cm target position, but were never greater than about 1×10^5 cpm for samples irradiated for 20 min in the polyethylene box.

Determination of Chlorine by the $^{37}\text{Cl}(n,\gamma)^{38}\text{Cl}$ Reaction. Chlorine-38 has a half-life of 37.3 min and emits gamma rays of 1.60- and 2.17-MeV energies. The main interference was caused by the Compton tail and escape peaks of the 2.75-MeV gammas from ^{24}Na produced by 14.5-MeV neutrons from $^{27}\text{Al}(n,\alpha)$. It was found possible to correct for ^{24}Na by spectrum stripping technique. The ^{24}Na spectrum between about 1.20 and 3.00 MeV is shown in Figure 3.

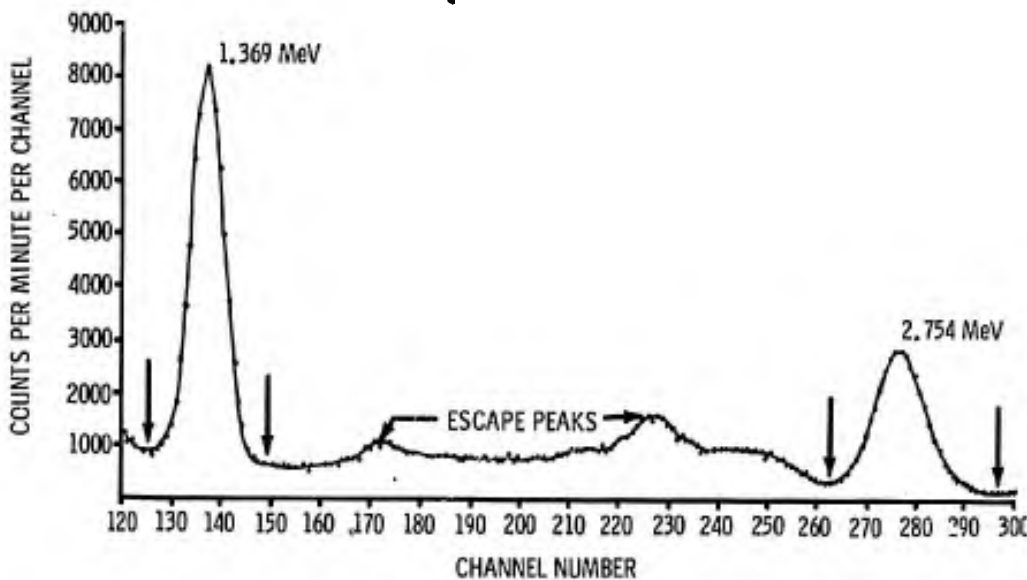


Fig. 3 Typical Gamma Scintillation Spectrum of ^{24}Na for Composite Propellant (Increment per channel is very nearly 0.01 MeV per channel.)

RICHARDSON and HARRISON*

Once the ^{24}Na spectrum was known, it was possible to calculate the ^{24}Na activity under the 1.60 MeV ^{38}Cl peak by multiplying the counting rate observed under the 2.75-MeV peak by the appropriate factor. The ^{24}Na activity under the 1.60 MeV ^{38}Cl peak could then be subtracted from the total activity to obtain the activity due to ^{38}Cl as shown in Figure 4.

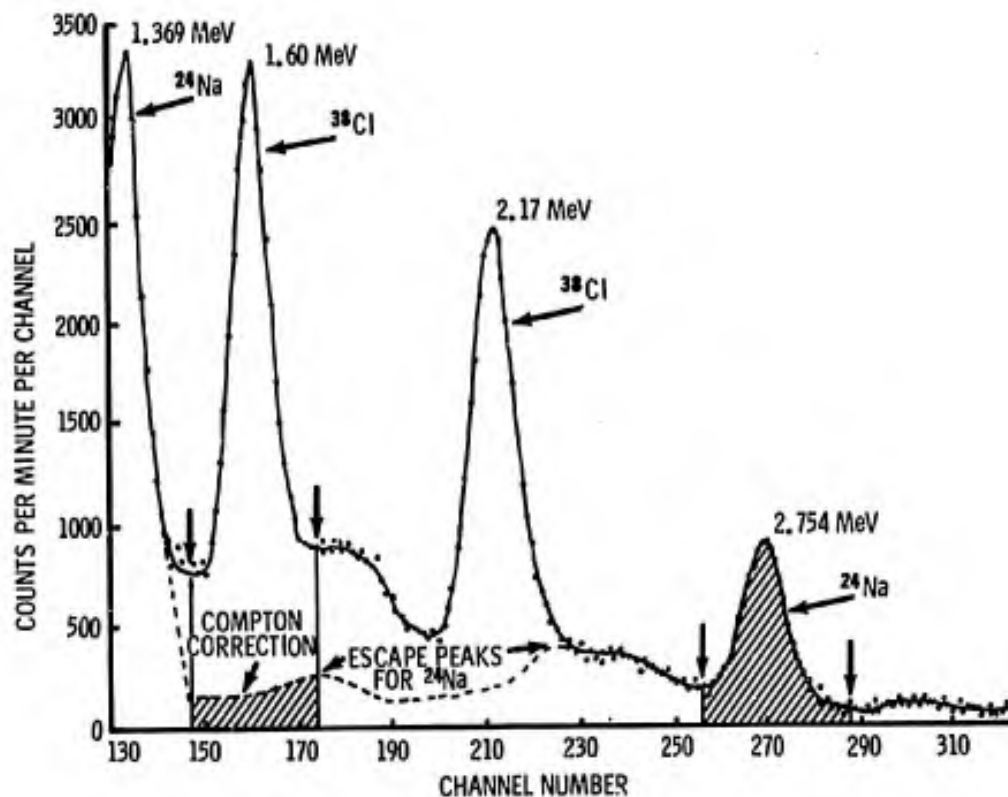


Fig. 4 Typical Gamma Scintillation Spectrum of ^{38}Cl and ^{24}Na for Composite Propellant (Increment per channel is slightly less than 0.01 MeV per channel. The spectrum was taken at 29.6 minutes after the end of a 15-minute irradiation with a mixture of 14.5 MeV and slow neutrons.)

Irradiations were of 10, 15, or 20 minute duration. It was necessary to wait about 25 min after irradiation end to allow the 1.78-MeV gamma of the 2.3 min ^{28}Al to decay out before counting. Zero-time activities for the 1.60-MeV peak ranged downward from a high of about 7×10^4 counts per 10 min for a generator target initially depleted to about one fourth of its maximum tritium content. With a fresh target it was possible to obtain about 300,000 counts per 10 minutes for the 1.60 MeV peak.

RESULTS AND DISCUSSION

As was mentioned earlier, the 12- to 13-gram samples used in these studies were prepared from slugs from Redstone Arsenal, Alabama. The slugs of cured propellant were prepared from larger batches of uncured propellant mix. Each batch weighed about 1 kilogram, and each slug, about 100 grams. The batches had a variety of compositions designed for a multiple regression analysis of X-ray fluorescence data (2). Relative percentages of each of the components varied over ranges of about 15% in the batches. The listed compositions (2) represented the weights of constituents used in preparing each of the respective batches. These will be referred to as nominal percentages in the remainder of the paper.

For the development of the activation analysis method, Batch 6 was made the reference standard to which all others were compared. The results are given as percentages in a particular batch relative to percentages in Batch 6. For data analysis, the absence of variations in composition among different samples of the same batch has been assumed. For most of the batches, two or three different samples were used.

Table I. Determination of Aluminum in
Propellant with ^{27}Mg from the $^{27}\text{Al}(n,p)^{27}\text{Mg}$
Nuclear Reaction Using 14.5 MeV Neutrons Alone

Batches Compared (Batch X/Batch 6)	Relative Percentage of Aluminum	Average of Relative Percentages of Aluminum
1/6	0.9682, 0.9795, 0.9849 ^a 0.9806 ^a , 0.9743 ^a , 0.9758 ^a	0.9772
2/6	0.8781, 0.8702	0.8741
3/6	1.0442, 1.0452, 1.0316	1.0403
4/6	0.9319, 0.9265, 0.9290	0.9291
5/6	1.0256 ^a , 1.0246 ^a , 1.0325, 1.0303, 1.0331, 1.0358, 1.0186, 1.0179	1.0273
7/6	0.9974, 1.0017	0.9996
8/6	0.8643, 0.8553, 0.8628, 0.8594	0.8605
10/6	0.9997, 0.9956, 0.9928, 0.9903	0.9946
11/6	0.9824, 0.9773	0.9799
12/6	0.9200, 0.9137, 0.9230	0.9189

*These values were computed through an intermediate ratio with respect to sample P2A.

RICHARDSON and HARRISON*

The results of the replicate analyses for aluminum and chlorine by activation analysis are listed in Tables I and II, respectively. The estimated relative standard deviation, s , for the 37 values for aluminum in Table I is only 5.5×10^{-3} , just slightly larger than the approximate relative standard deviation for counting statistics, which is about 4×10^{-3} . The value of s for the 12 values in Table II of Batches 3 and 7 for chlorine is 8.5×10^{-3} . If the replicates for Batches 10 and 11 are pooled with those of 3 and 7, s becomes 9.4×10^{-3} . The increase is due to the two values for Batch 4 which were obtained, respectively, with two different counting systems using different counting geometries. Even so, both values of s for chlorine are only slightly larger than the approximate value of 8×10^{-3} for counting statistics alone. For both aluminum and chlorine, random deviations other than those due to counting statistics appear to be smaller than 0.2%. Random errors caused by improper techniques of sampling, sample rotation, and sample orientation during counting, as well as those from interfering activities and neutron beam fluctuations are apparently quite small.

Table II. Determination of Chlorine
in Propellant Samples Using ^{38}Cl from
the $^{37}\text{Cl}(n,\gamma)^{38}\text{Cl}$ Nuclear Reaction

Batches Compared (Batch X/Batch 6)	Relative Percentage of Chlorine	Average of Relative Percentages of Chlorine
3/6	1.0004, 0.9878, 1.0075	0.9986
4/6	0.9958 ^a , 0.9697	0.9828
7/6	1.0028, 1.0153, 1.0115, 1.0004, 1.0091, 0.9953, 1.0052 ^b , 1.0096 ^b , 0.9900	1.0044
10/6	1.0030 ^a	1.0030
11/6	0.9936 ^a , 0.9956 ^a	0.9946

^aThese values were determined with the RIDL 400-channel analyzer with the sample placed between two 3- x 3-inch NaI(Tl) crystals. All others were determined with the TMC 400-channel analyzer as described in the text.

^bThese values are also included in Table III. The mean value for the seven other values for Batch 7 is 1.0035.

RICHARDSON and HARRISON*

The primary advantage of having a mixture of 14.5-MeV and slow neutrons is to make possible the determination of both aluminum and chlorine with a single irradiation. Table III shows the results of such a determination and compares them with those of earlier irradiations. Even though the level of ^{27}Mg activity was appreciably lower than when only 14.5-MeV neutrons were used, the values obtained for aluminum are in good agreement with those determined with the higher 14.5-MeV fluxes. The agreement for chlorine is expected, since all other ^{38}Cl values for Batch 7 were determined in the same way as those for this irradiation. The individual relative standard deviations for each element for counting statistics are each less than 1×10^{-2} .

Table III. Determination of Aluminum and Chlorine in Propellant Using ^{27}Mg and ^{38}Cl from the $^{27}\text{Al}(n,p)^{27}\text{Mg}$ and $^{37}\text{Cl}(n,\gamma)^{38}\text{Cl}$ Nuclear Reactions in the Same Irradiation

Element	Batches Compared (Batch X/Batch 6)	Relative Percentages	Relative Percentages from Other Experiments ^a
Al	7B/6	0.9953, 0.9850	0.9996
Cl	7B/6	1.0052 ^a , 1.0096 ^a	1.0035

^aSee Tables I and II.

The technique involving a mixture of 14.5-MeV and slow neutrons should be rather generally useful in other systems also. It indicates an expanded flexibility for 14-MeV neutron generators which has not as yet been widely publicized.

A comparison of the activation analysis results for both aluminum and chlorine to those for X-ray fluorescence and to the nominal percentages is given in Table IV. The overall agreement between the various values for each batch is really quite good. Both activation analysis and X-ray fluorescence methods appear to be adequate for quality control purposes. There are, however, some small but significant differences evident in the data, which should be discussed.

Table IV. Comparison of Neutron Activation and X-Ray Fluorescence Analyses of Composite Propellants

Batch	Aluminum Ratios				Chlorine Ratios			
	Nominal ^a	AA	X-Ray Cured ^b	X-Ray Uncured ^b	Nominal ^a	AA	X-Ray Cured ^b	X-Ray Uncured ^b
1	---c	0.9772	0.9553	0.9782	---c	---	---	---
2	0.8822	0.8741	0.8726	0.8959	0.9997	---	1.0038	0.9935
3	1.0401	1.0403	1.0413	1.0341	0.9804	0.9986	0.9614	0.9805
4	0.9175	0.9291	0.9222	0.8995	0.9805	0.9828	0.9792	0.9811
5	1.0185	1.0273	1.0227	1.0144	0.9599	---	0.9560	0.9576
7	0.9771	0.9996	0.9737	0.9964	0.9779	1.0044	0.9798	0.9823
8	---c	0.8605	---	---	---c	---	---	---
10	0.9952	0.9946	0.9898	1.0030	0.9951	1.0030	0.9968	0.9894
11	0.9773	0.9799	0.9904	0.9773	0.9768	0.9946	0.9740	0.9792
12	0.8965	0.9189	0.8983	0.8852	1.0160	---	1.0154	1.0180
Pooled s (within replicates)		5.5X10 ⁻³	1.0X10 ⁻²			9.4X10 ⁻³	6.4X10 ⁻³	
s _{mean} (4 samples per batch)			5.2X10 ⁻³				3.2X10 ⁻³	
Degrees of Freedom		27	27			12	27	
RMSE		1.2X10 ⁻²	6.7X10 ⁻³	1.2X10 ⁻²		1.7X10 ⁻²	2.5X10 ⁻³	3.6X10 ⁻³
s _{counting}		4X10 ⁻³	5X10 ⁻³			8X10 ⁻³	1.4X10 ⁻³	

^aFrom data of Reference (2) ^bFrom data of Reference (7) ^cThese batches from Redstone were incorrectly prepared.

The root-mean-square-error (RMSE) for aluminum determined with 14.5-MeV neutrons alone is 1.2×10^{-2} , and the differences between nominal and estimated aluminum percentages for Batches 3, 4, 5, 7, and 12 are significantly greater at the 95% confidence level than can be accounted for by the estimated random error. Note, however, that if Batches 7 and 12 are withdrawn from consideration, the RMSE for the others drops to only 7.7×10^{-3} which is much more in line with the s value of 5.5×10^{-3} . Such large errors could be in part due to incorrect nominal percentages for these particular batches. The chlorine values from ^{38}Cl for Batches 3 and 7 are also significantly in error, which indicates either a bias in the activation analysis method or incorrect nominal compositions.

One rather curious aspect of the X-ray fluorescence data on cured samples is that the RMSE for each chlorine batch is appreciably smaller than the s_{mean} . This indicates that the X-ray analysis contains an intrinsic characteristic which makes its values appear more accurate than they actually are. One such characteristic could be that the X-ray equations which were derived from the nominal percentages were then used to compute the values in the table. Because of this, it is quite possible that appreciable errors in nominal percentages have been demagnified to the point where they have gone unnoticed by the X-ray fluorescence procedure.

The two most likely causes for bias in the activation analysis method are self-shielding and self-absorption. As is well known, self-absorption depends upon sample density and self-shielding upon the percentages of elements which have significant macroscopic cross-sections for neutrons. The data for the present studies involving samples with similar compositions and densities have been carefully scrutinized for any evidence directly relating error magnitude to sample density, aluminum percentage, or chlorine percentage. No such evidence has been found. As an example, batches with nominal relative percentages ranging from as low as 0.8965 to as high as 1.0273 show significantly high ratios for activation analysis. No values are significantly low. Such behavior points away from errors caused by self-absorption and self-shielding and toward an error in the nominal percentage of Batch 6 to which all other were compared.

Further data will be needed to conclusively establish the exact causes for errors in the X-ray fluorescence and activation analysis methods, but, for the present, much of the evidence from the activation analysis studies seems to hint at incorrect nominal percentages for some of the batches. If some of the nominal values are incorrect, then the ^{27}Mg and ^{38}Cl methods may actually be more accurate than is now indicated by the respective 1.2 and 1.7% limits.

RICHARDSON and HARRISON*

The primary advantage of the X-ray fluorescence technique for quality control is its capability of directly determining all four main components of the propellants considered here, while activation analysis at its present state of development is limited to only two.

On the other hand, activation analysis has relatively minor matrix effects compared to those of X-ray fluorescence and can be more easily extended beyond the quality control limits to cover wide percentage ranges of the elements to which it is sensitive.

CONCLUSIONS

Aluminum and chlorine can be determined simultaneously with a precision of better than $\pm 1\%$ by activation analysis utilizing a mixture of 14.5 MeV and slow neutrons. The accuracy compares favorably with X-ray fluorescence and indicates that activation analysis can be a valuable method for the quality control of solid composite propellants.

ACKNOWLEDGMENT

The authors thank the staff at the Nuclear Effects Directorate, Army Missile Test and Evaluation, White Sands Missile Range, New Mexico, for their assistance in making possible the many irradiations. We are also grateful to Bernard J. Alley and co-workers at the Propulsion Laboratory, Redstone Arsenal, Alabama, for supplying us with the standard propellant samples. Mr. Alley's comments and his kind offer to let us use the X-ray fluorescence data presented in this paper should not go unmentioned.

REFERENCES

1. B. J. Alley and J. H. Higgins, Bulletin of 18th JANAF Panel Meeting, Thiokol Chemical Corporation, Elkton, Maryland, August 1962, SPIA/AC-18, Johns Hopkins University, Silver Spring, Maryland, October 1962, pp 123-140
2. B. J. Alley, Bulletin of the 20th Meeting ICRPG Working Group on Analytical Chemistry, United Technology Corporation, Sunnyvale, California, June 1964, CPIA Publication No. 52, Johns Hopkins University, Silver Spring, Maryland, July 1964, pp 279-88
3. M. H. Rison, W. H. Barber, and P. E. Wilkniss, Radiochimica Acta, 7(4), 196, (1967)

RICHARDSON and HARRISON*

4. M. H. Rison, W. H. Barber, and Peter Wilkniss, Analytical Chemistry, 39, 1028 (1967)
5. A. E. Richardson and Alex Harrison, Analytical Chemistry, 41, 1396 (1969)
6. I. G. B. Cook and J. F. Duncan, Modern Radiochemical Practices, Oxford University Press, Amen House, London, 1958, p 56
7. B. J. Alley, Propulsion Laboratory, U. S. Army Missile Command, Redstone Arsenal, Alabama, private communication, 1969

ON THE PROPAGATION OF HIGH INTENSITY,
RELATIVISTIC ELECTRON BEAMS

THOMAS G. ROBERTS
U. S. ARMY MISSILE COMMAND
REDSTONE ARSENAL, ALABAMA

INTRODUCTION

Intense beams of relativistic electrons have been extracted from the electrode space of flash X-ray machines and projected into plasma columns and drift spaces. In the plasma columns the beam pinches itself and propagates to a target at the end of the discharge (1-3). The plasma column is produced by a conventional pinch discharge in argon and the magnetic field of the plasma column is sufficient to guide the high energy beam around rather sharp curves with little loss of energy (4).

In addition to the very interesting properties of the beam itself, and its applications in thermonuclear work, the possibility of using these beams for a relatively inexpensive, ion accelerator (5-9) which may produce intense pulses of heavy ions with energies as high as 10^{12} eV per nucleon has recently stimulated this research. Beams have now been produced (10) with intensities beyond the generally accepted theoretical limit. The limiting current was established by Alfven (11) in 1939, and Lawson (12) further elaborated the significance of this limit. A theory (13) has been offered to explain how the Alfven limit is exceeded. In this theory it is assumed that the current distribution is nonuniform in such a way that the current density and the self-magnetic field are concentrated in a skin depth less than the beam's radius and near the surface of the beam. In this case the limiting current could be increased by a factor of $(a/2L)$ where a is the beam's radius and L is the skin depth. However, such a current distribution is not an equilibrium configuration and could not maintain itself. Therefore, it is the purpose of this paper to describe the principal experimental results so far obtained, and to derive an expression for the maximum current which a beam may possess by use of the Bennett theory (14, 15) and the equilibrium current distribution which the beam must assume. It will also be shown that this expression reduces to the Alfven limit in a frame in which the beam's space charge is fully neutralized, and indicates that beams

ROBERTS

which exceed the Alfvén limit may be expected to propagate in the laboratory frame.

EXPERIMENTAL

Two different methods have been developed for producing high current pulses of electrons at relativistic energies. In one of these (16) a Van de Graaff generator charges a 3-meter long coaxial capacitor whose central electrode is an extension of the terminal of the generator column. A potential of several megavolts is accumulated on the terminal, and a triggered spark gap on the symmetric axis of the terminal is used to deliver the energy to the high voltage electrode of the discharge tube. Supported from this electrode is a cold cathode, and the sudden application of the high negative potential to this cold cathode produces emission of tens of thousands of amperes at several megavolts for pulses of the order of 20 nanoseconds.

In the other method, (17) three coaxial cylinders are used as illustrated schematically in Fig. 1. One end of the inner cylinder is connected to the high voltage terminal of the discharge tube, A. The rounded end of the intermediate cylinder is close to the rounded end of the inner cylinder. The outer cylinder is the wall of the tank; the tank is filled with oil except in the discharge tube.

A reflex surge generator, M, is used for charging the middle cylinder in a time of the order of 0.1 microsecond, and this greatly overvolts the spark gap at the rounded end of the intermediate cylinder. The release of the charge between the middle cylinder and the inner cylinder and between the middle cylinder and the outer cylinder is like the discharge of the transmission lines of a Blumlein circuit. As soon as the wave has passed from the gap to the other end of the inner cylinder, A, the voltage across the discharge tube rises from zero to some voltage less than twice the initial potential to which the middle cylinder was charged. The pulsed high voltage is applied to the cold cathode, K, in the discharge tube. The application of this very high potential, V, between the cathode and the flat anode draws a very high current of electrons from the cathode. This type of machine has been made to produce pulses of 100,000 amperes at 12 megavolts for 4×10^{-8} second or of 500,000 amperes at several hundred kilovolts for 4×10^{-8} second. It was this type of machine which was used in the experiments to be described in the following paragraphs.

1. Propagation in a Plasma Column

In order to inject the intense pulse of relativistic electrons into the ionized medium, the thick central portion of the anode of the high voltage tube was replaced with a thin metal sheet, F. A linear pinch discharge in argon was coupled to the anode (Fig. 1). The linear pinch had a glass tube which was 4 inches in diameter, and the plasma column length could be varied from a few inches to

ROBERTS

6 feet. Typical operating conditions for the linear pinch were:

- a. The total circuit inductance was of the order of 10^{-6} henry.
- b. The initial mass density of the argon was 1.7×10^{-8} gram per cubic centimeter, which corresponds to a particle density of 10^{15} particles per cubic centimeter.
- c. The voltage across the capacitor bank was of the order of 1.5×10^4 volts.
- d. The rate of increase of current was of the order of 3×10^{10} amperes per second.
- e. The time to pinch was of the order of 1.6×10^{-6} second.
- f. The average sheath velocity was 3.6×10^6 centimeters per second.
- g. The current at the time of the pinch was of the order of 5×10^4 amperes.

The pulse of relativistic electrons was usually injected into the plasma column before the linear pinch had reached a minimum radius for the first time. However, during some experiments the relativistic electron beam was injected when the plasma diameter was a minimum and also after the plasma had thermalized and the plasma diameter was expanding. The results obtained when the plasma diameter was a minimum were different from those reported here and will be discussed elsewhere (18).

The plasma current in the linear pinch was in such a direction that its magnetic field prevented the high voltage electrons from striking and destroying the glass wall; instead it turned them back into the plasma column. The injected beam pinched itself to a radius which was smaller than that of the plasma while propagating to the far end of the linear pinch tube. The damage to the target which was embedded in the electrode of the linear pinch indicated that most of the energy in the injected pulse, which at times was as high as 10^4 joules, had been delivered to the target. This is illustrated in Fig. 2, which is a photograph of an Inconel target that was hit with about 5×10^4 amperes at about 5×10^6 volts for approximately 4×10^{-8} second. The rapid loading of the front surface with this kind of impulse produced a momentum wave in the material which was strong enough to cause the back surface to spall. It should be pointed out that the injected beam seemed to lose negligible energy in propagating the length of the plasma column. For example, the extent of the target damage seemed to be the same whether the plasma column was a few inches or 6 feet in length.

ROBERTS

Because of the effect of the magnetic field of the plasma current on the high energy electrons it was felt that the plasma column could be used as a guide for the injected beam. However, to perform these experiments it was necessary to produce a curved plasma column which was at least as stable as the straight plasma columns during the time of passage of the injected beam, and for future work it was required that the curved plasma column remain stable after passage of the beam. That is, the transport of the injected beam around the curve must not cause a perturbation which would drive the plasma column unstable. A simple method for producing such a curved, stable plasma column was devised by tailoring the return current distribution so that the linear pinch discharge is partially back-strapped only on the curved portion. Thus, the high voltage beam was injected into a plasma column which contained a 90-degree turn on a 6-inch radius, and it was found that the beam is guided around the bend with only a little loss of total energy. Figure 3 shows two targets that were obtained with similar beams. The one on the left was located only 18 inches from the anode with just a straight pinch; the one on the right was impacted after the beam had propagated around the curve and had covered a distance of 4.5 feet. It may be seen from the magnitude of the back spall that only a small loss of energy occurred. The injected beam here was about 3×10^4 amperes at about 3 megavolts, and the plasma column which was used is shown in Fig. 4.

One result of these experiments that was not included in any of the theories was the existence of an induced return current and its effect on the behavior of the injected electron beams. A first attempt to include the return current was made by Roberts and Bennett (3), who discerned that the magnetic field was produced by the plasma current density, the injected current density, and the induced return current density. However, it was assumed that the plasma conductivity was infinite so that the induced return current was always equal to injected current. It has been suggested (9, 15) that this induced return current might be used to explain the propagation of high v/γ beams. However, the return current is not expected to exist except when dI/dt is different from zero, and there would be no return current for a beam in a closed loop, or for a steady state beam.

2. Propagation in Drift Tubes

In these experiments a drift tube was connected to the anode of the flash X-ray machine instead of the linear pinch. The drift tube was filled with a gas so that the beam could be injected into different ambient pressures, and the experimental arrangement was such that it would lend itself to several types of diagnostic procedures. For example, the injected current density as a function of the distance from the anode could be measured qualitatively by the use of thin films. The transmission coefficient of these films at a certain wavelength in the visible was changed when the high energy

ROBERTS

electron beam passed through them. This procedure can be made quantitative by using a calorimeter for calibration. Calorimeters were also used to measure the beam's total energy and the energy distribution with radius at injection. The average energy of the electrons is measured by the use of dose depth dosimeters which are usually mounted in the center of the calorimeters.

These calorimeters were used to determine the properties of the injected beams before the linear pinch was coupled to the flash X-ray machine in the latter experiments.

The bulk of the work on propagation in drift tubes is reported in references 2, 5, 9, and 10, where studies of the beams have been made as a function of the pressure of the ambient gas, the shape of the drift tube, and the magnitude of the injected current. The beam was found to propagate in different modes at different ambient gas pressures. The image currents in the walls of the drift tubes allow the beam to propagate through various shaped tubes, and beams of 200 kiloamperes ($v/\gamma = 4$ to 6) have been made to propagate through drift tubes. These high v/γ beams were used in one of the experiments (9) where ions were accelerated to energies in excess of the beam's energy.

THEORY

The mutual interaction between charged particles in a beam in vacuum approaches zero when v , the velocity of the charged particles, approaches c , the velocity of light. However, the sign of the interaction cannot change, and since the beams emerging from beam-forming devices are divergent and since the mutual Coulomb repulsion between particles increases this divergence, it is necessary partially to neutralize the space charge of the beam before the beam's self-magnetic field can prevent or overpower the tendency of the beam to diverge. If particles are treated as moving with a constant velocity so that acceleration due to external fields and the Abraham-Dirac correction may be disregarded, then the Lorentz force equation describes the dynamics of a moving charge adequately (when radiation losses are also neglected):

$$\gamma m \frac{d\vec{v}}{dt} = -e(\vec{E} + \vec{v} \times \vec{B}) . \quad (1)$$

The transverse mass on the left of equation (1) increases with velocity through γ , and the Lorentz-force, $\vec{F}_m = -e(\vec{v} \times \vec{B})$, due to the magnetic self-field \vec{B}_s , is opposite in direction to the Coulomb force, $\vec{F}_e = -e\vec{E}_s$, caused by the repulsive electric self-field. The ratio of these forces is

$$\vec{F}_m \vec{F}_e^{-1} = v^2/c^2 = \beta^2 . \quad (2)$$

However, the presence of positive ions with random vectorial velocities in a beam of fast electrons will not affect the magnetic

ROBERTS

self-field of the fast electrons, and the ratio $\vec{F}_m \vec{F}_e^{-1}$ can become greater than unity when the space charge is only partially neutralized. For example, if the space charge of the fast electrons is partially neutralized by $f \cdot N$ ions per unit length of the beam, then the force ratio becomes

$$\vec{F}_m \vec{F}_e^{-1} = \beta^2 / (1 - f), \quad (3)$$

and the beam may converge if

$$\beta^2 / (1 - f) > 1. \quad (4)$$

Here, it may be seen that if f is small enough, then no amount of current can cause the beam or even part of it to focus - much less to over-focus.

Alfven treated a beam such as this in a frame in which $f = 1$ and found that the maximum current which the beam may possess is determined by

$$\frac{v}{\gamma} = 1, \quad (5)$$

where v is the number of electrons per unit length of the beam, N , times the classical electron radius, e^2/mc^2 .

If a beam of fast electrons is injected into an ionized or ionizable medium, its behavior in the absence of external forces will depend on the amount of the injected current, the average transverse energy per particle, ψ , at injection (the beam's initial divergence), and the properties of the medium into which the beam is launched. For example, if a beam which contains more current than the Bennett critical current is injected into an ionized or ionizable medium, a nonsteady situation is produced. The beam will attempt to neutralize itself by preferentially ejecting the slow-moving background electrons, and at the same time the beam will decrease in diameter. The decrease in diameter is a result of the beam's self-magnetic field. This magnetic field does no work on the electrons but transforms downstream energy into transverse energy; that is, the decrease in configuration space is accompanied by a corresponding increase in velocity space so that ψ , and therefore the value of the Bennett critical current, is increased while the value of the beam's current is decreased. This same self-magnetic field also tends to prevent the space charge neutralization from going to completion. Both these processes continue until the current in the beam is equal to the critical current. At this time an equilibrium radius and current distribution is reached and the beam continues to propagate in this mode as long as losses can be neglected.

The current is now related to the beam parameters by

$$I = c[2N\psi + e^2 N^2 (1 - f)^2]^{1/2}, \quad (6)$$

ROBERTS

where, as before, N is the number of fast electrons per unit length; ψ is the average transverse energy per fast electron; and the net charge per unit length is given by $q = -eN(1 - f)$, with f being the fraction of the space charge which is neutralized by $f \cdot N$ background ions per unit length of the beam. It has been assumed that the temperature of the background ions is zero (which does not affect the results), and that the beam has cylindrical symmetry. Equation (6) has been written for a fast electron beam in the laboratory frame, but when viewed from other frames both the current and therefore the self-magnetic field and the net charge per unit length will have different values. That is, a beam which is fully space-charged neutralized in one frame will appear to have a net charge in other reference frames, but the form of equation (6) will be the same in all frames. For example, if n_e and n_i are the electron and ion densities in the laboratory frame in which the ions are at rest, and n_e' and n_i' are their densities in a frame at rest with respect to the electrons, then

$$n_e' = (1/\gamma)n_e \quad n_i' = \gamma n_i \quad (7)$$

Therefore, one would expect these beams at equilibrium to be positively charged in the electrons' rest frame and negatively charged in the laboratory frame.

If a current is defined by

$$I_\psi = c[2N\psi]^{1/2} \quad (8)$$

then equation (6) may be solved for the fraction of the space charge which is neutralized at equilibrium

$$f = 1 - \frac{\bar{v}_{||}}{c} \left(1 - \frac{I_\psi^2}{I^2} \right)^{1/2} \quad (9)$$

where $\bar{v}_{||}$ is the average downstream velocity of the fast electrons. The current I_ψ for a fully space-charged neutralized beam ($f = 1$) is just that current which is required to overcome the thermal tendency of the beam to expand, and $I_\psi \leq I$.

By writing $Ne\bar{v}_{||}$ for I , equation (6) can also be solved for the average transverse energy per particle:

$$\psi = \frac{Ne^2 \beta_{||}^2}{2} - \frac{Ne^2 (1 - f)^2}{2} \quad (10)$$

Now if the average transverse energy per fast electron can be written as $\frac{1}{2}\gamma mc^2 \beta_\perp^2$, where $\beta_\perp^2 = \bar{v}_\perp^2/c^2$, and $\bar{v}_\perp^2 = (\bar{v} - \bar{v}_{||})^2$ is an average transverse velocity for the electrons, then equation (10) is reduced to the following relation between β_\perp^2 and $\beta_{||}^2$:

$$\beta_\perp^2 = \frac{\gamma}{2} [\beta_{||}^2 - (1 - f)^2] \quad (11)$$

ROBERTS

Solving equation (9) for $(1 - f)^2$ and substituting into equation (11) gives

$$\beta_{\perp}^2 = (v/\gamma \cdot I_{\psi}^2/I^2) \beta_{||}^2. \quad (12)$$

Thus, in order to have a beam the total current must be such that

$$v/\gamma \cdot I_{\psi}^2/I^2 \ll 1. \quad (13)$$

Equation (13), gives rise to the theoretical limit for the amount of current which a beam may possess as

$$v/\gamma \cdot I_{\psi}^2/I^2 = 1. \quad (14)$$

This reduces to the Alfvén limit expressed in Lawson's notation for the case of a fully space-charged neutralized beam ($f = 1$), and implies that beams, in the laboratory frame, with $v/\gamma > 1$ may be expected to propagate. For example, a 500-keV beam in which $1/\gamma^2$ of the space charge is neutralized would be expected to propagate as long as the current does not exceed 224 kiloamps, and a similarly neutralized beam at 5 MeV might carry a current as high as 1300 kiloamps.

REFERENCES

1. Roberts, T. G., The Experimental Verification of Self-Focusing in Intense, Relativistic, Electron Beams, Report No. RR-TR-65-17, U. S. Army Missile Command, Redstone Arsenal, Alabama, 1965.
2. Graybill, S. E., and Nablo, S. V., Observation of Magnetically Self-Focusing Electron Streams, App. Phys. Letters 8, 18, (1966).
3. Roberts, T. G., and Bennett, W. H., The Pinch Effect in Pulsed Streams at Relativistic Energies, J. Plasma Phys. 10, 381, (1968).
4. Roberts, T. G., Guiding of Self-Focused Relativistic Electron Beams, Report No. RR-TR-67-16, U. S. Army Missile Command, Redstone Arsenal, Alabama, 1967.
5. Graybill, S., Uglorn, J., and Nablo, S. V., Bull. Am. Phys. Soc. 56, (1968).
6. Veksler, V. I., Atomnaya Energiya 2, 427, (1957).
7. Veksler, V. I., Usp. Phys. Nauk. 66, 99, (1958).
8. Intense MeV-Electron Beams and Prospects for Accelerators, Physics Today, 59, June 1969.
9. Rander, J., Ecker, B., and Yonas, G., Ion Acceleration With High v/γ Electron Beams, Report No. PIIR-9-70, Physics International Company, December 1969.

ROBERTS

10. Yonas, G., and Spence, P., Experimental Investigation of High v/γ Electron Beam Transport, Report No. PIFR-106 (DASA 2175), 1968.
11. Alfven, H., On The Motion of Cosmic Rays in Interstellar Space, Phys. Rev. 55, 425, (1939).
12. Lawson, J. D., Perveance and the Bennett Pinch Relation in Partially Neutralized Electron Beams, J. Electron Control 5, 146, (1958).
13. Rostoker, N. Bull. Am. Phys. Soc. 14, 49, (1968).
14. Bennett, W. H., Magnetically Self-Focusing Streams, Phys. Rev. 45, 890, (1934).
15. Bennett, W. H., Self-Focusing Streams, Phys. Rev. 98, 1584, (1955).
16. Nablo, S. V., Personal Communication, Ion Physics Corporation, Burlington, Massachusetts.
17. Martin, D., Personal Communications, Physics International Company, San Leandro, California.
18. Roberts, T. G., and Bennett, W. H., Experimentally Observed Beam-Plasma Instability, Presented to the J. of Plasma Physics, March 1970.

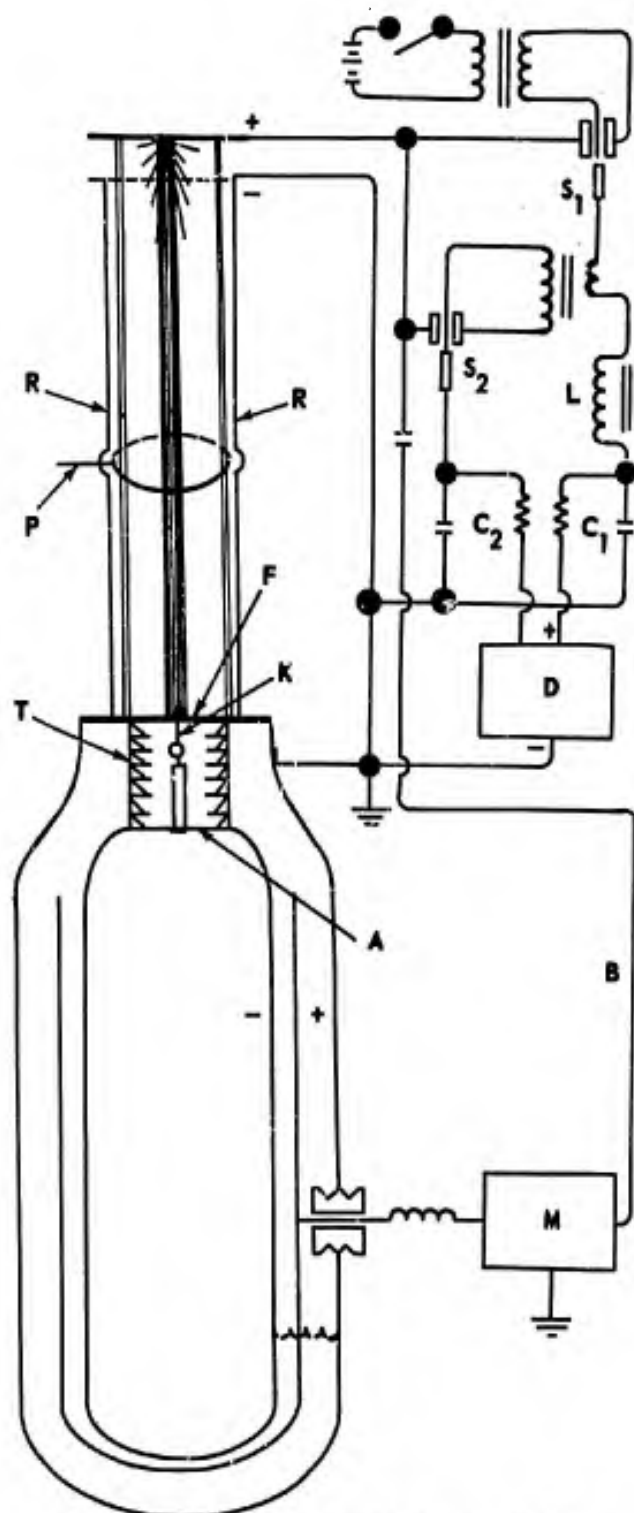


FIGURE 1. EXPERIMENTAL ARRANGEMENT

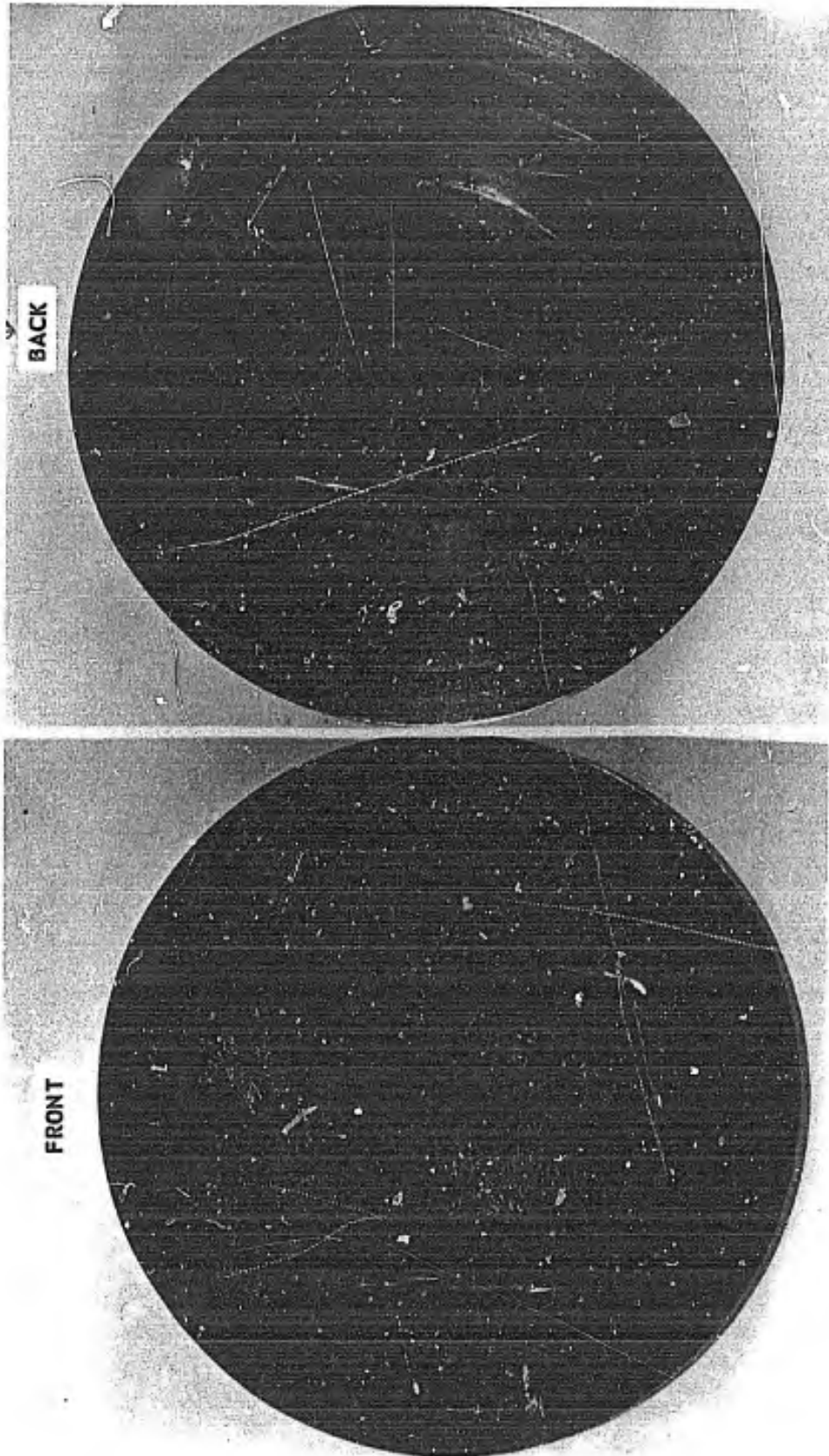


FIGURE 2. DAMAGE TO INCONEL TARGET 38 mm IN DIAMETER AND 4.8 mm THICK, IMPACTED WITH A 50,000-A, 5-MeV, 3×10^{-6} -sec BEAM

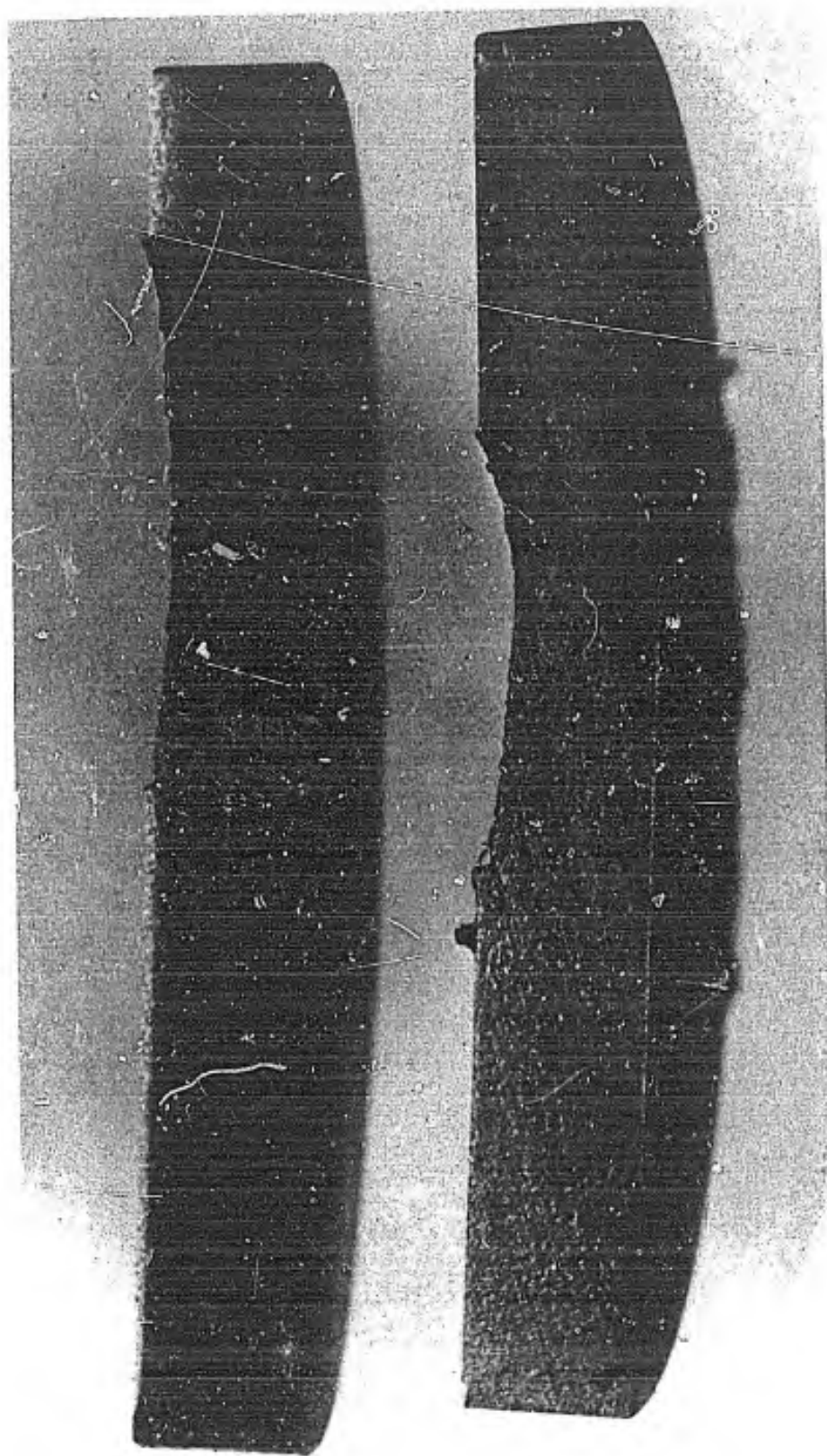


FIGURE 3. TWO TARGETS CUT TO SHOW THE MAGNITUDE OF THE BACK SPALLS,
LEFT TARGET FROM A STRAIGHT TUBE AND RIGHT TARGET FROM A CURVED TUBE



FIGURE 4. TIME INTEGRATED PHOTOGRAPH OF PINCH PLASMA IN CURVED TUBE
USED TO GUIDE THE HIGH VOLTAGE ELECTRON BEAM

TACTICS IN THE DEVELOPMENT OF MINE DETECTOR DOGS

JOHN J. ROMBA
U. S. ARMY LAND WARFARE LABORATORY
ABERDEEN PROVING GROUND, MARYLAND 21005

Dogs have been known to find hidden explosive artifacts and to provide behavior indicators of the detections. (1)(2) The United States Army during World War II devised a method for training dogs to discover buried metallic and non-metallic mines, trip wires and booby traps. The dog indicated the object's position by sitting from one to four paces distant from it. The dog was worked on-leash in mine-fields and on reconnaissance patrols. The principle of avoidance was the basis for learning - the dog was taught to fear and avoid the artifacts. The method apparently produced some behavior problems, e.g., the indicator response was often made too distant from the object to be of much use in locating it, and the dogs occasionally refused to move forward in search.

This paper describes the development and characteristics of two other U.S. mine dog systems. The Mine Detection Dog was recently made operational and has undergone a 6 month evaluation in RVN. (3) The Specialized Mine Detection Dog is currently in development. The training procedures for both have been based on the reward or approach principle of learning.

THE MINE DETECTION DOG

The operational Mine Detection Dog works off-leash about 30 meters ahead of a patrol on trails and in open fields at a speed of about 3 km/hr. It locates explosive ordnance, surprise firing devices and trip wires by sitting within two feet of them. This system is essentially similar to the British Arms Recovery Dog concept, except that the latter uses the on-leash mode and lacks a trip wire finding capability. (2)

Exploratory Work in Stimulus Learning

The success of a dog's ability to make the conditional sit response correctly to some objects and reject others during military

ROMBA

operations depends on what it learned in mine detection training. Experimental data show that the dog learns a good recognition to a single previously neutral odor in several hundred trials, and reliable perceptions at threshold levels of the same odor stimulus in a thousand or more trials. Clearly, no dog can be given discrimination training to each of the many kinds of available U. S. and foreign ordnance and to the vast set of home-made surprise firing devices, and later be expected to recognize all of them when encountered during operations. But, according to the generalization learning process, if an animal learns to respond to a particular stimulus, other previously neutral stimuli will also elicit the conditioned response if the stimuli are judged perceptually "similar." Early in the system development, the assumption was made that a dog could make a correct determination about many explosive artifacts never before experienced, on the basis that some similarity of components runs across these objects. A mine simulant was thought to be an appropriate object for obtaining stimulus generalization learning, and was used in the early exploratory work. It was comprised of broken pieces of a Claymore mine, a filter paper dusted with an explosive powder, metal pieces, field wire, and a dab of cosmoline, all enclosed in a piece of cloth and tied. Later, in production training, the first phases of learning were accomplished with mine simulants, which containing materials were now enclosed in a "cricket can," and the latter phases used 6 or more representative explosive ordnance pieces to supposedly complete the generalization process.

The early work investigated the conditions under which dogs can detect mines and the factors which affect their performance. The first experiment attempted to find out how well dogs could locate hidden mine simulants. Following stimulus learning, the mine simulant objects were tossed between one to three feet beyond the edge of a narrow dirt road into semi-dense brush. Eight mine simulants were positioned randomly along 150 yards of the road. Food was used to reward sit responses within 2 feet of the found object. A correction technique was used whenever a dog went past the planted mine: The dog was recalled and made to sit at the mine position for one minute. It was given a chance to approach again the missed mine position from a point about 10 yards back down the road. If the dog found the mine on the second try, it was praised and petted, but not food rewarded. Ultimately, all four dogs used showed performances which stabilized at 1 to 3 correct mine simulant finds out of 8, on the average, for any run. At that point, it was decided to give the dogs more trials per problem by having them run in the reverse direction over the same course. Based on learning principles relating to delayed response, memory was not expected to play much part in finding the mines, the location of which were experienced in the first leg of the run. All dogs made almost perfect runs on the second leg.

ROMBA

The second experiment was designed to test the hypothesis that dog odor traces left by a sitting dog are a significant cue used by the dogs to find the mine simulants. All dogs were tested over the same programmed run. Every dog had an equal chance to be the first animal run on any day. The first dog continued to show no better performance than that made earlier on a newly encountered mine trail. However, dogs in the second, third and fourth positions made perfect or near perfect runs. The conclusion was clear that dogs can find mines by tracking the odors of other dogs which had also found them.

Another experiment tried to establish how well dogs could find mines which were more than two feet from positions sat at by other dogs. Only two dogs were run on any programmed trail. The first dog sat at every mine on the run for one minute, either as a correct response or by correction. At the end of the sitting time, the mine was picked up and tossed 3 to 8 feet from the original position. The second dog typically showed strong search behavior about the position where the first dog sat. There appeared little or no approach in the direction of the mine object until it came to within about two feet of the object.

Detection Strategy

Further observations made during the training of dogs for operational use showed that the animals made use of secondary cues, such as disturbed earth odors and human odor traces, in finding hidden mines.

A simple test was conducted with trained Mine Detection Dogs to determine if ordnance objects which lacked emplacement associated cues could readily be found. A minelayer dropped fragmentation grenades 2-3 feet to the side of a trail, while walking at a rapid pace. All objects could be seen by anyone passing by. Results showed that the dogs found and sat at 30 per cent of the grenades. It seems that, because of the apparent weakness of most mine odors, a mine dog must learn to recognize other stronger cues which are frequently associated with mine emplacement, if it is ever to become an effective mine finding instrument. The secondary cues and not the mines or any of their components appear to elicit the classic "alerting" response, followed by a search for the odor source. It is then that the dog can finally make a determination if a mine is present.

Another simple test was made to find out whether the dogs recognized mine odors as such. Two special problems were included in runs, for eight animals, which also had the usual number of mine artifact problems. For one new problem, holes were dug and conditionally neutral objects, such as empty milk cartons and empty soft drink bottles and cans, were buried and camouflaged. In the other problem, holes were dug, nothing put in them, and camouflaged. Three of eight dogs inspected the holes containing the neutral objects, but did not sit at them. Five dogs found the holes and sat at them. In this

ROMBA

same group, all dogs discovered the holes which did not have anything in them. Four sat by them and four did not. This test showed that perhaps there is some recognition for the class of objects called explosive artifacts, but the notion that some dogs are finding mines without smelling mine odors or their components cannot be discounted. The strategy of some dogs may be merely to determine if there is some object present - any object - at a position which gives off reinforcing secondary cues. During these tests, it was also found that trained dogs rarely give false responses in the absence of secondary cues or conditional artifacts.

The detection of trip wires is probably made by sight, but before the sighting is made, in most cases, the dog stops abruptly on the track of the person which laid the trip wire across the line of movement.

Versatility

In a debriefing, two mine dog handlers reported that their dogs made clear readable reactions to Viet Cong waiting in ambush. The handlers were able to "read their animals" and correctly identify the odor stimulus which elicited the behavior. It is inherent in the dog to alert to humans naturally, but these reactions are not readily observable in some dogs, and the reaction can be extinguished through experience in others. However, procedures are simple for obtaining and maintaining this secondary detection capability without diminishing the dog's ability to find mines.

Several instances were related of mine dogs finding camouflaged ground cavities, i.e., punji pits, cache holes, etc. The phenomenon can be predicted from the procedures which bring about the mine finding behavior. During training, mines and holes in the ground frequently are closely associated. Ground cavity odors become discriminatory stimuli to a mine dog when they aid in getting the dog to a place where mines are likely to be found. The dog's behavior while checking out a ground cavity for the presence of mines is so strikingly characteristic that the handler will himself investigate the area of dog interest, even when the dog happened to move on without sitting.

The conditioned sit response is not appropriate when made to human and ground cavity stimuli. In one instance, an observable momentary distraction by the dog must be accepted as the indicator of stimulus presence. In the other, the stimulus is an integral part of the dog's mine finding strategy and the investigatory response should be the indicator.

The mine dog can be used to clear a path through a mine-field, if it had been recently laid, without any additional training. And such a field could be systematically cleared with an adjustment only in the dog's terrain-working behavior.

ROMBA

The assignment of more than one handler to each dog is being tried. The handlers alternate in grooming the dog and providing it with exercise and maintenance training on an equal basis. The dog should work with any handler assigned to it, regardless of the kind of personal relationship established between them - the handler should otherwise serve as a vehicle for getting the hungry animal to a place where it can find food. To show also that most dogs will quickly adapt to a new handler, a test was arranged to have dogs run on a practice mine trail with a stranger handler. The handler was given one minute to become acquainted with each dog before a run. The criteria of good cross-handler working ability was moving out on command and purposefully going down the trail for a distance of 50 yards. Fourteen of seventeen dogs met these criteria.

Operational Evaluation

Fourteen Mine Detection Dogs were sent to the Republic of Vietnam for a 6-month evaluation and a partial summary of results follows: The mine dogs made 76 positive responses on ordnance and trip wires; 21 positive responses on tunnels, punji pits, caches and spider holes; 6 alerts on enemy personnel; and 14 alerts that were not checked by the supported unit. There were 12 confirmed cases where mine dogs missed an artifact. Several misses were on ordnance and explosives that had been emplaced for a long period. Two misses were 30-pound plastic mines of ammonia nitrate. Three misses were antitank mines. Two of these misses occurred after heavy rains. Both were also missed by mine sweep teams. Detecting ordnance that had been emplaced for a long period seemed to be a problem for the mine dogs. (3)

SPECIALIZED MINE DETECTION DOG

The Specialized Mine Detection Dog System is now in development. It was designed to locate plastic antipersonnel fragmentation mines which were buried for durations of several months or longer. The dogs shall be used off-leash between guide tapes in minefields and make their conditioned sit response within two feet of the buried mine.

The British Mine Dog is also a minefield dog (2), but the system differs importantly from the current one in the way that the respective dogs locate mines. The assumption guiding our procedures is that there are no accessory cues other than mine odors in some minefields which can guide the animal to a mine's location. The British Mine Dog appears to be using mine-emplacement generated secondary cues in its strategy because the animal has difficulty locating mines as emplacement duration increases.

In training the dog, odors from earth disturbance made during daily mine laying must be reduced considerably. The procedure

ROMBA

which is used to reduce these odors is one which does not require hole digging for mine burial. Several hundred upright ceramic sleeves shall be emplaced throughout the experimental minefield and shall remain in place for the duration of minefield use. Into them shall fit ceramic containers, some of which hold soil and a mine, and others which hold only soil. The containers can be removed and replaced with other containers for any test session. The entire field then shall be given a light raking to hide container positions from sight.

The presence of human odor traces during trial runs can be minimized if the person who lays out the minefield daily does not thereby make physical contact with the ground. A cart was designed for use in the training minefield. It permits the minelayer to lie prone about 14 inches above ground level while he does his work.

Feasibility of the Specialized Mine Dog System shall be tested in mid-1970 on a 9-month old minefield at the Aberdeen Proving Ground, Maryland.

FUTURE RESEARCH

An olfactometer was designed recently to study experimentally some of the factors which relate to mine detection by dogs. The instrument precisely regulates the quality and intensity of odor stimuli, uncontaminated by affecting impurities. Air flow, shown in the diagram of figure 1, begins at the motor compressor and passes through a vessel immersed in an isopropyl alcohol and dry ice bath - the air is purified by means of condensation at low temperature. At valve X, the flow is diverted into any of three odor producing branch lines. In our work, the liquid sparger was used specifically to obtain conditioning of animal behaviors which were required later for testing experimental odorants. Amyl acetate provided an easily discriminable odor for this pre-experimental purpose. The sample chamber in the second branch can contain solid substances such as explosives and ordnance items. The third branch leads to a series of simulated environmental fields, consisting principally of tubs containing soil and Bell jar housings. The saturated odorants and several dilution intensities are shown as lines A through J on both sides of the manifold. The system is in flow equilibrium - the lines are either opened to the manifold or to waste. Once the saturation levels have been determined for any odorant line, they should remain constant throughout a session.

The instrument is capable of delivering one or two qualitatively different odorants or clean air to the animal on any trial. For example, the air flow from the sample chamber containing a mine could mix with the air flow from one of the tubs containing only soil and be delivered to the animal on the same trial. In this manner, the odor intensities from the mine and soil can each be systematically varied during an experimental session, and the effects of one on

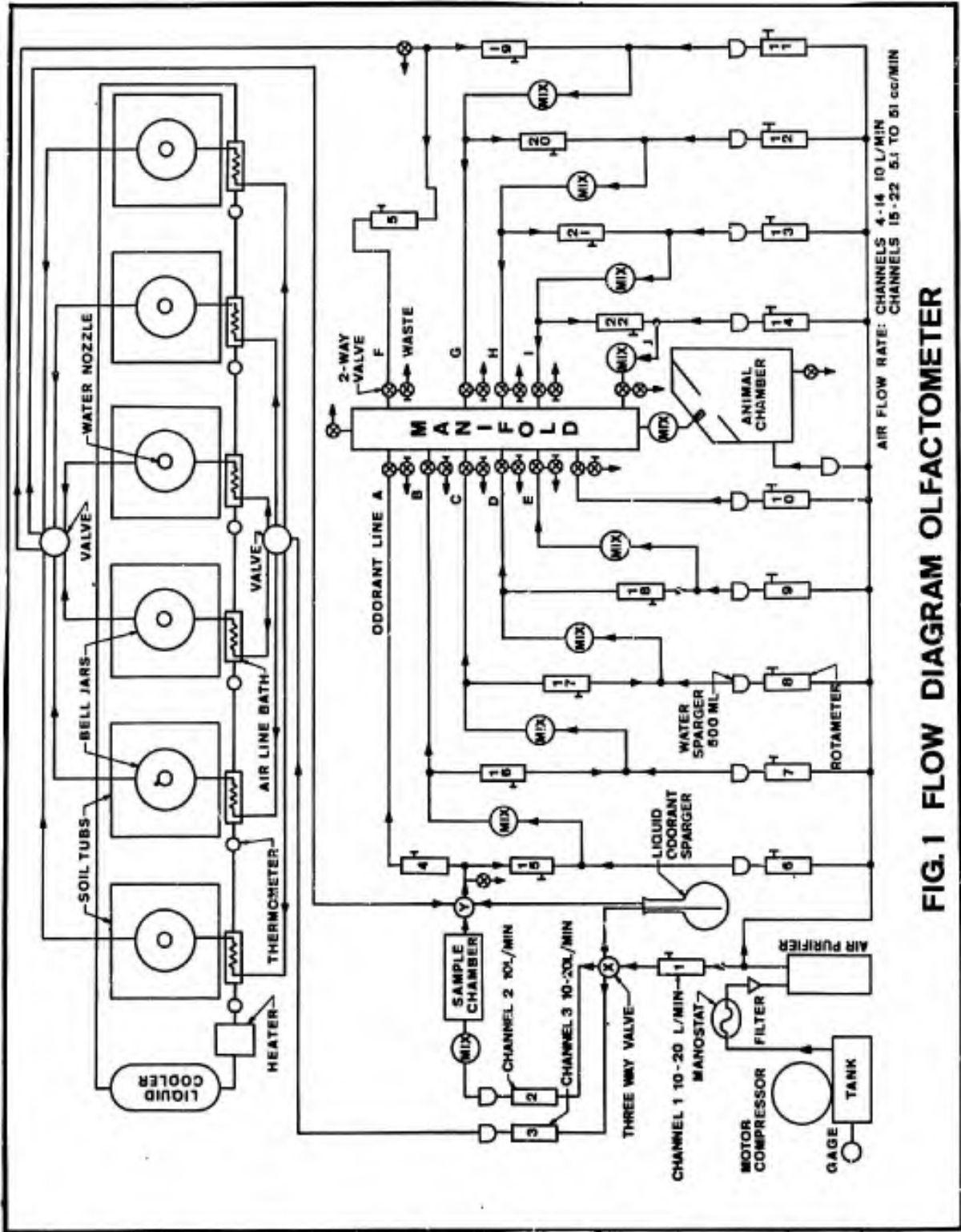


FIG. 1 FLOW DIAGRAM OLFACTOMETER

ROMBA

the other can be established.

Matters of importance to developers of detector-dog systems are: The olfactory sensitivity of the dog to various substances of military significance. From the limited data available on the dog's olfaction capabilities, this animal shows remarkable odor detecting powers, although degree of sensitivity will be expected to vary considerably over the broad spectrum of discriminable odors - the dog's ability to smell some floral scents apparently is no better than what man can do. The masking effects of background mediums on the conditional odorant. Except as a laboratory phenomenon, the conditional odorant shall appear with other odors in air that the dog normally breathes and are expected to exert some masking. Individual animal differences in discriminability. The selection of dogs for any detector program on the basis of olfactory acuity should be made on how the dogs are distributed along the sensitivity continuum and how various sensitivity levels affect performance in applied situations. The effects of training conditions and procedures on the system performance. The selection of the correct training variables depends currently on the skills and experiences which the developer hopefully has had in related fields of animal learning. Procedures selected for the systems must at some time be experimentally evaluated for appropriateness and effectiveness.

The improvement of present detector-dog systems and the development of other systems will come about through continuing evaluation of fielded systems and through experimental work in both open-field trials and the laboratory, the latter conducted especially with olfactometry.

REFERENCES

- (1) War Department Technical Bulletin TB 10-396-1, Mine Detection Dog (M-Dog), 1944.
- (2) The War Office, Training of War Dogs. WO Code No. 9746, March, 1962.
- (3) ACTIV. 60th Infantry Platoon (Scout Dog) (Mine/Tunnel Detector Dog) Final Report: Project No. ACG-65F, December 1969.

THE USE OF MARTENSITE MATERIALS IN THE DESIGN
OF THERMALLY ACTIVATED SPRINGSFREDERICK ROTHWARF, ARTHUR AUERBACH and DONALD FORD
Pitman-Dunn Research Laboratories
Frankford Arsenal, Philadelphia, Pa.

INTRODUCTION

Many intermetallic compounds exhibit some rather interesting elastic properties associated with certain phase transitions known as martensite transformations (1-5). Certain alloys such as NiTi and AuCd exhibit such crystallographic changes on cooling from a body-centered cubic high temperature phase (htp) to a low temperature phase (ltp) of lower symmetry. The ltp is usually a twinned structure whose twins are very mobile under the application of stress. A specimen may deform plastically entirely by movement of twin boundaries. The elastic moduli of such materials can be significantly modified by these twinning effects. Interesting "memory" properties are also exhibited by these alloys. For example, if a severely cold-worked sample is constrained to a given shape while being given a special anneal in the htp, this shape will be retained on cooling to the ltp and then subsequently "remembered" everytime it is heated to the htp even though the sample may have been severely plastically deformed in the ltp. This "memory" is exhibited by the fact that the sample will regain its original htp shape when it is heated above its characteristic transformation temperature. These alloys exhibit large differences in their htp and ltp force constants. This fact when coupled with their "memory" properties make these alloys particularly interesting for use as thermally activated springs. The purpose of this paper is to review some of the properties of these materials and to explore some of the problems involved in their use in the design of thermally activated springs that might find use in electro-mechanical fuzes, switches, and timing devices.

SOME PROPERTIES OF MARTENSITE MATERIALS - A REVIEW

For some time it has been well known that certain metallic systems undergo solid state phase transitions which involve a change in crystal structure but none in chemical composition. Such phase changes which involve no long-range diffusion are known as diffusionless transformations. This kind of reaction includes a type known as the martensite transformation that exhibits certain characteristic

crystallographic features which have been reviewed by Bilby and Christian, (1) and Christian, (2) and Christian, Read, and Wayman, (3) and Wayman (4). In general, on cooling, these reactions involve the transformation of the crystal to a phase of lower symmetry, e.g., the gold-cadmium system, where the high temperature CsCl cubic phase transforms to an orthorhombic phase on cooling at about 60°C for the 47.5 at % cadmium composition (5). The most significant feature (in fact, the one proposed (1) as a criterion for these reactions) is a characteristic shape change which takes place as a given volume of the crystal transforms (6,7).

The martensite transformations occur on cooling below some transformation temperature, M_s , but they also can be induced by the application of various stresses. The effective elastic moduli of such materials can be significantly modified by these twinning effects. Later in this report we shall have occasion to determine such effective moduli from experimental stress-strain curves.

In general, the application of a stress gives rise to a change in the M_s temperature. Intrater, Chang, and Read (8) reported the effect of a tensile stress on the M_s of annealed Au 47.5 at % Cd alloys. They found parallel upward shifts of the transformation temperatures for heating and cooling. In both cases the magnitude of the shift was proportional to the applied stress. These results were in part due to the fact that the length increase during transformation on cooling and the length decrease on heating were equal. Cross (9) has obtained similar results for NiTi. Application of the appropriate form of the Clausius-Clapeyron Equation permitted calculation of the heat of transformation, λ_m . We shall find below that this will be an important quantity to know for the calculation of the thermal energy needed to operate special springs made from martensite materials.

Some interesting changes in the mechanical properties of a material accompany the crystallographic changes that occur during a martensite transformation (10,11). Buehler, Gilfrich, and Wiley, (12) who studied the intermetallic compound NiTi with stoichiometric composition, reported some interesting memory effects associated with the martensite transformation in this alloy. They found that if an initially straight wire is deformed at room temperature by coiling it into a helix, and is then heated, the wire rapidly straightens out to its original shape at about 65°C. The demonstration apparently can be repeated an indefinite number of times. This memory phenomenon has been used in the design of several interesting electro-mechanical relaxation oscillators, (9,13) as well as in several models of expanding antenna arrays for our space program (9). This rapid reversion of a sample to its original shape on heating has also been observed in the gold-cadmium alloys, where it could be accounted for in terms of the crystallography of the transformation (14).

There is also a large change in the elastic constants that accompany the phase change. For example, in the NiTi stoichiometric material, the effective Young's modulus E has been found to change by a factor of approximately 3 to 4 on heating. Such a result can be calculated from the force vs displacement data for a NiTi rod shown in Figure 1. Similar properties were exhibited by the AuCd alloys (15). Such a large change in Young's modulus makes such materials very attractive for the construction of special thermally activated springs, whose design will be discussed below.

We shall base our spring design calculations entirely on the properties of the NiTi alloys as typical martensite materials. There are two reasons for this choice. First, an extensive literature documenting the physical properties of this system already exists. Much of this work has been accomplished by the group at the Naval Ordnance Laboratories (NOL) which has done considerable work on this system (16-21). In fact, the alloys near the stoichiometric composition have been given the trade name Nitinol (nickel titanium-Naval Ordnance Laboratory) in recognition of the extensive research done by the NOL people on this material. The second reason for our choice of Nitinol is that the equiatomic compound is reasonably ductile at room temperature and below so that the material can readily be fabricated into sheet and wire stock useful in a variety of devices. In this respect Nitinol seems to be rather exceptional in that most martensite materials having a high temperature cesium chloride phase are quite brittle. This brittleness of most interesting materials no doubt has been a deciding factor in preventing the commercial utilization of the interesting mechanical properties of such materials.

In some applications it might be desirable to have a different M_s than that available with Nitinol. It is possible to accomplish this by adding a third element to a given alloy or by choosing other related binary alloys. For example, Rothwarf and Muldrew (22) have demonstrated that the transformation temperature of AuCd alloys can be lowered significantly by the addition of silver. Similarly, Wang (23) has shown that M_s can be varied over a wide range of temperatures for a series of CsCl-type equiatomic phases in binary alloys of transition elements such as TiFe, TiCo, TiNi, ZrRu, and ZrPd. Many other binary alloys exist that exhibit martensite transformations. These include CuAl, CuSn, CuZn, AuCu, AuMn, MnAs, MnBi, AgCd and AgZn. Such materials have a variety of M_s temperatures which vary with deviations from stoichiometry. Thus, it seems that it might be possible to choose a material with an M_s suitable for any given application.

THE DESIGN OF THERMALLY ACTIVATED SPRINGS

Cantilever Springs. In discussing the elastic properties of martensite materials we mentioned the fact that the Young's modulus E for NiTi can change by a factor of 3 to 4 on heating. The

tensile measurements of Cross (9) give $E_{ltp} = 3.5 \times 10^6$ psi (2.42×10^{11} dynes/cm²) at 38° C and $E_{htp} = 11.5 \times 10^6$ psi (7.94×10^{11} dynes/cm²) at 71° C. Using the same material (kindly furnished to us by Mr. Cross) we have carried out a series of studies to acquaint ourselves with the peculiar properties of this material. In Figure 1 we show the force vs displacement characteristics for a NiTi rod having a diameter of 0.254 cm and a length of 11.2 cm when it was used as a cantilever spring. The ltp curve taken at room temperature ($T = 23^\circ$ C) shows a large mechanical hysteresis on unloading. The htp curve, taken with the sample heated to 150° C by passing a current of 15 amperes through it, shows a much steeper loading behavior and far less hysteresis than does the ltp curve. From the slopes of the loading curves, Young's modulus E can be determined. This is done by invoking the relationship for a cantilever rod supported at one end (24):

$$E = \frac{64FL^3}{3\pi d^4Y} \quad (1)$$

where F is the force in dynes applied at a distance, L centimeters, from the point at which the rod of diameter, d centimeters, is clamped. Y is the displacement in centimeters of the free end from its straight rest position. Using this equation and our measurements, we obtained an $E_{ltp} = 2.24 \times 10^{11}$ dynes/cm² and $E_{htp} = 7.28 \times 10^{11}$ dynes/cm² which gives good agreement with the tensile results of Cross. Equation 1 may be used to design thermally activated cantilever springs, whose various modes of operation will now be discussed.

Modes of Spring Operation. Figure 1 is also useful for illustrating the possible modes in which a thermally activated spring might be used. For certain applications, it might be useful to have a given load undergo some displacement on heating. Such a case is shown in Figure 1 as the horizontal line (1) at a force of 1.5×10^5 dynes. Obviously work can be obtained from application of such a method. However, the efficiency of the process is small. By measuring the power and the time needed to transform the rod from the ltp to the htp for the situations shown in Figure 2, it was determined that the work performed was only 0.01 to 0.05% of the energy needed to heat the sample into the htp. It is interesting to note that, within certain limits, the greater the load, the greater the work one can obtain from the process. This behavior is clearly illustrated in Figure 2 where the displacements obtained for a number of heating and cooling cycles are shown for different masses hung from the end of a NiTi rod of nearly the same composition and dimensions as that discussed in Figure 1. The sample was heated into its htp by passing a 15-ampere current through it. Liquid nitrogen was then used to quickly cool it back to room temperature. A cathetometer was used to observe the equilibrium end points in each phase. It is clear that the cycling was quite reproducible. The vertical line (3) in Figure 1 demonstrates the large increase in

force that is possible if the rod were constrained to a nearly constant displacement on heating to the htp. Again, it is apparent from Figure 1 that a greater force can be obtained when the rod is constrained at a greater displacement. In general, a given device will operate between the extreme cases (1) and (3), i.e., along a line such that the spring will contract (in this case) when it is heated, as is shown by line (2). It is conceivable that these modes for operating such springs can find considerable application in a variety of temperature activated electromechanical devices.

Helical Springs. It is useful to consider the design problem encountered in using thermally activated helical springs. The pertinent design equations and an illustrative example will now be presented. A useful characteristic of a helical spring is the force constant, F_0 , necessary to compress it a unit distance. F_0 is also known as the scale of the spring. In general, one has from Hooke's Law:

$$F = F_0 y, \quad (2)$$

where F is the force required to compress the spring a distance, $y = (L_0 - L_{htp})$, and L_0 is the uncompressed length of the spring. For a helical spring made of cylindrical wire stock of diameter d , one has (25)

$$F_0 = \frac{d^4 G}{8iD^3 k} = \frac{dG}{8ic^3 k} \quad (3)$$

where G is the modulus of elasticity in shear or torsion, D is the diameter of the spring, i is the number of active coils, which is greater by one-half coil than the number of free coils (26), and k is a stress factor which is a function of the diameter ratio, $c = D/d$, the spring index. For closely coiled springs

$$k = \frac{4c-1}{4c-4} + \frac{0.615}{c} \quad (4)$$

Maleev (25) plots k vs c and shows that the stress factor increases very rapidly with the decrease of the spring index, c . Usually it is advisable to have $c \geq 3$. The shear modulus, G , is theoretically related to Young's modulus, E , by the relation

$$G = \frac{E}{2(1 + \nu)} \quad (5)$$

where ν is Poisson's ratio which is 0.33 (12) for NiTi.

In designing a thermally activated spring to provide a given force (curve 3, Figure 1) in the htp, one need consider only the high temperature elastic constants for use in Equations 3 and 5. For example, it was desired to have a compressed spring to activate

ROTHWARF, AUERBACH and FORD

a mechanical chain of events on being heated. A final force, F_{htp} , of 4 oz (2.8×10^4 dynes) was required from a spring with a constrained length, L , of 0.250 inches (0.635 cm) and a maximum diameter, D , of 0.250 inches (0.635 cm). It was also desired to minimize the length of wire, L_w , to be heated.

$$L_w = \pi i D \quad (6)$$

The problem was to determine an uncompressed spring length, L_0 , and the corresponding initial pitch of the spring, P_0 , where

$$P_0 = i/L_0 \quad (7)$$

Several solutions are possible to this problem depending upon the choice of wire and spring diameters. Using Equations 2 and 3, one finds

$$L_0 = L_{\text{htp}} + (F/F_0)_{\text{htp}} = L_{\text{htp}} + \frac{F_{\text{htp}} 8ic^3 k}{dG_{\text{htp}}} \quad (8)$$

or

$$L_0 = L_{\text{htp}} + \alpha i \quad (9)$$

and

$$\alpha = \frac{8F_{\text{htp}} c^3 k}{dG_{\text{htp}}}$$

where α is the compression per turn. Using $E_{\text{htp}} = 7.9 \times 10^{11}$ dynes/cm² which is Cross' value at 71° C, one can obtain $G_{\text{htp}} = 3.0 \times 10^{11}$ dynes/cm² from Equation 5. If one chooses $d = 0.010$ inches (0.025 cm) and $D = 0.125$ inches (0.318 cm), then $c = D/d = 12.5$, and from Equation 4 one has $k = 1.12$. Substituting the appropriate values in Equation 9, one finds $\alpha = 6.4 \times 10^{-2}$ cm/turn. If one chooses $i = 5$ turns for some mechanical stability, then $L_0 = L_{\text{htp}} + 5\alpha = 0.635 \text{ cm} + 0.320 \text{ cm}$, $L_0 = 0.995 \text{ cm}$ and $P_0 \cong 5$ turns/cm. Of course, a somewhat shorter spring with fewer turns would also have satisfied the constraints.

One can simply evaluate the other cases illustrated in Figure 1 by using the suitable htp and ltp values of G in the design equations as well as the pertinent spring dimensions for a particular design.

SOME THERMAL CHARACTERISTICS OF NITINOL

Heat Capacity and Heat of Transformation. It is, of course, important that one know the thermal energy needed to activate a

spring. In general, this requires a knowledge of the specific heat as a function of temperature for the material in its low and high temperature phases. In addition, for a given martensite transformation there is a heat of transformation, λ_m , which can be a large fraction of the heat necessary to activate a spring. We shall again consider the data available for Nitinol and shall find that certain complications exist.

Berman, West, and Rozner (27) have studied the heat capacity of an equiatomic NiTi alloy in the temperature range from 25° to 220°C. For their sample, which had been vacuum arc-melted, hot-swaged, annealed 2 hours at 800° C, and cooled overnight in the furnace at a vacuum of 10^{-6} Torr, they obtained certain anomalous effects on three successive cycles. In Figure 3 we have replotted their results for their second run. Between 65° and 110° C, a large peak appears in the specific heat curve. The area labelled B (above the horizontal dashed line) represents the λ_m . For three successive runs they obtained a smaller λ_m . The three heats of transition listed in chronological order were 4150 J/mole, 3831 J/mole, and 3375 J/mole. The estimated uncertainty in each case was 10 J/mole or less, so that clearly the heat of transition exhibited anomalous behavior on cycling. The values reported by Berman et al. are considerably larger than those reported by previous workers. Wang, Buehler, and Pickart (28) reported a λ_m of 2600 J/mole for an alloy having 51 at % Ni, while Dautovich, Melkvi, Purcy, and Stager (29) found a value somewhat higher than this for a 50 at % Ni alloy. The work of Dautovich et al. was consistent with the results of Wasilewski, Butler, and Hanlon (30) who obtained a λ_m of 3100 J/mole for an equiatomic NiTi alloy. It should be pointed out that the various investigating groups used somewhat different heat treatments for this material. The variation in heat treatment might play a significant role in determining the value of λ_m because of the various stress levels that might have existed in the alloys at the time a measurement was begun. The striking decrease in λ_m observed by Berman et al. for successive runs may well be evidence for this type of effect. Of course, the effects of different impurity concentrations and differences in composition may also be determining factors in giving the observed variations in λ_m .

Some recent data presented by Buehler and Cross (31) may be evaluated to show the effect that stresses play in changing λ_m and T_m , the midpoint temperature of the martensite transformation. Cross maintained a fixed strain in a 100-mil diameter, 6-inch length of Nitinol rod (49.6 at % Ni) by increasing the tensile force as temperature was increased. The force necessary to maintain a given strain was found to increase steeply in the region of the martensite transformation and then leveled off to a constant value above the transformation region. Furthermore, as the strain was increased T_m increased. Such behavior is similar to that observed for the Au 47.5 at % Cd alloys by Intrater, Chang, and Read (8) for the effect of tensile stress. Cross' results are shown in Figure 4. Applying

the appropriate form of the Clausius-Clapeyron Equation (8) to these data one can obtain λ_m as a function of strain:

$$\lambda_m = \frac{T_m \epsilon}{\rho(1-\epsilon)} \left(\frac{\partial \sigma}{\partial T} \right)_\epsilon \quad (10)$$

where ϵ is the constant strain maintained as the stress, $\sigma = F/A$ in dynes/cm², is varied with the absolute temperature, T , in °K, and ρ is the NiTi density, 6.45 grams/cm³, while A is the cross-sectional area of the 100-mil rod. In evaluating λ_m , we have chosen the values for $(\partial F/\partial T)_\epsilon$ from the curves in Figure 4, at a temperature, T_m , which represents the point at which 50 percent of the final constant high temperature force has been applied. The results for λ_m and T_m as a function of strain, ϵ , are presented in Figure 5. It is clear that λ_m rises continuously with strain up to a value of 58 J/gram (6200 J/mole) for a strain of 10 percent. The values of λ_m reported by the workers mentioned above are comparable to those calculated using Equation 10 for strained material.

The total heat per unit mass, Q/m , needed to raise the temperature of a spring from 25° C to 110° C can be written as

$$Q/m = \int_{25^\circ\text{C}}^{110^\circ\text{C}} C^*(T)dT + \lambda_m \quad (11)$$

The upper limit of 110° C was chosen since Figure 3 indicates that the transition is essentially completed by 110° C. $C^*(T)$ represents the nearly horizontal curve of Figure 3 which does not include the peak region, B. On evaluating the first term of this expression, one obtains a value of 4250 J/mole, which is comparable to the λ_m values reported by Berman et al. Thus, it is clear that any variations in λ_m on cycling would yield significant variations in the heat needed to operate a spring. It would also be of great importance to have a standardized heat treatment procedure that would yield a rather well controlled value of λ_m . This would be especially true for those applications where a limited quantity of heat would be available to drive the transformation.

Thermal Diffusivity and Thermal Conductivity. Springs such as we have been discussing can be activated in several ways: by infrared or solar radiation; electrical heating; or thermal conduction of heat down the length of the spring. In the first two cases the heat is supplied somewhat uniformly along the length of the spring and more than enough energy is usually available to raise the sample temperature above its transformation temperature. In the last case, however, one is usually concerned with transferring heat down a spring from a heated end and one deals with a situation where only a limited amount of energy may be available. This end may be connected directly to some source of energy or may be connected to

some conduction rod which brings the heat from some remote source. One may be required to deal with heat sources whose power output varies with time, i.e., the temperature vs time waveform at the heated end of the rod might be a delta function, a single square wave of a certain duration, a sinusoid, or a step function. In each case one would like to know the temperature distribution along the spring as well as the resultant mechanical response that one might expect as a function of time. It is conceivable that under certain conditions a spring might not be fully transformed along its entire length and thus its effective force constant would lie somewhere between those characteristic of the ltp and htp. In any case the standard differential equation for heat flow would have to be satisfied (32)

$$\frac{\partial T}{\partial t} = D \frac{\partial^2 T}{\partial X^2} - \frac{2H}{\rho c R} T \quad (12)$$

where we have assumed that a given spring can be represented as a finite thin rod and where the thermal diffusivity, D , is given by

$$D = \frac{k}{\rho c} \text{ in cm}^2/\text{sec} \quad (13)$$

k is the thermal conductivity in watts/cm²-°K, ρ is the density in g/cm³, c is the specific heat in J/g-°K, H is the surface conductance losses due to radiation and convection in watts/cm²-°K, and R is the radius of the rod.

Goff (33) gives a value for the thermal conductivity at 300°K as being 0.20 watts/cm-°K, while a value of 51.1 J/°K-mole (0.49 J/g-°K) can be calculated from the data of Berman et al. (27) for the value of the specific heat at the same temperature. The density of NiTi is listed as 6.45 g/cm³ by Buehler (16). Thus, the diffusivity, D , for NiTi is 0.063 cm²/sec. This is a factor of over 19 smaller than the diffusivity of copper ($D_{Cu} = 1.22$ cm²/sec). This low diffusivity for Nitinol thus leads to difficulties in employing it for applications that require a fast thermal response. The low thermal conductivity also requires that in a steady state situation Nitinol sustain large temperature gradients. Thus, in applications that require heat conduction to activate a spring it is possible that the total length of material in a given spring may not transform unless a very high temperature pulse is applied to the heated end. It is clear that where such an application is of importance, a martensite material with better thermal characteristics than Nitinol is desirable. Nevertheless, the thought occurred to us that the characteristics of Nitinol might be improved by plating with copper to give a composite with more desirable thermal properties.

A detailed experimental study was undertaken by Rothwarf, Auerbach and Ford (34) to determine the thermal and mechanical

characteristics of copper-plated Nitinol rods. In that work certain effective thermal parameters were defined for Nitinol-copper composite rods for use in the analysis of the heat flow problem. It was assumed that the composite rod could be represented by an equivalent rod with certain effective properties: a density, ρ^* ; a specific heat, c^* ; a thermal conductivity, k^* , and a diffusivity, D^* , that could be derived from the separate thermal properties of the Nitinol and the copper. It was further assumed that the temperature was constant through a given cross section, i.e., that the temperature varied only along the length of the rod so that the one-dimensional heat flow equation, Equation 12 was applicable. An experimental study of the steady-state temperature distribution along a composite rod gave support to the assumptions. Therefore, this formulation was used by Friedman (35) to obtain the pertinent parameters needed in evaluating the time-dependent solutions to the heat flow equation for copper-plated Nitinol rods when certain time-varying sources of heat were applied to one end.

Elastic Properties. Even though copper plating increased the effective diffusivity and thus decreased the thermal response time of a given Nitinol rod, the effect of such a procedure on the elastic properties was not readily apparent. Extensive measurements of the force versus displacement curves were taken for a rod after each new layer of copper had been deposited (34). It was found that copper plating tends to eliminate the large differences in the elastic constants that exist between the high and low temperature phases of Nitinol. A theory was developed (34) which closely describes the elastic behavior of composite copper-Nitinol rods in terms of the Young's moduli of the copper and the Nitinol. The above studies showed that while diffusivity is increased by copper plating, the deflection or force changes, which accompany the transformation of the copper-Nitinol composite decrease. Nevertheless, for certain stringent design constraints one might wish to sacrifice some of the memory properties for the more rapid thermal response which can be had with copper plating.

NITINOL SPRINGS AS COMPONENTS IN SMALL CALIBER FUZES

This study was initiated to evaluate the possibility of using "memory" metals as thermally activated springs in small caliber fuzes. It soon became quite clear that either there was insufficient data available in the literature to evaluate most of the "memory" materials for this application or that they did not possess sufficient ductility to permit their fabrication into spring stock. The only material found that satisfied both of these criteria was Nitinol. However, its low thermal diffusivity makes its usefulness for this application uncertain.

To thermally activate a Nitinol spring fully, approximately 6800 J/mole (64 J/gm) are needed. If one considers the helical spring described above as being typical of the size needed in a

fuzing application (it is 5 centimeters in length, which corresponds to a mass of 0.016 grams), one would require an energy of approximately 1.0 J to activate the spring. In the case of a small caliber fuze, two methods of obtaining this energy were considered. The first was from the aerodynamic heating of the projectile itself while it was in flight. The other was the use of a resonance effect which might pump enough energy into the projectile interior during the portion of the flight when ultrasonic velocities were attained. In each case, the heat for activation of the spring was to be supplied via conduction down the length of the spring. In a companion report (35) Friedman has solved the heat flow equation, Equation 12, by assuming certain pertinent boundary conditions derived from a knowledge of typical projectile aerodynamic characteristics. He concludes that the usefulness of Nitinol is just marginal for this application. Under certain geometric conditions and with a certain copper plating it might just be possible to attain the desired force to initiate a certain train of mechanical events within some specified time.

CONCLUSIONS

The use of martensite memory materials in the design of thermally activated springs is an intriguing concept. This is a concept that can definitely be implemented for a number of practical applications by using the Nitinol alloy. However, this particular alloy has poor thermal properties that preclude its use in devices that must respond rapidly to thermal inputs. For its use in a disarming device Friedman recommends that an attempt be made to construct such a device, but indicates that its usefulness is just marginal. It is clear that much more basic research is needed on the metallurgical, mechanical, and thermal properties of other martensite systems. This can be a long, tedious process with no assurance of ultimate success in achieving better thermal properties since most alloys have poor thermal properties. Thus, a value judgement must be made by management as to whether the intriguing applications of these materials justify the extensive research program necessary to develop suitable materials.

ACKNOWLEDGEMENTS

The authors wish to thank Dr. P. D. Flynn for several helpful discussions concerning the mechanical properties of composite structures. We also wish to thank Mr. C. Friedman for useful discussions in the development of this work. The authors further wish to extend their appreciation to Mr. W. B. Cross of the Goodyear Aerospace Corporation for lending test samples and for making his unpublished data available. His work was being done under NASA Contract No. NAS1-7522. In addition, thanks are due Prof. L. Muldawer of Temple University for a critical reading of this work. Helpful discussions with Dr. W. J. Buehler of the Naval Ordnance Laboratory are also gratefully acknowledged.

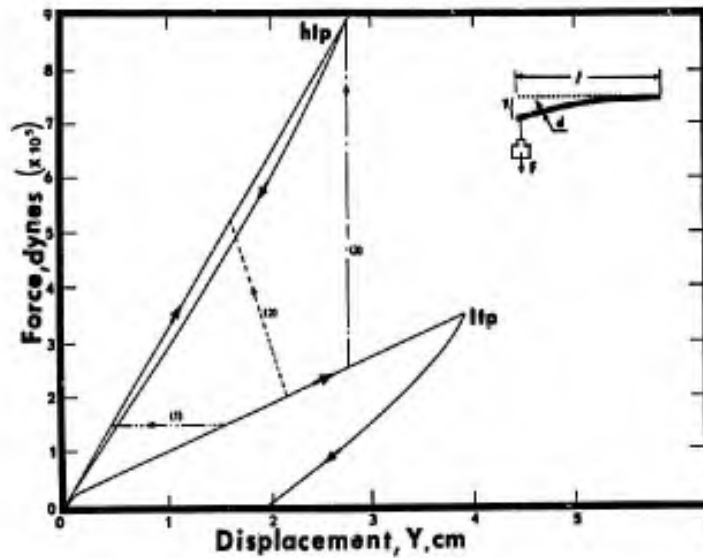
REFERENCES

1. B. A. Bilby and J. W. Christian, The Mechanism of Phase Transformations in Metals. The Institute of Metals, London, 1956, p. 121.
2. J. W. Christian, The Theory of Transformations in Metals and Alloys. Pergamon Press, Oxford, 1965.
3. J. W. Christian, T. A. Read, and C. M. Wayman, "Crystallographic Transformations," Chap. 22 in Intermetallic Compounds, J. H. Westbrook, ed. John Wiley & Sons, Inc., New York, 1967.
4. C. M. Wayman, Introduction to the Crystallography of Martensitic Transformations. The MacMillan Company, New York, 1964.
5. D. S. Lieberman, M. S. Wechsler, and T. A. Read, *J. Appl. Phys.* **26**, 473 (1955).
6. H. Birnbaum and T. A. Read, *Trans. AIME* **218**, 662 (1960).
7. J. W. Christian, *ibid*, p. 787.
8. J. Intrater, L. C. Chang, and T. A. Read, *Phys. Rev.* **86**, 598 (1952).
9. W. B. Cross, Goodyear Aerospace Corp., Akron, Ohio, private communication.
10. D. S. Lieberman, private communication.
11. L. Muldawer and F. Rothwarf, unpublished results.
12. W. J. Buehler, J. V. Gilfrich, and R. C. Wiley, *J. Appl. Phys.* **34**, 1475 (1963).
13. W. J. Buehler, Naval Ordnance Laboratory, White Oak, Maryland, private communication.
14. J. W. Christian, T. A. Read, and C. M. Wayman, *ibid*, p. 446.
15. H. Weinstock, Bachelor of Arts Thesis, Temple University, 1955, unpublished.
16. W. J. Buehler and R. C. Wiley, "The Properties of TiNi and Associated Phases," unpublished report NOL TR 61-75, 3 Aug 61 (AD No. 266607).
17. W. J. Buehler, "Intermetallic Compound Based Materials for Structural Applications," presented at the Seventh Navy Science Symposium: Solution to Navy Problems Through Advanced Technology, held 14-16 May 1963 at U. S. Naval Aviation Medical Center, Pensacola, Florida, Vol. 1, p. 1 of unpublished proceedings (AI No. 657400).
18. D. M. Goldstein, W. J. Buehler, and R. C. Wiley, "Effects of Alloying Upon Certain Properties of 55.1 Nitinol," unpublished report NOL TR 64-235, 28 May 1965 (AD No. 618681).
19. A. G. Rozner and W. J. Buehler, "Low Temperature Deformation of the TiNi Intermetallic Compound," unpublished report NOL TR 66-38, 1 March 1966 (AD No. 633220).
20. W. J. Buehler and F. E. Wany, "Study of Transition Element Intermetallic Compounds," presented at the Ninth Navy Science Symposium, Washington, D.C., 5-6 May 1966.
21. Frederick E. Wang, ed., Proceedings of Symposium on TiNi and Associated Compounds, held at Naval Ordnance Laboratory, Silver Spring, Maryland, 3-4 April 1967, NOL TR 68-16. These proceedings have been published in the *J. Appl. Phys.* **39** (1968).

ROTHWARF, AUERBACH and FORD

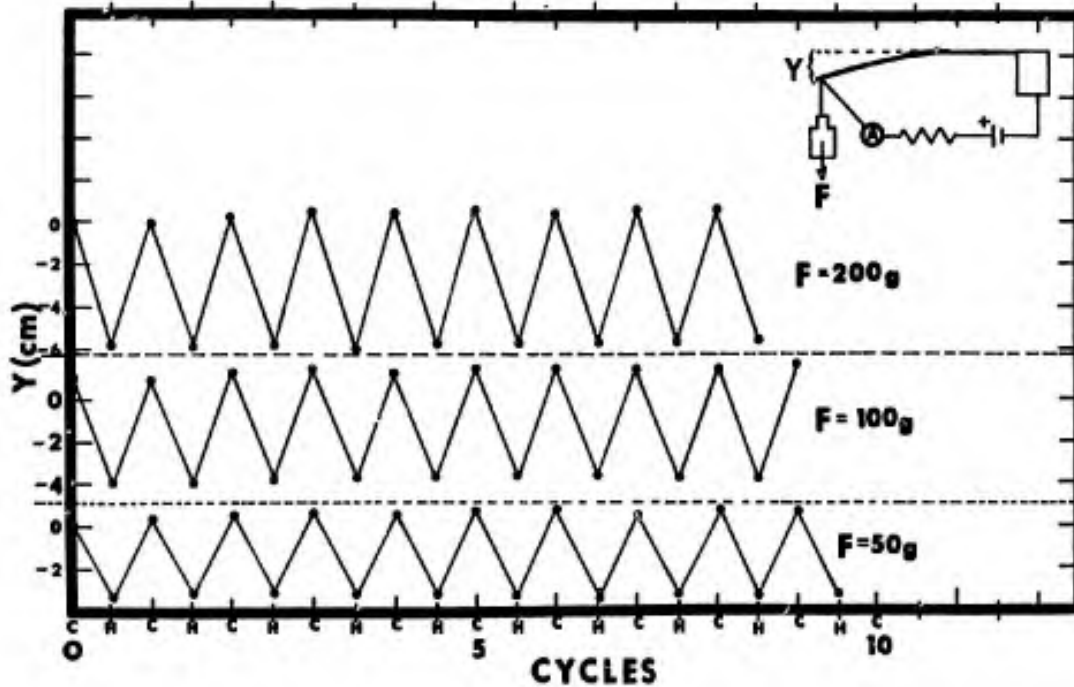
22. F. Rothwarf and L. Muldower, J. Appl. Phys. 33, 2531 (1962).
23. Frederick E. Wang, J. Appl. Phys. 38, 822 (1967).
24. John Prescott, Applied Elasticity, Dover Publications, New York, 1946, pp 34-37, 50-52, 59-60.
25. V. L. Maleev, Machine Design, International Textbook Co., Scranton, Pa., 1939, Chap. 17.
26. R. F. Fogt, Trans. A.S.M.E., June 1934, RP-56-4, p. 469.
27. H. A. Berman, E. D. West, and A. G. Rozner, J. Appl. Phys. 38, 4473 (1967).
28. R. E. Wang, W. J. Buehler, and S. J. Pickart, J. Appl. Phys. 36, 3232 (1965).
29. D. P. Dautovich, Z. Melkvi, G. R. Purdy, and C. V. Stager, J. Appl. Phys. 37, 2513 (1966).
30. R. J. Wasilewski, S. R. Butler, and J. E. Hanlon, J. Metals 17, 1059 (1965).
31. W. J. Buehler and W. B. Cross, "55-Nitinol-Unique Alloy Wire for Self-Erectible Space Structures." Presented at the Wire Association Inc., Non-ferrous Dib. Meeting, Huntsville, Alabama, 3-4 April 1968.
32. H. S. Carslow and J. C. Jaeger, Conduction of Heat in Solids, 2nd ed. Oxford University Press, London, 1947, Chap. 4, pp 139-140.
33. J. F. Goff, J. Appl. Phys. 35, 2919 (1964).
34. F. Rothwarf, A. Auerbach, and D. Ford, "The Use of Martensite Materials in the Design of Thermally Activated Springs," Frankford Arsenal Report M68-38-1, November 1968.
35. C. Friedman, "Heat Conduction Properties of a Thermally Activated Fuze Device," Frankford Arsenal Report M68-38-2, November 1968.

ROTHWARF, AUERBACH and
FORD



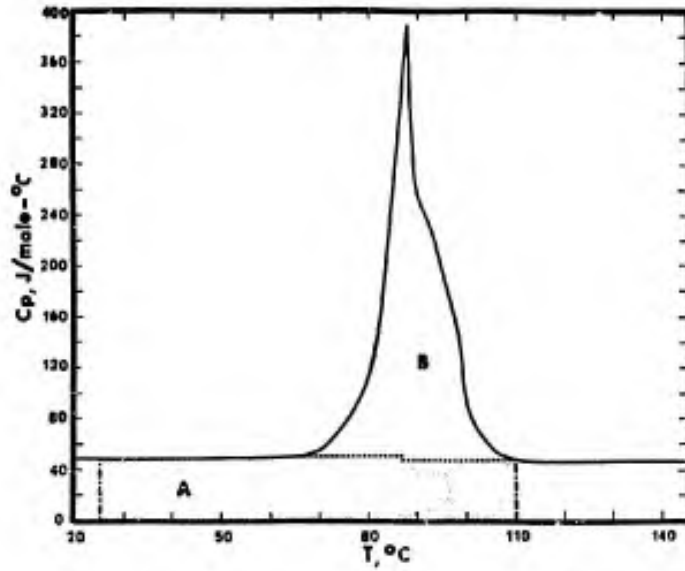
- Three different modes of spring operation are indicated - (1), (2), and (3).
- (1) A given load can undergo a cyclic displacement on heating and cooling;
 - (2) A large increase in force is possible if the rod is constrained to a nearly constant displacement on heating to the htp;
 - (3) An intermediate case between (1) and (2).

Figure 1. Force vs Displacement Curves for a Nitinol Rod (0.254 cm diameter, 11.2 cm long from point of support to point at which the weight is suspended) in its High Temperature Phase (htp) at 150° C, and Partially Transformed to its Low Temperature Phase (ltl) at 23° C



Different sets of measurements for various masses suspended from the end of the rod indicate that the greater the load, the greater the work one can obtain from the process.

Figure 2. Displacements for a Number of Heating and Cooling Cycles for a NiTi Rod



The area labelled B represents the heat of transformation, λ_m .

Figure 3. Specific Heat of NiTi vs Temperature

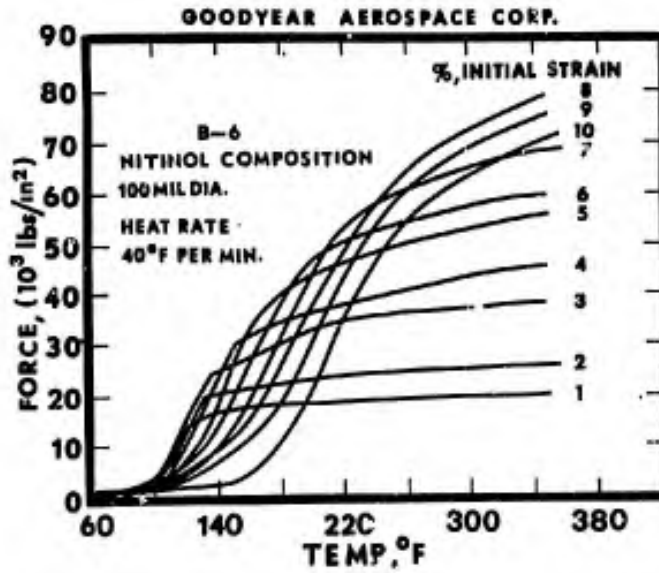


Figure 4. Force required to Maintain a Fixed Strain, ϵ , in a 100-mil diameter Nitinol Rod vs Temperature

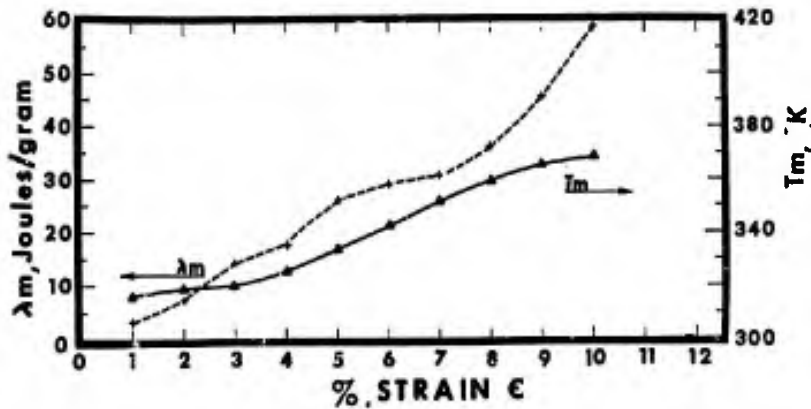


Figure 5. The Heat of Transformation, λ_m , predicted from the Clausius-Clapeyron Equation, vs Strain, ϵ ; the Midpoint Temperature, T_m , of the Martensite Transformation, on Heating at Constant Strain, vs Strain

THE EFFECT OF UNDIFFERENTIATED MASS
PUNISHMENT OF THE COHESIVENESS OF THE
GROUP AND THE ATTRACTIVENESS OF THE REBEL

WILLIAM B. SEELY, LIEUTENANT COLONEL, INFANTRY
OFFICE OF MILITARY PSYCHOLOGY AND LEADERSHIP
UNITED STATES CORPS OF CADETS
WEST POINT, NEW YORK

This paper will summarize some of the social psychological research conducted in the area of mass punishments and related group factors, and will describe a recent study investigating specific aspects of group dynamics occurring in a mass punishment situation.*

The American Soldier (16) reported results of investigations concerning the use of group punishments in the U.S. Army in World War II. An analysis of reported situations by servicemen indicated that mass punishments were not effective in situations such as punishment of a group for one man who went AWOL, or punishment of a whole unit because a subunit failed an inspection. However, punishment of a small group for failure to pass an inspection tended to be effective in forcing the group to work together and influencing the behavior of the members who caused the group to fail. Other results indicated that a majority of officers questioned believed group punishment to be ineffective under any circumstances. Thus, no firm conclusions were drawn concerning the efficacy of group punishments. The authors suggested that because group punishments are employed to direct informal group controls to enforce a formal position, this area of investigation would lend itself well to further systematic experimentation.

History has shown that on a large scale, effect of mass punishments on group cohesiveness can be unpredictable. Indeed, morale and optimism can increase abnormally as resentment against the punisher leads to determination to succeed and to secure revenge. This apparently occurred in Britain in response to the Nazi blitz in World War II, and a similar reaction apparently occurred in North Vietnam as a result of U.S. bombing there. On the other hand, where the threat of defeat has been overpowering or where the attacks have been

*Originally presented as a thesis in fulfillment of requirements for the degree of Master of Arts at the University of Texas, 1968.
Faculty advisors were Dr. Elliot Aronson and Dr. Robert Helmreich.

SEELY

unexpected or unusual either in intensity or in form, morale and cohesiveness can break down, as occurred in Tokyo and in Hiroshima when they suffered intense and unusual aerial attack at the end of World War II (18). Generalizing to small groups is perhaps not appropriate here, although such historical examples do serve to indicate that the results of punishing a group can be a complex matter.

Some theoretical aspects relating to the problem of group punishment have been investigated extensively in social psychology during recent years, although not necessarily in the specific context of group sanctions. Dollard, et al (7) proposed a frustration-aggression hypothesis, which states generally that frustration, or any condition that directly or indirectly prevents an organism from attaining a desired goal, produces instigations to some form of aggression. The hypothesis further implies that aggression will be more inhibited when the agent of frustration is powerful and capable of retaliation than when he is weak and impotent. Paraphrasing this in a military context, Jones and Gerard (11) stated that soldiers are probably less frustrated when they are "chewed out" by a top sergeant than by an acting squad leader. Berkowitz (1) placed it in the context of family social norms by saying that it was more socially permissible for the father to spank his child than the child to hit his father. Aggression against more powerful adversaries apparently does not pay.

There is considerable additional evidence that aggression is more likely to be expressed toward low-status than high-status instigators of frustration. In paper and pencil tests, identical frustrations caused by parents on one form of the test and siblings on the other, caused the subjects to respond much less aggressively on the items referring to parent-originated frustrations (5). An experiment in a military setting showing this differential expression of aggression was conducted by Thibaut and Reicken (17). Air Force reservists were exposed to a highly realistic situation in which they heard an officer in the Air Force giving another man orders in a highly insulting manner, deliberately calculated to evoke feelings of hostility in anyone who heard what was being said. Each subject was then given the opportunity to talk to the insulting officer. As expected, relatively little aggression was communicated when the insulter was of higher military rank than the subject, whereas a great deal was expressed when he was of lower rank. A simple cue of relative status in a social situation, e.g., a uniform, can operate as a powerful deterrent to the expression of aggression.

Horwitz (8) performed an experiment testing this same idea of using differential power as the source of frustration in a frustrating situation, and he also found that where power of the frustrater was considered by the subjects to be legitimate, the level of expressed hostility by the subjects was low; conversely when the power of the frustrater was not considered to be legitimate, expressed hostility was high.

Such findings, then, would indicate that a group being punished will manifest less overt resistance or aggression toward a higher ranking punisher, or frustrater, than a lower ranking punisher/frustrater. Other findings suggest that arbitrary frustration situations lead to more hostility than nonarbitrary situations, with no reference to the status of the frustrater (13). Cohen (6) found that subordinates tend to be threatened more by the leader's use of power where the situation offers few guidelines and cues for action. When the leader exercises power in a well-defined situation, the individual is less likely to see the situation as threatening. Burnstein and Worchel (3), in an experiment involving groups of subjects exposed to arbitrary and nonarbitrary frustration situations, attempted to determine whether the relative absence of aggression following nonarbitrary frustration was due to lower instigation or greater inhibition. They found that the arbitrary frustrater was more severely rejected than the nonarbitrary one. More interestingly, the subjects' evaluation of the conduct of the experiment, and of themselves, was considerably lower in the nonarbitrary than in the arbitrary condition. This would give support to the greater influence of differential inhibition over differential instigation, since the instigator was held as a constant condition. The more arbitrary the frustration, the more direct the expression of aggression; on the other hand, the less arbitrary the frustration, the more inhibition that takes place, with accompanying internal degradation by the subject of himself and the situation. These findings, then, would generally suggest that unexpected sanctions, or lack of sanctions, taken against group members would be more disrupting and would break down group cohesiveness more than actions or sanctions taken that were expected or predictable.

Referring to examples of community stress, such as famine and bombings, Janis (9) suggested that new behavior patterns can develop in response to this group or mass frustration. Janis (10) also observed in a military situation examples of the way men react to anticipated punishment for showing any signs of anger in the presence of oppressive superiors indoctrinated with the principle that a good military leader must punish any soldier who protests against a frustrating order, no matter how arbitrary or humiliating it may be. During basic training the soldier is taught to expect instant retaliation for the slightest gesture of defiance towards authority. Janis suggested that this sensitivity to difference in military rank becomes ingrained in the soldier's thought and action (10).

Group cohesiveness and deviation from group norms are factors that relate to any investigation of the effects of sanctions taken against a group. Evidence shows that when members of a group strive to satisfy their individual wants through group goals, any deviant member is coerced and deviant behavior is punished (2). Pepitone and Reichling (14) performed an experiment comparing expression and hostility within high-cohesive groups and within low-cohesive

SEELY

groups; their results showed that high-cohesive groups were able to express more hostility than low-cohesive groups, and that hostility expressed by high-cohesive groups was more direct than that expressed by low-cohesive groups. An interesting question arising from this would be, is the obverse also true: do different conditions of perceived ability to express oneself against a hostility-creating situation have any effect on raising or lowering the cohesiveness of the group?

Recent historical examples of group punishment and related factors can be cited in the current Arab-Israeli conflict. A typical situation reported by the news media has been the following: an Israeli military force occupies an Arab village. An Arab saboteur kills some Israeli troops by blowing up a truck; the Israelis, after failing to uncover the culprit, respond in turn by punishing the entire village as a reprisal measure, either by burning down some houses, or otherwise imposing restrictions on the entire village, in order to prevent recurrences of acts of sabotage. Some interesting questions arise out of this: do the Israelis succeed in preventing recurrences, or do they only succeed in making a martyr of the saboteur and crystallizing the feelings of the Arab villagers against the Israeli authority? Is the previous treatment of the villagers in the hands of the occupying Israelis a factor in the resulting attitude of the villagers after the mass punishment? Does the perceived ability by the Arab villagers of the occupying forces to exact punishment have an influence on their reaction to the mass punishment? Does the saboteur receive more support from the other villagers as a result of the punishment imposed by the Israelis, or is he despised for having caused grief for the entire village? In the absence of follow-up information resulting from a complete on-the-spot investigation by making surveys, follow-up studies, taking attitude measures and so forth, one can only surmise what the answers to these questions would be. Even if such an investigation could be performed, what are the relevant factors in such a multifaceted situation?

It was decided to design a laboratory experiment which would provide an examination of some of these factors. The following hypothesis was proposed: If a member of a group performs a rebellious act against higher authority--the identity of the "rebel" being known to the rest of the group but not known to the higher authority--the cohesiveness of the group as well as the group esteem of the rebel will change differentially, depending on certain factors, which are: 1) formal power ascribed to the authority, 2) general manner displayed toward the group by the authority, and 3) whether or not mass punishment is administered to the group by the authority.

It was predicted that in the conditions involving the authority's general manner manifested toward the group, there would be a main effect of higher group cohesiveness, and more liking for the rebel by the group, when the authority was harsh and tyrannical in manner than when he was mild and fair in manner. This was based

SEELY

on the reasoning that the harsh authority would evoke feelings of hostility in the subjects, and the rebel's act would serve as a projected act of perceived retaliation against the harsh authority. Likewise, the rebel's act performed against a fair authority, who had been treating the group well, would be reacted against by the subjects in the form of rating the rebel lower, and also generalize to disruption and confusion as a result of this unexpected act, producing lower group cohesiveness.

Also predicted was an interaction of rank and punishment in both group cohesiveness and in liking for the rebel. With a punishing lower-ranking authority, group cohesiveness would increase and the rebel would be liked more than with a non-punishing lower-ranking authority, since it was expected that the subject would perceive the lower-ranking authority as relatively "reachable", or relatively close to his own level. The rebellious act would be perceived as a vicarious "getting even" with the punisher; the subject would mentally support the deed of the rebel performed against the lower-ranking authority, who is the tangible, reachable symbol of the establishment. On the other hand, it was predicted that with a higher-ranking authority, who was considerably higher in the power structure and "out of reach", any rebellious act would be considered suicidal, as it were. A punishing higher-ranking authority would only confirm their worst suspicions about how someone high in the power structure would act; this would result in a lower group cohesiveness rating and a lower rating for the rebel. But a non-punishing higher-ranking authority would be perceived as reacting to the rebellious act in a manner totally unexpected from someone so high in the power structure. The subject would experience feelings of relief and having "gotten away with it", considering the authority figure a "patsy", with resulting higher group cohesiveness and a higher rating for the rebel.

To explore the hypothesis the following situation was created: a group of military trainees, all at the same experience level in the service but not previously acquainted with each other, would be brought together ostensibly for a discussion session with instructions that they were to rate the group and each individual at the end of the discussion. Each group would consist of five naive subjects and one accomplice. The discussion moderator, who also initially instructs the group on the procedure for the discussion, would either wear the uniform of a captain or a staff sergeant, depending on the condition. The discussion moderator also would act either in an extremely harsh and tyrannical fashion, or in a fair and moderate fashion, also depending on the condition. After conducting the discussion with the group, the discussion moderator would leave the room on a pretext, and during his absence the accomplice in the group would write a profanity on the blackboard. This would be the act of rebelliousness. Upon the return of the moderator, he would either punish the entire group for the deed, or admonish the group and not punish them. A questionnaire would then be

SEELY

given to the members of the group by a confederate introduced as a civilian psychologist, after the moderator left the room again. This questionnaire would be given in order to obtain the dependent measures of 1) the cohesiveness of the group compared across all conditions, and 2) the degree of liking/disliking for the rebel compared across all conditions. Thus the experiment is a 2x2x2 factorial. Variable A, rank of the authority, has two levels: higher rank (captain) and lower rank (staff sergeant). Variable B, prior manner of the authority toward the group, has two levels: harsh and mild. Variable C, punishment by the authority, has two levels: punishment and no punishment.

The experiment was conducted at the Personnel Research Laboratory at Lackland Air Force Base. 114 men, who were Air Force enlistees in their sixth day of training, were used as naive subjects. The discussion moderator, dressed as either an Air Force captain or an Air Force staff sergeant, briefed each group by telling them that they were to participate in a short group discussion exercise which was part of a research project being conducted by the Personnel Research Laboratory on the effectiveness of different methods of communication. The actual purpose for the discussion group set-up was to provide a vehicle to permit interaction of the group members and the discussion moderator, and to provide a rationale for placing the group together for the manipulation. The group was told that they had been especially selected for the exercise and that their performance would be rated and the results compared with those of other similar groups participating in the research. This was done in order to create an initial degree of group spirit and cohesiveness and to add interest and incentive to their participation. They were further briefed that upon completion of their discussion, a civilian research psychologist would give them a questionnaire supposedly designed to elicit their comments as to the effectiveness of the group discussion method of communication. This was done in order to provide a cover for introducing the dependent variable, which provided the necessary measures for the experimental conditions.

The discussion was then conducted by the moderator who asked questions relating to a general discussion topic, giving everyone in the group, including the rebel, a chance to talk at least once in order to provide a basis for rating the group members. At the end of 5-7 minutes the moderator concluded the discussion and stepped out of the classroom, ostensibly to look for the psychologist. When the moderator closed the door, the rebel looked around furtively for a few seconds, then jumped up, ran up to the blackboard, and wrote "GO TO HELL" in large letters, then sat down again. The discussion monitor then reentered the classroom, pretended to notice the profanity on the board, and then thoroughly lambasted the group as a whole, being careful not to permit anyone to indicate who the culprit was. The moderator accused the group of conspiracy and otherwise made it clear that he thought the entire group was to blame. Then the moderator either told the subjects they would all get a stiff punishment,

or he would not punish the group, passing it off by giving the impression that it was too much "red tape" to go through to get them punished. Once this was completed and the profanity was erased, the psychologist-accomplice entered the room and the moderator left again. This was done in order to minimize any biases concerning the moderator from affecting the subjects' ratings on the questionnaire.

Upon completion of the questionnaire, the subjects were then thoroughly debriefed by the experimenter as to the true nature of the experiment. Virtually all the subjects displayed relief when learning of the true nature of the experiment, and most showed considerable interest in its outcome by virtue of their comments and questions. Six subjects out of 120 used were dropped from the results because of suspicions expressed by them during the debriefing concerning the true nature of the experiment.

The questionnaire given to all subjects just prior to the conclusion of the experiment consisted of seven items. Three items were critical and were those used to determine the cohesiveness of the group and the degree of liking or disliking for the rebel. The items were scaled from 1 to 7, with each member of the group required to rate all the other members of the group for each item. Degree of group cohesiveness was determined by totalling the mean scores of all group members, excluding the ratings of the rebel, for the three critical items and determining the mean within each cell. Degree of liking for the rebel was determined by totalling the raw score ratings for the rebel by the other group members in the three critical items and determining the mean score rating each cell. One other item was designed to examine any significant results attributable to birth order effects; no significance was found in this regard.

The results only partially confirmed the tentative predictions. The comparison of group cohesiveness, or liking of the group by its members, was made by an analysis of variance of the sum of the individual means of three critical dependent measure items on the questionnaire, excluding the ratings of the rebel by the other members. The means are shown in Table I. The results of the analysis are shown in Table II. The analysis showed three areas of significance: a harsh-mild main effect ($p < .0001$), with the harsh moderator producing a less cohesive group; a rank-punishment interaction ($p < .05$); and a rank-harshness-punishment triple interaction ($p < .05$). The highly significant general harshness effect was counter to that predicted initially. It had been caused by the harsh treatment producing a feeling of derogation within the group and subsequent feeling of low worth. The group members were told by the moderator that they were in effect worthless; the groups in the harsh condition may have internalized this verbal abuse, and reflected this in their rating of the group. An alternate explanation for the low cohesiveness of the harsh groups is that during the discussion session the members of the harsh group were not permitted to

SEELY

talk freely to express their opinions and to share their views with the other members. On the other hand, in the mild condition, the group had a free exchange of ideas and group participation, which may have an overriding factor in the evaluation of the group by the members. As seen in Table I, the mild conditions across rank and punishment all ranked high in cohesiveness, with almost identical mean scores ($\bar{X} = 16.34, 16.07, 16.35, \text{ and } 16.05$).

The significant interactions that occurred with regard to group cohesiveness tend to support the predicted effect. One interpretation considered to be plausible is the following: again referring to Table I, it appeared that a harsh sergeant, as compared to a harsh captain, was not perceived as a threat to the group as such, in the punishment condition. He was apparently seen as closer to the group in status, and secondly, he was acting in a manner already familiar and expected by the trainees. Because of their being accustomed to such treatment from a harsh sergeant, the group members did not perceive this as demeaning treatment to the group, and did not suffer a loss of self-esteem; they tended to band together against this common, familiar threat, and were relatively high in cohesiveness as a result ($\bar{X} = 15.46$). A harsh sergeant in the no-punishment condition, on the other hand, may have caused an unexpected situation by not punishing what was surely a punishable deed. It may have been perceived as an incongruous, confusing situation which produced no banding together of the group members, resulting in lower group cohesiveness ($\bar{X} = 13.92$).

The treatment of the group by a harsh captain appeared to have the opposite effect on group cohesiveness than by a harsh sergeant. The high-ranking moderator was on a higher authority level, and less familiar to the subjects than a lower-ranking sergeant with whom they had more experience. A captain may have been considered more out of reach, less accessible, and, with more perceived power, impossible to fight back against by showing group solidarity. When the captain told them that they were worthless, and were punished, the group members in effect may have believed it, and with the feeling of derogation of the group there resulted a low group self-esteem and a lack of cohesiveness ($\bar{X} = 11.71$). On the other hand, the harsh captain in the no-punishment situation was perceived as not so unusual, since the normal operating cues for an officer were not as familiar to the subjects as were the expected reactions of a harsh sergeant. Since the group was not punished, the members possibly did not feel the loss of self-esteem experienced when they were punished, and thus the cohesiveness of the group remained higher.

The comparison of liking for the rebel consisted of an analysis of variance of the sum of the raw score ratings of the rebel by the other group members, for the three critical dependent measure items. The means are shown in Table III. The results of the analysis are shown in Table IV. The analysis showed that a significant finding

was a main effect of punishment ($p < .05$), i.e. the rebel was liked better under a no-punishment condition than under a punishment condition, independent of either rank or prior manner of the discussion moderator; this is counter to the prediction of an interactive effect of rank and punishment on liking for the rebel. The means in Table III show that in every case except for the harsh captain, there was an indication of differential effect of punishment and no punishment on liking for the rebel. In the case of the harsh captain condition there was a slight indication of liking the rebel more under the punishment condition ($\bar{X} = 6.40$) than under the no-punishment condition ($\bar{X} = 6.21$), although the difference does not begin to approach significance. A possible explanation for the practically level rating of the rebel under the harsh captain over the two punishment conditions is that the rebellious act against such a tough, high-ranking, untouchable, aloof moderator had such a shattering effect on the subjects, that they were in a state of shock; all that transpired after that, i.e., the act of either punishing or not punishing, made little difference in the rating of the rebel.

The punishment main effect significance is clearly the dominating tendency and washes out any difference attributable to the other variables. If the group was punished, the source of their frustration (the rebel) was going to suffer accordingly. If the group was not punished, which was an action contrary to the subjects' expectations, the rebel was perceived to have gotten away with something and was accordingly not rated as low by the group members as in the punishment condition.

It should be noted that the ratings in Table III are on a scale from 3 to 21; disliking very much to liking very much. Thus, the rating of the rebel, which is significantly higher in one condition than in another, cannot be considered so much to be a greater liking for the rebel, as it is a "less disliking". In no condition was the rating of the rebel higher than 7.64 (i.e., the sergeant-mild-no punishment condition) on a scale of 3 to 21. The rebel was always rated lower than the group mean, in all conditions.

Since rank did not make a significant difference in liking for the rebel, it appears that the prediction concerning effects of rank interacting with punishment on liking for the rebel was incorrect. This may have been caused by an insufficient difference in the perception by the subjects of the relative hierarchical status between a sergeant and a captain. Both ranks were apparently perceived to be acting in accordance with their vested authority, or the authority that the trainee subjects had become accustomed to seeing in their short time in the service. Therefore no greater degree of hostility was expressed toward the vested authority in the form of rating the rebel higher, in terms of rank differences of the moderator. However, it was felt that an attempt to either raise the officer's rank or lower the NCO's rank in the experimental design would

SEELY

have evoked too much suspicion in the subjects.

The harsh-fair main effect with respect to liking for the rebel also was not significant. Again it appears that the portion of the prediction concerning the effects of authority manner on liking of the rebel was inaccurate. A possible explanation is that the harsh treatment they were subjected to was something they had grown accustomed to suffering, and that it had become a way of life in their short six days in the Air Force. The mild treatment was what they were more accustomed to in civilian life; once the moderator cued them to his mild manner, perhaps it also did not appear to be out of line, particularly since the setting (a laboratory classroom) was a different one from where they had been receiving the harassing treatment up to that time.

From the results and discussion thus enumerated, the following conclusions are suggested:

1) A rebellious act against authority can best be handled, in terms of forcing the group to derogate the rebel and otherwise not support his actions, by immediate and forceful punishment imposed on the group by the authority. Prestige of the authority and manifested manner of the authority are of some effect, but not significantly so.

2) The breaking down of group cohesiveness--cohesiveness being manifested in defiance of authority as a result of the action by the rebel--may occur if the group is subjected to unexpected, or unfamiliar, treatment, as opposed to routine, predictable treatment. This is suggested by the interaction of rank and punishment in the harsh treatments of the experiment, where there was a tendency for group cohesiveness to be less when the behavior of the authority was apparently not that expected in the usual situation (for example, the results suggested that a harsh sergeant who punished the group did not reduce group cohesiveness as much as a harsh sergeant who did not punish the group; likewise, there was a suggestion that a harsh captain who punished the group reduced group cohesiveness more than a harsh captain who did not punish the group). Thus, a group may be more cohesive when it can more readily cope with the situation and can recognize the pattern of events with expected outcomes. This would give support to earlier findings (13, 8, 3, 6).

This experiment also tends to support what Janis (9) hypothesized regarding the attitude formation of the basic military trainee. He commented that the inductee (referring to the Army) faces a new set of demands from the social environment, a new sub-culture, one which he must rapidly adjust to, adhering to new attitudes if he is to escape punishment. It appears that the present experiment showed that even six days was quite sufficient to acquire these new attitudes necessary for survival.

SEELY

Possible implications for the future are indicated by the results of this study. Useful information was obtained which can serve as a starting point for future investigations in this field. The question which needs special emphasis in any future study is that of the effect of punishment under different circumstances. In future studies it would be useful to measure varied degrees of punishment on a group in order to get a better delineation of differences in effects, keeping in mind also the important variables of ascribed power, and general attitude or leadership style manifested by the power source.

BIBLIOGRAPHY

1. Berkowitz, L. (1958). The expression and reduction of hostility. Psychological Bulletin, 55, 257-283.
2. Berkowitz, L., and R. C. Howard (1959). Reactions to opinion deviates as affected by affiliation need and group member interdependence. Sociometry, 22, 81-91.
3. Burnstein, E., and P. Worchel (1962). Arbitrariness of frustration and its consequences for aggression in a social situation. Journal of Personality, 30, 528-541.
4. Cartwright, D., and A. Zander, eds. (1960). Group Dynamics, 2nd Edition. Evanston, Ill.: Row, Peterson and Company.
5. Cohen, A. R. (1955). Social norms, arbitrariness of frustration and status of agent of frustration in the frustration-aggression hypothesis. Journal of Abnormal and Social Psychology, 51, 222-226.
6. Cohen, A. R. (1959). Situational structure, self-esteem and threat-oriented reactions to power. In D. Cartwright, ed., Studies in Social Power. Ann Arbor: The University of Michigan, pp. 35-52.
7. Dollard, J., L. Doob, N. Miller, and R. Sears (1939). Frustration and Aggression. New Haven: Yale University.
8. Horwitz, M. (1958). The veridicality of liking and disliking. In R. Taguiri, and L. Petrullo, eds., Person Perception and Interpersonal Behavior. Stanford: Stanford University Press.
9. Janis, I. L. (1945). Psychodynamic aspects of adjustment to Army life. Psychiatry, 8, 159-176.
10. Janis, I. L. (1966). Stress and Frustration. Unpublished manuscript. Yale University.
11. Jones, E. E., and H. B. Gerard (1967). Foundations of Social Psychology. New York: John Wiley and Sons, Inc.
12. Krech, D., R. S. Crutchfield, and E. L. Ballachey (1962). Individual in Society. New York: McGraw-Hill Book Company.
13. Pastore, N. (1952). The role of arbitrariness in the frustration-aggression hypothesis. Journal of Abnormal and Social Psychology, 47, 728-731.
14. Pepitone, A., and G. Reichling (1955). Group cohesiveness and the expression of hostility. Human Relations, 8, 327-337.

SEELY

15. Pepitone, A. (1964). Attraction and Hostility. New York: Atherton Press.
16. Stouffer, S. A., E. A. Suchman, L. C. DeVinney, S. A. Star, and R. M. Williams, Jr. (1949). The American Soldier: Adjustments During Army Life. Volume I of Studies in Social Psychology in World War II. Princeton: Princeton University Press.
17. Thibaut, J. W., and H. W. Riecken (1955). Authoritarianism, status, and the communication of aggression. Human Relations, 8, 95-120.
18. Warnken, R. D. (1965). The psychological effect of mass casualties. In Military, Political and Psychological Implications of Massive Population Casualties in History, Volume IV. Washington, D. C.: Historical Evaluation and Research Organization, pp. 59-104.

		Harsh	Mild
Punishment	Captain	11.71	16.34
	Sergeant	15.46	16.07
No Punishment	Captain	14.57	16.35
	Sergeant	13.92	16.05

*Rating scale runs from 3 to 21 (the sum of 3 scores on a scale of 1 to 7). Mean of harsh cells is 13.92. Mean of mild cells is 16.20.

Table I. Group Cohesiveness: Cell means of the sum of the individual means of critical dependent measure questions, excluding ratings of the rebel*.

Source	df	M.S.	F	p
Total	113	9.279		
Between	7	37.051		
A (Rank)	1	11.355	1.5253	n.s.
B (Harshness)	1	148.804	19.9877	<.0001
C (Punishment)	1	3.063	.4115	n.s.
AB	1	23.958	3.2180	n.s.
AC	1	34.948	4.6943	<.05
BC	1	3.072	.4127	n.s.
ABC	1	34.157	4.5880	<.05
Within	106	7.445		

Table II. Group Cohesiveness: Analysis of variance of the sum of the individual means of critical dependent measure questions, excluding ratings of the rebel.

		Harsh	Mild
Punishment	Captain	6.40	5.62
	Sergeant	4.71	4.87
No Punishment	Captain	6.21	7.36
	Sergeant	6.87	7.64

* Rating scale runs from 3 to 21 (the sum of 3 scores on a scale of 1 to 7). Mean of punishment cells is 5.40. Mean of no-punishment cells is 7.02.

Table III. Liking for Rebel: Cell means of the sum of the raw score ratings of the rebel by the other group members for critical dependent measure questions*.

Source	df	M.S.	F	p
Total	113	16.963		
Between	7	16.720		
A (Rank)	1	3.980	.2344	n.s.
B (Harshness)	1	2.943	.1733	n.s.
C (Punishment)	1	74.738	4.4017	<.05
AB	1	.578	.0340	n.s.
AC	1	20.215	1.1906	n.s.
BC	1	11.569	.6814	n.s.
ABC	1	3.021	.1779	n.s.
Within	106	16.979		

Table IV. Liking for Rebel: Analysis of variance of the sum of the raw score ratings of the rebel by the other group members for critical dependent measure questions.

CHEMILUMINESCENT ORGANIC PHOSPHIDES

GILBERT P. SOLLOTT, JONATHAN L. SNEAD, and RICHARD A. STRECKER
PITMAN-DUNN RESEARCH LABORATORIES, FRANKFORD ARSENAL
PHILADELPHIA, PENNSYLVANIA

In 1959, Issleib and Tzschach reported that lithium dicyclohexylphosphide (LHP = R_2PLi ; R = cyclohexyl) yields an "extremely" strong yellow-green chemiluminescence with traces of oxygen (1). This was followed by reports in 1961 that compounds of the type, $R(Li)P-(CH_2)_n-P(Li)R$, chemiluminesce as intensely as LHP when R = cyclohexyl and n = 5 (2), and only weakly when R = phenyl (3). The chemiluminescence spectra were not reported, and no further investigation of the chemiluminescence of these compounds has been published. The subject of phosphide chemiluminescence has been entirely overlooked in recent reviews of chemiluminescent reactions (4,5), and is characterized to date by relative obscurity. In general, organophosphorus compounds have not been the subject of chemiluminescence research.

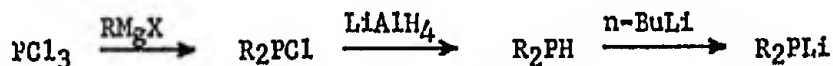
The present work was undertaken to determine the variability of the emission characteristics of organic phosphides with change in molecular structure; to identify the emitting species responsible for the observed chemiluminescence; and to gain some insight into the mechanism of the chemiluminescent oxidation.

RESULTS AND DISCUSSION

Synthesis and Chemiluminescent Characteristics of Organic Lithium Phosphides

LHP was originally prepared (1) by the action of phenyllithium on $(C_6H_{11})_2PH$ obtained by $LiAlH_4$ reduction of $(C_6H_{11})_2P(S)-P(S)(C_6H_{11})_2$. The disulfide was prepared from cyclohexyl Grignard reagent and $PSCl_3$. We have found it more convenient, however, to prepare in situ the phosphine by $LiAlH_4$ reduction of the phosphinous chloride, $(C_6H_{11})_2PCL$, formed from PCl_3 and cyclohexyl Grignard reagent. All other phosphines employed in this work were similarly prepared. Lithium dicyclopentylphosphide could not be obtained from phenyllithium and the secondary phosphine, and was unlike LHP

in this respect. The compound was obtained using the more basic *n*-butyllithium, and in general, all phosphides with the exception of LHP were prepared with this reagent. The following represents the sequence of reactions employed in the preparation of the phosphides.



We have discovered that lithium diphenylphosphide is a strong emitter when precipitated from petroleum ether. This compound was previously isolated as the dioxanate, and as such did not exhibit chemiluminescence (1). We have also obtained the unsolvated di-*p*-tolylphosphide, and in the alkyl series, *n*-butyl-, *s*-butyl-, and *t*-butylphosphides from petroleum ether, and observed their chemiluminescence. The tolylphosphide was comparable to phenyl in emission intensity, while the alkylphosphides were generally weaker. The *t*-butylphosphide showed solubility in ethyl ether, and did not chemiluminesce when precipitated from that solvent due to co-crystallization with solvent. Lithium dicyclopentylphosphide, however, was found to be insoluble in ether, like LHP, and chemiluminesced strongly when formed in that solvent. Lithium dicycloheptylphosphide, precipitated from petroleum ether, proved to be a weak emitter.

Besides the requirement that the phosphide molecule be unsolvated if it is to chemiluminesce, the presence of a suitable cyclic group on phosphorus apparently is necessary if the phosphide is to be a strong emitter. Table I summarizes the luminescence data obtained on the new phosphides as well as LHP.^a LHP and the cyclopentylphosphide produced an unusual type of chemiluminescence spectrum consisting of two broad bands, one, relatively strong (primary emission), the other, weak (secondary emission). The latter had peak intensities approximately 20% of the former. In the case of the remaining phosphides, the secondary bands were extremely weak, and were either undetected or poorly defined in the region, 450-500 m μ . LHP, exposed under dry nitrogen to traces of oxygen, was found to chemiluminesce with intensities comparable to that displayed by tetrakis(dimethylamino)ethylene (7) in air. The duration of the emission of the aromatic phosphides was noticeably shorter than that of LHP.

^aK. Issleib and F. Krech (6) have reported the preparation of lithium di-*t*-butylphosphide in petroleum ether without mentioning that the compound chemiluminesces.

Table I. Chemiluminescence of R₂PLi

R	Color of Emission	Relative Intensity ^a	Primary Emission $\lambda_{\max.} \pm 3, \text{m}\mu$	Secondary Emission $\lambda_{\max.} \pm 3, \text{m}\mu$
cyclopentyl	yellow	strong	556	479
cyclohexyl (LHP)	yellow-green	very strong	531	463
cycloheptyl	blue-green	medium	507	b
phenyl	yellow	strong	558	c
p-tolyl	yellow	strong	555	b
t-butyl	yellow-green	medium	532	c
s-butyl	light blue	weak	456	c
n-butyl	yellow-green	very weak	525	c

^aVisual comparison. The compounds were exposed under dry nitrogen to traces of oxygen. ^bNot detected. ^cPoorly defined in the region, 450-500 $\text{m}\mu$.

The data in Table I show that the wavelength of the emitted light is sensitive to relatively minor change in the structure of the organic group. Shifts of the primary emission band of approximately 60 $\text{m}\mu$ and 70 $\text{m}\mu$ to longer wavelength were obtained in going from the s-butyl group to the n-butyl and t-butyl groups, respectively. Going from cycloheptyl to cyclohexyl to cyclopentyl produced successive red shifts of approximately 20 $\text{m}\mu$ each. The wavelengths obtained for phenyl and p-tolyl, however, were nearly identical.

Since the wavelength for phenyl [σ^* value, +0.60 (8)] was practically the same as that obtained for the cyclopentyl group [σ^* value, -0.20 (8)], no simple correlation is seen to exist between wavelength of the emissions in general (Table I) and the polar substituent (σ^*) constants (8) for the organic groups. The effect exerted on the chemiluminescence by the organic group attached to phosphorus is likely a combination of resonance and steric effects superimposed on inductive effects to which the σ^* constants are essentially related. Steric effects would alter the bond angles (thus the hybridization of phosphorus), and could thereby affect the chemiluminescent oxidation. Resonance effects such as hyperconjugation involving the phosphorus 3d orbitals should also be important. Although the increased wavelength of the emission of the cyclopentylphosphide over the cyclohexylphosphide (Table I) is in accord with

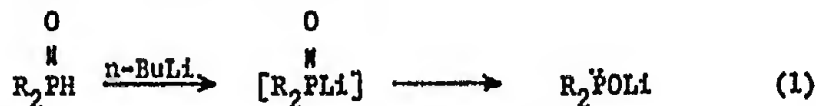
the σ^* values for cyclopentyl and -hexyl [-0.20 and -0.15, respectively (8)], the increase may be due to the effect of delocalizable " π " electrons of cyclopentyl, as compared to the lesser effect of the hyperconjugative type of resonance interaction presumably shown by cyclohexyl (9). In the case of the alkyl groups, where the predicted increase in wavelength would be $n\text{-C}_4\text{H}_9 < s\text{-C}_4\text{H}_9 < t\text{-C}_4\text{H}_9$ based on their σ^* values [-0.13, -0.21, and -0.32, respectively (8)], emission occurred at lowest wavelength in the case of $s\text{-C}_4\text{H}_9$ (Table I). The behavior shown by this series, moreover, cannot be attributed solely to steric or hyperconjugative effects.

Fluorescence and Electron Spin Resonance Studies, Emitting Species, and Mechanism of Phosphide Chemiluminescence

LHP which is slightly oxidized (as isolated in this work) produced a fluorescence spectrum (after subsidence of the chemiluminescence emission) consisting of two broad bands with maxima coinciding with those of the phosphide chemiluminescence spectrum. Continued exposure of LHP to traces of oxygen caused the strongly chemiluminescent, light-yellow powder to convert to a white solid which exhibited only the secondary component of the chemiluminescence spectrum (Table I). This served as evidence that two different species produce the primary and secondary emissions, and that the primary emitter arises prior to the secondary emitter en route to the final oxidation product.

The secondary emissions in the chemiluminescence spectra of LHP and its cyclopentyl homolog were found to correspond reasonably well with the fluorescence of solid lithium dicyclohexyl- and dicyclopentylphosphinates [$\text{R}_2\text{P}(\text{O})\text{OLi}$; $\text{R} = \text{C}_6\text{H}_{11}$ and C_5H_9 , respectively] (Table II). The phosphinates were isolated as the final products of the controlled oxidation of the phosphides, and it appears that electronically activated phosphinate molecules may be responsible for the secondary chemiluminescence emissions.

Solid lithium dicyclohexylphosphinite ($\text{R}_2\text{P}(\text{O})\text{Li}$; $\text{R} = \text{cyclohexyl}$)^a, obtained by the interaction of *n*-butyllithium with dicyclohexylphosphine oxide (eq. 1), was discovered to be very weakly chemiluminescent at 490 $\text{m}\mu$, the wavelength differing from those encountered in LHP chemiluminescence (Table II).



^aR = cyclohexyl whenever R is used hereinafter.

Table II. Chemiluminescence and Fluorescence of Organophosphorus Compounds

Compound	Chemiluminescence $\lambda_{\text{max.}} \pm 3, \text{ m}\mu$	Fluorescence $\lambda_{\text{max.}} \pm 3, \text{ m}\mu$
$(\text{C}_6\text{H}_{11})_2\text{PLi}$ (LHP)	463 ^a , 531 ^b	
$(\text{C}_6\text{H}_{11})_2\text{POLi}$	490	
$(\text{C}_6\text{H}_{11})_2\text{P(O)OLi}$		460
$(\text{C}_5\text{H}_9)_2\text{PLi}$	479 ^a , 556 ^b	
$(\text{C}_5\text{H}_9)_2\text{P(O)OLi}$		470

^aSecondary emission. ^bPrimary emission.

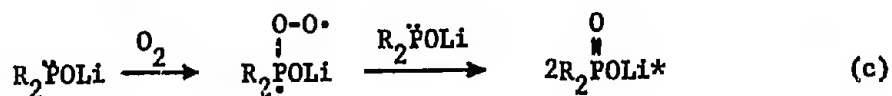
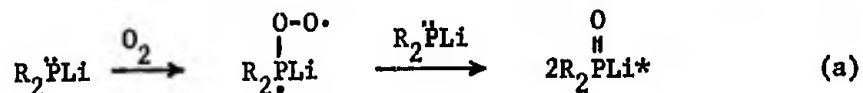
The phosphinite produced no fluorescence near 531 $\text{m}\mu$,^a the wavelength of the primary chemiluminescent emission of LHP. Thus, R_2POLi^* is not considered to be the species producing the primary component of the phosphide chemiluminescence spectrum. It is suggested, rather, that the metastable tautomer, $\text{R}_2\text{P(O)Li}^*$, is produced during the chemiluminescent oxidation (below), and is the emitting species.

When the phosphinite was co-precipitated with LHP upon reaction of n-butyllithium with the phosphine oxide in the presence of unoxidized dicyclohexylphosphine, the solids were observed to glow in a limited oxygen atmosphere, with a weak, green emission that quickly changed to light blue. The latter emission corresponded in wavelength (463 $\text{m}\mu$) to both the secondary emission of the phosphide chemiluminescence, and the fluorescence of the phosphinate

^aSome fluorescence generally occurred in the region of 460 $\text{m}\mu$, but this may be due to a small amount of $\text{R}_2\text{P(O)OLi}$ present as contaminant.

[R₂P(O)OLi] (Table II). Since the oxidation of R₂POLi in the absence of R₂POLi did not produce the secondary (blue) chemiluminescence emission, this behavior is understandable on the basis that phosphinite and phosphide oxidations are intermolecular processes involving pairs of salt molecules.

The following sequence is suggested to account for the observed chemiluminescence emissions of LHP and the phosphinite.



This sequence is based on the assumption that R₂POLi and R₂POLi, entirely free of oxidation products, do not fluoresce at 531 and 490 mμ, respectively. Steps (a), (b), and (c) are similar to the scheme proposed for the air oxidation of secondary phosphines to phosphine oxides (10). R₂P(O)Li*, generated in step (a) might undergo emission prior to, or simultaneously with tautomerization to R₂POLi. Thus



The species, R₂P(O)Li*, arising in step (b) would be essentially nonluminescent (as a result of energy transfer), or alternatively generated as a ground-state molecule, based on the fact that the blue emission attributed to R₂P(O)OLi* is visually observable. Similarly,

one of the pair of excited molecules depicted as arising in each of steps (a) and (c) may be either nonluminescent or alternatively generated in the ground-state. The species, $R_2P(O)OLi^*$, produced in steps (b) and (c) would emit at different wavelengths (463 and 490 $m\mu$, respectively), possibly as a result of different solvation effects in the solid state.

Finally, esr data confirm the free-radical character of the chemiluminescent process. Oxidation of several phosphides (s-butyl, cyclohexyl, and phenyl) in the solid state produced a free radical which was detected by electron spin resonance and whose signal was observable at room temperature for several days following outgassing. The esr spectrum obtained from lithium diphenylphosphide showed an unsymmetrical signal ($g = 2.0067$) with two weak satellites ($g = 1.990$ and 2.019) attributable to an oxygen radical and the influence of the crystal field. The satellites did not appear upon oxidizing the phosphide in ether solution and the signal obtained ($g = 2.0067$) exhibited increased symmetry. This is the expected consequence of eliminating the crystal field effects. The observed esr signal could be due to radicals such as depicted above. Since they are generated from salt molecules, however, such radicals are more precisely represented as anion radicals, e.g., $[R_2\overset{\ominus}{P}-O-O\cdot]^-$. Similar (though uncharged) radicals have been postulated as intermediates arising during oxidation of R_2PH (10) and R_3P (11).

EXPERIMENTAL

General

Melting points are uncorrected. Analyses were performed on a Hewlett-Packard F&M 185 Carbon, Hydrogen, Nitrogen analyzer. Solvents [ethyl ether, petroleum ether (b.p. 30-55°)] were dried over $LiAlH_4$. Infrared spectra were obtained on Nujol mulls or neat compounds using a Perkin-Elmer 21 infrared spectrophotometer. ESR spectra were obtained from solid samples using a Varian 4500 electron spin resonance spectrometer. Precipitation and other manipulations of air-sensitive materials were done in a Whittaker, Mark V-A, controlled atmosphere system. The chamber was evacuated to 1 micron, then back-filled with Baker (99.997%) nitrogen.

Emission Spectra

Chemiluminescence spectra were taken from suspensions of solid samples in Nujol with oxygen passing through, in a holder that excluded background light. A Photovolt 520-M photometer with 28-B photomultiplier tube was used with a Jarrell-Ash 82-000 scanning spectrometer, and a recorder.

Fluorescence and some chemiluminescence spectra were obtained from solid samples using a Perkin-Elmer MPF-2A fluorescence spectrophotometer. The samples for fluorescence were excited by 370 or 400-m μ lines of a high-pressure xenon lamp using Corning filter 7-54 with maximum transparency at 370 m μ .

Phosphinous Chlorides

(C₆H₅)₂PCl was obtained commercially. (C₆H₁₁)₂PCl, (C₅H₉)₂PCl, (C₇H₁₃)₂PCl, (s-C₄H₉)₂PCl, and (t-C₄H₉)₂PCl (12), (n-C₄H₉)₂PCl (13), and (p-CH₃C₆H₄)₂PCl (14) were prepared by reactions similar to those described in the literature.

Phosphines

The phosphines were prepared by reduction of the appropriate phosphinous chloride in situ with an excess of LiAlH₄, and purified by vacuum distillation through a 13 cm. Vigreux column, at the following temperatures and pressures.

- (n-C₄H₉)₂PH, 45-47°/1 mm. [lit. (15) 68-70°/14 mm.]
- (s-C₄H₉)₂PH, 39-40°/6 mm. [lit. (16) 162-165°]
- (t-C₄H₉)₂PH, 44-47°/15 mm. [lit. (17) 38-40°/13 mm.]
- (C₆H₁₁)₂PH, 81-82°/0.5 mm. [lit. (18) 105-108°/3 mm.]
- (C₆H₅)₂PH, 98-100°/1 mm. [lit. (19) 100-102°/1.5 mm.]
- (C₅H₉)₂PH, 76-78°/0.8 mm.
- (C₇H₁₃)₂PH, 100-102°/0.5 mm.
- (p-CH₃C₆H₄)₂PH, 112-114°/0.5 mm.

The infrared spectra of the phosphines showed P-H stretching in the region of 2400 cm.⁻¹, and lacked absorption for P=O and P-O-.

(C₅H₉)₂PH and methyl iodide in ethanol gave the methiodide, m.p. 156-159° (ethanol/ether). Anal. Calcd. for C₁₁H₂₂PI: C, 42.32; H, 7.10. Found: C, 42.17; H, 6.99.

(C₇H₁₃)₂PH and methyl iodide in ethanol gave the methiodide, m.p. 129-131° (ethanol/ether). Anal. Calcd. for C₁₅H₃₀PI: C, 48.92; H, 8.21. Found: C, 48.82; H, 8.20.

(p-CH₃C₆H₄)₂PH was air-oxidized to produce the phosphine oxide, m.p. 93-96° (unrecrystallized) [lit. (12) 94-96°].

Lithium Phosphides

The phosphides were precipitated by the dropwise addition of n-BuLi (0.15 mole) in hexane to the appropriate phosphine (0.1

mole) in petroleum ether (50 ml.). The products were collected on a filter and washed with petroleum ether.

Chemiluminescence data are given in Table I. An attempted examination of $(C_6H_{11})_2PLi$ for fluorescence produced a spectrum very similar to the chemiluminescence spectrum. However, under the conditions employed during preparation of the samples for fluorescence, some oxidation occurred such that the observed fluorescence is attributed to products of oxidation.

Although $(C_6H_{11})_2PLi$ precipitated from solution when C_6H_5Li was used in place of $n-BuLi$, $(C_5H_9)_2PLi$ could not be obtained in the same manner. Both phosphides were additionally obtained using $n-BuLi$ with ethyl ether as solvent in place of petroleum ether. $(t-C_4H_9)_2PLi$, a yellow, chemiluminescing solid when precipitated from petroleum ether (above), showed partial solubility in ethyl ether, and precipitated, after forming in that solvent, as a white, etherated (20), non-luminescing solid, gradually turning yellow with loss of solvent on standing.

Lithium Phosphinates

The products obtained by the slow oxidation of solid $(C_6H_{11})_2PLi$ and $(C_5H_9)_2PLi$ under nitrogen containing traces of oxygen, produced infrared spectra, each with strong bands near 1160 cm.^{-1} and 1050 cm.^{-1} consistent with phosphinate structures (21). Fluorescence data are given in Table II. Acidification of aqueous solutions of the salts with hydrochloric acid yielded precipitates of the phosphinic acids.

Lithium Dicyclohexylphosphinite

Dicyclohexylphosphine oxide, m.p. $74-76^\circ$ [lit. (24) $76-77^\circ$], was prepared by air oxidation of the phosphine, by a procedure similar to that described in the literature (10). The phosphinite was then precipitated by the dropwise addition of $n-BuLi$ (0.018 mole) in hexane to the phosphine oxide (0.018 mole) in oxygen-free petroleum ether (50 ml.). The product was collected on a filter and washed with petroleum ether. The chemiluminescence wavelength is given in Table II. Examination of another sample for fluorescence showed some emission in the region of $460\text{ m}\mu$, possibly due to a small amount of contaminating phosphinate. Slow oxidation under nitrogen containing traces of oxygen, produced the phosphinate which was converted to its phosphinic acid, as above.

SUMMARY

The synthesis, relationship of emission characteristics to molecular structure, and mechanism of the chemiluminescence of organic lithium phosphides (R_2PLi) have been investigated. It was

SOLLOTT, SNEAD, and STRECKER

found that phosphides in general are chemiluminescent, but become non-luminescent when co-crystallized with solvent. Aromatic phosphides were discovered to be relatively strong emitters. Strongest emission was found among cycloalkylphosphides; weakest among alkylphosphides. Strong emission apparently requires the presence of a suitable cyclic group on phosphorus.

The phosphides produce an unusual type of chemiluminescence spectrum consisting of primary and secondary emissions. The strong primary emission was sensitive to relatively minor change in structure of the organic group, undergoing shifts of 20 m μ to 70 m μ , and color variation from blue to yellow-green to yellow. No simple correlation was seen to exist between emission wavelength and polar substituent (σ^*) constants. Rather, the effect of the organic group on the chemiluminescence is likely to be a combination of resonance (including hyperconjugation) and steric effects superimposed on inductive effects.

Conditions were discovered under which it was possible to eliminate the strong, yellow-green emission of lithium dicyclohexylphosphide [(C₆H₁₁)₂PLi], and visually observe the blue emission. Probable excited species, responsible for the chemiluminescent emissions, were identified via matching with fluorescence data obtained on intermediate and final products of the oxidation of the phosphide. Lithium dicyclohexylphosphinite [(C₆H₁₁)₂POLi] was discovered to chemiluminesce weakly, and this emission plus the secondary emission of the phosphide were attributed to excited phosphinate [(C₆H₁₁)₂P(O)OLi*] emitting at different wavelengths possibly as a result of different solvation effects in the solid state. The primary emission of the phosphide was attributed to an electronically activated tautomer of the phosphinite molecule [viz., (C₆H₁₁)₂P(O)Li*].

A mechanism was proposed to account for the observed chemiluminescent emissions of the phosphide and phosphinite, in which the oxidations are considered to be intermolecular processes involving pairs of salt molecules via intermediate formation of an anion radical {e.g., [(C₆H₁₁)₂P \ddot{P} -O-O \cdot]⁻}. Electron spin resonance data were obtained, supporting the existence of such species.

ACKNOWLEDGMENT

The authors wish to thank Dr. M. Codell for helpful discussions concerning the esr spectra.

REFERENCES

1. K. Issleib and A. Tzschach, Chem. Ber., 92, 1118 (1959).
2. K. Issleib and G. Döll, ibid., 94, 2664 (1961).
3. K. Issleib and F. Krech, ibid., 94, 2656 (1961).
4. K. D. Gundermann, Angew. Chem. internat. edit., 4, 566 (1965).
5. V. Ya. Shlyapintokh, O. N. Karpukhin, L. M. Postnikov, V. F. Tsepalov, A. A. Vichutinskii, and I. V. Zakharov, Chemiluminescence Techniques in Chemical Reactions, translation from Russian, Consultants Bureau, New York, 1968, Chap. 1.
6. K. Issleib and F. Krech, J. Organometallic Chem., 13, 283 (1968).
7. H. E. Winberg, J. R. Downing, and D. D. Coffman, J. Am. Chem. Soc., 87, 2054 (1965), and references cited therein and in 4.
8. R. W. Taft, Jr., in M. S. Newman (ed.), "Steric Effects in Organic Chemistry", Chap. 13, Wiley, New York, 1956.
9. H. H. Jaffé and M. Orchin, "Theory and Applications of Ultra-violet Spectroscopy", Wiley, New York, 1962, p. 254.
10. M. M. Rauhut and H. A. Currier, J. Org. Chem., 26, 4626 (1961).
11. R. F. Hudson, "Structure and Mechanism in Organo-Phosphorus Chemistry", Academic Press, Inc., London, 1965, p. 292.
12. W. Voskuil and J. Arens, Rec. Trav. Chim., 82, 302 (1963).
13. K. Issleib and W. Seidel, Chem. Ber., 92, 2681 (1959).
14. R. Montgomery and L. Quin, J. Org. Chem., 30, 2393 (1965).
15. H. Fritzsche, U. Hasserodt and F. Korte, Chem. Ber., 98, 1681 (1965).
16. A. R. Stiles, F. F. Rust, and W. E. Vaughan, U. S. Patent 2,803,597 (1957); cf. Chem. Abstr., 52, 2049p (1958).
17. H. Hoffman and P. Schellenbeck, Chem. Ber., 99, 1134 (1966).
18. H. Niebergall and B. Langenfeld, ibid., 95, 64 (1962).
19. W. Kuchen and H. Buchwald, ibid., 91, 2871 (1958).
20. K. Issleib and F. Krech, J. Organometal. Chem., 13, 283 (1958).
21. N. Colthup, L. Daly and S. Wiberley, "Introduction to Infrared and Raman Spectroscopy", Academic Press, New York, 1964, p. 300.
22. A. Stiles, F. Rust and W. Vaughan, J. Am. Chem. Soc., 74, 3282 (1952).
23. B. B. Hunt and B. C. Saunders, J. Chem. Soc., 2413 (1957).
24. A. Herstellung in Houben-Weyl's "Methoden der Organischen Chemie, Organische Phosphorverbindungen", Vol. 1, G. Thieme Verlag, Stuttgart, 1963, p. 197.

**MICROCLIMATE-CONTROLLED (THERMALIBRIUM)
CLOTHING SYSTEMS FOR MILITARY APPLICATIONS**

LEO A. SPANO AND VINCENT D. IACONO
U. S. ARMY NATICK LABORATORIES
NATICK, MASSACHUSETTS 01760

1. INTRODUCTION

Progress in weapons development has emphasized the need for multifunctional clothing to protect the individual exposed to extreme climates and/or toxic environments. This need is particularly acute when individuals are engaged in disposing toxic munitions or operating military equipment such as armored vehicles, helicopters or low-speed aircraft in hot and hot-humid environments. To meet these needs, the U.S. Army has designed and developed microclimate-controlled clothing. The basic difference between this type of clothing and conventional protective ensembles is the technique used to control the flow of heat and sweat from the skin surface to the outside environment. In microclimate-controlled clothing such control is accomplished by closed-loop circulation of heated or cooled fluids close to the skin surface or by circulation of heated ambient or conditioned air inside the clothing. In conventional clothing such control is attempted by varying the number and type of clothing layers worn at one time.

To function best the human body should not be restricted in locomotion and other physical activities; should be protected against excessive heat, cold and other disabling environments; and should be maintained in thermal balance. Clothing, no matter of what type, is not fully adequate in any of these respects. The inadequacies can become critical in the case of military clothing. Protection against toxic environments can usually be realized by employing fabrics and treatments specifically developed to defeat such toxic agents. A high degree of clothing adjustability can be achieved by novel pattern designs. However, to maintain the clothed individual in thermal balance the heat and sweat produced by the body must be transported to the outside environment at the same rate the individual produces it. In other words military clothing, to function best, must be dynamically responsive to body needs. This is no simple task. No pro-

protective clothing available in military supply channels presently meets this criterion.

2. DESIGN PRINCIPLES

The building blocks conceptually needed for microclimate-controlled protective clothing systems are shown in Fig. 1. Principal components of microclimate-controlled clothing are:

1. The basic ensemble which provides all the protective capabilities necessary for the specific mission.
2. A microclimate distribution garment tailored for the specific activity.
3. A powered microclimate regulation device to control the temperature, humidity and flow rate of the ventilating air or circulating fluid moving through the distribution garment.

Environmental protection is realized through the insulative properties of the basic ensemble and is augmented by the energy transported by the conditioned air or fluid moving through the microclimate distribution garment. Protection against toxic agents and thermal radiation from nuclear and flame weapons is accomplished by extensive use of clothing materials and treatments developed specifically to meet such military requirements. Stretch-type materials and bias-cut fabrics are used extensively to achieve a high degree of clothing adjustability. Use of such materials and cutting techniques bridge over several problems which, to date, have precluded the engineering of close-fitting clothing that impose little or no restriction on body movement.

Microclimate distribution garment. The microclimate distribution garment is either a spaced ventilated undergarment through which conditioned or ambient air flows and is distributed over the body surface, or it is a knitted undergarment through which a closed loop network of flexible "Tygon" vinyl plastic tubing is interwoven to provide a closed path for the liquid circulating through the garment. Selection of either type (gaseous or liquid) as well as its specific design and surface coverage, i.e., total body or torso, is dependent on the specific protection needed and the environment in which such protection must be given.

Figures 2 and 3 show a typical total body and torso air distribution garment, respectively. Figure 4 shows a typical water-cooled undergarment and a water-cooled vest. For example, cooling of tank crewmen operating in hot and/or hot-humid areas can be easily achieved by ventilating the torso area with conditioned air or by circulation of cool water through a water-cooled vest. However, when these vehicles are operating in a toxic environment all ventilating air for microclimate control must be filtered prior to its use in the clothing. Consequently, under these conditions, a

closed-loop, water-cooled system for tank crewmen would be preferred.

Powered microclimate regulation devices. To control the temperature, humidity and flow rate of the ventilating air or the temperature and flow rate of the circulating water, powered heat regulation devices must be available. These may be battery-powered, self-powered or remotely powered from the vehicle in which the individual is performing his mission. The low power density of rechargeable batteries limits their use to clothing systems that are required to protect the individual for periods of 2 to 3 hours. However, the technology in semiconductor materials is such that it is possible to engineer self-powered heat regulation devices for protective clothing. Figure 5 shows a thermoelectric powered heating-ventilating system capable of delivering continuously 18 cfm of heated or ambient air at a static pressure of four inches of water. This unit fully fueled for 8 hours of continuous operation weighs 11.9 lbs. The operation of this unit is shown in Fig. 6.

3. PROTECTIVE CLOTHING SYSTEM FOR EXPLOSIVE ORDNANCE DISPOSAL

This system (Fig. 7) consists of a one-piece butyl-coated ensemble; a spaced microclimate distribution garment worn directly under the coated butyl layer; insulated butyl boots; butyl handwear; a shoulder suspended helmet; a lightweight communication headset; and a battery-powered ventilating backpack for microclimate control and life support. All components are shown in Fig. 8. The design and surface coverage of the microclimate distribution garment selected for this system is critical and was specifically tailored to perform several functions. The distribution garment chosen is a five-layer-spaced system through which the ventilating air in contact with the skin surface is forced to move to the extremities, then reverse its path and move countercurrently through a spaced layer parallel to but separated from the ventilating layer before the air is discharged to the outside environment.

The flow path of the ventilating air through the fabric system is shown in Fig. 9. Partitioning of the ventilating stream from the exhaust stream assures high turbulence over the skin surface. This effectively increases the overall heat and mass transfer coefficients prevailing on the skin surface. This also increases the cooling capability of the total system. The partitioned exhaust air serves as a buffer layer between the outside environment and the ventilating air in contact with the skin surface. Such a buffer layer increases the insulative characteristics of the total clothing by shielding the ventilating air stream against heat leakage into the clothing when exposed to solar radiation; it augments the protective capabilities of the system by purging any in-board leakage of toxic agents that could penetrate the outer butyl-coated fabric garment through punctures or tears. The redundant butyl-coated fabric layer used to separate the ventilating and exhaust air streams serves as a secondary barrier to potential penetration of toxic agents.

SPANNO and IACONO

All materials used in the fabrication of this ensemble are either stretchable or cut on the bias to achieve a high degree of mobility. The ensemble is relatively form-fitting and highly flexible. Butyl insulated boots and butyl gloves are used to protect the extremities. Connection of the handwear and footwear to the suit is achieved by locking plastic disconnects. A gas-sealing zipper is used for the main closure of the suit. All hardware connectors and closures are shielded by butyl rubber protectors.

Helmet. The helmet consists of a rigid polycarbonate shell with a large clear area to provide nearly unrestricted visibility. It is supported on the shoulders and its position is adjustable on either side for better fit. Ventilating air for breathing and cooling is delivered to the head area through a built-in manifold in the air distribution garment. At the base of the visor there is an oral-nasal deflector to direct exhaled gases away from the visor. This prevents fogging on the visor and CO₂ buildup in the helmet. The deflector is currently being redesigned to permit direct breathing from various types of emergency-breathing, life-support devices.

Life Support System for EOD. The connecting link between the suited man and the outside environment is the life-support backpack. This consists of three basic components: (1) a high efficiency blower; (2) an expendable filter; and (3) a power pack to drive the blower. The expendable filter and blower are located in a molded plastic housing carried on the upper section of the man's back. The power pack consists of two waist-belt-suspended pouches containing rechargeable Ni-Cd batteries. The power pack is readily accessible for fast replacement in contaminated environments.

Disposable Filter. The disposable filter whose capacity is approximately four times that required for a normal EOD mission was specifically designed to clean all ventilating air entering the suit to the same degree now provided by the M-17 Field Protective Mask. Figure 10 shows the filter canister and its location when nested in the backpack. While it has been established that nearly all Army EOD missions can be handled by using the filtered-air life-support backpack, the protective ensemble is designed to be easily interphased to a self-contained air supply system when CB agents contamination is anticipated to be exceedingly high.

4. AIR-CONDITIONED CLOTHING FOR ARMY AIRCREWMEN

The Army's extensive use of helicopters and other aircraft to provide logistical and tactical support to ground troops in Southeast Asia brought into focus the need for an air-conditioned clothing system to relieve the physiological stress imposed by hot-humid environments on the individual flying such aircraft. Generally, the only type of environmental control provided in current Army aircraft is ventilation of the cabin area by ram air entering through air scoops while the aircraft is in flight. Although this method of purging the

SPANNO and IACONO

cabin when flying is of definite value, frequently such cabin ventilation with ambient air has been found inadequate because of the low altitude. The problem becomes much more severe when such aircraft are required to remain on the flight line for prolonged periods prior to actual take-off. During these pre-flight delays the temperature and humidity in the cabin area become very stressful. Many flights may have been aborted following such pre-flight delays because pilots could not continue in the stressful environments prevailing inside the aircraft.

Spaced Garments. To alleviate these conditions the U.S. Army Natick Laboratories engineered a spaced garment to be worn directly over the underwear and under the standard high temperature resistant "Nomex" flight clothing and associated equipment, i.e., the aircrew armor, the life jacket, and the harness used in such aircraft as the Mohawk to secure the pilot and navigator to the ejection seats. Development of the air conditioning equipment to condition aircrewmen's clothing is the responsibility of another agency and will not be discussed here. However, studies conducted at Natick provide the information necessary for such development.

Air Distribution System. The air distribution system, shown in Fig. 11, consists of a layer of spacer fabric sandwiched between two layers of Lycra fabric. This material was selected to provide adequate spacing for air circulation between the two Lycra fabrics while maintaining a low air flow resistance. Air manifolds located between the two Lycra fabrics and near the lumbar region assure air circulation to the chest and back section of the torso.

Conditioned air enters the distribution garment through two quick-disconnect fittings, one connected to the left air manifold and the other connected to the right air manifold. The garment configuration resembles an abbreviated, one-piece underwear. As shown in Fig. 11, the garment can be put on or taken off simply by opening or closing the "Velcro" front closure running from the neck (jugular notch) over the thorax, the abdomen to the iliac region, and then to both thighs. The air distribution system has exceptional adjustability; consequently, it imposes little or no restriction of body movement on the individual wearing it. This adjustability is achieved by bias cutting of the spacer fabric and by adding stretchable panels in those areas where body movement requires extensive dimensional change of the garment. Since all fabrics used are air permeable, flow of both sensible and insensible perspiration leaving the body surface is not impeded. Circulation of the conditioned air over the skin surface for body cooling is assured by the low air permeability of the flight suit, the aircrewman armor and other personal equipment worn over the air distribution garment. Figure 12 shows three soldier volunteers wearing the air-conditioned clothing and fully dressed for combat mission.

5. PERFORMANCE OF THE EOD CLOTHING

The physiological adequacy of this clothing system was checked by soldier volunteers performing work equivalent to EOD activities while exposed to the following chamber environments: (1) 105°F and 20% RH; (2) 95°F and 50% RH; (3) 85°F and 96% RH; and (4) 85°F and 75% RH. These studies were conducted by the U. S. Army Research Institute of Environmental Medicine at Natick. Figure 13 shows the physiological response of one of the test subjects as reflected by the rectal temperature T_r , body temperature T_b , and the mean-weighted skin temperature T_s as a function of exposure time. The sharp decrease followed by the sharp rise in T_b and T_s during the first hour of the study reflects the high evaporative-cooling capability of the system when the skin surface is saturated with sweat. Then, as the skin surface dries, the cooling rate decreases to that required to keep the body thermally neutral. This effect is reflected by the relatively constant T_r , T_b , and T_s prevailing during the last hour of the test.

To confirm the system's protective capability when an individual is exposed to toxic agents, tests were conducted by the Medical Research Laboratory at Edgewood Arsenal. Three soldier volunteers dressed in the EOD Clothing were exposed inside a chamber laden with chloropicrin gas. The concentration of chloropicrin in the chamber was set at 1000 mg/m³. This concentration is estimated to be approximately ten times higher than any condition expected in a field mission. The chamber temperature and humidity during the tests were maintained between 108 and 110°F and approximately 20% RH. Each of the three volunteers was exposed twice. Each study lasted two hours. During the first hour each individual was required to walk around the chamber, and during the second hour he was required to perform light exercise. Heart rate and rectal temperature were monitored continuously. At no time during the six 2-hour exposures did the rectal temperature exceed 102°F nor the heart rate reach 180 beats per minute. At the end of each test the subject, while still in the chamber, was asked to disconnect the air hoses at the suit inlet fittings to simulate exchange of a spent backpack for a fresh one. No leaks of chloropicrin gas were detected by the subjects at any time during the studies. At the completion of each test all three subjects stated that under the conditions of test they were reasonably comfortable. Under the same conditions, an individual wearing the standard M-3 Toxicological Protective Suit shown in Fig. 14 would have collapsed from heat stress in less than thirty minutes.

6. PERFORMANCE OF THE AIR-CONDITIONED CLOTHING FOR ARMY AIRCREWMEN

The effectiveness of this clothing system was checked by soldier volunteers exposed to environments simulating those in a typical aircraft waiting to take off in a hot-humid area. The

objective of these studies was to demonstrate the degree of physiological stress imposed under such conditions and determine to what degree such stress can be reduced by the use of air-conditioned clothing.

After selecting the proper size clothing system, each test subject was weighed nude, and then weighed again when fully dressed. Following the weighing, each subject entered the climatic chamber and sat at rest, simulating his pre-flight period in the aircraft. Figure 15 shows test subjects in the chamber. Temperature and humidity in the chamber were set at 125°F and 25% RH. This high-temperature and low-humidity condition was used to simulate the "greenhouse" effect of solar heat passing through the plastic canopy of an aircraft. This effect produces a high radiant heat condition within the aircraft cabin. It should be noted that the total enthalpy of the environment at 125°F and 25% RH (48.9 Btu/lb) reflects the exact enthalpy of the hot-humid environment prevailing outside an aircraft under ambient conditions of 95°F with an 83% relative humidity. Each test subject was continuously monitored while in the chamber to record his physiological responses to the stressful environment. Specific physiological measurements taken included: (a) Rectal temperature (T_r); (b) Mean weighted skin temperature (T_s); (c) Heart rate; (d) Metabolic heat production (M); and (e) Sweat production. Mean body temperature (T_b) was calculated as the weighted average of $1/3T_s + 2/3T_r$.

Each subject was tested wearing both the standard flight clothing and the air-conditioned aircrewman clothing system with half the men wearing each item each day to assure that any significant differences obtained were attributable to using the conditioned aircrewmen's clothing and not to differences between individuals or to acclimatization. Consequently, the physiological response of each test subject when wearing air-conditioned aircrewmen clothing could be compared directly with the response of the same individual when wearing standard flight clothing.

Results from these studies suggest that personnel wearing the standard flight clothing and equipment used when flying military aircraft in hot and hot-humid areas are under a severe heat stress if, fully dressed for combat missions, they are required to sit in the aircraft on the flight line for extended periods prior to being cleared for take-off. This is reflected by the rise in body temperature, sweat production and heart rate. Figures 16 and 17 show two typical cases of heat exhaustion following these exposures to the simulated air craft cabin environment (125°F and 25% RH) used for these studies. Figure 18 shows the mean rise in rectal temperature of the same individual when using the air-conditioned clothing and when using the standard flight clothing and equipment now required for combat missions in Southeast Asia. It is apparent that when wearing the air-conditioned clothing the individual was essentially

SPANNO and IACONO

in thermal balance. Figure 19 shows the change in body temperature as a function of time. It also shows that the body temperature of individuals wearing the standard flight clothing rose approximately 2°F per hour, while men wearing the air-conditioned clothing show little change or no change.

Sweat production rates obtained in these studies also show significant differences. Figure 20 shows that the sweat production of individuals dressed in standard clothing is approximately 2.3 times higher than that when wearing the air-conditioned clothing. The sweat evaporation rate when using the air-conditioned clothing was found to be 1.7 times greater than that realized when wearing the standard flight clothing. It can be predicted from these data that extended exposure of crewmen wearing standard flight clothing to these hot conditions would lead to physiological exhaustion. However, when using air-conditioned clothing they could be exposed indefinitely without imposition of any significant stress.

7. CONCLUSIONS

Clothing, regardless of type, restricts normal body motion and obstructs the transport of heat and sweat from the skin surface to the outside environment. This is particularly true of military clothing which must provide protection against a multitude of natural environments and man-imposed toxic hazards. No protective clothing available in military supply channels remotely approaches the dynamic responsiveness the body requires of clothing.

Studies by U. S. Army Natick Laboratories show conclusively that close control of the microclimate inside clothing can bridge over many technical problems which now preclude the engineering of multifunctional clothing systems for military applications.

Although the technical feasibility of microclimate-controlled clothing for general field use is still a long-range goal of the Army, the use of such systems for special applications is now a reality. Besides the two systems discussed in this paper several other functional systems based on the same design principles have been delivered and are now in actual use, or are scheduled for field testing by the U. S. Army. Typical of these are the protective clothing system delivered to NASA Manned Spacecraft Center, Houston, Texas for use by rescue personnel entering the space vacuum chamber; the environmental protective ensemble delivered to NASA Marshall Space Flight Center at Huntsville, Alabama, to be used in checking the Saturn V booster; the microclimate-controlled clothing for tankcrewmembers, and the Protective clothing used by laboratory personnel at Ft. Detrick.

SPANO and IACONO

It can be concluded that substantial progress has been made toward the development of scientific, fully effective, protective clothing, capable of sustaining soldiers in the most adverse environments.

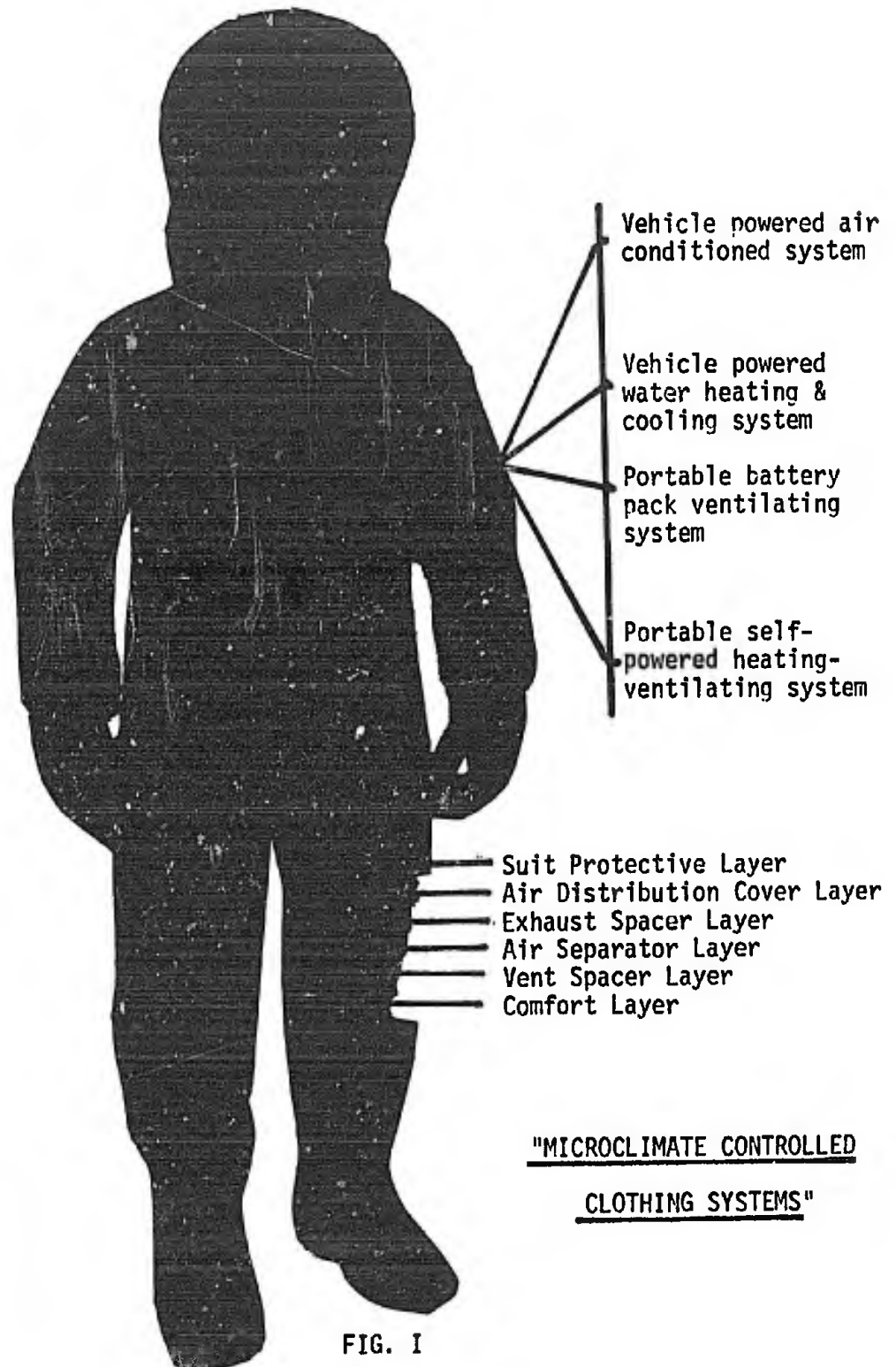


FIG. I



Fig. 2. Total body, air distribution garment



Fig. 3. Torso, air distribution garment



Fig. 4. Water-cooled vest and undergarment

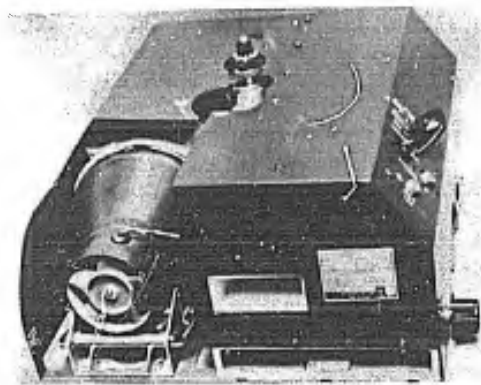


Fig. 5. Thermoelectric unit

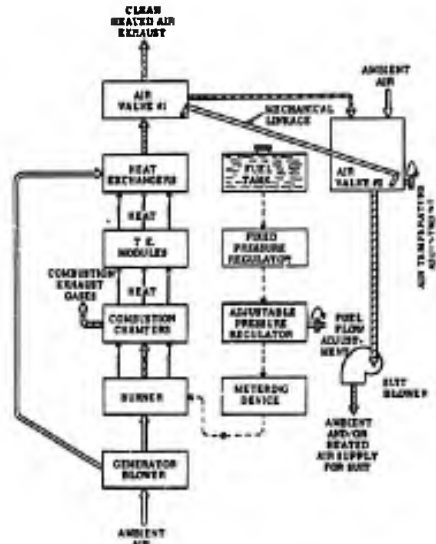


Fig. 6. Flow diagram of thermoelectric unit



Fig. 7. EOD man working

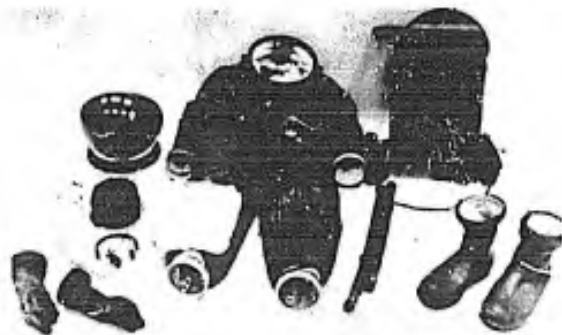


Fig. 8. EOD ensemble components

SPANO and IACONO

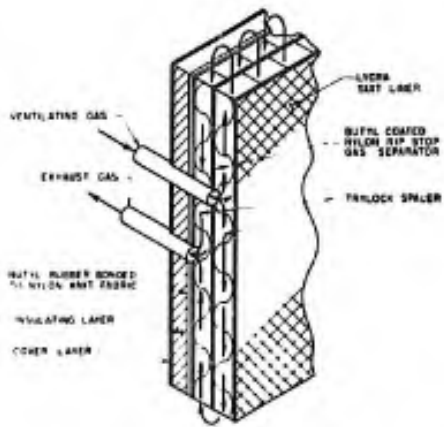


Fig. 9. Flow path through fabric system

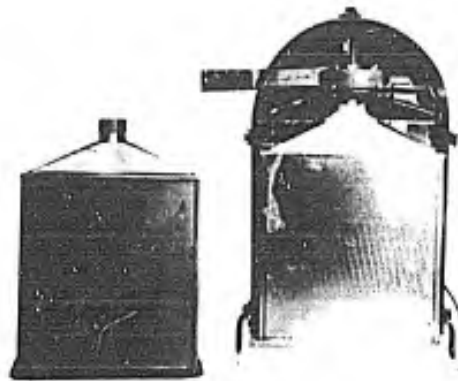


Fig. 10. Filter and its location in the pack



Fig. 11. Air distribution garment



Fig. 12. Aircrewmen wearing air-conditioned clothing

SPANO and IACONO

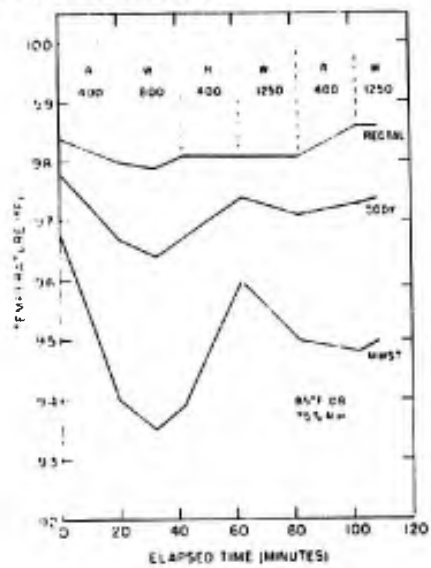


Fig. 13. Physiological responses during test



Fig. 14. M-3 toxicological protective suit and its components



Fig. 15. Test subjects in chamber



Fig. 16. Heat casualty



Fig. 17. Heat casualty

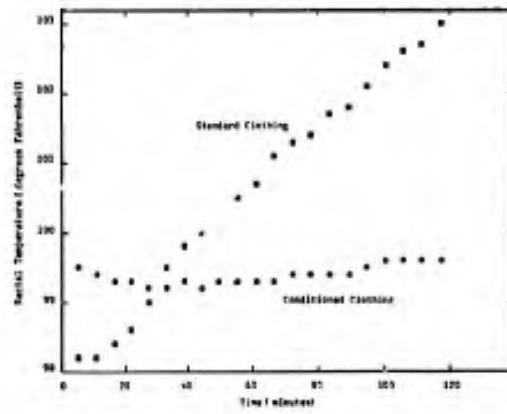


Fig. 18. Rectal temperature as a function of time

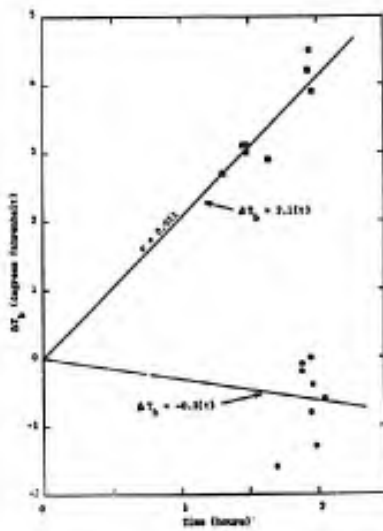


Fig. 19. Body temperature as a function of time

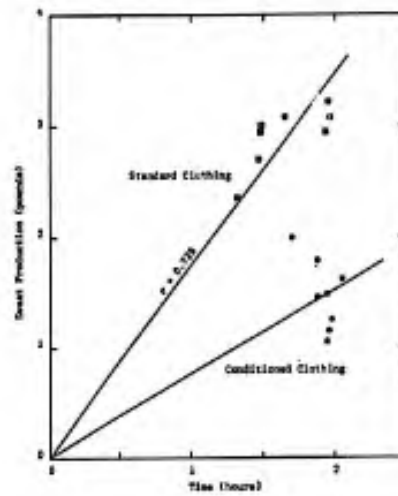


Fig. 20. Sweat production as a function of time.

NEODYMIUM YAG LASER FOR OPTICAL RADAR APPLICATIONS

JOHN W. STROZYK and VINCENT J. ROSATI
Electronic Components Laboratory
United States Army Electronics Command
Fort Monmouth, New Jersey 07703

Laser systems can be grouped into three general areas of use, military, commercial and laboratory. Examples of this grouping would be ruby rangefinders (military), laser welders (commercial) and high power lasers for plasma studies (laboratory). Of these areas, the largest emphasis has been given to military applications in the surveillance and communications fields. The application of the laser to military problems has been widely accepted and the extension to commercial uses is being pursued vigorously by many organizations. Therefore, the development of a general purpose surveillance device, which satisfies the existing requirements as well as promises to provide new ones, is highly desirable.

Ideally, such a surveillance system should be capable of providing range, azimuth, elevation and velocity information in both search and track modes of operation. This system might also be expected to provide guidance or beacon functions and be relatively small but not necessarily man portable at this stage. The design of such a system involves many parameters with power output, PRF and pulse width being of primary importance. The power output will determine the range limit, the PRF will determine what, how much, and how fast the information may be obtained, and the pulse width will effect the accuracy of the data. These parameters will of course govern or be governed by the receiver design, and at present they are the most difficult to control or predict.

Unfortunately, the development of such a laser system is at about the same stage that microwave radar was 20 or 25 years ago. This is primarily due to the efficiency and low PRF's of most lasers. Following the development of the Nd:YAG laser at Bell Telephone Laboratories (1) the Electronic Components Laboratory at Fort Monmouth, initiated a program for the design of a high repetition rate laser device. This effort resulted in a relatively simple Nd:YAG device with characteristics worthy of optical radar

feasibility studies over short ranges, the results of which are presented here.

All radars, including optical ones, can be described by the same basic black boxes. Figure 1 illustrates the simple requirements and includes the Nd:YAG laser as the transmitter, telescope optics for beam collimation, telescope optics to collect returning signals, a photomultiplier to process the signals and an oscilloscope to display the information. The design of each unit or component will be fixed by the laser characteristics and to some extent by the intended application (i.e. simple range data as compared to range rate data). The analysis or design of any radar system inevitably involves a radar range equation in one form or other. This approach is applicable to laser radars and has been used by many people under the assumption of having diffuse targets and constant atmospheric parameters. The results, while only approximations, are of acknowledged use and are developed here.

Consider the problem illustrated in figure 2. It is required that the maximum range for a given power output, or conversely, the minimum power output for a specified target and range, be determined as functions of the system parameters.

With a laser peak power output of P_0 Watts and a transmitter optics efficiency of k_1 , the power at the target can be expressed as

$$1) \quad P_T = k_1 (T_{air}) P_0 \frac{A_T}{A_B} ,$$

where: T_{air} represents the atmospheric losses due to absorption and scattering

$$\begin{aligned} A_T &= \text{area of the target} \\ A_B &= \text{area of the beam.} \end{aligned}$$

The power at the receiver, for a Lambertian type target surface, will be

$$2) \quad P_R = \left[k_1 k_2 (T_{air}^2) A_R P_0 \frac{\rho}{\pi} \cdot \frac{A_T}{A_B} \right] \frac{1}{R^2} ,$$

with A_R = area of the receiver
 R = distance to the target
 ρ = reflectivity of the target.

The beam area at a specific range R , is, in terms of the laser divergence:

$$A_B = \frac{\pi R^2 \phi_1^2}{4},$$

which when introduced into equation 2 gives

$$3) \quad P_R = \left[4 k_1 k_2 (T_{air}^2) A_R P_0 \frac{\rho}{\pi^2} \cdot \frac{A_T}{\phi_1^2} \right] \frac{1}{R^4}.$$

This case represents the problem when the target area is much less than the beam area.

For the case of the target area \geq beam area, the power at the receiver is:

$$4) \quad P_R = \left[k_1 k_2 (T_{air}^2) A_R P_0 \frac{\rho}{\pi} \right] \frac{1}{R^2}.$$

Another special case which is receiving considerable attention at present involves wire like targets. For this case the power at the receiver is given by

$$5) \quad P_R = \left[4 k_1 k_2 (T_{air}^2) A_R P_0 \frac{\rho}{\pi^2} \cdot \frac{d}{\phi_1} \right] \frac{1}{R^3},$$

where: d = diameter of the wire.

Of course, most targets will have a combined diffuse and specular nature which is not included in these power relations. In addition, the case for wire targets would be modified for wires consisting of multiple strands which are twisted into cables. Many high frequency radar operators have noted enhanced reflections, as we have, due to cable wrapping, and indeed have been able to determine the pitch and distance between wraps.

With the power at the receiver given by equation 3, 4 or 5 the signal current at the cathode of the detector can be determined using

$$6) \quad i_s = \frac{P_R e Q(\lambda)}{h\nu} \text{ amps.}$$

With $Q(\lambda) \doteq 5 \times 10^4$ for an S-1 cathode at an operating wavelength of 1.06 microns, the computed signal current is

$$6a) \quad i_s \doteq (4.3 \times 10^{-4}) P_R \text{ amps.}$$

In order to distinguish this signal, the receiver noise must be less than, or at least equal to, the signal current unless special techniques are employed.

The noise in the receiver has two components, shot noise at the cathode and the Johnson noise of the load. The shot noise consists of two components, the dark current and the background induced current. Then the total rms shot noise at the cathode can be expressed as:

$$7) \quad (i_n)_s = [2eB(i_d + i_b)]^{1/2} \text{ amps,}$$

with i_d = dark current component
 i_b = background induced current
 B = electrical bandwidth of system.

The dark current component is a function of the cathode type, size and operating temperature. For the tube used, the surface area is $\sim 8 \text{ cm}^2$, temperature $\sim 25^\circ\text{C}$, which results in a dark current on the order of $i_d \doteq 8 \times 10^{-12}$ amps.

The background noise contribution, i_b , can be determined using solar radiation figures for a bright day as the worst case. This would give typical background noise powers as a function of the receiver parameters. For a blue sky background, appropriate for this application, the background induced current can be calculated using

$$7a) \quad i_b \doteq (4.3 \times 10^{-4}) J_\lambda A_R k_2 \Omega_R \Delta\lambda.$$

For the values $J \doteq 7 \times 10^{-7} \text{ Watts cm}^{-2} \text{ ster.}^{-1} \text{ \AA}^{-1}$
 $A_R \doteq 55 \text{ cm}^2$ $k_2 \doteq 0.4$
 $\Delta\lambda \doteq 200 \text{ \AA}$ $\Omega_R \doteq 8 \times 10^{-7} \text{ ster.}$

which assumes the receiver field of view equals the transmitter field, a background noise, $i_b \doteq 1.1 \times 10^{-12}$ amps is obtained. These operating conditions would be considered the best available (equal fields of view) while the background level is at its worst. In actual operation, this is seldom realized. Thus, for this system, the receiver is marginally dark current limited.

STROZYK and ROSATI

Using these values of noise currents, the total shot noise in the system, for a 4 MHz electrical bandwidth is

$$8) \quad (i_n)_s = 3.4 \times 10^{-12} \text{ amps} \quad (B = 4 \text{ MHz})$$

at the cathode.

The remaining noise components, the Johnson noise is given by

$$9) \quad i_J = \left[\frac{4 K T B}{R} \right]^{\frac{1}{2}} \text{ amps.}$$

For this system, $B = 4 \text{ MHz}$, $R = 100 \text{ ohms}$, $K = 1.38 \times 10^{-23} \text{ Joules/}^\circ\text{K}$ and $T = 300^\circ\text{K}$, which yields a value of $i_J = 2.56 \times 10^{-8} \text{ amps}$.

This component when compared with the shot noise contribution after it is amplified by the dynode stages of the tube, is seen to be ~ 2 orders of magnitude below the shot noise, and can be neglected. The shot noise components could, if desired, be reduced by cooling the tube (reduces i_d) or by using a narrower band optical filter (reduced i_b) neither of which was accomplished during these tests.

With this value of noise current and the signal currents given in terms of the power at the receiver, one can calculate the power required to yield a specified signal to noise ratio (SNR). For a $\text{SNR} \approx 1$, the incident power on the cathode would have to be $\sim 3.2 \times 10^{-8} \text{ Watts}$.

If one plots equation 6a in terms of the photomultiplier anode current versus the range, in terms of target reflectivity and power output, a family of curves will be generated. This has been done in figure 3 for the case of a beam filling target (equation 4). For typical targets, the reflectivity might be expected to vary from 0.5 to 0.01 at 1.06 microns, except for cooperative targets (mirror, prisms) which were not employed. If a fixed power output of 1 kW is used, the product as shown in figure 3 will allow for some extrapolation from diffuse to specular targets. The photomultiplier gain for this system has been measured at 10^6 , and is incorporated into the plot.

The transmitter assembly for this study consisted of a water cooled, continuously pumped Nd:YAG rod with a rotating Q-switch mirror arrangement. Its complete characteristics are summarized in figure 4. A detailed analysis of the design of the laser assembly has been presented elsewhere and will not be included here (2).

From the preceding analysis and the laser characteristics listed, it was determined that the system could be used on beam filling targets out to ~ 4000 meters and have a $SNR \approx 1$. In addition to this, the high PRF could be utilized rather simply to extract the signals from the noise using integration techniques, if it proved necessary. The data display consisted of two forms of visual read-out. Initially an "A" type oscilloscope presentation was employed when fixed targets at less than 3000 meters were involved. This was further augmented with a raster type of presentation using "Z" axis modulation for more distant as well as moving targets. The raster display allows for retrieval of signals below the noise level, a feature not available in the "A" type presentation. In addition, this raster display is similar to a "B" type radar scope and could easily be converted to provide azimuth or height information if desired. Both methods of display utilize an integration time set by the oscilloscope and the operators eye or camera.

In the case of the raster display a definite target indication could be obtained using on the order of 5 to 10 pulses, depending on target type and range. The introduction of additional electronics could allow this to be lowered to the 2 pulse level if required. Also, since it is a high PRF system, operator experience can be utilized in making decisions similar to microwave radar systems. Figure 5 shows the system schematically and figure 6 is a photograph of the unit in operation at Fort Monmouth.

Initially, this system was placed in operation under various weather conditions on fixed targets. For these studies only the "A" type presentation was required and data typical of this operation is shown in figures 7 and 8. Figure 7 illustrates the echo returns from a painted structural tower at a range of 1000 meters during heavy rainfall and general overcast conditions with some ground fog. Figure 8 shows multiple echos from a 0.780 inch diameter wire and a roof at ranges of 500 meters and 1100 meters. These echos were obtained under heavy rain, overcast and bright sunshine conditions. Note the various noise levels as well as signal level conditions. The wire and the tower represent the case in equation 5 while the roof comes under equation 4.

Following these results, the raster display was added to allow signal retrieval at $SNR \approx 1$ or less, and more distant as well as moving targets were examined. Unfortunately various weather conditions could not be examined during these later studies.

In an effort to establish the maximum range capability of the unit, a black water tower was elected as a suitable beam filling target, most closely approximating the conditions of equation 4. The results of this test are shown in figure 9 for both the "A" and raster type displays. The range is 4300 meters which is in fair agreement with the plot in figure 3 considering the assumptions

made there. This data not only illustrates the range of the unit, but also the effectiveness of the raster display in enhancing the echo.

Having established a useful maximum range for the unit, attention was directed at the evaluation of it for various other uses.

The ability to perform such tasks as perimeter defense and terrain mapping were examined by manually scanning the device through approximately 45 degrees while recording the echos. The results are shown in figure 10 for targets out to approximately 1500 meters and as close as 50 meters. In addition, automobiles and trucks traveling at speeds of 30 to 70 mph were recorded intercepting the beam. The targets in figure 10 represent trees, wires, poles, radio towers, buildings, and columns of white smoke.

To evaluate its potential as a radar unit, a U. S. Army H-19 helicopter was employed. The helicopter was manually tracked through two types of approaches, directly toward the unit and normal to it. The results of the pass directly into the unit are shown in figure 11. The target was manually acquired at a range of 3000 meters and tracked to within 100 meters of the site. The echos are broken in places due to the difficulty of manual tracking such a large unit. From the data obtained, the helicopters velocity was computed and verified as ~ 52.9 knots. Similar data for the pass normal to the site was obtained at ranges out to 2500 meters. These tests were run at several times with no appreciable difficulties, other than manual tracking, observed.

In addition to these tests, such examinations as guidance capabilities were checked along with system resolution. Under daylight conditions a hand-held image converter could pick up and follow the beam on targets out to ~ 1000 meters. The resolution, while not directly measured, was good enough to distinguish birds and wire insulators, when studies involving wire detection were performed, at ranges up to 500 meters.

Having demonstrated some of the possible uses of this system, it remains now to refine and add to it. Some improvement in receiver performance could be obtained with better optical filters and cooling techniques. The largest improvements could be had by increasing the power output, which is easily accomplished using higher quality rods such as Nd:Lu:YAG. With the exception of the above changes, the most important system modification would be the addition of a continuous or sequential scanner, perhaps in the form of a rotating wedge or vibrating mirror. Since a few pulses will establish the existence of a target and possibly its speed, a scanner can be built to overlap different areas in space. Error signals generated by the scanner or the receiver could easily be made to drive servo positioners which control the platform. This would then form the foundation for a true search and track optical

STROZYK and ROSATI

radar. Other changes, to accomplish military missions depend entirely upon the mission and are too numerous to describe in full. One obvious application is high performance aircraft or missile guidance which is extremely compatible with the high PRF.

REFERENCES:

- (1) Contract # DA-36-039-AMC-02333(E), Final Report. Bell Telephone Laboratories, Murray Hill, New Jersey.
- (2) Contract # DA-28-043-AMC-00326(E), Final Report. Hughes Aircraft Company, Culver City, California.

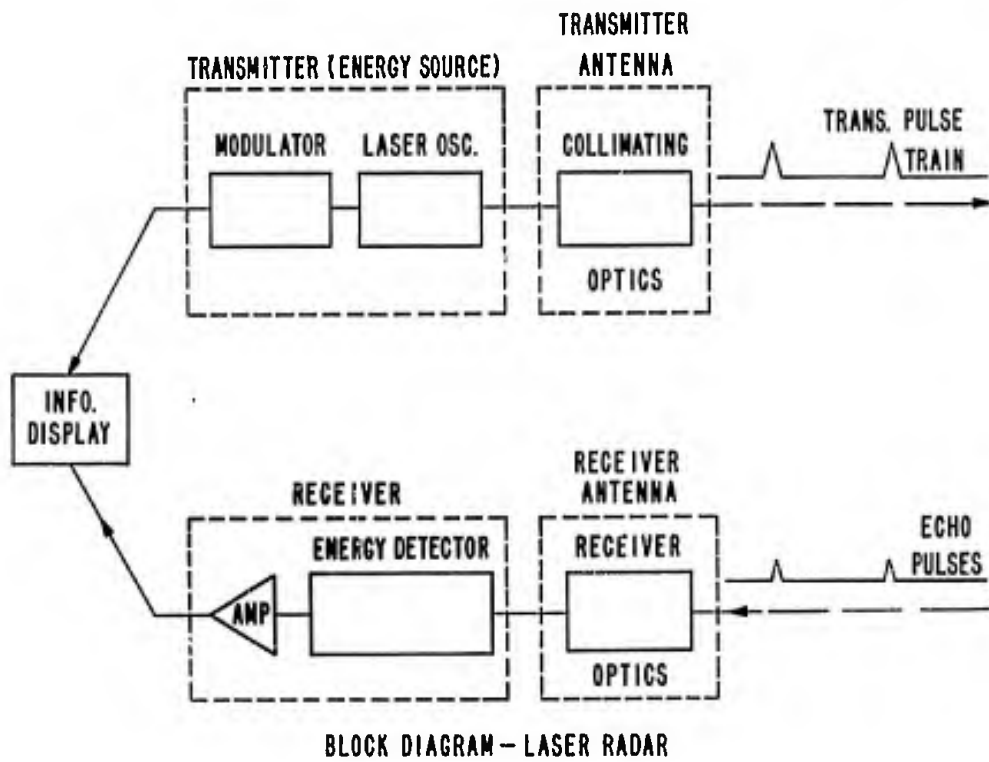
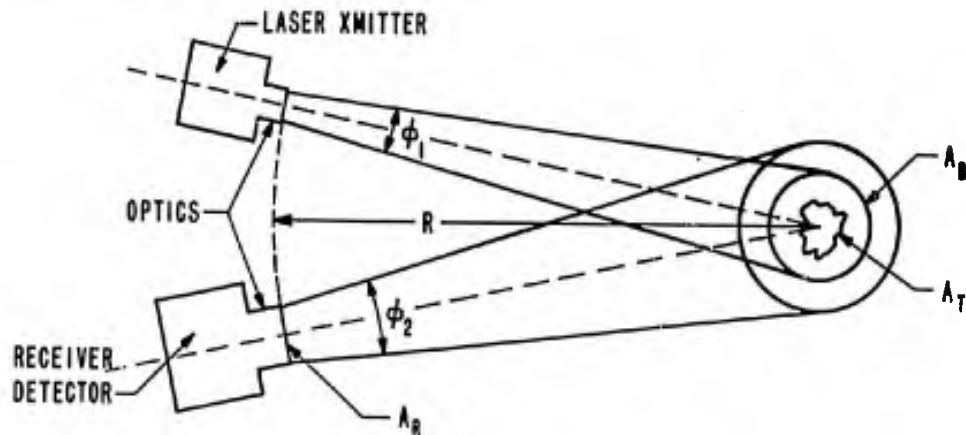


Figure 1.



- | | |
|----------------------------------|---|
| A_R - AREA REC. | R - RANGE |
| A_B - AREA BEAM @ R | k_1 - XMIT. OPTICS COEF. |
| ϕ_1 - XMITTER FIELD OF VIEW | k_2 - REC. OPTICS COEF. |
| ϕ_2 - REC. FIELD OF VIEW | T_{AIR} - ATMOSPHERE LOSS CONSTANT
(ABSORPTION & SCATTERING) |
| A_T - AREA TARGET | ρ - TARGET REFLECTIVITY |
- SYSTEM PARAMETERS**

Figure 2.

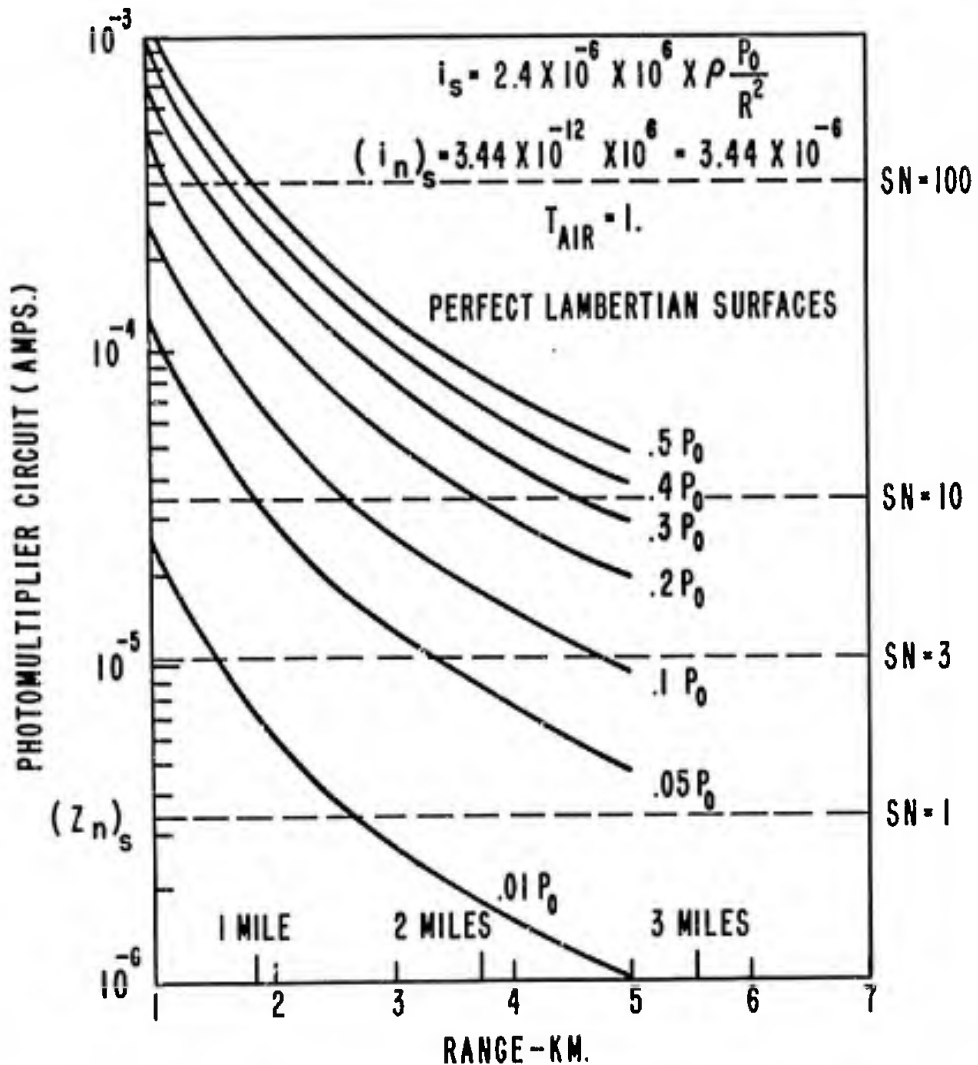


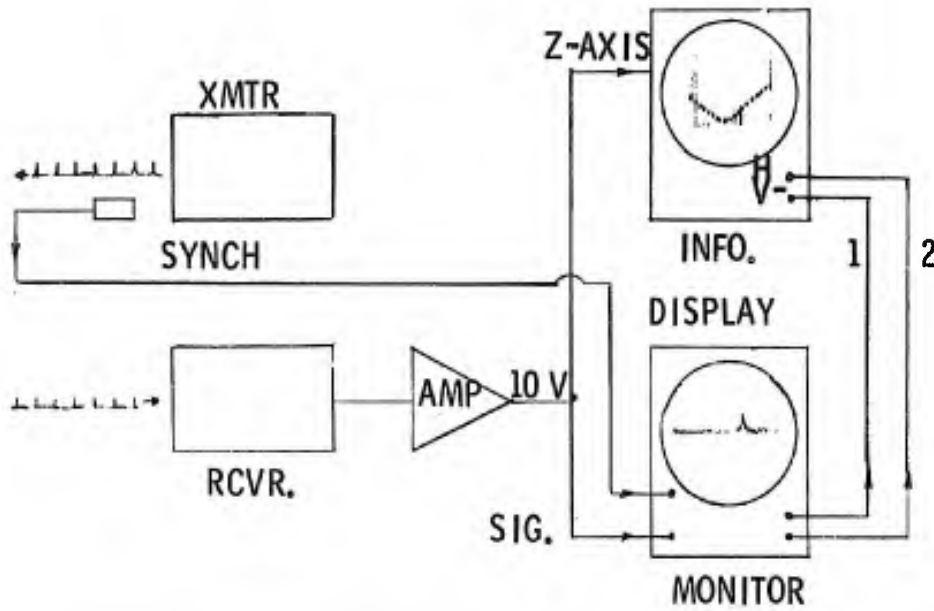
Figure 3. Anode current from range equation considerations.
Target = Beam size.

LASER CHARACTERISTICS

AVERAGE POWER ~ 1Watt
 PRF 500-5000 pps
 PULSE WIDTH 0.2 - 0.3 μ sec. DUTY CYCLE = 1.25 × 10⁻³
 PEAK POWER ~ 1 KW max.
 BEAM DIVERGENCE ~ 6 - 10 m rad. (P_R & T dep.)
 ROOM TEMPERATURE WATER COOLED OPERATION.
 CW PUMPING 1 - 1.3 KW max.

Figure 4.

SYSTEM DIAGRAM



- 1. SAWTOOTH, (RASTER FRAME)
- 2. SAWTOOTH, (RASTER LINE)

Figure 5.

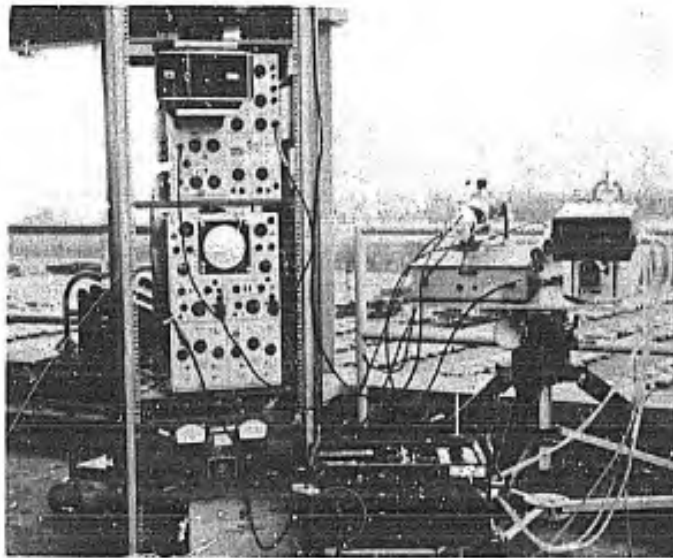


Figure 6. System in use.

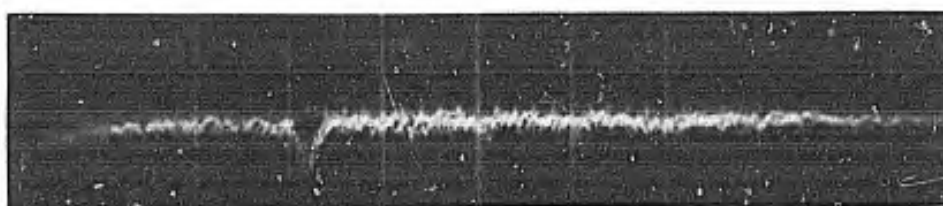
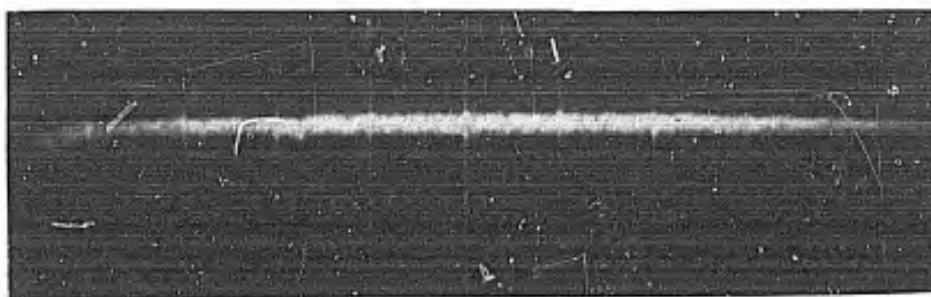


Figure 7. Radio tower, range 1000 meters:
Top trace - heavy rain: Bottom trace - overcast.

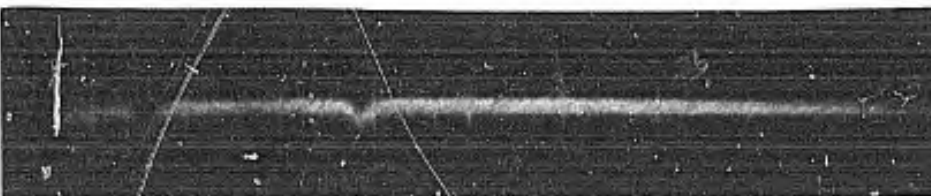
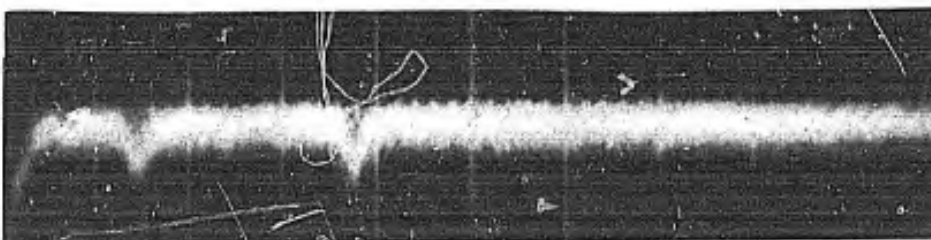
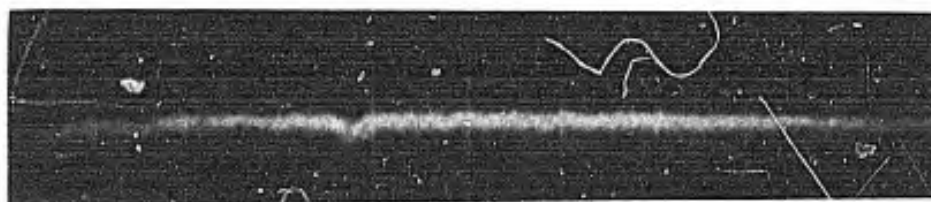


Figure 8. Wires and roof, ranges 500 meters and 1100 meters:
Top - heavy rain: Middle - bright sun: Bottom - overcast.

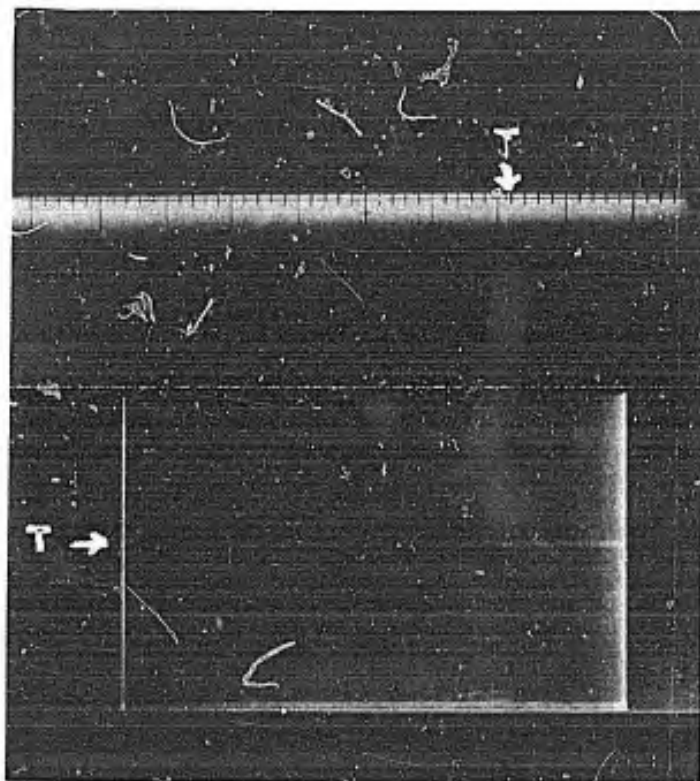


Figure 9. Beam filling target, range 4300 meters, bright sun.
Top trace - "A" type: Bottom trace - raster.



Figure 10. Terrain Mapping Operation. Targets vary in range from 50 to 1500 meters.

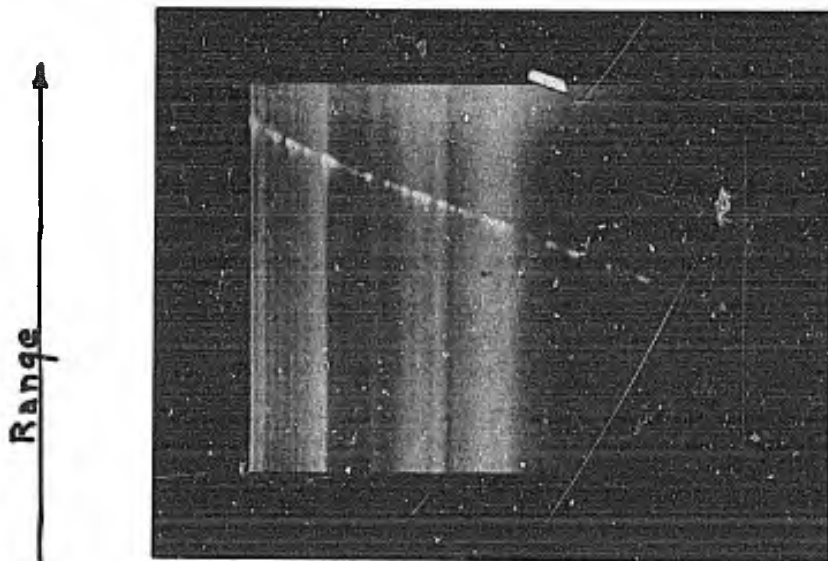


Figure 11. Manual Tracking of H-19 Helicopter. Range starts at 3000 meters, velocity 52.9 knots.

A LIGHTWEIGHT ELECTRONIC SCANNING RADAR

HAROLD N. TATE
CS, TA&SI LABORATORY, USAECOM
FORT MONMOUTH, NEW JERSEY

BACKGROUND

Current vintage combat surveillance radars, used in forward areas, utilize antennas requiring mechanical motion to scan the battlefield. This motion is easily detected (visually) by enemy patrols, thus making the radars vulnerable to enemy attack. The experimental radar described herein employs inertialess techniques which permits scanning a given azimuth sector without any physical motion of the antenna. Figure 1 is a sketch depicting the concept. The radar consists of a receiver-transmitter unit (RTU) and a remote-control unit (RCU). The antenna is made up of 16 line sources forming a flat plate array. The remote control unit shown here utilizes a cathode ray tube as a doppler "B" type display. The RCU is capable of being remotely located up to 50 feet so as to afford operation from a secure position (foxhole). Figure 2 is a plan view showing the sector width scanned and the rough azimuthal beamwidth. There are thirty discrete beam positions of 50 mils each. The scanning commands are generated in a small laboratory-developed beam steering computer. Since the azimuth beam steps in 50 mil increments, monopulse techniques are employed in azimuth with the idea of obtaining more precise azimuth data. Such a scheme is shown in Figure 3. The antenna is split electrically thus permitting the generation of sum and difference patterns. The difference pattern (A-B) is the error function which is utilized to obtain sense with respect to a given boresight position. The meter at the upper right is shown just to indicate a possible method of displaying the location of a given target with respect to the boresight. There are thirty such boresight positions which are determined by the 5-bit logic coming from the beam steering computer. A front view of the first experimental antenna is shown in Figure 4. It consists of an array of milled slots. Each of 16 vertical columns are located on a single flat aluminum plate. Each column of slots is milled in the front face of a ridged waveguide channel. Figure 5 is a rear view of the same array showing the power

TATE

divider and the 16, 4-bit ferrite phase shifters. The driver is an integral part of each phase shifter. The automatic azimuth scanning can be over-riden by a manual control. The beam can quickly be placed on any one of the 30 azimuth beam positions at the will of the operator and a doppler range gate can be positioned on targets to determine their classification (vehicle or personnel). The automatic azimuth scan can also be resumed at the will of the operator. Test results on this antenna have shown that mutual slot coupling limits the sector width to ± 500 mils. The cost of fabricating such an array in production would no doubt prove quite costly. Therefore, other approaches are under consideration. Figure 6 is a photo-etched line source fabricated in polyguide. The edges are bound by rivets thus forming a dielectrically loaded waveguide with etched slots in one face. OSM connectors have been placed at both ends. By feeding one end and measuring the power collected at the far end, the efficiency of the traveling wave line source can be determined if the dielectric and connector losses are known. Samples have been designed and fabricated. They are currently being tested and evaluated. Should these results prove satisfactory, 16 such line sources will be etched in a single sheet of polyguide. Our friends, at Harry Diamond Laboratories, have demonstrated that the rivets can be omitted by plating through the rivet holes. Should this prove to be the case, truly inexpensive lightweight antennas can be mass produced to solve not only our problem but many others. This truly lightweight antenna will require that a review be made of the other antenna components contributing excessive weight. This has already been initiated. The relative size of the ferrite and diode phase shifters are shown in Figure 7. The ferrite phase shifter weighs 1.25 pounds as compared with 2.5 ounces for the diode phase shifter shown in this figure. From the standpoint of developing small, lightweight radars, there is no question in one's mind which phase shifter is superior. The insertion losses, insertion phase and phase reciprocity of the ferrite phase shifters was poorer than that of the diode phase shifters. Figure 8 depicts some of these data on the diode phase shifters. Columns 3 and 4 show the insertion loss as a function of the 16 phase states. Column 5 is a measure of the loss reciprocity looking into ports 1 and 2. Columns 6 and 7 show the exact measured phase over the 16 phase states. The lower this number, the better the phase shifter. These values are shown for a frequency of 5600 MHz but are indicative of those measured at 5600 ± 200 MHz.

DISPLAY UNIT

Our current display is a cathode ray tube (CRT). It is a "B" type indicator which displays 5000 meters range versus ± 750 mils in azimuth. This permits an azimuth coverage of approximately ± 800 mils. We currently display moving targets, only. Since there are 50 elements in range and 30 elements in azimuth, 1500 bits presents the maximum display capability. The CRT has a very poor form factor for man-packed radars. It also requires large acceleration voltages for a reasonable light output. These disadvantages may be overcome by

resorting to the use of a solid-state display. The display under consideration is one consisting of a matrix of 50 by 30 gallium arsenide light emitting diodes with appropriate drive circuits. This display not only has an excellent form factor but the light output is quite bright and the operating voltage required is the order of 12 volts DC as compared with kilovolts for the CRT. The same digital logic required for giving the phase shifters the azimuth scanning commands is utilized to keep the CRT and solid state displays in step with each azimuth pointing angle. The video is processed in the MTI unit and only moving targets are fed serially into the display. The solid state display is capable of holding a picture for long periods of time, thus permitting the updating of prior information. This will permit the operator to observe traffic patterns over a large area.

MOVING TARGET INDICATOR

The moving target indicator (MTI) unit consists of 50 contiguous miniaturized range gate filters, mounted on a mother board. The unit is housed in the remote control unit. One of the range gate filters is shown in Figure 9. The lower cutoff frequency is currently operator-adaptive, and rolls off at 12 dB per octave. This feature permits the operator to adjust the display for a constant false alarm rate depending upon the wind velocity (clutter spread). Plans are being made to sample the clutter and make the cutoff frequency automatically adaptive to windblown clutter.

TRANSMITTER - LOCAL OSCILLATOR

Often, the transmitter - local oscillator combination is responsible for the major power dissipated by the radar. During the development of this breadboard radar, a novel transmitter - local oscillator was conceived. Its operation can best be described by referring to Figure 10. A triode cavity serves as single, high level pulse transmitter and a gated, low power local oscillator. The transmitter - local oscillator is keyed with a high level pulse ($\approx 1000v$) during the time interval "S". The common transmitter - local oscillator generates a microwave pulse of the order of 200 watts peak at frequency f_1 . This signal reaches the antenna via the circulator. During the receive time, R_t , a low level voltage ($\approx 175V$) keys the common transmitter - local oscillator and it generates a gated low level (100 mw) microwave signal at frequency f_2 . This signal reaches the mixer at a reduced level of (-20 dB) and serves as the local oscillator injection for the mixer. Echo returns at $f_1 \pm f_d$ also enter the mixer via the antenna-circulator and limiter where they are heterodyned with f_2 . The difference frequency $(f_1 - f_2) \pm f_d$ is then selected by the IF amplifier. During the dead time "D_p" the device is completely passive and only the heater is dissipating power. This device has now been utilized in a system with excellent success. Tests have been conducted over a wide temperature range and the local oscillator tracks the high level transmitter frequency remarkably well. No automatic frequency circuitry

TATE

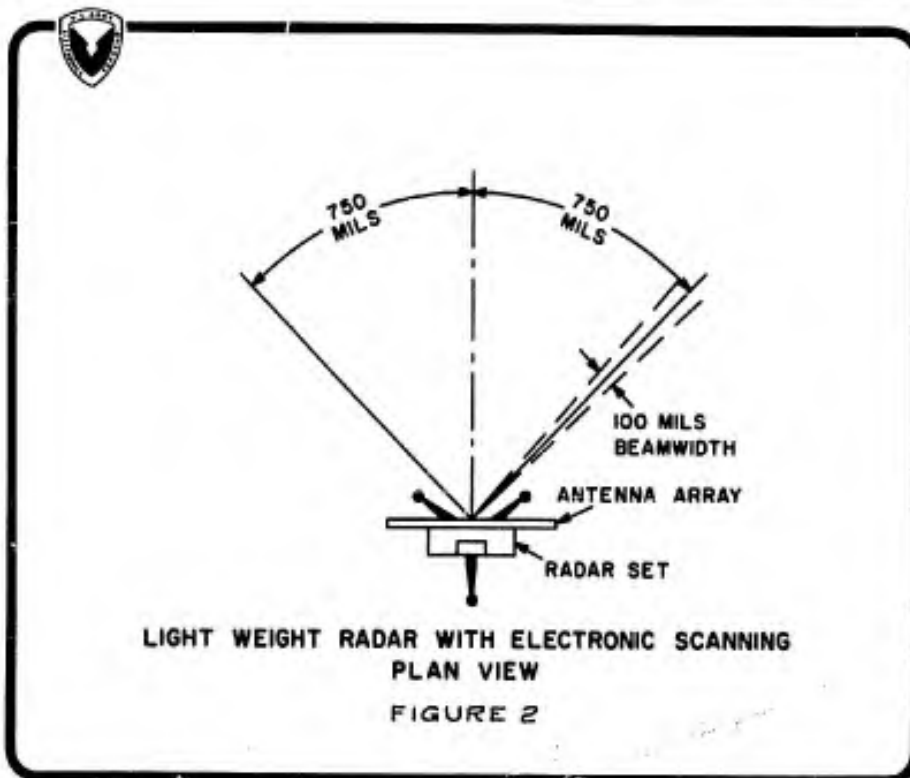
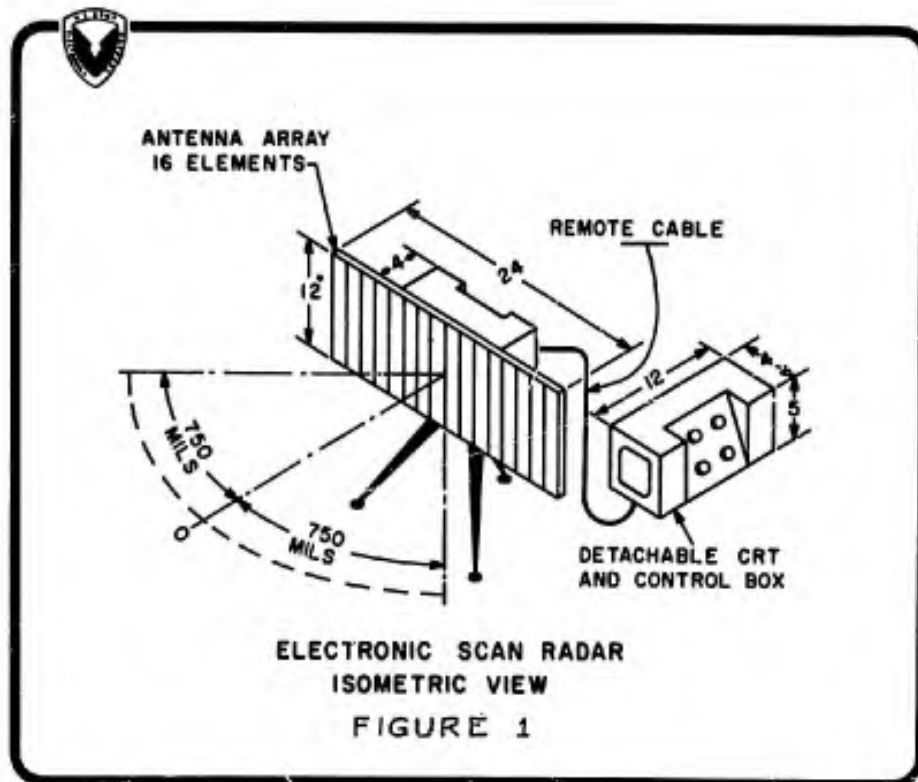
is required. This simplifies the radar circuitry considerably and should be reflected in lower manufacturing, training and maintenance costs. Figure 11 is a photograph of the device. Additional effort is underway to increase the output power and improve the azimuth resolution of the system in order to extend the useful range of the radar set. To this end a 1 kilowatt transmitter is currently being tested and evaluated. The device is shown in Figure 12. Some of the improved radar characteristics are shown in Figure 13. The transmitter's peak power has been increased from 0.2 to 1 kilowatt peak and the azimuth resolution has been improved to 50 mils. These changes should result in an increase in range by a factor of 2 times.

SUMMARY

In summary, some of the objectives of the program have been achieved. Others have not been brought to fruition as of this writing. However, there is sufficient component test data to show that a complete breadboard system incorporating the improved techniques described herein, will be in operation in our laboratory during the summer of 1970.

ACKNOWLEDGMENTS

Acknowledgments are in order for the fine work of Mr. George Hrivnak and Mr. Russell Gilson, of the Components Laboratory, on the Beamsteering Computer and Range Gate Filters respectively.



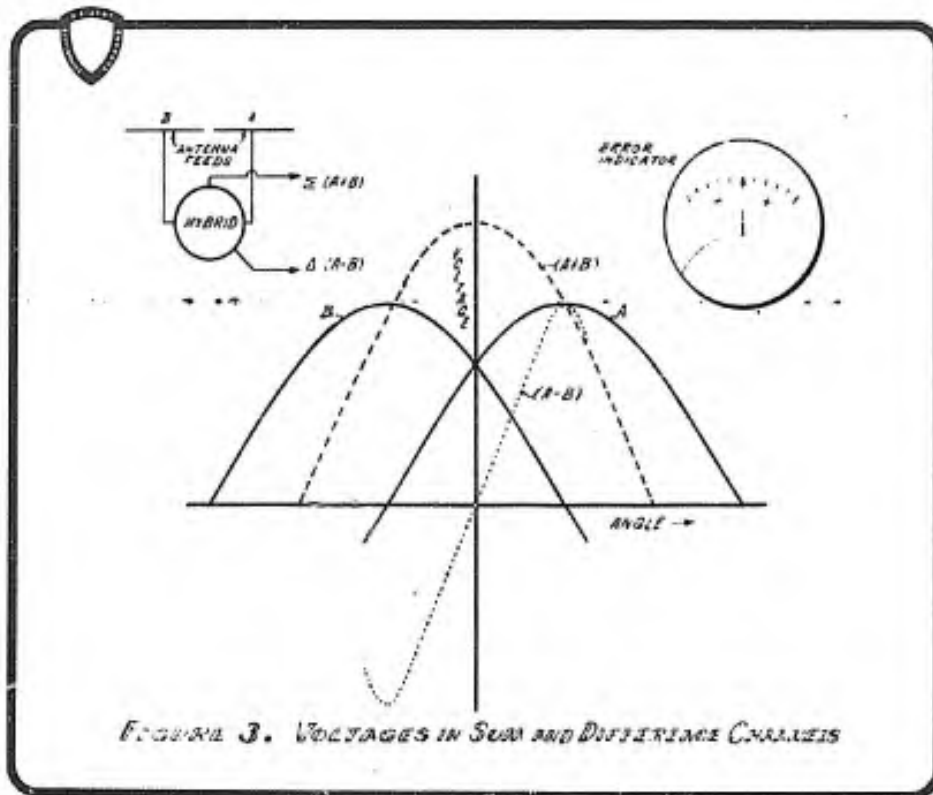


FIGURE 3. VOLTAGES IN SUM AND DIFFERENCE CHANNELS

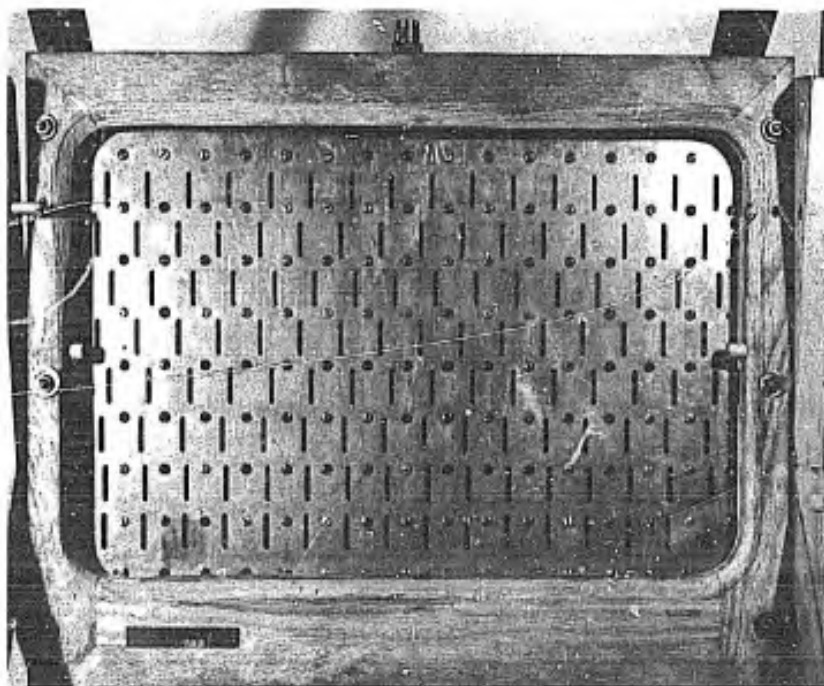


FIGURE 4

TATE

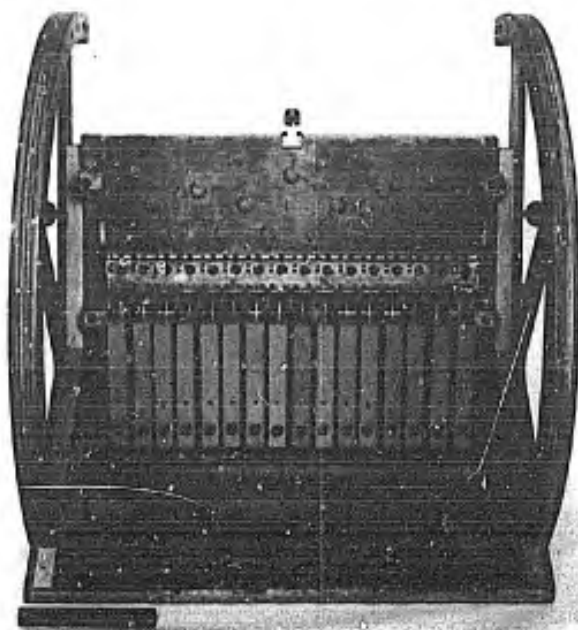
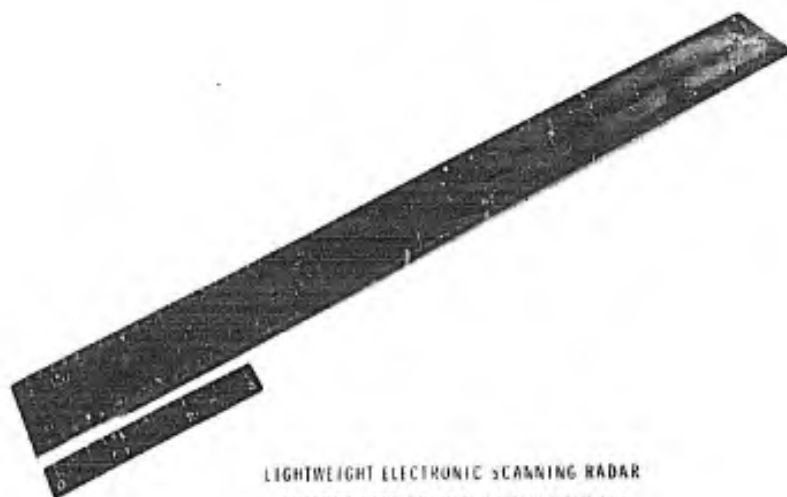


FIGURE 5



LIGHTWEIGHT ELECTRONIC SCANNING RADAR
ANTENNA LINE SOURCE ISLOTTED ARRAY

FIGURE 6

TATE

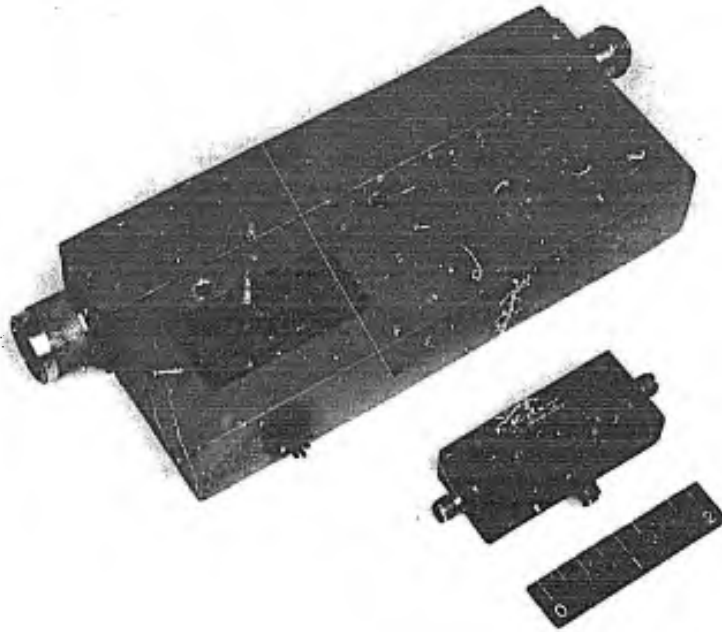



FIGURE 7



C^B BAND DIGITAL PHASE SHIFTER **MICROWAVE ASSOC. MODEL NO. 8388-8C104**
FT. MON. 1/2/70

UNIT 7		AND 7 OUT					
OCT#	CODE	IL1	IL2	DEL-IL	PH1	PH2	DEL-PH
F = 5600.							
00	1	-1.63	-1.60	.04	.00	-.40	-.40
01	2	-1.56	-1.54	.02	-22.20	-22.80	-.60
02	3	-1.46	-1.45	.01	-43.90	-44.50	-.60
03	4	-1.42	-1.42	.00	-66.80	-67.20	-.40
04	5	-1.39	-1.38	.01	-89.50	-89.50	.00
05	6	-1.40	-1.38	.02	-111.90	-112.00	-.10
06	7	-1.32	-1.34	-.02	-133.30	-133.50	-.20
07	8	-1.31	-1.32	-.01	-156.40	-156.40	-.20
10	9	-1.57	-1.56	.00	-179.10	-179.50	-.40
11	10	-1.54	-1.55	-.01	-201.50	-202.00	-.50
12	11	-1.69	-1.69	-.01	-224.20	-224.60	-.40
13	12	-1.68	-1.68	.00	-247.50	-247.90	-.40
14	13	-1.65	-1.64	.01	-270.90	-270.90	.00
15	14	-1.65	-1.61	.04	-293.20	-293.30	-.10
16	15	-1.68	-1.70	-.03	-316.20	-316.20	.00
17	16	-1.65	-1.67	-.01	-339.30	-339.30	.00

FIGURE 8

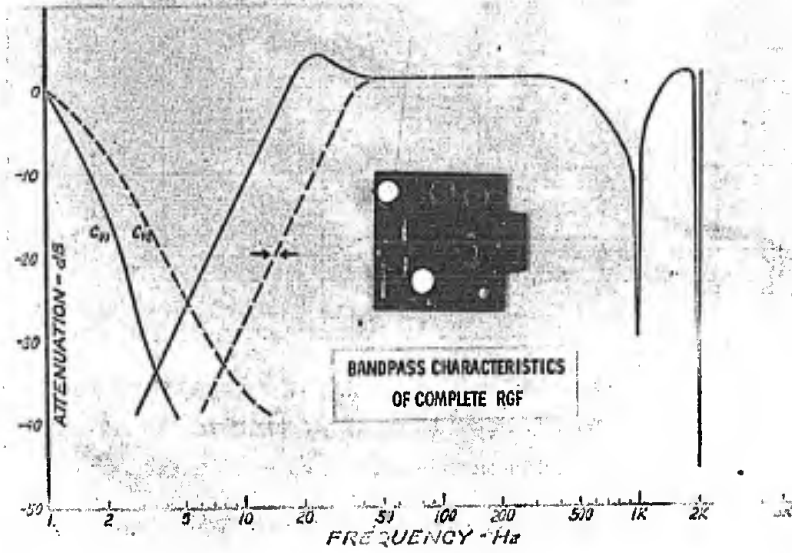


FIGURE 9

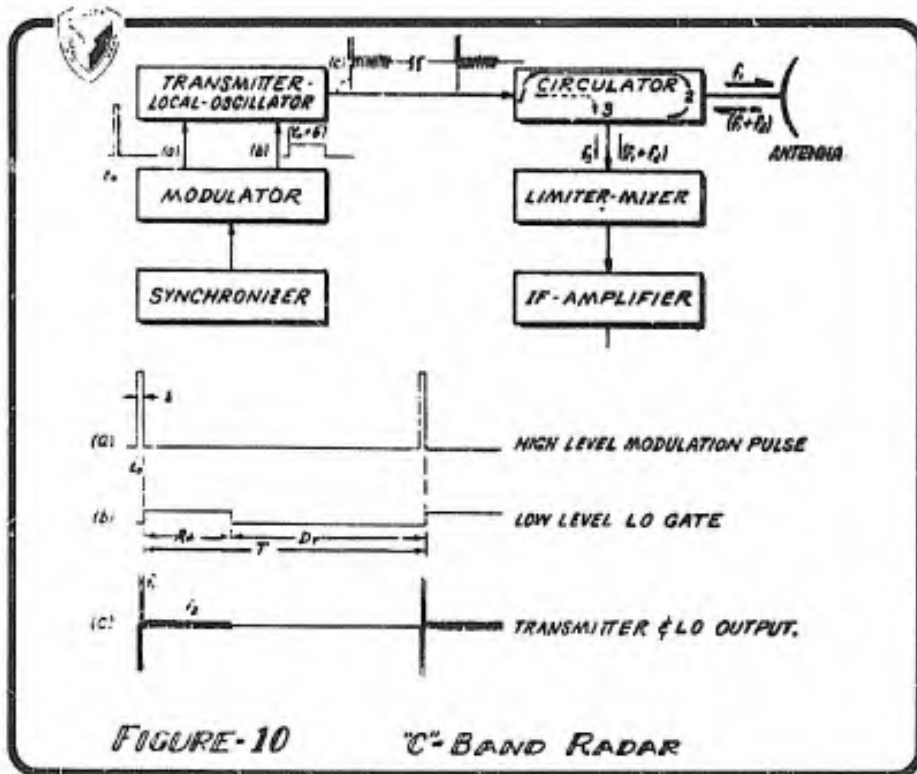
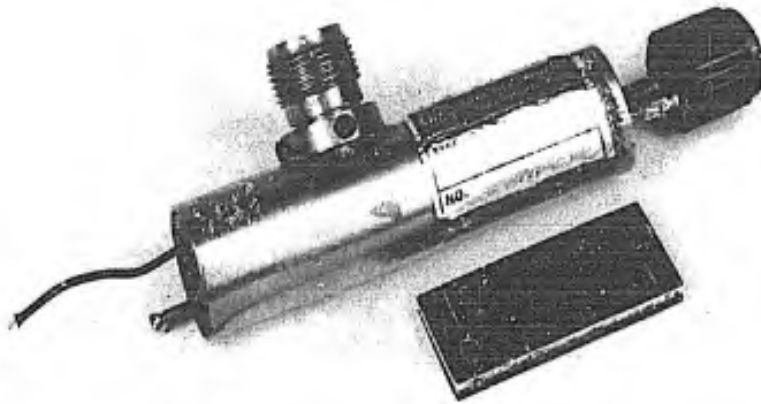


FIGURE-10 C-BAND RADAR

TATE



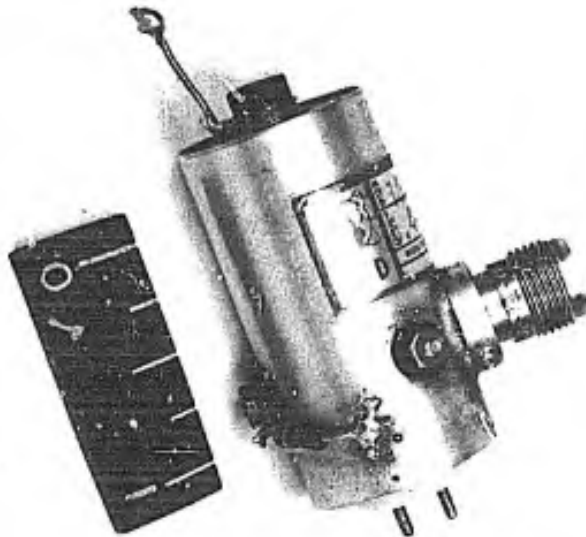
DUAL MODE - L. O. TRANSMITTER

TUBE TYPE - PLANAR TRIODE

FREQUENCY - 5.4 GHz - 5.9 GHz

POWER OUTPUT - 100 WATTS PEAK

FIGURE 11



HIGH POWER TRANSMITTER

TUBE TYPE - PLANAR TRIODE

FREQUENCY - 5.4 GHz - 5.9 GHz

POWER OUTPUT - 1000 WATTS PEAK

FIGURE 12

PERTINENT RADAR CHARACTERISTICS

FREQUENCY	-----	5.4 - 5.9 Gc/s
XMTR POWER	-----	1 KW (P)
PULSE WIDTH	-----	0.25 - 0.5 μ SEC
PRF	-----	2 ± 0.2 Kc/s
ANTENNA	-----	INERTIALESS SCAN
ANT. BW		
- AZIM	-----	\pm 50 MILS
- ELEV	-----	\pm 200 MILS
ANT SCAN WIDTH	-----	\pm 800 MILS
DISPLAYS	-----	"B" & AURAL

FIGURE 13

COMPARATIVE ANALYSIS OF MANDIBULAR AND MID-FACE FRACTURES
IN MISSILE AND BLUNT TRAUMA: 4,015 CASES

LAWRENCE E. TINDER, LTC, DC
LETTERMAN ARMY INSTITUTE OF RESEARCH
SAN FRANCISCO, CALIFORNIA 94129

Although most reports on facial fractures have been limited to fractures of the mandible due to blunt trauma, some studies¹⁻¹⁰ have been concerned with fractures of the middle third of the facial skeleton. In the last century, Le Forte¹ described fractures of the zygomatico-maxillary complex and the detachment of facial bones from the facial skeleton along particular planes of cleavage. More recently, Rowe and Killey² established a series of comparison tables using the Le Forte classifications of facial fractures. Their studies, particularly when supplemented with data of other investigators,³⁻¹⁰ stand as the most comprehensive review on facial fractures due to blunt trauma.

The ratio of mandibular fractures to mid-face fractures due to blunt trauma historically has been considered to be 2 to 1; however, a rise in the incidence of mid-face fractures has been noted in recent reports on both civilian and military patients.¹¹

It is conjectured that the rise in mid-face fractures in military patients is related to the high deployment of sophisticated weapons in present day combat activities. The technological advancements of these weapons have resulted in greater diversity and magnitude of trauma than previously experienced.¹² This investigation is confined to the analysis of data on facial fractures subsequent to some of these forms of trauma.

The purpose of this study was to compare the relative occurrence of mandibular, mid-face, and combination fractures of the mandible and mid-face due to various types of trauma which have afflicted members of the U.S. Army. An additional purpose of this study was to formulate a basis for comparatively evaluating facial injuries caused by diverse forms of missile and blunt trauma.

MATERIALS and METHODS

This study was based on data obtained in a survey of oral and maxillofacial injuries at selected U.S. Army hospitals in Vietnam during a two-year period ending 30 June 1969, and at selected military installations in the continental United States, Berlin, and Hawaii during a one-year period ending 30 June 1968. Data were obtained from reports submitted by attending Army dentists. Most of the patients who were reported to have suffered facial bone fractures were active duty U.S. Army personnel.

Accumulated data concerning patients with facial fractures were divided into four general categories of trauma and arbitrarily placed in a convenient order: (1) bullet trauma, (2) missile fragment trauma, (3) "non-ballistic" missile trauma, and (4) blunt trauma. "Non-ballistic" missiles included rocks, gravel, glass, falling debris, and hurled objects. The order selected for blunt trauma injuries was: vehicular accidents, miscellaneous accidents, sports accidents, and altercations.

The specific facial bones investigated in these trauma categories were the mandible, maxilla, malar, and nasal bones. The zygomatic arch and the floor of the orbit were also included as separate entities. The mandibular fractures were further characterized as those with evidence of comminution and those with evidence of avulsion.

Each trauma category was analyzed with electronic data processing equipment for the incidence of single and concomitant facial bone fracture cases, plus the incidence of specific facial bones fractured in concomitant cases. From this data the following information was assembled: (1) fractures of the mandible only, (2) fractures exclusive to one or more mid-face bones, and (3) combination fractures of the mandible and one or more mid-face bones.

In order to better relate to the literature on facial fractures, the mandibular, mid-face, and combination fractures were expressed in ratio form. This was accomplished by selecting mandibular fractures as the reference point from which comparisons would be made (mandibular fractures were assigned the value of one). The values for mid-face and combination fractures were adjusted accordingly. This procedure was also carried out on data reported in previous studies by Rowe and Killey² and Schuchardt et al.³

RESULTS

A total of 4,015 facial fracture patients were included in this study, of which 67.4 percent (2,705) were injured by missiles and 32.6 percent (1,310) were injured by blunt trauma.

TINDER

In the missile group: 23.6 percent (638) of the individuals were injured by bullets, 45.4 percent (1,228) were injured by missile fragments, and 31.0 percent (839) were injured by "non-ballistic" missiles. All of the bullet and fragment injuries and about one-quarter of the "non-ballistic" missile injuries were sustained under combat circumstances.

In the blunt trauma group: 35.3 percent (464) were associated with vehicular accidents, 16.2 percent (213) were involved in miscellaneous accidents, 5.1 percent (67) were sports-related accidents, and 43.6 percent (573) of the blunt trauma fractures were caused by altercations. About half of the vehicular accidents and about half of the miscellaneous accidents were sustained under combat circumstances.

Table I reveals the four general categories of trauma and the sub-categories of blunt trauma arranged in order of their respective single and concomitant facial bone fracture incidences. Table II shows the specific facial bones involved in those cases where only one bone was fractured. In all categories of trauma where only one facial bone was fractured, the mandible was most frequently involved. The nasal bone ranked second in frequency of specific bones fractured. The individual facial bones intimately associated with the zygomatico-maxillary complex (malar, zygomatic arch, and orbital floor) infrequently occurred as single facial bone fractures. The greater part of the maxilla is anatomically less intimately associated with the complex. Hence, a moderate incidence of maxillary fractures alone was observed. Table III shows the concomitant fracture cases, and enumerates the specific facial bones which were fractured. In general, the bones of the zygomatico-maxillary complex had the highest incidences of fractures in the concomitant fracture cases. Table IV revealed that mandibular comminution and mandibular avulsion were generally more common in combination fractures than in mandibular fractures alone. These tables served as the basis for the following observations:

Bullet trauma:

Bullet wounds had the lowest incidence of single bone fracture cases (see Table I) mainly because of the infrequent occurrences of nasal bone fractures alone or single fractures of the bones of the zygomatico-maxillary complex (see Table II). Although mandibular fractures alone were relatively common, the infrequency of solitary fractures of mid-facial bones accounted for the low incidence of exclusive mid-face fractures (see Table V) and the low ratio of mid-face fractures to mandibular fractures (see Table VI) in this group.

However, bullet wounds had the highest incidence of concomitant facial fracture cases (see Table I) with correspondingly high rates of specific facial bone fractures (see Table III). Moreover, the high incidence of mandibular fractures in those cases

TINDER

with concomitant fractures (see Tables III and V) is sufficient to effect a comparatively high ratio of combination fractures when compared to the solitary mandibular fractures (see Table VI).

Mandibular comminution and mandibular avulsion were most often noted in bullet trauma. They occurred eight percent more frequent when the mandible was fractured alone than when fractured in combination with mid-face bones. In each fracture group, mandibular comminution was approximately 25 percent more common than mandibular avulsion (see Table IV).

Fragment trauma:

Although concomitant fracture cases were less frequent (see Table I) and the rates of specific bones fractured in these cases were less for fragment trauma than for bullet trauma (see Table III), a higher percentage of exclusive mid-face fractures was recorded for fragment trauma (see Table V). This was due to the relatively high number of solitary fractures of the maxilla or nasal bones (see Table II) plus the relatively low number of solitary or concomitant mandibular fractures (see Table III). The net effect was that exclusive mid-face fractures subsequent to fragment wounds were 16.5 percent more common than mandibular fractures alone (see Table V). Although lower in value than in bullet trauma, the incidence of mandibular comminution due to missile fragments was about equal in mandibular fractures alone and combination fractures. In each fracture group, mandibular comminution was approximately 30 percent more common than mandibular avulsion (see Table IV).

"Non-ballistic" missile trauma:

In contrast to bullet and fragment trauma, "non-ballistic" missile trauma was rarely associated with tissue penetration. The incidence of single facial bone fractures due to "non-ballistic" missiles was closer numerically to blunt trauma than it was to penetrating types of missiles (see Table I). Although the highest percentage of nasal fractures alone were recorded in "non-ballistic" missile wounds, the rates of other facial bone fractures either as single or concomitant fractures were relatively low (see Tables II and III). In addition, this high frequency of nasal fractures was primarily responsible for a 17 percent higher rate of exclusive mid-face fractures than solitary mandibular fractures in this group (see Table V).

In combination fractures due to "non-ballistic" missiles, the incidence of mandibular comminution was more than twice and the incidence of mandibular avulsion was more than five times the respective values computed for mandibular fractures alone (see Table IV).

Blunt trauma:

Analysis of the sub-categories of blunt trauma revealed that vehicular accidents had the lowest incidence of single facial

TINDER

bones fractured concomitantly (see Table III). The relatively low frequency of nasal fractures alone (see Table II) was largely responsible for the relatively low incidence of exclusive mid-face fractures in vehicular accidents. The incidence of combination fractures (see Table V) was high enough to make the ratio of these fractures to that of mandibular fractures alone greater in vehicular accidents than in any other form of trauma (see Table VI).

The frequent occurrence of mandibular or nasal fractures only in miscellaneous and sports accidents (see Table II) accounts for these types of trauma having higher incidences of single facial bone fractures than did vehicular accidents (see Table I). In addition, the incidence of concomitant fractures in these accidents was much lower than in vehicular accidents. Furthermore neither the mandible nor the nasal bones were involved in concomitant fractures due to sports accidents (see Table III). Sports accidents were clearly either a mandibular or a mid-facial bone fracture exclusively (see Table V).

The highest incidence of single facial bone fractures was found in altercations (see Table I). The lower jaw and the nose were such specific targets that over 81 percent of the altercations which resulted in facial fractures had a fracture of either the mandible alone or the nasal bones alone (see Table II). The few concomitant fractures which resulted from altercations rarely included the mandible or nasal bones (see Table III).

Mandibular comminution due to blunt trauma was approximately twice as frequent in combination fractures as in mandibular fractures alone; yet lower than in the other major categories of trauma. Mandibular avulsion occurred in about 10 percent of the combination fracture patients but rarely occurred in solitary mandibular fractures (see Table IV).

DISCUSSION

The current literature on facial fractures does not afford sufficient data for valid comparisons of facial fractures caused by diverse forms of trauma. The literature, predominately, has been more concerned with mandibular fractures than mid-face fractures, treatment more than cause, and blunt trauma more than the other forms of trauma.

Although most of the data used for this study were related to patients who received facial fractures in combat situations, approximately one-third of the data sample involved persons acquiring facial fractures in situations (vehicular accidents, altercations, sports accidents, etc.) comparable to those commonly occurring in the civilian community.

TINDER

Missile trauma:

In contrast to blunt trauma, missile impact sites on the face are more random in distribution. It is conjectured that if data were compiled for a significant number of cases (including those which were fatal), this distribution would be uniform over the surface area. This study was based on the premise that, in non-fatal cases, the incidence of mid-face fractures would be lower in the more lethal forms of missile trauma, and that the relative distribution of mandibular, mid-face, and combination fractures would reveal a pattern based on the relative potency of various forms of missiles.

The comparatively low incidence of exclusive mid-face fractures (34.3 percent) due to bullets suggests that only persons receiving a tangential hit to the mid-face would survive. The high incidence of combination fractures (20.6 percent), where the trajectory of the bullet aligns with the mandible and mid-face, strengthens this supposition.

The 18.6 percent higher incidence of mid-face fractures due to fragments suggests that individuals are more able to survive direct hits to the mid-face by fragments than by bullets. This is due in fact to the penetration depth of missile fragments being less than that of bullets, due to the lower momentum and higher retardation of the fragments. In addition, the irregular configurations of fragments cause a more rapid retardation of momentum upon penetration into the facial tissues and thus a more rapid release of expended energy nearer the surface than occurs with bullet wounds. This is extremely important in the mid-face area where further penetration and deeper release of energy would seriously affect vital structures.

In combat situations, explosions will frequently "shower" individuals in the immediate area with rocks, gravel, glass, falling debris, and other secondary missiles. These "non-ballistic" missiles (including hurled objects) have lower velocities, momenta, and energy levels than either bullets or missile fragments. Therefore, these missiles cause a relatively higher incidence of non-fatal mid-face fractures than bullets because of their lower potency. Although missile fragments and "non-ballistic" missiles each had 17 percent more mid-face fractures than mandibular fractures alone, the comparatively low incidence of combination fractures by "non-ballistic" missiles is attributed to the less severe type of forces involved in this class of trauma.

Unlike bullet trauma, the relatively low incidence of mandibular fractures subsequent to missile fragment and "non-ballistic" missile trauma suggests that these insults are often of insufficient magnitude to cause mandibular fractures, but still are of sufficient force to create fractures of the mid-face. The comparatively low incidence of combination fractures due to fragment and "non-ballistic" missiles indicates the relatively low magnitude

TINDER

of these trauma as compared to that of bullets.

Higher incidences of mandibular comminution and mandibular avulsion were recorded for penetrating missiles (bullets and missile fragments) when the mandible was fractured alone rather than in combination with mid-facial bones. The contrast was greatest in bullet trauma and was related to the consistently high level of kinetic energy associated with this type of trauma. In bullet trauma, when this level of energy was confined to mandibular fractures alone, a higher degree of comminution and avulsion was recorded than when the energy was dissipated by the fracturing of additional facial bones.

The highly variable masses and velocities associated with "non-ballistic" missiles gave "non-ballistic" missile trauma the widest range of insulting magnitude. It is presumed that combination fractures were caused by the more severe levels of energy which in effect developed higher incidences of mandibular comminution and mandibular avulsion.

Blunt trauma;

Although the mandible encompasses less surface area than the more fragile mid-face skeleton, its higher incidence of fracture subsequent to blunt trauma insults is considered to be due to its exposed position and the direction from which blunt trauma blows commonly strike the face. In this population sample, a number of blunt trauma injuries were the result of altercations. The traditional target in such situations is most often the mandible.

The relative incidence of mid-face fractures is appreciably higher than that reported in previous studies by Rowe and Killey² and Schuchardt et al.³ This is consistent with Dingman's contention¹ that a rise in the incidence of mid-face fractures becomes apparent when military reporting and high-speed transportation accident cases are considered. Although a specific comparison cannot be made because of the diversity of accidents and circumstances between studies, in contrast to the combined data of these investigators,^{2,3} exclusive mid-face fractures subsequent to blunt trauma were found to be 14 percent higher and combination fractures were 4 percent higher; mandibular fractures occurred 22 percent less frequently. These variations are considered to be due to the more aggressive activities characterizing a military population; the magnitude of blunt trauma forces is considered to be higher. As Rowe and Killey² contend, blunt trauma forces of higher magnitude effect a relative increase in the incidence of mid-face fractures when compared to mandibular fractures.

SUMMARY

Data pertaining to 4,015 facial fracture cases due to various types of trauma were examined to determine the relative incidence of: mandibular fractures alone, exclusive fractures of one or more mid-face bones, and combination fractures of the mandible and one or more mid-face bones for each form of trauma. These findings were expressed in ratio form. On analysis the following observations were made:

1. In bullet trauma: 45.1 percent of the patients had mandibular fractures alone, 34.3 percent had exclusive mid-face fractures, and 20.6 percent had combination fractures of the mandible and one or more mid-face bones. Expressed as a ratio, with mandibular fractures alone assigned a value of one, these values became 1 to 0.760 to 0.454 for bullet trauma.

2. In fragment trauma: 36.4 percent of the patients had mandibular fractures, 52.9 percent had exclusive mid-face fractures, and 10.7 percent had combination fractures. Expressed as a ratio, these values became 1 to 1.454 to 0.293 for missile fragment trauma.

3. In "non-ballistic" missile trauma: 37.9 percent of the patients had mandibular fractures, 55.7 percent had exclusive mid-face fractures, and 6.4 percent had combination fractures. Expressed as a ratio, these values became 1 to 1.437 to 0.201 for "non-ballistic" missile trauma.

4. In blunt trauma: 48.0 percent of the patients had mandibular fractures alone, 43.6 percent had exclusive mid-face fractures, and 8.4 percent had combination fractures of the mandible and one or more mid-face bones. Expressed as a ratio, these values became 1 to 0.908 to 0.175 for blunt trauma.

BIBLIOGRAPHY

1. LE FORT, R. Fractures de la machoire superieure Congr. int Med., Paris, Sect. Chir. gen., pp. 275 (1900).
2. ROWE, N.L. and KILLEY, H.C. Fractures of the Facial Skeleton. Williams and Wilkins, Baltimore, 1968.
3. SCHUCHARDT, K., BRICHETTI, L.M., and SCHWENZER, N. Fractures of the Facial Skeleton: Statistical Report on 1,566 instances. Dental Abstracts, Chicago, 6:277, 1961.
4. MALLET, S.P. Fractures of the Jaw. A Survey of 2,124 Cases. J. Amer. Dent. Assn. Dent. Cosmos 41:657, 1950.
5. RAWSON, R.L. and FORDYCE, G.L. Complex Fractures of the Middle Third of the Face and Their Early Treatment. Brit. J. Surg. 41:255, 1953.
6. KULOWSKI, J. Facial Injuries: A Common Denominator of Automobile Casualties. J. Amer. Dent. Assn. 53:32, 1956.
7. LINDSTROM, D. Comparative Survey of Jaw Fractures During the Years 1948-1958. Dent. Abstr. 5:596, 1960.
8. MC COY, F.J., CHANDLER, R.A., MAGNAN, C.G., MOORE, J.R. and SIEMSEN, G. An Analysis of Facial Fractures and Their Complications. Plast. & Reconstr. Surg. 29:381-391, Apr. 1962.
9. KRØMER, H. Den Dentaikirurgiske Behandling av Kjevfracturer. Oslo: Fabritius and Sonner, 1954.
10. KAZANJIAN, V.H. Fracture of the facial bones. In Experience in the Management of Fractures and Dislocations. Ed. Wilson, P.D., Philadelphia: Lippincott., 1938.
11. DINGMAN, R.O. and NATVIG, P. Surgery of Facial Fractures. Philadelphia: W.B. Saunders, 1967.
12. TINDER, L.E., OSBON, D.B., LILLY, G.E., SALEM, J.E., and CUTCHER, J.L. Maxillofacial Injuries Sustained in the Vietnam Conflict. Milt. Med. Vol. 134:9, 668-672, Sept. 1969.

TINDER

TABLE I
INCIDENCE* OF SINGLE AND CONCOMITANT FACIAL BONE FRACTURES

<u>Cause of Injury</u>	<u>Single Facial Bone Fractures</u>	<u>Concomitant Facial Bone Fracture Cases</u>
Bullets	353 (55.3)	285 (44.7)
Fragments	753 (61.3)	475 (38.7)
"Non-ballistic" missiles	618 (73.7)	221 (26.3)
Blunt trauma:	988 (75.4)	322 (24.6)
Vehicular accidents	274 (59.3)	188 (40.7)
Miscellaneous accidents	162 (77.9)	46 (22.1)
Sports accidents	54 (80.6)	13 (19.4)
Altercations	498 (86.9)	75 (13.1)
All forms of trauma	2,712 (67.5)	1,303 (32.5)

* Numbers in parenthesis are percentages calculated on the basis of the total number of patients in each trauma category.

TABLE II
 * INCIDENCE OF SPECIFIC SINGLE FACIAL BONE FRACTURES

Cause of Injury	Mandible	Nasal	Maxilla	Malar	Zygomatic Arch	Orbital Floor
Bullets	288 (45.1)	10 (1.6)	30 (4.7)	2 (0.3)	20 (3.1)	3 (0.5)
Fragments	447 (36.4)	95 (7.7)	165 (13.4)	27 (2.2)	none	19 (1.5)
"Non-ballistic" missiles	318 (37.9)	242 (28.8)	34 (4.1)	8 (1.0)	13 (1.5)	3 (0.4)
Blunt trauma:	629 (48.0)	239 (18.2)	71 (5.4)	21 (1.6)	21 (1.6)	7 (0.5)
Vehicular accidents	175 (37.9)	43 (9.3)	34 (7.4)	14 (3.0)	6 (1.3)	2 (0.4)
Miscellaneous accidents	100 (48.1)	41 (19.7)	14 (6.7)	1 (0.5)	4 (1.9)	2 (1.0)
Sports accidents	28 (42.0)	15 (22.4)	6 (9.0)	2 (3.0)	3 (4.5)	none
Altercations	326 (56.9)	140 (24.4)	17 (3.0)	4 (0.7)	8 (1.4)	3 (0.5)
All forms of trauma	1,682 (41.9)	586 (14.6)	300 (7.5)	58 (1.4)	54 (1.3)	32 (0.8)

* Numbers in parenthesis are percentages calculated on the basis of the total number of patients in each trauma category.

TABLE III
INCIDENCE* OF SPECIFIC FACIAL BONES FRACTURED CONCOMITANTLY

Cause of Injury	Mandible	Nasal	Maxilla	Malar	Zygomatic Arch	Orbital Floor
Bullets	131 (20.5)	123 (19.3)	250 (39.2)	188 (29.5)	122 (19.1)	159 (24.9)
Fragments	131 (10.7)	162 (13.2)	402 (32.7)	297 (24.2)	190 (15.5)	232 (18.9)
"Non-ballistic" missiles	64 (7.6)	73 (8.7)	175 (20.8)	166 (19.8)	127 (15.1)	134 (16.0)
Blunt trauma:	110 (8.4)	115 (8.8)	235 (17.9)	252 (19.2)	204 (15.6)	210 (16.0)
Vehicular accidents	86 (18.6)	92 (19.9)	153 (33.1)	140 (30.3)	112 (24.2)	120 (26.0)
Misc accidents	8 (3.8)	12 (5.8)	28 (13.5)	38 (18.3)	25 (12.0)	33 (15.9)
Sports accidents	none	none	8 (11.9)	10 (14.9)	9 (13.4)	9 (13.4)
Altercations	16 (2.8)	11 (1.9)	46 (8.0)	64 (11.2)	58 (10.1)	48 (8.4)
All forms of trauma	436 (10.9)	473 (11.8)	1,062 (26.5)	903 (22.5)	643 (16.0)	735 (18.3)

* Numbers in parenthesis are percentages calculated on the basis of the total number of patients in each trauma category.

TABLE IV
INCIDENCE* OF COMMINUTION AND AVULSION IN MANDIBULAR FRACTURES

Cause of Injury	Mandibular Fractures Alone		Combination Fractures	
	Comminuted	Avulsed	Comminuted	Avulsed
Bullets	260 (90.3)	188 (65.3)	108 (82.4)	74 (56.5)
Fragments	323 (72.3)	190 (42.5)	93 (71.0)	56 (42.7)
"Non-ballistic" missiles	66 (20.8)	16 (5.0)	36 (56.3)	16 (25.0)
Blunt trauma:	158 (25.1)	6 (1.0)	55 (50.0)	12 (10.9)
Vehicular accidents	58 (33.1)	6 (3.4)	47 (54.7)	8 (9.3)
Miscellaneous accidents	25 (25.0)	none	4 (50.0)	2 (25.0)
Sports accidents	5 (17.9)	none	none	none
Altercations	70 (21.5)	none	4 (25.0)	2 (12.5)
All forms of trauma	807 (48.0)	400 (23.8)	292 (67.0)	158 (36.2)

* Based on the number of mandibular fractures alone and concomitant mandibular fractures in each trauma category.

TINDER

TABLE V
INCIDENCE* OF FACIAL BONES FRACTURED BY VARIOUS CAUSES

<u>Cause of Injury</u>	<u>Mandibular</u>	<u>Mid-Face</u>	<u>Combination</u>
Bullets	288 (45.1)	219 (34.3)	131 (20.5)
Fragments	447 (36.4)	650 (52.9)	131 (10.7)
"Non-ballistic" missiles	318 (37.9)	457 (54.5)	64 (7.6)
Blunt trauma:	629 (48.0)	571 (43.6)	110 (8.4)
Vehicular accidents	175 (37.9)	201 (43.5)	86 (18.6)
Miscellaneous accidents	100 (48.1)	100 (48.1)	8 (3.8)
Sports accidents	28 (42.0)	39 (58.2)	none
Altercations	326 (56.9)	231 (40.3)	16 (2.8)
All forms of trauma	1,682 (41.9)	1,897 (47.2)	436 (10.9)
Previous study, year:			
Rowe and Killey, 1955	336 (67.2)	118 (23.6)	46 (9.2)
Rowe and Killey, 1965	535 (53.5)	383 (38.2)	82 (8.2)
Schuchardt et al, 1961	1,174 (75.0)	324 (20.7)	68 (4.3)
Schuchardt et al, 1966	773 (59.0)	450 (34.3)	88 (6.7)
Previous studies combined	2,818 (64.4)	1,275 (29.1)	284 (6.5)

* Numbers in parenthesis are percentages calculated on the basis of the total number of patients in each trauma category.

TINDER

TABLE VI
ADJUSTED RATIOS OF FRACTURE INCIDENCES

Cause of Injury	Mandibular	Mid-Face	Combination
Bullets	1	0.760	0.455
Fragments	1	1.454	0.293
"Non-ballistic" missiles	1	1.437	0.201
Blunt trauma:	1	0.908	0.175
Vehicular accidents	1	1.149	0.491
Miscellaneous accidents	1	1.000	0.080
Sports accidents	1	1.393	0.000
Altercations	1	0.709	0.049
All forms of trauma	1	1.128	0.259
Previous study, year:			
Rowe and Killey, 1955	1	0.351	0.137
Rowe and Killey, 1965	1	0.716	0.153
Schuchardt et al, 1961	1	0.276	0.058
Schuchardt et al, 1966	1	0.582	0.114
Above studies combined	1	0.452	0.101

STRUCTURE AND LATTICE DYNAMICS OF METAL AZIDES AND
THEIR RELATIONSHIP TO STABILITY

SAMUEL F. TREVINO, CHANG S. CHOI, ZAFAR IQBAL,
RICHARD D. MICAL, HENRY J. PRASK AND KRISHNARAO R. RAO
EXPLOSIVES LABORATORY, FRL, PICATINNY ARSENAL
DOVER, NEW JERSEY

I. INTRODUCTION

At the 1966 Army Science Conference a paper by Boutin, Prask and Trevino was presented which attempted to relate the low frequency molecular motions in solid explosives to the ease of initiation of detonation (1). The neutron scattering data and the model proposed were comparatively crude because of the inability to assign observed vibrational frequencies to particular lattice or molecular modes. In order to obtain a detailed and quantitative physical picture it was necessary to have more complete information on the crystal structures of the explosives, and to develop and apply improved techniques to resolve the spectra of molecular motions in crystals.

Any attempt to obtain and interpret such information represents an ambitious endeavor, taxing the state-of-the-art of molecular spectroscopy. Nevertheless, a systematic approach has been developed supplementing the experimental techniques of neutron spectroscopy with optical spectroscopy and applying normal coordinate analyses to interpret the data. The approach is wide-ranging, considering both inorganic and organic explosives together with temperature and pressure effects. This paper, dealing with the structure and lattice or molecular dynamics of inorganic azides at room temperature, presents one facet of the program which has yielded significant advances in technique and in our understanding of explosives stability.

The inorganic azides are militarily important substances, having explosive behavior which ranges from stable to extremely sensitive (2,3). They also have relatively simple crystallographic structures and offer the best prospects for a quantitative description of the lattice dynamics of a homologous series of explosive substances. As described at the 1968 Army Science Conference (4), the structure of lead azide was shown to be more complex than previously supposed, and the present paper confirms a similar complexity in the azide ion structure of

TREVINO, CHOI, IQBAL,
MICAL, PRASK and RAO

barium azide. However, as described below these discoveries, while complicating an already difficult task, are in themselves important contributions to the interpretation of the stabilities of the substances in terms of structure and molecular dynamics.

II. THEORY

Lattice dynamics provides a quantitative description of atomic and molecular motions in crystals and of the forces of interaction which produce the motions. It has been shown conclusively that changes in such microscopic behavior greatly affects macroscopic properties (5); e.g. lattice dynamics determine thermodynamic and transport properties, and reflect the presence of defects and anharmonicity, all of which markedly affect explosive properties.

The usual method of expressing the equations of motions of the particles in a crystal is in terms of cartesian displacement coordinates. With this coordinate system, the potential energy of the crystal in the adiabatic and harmonic approximation is written as (6):

$$2V = \sum_{\substack{\vec{n}-\vec{n}' \\ \alpha, \alpha'}} \phi_{\alpha, \alpha'}^{\vec{n}-\vec{n}'} \cdot \vec{x}_{\alpha}^{\vec{n}} \cdot \vec{x}_{\alpha'}^{\vec{n}'} \quad (1)$$

where α numbers the S particles in the \vec{n} th primitive cell. The properties of the force constant matrix ϕ are dependent upon the type of force field used to describe the interaction of the various particles and must be consistent with the symmetry of the crystal. The dynamical matrix $D_{\alpha\alpha'}(\vec{k})$ is formed as

$$D_{\alpha\alpha'}(\vec{k}) = (M_{\alpha\alpha'})^{-1/2} \sum_{(\vec{n}-\vec{n}')} \phi_{\alpha\alpha'}^{\vec{n}-\vec{n}'} e^{2\pi i \vec{k} \cdot (\vec{n}-\vec{n}')} \quad (2)$$

and the equations of motion to be solved are

$$\sum_{\alpha'} D_{\alpha\alpha'}(\vec{k}) L_{\alpha'j}(\vec{k}) = L_{\alpha j}(\vec{k}) \omega_j^2(\vec{k}) \quad (3)$$

where $\omega_j(\vec{k})$ and $\hbar\vec{k}$ are, respectively, the vibrational frequency and quasi momentum of the j th mode phonon and M_{α} is the mass of the α th atom. "Phonon" is the term given to the quantized plane wave of wavelength, $\lambda = 2\pi/k$ and energy, $E = \hbar\omega_j$, in terms of which the vibration is described. The quantity $L_{\alpha j}(\vec{k})$, called the polarization vector, describes the magnitude and phase of the motion of the α th particle when the phonon (j, \vec{k}) is excited. The determination of $\omega_j(\vec{k})$ and $L_{\alpha j}(\vec{k})$ characterizes a vibration, and the functional dependence of these quantities is determined by crystal symmetry and the force field between particles. The measurement of these two functions is the aim of experimental lattice dynamics. It should be mentioned that thermodynamic properties, such as specific heat, depend directly on all $\omega_j(\vec{k})$.

TREVINO, CHOI, IQBAL,
MICAL, PRASK and RAO

III. EXPERIMENTAL

The principal experimental techniques used are Raman and infrared spectroscopy, and both incoherent (INIS) and coherent (CNIS) neutron inelastic scattering. With the exception of CNIS the techniques have been employed previously in the study of explosives (3) but not in a coordinated approach. In many instances previous results could not be interpreted because the crystal structures and crystal symmetry were not known in detail.

A. Structure Determination

A knowledge of crystal structure is essential for the interpretation of the experimental data. Neutron diffraction as a method for crystal structure determination, was used to complement x-ray diffraction because numerous physical factors can prevent a complete structure determination by x-rays. In the particular case of the azides, light-atom positions may be obscured when heavy atoms are also present as occurs with azide ions in the presence of lead in PbN_6 . In addition, x-rays sometimes cause decomposition of azide crystals.

B. Determination of Lattice Dynamics

1. General: Two quantities can be used to measure the interaction of radiation with matter; namely, the energy exchanged between the radiation and the sample, and the momentum transferred during the interaction. Figure 1 compares the various types of radiation used to determine the positions and dynamics of atoms in crystals. The ordinate and abscissa of Figure 1 show the logarithm of energy transfer (in eV) and momentum transfer (in \AA^{-1}). Infrared and Raman radiation can exchange energy over a rather large range but are restricted to very small momentum transfers because of their large wavelength. X-rays and electrons can be used to study spatial correlations, as indicated by the range of momentum transfer available to them, but are very difficult to use in the study of dynamics for their energy is quite large. The range of application of Brillouin scattering and γ -rays can be deduced from their position on the graph. Neutrons have the unique property of being able to simultaneously satisfy the requirements of energy and momentum most suited to the study of lattice dynamics. However, these unique properties of neutrons cannot always be used to advantage. (A noteworthy feature of this representation is the large region in energy-momentum space for which no technique has been found.)

2. Techniques: Conventional Raman and infrared techniques were employed in the measurements presented here and details are discussed as appropriate in the Results section.

Coherent inelastic neutron scattering (CNIS) is a relatively new technique (6) and has been applied to the azides for the first time in this work. An investigation of the dynamical properties of a crystal by means of CNIS is, in principle, capable of revealing the most detailed information concerning the force fields which are characteristic of the crystal. This technique, alone, can result in the direct measurement of the complete dispersion relations,

TREVINO, CHOI, IQBAL,
MICAL, PRASK AND RAO

$\omega_j(\vec{k})$ as functions of \vec{k} . A great difficulty which is normally encountered by spectroscopists in attempts to define force fields is the limited number of frequencies which can be obtained as opposed to the number of adjustable parameters in the definition of the force constants. In the case of CNIS there is explicitly the promise of obtaining many frequencies $\omega_j(\vec{k})$ all of which depend on the same set of parameters in a known manner as a function of crystal structure and wave vector \vec{k} .

The expression for the scattering probability, wherein a neutron interacts with the phonon of energy $\hbar\omega_j(\vec{k})$ and momentum $\hbar\vec{k}$, is governed by the so-called "inelastic structure factor"

$$f_j^2(\vec{k}) = \left| \sum_{\vec{n}, \alpha} \vec{k} \cdot \vec{L}_{\alpha j}(\vec{k}) S_{\alpha} \omega_j^{-1/2}(\vec{k}) e^{-2W_{\alpha} + i\vec{K} \cdot \vec{R}_{\alpha}} e^{2\pi i \vec{T} \cdot \vec{R}_{\vec{n}}} \right|^2 \quad (4)$$

$$\times \delta(\vec{K} - 4\pi\vec{T} - \vec{k}) \delta(E_f - E_i \pm \hbar\omega_j(\vec{k}))$$

In eqn. (4), $\vec{K} = (\vec{k}_f - \vec{k}_i)$ is the momentum transferred by the neutron, $\vec{R}_{\vec{n}}$ and \vec{R}_{α} are position vectors for the n th unit cell and α th atom, respectively, S_{α} is the scattering length for the α th atom, and $4\pi\vec{T}$ is the lattice vector in reciprocal space. The two δ -functions express conservation of energy and momentum i.e.

$$\delta(\vec{K} - 4\pi\vec{T} - \vec{k}) \cdot \delta[E_f - E_i \pm \hbar\omega_j(\vec{k})] = 1$$

when the energy ($E_f - E_i$) and momentum transferred (\vec{K}) by the neutron equal, respectively, the energy [$\hbar\omega_j(\vec{k})$] and quasi momentum ($4\pi\vec{T} + \vec{k}$) of the j , k th phonon; if not, the δ -functions - and structure factor - are zero.

A systematic procedure has been devised for the measurement of the dispersion relations by CNIS (16). The method known as the "Constant Momentum Transfer" technique can be understood with the aid of Figures 2 and 3. Figure 2 is a schematic of the triple axis spectrometer used in the measurements. The three crystals labelled X1, S and X2 correspond to the monochromator, sample, and energy analyzer respectively. The various angles are labelled. Figure 3 is a schematic of the geometry in reciprocal space. The vectors correspond to quantities previously defined and are so arranged as to satisfy the momentum conservation condition. In the configuration pictured in the figures an attempt is made to measure the energy $\hbar\omega$ of the phonon with wave vector \vec{k} . The method consists in holding $\vec{K} = \vec{k}_f - \vec{k}_i$ constant, and therefore \vec{k} fixed, while changing either k_f or k_i such that the energy transfer $E = \frac{\hbar^2}{2m} (k_f^2 - k_i^2)$ varies until the energy conservation condition is satisfied.

When this condition is attained, the cross-section will increase and a measure of $\hbar\omega = E$ is obtained. The procedure is repeated for a new \vec{K} (and therefore a new \vec{k}) until the entire dispersion relation $\omega_j(\vec{k})$ is obtained along a given direction. Although a most powerful experimental technique, in practice the following limitations are encountered: 1) With presently available reactor neutron fluxes,

TREVINO, CHOI, IQBAL,
MICAL, PRASK and RAO

very large single crystals ($\sim 10\text{cm}^3$) are necessary to obtain sufficient scattered neutron intensity; 2) Symmetry-dependent selection rules - although not, in general, the same as for optical measurements - limit the observable modes; 3) The CNIS cross-section is essentially inversely proportional to phonon energy so that modes with $hw > 150\text{cm}^{-1}$ become difficult to observe.

IV. RESULTS

A. General

The inorganic azides form a family of compounds exhibiting a broad range of properties of immediate military interest. For example, α -lead azide and $\text{Ba}(\text{N}_3)_2$ both of which possess similar complex structural properties, as this work confirms, differ markedly in explosive behavior; in contrast, several of the stable alkali azides possess, very nearly, the same relatively simple crystal structure as AgN_3 , which is a sensitive primary explosive. A knowledge of the lattice dynamics is essential for the understanding of these differences.

B. Alkali Azides

The alkali azides, because of their relative simplicity, constitute the best starting point for detailed studies of metal azides. The structures up to CsN_3 have been determined by x-ray diffraction (3). For these reasons previous lattice-dynamical studies of azides deal almost exclusively with these compounds (3). These experimental studies were limited to Raman and intermediate infrared spectroscopy, and the one dispersion curve calculation performed considered only $\vec{k} = 0$ modes (7).

1. Potassium Azide: In this work KN_3 has been studied by means of coherent neutron inelastic scattering (CNIS), far-infrared, high-resolution intermediate infrared and Raman spectroscopy. A complete lattice-dynamical calculation of the normal modes of vibration has been made, all observed modes assigned, and all atomic interactions inferred.

For the CNIS measurements, no single crystal of sufficient size was available. A pseudo-single crystal composed of thirty solution-grown KN_3 "crystallites" (each $\sim 1.5 \times 1.5 \times 0.3$ cm) was built-up and aligned using a neutron diffractometer. (It is perhaps worth mentioning that after the best crystallite growing method had been developed, approximately two months were required for final crystal growing and another month for pseudo-crystal fabrication.) The CNIS measurements were performed on the Picatinny Arsenal triple-axis spectrometer at the AMMRC Reactor (Watertown, Mass). Measurements were made in the highest symmetry direction, [001], and in a second high-symmetry direction, [110]. The complete set of phonons measured are shown in Figure 5.

Concurrent with the CNIS measurements, KN_3 films were studied by far infrared spectroscopy while medium infrared and Raman measurements were performed on single crystal samples. The space group for KN_3 is D_{4h}^{18} for which factor group selection rules

TREVINO, CHOI, IQBAL
MICAL, PRASK and RAO

predict translatory lattice modes of symmetry species $A_{2g}(1)$, $E(1)$, $A_{2u}(1)$, $B_{1g}(1)$, and $E_u(2)$; rotatory lattice modes are predicted as $A_{2g}(1)$, $B_{1g}^+(1)$ and $E_g(1)$. Of these A_{2u} and E_u are allowed in the first-order infrared spectrum, while B_{1g} and E_g are allowed in the first-order Raman spectrum.

All allowed first-order infrared and Raman modes were observed, the latter confirming Bryant's earlier work (8). Second-order spectra were also obtained (i.e. combination bands with ν_1 and ν_2) for which factor group selection rules are also known. Table 1 shows observed frequencies and assignments for KN_3 (also RbN_3 and CsN_3) based on the above measurements and factor group analysis. The detailed spectra are shown in ref (7).

Table 1

Observed Rotatory and Translatory Modes at $k=0$ in Alkali Azides

Symmetry Species	KN_3	Experimental (cm^{-1})	
		RbN_3	CsN_3
R(E_g)	147	126	108(a)
T(A_{2u})	166	144	124
R(B_{1g})	150	140	153(a)
T(E_g)	102	65	42(a)
T(E_u)	{ 130 80	96 76	90 46

(a) Values taken from reference 8.

The first full lattice-dynamical calculation for any metal azide was carried out for KN_3 by means of the theoretical approach described in Section II. A rigid-ion model was formulated in which each atom of the KN_3 "molecule" was assigned a charge; short range repulsive forces were introduced between nearest and next-nearest ions, and covalent forces employed between azide nitrogens. With three degrees of freedom per atom and eight atoms per primitive unit cell, the resultant dynamical matrices (Eqn. 3) were dimensionally 24×24 . The force field and ionic charges were refined by least-squares techniques to obtain observed frequencies at representative k values. The interaction model is described in detail in Table 2 and atom positions shown in Figure 4. The calculated $\hbar\omega_j(\vec{k})$ for the [001] direction are shown as solid curves in Figure 5 along with all measured frequencies, and the corresponding force constants are listed in Table 2. The calculated acoustic modes do not reproduce measured values completely satisfactorily; however, overall agreement between the measurement and calculations is reasonably good. It should also be pointed out that of the many lattice modes in KN_3 the inelastic structure factors (Eqn. 4) show only five to be observable in any crystallographic direction. Because of the limitations discussed in section III.B.2, only two were observed in our measurements.

Table 2
Force Field and Force Constant Values for KN₃

<u>Force Constants</u>	<u>Interacting Atoms</u>	<u>Values</u>
f (K-K) (m dynes/Å)	(1)-(2)	.019
f (K-N)	(1)-(4)	.284
"	(1)-(8)	.284
"	(2)-(5)	.284
"	(2)-(7)	.284
f' (N-N)	(5)-(6)	.07
"	(4)-(6)	.07
"	(7)-(3)	.07
"	(8)-(3)	.07
f'' (N-N)	(3)-(6) axial azides	.141
F _r	Δr, (3)-(5) (6)-(7)	13.385
	Δr, (3)-(4) (6)-(8)	13.385
f _r	Δr ₁ Δr ₂ interaction	1.753
H _θ	(4)-(3)-(5)	.365
	(7)-(6)-(8)	.365
Z(K)/e	K(1), (2)	.6
Z(N)/e	N(3), (6)	.2
Z(N')/e	N(4), (5), (7), (8)	-.4

2. Rubidium and Cesium Azides: Optical spectroscopic measurements, as those on KN₃, were carried out for RbN₃ and CsN₃ (7). CNIS measurements have not yet been begun because of the difficulties of sample preparation. Both RbN₃ and CsN₃ also have D_{3h}¹⁸ space groups so that factor group analysis and the symmetry species of k=0 allowed modes follows that of KN₃. The observed frequencies and assignments are shown in Table 1. These results provide an excellent starting point to the solution of the full lattice-dynamical problem. Calculation of the k=0 frequencies with the KN₃ force field, after appropriate mass and interatomic distance changes, are in progress, and extension to k≠0 values will be completed with CNIS measurements.

C. Divalent Azides

The divalent azides, as a class of compounds, are structurally much more complex, than the monovalent azides. In further contrast, essentially all of the divalent azides are explosives and of practical interest. The complexity of the divalent azides has prevented lattice-dynamical studies of these compounds except for infrared investigations of the internal modes of the azide ion (3). Furthermore, until 1967 Sr(N₃)₂ was the only divalent azide for which the detailed structure had been determined. Since that time the structure of cupric azide has been completely determined by x-ray diffraction (9) and that of α-lead azide by neutron diffraction (4). Lead azide, which is of great interest as an explosive, presents - as shown by the presence of four distinct azide types - a most formidable problem for lattice-dynamical studies. However, early infrared work and later EPR measurements suggested that Ba(N₃)₂

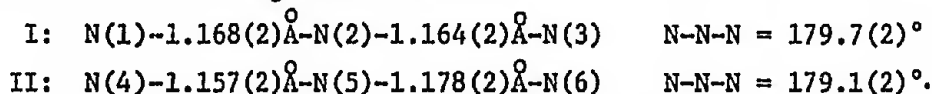
TREVINO, CHOI, IQBAL
MICAL, PRASK and RAO

also contains more than a single azide type. In addition, single crystals of sufficient size for neutron diffraction and optical studies could be grown and handled. Therefore, $\text{Ba}(\text{N}_3)_2$ was chosen for initial detailed study of the divalent metal azides.

1. $\text{Ba}(\text{N}_3)_2$ Structure: $\text{Ba}(\text{N}_3)_2$ was prepared and investigated for the first time in single crystal form in 1965 (10). It was determined that the lattice parameters of the monoclinic unit cell were $a = 9.59$, $b = 4.39$, $c = 5.42\text{\AA}$ and $\beta = 99.75^\circ$ with 2 molecules per unit cell. Later x-ray work by Abel and Glen of this laboratory confirmed the lattice parameters, but could provide no further information, most probably because the crystal deteriorates in x-radiation.

In the present work (10) a cylindrical single crystal ($\sim 2\text{mm}$ diameter, 12mm long) was employed. A total of 776 reflections were scanned with the Picatinny Arsenal neutron diffractometer at the AMMRC Reactor, of which 632 reflections showed measurable intensity. No intensity changes due to irradiation were observed. A systematic absence of $(0k0)$ reflections for $k = 2n+1$ and the $N(Z)$ intensity statistics test established the space group as $P2_1/m$. A study of the observed intensities with reference to $P2_1/m$ space group and a Patterson synthesis established approximate atomic positions, and these were employed in the initial full-matrix least squares refinement of data. The final refinements included anisotropic temperature factors, secondary extinction coefficients, and individually weighted observed data based on counting statistics. The final discrepancy factor was $R = 0.041$, $WR = 0.039$.

The crystallographic structure is shown in Figure 6. It is composed of an infinite chain of Ba-N bonds which run between the barium atoms and two distinct azide groups denoted I and II. Their configurations are



$\text{Ba}(\text{N}_3)_2$, therefore, possesses a symmetric azide group (I) as is found in the monovalent azides, but also an asymmetric azide group (II) as is found in $\text{Cu}(\text{N}_3)_2$ and $\alpha\text{-Pb}(\text{N}_3)_2$.

2. $\text{Ba}(\text{N}_3)_2$ Dynamics: Infrared and laser-excited Raman were used to study the $k=0$ vibrations of single crystal $\text{Ba}(\text{N}_3)_2$ over the entire 30 to 4000 cm^{-1} frequency range. CNIS measurements were not possible because of the limited size and number of single crystals available. However, the optical measurements constitute the most complete, high-resolution study of any non-alkali-metal azide to date (11).

For the normal infrared measurements, the crystals were mounted with the b axis approximately perpendicular to the incident beam. Polarized light studies in the infrared were made with the electric vector parallel and perpendicular to the b axis on the (100) plane. Raman scattering measurements were made in the perpendicular scattering configuration using different crystal orientations. The medium infrared spectra were obtained using a model 621 Perkin Elmer grating spectrophotometer with a microscanning

TREVINO, CHOI, IQBAL
MICAL, PRASK and RAO

attachment over the frequency region between 400 and 4000 cm^{-1} . A microsampling Hofman dewar with CsI windows was used for obtaining the spectra at 80°K. Polarized infrared spectra were obtained using a silver chloride plate polarizer. The far infrared reflection spectrum was measured on a pure BaN_6 pellet using a Perkin Elmer 301 spectrophotometer. The Raman spectra were obtained using He-Ne and Argon ion lasers and a Spex Model 1400 double monochromator with photon counting detection system.

The neutron diffraction structure determination allowed factor group analysis and correlation between factor and molecular groups for $\text{Ba}(\text{N}_3)_2$. The 42 expected fundamental modes belong to species $A_g(14)$, $B_g(7)$, $A_u(7)$, $B_u(14)$ of which vibrations of A_u and B_u symmetry are infrared active; vibrations of A_u symmetry are polarized parallel to the b axis whereas vibrations of B_u symmetry are polarized along a and c axes. The vibrations of A_g and B_g symmetry are Raman active, the former being approximately polarized and the latter depolarized. With this basis and the experimental techniques described in the previous paragraph, essentially all vibrational modes at $k=0$ were assigned. It is significant that analysis of the observed frequencies independently confirms the existence of two types of azides and the structure as determined by neutron diffraction. A partial list of the 113 observed fundamental and combination modes is given in Table 3 along with assignments.

V. CONCLUSIONS

The results described in Section IV show that by means of a closely coordinated effort in which all necessary structural and spectroscopic experimental techniques are employed, the lattice dynamics of complex compounds such as metal azides and other explosives can be elucidated.

For the first time dispersion curves of a metal azide, KN_3 , have been measured, interatomic forces inferred from a full lattice-dynamics calculation and reasonable agreement obtained for both optical ($k=0$) and CNIS ($k \neq 0$) data. These results are immediately applicable to Rb, Cs and Ag azides; optical data and assignments have been obtained for RbN_3 and CsN_3 .

It has long been a postulate of the thermal theory of explosion that a detonation regime in a solid can be sustained only when the thermal conductivity of the solid is relatively small so that heat imbalance can be maintained. On the microscopic level partially successful correlations have been proposed between electronic properties such as band gap and ionization potential and explosive sensitivity. The present work shows a correlation between relative stability and microscopic properties not possible from previous work. The order of symmetry of a lattice determines the degree of anharmonicity; this arises from phonon-phonon interactions and is inversely proportional to λ , the phonon mean free path. It has also been shown that λ is directly proportional to thermal conductivity. A solid having a low order of symmetry has a

TREVINO, CHOI, IQBAL
 MICAL, PRASK and RAO

Table 3

Vibrational Frequencies of Ba(N₃)₂

Observed Bands (cm ⁻¹)		Assignments and Remarks
<u>Infrared</u>	<u>Raman</u>	
42 w		R(A _u or B _u)
	53 s	R(A _g) polarized
64 w		R(A _u or B _u)
	103 w	2R(A _g) R(Ag)~52
114 s		T(A _u or B _u)
	127 w	2R(A _u or B _u)
140 m		T(A _u or B _u)
	140 w]	T(B _g) polarized
	151 s]	
	162 m]	
164 s		T(A _u or B _u)
190 w		T(A _u or B _u)
	184 w]	T(A _g) polarized
	195 m]	
	208 m]	
	434 w]	
629 vs		v ₂ (B _u)
633 s		v ₂ (A _u)
	638 w]	v ₂ (A _g or B _g)
	651 w]	
825 w		v ₂ (B _u)+T(A _g) T(A _g)~196
838 w		v ₂ (B _u)+T(A _g) T(A _g)~209
1251 m	1252 w]	2v ₂ (A _g)
1263 m	1264 w]	
1293 m	1294 w]	
1309 w		1263+R(A _u or B _u) R~46
1312 w		1251+R(A _u or B _u) R~61
1364 m	1363 s	v ₁ (A _g) Raman depolarized
1375 w	1372 w	v ₁ (A _g)
1405 w		v ₁ +R(A _u or B _u) R~42
2134 vs]		v ₃ (B _u)
2150 vs]		
2190 vs]		
2227 vs]		

TREVINO, CHOI, IQBAL
MICAL, PRASK and RAO

correspondingly low λ and is therefore more sensitive to the input of thermal energy. Consequently as one goes from KN_3 (D_{4h}) to AgN_3 (D_{2h}) one expects thermal sensitivity to increase, and this is dramatically observed experimentally.

In the divalent metal azides, a quantitative ordering of the degree of crystal symmetry is difficult to make because of their structural complexity. It is clear, however, that $\text{Ba}(\text{N}_3)_2$ possesses higher symmetry, and therefore a higher λ than $\text{Cu}(\text{N}_3)_2$ and $\alpha\text{-Pb}(\text{N}_3)_2$; experimentally $\text{Ba}(\text{N}_3)_2$ exhibits a markedly lower sensitivity. A further consideration - not possible previously because the structures were not known - is that thermal sensitivity increases with the degree of asymmetry of the azide ions: $\text{Ba}(\text{N}_3)_2 < \alpha\text{-Pb}(\text{N}_3)_2 < \text{Cu}(\text{N}_3)_2$. This suggests an additional phonon-phonon coupling dependent upon the degree of covalency of the metal-azide bond.

In summary, the present work shows that the determination of the lattice dynamics of a homologous series of complex explosive substances is feasible. Furthermore, a consideration of the structures and lattice dynamics of metal azides shows a direct correlation with the relative stabilities of these materials.

VI VI. ACKNOWLEDGEMENTS:

The authors are indebted to Dr. R.F. Walker for valuable discussions and guidance concerning this work, to Mr. L.H. Eriksen for his interest and support, and to Dr. J.V.R. Kaufman who initiated this program and has supported it since its inception.

References

1. H. Boutin, H. Prask and S. Trevino, Army Sci. Conf. Proc. (AD 634 615), Vol I, 49 (1966).
2. F.P. Bowden and A.D. Yoffe, "Fast Reactions in Solids", (Butterworths, London, 1958) and references cited therein.
3. A.D. Yoffe, in "Developments in Inorganic Nitrogen Chemistry", Coburn, Ed. (Elsevier, Amsterdam, 1967), pp. 73-149, and references cited therein.
4. C.S. Choi and H. Boutin, Army Sci Conf. Proc. (AD 837 098), Vol I, 147 (1968); Acta Cryst. B25, 982 (1969).
5. Reviewed, in part, at "Explosive Chemical Reactions Symposium", T.C.P. O-2, Durham, N.C., Oct 1968.
6. Reviewed in "Thermal Neutron Scattering", P.A. Egelstaff, Ed. (Academic Press Inc., New York, 1965).

TREVINO, CHOI, IQBAL
MICAL, PRASK and RAO

7. Z. Iqbal, M.L. Malhotra and K.D. Moeller, Physics Letters 31A, 73 (1970), and references cited therein.
8. J.I. Bryant and R.L. Brooks, J. Chem. Phys. 43, 880 (1965); J.I. Bryant, Ibid. 45, 689 (1966).
9. R. Söderquist, Acta Cryst. B24, 450 (1968); I. Agrell, Acta Chem. Scand. 21, 2647 (1967).
10. C.S. Choi, Acta Cryst, in press, and references therein.
11. Z. Iqbal, S. Mitra and C. Brown, J. Chem. Phys., in press.

TREVINO, CHOI, IQBAL,
MICAL, PRASK and RAO

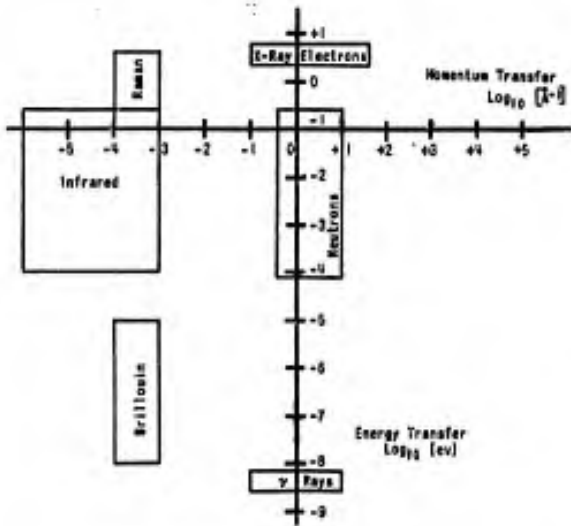


Figure 1. THE RANGE OF ENERGY AND MOMENTUM TRANSFERS ATTAINABLE BY VARIOUS EXPERIMENTAL TECHNIQUES

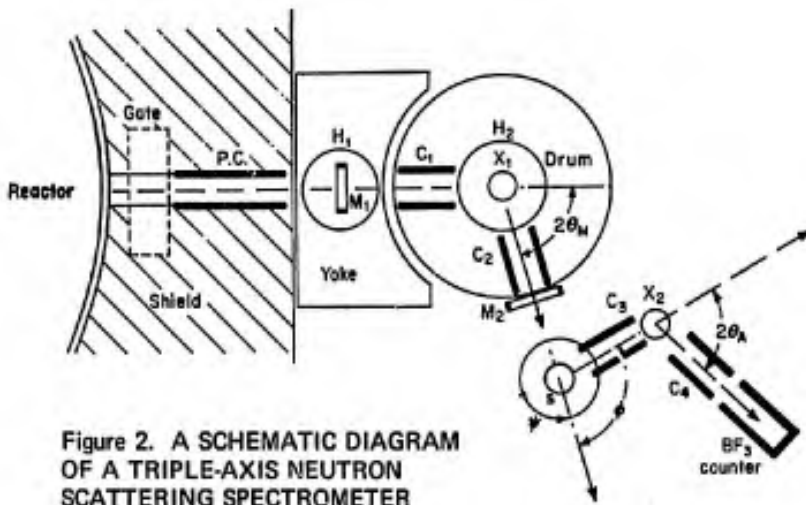


Figure 2. A SCHEMATIC DIAGRAM OF A TRIPLE-AXIS NEUTRON SCATTERING SPECTROMETER

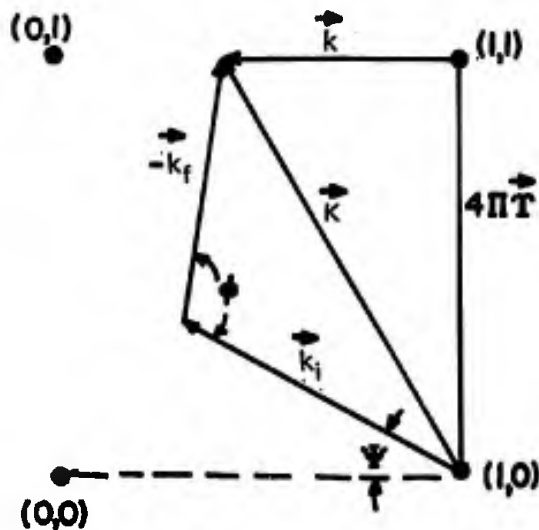


Figure 3. THE WAVE VECTORS IN THE RECIPROCAL LATTICE FOR THE MEASUREMENT OF A PHONON OF QUASI-MOMENTUM $\hbar\vec{k}$ BY COHERENT NEUTRON INELASTIC SCATTERING

TREVINO, CHOI, IQBAL,
MICAL, PRASK and RAO

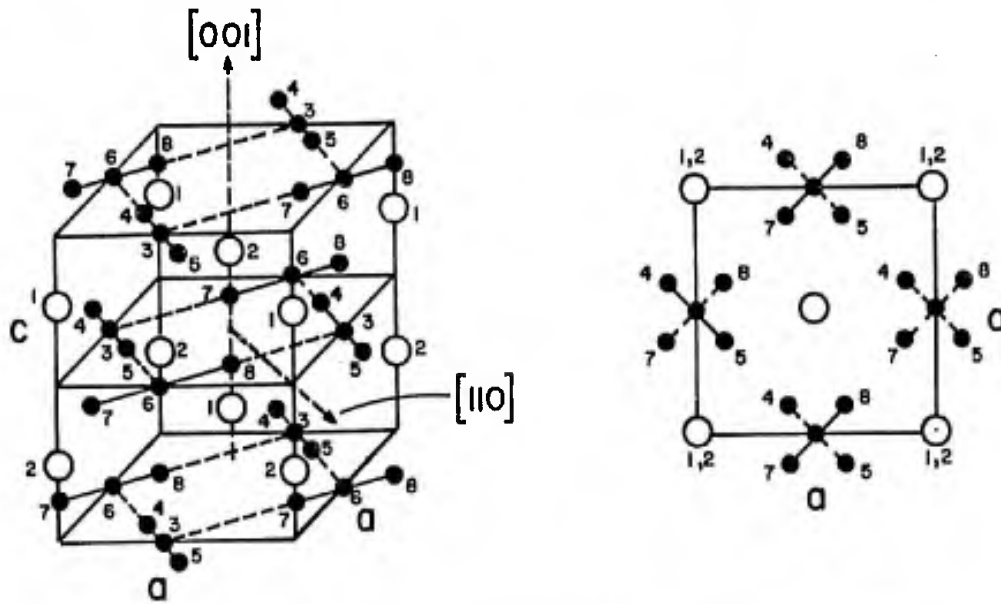


Figure 4. Perspective view of the unit cell of KN_3 and a projection of atom positions on the (001) plane; open circles denote potassium ions.

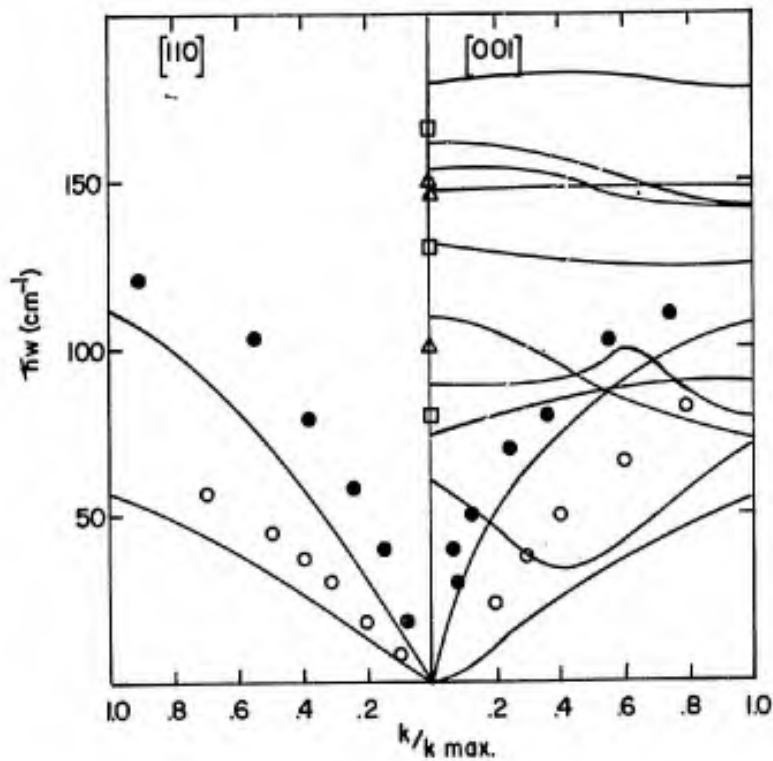
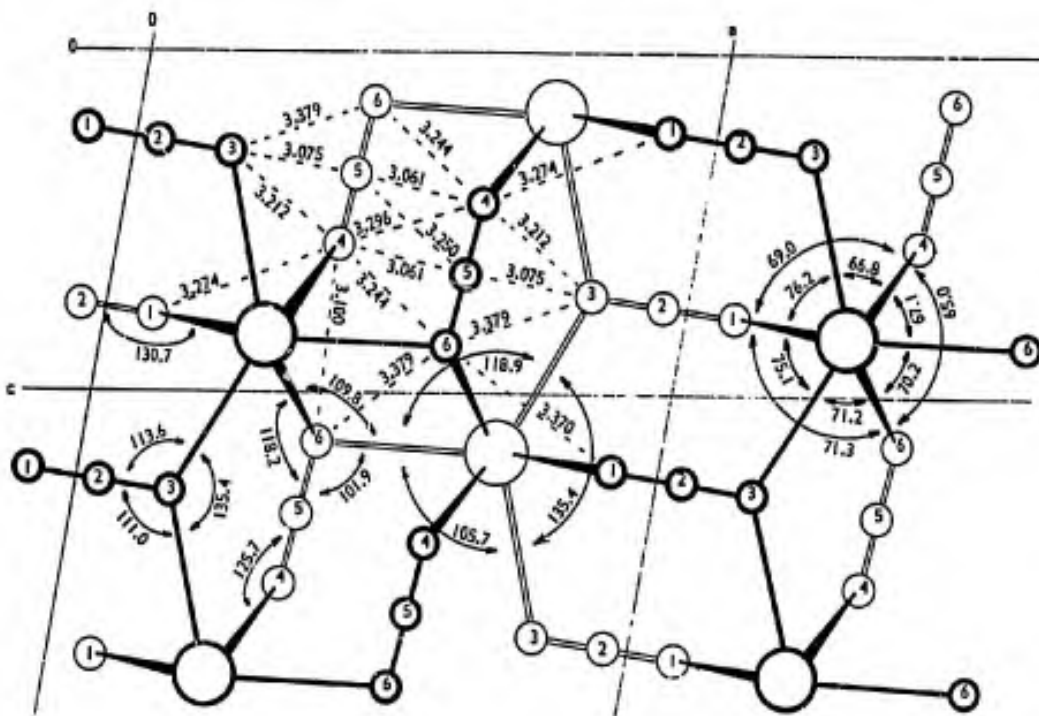
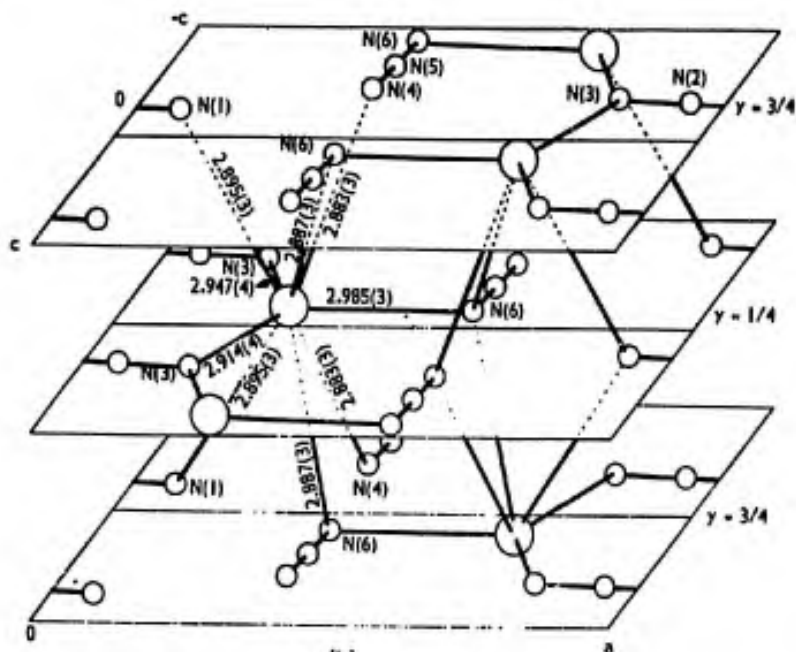


Figure 5. Experimental data and calculated dispersion curves (solid curves) for KN_3 ; ● = CNIS, longitudinal modes, ○ = CNIS, transverse modes, Δ = Raman data, □ = far infrared data.

TREVINO, CHOI, IQBAL,
MICAL, PRASK and RAO



(a)



(b)

Figure 6. The upper figure shows the atomic arrangement of $\text{Ba}(\text{N}_3)_2$ projected on the (010) plane. The larger circles correspond to Ba atoms, the smaller circles with inset numbers to nitrogens. Darker circles represent atoms on the $y = \frac{1}{4}$ plane; lighter circles correspond to atoms on the $y = \frac{3}{4}$ plane. The lower figure is a perspective view of the crystal structure of $\text{Ba}(\text{N}_3)_2$.

GENETIC TRANSFORMATION IN THE GENUS PASTEURELLA

FRANKLIN J. TYERYAR, JR. and WILLIAM D. LAWTON
U. S. ARMY BIOLOGICAL LABORATORIES
FORT DETRICK, MARYLAND

The mechanisms of virulence of bacteria pathogenic for man have been investigated primarily by immunological and biochemical approaches. By comparison of antigenic makeup and metabolic activities of virulent and avirulent organisms, one hopes to find characteristics associated with virulence. These characteristics then serve to distinguish the virulent and avirulent types in vitro. Studies of virulence at the chromosomal level can then be initiated, if a gene exchange system is available. Ideally, immunological, biochemical, and genetic studies should be conducted simultaneously. Indeed, the genetic transfer of a virulence factor may provide a significant antigenic or metabolic alteration in the recipient which could be detected and correlated with virulence.

We initiated a study of the genetics of the bacterial genus Pasteurella because this genus includes several human pathogens whose mechanisms of virulence are virtually unknown. It is the purpose of this report to describe genetic transformation of Pasteurella novicida. This type of genetic exchange is accomplished by the uptake and integration into the host chromosome of exogenously supplied deoxyribonucleic acid. This phenomenon has not been previously observed for any members of the genus Pasteurella.

METHODS AND MATERIALS

Bacterial strains. Cultures of Pasteurella novicida U112 were obtained from LTC John Marshall, U. S. Army Medical Research Institute of Infectious Diseases, and from Dr. Cora Owen, Rocky Mountain Laboratory, Hamilton, Montana.

TYERYAR and LAWTON

Media. Cultures were routinely grown on glucose-cysteine-blood agar (GCBA, 4) slants and plates. Transformants to streptomycin resistance were obtained on GCBA containing the antibiotic. Transformants to nutritional independence were recovered on the defined medium of Chamberlain (3). Cells for DNA isolation and mutagen treatment were grown in Brain Heart Infusion broth (BHI) supplemented with 0.1% cysteine·HCl.

The composition of the liquid transformation medium in g/L was: L-arginine, 0.4; L-aspartic acid, 0.4; L-cysteine·HCl, 0.2; DL-methionine, 0.4; spermine phosphate, 0.04; NaCl, 15.8; $\text{MnSO}_4 \cdot \text{H}_2\text{O}$, 0.75; $\text{MgSO}_4 \cdot 7\text{H}_2\text{O}$, 6.0; $\text{CaCl}_2 \cdot 2\text{H}_2\text{O}$, 2.94; and tris (hydroxymethyl) aminomethane, 6.05.

Bacterial mutants. Spontaneous streptomycin-resistant (Sm^r) mutants of *P. novicida* and *Pasteurella tularensis* were obtained on GCBA plates containing 1 mg/ml of streptomycin sulfate. Mutants of *P. novicida* auxotrophic for tryptophan (Trp^-) and adenine (Ade^-) were obtained by exposing wild-type cells to N-methyl-N'-nitro-N-nitrosoguanidine (NTG). Cells grown 16 hr in BHI + cysteine were sedimented by centrifugation and resuspended in a sterile solution of 100 $\mu\text{g}/\text{ml}$ of NTG in gel-saline (5). The suspension was incubated at 37 C for 30 min, after which the cells were centrifuged and resuspended in fresh BHI + cysteine medium. The cells were then diluted and plated on GCBA. Mutants were detected by picking colonies to the defined medium of Chamberlain (3) and the medium supplemented with additional amino acids, purines, and pyrimidines for which nutritional dependence was desired.

Preparations of transforming deoxyribonucleic acid (DNA). Cells of the varicus *Pasteurella* species were grown in BHI + cysteine overnight at 37 C on a reciprocating shaker. The cells were removed from their growth medium by centrifugation and their DNA was isolated by the method of Marmur (10). The purified DNA from each culture was dissolved in SSC (0.15 M NaCl + 0.015 M sodium citrate), and its concentration was determined by the method of Burton (2).

Transformation procedures. Assays for transformability of *P. novicida* Sm^s to Sm^r were performed essentially as described by Bove for *Moraxella* (1). Recipient cells were grown overnight at 37 C on a GCBA plate. The growth was removed with 2 ml of gel-saline, diluted to approximately 1×10^{10} cells/ml, and 0.1 ml of the cell suspension was mixed with 0.1 ml of Sm^r DNA on the surface of GCBA plates (25 ml of GCBA per plate). The plates were incubated at 37 C and, at hr intervals, the agar from each plate was transferred to a large petri dish containing 50 ml of

GCBA + 1.5 mg/ml of streptomycin sulfate. Incubation was continued at 37 C and Sm^r colonies were scored after 48 hr. Control plates contained cells alone, cells + Sm^r DNA + deoxyribonuclease (100 µg), or cells + Sm^s DNA.

Transformations of auxotrophic mutants were determined by spreading 0.1 ml of recipient cells, prepared as described above, plus DNA, on the surface of Chamberlain's agar.

Cells used in liquid medium transformations were prepared as described above except that, for many of the experiments, the cells were washed repeatedly with gel-saline before use. The transformations were conducted in a volume of 1 ml (0.1 ml cells, 0.1 ml DNA, and 0.8 ml medium) in a cotton-stoppered test tube. The reactions were terminated by the addition of Mg⁺⁺-activated deoxyribonuclease at a final concentration of 50 µg/ml. Reaction tubes were incubated in a slanted position at 37 C on a reciprocating shaker. Suitable dilutions were then plated onto the appropriate media and incubated for 48 hr at 37 C. Transformation frequencies are expressed as transformants/recipient cells X 100.

RESULTS

Transformation of *P. novicida*. The data in Table 1 demonstrate that *P. novicida* picks up and integrates exogenously supplied DNA. Colonies resistant to streptomycin only occur in significant numbers when recipient cells are incubated in the

Table 1. Transformation of *Pasteurella novicida* on agar plates

Experiment No.	Recipient	Cells per plate	DNA		Deoxyribonuclease ^{a/}	Colonies per plate
			Source	µg/plate		
1	Sm ^s	6.5 x 10 ⁸	Sm ^r	108	-	Sm ^r 300
				108	+	3
				0	-	2
2	Trp ⁻	1.4 x 10 ⁹	Trp ⁺	62	-	Trp ⁺ > 1,000
				62	+	0
				0	-	0
				10.8	-	> 1,000
				1.1	-	153
				0.1	-	17
				0.01	-	5
	Trp ⁻	30	-	0		
3	Ade ⁻	6.0 x 10 ⁷	Ade ⁺	10.8	-	Ade ⁺ > 1,000
				1.1	-	> 1,000
				10.8	+	0

^{a/} Deoxyribonuclease concentration = 100 µg/plate

presence of DNA carrying the Sm^r locus. Furthermore, the reaction is obliterated by deoxyribonuclease. Similar results were obtained for auxotrophic mutants. The number of wild-type colonies observed was dependent on the concentration of DNA employed, with as little as 0.01 μ g per plate producing a significant number of transformants.

Liquid transformation medium. Although the mixing of recipient cells and DNA on agar plates was satisfactory for demonstrating transformation, this procedure does not permit quantitative assessment of such parameters as maximum levels of transformation, factors affecting the physiological state of cells for transformation (competence), and the kinetics of transformation. Such studies could only be made by exposing the cells to DNA in a liquid medium.

A satisfactory transformation medium was developed by modifying Chamberlain's medium. As shown in Table 2, Ca^{++} was required for transformation, and Mg^{++} would not substitute for this requirement. For assessment of Ca^{++} requirement, the transformation medium contained all components including 1×10^{-2} M

Table 2. Effects of calcium and magnesium on transformation of *P. novicida* (Trp⁻) ^{a/}

Ion concentration in M	Trp ⁺ transformants per ml	Transformation, %
Ca^{++}	6.6×10^1	0.0002
10 ⁻⁴	1.2×10^2	0.0004
10 ⁻³	1.1×10^3	0.004
5×10^{-3}	1.5×10^3	0.006
10 ⁻²	3.2×10^4	0.11
2×10^{-2}	2.7×10^4	0.13
3×10^{-2}	3.5×10^4	0.13
5×10^{-2}	3.1×10^4	0.09
Mg^{++}	1.7×10^4	0.06
10 ⁻⁴	3.2×10^4	0.12
10 ⁻³	3.5×10^4	0.12
5×10^{-3}	4.0×10^4	0.11
10 ⁻²	4.0×10^4	0.16
2×10^{-2}	2.3×10^4	0.09
5×10^{-2}	2.6×10^4	0.13

^{a/} DNA concentration = 25 μ g/ml

TYERYAR and LAWTON

Mg⁺⁺, and the levels of Ca⁺⁺ were varied. Similarly, for evaluation of Mg⁺⁺ effects, the complete medium contained 2×10^{-2} M Ca⁺⁺, and the levels of Mg⁺⁺ were varied. Additional experiments showed that none of the other ions present in the medium would satisfy the Ca⁺⁺ requirement, but their presence appeared to raise the overall frequency of transformation.

Optimal yields of transformants were obtained within a pH range of 6.0 to 7.0 (Figure 1); accordingly, subsequent experiments were conducted at pH 6.8.

Kinetics of transformation. The yield of Trp⁺ transformants was maximal after approximately 20-35 min exposure to DNA, and further incubation with DNA did not significantly increase the number of prototrophic colonies (Figure 2).

Transformation as a function of DNA concentration. As shown in Figure 3, Trp⁺ transformants increased linearly as the DNA concentration was increased up to a saturation level of about 0.5 µg/ml. This type of dose-response curve is characteristic of most bacterial transformation systems and is interpreted to mean that each transformant is the result of one bacterium interacting with one molecule of the transforming DNA (6).

Competence as related to the growth cycle. Competent recipient cells were obtained following 16 hr growth on GCBA plates; transformation frequencies of 0.1 to 0.3% were routinely observed. For other transformable species of bacteria, the capacity to be transformed usually develops at certain periods of their growth cycles (8). Therefore, we determined if such periods of competence existed for *P. novicida*. An overnight culture (Trp⁻), grown in Chamberlain's medium supplemented with 50 µg/ml of L-tryptophan, was diluted 1:250 in fresh medium and incubated at 37 C on a shaker. Growth was measured by the increase in viable cells. At various times during the growth curve, the cells were tested as recipients for transformation. The results of one such experiment are shown in Figure 4. *P. novicida* could be transformed throughout the entire growth cycle. The frequency declined in the stationary phase, but significant levels of transformation were detectable even after 26 hr. It was also observed that frequencies of greater than 1% transformation were obtained when cells were grown in liquid medium.

Heterologous recombination. Since *P. novicida* appears closely related to *P. tularensis*, the question arises whether this relationship would permit interspecies transformation;

i.e., would P. novicida take up and integrate DNA that had been isolated from P. tularensis? The data in Table 3 demonstrate that P. novicida - P. tularensis recombinants occurred quite readily. We have obtained similar results for streptomycin resistance transfer and adenine biosynthesis.

Table 3. Heterologous transformation of P. novicida (Trp⁻)

Trp ⁻ recipient cells/ml	Donor DNA ^{a/}	Trp ⁺ transformants/ml
6.4 x 10 ⁷	<u>P. novicida</u>	2.5 x 10 ⁵
	<u>P. tularensis</u>	
	SCHU	4.2 x 10 ⁴
	LVS	4.4 x 10 ⁴
	38-A	3.6 x 10 ⁴
	Vt 68	2.3 x 10 ⁴
	O'Hara	3.0 x 10 ⁴

^{a/}DNA concentration = 20 μg/ml

DISCUSSION

Pasteurella novicida is a unique organism in several respects. This organism has been isolated from nature only once, and was tentatively identified as P. tularensis on the bases of observed pathogenicity, pathology, and cellular and colonial morphology (9). The isolate, however, was serologically different and failed to be agglutinated by antiserum against P. tularensis. Additional studies indicated that it was a previously undescribed bacterium, thereby resulting in a separate species designation (9, 11).

Our studies further illustrate the similarities and disparities between P. novicida and P. tularensis. The formation of heterologous recombinants by P. novicida demonstrates that these species are closely related, but the reduced levels of transformation observed when P. tularensis DNA provided genetic information suggests that significant differences exist at the molecular level. Genetic relatedness of the two species

TYERYAR and LAWTON

was postulated by Ritter and Gerloff (12) on the basis of DNA-DNA hybridization studies. It is anticipated that our gene exchange system will serve as a tool for studying antigenic and virulence determinants of both P. novicida and P. tularensis, as well as studying the genetic relatedness of the various members of the genus.

Although P. novicida is the only member of the genus Pasteurella possessing the mechanisms for bacterial transformation (discovered thus far), the requirements and characteristics of its transformation are not significantly different from most other bacterial transformation systems. For example, Ca^{++} is required for transformation of Neisseria meningitidis and Bacillus subtilis (8). The DNA-dose response curve, kinetics of transformation, and pH optimum for transformation obtained for this system are characteristic for bacterial transformation systems in general (8).

The state of competence is an ill-defined physiological phenomenon for recipient bacterial cells, and each system has its own set of conditions for achieving this state. For example, Diplococcus pneumoniae, Hemophilus influenzae, and Bacillus subtilis reach maximal competence when the cells are grown to the latter part of the growth cycle and/or the beginning of the stationary phase, where metabolic activities of the cells are not maximal. It has been suggested that conditions of unbalanced growth contribute to the formation of the competent state in these species (8). In contrast, Neisseria meningitidis exhibits maximal transformability in the early logarithmic phase of growth, suggesting that its competence is related to a high metabolic rate of the recipient cells (7). The competent state of P. novicida cells grown in a defined liquid medium appears to be associated with actively dividing cells; i.e., the proportion of the transformants to viable cells was constant throughout the logarithmic phase of growth, and diminished in the stationary growth phase. The apparent ease of producing the competent state for P. novicida cells is quite unusual among bacterial transformation systems and is a phenomenon deserving of investigation in more detail.

CONCLUSIONS

Streptomycin-sensitive cultures of Pasteurella novicida can be transformed by deoxyribonucleic acid (DNA) extracted from streptomycin-resistant cultures of P. novicida or P. tularensis. Similarly, cultures nutritionally dependent on tryptophan or adenine for growth can be transformed to nutritional independence for these requirements by DNA carrying the appropriate allele from P. novicida or P. tularensis.

The formation of hybrid recombinants establishes the close genetic relatedness of P. novicida and P. tularensis, but the reduced frequency of transformation observed when P. tularensis serves as the donor suggests significant differences at the molecular level.

The ability of P. novicida to undergo transformation, i.e., become competent, is not restricted to a short phase of the growth cycle, but is present uniformly throughout the logarithmic and early stationary phase of growth. In most other respects, the requirements and characteristics of the P. novicida transformation system are similar to those of several other bacterial transformation systems.

LITERATURE CITED

1. Bövre, K. Acta Pathol. Microbiol. Scand. 61, 457, (1964).
2. Burton, K. Biochem. J. 62, 315, (1956).
3. Chamberlain, R.E. Appl. Microbiol. 13, 232, (1965).
4. Downs, C.M., Coriell, L.L., Chapman, S.S., and Klauber, A. J. Bacteriol. 53, 89, (1947).
5. Eigelsbach, H.T., and Downs, C.M. J. Immunol. 87, 415, (1961).
6. Hotchkiss, R.D. in The chemical basis of heredity (eds. W.D. McElroy and B. Glass), The Johns Hopkins Press, Balto., Md., 321, (1957).
7. Lie, S. Acta Pathol. Microbiol. Scand. 64, 119, (1965).
8. Spizizen, J., Reilly, B.E., and Evans, A.H. Ann. Rev. Microbiol. 20, 371, (1966).
9. Larson, C.L., Wicht, W., and Jellison, W.L. Pub. Health Rep. 70, 253, (1955).
10. Marmur, J. J. Mol. Biol. 3, 208, (1961).
11. Owen, R.R., Burkner, E.O., Jellison, W.L., Lackman, D.B., and Bell, J.F. J. Bacteriol. 87, 676, (1964).
12. Ritter, D.B., and Gerloff, R.K. J. Bacteriol. 92, 1838, (1966).

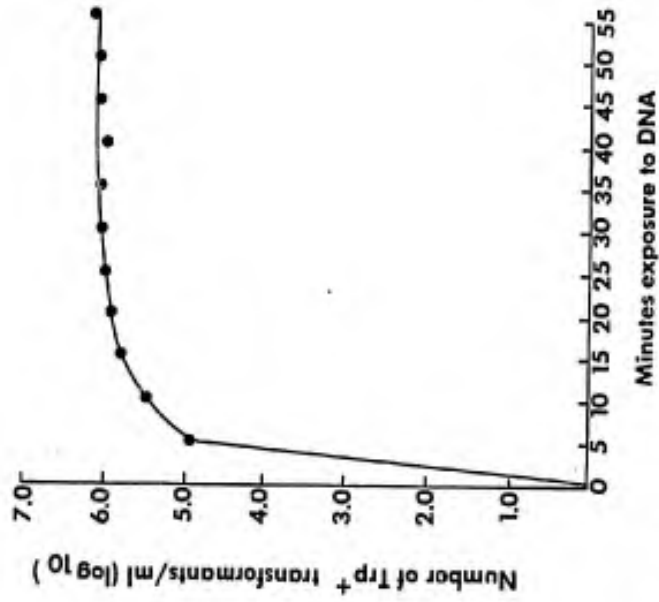


Figure 2. Kinetics of transformation of *P. novicida* (Trp⁺)

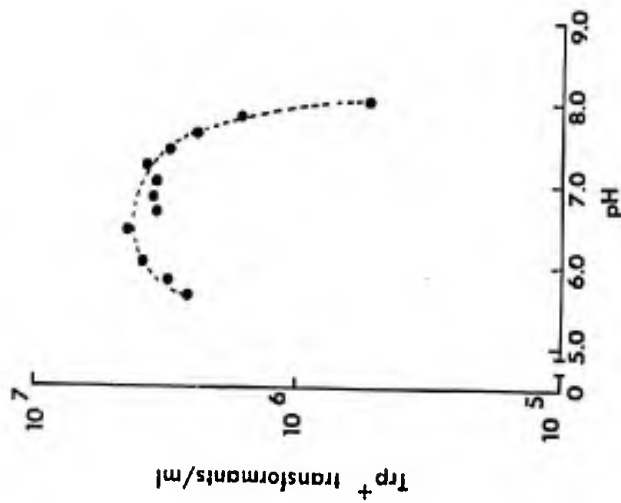
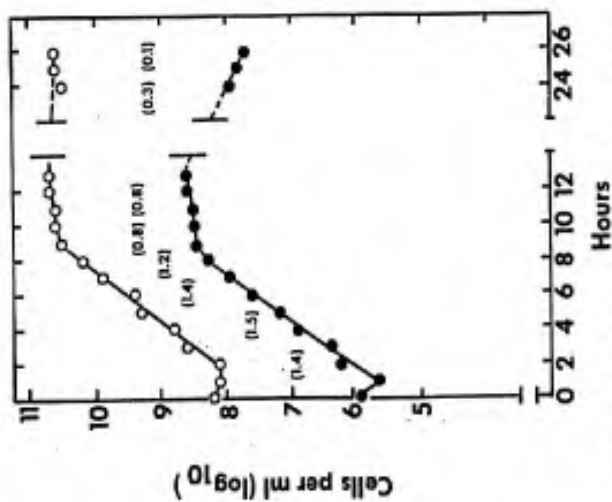


Figure 1. Effect of pH on transformation of *P. novicida* (Trp⁺)



- Numbers in parentheses = % transformation
- Total number of recipient cells per ml
- Total number of Trp⁺ transformants per ml

Figure 4. Competence related to the growth cycle of *Pasteurella novicida*

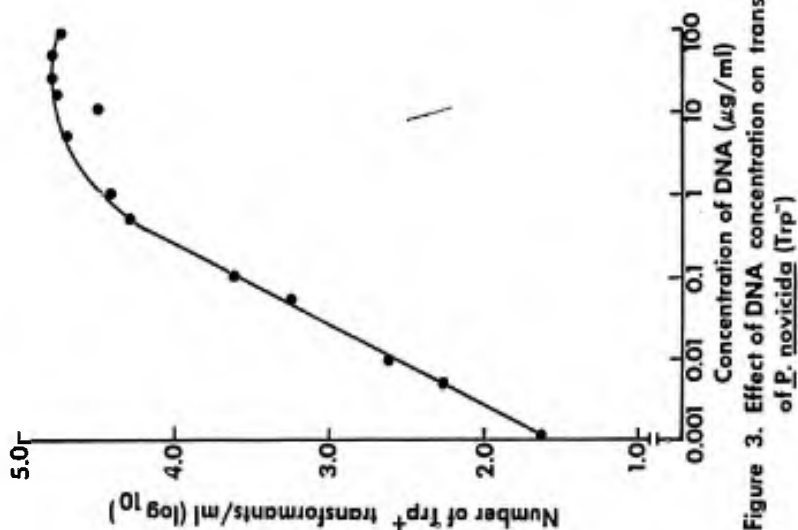


Figure 3. Effect of DNA concentration on transformation of *P. novicida* (Trp⁺)

MASS FLOW, VELOCITY AND IN-FLIGHT THRUST
MEASUREMENTS BY ION DEFLECTION

C. RANDE VAUSE
ROBERT S. RUDLAND, CAPTAIN, ORD C
U.S. ARMY AERONAUTICAL RESEARCH LABORATORY
AMES RESEARCH CENTER, MOFFETT FIELD, CALIFORNIA

INTRODUCTION

The desire to maximize performance and utility of airmobile systems in battle tactics has led to sophisticated advances in many areas such as fire control, navigation, and aircraft stability and control. However, similar advances in more accurate measurement of aircraft velocity and installed thrust have not kept pace. Systems currently in use for these purposes have been used in generally the same form for over fifty years.

The performance of V/STOL aircraft is significantly dependent upon forward velocity. An example is the take-off maneuver under overload condition for a helicopter in ground effect. Figure 1(1) shows the power required for various V/STOL aircraft, out of ground effect in 1-g flight. The large reduction of power required with forward speed is apparent. The ground effect produces lift augmentation at hover, as shown in figure 2, which permits lift-off with an overload. By increasing forward speed while still in ground effect, a good pilot can increase available thrust to take off with maximum overload. The optimum trajectory which assures maximum safety, however, is very sensitive to forward velocity.

The example cited above illustrates the need for a good airspeed indicating system, accurate especially at low speeds. Such a system is important for both performance testing and actual flight operation.

The importance of accurate thrust measurement may be easily appreciated by considerations of both research and operational requirements. The ability to optimize a given engine installation is highly dependent upon the ability to accurately determine engine installed thrust and to separate this from the aerodynamics of the airframe and inlet. This separation permits intelligent assessment of areas of research for potential improvement. Further, the accurate

VAUSE AND RUDLAND

knowledge of thrust available under operational conditions is valuable in terms of both operational efficiency and maintenance effectiveness. Since the entire payload of some vehicles in hover is represented by from 6 to 10 percent of the thrust available, errors of as little as 3 percent represent 50 percent of payload capability. Safety of operation would be greatly enhanced by accurate thrust indication in the cockpit. Field maintenance and Time-Between-Overhauls could be performed and established much more effectively with an accurate indication of installed thrust which, in turn, indicates general engine condition.

These recognized requirements inspired an investigation of the use of gaseous (ion) discharge sensors to achieve adequate measure of aircraft velocity and installed thrust.

GENERAL CONCEPT OF MEASUREMENT OF GAS DISCHARGE SENSORS

Background of Gas Discharge Sensors

The application of gaseous (ion) discharges to measure velocity has been the subject of considerable investigation for better than a hundred years. However, the multitude of problems involved when working with coronas has precluded the development of practical instrumentation for measuring mass flow or velocity. For example, in an early investigation by Werner⁽²⁾, the interaction between the free stream velocity and the actual discharge process was examined. When working at steady state corona current levels, the variation in the discharge current was found to be proportional to changes in free stream velocity. The sensing apparatus, however, suffered from low sensitivity and high background noise as well as electrode disintegration.

In an investigation done by Fuchs⁽³⁾, the interaction between the free stream velocity and the collected current was examined. Working at low levels, where the voltage is nearly a linear function of the current, the free air stream velocity was found to significantly alter the magnitude of the collected ion current by blowing ions away from the electrodes before they could be collected suggesting that the altered current might be a measure of stream velocity. However, the variation in current with velocity was found to be nonlinear, which limited its usefulness for anemometric purposes.

Other investigations undertaken depended, in one way or another, upon the motion of ions in the free stream. The ions formed in the discharge process migrate to one of the electrodes under the influence of an electric field applied perpendicular to the free stream velocity. During this migration, the ions are assumed to obtain a component equal to the free stream velocity. Thus, by monitoring the motion of these ions, the free stream velocity can be

determined. One scheme using this principle was investigated by Townsend in 1937⁽⁴⁾ and later by Saheki in 1946⁽⁵⁾ in which the translation of a column of ionized air produced by a spark discharge was used to measure boundary layer velocities. The discharge process, however, was found to have altered the flow field because of the large current flow and the heat energy associated with the spark.

In general, the difficulties encountered by each of the above investigators when trying to measure velocity with a gas discharge anemometer were in some way related to the unsteadiness of the ion current, or to flow distortion caused by the introduction of the high energy spark discharge into the flowing gas.

These two observations suggested a whole new approach. Investigations by Durbin of Princeton University showed that a gas flowing between a source electrode and a flat collecting electrode not only significantly altered the collected ion current as shown by Fuchs, but also significantly altered the landing point of the ion stream, and that the deflection of the ion stream was related to the momentum of the air passing between the source and the collector. During the course of these initial studies, it also became evident that flow distortion due to the addition of a high energy spark could be avoided by using a much lower potential glow discharge source.

Based upon this ion drift principle, several variations in sensors were built at the Army Aeronautical Research Laboratory for investigations of the adequacy of this concept for measurement of velocity and mass flow.

Description of Ion Drift Anemometer

A coaxial configuration, illustrated in figure 3, appears to have the most general application, and has been chosen to demonstrate the principles of an ion drift anemometer. This configuration employs a "sheet" of ions created near the edge of a disc shaped electrode. When a high positive potential is applied, ions are created near the positive center electrode. With no axial velocity through the sensor, the ions drift radially, undisturbed in an ever broadening beam toward the outer negative resistive collector (in this case, a helical coil). The current distribution (figure 4) on the collector is Maxwellian and the current peak is directly opposite the outer electrode axial position.

As a gas is passed through the sensor, the ions are given an axial velocity component equal to the local gas velocity, which shifts the current peak to a new downstream location directly proportional to the velocity and density of the gas. Figure 5 shows a circuit diagram of how the shift in the current peak might be measured. If the current through both sides of the circuit is balanced initially, then the imbalance in current caused by the shift in the

VAUSE AND RUDLAND

current peak can be amplified and used to adjust a variable resistor to restore the current balance.

The initial mathematical model indicates that the ion deflection, and hence, the resistance correction or sensor output, is linear with the momentum flux (ρU) of the gas through the sensor.

Derivation of Drift Equation

The great difficulty in writing the field equations for a disc and rod made it more feasible to use two coaxial cylinders (no disc) for purposes of analysis. Considering these two cylinders, the ion deflection equation can be derived as follows:

The electric field, E , at location, r , between two infinitely long coaxial cylinders is typically given by

$$E(r) = \frac{V}{r \ln (r_2/r_1)} \quad (1)$$

where V is the electric potential difference between the cylinders and where r_1 and r_2 are the radii of the inner and outer cylinders.

The mobility constant, K , of the flowing gas is the ratio of the ion velocity (in the radial direction for this case), v_r , and the electric field, E , that produces the velocity. As long as the ion velocity is much less than the thermal velocity for the gas, the mobility constant is inversely proportional to the gas density and can be expressed as

$$K(r, \theta) = \frac{v_r (r, \theta)}{E(r)} = K_{NTP} \frac{\rho_{NTP}}{\rho(r, \theta)} \quad (2)$$

where ρ is the gas density and NTP denotes the value at "normal temperature and pressure".

By inspection (figure 6) it is seen that the expression for the ion deflection, D , along a radial line, is given by

$$D_r = \int_{r_1}^{r_2} \frac{U(r)}{v_r(r)} dr \quad (3)$$

where U is the local free stream gas velocity. Integrating this expression from 0 to 2π gives the mean ion deflection around the circumference.

$$D = \frac{1}{2\pi} \int_0^{2\pi} \int_{r_1}^{r_2} \frac{U(r, \theta)}{v_r(r, \theta)} dr d\theta \quad (4)$$

VAUSE AND RUDLAND

Combining equations (1), (2), and (4) the complete deflection equation is obtained and given by

$$D = \frac{1}{2\pi} \int_0^{2\pi} \int_{r_1}^{r_2} \frac{U(r,\theta) \rho(r,\theta) \ln(r_2/r_1)}{K_{NTP} \rho_{NTP} V} r dr d\theta \quad (5)$$

However, by taking the constant

$$\frac{\ln(r_2/r_1)}{K_{NTP} \rho_{NTP} V}$$

outside the integral, and letting

$$c = \frac{2\pi K_{NTP} \rho_{NTP} V}{\ln(r_2/r_1)} \quad (6)$$

the expression for the deflection reduces to

$$D = \frac{1}{c} \int_0^{2\pi} \int_{r_1}^{r_2} U(r,\theta) \rho(r,\theta) r dr d\theta \quad (7)$$

Note now that the integral is exactly the expression for the mass flow of the gas through the sensor, \dot{m} . It is seen that the mean deflection of the ion sheet is linearly related to the integrated mass flow and is simply given by

$$D = \frac{\dot{m}}{c} \quad (8)$$

where the constant of proportionality, c , is dependent only on known physical constants and the applied voltage.

Assumptions

Consider now the assumptions made in this analysis:

1. The electric field intensity is inversely proportional to the radial distance from the electrode. In a coaxial geometry with a potential difference applied between center electrode and outer cylinder, the electric field varies as $1/r$ providing the additional fields due to space charges are small. At the relatively low current densities employed in this system, errors associated with space charges are negligible.
2. The two-dimensional cylinders are a good approximation to the real case. For the two-dimensional cylinders to be an accurate approximation to the real case, the center disc must not affect the

electric field created between the center rod and the surrounding collector. A computer program, run at Princeton University, computes and plots the field lines for the configuration used in this sensor. Results of that analysis indicate that the distortion in the electric field generated by the disc is negligible, except within a small region about the disc itself; i.e., for all practical purposes, the high voltage disc acts solely as an ion source and has no effect on the field between the center rod and the outer cylinder.

3. The ion current is distributed uniformly around the periphery of the system to ensure uniform weighing of the gas flow. This requirement is ensured by the uniformity of construction of the ion source.

4. The ion mobility is inversely proportional to the gas density. This condition is satisfied only when the gas molecule thermal velocity is greater than or comparable to the ion velocity caused by the acceleration of the ions in the electric field.

For air at sea level, the mean thermal velocity is about 340 meters/sec. This velocity can be induced in an air molecule when the electric field strength is about 0.1 volts per mean path, λ . i.e.,

$$E = 0.1/\lambda \quad (9)$$

In the coaxial geometry we can solve for the minimum distance from the disc, r_{\min} , below which the thermal velocity will be exceeded, and the assumption will no longer hold.

A conservative estimate for r_{\min} can be obtained by the following approximation. Because major changes in the electric field occur only near the edge of the disc, the disc electrode can be visualized as a ring of wire with wire diameter equal to the disc thickness and radius of curvature equal to the disc radius. Since the radius of curvature of the ring is much larger than the radius of the wire, and since the ring is equi-distance from the collector at all times, in the vicinity of the electrode this electrode-collector configuration can be nearly approximated by a wire stretched above a plane.

The electric field for a wire above a plane is given by

$$E(r) = \frac{V}{r \ln (2h/r_d)} \quad (10)$$

where V is the applied voltage, r is the distance from the wire in the direction normal to the plane, h is the wire height above the plane, and r_d is the wire radius equal to half the disc thickness. A typical example of r_{\min} may be obtained by inserting representative values for a coaxial mass flow system into equation (10) and

VAUSE AND RUDLAND

solving for $r = r_{\min}$, the radius at which these conditions are exceeded. If

$$\begin{aligned} E &= 0.1/\lambda & h &= 1.43 \times 10^{-2} \text{ meters} \\ \lambda &= 6.6 \times 10^{-8} \text{ meters} & r_d &= 2.54 \times 10^{-5} \text{ meters} \\ V &= 10 \text{ KV} \end{aligned}$$

then $r_{\min} = 0.9 \text{ mm}$

This is only a trivial distance and represents only a very small part of the cross sectional area.

Thus, in the coaxial configuration the ion mobility is inversely proportional to the gas density in all but a trivial portion of the flow.

Experimental Results

Tests were conducted to demonstrate experimentally the adequacy of equation (8) by determining, (a) the relationship between ion deflection and mass flow, and (b) the dependence or independence of the meter output on cross sectional velocity profile.

A special calibration rig was found necessary to determine the ion deflection mass flow relationship at very low mass flows. The calibration rig is shown in figure 7. Air was discharged through the sensor from a compressed air bottle hung on the calibration balance. A strain gage placed between the balance arm and the support structure measured any change in weight of the stored air. The output from the strain gage was fed into a data recorder and plotted against time. The instantaneous slope of that plot represents the mass rate of flow, ρAU , of the air from the bottle, which is what the sensor measures. A constant flow rate, and thus a constant slope, was maintained during the run by use of valves and a pressure regulator. Flow rates were set by adjusting the regulator. Long running times further increased the accuracy of the calibration.

Figure 8 shows the sensor used. Here it is mounted in a length of pipe adaptable to the calibration rig.

Figure 9 is a sample plot of the data obtained. The symbols are data from the calibration stand. The solid black line was faired from points theoretically predicted from equation (7). Experimental and predicted data agree within less than 1 percent error.

Calibrations at higher mass flows were obtained by installing the sensor in the AARL 7 by 10 foot wind tunnel. A calibrated pitot tube was used to measure the tunnel velocity. The velocity was corrected by the density ratio to give the mass flow. Figure 10 is a plot of data obtained by this method. Here, again, the solid

VAUSE AND RUDLAND

line indicates the values predicted by the drift equation. Note that the sensor sensitivity can be varied, as is indicated by the differences in slopes of figures 8 and 9, to give the accuracy required over a given velocity range.

It is readily seen that the mass flow and the ion deflection are indeed linearly related as predicted, even at low flow rates.

Two sensors were placed in series to determine the sensitivity of the mass flow measurement by the ion drift sensor to variations in the velocity profile. This technique is illustrated in figure 11. The first sensor was in undisturbed flow, and was used to measure the true flow rate. Between the first and second sensor, a butterfly valve was installed to create a nonuniform velocity distribution. A pitot rake was mounted at the entrance to the second flow meter so that the actual velocity profile could be determined. Figure 12 shows the results of these tests for one configuration. Figure 13 shows the (typical) related velocity profile. As is readily seen, the effects of major changes in the velocity profile cause only small changes in the measurement of mass flow.

Although the equation for the mass flow/ion deflection derived above is only a first order approximation, the theoretical and empirical results correspond exceptionally well. As predicted, the meter does indeed measure the mean mass flow, independent of the cross sectional velocity profile, except in very extreme cases. At this writing, the actual resolution obtainable with an ion drift anemometer has not been ascertained. With the present sensor and related instrumentation, a resolution of velocity to 0.10 ft/sec, or equivalently of mass flow to 7.56×10^{-3} lb/sec/ft², is believed to be of the proper order of magnitude.

A flow sensor of this order is a major contribution to flow measurements. The ion drift principle is adaptable to a wide range of geometries, suggesting its use for many types of test and research equipment, in particular. Applications for velocity, mass flow and jet engine thrust measurements, boundary layer studies, environmental research and space exploration are being investigated by various groups.

GAS DISCHARGE SENSOR AS A VELOCITY METER

As indicated earlier, one ion drift application of particular interest and significance to the Army is to measure airspeed for V/STOL aircraft. The problems associated with this application and the advances already achieved at AARL now will be discussed.

Sampling Problem

Several problems arise when attempts are made to measure

VAUSE AND RUDLAND

forward velocities on V/STOL aircraft. One problem deals with the location of the sensor. Either the sensor must be located away from the flow disturbed by the aircraft, or the sensor must be insensitive to the disturbed flows. On test aircraft, long, nose-mounted booms have been used to locate the sensor away from disturbances; this, however, is impractical for operational use. Consequently, considerable effort has been expended to establish a satisfactory method for extracting the horizontal components of airspeed, both lateral and longitudinal, in regions influenced by the aircraft.

Another problem is one of sensing accurately velocities ranging from zero to as high as 300 feet per second on some compound helicopters and to much higher velocities on other V/STOL aircraft.

There are two additional aspects to this sampling problem. Errors can be generated by the disturbance of the flow due to the presence of the measuring device and the very small momentum or pressure available in the flow make it difficult to activate the measurement device. A survey of current sensor systems failed to reveal any capable of adequately coping with these problems.

The first system to deal satisfactorily with the problems associated with V/STOL airspeed measurement is a gas discharge anemometer developed at the AARL called VAMS^{6,7} (Vector Airspeed Measuring System).

VAMS

In the foregoing, an ion drift anemometer has been shown to be sufficiently sensitive and to have adequate range to measure accurately the wide variety of airspeeds encountered by V/STOL aircraft. By proper mounting (as discussed below), the problems associated with flow distortion and sensor location can be virtually eliminated, and by using multi-sensors, the vector components of airspeed can be obtained.

As would be expected, experimental results from tests of the ion drift anemometer show that the velocity of the air passing through a small hole in the diameter of a right circular cylinder of large aspect ratio is the component of free stream velocity normal to the cylinder. Figure 14 shows the results of a wind tunnel test on such a cylinder. As the cylinder is yawed from zero to ninety degrees to the free stream, the velocity measured in the hole is seen to vary quite closely with the cosine of the yaw angle. The solid line is a true cosine curve and is drawn in as a reference for comparison. By this method translation velocities of an aircraft can be accurately determined, even in a downwash region where the incidence angle is high.

The VAMS concept effectively deals with the three basic

VAUSE AND RUDLAND

difficulties associated with helicopter airspeed measurement. The vector extraction method using a circular cylinder solves the sampling problem and minimizes the errors due to flow distortion generated by the presence of a measuring system. The ion sensing method solves the problems associated with measuring the low airspeeds.

There are several other important advantages to the VAMS system. The sensor has no moving parts. It can easily be mounted on the aircraft. The output function is intrinsically bidirectional and is linear with airspeed, through zero. Hence, a very simple calibration is accomplished by knowing a single velocity other than zero and zero. The calibration can also be predicted mathematically to within 1 percent. A wide selection of velocity ranges may be provided for using a single sensor - ranging from fractions of a foot per second to near sonic velocities, thus making it suitable for helicopters, as well as most V/STOL aircraft.

Further tests are being conducted on parameter dependence. Recently, the VAMS has been flown and tested on an operational V/STOL aircraft. Preliminary results indicate that accuracy predicted was obtained.

GAS DISCHARGE SENSOR AS A THRUST METER

Another application of the ion drift concept, as indicated previously, is the measurement of installed thrust for jet engines. The successful application of this concept requires that its basic simplicity can be maintained; that is, a simple installation in the gas generator with a source at the engine shaft axis and a collector in the engine outer wall. An ion drift meter would be required in both engine inlet and exit.

The basic equation for thrust, which can be obtained from any standard text on propulsion, is

$$T = m_i(U_e - U_\infty) + m_f U_e \quad (11)$$

where

T = net thrust

m_i = mass flowing through the inlet

m_f = mass added or lost in engine

U_∞ = free stream velocity

U_e = exit gas velocity in the far wake

However,

$$m_i + m_f = m_e$$

where

m_e = mass flowing through the engine exit

The thrust equation can be expressed in the following form:

$$T = m_i^2 \left[\left(\frac{m_e}{m_i} \right)^2 \frac{1}{\rho_e A_e} - \frac{1}{\rho_i A_i} \right] \quad (12)$$

The difficulties in evaluating this equation have resulted from the inability of present measuring systems to determine the engine inlet free stream capture area A_i and problems associated with measuring the density in the far wake of the engine exit stream tube. The ion drift mass flow meter provides a means of evaluating the inlet momentum term ($1/\rho_i A_i$).

The second term in equation (12) now can be easily and accurately determined with the ion drift meter in the inlet, which will provide an accurate measure of inlet stream tube mass flow and the free stream velocity, even though nonuniformities in temperature and pressure profiles may be present. The thrust equation can be rearranged to reflect this capability.

Note that

$$m_i = \rho_i A_i U_\infty$$

or

$$\rho_i A_i = \frac{m_i}{U_\infty}$$

and equation (12) can be written

$$T = m_i^2 \left[\left(\frac{m_e}{m_i} \right)^2 \frac{1}{\rho_e A_e} - \frac{U_\infty}{m_i} \right] \quad (13)$$

However, the first term is not so easily evaluated since problems of temperature and contaminants appear to preclude using the ion drift meter in the engine exit. Therefore, substitutions can be made in equation (13) to reflect conventional methods of determining engine exit mass flow by integration of exit rakes.

$$T = m_i^2 \left[\left(\frac{m_e}{m_i} \right)^2 \frac{R_e \bar{t}_e}{\bar{P}_e A_e} - \frac{U_\infty}{m_i} \right] \quad (14)$$

where R_e is the gas constant
 \bar{t}_e is the mean static temperature
 \bar{P}_e is the mean static pressure

all measured in the engine exhaust products at a point in the far wake stream tube.

To accurately determine the value of the first term requires specifically the value of $R_e \bar{t}_e / \bar{P}_e A_e$. Physical limitations require these parameters to be measured at the engine exit, rather than in the far wake of the exhaust stream tube. This limitation induces errors in the thrust measurement obtained by mass flow.

VAUSE AND RUDLAND

(This is also the case in the more conventional method of measurement.)

Since the exhaust tube measurements must be made at the engine exit, equation (14) must be rewritten in terms of the variables at the exit station, and a term added to account for the exit stream tube losses. The following expression results.

$$T = m_i^2 \left[\left(\frac{m_e}{m_i} \right)^2 \frac{C_2 R_2 \bar{t}_2}{\bar{P}_2 A_2} - \frac{U_\infty}{m_i} \right] + F' \quad (15)$$

Comparing this equation with that for the conventional method for measuring thrust by the integration of both inlet and exit rakes clearly indicates the advantages of the ion drift meter in the inlet. The equation for the conventional method is:

$$T = m_i^2 \left[\left(\frac{m_e}{m_i} \right)^2 \frac{C_2 R_2 \bar{t}_2}{\bar{P}_2 A_2} - \frac{C_1 R_1 \bar{t}_1}{\bar{P}_1 A_1} \right] + F \quad (16)$$

In equations (15) and (16) the C's are correction factors for nonuniform profile losses, stations 1 and 2 are engine inlet and exit planes, and F includes both inlet and exit stream tube losses where F' includes only the exit stream tube losses.

The primary advantage obtained by ion drift mass flow thrust measurement is the high accuracy with which the inlet momentum drag can be determined. Simplicity of installation, would make it desirable to obtain \bar{t}_2 and \bar{P}_2 by a single measurement, either at the engine exit wall or the center body and eliminate the need for exit rakes. An error analysis must be performed to determine the accuracy with which this term can be obtained using a single representative pressure and temperature measurement, and assuring the capability to determine a correction factor for nonuniformity of profiles of temperature and pressure. It must also be recognized that the error due to F' must be included in the analysis. Corrections for this factor have been obtained by others and can be applied with reasonable accuracy. Even though simplicity of installation may not be obtained, the case of the inlet ion drift meter with conventional exit measurements would be a significant improvement over current systems.

A possible limitation for installation of the meter in large engines should be noted. When the distance between the ion source and the collector become large, the axial drift becomes large. This fact may produce practical limits to the gap dimensions and, consequently, installation length of a workable meter in the engine inlet.

REFERENCES

1. Carpenter, Paul J., "Design Trends in Future Helicopters, Compounds, and Composite Aircraft", Presented at International Congress of Subsonic Aeronautics, New York Academy of Sciences, April 3-6, 1967.
2. Werner, F.D. and Anderson, J.R., "Investigation of a Corona Discharge for Measurement in Airflow", AF 33 (038) 15833, July, 1951.
3. Fuchs, W. and Schumacher, G., "Tests with an Alternating Current Glow Anemometer under Steady Conditions", Translated by NRCC, No. TT-78.
4. Townsend, H.C.H., "Hot Wire and Spark Shadowgraphs of the Air Through an Air-Screw", Phil. Mag. (7), 14, 1932.
5. Saheki, Y., "On the Measurement of Wind Velocity Distribution by the Electric Spark Method", Hokaido Faculty of Eng. Memoirs, 8 (1947) Translated by E. Hope.
6. Durbin, E.J., Born, G., and Vause, R., "A Vector Airspeed Measuring System (VAMS) for Helicopters and Other V/STOL Aircraft", American Helicopter Society, Inc. 25th Annual National Forum Proceedings, May 14-16, 1969, Washington, D. C.
7. Vause, R., Durbin, E.J., and Born, G., "A System for Measuring the Vectorial Components of Airspeed for VTOL Aircraft", Proceedings of the USAEC/AAAA/IN Technical Symposium on Navigation and Positioning, September 23-25, 1969, Fort Monmouth, N.J.

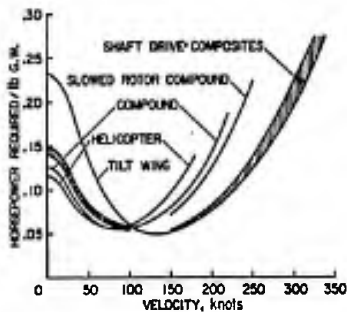


Figure 1. Horsepower required per pound of gross weight to maintain level flight.

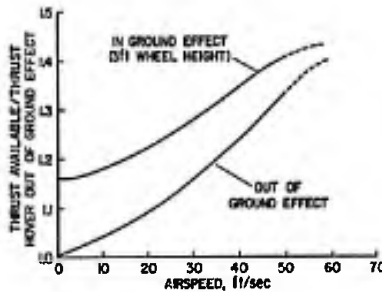


Figure 2. Thrust available as a function of airspeed and ground effect.

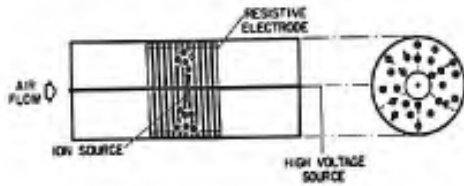


Figure 3. Velocity meter, concentric configuration.

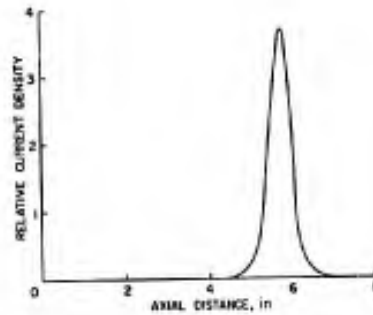


Figure 4. Typical ion current distribution.

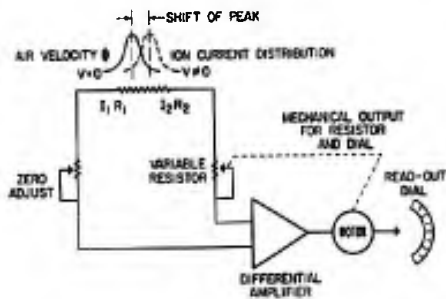


Figure 5. Amplifier circuit to measure current peak shift.

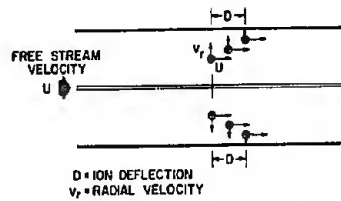


Figure 6. Ion velocity components.

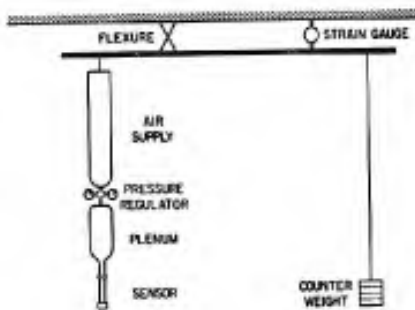


Figure 7. Calibration balance rig.



Figure 8. Pipe mounted ion drift sensor.

VAUSE AND RUDLAND

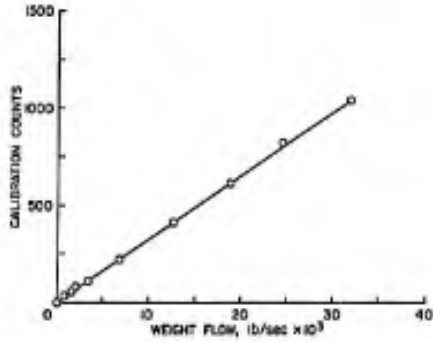


Figure 9. Calibration plot for mass flow meter.

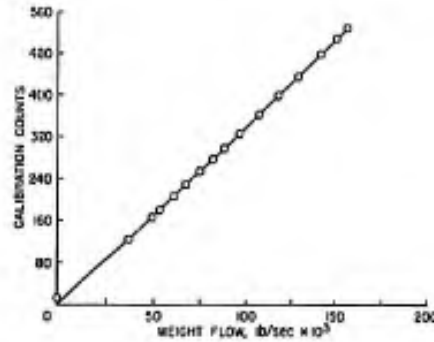


Figure 10. Calibration plot for mass flow sensor.

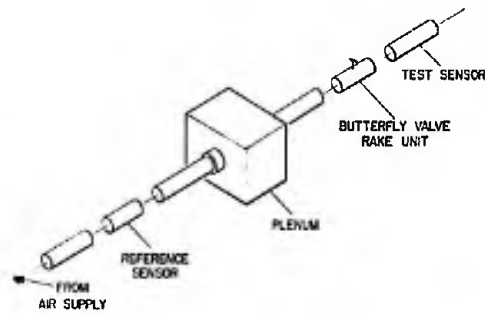


Figure 11. Tandem sensor test set up.

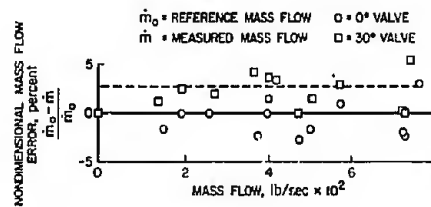


Figure 12. Non-dimensional mass flow error for undisturbed flow and highly disturbed flow.

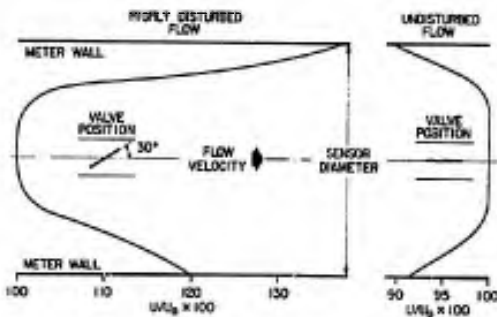


Figure 13. Representative velocity profiles as measured ahead of the sensor.

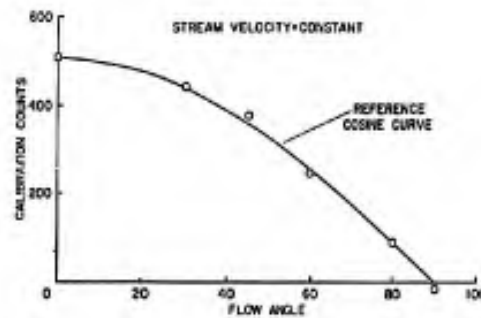


Figure 14. Experimental results of vectorial airspeed measurement.